



HAL
open science

Synthesis and characterization of composite materials based on alkali-activated materials incorporating mineral oils for the management of tritiated oils

Charles Reeb

► **To cite this version:**

Charles Reeb. Synthesis and characterization of composite materials based on alkali-activated materials incorporating mineral oils for the management of tritiated oils. Other. Centrale Lille Institut, 2022. English. NNT : 2022CLIL0020 . tel-04090737

HAL Id: tel-04090737

<https://theses.hal.science/tel-04090737v1>

Submitted on 6 May 2023

HAL is a multi-disciplinary open access archive for the deposit and dissemination of scientific research documents, whether they are published or not. The documents may come from teaching and research institutions in France or abroad, or from public or private research centers.

L'archive ouverte pluridisciplinaire **HAL**, est destinée au dépôt et à la diffusion de documents scientifiques de niveau recherche, publiés ou non, émanant des établissements d'enseignement et de recherche français ou étrangers, des laboratoires publics ou privés.

CENTRALE LILLE

THESE

Présentée en vue d'obtenir le grade de

DOCTEUR

Spécialité : Chimie des Matériaux

Par : Charles, Edouard REEB

Doctorat délivré par CENTRALE LILLE

Titre de la thèse :

Synthèse et caractérisation de composites à base de matériaux alcali-activés incorporant des huiles minérales pour la gestion des huiles tritiées

Synthesis and characterization of composites based on alkali-activated materials incorporating mineral oils for the management of tritiated oils

Soutenue le 04 novembre 2022 devant le jury d'examen :

Présidente	Pr. Gaëlle FONTAINE, Professeur des Universités, Centrale Lille Institut
Rapporteur	Pr. John PROVIS, Professeur des Universités, Université de Sheffield, Grande-Bretagne
Rapporteur	Dr. Pierre, BAUDUIN, Directeur de Recherche, ICSM
Examineur	Pr. Martin CYR, Professeur des Universités, Université de Toulouse
Examinatrice	Dr. Véronique BAROGHEL-BOUNY, Directrice de Recherche, Université Paris-Est
Directeur de Thèse	Dr. Christel PIERLOT, Maître de conférences, Centrale Lille Institut
Co-Directrice de Thèse	Pr. Catherine DAVY, Professeur des Universités, Arts et Métiers - Campus d'Angers
Encadrant	Dr. David Lambertin, Directeur de Recherches, CEA Marcoule
Invité	Dr. Cau Dit Coumes Céline, Directrice de Recherches, CEA Marcoule

Thèse préparée aux laboratoires :

- CISCO, UCCS, Ecole Doctorale SMRE 104
- LCBC, CEA Marcoule

Remerciements

Je tiens tout d'abord à remercier sincèrement mon encadrement de thèse. Chacun à votre manière, vous avez contribué à faire de ce travail une belle réussite. Christel, je te remercie pour ta bonne humeur et ta positivité à chaque instant. J'ai adoré cette première année à Lille mêlant discussions de laboratoire, matchs de tennis et repas du midi aux petites côtes. Merci Catherine pour m'avoir toujours plus challengé, j'avoue en avoir même eu un peu marre quelque fois, mais je sais que c'était dans le but d'améliorer la qualité de notre travail. Tu es une pile, parfois difficile à suivre, mais tu as surtout été une maman et une locomotive. Et enfin, merci à toi David pour tes conseils, ton écoute et ton soutien dans les moments difficiles. J'ai commencé avec un encadrant de thèse et je peux dire que je termine aujourd'hui avec un ami.

Je tiens ensuite à remercier les membres du jury d'avoir accepté de juger ce travail de thèse et plus particulièrement mes deux rapporteurs, John PROVIS et Pierre BAUDUIN, pour le temps consacré à l'évaluation de ce mémoire de thèse.

Je remercie les membres de l'équipe de recherche CISCO basée à Lille, où tout a commencé, pour m'avoir chaleureusement accueilli. Malgré la difficile période de COVID, nous aurons beaucoup rigolé et vous quitter aura été dur. Plus particulièrement, Agathe, merci de m'avoir intégré et te redécouvrir aura été un plaisir. Tristan et Greg, vous êtes incroyables et je vous remercie pour tous ces bons moments passés ensemble.

Je remercie également l'ensemble des membres du LCBC. Un grand merci Matthieu B. pour ton aide lors de mes débuts à Marcoule. Adrien, David R., Thomas, Géraldine, Karine, Pascal, merci pour votre aide précieuse au labo et « perdre » un peu de temps à discuter avec vous aura toujours été un plaisir. Merci Céline pour ton temps et tes conseils qui sont toujours les bienvenus. Je remercie spécialement la team Lambertin-GEOIL (Matthieu B., Vincent C., Matthieu D.C., Abdelaziz) avec qui les synergies de travail furent fructueuses et toujours très agréables. Merci enfin à nos secrétaires adorées, Kelly et Magalie, surtout lorsqu'on déteste la paperasse comme moi...

Je souhaiterais ensuite remercier quelques personnes pour leur aide ponctuelle et leur gentillesse :

- Cyrille MERCIER de l'Université de Valenciennes et du Hainaut-Cambrésis (UVHC) pour les analyses RMN qu'elle a réalisées.
- Pardis SIMON de l'Université de Lille pour les analyses XPS qu'elle a réalisées et pour le temps qu'elle m'aura accordé pour le traitement des données.
- Renaud PODOR de l'ICSM pour ses observations par MEB environnemental.

Je remercie profondément tous mes collègues doctorants, post-doctorants, CDD et stagiaires que j'ai connu : Birsen, Georges, Aline, Nicolas, Kahina, Jihane, Pauline, Gabriel,

Loan, Laure, Hicham, Richard, Théo, Sophie, Steph, Benoit, Rachel, Charles B., Sébastien, Simon, Charly, Axel, Pierre-Francois, Nicolas, Thomas, Oriane, François, Pia, Laura D., Lucas. Cette liste est non-exhaustive et je m'excuse auprès des personnes que j'oublierais ici et je n'ai pas non plus la place pour développer des remerciements au cas par cas, mais merci à vous, sincèrement, pour les bons moments passés ensemble. Je me permets quand même de remercier particulièrement Axel, d'avoir rendu nos interminables trajets en bus plus intéressants et de m'avoir permis d'intégrer la famille OVS.

Un grand merci à mon coloc Hugo pour m'avoir changé les esprits de thésard, le soir, en me parlant la langue du pinard.

Je tiens aussi à remercier un couple que j'adore, Oriane et Rémy, pour leur accueil lors de mes premières missions à Marcoule. Grâce à vous, démarrer mon aventure sudiste fut beaucoup plus facile et agréable et je n'oublierais jamais ce que vous avez fait pour moi.

Enfin, pour finir, je souhaiterais dire un grand merci à ma famille. La distance nous sépare et je rentre moins souvent ces dernières années mais sachez que votre présence est un soutien inébranlable pour pouvoir avancer sereinement dans ma vie. Je remercie particulièrement mes parents qui me supportent depuis 28 ans et que j'espère rendre fiers.

Summary

INTRODUCTION AND CONTEXT	1
1. TREATMENT OF RADIOACTIVE LIQUID ORGANIC WASTES (RLOW).....	5
1.1. TYPOLOGY AND ORIGIN OF RLOW	6
1.2. REFERENCE PROCESS FOR THE TREATMENT OF RLOW: INCINERATION	6
1.3. ALTERNATIVE PROCESSES	8
1.4. DIRECT CONDITIONING	9
1.4.1. <i>NOCHAR® technology (Absorption)</i>	9
1.4.2. <i>Cementation</i>	9
2. TRITIATED WASTES	10
2.1. TRITIUM AND ITS NUCLEAR CHARACTERISTICS.....	10
2.2. PHYSICOCHEMICAL PROPERTIES OF TRITIUM.....	11
2.3. ORIGINS OF TRITIUM.....	12
2.4. STRATEGY FOR THE TREATMENT OF TRITIATED WASTES.....	13
2.4.1. <i>Interim storage</i>	13
2.4.2. <i>Preliminary treatment</i>	13
2.4.3. <i>Direct conditioning</i>	14
2.4.4. <i>Tritium scavengers within tritiated waste packages</i>	15
3. THE CASE OF TRITIATED INDUSTRIAL OILS: WHAT STRATEGY?	17
3.1. ORIGIN OF TRITIATED INDUSTRIAL OILS	17
3.2. SCIENTIFIC ISSUES AND RESEARCH STRATEGY	17
REFERENCES	22
CHAPTER I	25
CHAPTER II	45
PREAMBLE CHAPTER II	49
1. EMULSIONS.....	50
2. SURFACTANTS.....	51
3. PICKERING EMULSIONS.....	53
4. SURFACTANTS AND SOLID PARTICLES	55
5. CONCLUSION.....	56
REFERENCES	57

CHAPTER II: EMULSIFICATION OF LOW VISCOSITY OIL IN ALKALI-ACTIVATED MATERIALS	59
ABSTRACT	59
1. INTRODUCTION.....	60
1.1. INDUSTRIAL CONTEXT.....	60
1.2. SCIENTIFIC BACKGROUND.....	60
1.3. AIMS AND SCOPES.....	63
2. EXPERIMENTAL	63
2.1. RAW MATERIALS	63
2.2. PREPARATION OF COMPOSITE MATERIALS	65
2.3. RHEOLOGY.....	65
2.4. DROPLET SIZE MEASUREMENTS	66
2.5. INTERFACIAL TENSION	67
2.6. DILUTED TERNARY SUSPENSIONS	67
3. RESULTS AND ANALYSIS.....	68
3.1. FORMATION OF THE AAM-OIL EMULSIONS	68
3.1.1. <i>Macroscopic observations</i>	68
3.1.2. <i>Rheology of fresh AAM</i>	69
3.1.3. <i>Analysis: formation of the emulsion</i>	72
3.2. PERFORMANCE OF AAM-OIL EMULSIONS THROUGH DROPLET SIZE MEASUREMENTS.....	73
3.2.1. <i>Droplet size measurements</i>	73
3.2.2. <i>Droplets velocity as an indicator for emulsion stability</i>	76
3.3. FORMATION AND STABILITY OF AAM-OIL EMULSIONS: EFFECT OF THE INTERFACIAL TENSION	77
3.3.1. <i>Direct measurement of the interfacial tension</i>	77
3.3.2. <i>Relationship between interfacial tension and OL droplet size</i>	79
3.4. FORMATION AND STABILITY OF AAM-OIL EMULSIONS: ROLE OF SOLID PARTICLES.....	80
3.4.1. <i>Influence of surfactants in the absence of particles (G1-G7 & L1-L7)</i>	80
3.4.2. <i>Influence of particles in the absence of surfactants (G8 & L8)</i>	80
3.4.3. <i>Influence of surfactants on the interaction between MK and liquid phases (G9-G14)</i>	82
3.4.4. <i>Influence of surfactants on the interaction between BFS and liquid phases (L9-L14)</i>	83
3.4.5. <i>Comparison and analysis of the diluted ternary suspensions</i>	83
3.5. DISCUSSION: TWO DISTINCT PATTERNS CONCERNING THE EFFECT OF SURFACTANTS DESCRIBE THE EMULSION FORMATION AND STABILITY.....	84
4. CONCLUSIONS.....	88
ACKNOWLEDGMENTS	89
APPENDIX A	90
APPENDIX B.....	92
REFERENCES.....	95

CHAPTER III	99
PREAMBLE CHAPTER III	103
1. CLASSIFICATION OF ALKALI-ACTIVATED MATERIALS	103
2. AAM WITH LOW CA CONTENT: GEOPOLYMERS.....	104
2.1. STRUCTURE.....	104
2.2. FORMULATION	105
3. AAM WITH HIGH CA CONTENT: C-A-S-H	106
3.1. STRUCTURE.....	106
3.2. FORMULATION	107
4. WATER PERMEABILITY OF AAM	108
REFERENCES	110
CHAPTER III: HOW ARE ALKALI-ACTIVATED MATERIALS IMPACTED BY INCORPORATING LOW VISCOSITY ORGANIC LIQUIDS?	113
ABSTRACT	113
1. INTRODUCTION.....	114
1.1. INDUSTRIAL CONTEXT.....	114
1.2. SCIENTIFIC BACKGROUND.....	114
1.3. AIMS AND SCOPES.....	115
2. MATERIALS AND METHODS	116
2.1. RAW MATERIALS	116
2.2. PREPARATION OF COMPOSITE MATERIALS	117
2.3. CHARACTERIZATION OF COMPOSITE MATERIALS.....	118
2.3.1. <i>Physical characterization.....</i>	<i>118</i>
2.3.2. <i>Chemical characterization.....</i>	<i>122</i>
3. RESULTS AND DISCUSSION	123
3.1. PHYSICAL CHARACTERIZATION.....	123
3.1.1. <i>Visual assessment of the incorporation of LVOL in hardened AAM</i>	<i>123</i>
3.1.2. <i>Influence of LVOL and surfactants on the mechanical strength and pore structure of AAM</i>	<i>125</i>
3.1.3. <i>Influence of surfactants on the emulsion in hardened AAM</i>	<i>132</i>
3.1.4. <i>Chemical characterization</i>	<i>137</i>
4. CONCLUSIONS.....	144
ACKNOWLEDGMENTS	145
APPENDIX.....	146
REFERENCES	152
CHAPTER IV	157

PREAMBLE CHAPTER IV	161
1. MANGANESE OXIDES	161
2. THE COMPLEX Γ -MNO ₂ STRUCTURE AND ITS IMPACT ON GETTER EFFICIENCY	162
3. THE GETTER TRAPPING MECHANISM	164
4. APPLICATION IN CEMENTITIOUS MATERIALS	165
REFERENCES	168
CHAPTER IV: TRAPPING PERFORMANCE OF ALKALI-ACTIVATED MATERIALS INCORPORATING A HYDROGEN/TRITIUM GETTER FOR THE CONDITIONING OF TRITIATED ORGANIC LIQUIDS	171
ABSTRACT	171
1. INTRODUCTION.....	172
1.1. INDUSTRIAL CONTEXT.....	172
1.2. SCIENTIFIC BACKGROUND.....	172
1.3. AIMS AND SCOPES.....	173
2. MATERIALS AND METHODS	174
2.1. RAW MATERIALS	174
2.2. MATERIALS PREPARATION.....	174
2.3. HYDROGEN TRAPPING PERFORMANCE	178
2.3.1. <i>Gamma irradiation experiments</i>	178
2.3.2. <i>Magnesium corrosion</i>	180
2.4. INTERACTIONS BETWEEN THE AAM POREWATERS AND THE GETTER	181
3. RESULTS AND ANALYSIS	181
3.1. H ₂ TRAPPING PERFORMANCE OF HARDENED AAM IN PRESENCE OF GETTER AND OL (MATERIALS B AND C)	181
3.2. CONTINUOUS H ₂ TRAPPING PERFORMANCE OF AAM IN PRESENCE OF GETTER (MATERIALS D)	183
3.2.1. <i>Trapping kinetics</i>	184
3.2.2. <i>Trapping efficiency</i>	184
3.3. INFLUENCE OF THE POREWATER CHEMISTRY ON THE Γ -MNO ₂ /AG ₂ O GETTER.....	187
3.3.1. <i>Interactions between porewaters and γ-MnO₂/Ag₂O getter</i>	187
3.3.2. <i>Interaction between sulfides and γ-MnO₂/Ag₂O hydrogen getter</i>	191
4. CONCLUSION.....	194
APPENDIX: INTERACTIONS BETWEEN THE AAM POREWATERS AND THE GETTER.....	195
REFERENCES	197
CHAPTER V.....	201
CHAPTER V: A NEW APPROACH FOR EVALUATING THE LONG-TERM CONFINEMENT OF RADIOACTIVE ORGANIC LIQUIDS IN GEOPOLYMERS.....	205

ABSTRACT	205
1. INTRODUCTION	206
1.1. INDUSTRIAL AND SCIENTIFIC CONTEXT	206
1.2. AIMS AND SCOPES	206
2. THEORETICAL BACKGROUND	207
2.1. SURFACE WETTING PROPERTIES	207
2.2. EXPERIMENTAL STRATEGY	209
2.2.1. <i>Determination of the SFE of GP</i>	209
2.2.2. <i>Determination of wetting envelopes</i>	210
2.2.3. <i>Prediction of wetting on a GP surface and experimental validation of the O-W approach</i>	210
3. MATERIALS AND METHODS	210
3.1. MATERIALS	210
3.1.1. <i>Preparation of the GP material</i>	210
3.1.2. <i>Organic liquids</i>	211
3.2. CONTACT ANGLE MEASUREMENTS	211
4. RESULTS AND DISCUSSION	211
4.1. CHARACTERIZATION OF Γ^{SD} , Γ^{SP} AND Γ^{S}	211
4.2. DETERMINATION OF THE GP WETTING ENVELOPES	213
4.3. EXPERIMENTAL VALIDATION OF THE OWENS-WENDT APPROACH	214
4.4. DISCUSSION ON THE PREFERENTIAL WETTING OF OL OR WATER ON GP SURFACE	215
5. CONCLUSIONS	216
REFERENCES	217
CONCLUSIONS AND FURTHER RESEARCH	219
1. MAIN ACHIEVEMENTS	221
1.1. FRESH STATE OIL EMULSION	221
1.2. OIL IMMOBILIZATION IN THE HARDENED STATE	222
1.3. GETTER EFFICIENCY IN AAM	223
1.4. OIL CONFINEMENT ON THE LONG-TERM	224
2. FURTHER RESEARCH	224
2.1. ENSURING OIL CONFINEMENT OVER TIME	224
2.2. ENSURING TRITIUM CONFINEMENT	225
REFERENCES	226
APPENDIX 1	227
APPENDIX 2	241

Introduction and context

Summary Introduction and Context

INTRODUCTION AND CONTEXT	5
1. TREATMENT OF RADIOACTIVE ORGANIC LIQUID WASTES (RLOW).....	5
1.1. TYPOLOGY AND ORIGIN OF RLOW	6
1.2. REFERENCE PROCESS FOR THE TREATMENT OF RLOW: INCINERATION	6
1.3. ALTERNATIVE PROCESSES	8
1.4. DIRECT CONDITIONING	9
1.4.1. <i>NOCHAR® technology (Absorption)</i>	9
1.4.2. <i>Cementation</i>	9
2. TRITIATED WASTES	10
2.1. TRITIUM AND ITS NUCLEAR CHARACTERISTICS.....	10
2.2. PHYSICOCHEMICAL PROPERTIES OF TRITIUM.....	11
2.3. ORIGINS OF TRITIUM.....	12
2.4. STRATEGY FOR THE TREATMENT OF TRITIATED WASTES.....	13
2.4.1. <i>Interim storage</i>	13
2.4.2. <i>Preliminary treatment</i>	13
2.4.3. <i>Direct conditioning</i>	14
2.4.4. <i>Tritium scavengers within tritiated waste packages</i>	15
2.4.4.1 Organic compounds.....	15
2.4.4.2 Metal hydrides	16
2.4.4.3 Mineral oxides.....	16
3. THE CASE OF TRITIATED INDUSTRIAL OILS: WHAT STRATEGY?	17
3.1. ORIGIN OF TRITIATED INDUSTRIAL OILS	17
3.2. SCIENTIFIC ISSUES AND RESEARCH STRATEGY	17
REFERENCES	22

Introduction and context

The use of radiological matter since the beginning of the 19th century has led and still leads to the production of radioactive wastes. Most of these wastes are generated in nuclear power plants, spent nuclear fuel reprocessing plants and other civilian and military nuclear facilities. To a lesser extent, research centers along with nuclear medicine also contribute to the production of nuclear wastes. These different applications lead to the formation of various types of radioactive wastes in terms of radiological activity, radionuclides lifetime, physical state, chemical composition, etc.

Nowadays, most of these wastes have an appropriate treatment method available for their safe disposal. This guarantees the durable protection of human health and the environment. However, some are still deprived of an appropriate treatment solution due to technical challenges and are temporarily stored in the vicinity of production sites. Among others, this is the case of metallic wastes producing high amounts of gaseous dihydrogen by corrosion, mixed tritiated wastes combining chemical toxicity and radiological issues, various organic liquid wastes, etc. [1] In France and in many other industrialized countries, liquids are strictly forbidden in all final disposal sites, whatever their chemical nature and their radiological activity [2]. They first need to be transformed in a solid state. This is generally done by incineration, which results in ashes that can be further conditioned. However, the radiological or physicochemical properties of some radioactive liquid wastes do not allow their incineration (e.g. high concentration of ^{14}C or ^3H , or the presence of halogen species leading to the formation of corrosive gas during incineration). In particular, tritiated organic liquid wastes are non-standard waste streams that have proven difficult to manage due to the high mobility of tritium; incineration is not adapted while avoiding outflows. There is a significant volume of existing tritiated organic liquid wastes, which have accumulated on production sites in the absence of a regulated management route. In addition, a much larger quantity will be produced in the coming years with the operation (and dismantling) of the ITER nuclear fusion reactor, which is under construction in the south of France. Therefore, an alternative process must be found for these tritiated liquid wastes that is reliable, robust and economically viable.

1. Treatment of radioactive liquid organic wastes (RLOW)

The challenge of RLOW disposal in a number of industrialized countries is exacerbated by a number of factors. The historical absence of a treatment and disposal route (with the exception of very limited scale incineration) have contributed to the development of a stockpile of legacy wastes which are aged, in some cases degraded, and both radiologically and chemically contaminated. These legacy RLOW pose a significant risk to both people and the environment, given their chemo- and eco-toxicity. As such, the concerned countries have been seeking alternative technologies for the treatment and disposal of RLOW.

1.1. Typology and origin of RLOW

The range of RLOW shows a great variability, with typical examples such as the following [3]:

- **Scintillation liquids** resulting from radiochemical analysis and consisting of at least one organic solvent (e.g. toluene, xylene, pseudocumene, diisopropylnaphthalenes, etc.) and one or more scintillators (e.g. PPO: 2,5-diphenyloxazole, butyl-PBD: [2(4-Biphenyl)-5-(4-tert-butylphenyl)-1,3,4-oxadiazole], p-terphenyl, etc.) [4]. In addition, emulsifiers are often present in large quantities in order to solubilize the radioactive species into aromatic solvents.
- **Extraction solvents** with the most commonly used one being tri-butyl phosphate (TBP), often diluted with light saturated hydrocarbons such as dodecane [5]. The industrial emergence of these wastes is due to nuclear fuel reprocessing, aiming at recovering uranium and plutonium. In some cases, other organic compounds are used for the extraction of heavy metals, including tri- and tertiary amino-compounds.
- **Miscellaneous liquids** arising from a variety of decontamination operations. Among others, these include toluene, carbon tetrachloride, acetone, alcohols, trichloroethane, etc. Aqueous solutions of organic acids, such as citric acid, picolinic acid, ethylene-diamine tetra-acetic acid (EDTA) are also commonly used in the decontamination of industrial equipments [6].
- **Industrial oils** (lubricating oils, hydraulic fluids, vacuum pump oils, cutting oils, greases, etc.) used for many purposes such as for reducing the friction between two surfaces in contact, protecting surfaces against the environment (e.g. corrosion, oxidation), dissipating heat, etc. In general, all these liquids are mainly composed of mineral oils and contain several hydrocarbon species (alkanes, naphthenic, aromatics) [7]. In addition, many additives are present (e.g. viscosity modifiers, anti-wear additives, friction modifiers, dispersants, detergents, corrosion inhibitors, etc.).

This highlights that RLOW require management steps that do not only take into account their radioactivity but also their varied chemical composition. It would be useful to have a single process for the wide variety they represent.

1.2. Reference process for the treatment of RLOW: Incineration

At a worldwide scale, the reference process for the treatment of RLOW consists in the mineralization of the wastes by incineration. Several industrial treatment units (incineration plants) are operated in various European countries and can process a part of RLOW. In France, at the CENTRACO facility managed by Cyclife, ashes and clinkers from the incineration of RLOW are further immobilized in an appropriate cement formulation and finally conditioned in shielded metallic drums of 400 L, which are exported as final wastes to industrial disposal sites held by

ANDRA (the French National Radioactive Waste Management Agency). However, it has been identified that some RLOW still fall outside the waste acceptance criteria for incineration [8].

For instance, radiological and physicochemical specifications for the CENTRACO incineration unit in France are given in Tables 1 and 2 respectively. Radiological limitations defined for the CENTRACO waste streams are given in mass activity per package with the value calculated with respect to the total net mass of the waste (Table 1). It is observed that the wastes accepted for incineration are of low radioactive activity.

Table 1: CENTRACO radiological acceptance specifications for RLOW.

Acceptation (Bq/g)	Direct	After particular agreement	Prohibited
α emitters	< 50	50 to 370	≥ 370
$\alpha\beta$ emitters with ^3H	< 20 000	20 000 to 40 000	$\geq 40 000$
$\alpha\beta$ emitters without ^3H	/	< 20 000	$\geq 20 000$
^3H	/	< 20 000	$\geq 20 000$
^{129}I	< 10	10 to 20000	$\geq 20 000$

Table 2: CENTRACO physicochemical acceptance specifications for RLOW.

Elements	Limit of mass concentration	
	Direct	After particular agreement
Cl	< 5.0 %	5.0 to 8.0 %
S	< 1.8 %	1.8 to 3.0 %
Phosphates (PO_4^{3-})	< 6.7 g.kg ⁻¹	6.7 to 10 g.kg ⁻¹
Nitrates (NO_3^-)	< 11 g.kg ⁻¹	11 to 16 g.kg ⁻¹
Br	< 0.50 g.kg ⁻¹	0.50 to 1.0 g.kg ⁻¹
F	< 0.05 g.kg ⁻¹	0.05 to 1.0 g.kg ⁻¹
Heavy metals total	< 280 mg.kg ⁻¹ (ppm)	280 to 400 mg.kg ⁻¹ (ppm)
Ni	< 65 mg.kg ⁻¹ (ppm)	65 to 100 mg.kg ⁻¹ (ppm)
Cd or Se	< 3.5 mg.kg ⁻¹ (ppm)	3.5 to 5.2 mg.kg ⁻¹ (ppm)
Hg	< 6.5 mg.kg ⁻¹ (ppm)	6.5 to 10.0 mg.kg ⁻¹ (ppm)
Co, Cr, Cu, Mn, Sb, Pb, Sn, Ti, V	< 20 mg.kg ⁻¹ (ppm)	20 to 40 mg.kg ⁻¹ (ppm)

In addition, the concentrations of the chemical elements present in RLOW need to be determined for Cl, S, phosphates, nitrates, Br, F and thirteen heavy metals which are Ni, Cd, Se, Hg, Co, Cr, Cu, Mn, Sb, Pb, Sn, Ti, and V. Limitations fixed for each chemical expressed in mass are given in Table 2. For some elements, the allowed concentration is limited to few ppm, which is very restrictive.

Finally, RLOW and their composites must have a viscosity allowing their pumping through the incinerator injection unit, which rules out, for instance, high viscosity oils and greases.

As a consequence, many RLOW do not meet the specifications of current industrial incineration units and constitute radioactive wastes that are yet deprived of an appropriate management solution.

1.3. Alternative processes

According to the International Atomic Energy Agency (IAEA) report [6], several alternative techniques for treating RLOW have been evaluated, such as wet oxidation, silver electrochemical oxidation, acid digestion, alkaline hydrolysis, phase separation by adduct formation, distillation, etc. Biological processes have also been considered [9]. At this stage, most of these studied technologies have not brought a satisfactory operational solution to the issue of RLOW for different reasons depending on the technologies [3], [6]. These are in particular:

- Insufficient performances (low yields, slow destruction kinetics).
- Lack of robustness regarding wastes variability and/or volumes.
- Incompatibility with organic components including heteroatoms (corrosion issues).
- Production of secondary wastes in high amounts.
- Difficulty to reach an acceptable economic balance.

It is to be noted that a supercritical water oxidation process (the DELOS facility) has been implemented in France at CEA Marcoule. It is operated to treat RLOW but with a limited processing capacity ($200 \text{ g}\cdot\text{h}^{-1}$) [10]. In 2020, 60 L of high activity RLOW were treated [11]. The successful operation of this pilot scale facility is an incentive for the development of a scaled-up unit ($1 \text{ kg}\cdot\text{h}^{-1}$) in order to reach industrial needs.

Moreover, some innovative mineralization technologies are still studied in on going R&D projects but with limited transfer readiness level (TRL) at this stage. This prevents an adequate assessment of their potential. In particular, this is the case of the MILOR industrial project in France, supported by the national research program “Investment for the Future” (PIA in French for *Plan d’Investissement d’Avenir*). It is conducted by CEA Marcoule in collaboration with the company A3I. This project aims at providing a versatile process for the treatment of RLOW accounting for their diversity. Two complementary processes are developed, allowing the mineralization of RLOW by applying plasma treatments [12]. The first process (IDOHL) uses an inductive plasma of

low power (5 kW) and is adapted for the treatment of halogenated liquids (with up to 70% of Cl content) free of mineral charges, such as scintillating liquids containing ^{14}C or ^3H . It is currently in the route towards industrialization but the treatment flow rate is limited ($100\text{-}150\text{ mL}\cdot\text{h}^{-1}$) due to the low plasma power [13]. The second process (ELIPSE) uses a plasma immersed in an aqueous solution, which directly absorbs the gases produced by incineration [14]. The flow rate of RLOW that can be treated is much higher ($3\text{ L}\cdot\text{h}^{-1}$) due to the higher power of the plasma (45 kW). First trials validated the technology with destruction rates close to 100% for varied RLOW such as TBP/dodecane, trichloroethylene and perfluorinated oils. However, this process is not yet ready for an effective industrial scale application.

1.4. Direct conditioning

Direct conditioning consists in encapsulating RLOW in a solid matrix in order to obtain composite materials, which can constitute the base of radioactive waste packages and fulfill the requirements of disposal facilities.

1.4.1. NOCHAR® technology (Absorption)

High technology polymers manufactured by NOCHAR® (USA) and used for the treatment of RLOW have demonstrated good results at test sites worldwide [15]. This technology consists of a range of granulated polymers such as acrylamide co-polymers, acrylate co-polymers or styrene block co-polymers. These polymers act by making strong physicochemical interactions with liquid wastes and are frequently blended together to capture and solidify waste streams that vary in chemical composition. The NOCHAR® polymer technology is mature and has been demonstrated to immobilize a wide range of RLOW such as oily, aqueous, acidic and basic waste streams [16]-[18]. The volumetric increase is generally low, typically of about 5-10% of that of the liquid waste stream. However, in some countries (e.g. France, UK), there are requirements for the acceptance of low-level waste disposal, in addition to radiological criteria, under which a waste form must have a minimum unconfined compressive strength (8 MPa in France). NOCHAR® itself does not meet this criterion and it was therefore suggested that NOCHAR®-solidified RLOW could be combined with cementation (i.e. incorporation into a cement-based matrix) in order to produce a final waste form compliant with the industrial handling, storage, transport and disposal requirements. The long-term stability of NOCHAR® polymers is also a question on hold, which yet freezes the acceptance of “nocharized” wastes for disposal in France [19]. Finally, it is to be noticed that NOCHAR® polymers are commercial products, which raises the question of NOCHAR® as a reliable option in the future (should the NOCHAR® company disappear).

1.4.2. Cementation

Cement-based materials are widely used for the direct conditioning of radioactive wastes due to numerous advantages, such as robustness (with regards to waste variability), low cost and easy

manufacturing process, high mechanical strength, excellent resistance to irradiation, possibility of treating large amounts of wastes, etc. [20], [21].

One of the first studies on the direct cementation of RLOW has been carried out in the USA in 1985 [22]. It consisted in the direct immobilization of a pump oil and a TBP/dodecane mixture in Portland cement with the addition of an emulsifier and a setting accelerator. However, ensuing studies have shown that the presence of organics in Portland cement pastes could cause delays in cement hydration and hardening, and structural defects leading to significant leaching of the organic compounds [23]-[25]. In addition, the incorporation of organic liquids in fresh Portland cement grout is generally difficult [26]. To overcome these issues, it has been recommended to implement an absorption step before the immobilization of RLOW in a Portland cement matrix [26]-[28]. However, for some difficult RLOW, the final result remains unsatisfying and the absorption step decreases the amount of RLOW that can be incorporated [26].

More recently, it has been shown that the conditioning of RLOW can be optimized by using geopolymers and related alkali-activated materials [29] as alternative mineral binders. From preliminary studies [30]-[32], the main advantages of directly conditioning RLOW using geopolymers instead of usual Portland cements are the following:

- The absence of RLOW/geopolymer interactions, which avoids delays in setting or negative effects on the final material properties.
- A highly beneficial emulsification of the RLOW in the alkaline activating solution.
- A high incorporation rate can be achieved (up to 60% vol), while maintaining sufficient mechanical properties.

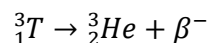
Therefore, geopolymers and related alkali-activated materials (AAM) appear to be promising solutions for the immobilization of RLOW and are becoming the focus of the nuclear community [33]. In particular, some successful studies have managed the direct conditioning of model liquids representing RLOW contaminated with alpha emitters in geopolymer materials [30], [34], [35]. This topic is also part of the on-going European PREDIS project on the predisposal management of radioactive wastes [36]. In PREDIS, an entire work package is dedicated to the direct conditioning of several troublesome RLOW in AAM. However, PREDIS will not deal with tritiated oils, which direct conditioning in AAM is the focus of this work.

2. Tritiated wastes

2.1. Tritium and its nuclear characteristics

Tritium was discovered in 1934 by Rutherford and identified by Alvaroz in 1937. It is a radioactive isotope of hydrogen written as ^3H or T. Its nucleus is made of one proton and two neutrons. It possesses an atomic mass of $3.0 \text{ g}\cdot\text{mol}^{-1}$. The half-life of tritium is 12.32 years. It is therefore a

short life radionuclide. During its radioactive decay into a stable isotope of helium (^3He), it emits a β^- particle (i.e. an electron) through the following reaction:



The β radiation emitted from the tritium decay is energetically low (5.7 keV). Accordingly, it is only thinly penetrating (its average free pathway in water is lower than 1.0 μm) and does not lead to any external irradiation of living organisms when it is present in the environment. Therefore, the harmfulness of tritium to living organisms only occurs in case of incorporation (e.g. ingestion).

2.2. Physicochemical properties of tritium

The chemical properties of tritium are identical to those of hydrogen of mass 1 (^1H) [37]. Whether of natural or anthropogenic origin, tritium is extremely mobile in the environment and in all biological systems. It exists in three different chemical forms [38]:

Tritiated water (HTO): Also known as “super heavy water”, this is the most abundant form of tritium in the environment. When tritium is not introduced into the environment in this form, HTO is most usually the result of gaseous tritium (HT) oxidation resulting from light or bacteria action.

Gaseous tritium or « tritiated hydrogen » (HT): This chemical form represents only a small fraction of tritium but it could become more important in the future with the development of nuclear fission reactors. As a result of oxidation processes, HT transforms into HTO and re-enters the water cycle.

Organically bound tritium (OBT): This form, in which tritium is bound to organic matter, results from tritium incorporated in various organic compounds during the synthesis process of living matter (e.g. photosynthesis). How stable tritium is within such compounds depends on the nature of the bond between the tritium and the organic molecule. A distinction is made between:

- **Exchangeable tritium:** There is an exchangeable fraction when hydrogen atoms bound to oxygen, sulfur or nitrogen are replaced by tritium and are readily accessible for new exchanges. This fraction of tritium bound in a labile form to biomolecules is in equilibrium with the concentration of tritiated water in the intracellular environment.
- **Non-exchangeable tritium:** In that case, tritium is covalently bound to a carbon. This is a permanent bond as long as the biomolecule itself is not transformed nor destroyed by an enzymatic reaction. Therefore, the amount of time that tritium remains incorporated in that form depends on the biomolecular turnover: fast in the case of molecules involved in the energy cycle, and slower in the case of structuring molecules or macromolecules such as DNA or energy reserve molecules.

In the form of tritiated water (HTO), tritium is extremely mobile in the environment and all biological systems, and thus quickly integrated into numerous cycles of the geo- and bio-sphere. Figure 1 shows how tritium is transferred in terrestrial environments [37]. It may be found in all hydrogenated molecules and associated both with water in tissue and with the organic material of plants and animals. The environmental toxicity of ^3H is related only to radioactive emissions of the pure, low-energy beta type and hence results mainly from uptake processes.

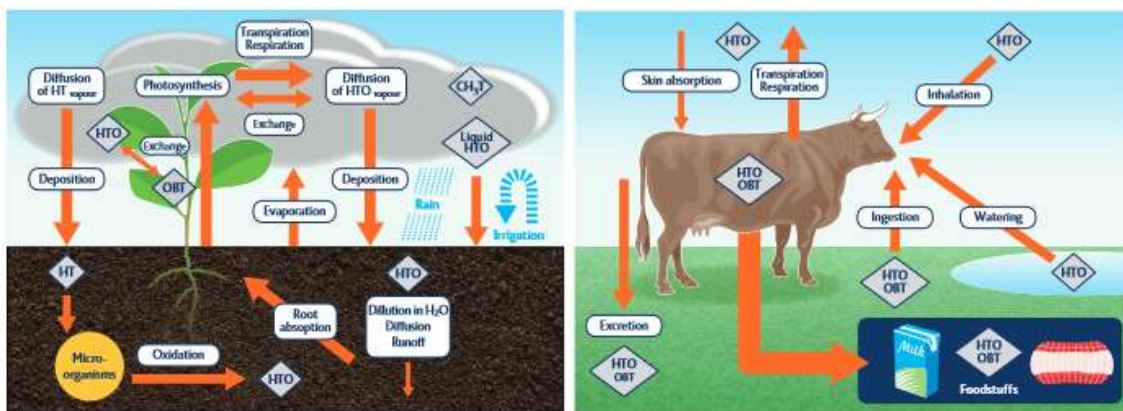


Figure 1: Tritium transfer in terrestrial environments at the air-soil-plant interfaces and in animals, including to foodstuffs [37].

2.3. Origins of tritium

Tritium is naturally present in the environment. It is mainly produced by the action of neutrons emitted from cosmic radiations on nitrogen and oxygen present in the atmosphere, representing an annual production of about 7.0×10^{16} Bq (0.20 kg) [38]. Around 99% of the tritium produced in the upper atmosphere is oxidized into tritiated water (HTO) and dispersed into surface water.

Tritium is also artificially present in the environment due to human activities, mainly from the nuclear industry (civilian nuclear reactors, military defense, and fusion). During the atmospheric trials of nuclear weapons, which mainly took place between 1945 and 1963, many radionuclides, including tritium, were released in the environment. These trials released about 650 kg of tritium in the atmosphere (240×10^{18} Bq) [37]. At present, given the half-life of tritium, about 35 kg of this tritium quantity remains, mainly in surface water [38]. This quantity can be compared against the permanent inventory of natural tritium, which is of about 3.5 kg (1.2×10^{18} Bq) [39].

Nowadays, most of fission nuclear reactors worldwide are pressurized water reactors. The main source of tritium arising from the operation of this kind of reactor is the neutron activation of bore ^{10}B and lithium ^6Li present in the primary heat transfer fluid [38]. Tritium is also produced during ternary fission of uranium and plutonium, but it mainly remains confined in the fuel. However, during the treatment of spent nuclear fuels, tritium is released from the dissolution of the fuel in the form of oxides. Additionally, some fission reactors use heavy water for their operation, in which tritium is produced by the neutron activation of deuterium [38]. This is the

case of CANDU reactors (CANadian Deuterium natural Uranium reactors). Currently, most of the tritium released worldwide by fission reactors is due to this type of reactors, while they produce only about 5% of the nuclear electrical supply. Tritium is also an important component of nuclear military arms, used to enhance the yield and efficiency of fission and thermonuclear weapons. Finally, the future ITER reactor, aiming at demonstrating the control of fusion energy, will make use of a large amount of tritium as a primary constituent of the fusion reaction [40].

All these artificial productions of tritium go alongside with the production of tritiated wastes that need to be taken care of. The majority of tritiated wastes is in a solid state with an estimated inventory of 4500 m³ in France in 2010. The future operation (and dismantling) of the ITER fusion reactor, using deuterium and tritium as fuel, will strongly contribute to the formation of tritiated wastes, with a solid production estimated at 30 000 m³ or 34 000 tons in 2060, while the production of liquid wastes is more difficult to anticipate [10], [41], [42].

2.4. Strategy for the treatment of tritiated wastes

All tritiated wastes release tritium over time in the form of gaseous tritium (HT or T₂) or tritiated water in liquid or vapor form (HTO or T₂O). The specific issue related to the treatment of tritiated wastes arises from the high mobility of tritium. The latter is difficult to contain within waste packages. Accordingly, safety authorities responsible for the acceptance of waste packages impose not only a radiological activity specification but also a criterion based on the out-gassing rate of tritium. Therefore, it is necessary to find adapted solutions for the disposal of this kind of radioactive wastes. Several strategies exist and are presented in Figure 2 [43].

2.4.1. Interim storage

The interim and safe storage of tritiated wastes is performed directly at production sites or on dedicated sites. The aim is to wait long enough for the radioactive decay to be sufficient for the wastes to fulfill acceptance criteria for their final disposal. Due to its short lifetime (half-life of 12.32 year), about 5% of the tritium inventory of a given tritiated waste disappears yearly. Hence, for tritiated wastes, in France, a storage period of about 50 years is generally sufficient to meet the acceptance criteria and allow wastes to be placed in disposal sites held by ANDRA [41]. The advantage of this method lies in its easiness and fast implementation but it does not fully avoid tritium release in the environment and should not be considered as the sole option.

2.4.2. Preliminary treatment

The implementation of a preliminary treatment aims at reducing the volumes of tritiated wastes or the tritium content of wastes (detritionation). This has several advantages [42]:

- Downgrade the primary waste classification, and allow the waste to be directly compatible with disposal criteria.

- Decrease the interim storage period and the surface of interim storage sites.
- Reduce radioprotection constraints for working people.
- Deplete atmospheric tritium out-gassing.
- Recycle the extracted tritium [10].

Several detritiation processes have been studied but most of them have been ruled out due to superficial detritiation performances and to the production of large amounts of secondary tritiated water. However, two efficient processes have been successfully executed [43]. One is a thermal treatment applied to metallic parts until their fusion. The other is incineration applied to soft housekeeping wastes.

Although they are interesting, these detritiation techniques still produce secondary tritiated wastes (mostly tritiated water), which also have to be managed [42].

2.4.3. Direct conditioning

The direct conditioning of short-lived wastes is mainly performed in cementitious materials. However, the high mobility of tritium suggests to design specific waste packages for reducing the rate of tritium release. Several strategies have been considered [44], [45]:

- Surface coatings (paraffin, grease, epoxy resin, wax, bitumen ...). Among these coatings, paraffin and bitumen seemed to be the most promising with the decrease of tritium release rate by more than one order of magnitude.
- The impregnation of cementitious materials by polymers such as polystyrene or polyethylene. The objective of the polymer is to fill the porosity of the cement. Monomers are introduced and polymerization is performed directly inside the hardened cementitious material by slightly increasing the temperature. The final composite material displays reinforced mechanical properties but the efficiency for tritium containment is questionable (thermal cracking is possible).
- The application of external liners made up of high-density polyethylene. They tend to act efficiently as physical barriers, but their long-term stability has not been studied.
- A multi-barrier approach combining high-density polyethylene liners with containers made of multi-layer walls and interlayer spacing filled with bitumen or vermiculite. This technique has proven to be very efficient to limit tritium release.

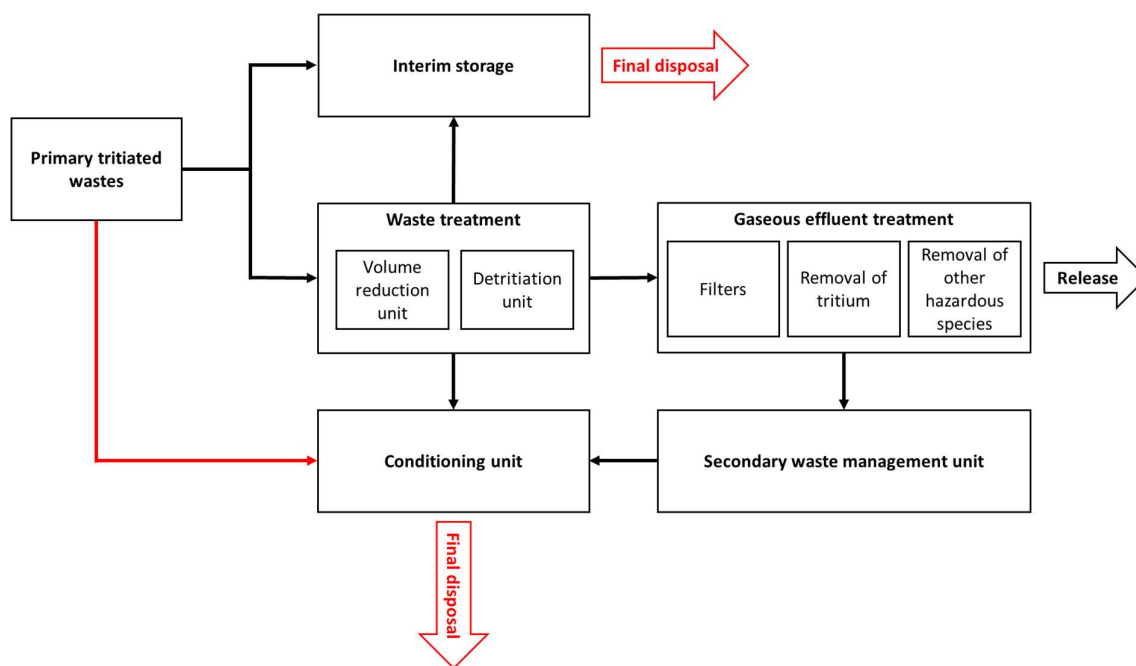


Figure 2: Strategy for the disposal of tritiated wastes adapted from [43].

2.4.4. Tritium scavengers within tritiated waste packages

Another possibility for the conditioning of tritiated wastes is to trap tritium directly within waste packages. This section deals with the issues related to gaseous tritium (HT). Several types of getters (i.e. trapping compounds) exist to limit the tritium outgassing rate by trapping gaseous tritium directly within waste packages. In order to be used as a solution for tritiated waste disposal, getters need to fulfill some specifications [46]:

- The trapping must be irreversible.
- The trapping kinetics must be fast and the trapping capacity must be high.
- The getter should be highly stable for tolerating strong temperature and/or pressure increase, exposure to irradiation, etc.
- The trapping must take place under atmospheric pressure and at room temperature.

Several types of chemical getters, which are based on chemisorption of H_2 (or HT) present in the vapor phase, have been studied. They can be divided in three main categories: organics, metal hydrides and metal oxides.

2.4.4.1 Organic compounds

In the 70s, Sandia National Laboratories developed organic getters based on 1,4-bis(phenylethynyl)benzene (DEB), dimerized-phenyl-propargyl-ether (DPPE) and 1,4-diphenylbutadiyne (DPB) with platinum or palladium as catalysts [47]-[50]. These scavengers are made up of alkene or alkyne species and the reaction mechanism is the hydrogenation of the

carbon-carbon double or triple bonds. This requires the use of catalysts in order to separate dihydrogen molecules in separate hydrogen atoms. However, this type of getter cannot be considered for the trapping of tritium because their melting point is generally low (80°C for DPPE to 180°C for DBE), which would be an issue in case of fire on the disposal site [46], [51]. Moreover, they are sensitive to gamma radiation exposure, which reduces their trapping capacity [52].

2.4.4.2 Metal hydrides

Hydride-forming metals or metal alloys can be used as hydrogen scavengers. After adsorption at the surface of the metal, dihydrogen molecules are dissociated in single hydrogen atoms, which can be inserted in the interstitial network of the metal structure. The most frequently used metals are palladium [53], zirconium and titanium [38], [54], [55]. However, the hydride formation generally requires high temperature and is therefore difficult to implement industrially [38]. Despite their efficiency, metal hydrides are also known to be reversible getters of hydrogen, especially in presence of water [38]. They are also sensitive to poisonous gases (O₂ and CO [56]), some are pyrophoric [38] and their behavior under irradiation is yet unanswered.

2.4.4.3 Mineral oxides

In the early 80s, Kozawa studied the trapping of dihydrogen using metal oxides in combination with several catalysts based on palladium, platinum and silver oxide [57]-[59]. Catalysts increase the trapping capacity and kinetics by allowing the fast dissociation of dihydrogen molecules in single hydrogen atoms. These atoms then diffuse inside the structure of the oxides to form metal oxide hydroxides. Among others, getters made of a combination of manganese oxide (MnO₂) and silver oxide (Ag₂O) seemed to be the most promising.

Several authors showed that MnO₂/Ag₂O getters allow an efficient trapping of H₂ at room temperature and atmospheric pressure [54], [59], [60]. Galliez [61] proposed a reaction mechanism explaining how MnO₂ is irreversibly transformed in MnOOH during the trapping of H₂. In 2011, a patent was filed dedicated to the trapping of tritium using a combination of manganese oxide, silver oxide and platinum black supported by zeolites [62]. The trapping of gaseous tritium (HT) is performed at the surface of the getter (metal oxide + silver oxide + platinum black), whereas tritiated water (HTO) is adsorbed at the surface of the zeolite. Also, Janberg et al. [63] highlighted the tritium trapping efficiency of MnO₂/Ag₂O getters during the transport of nuclear waste packages. Finally, mineral oxides, and more specifically MnO₂/Ag₂O getters, are thermally stable in addition to their resistance against irradiation exposure [64], [65].

Accordingly, the use of metal oxides, and more specifically MnO₂/Ag₂O blends, seems to be the most promising option for gaseous tritium confinement, as it best fulfills all the specifications for disposal, especially in terms of efficiency, stability and safety [46], [51], [66].

3. The case of tritiated industrial oils: What strategy?

3.1. Origin of tritiated industrial oils

In tritium-related facilities, a large amount of tritiated contaminated oils is produced, mainly through the tritium-hydrogen (H-T) isotope exchange reaction [67]. For instance, tritium reacts with hydrocarbons, which are the major constituents of oily wastes, to form tritiated hydrocarbons [68]. In the presence of oxygen, tritium and hydrocarbons may further undergo radiochemical oxidation to produce stable tritiated oxides, such as alcohols, carbonyl compounds and carboxylic acids [67]-[69]. The resulting wastes are complex and it is essential to develop economic and efficient methods to dispose of these tritium-containing wastes. At present, two main directions for the safe management of tritiated oils are being investigated. A first approach is based on decontamination, which, in its ideal form, should allow for both an easy recovery of tritium and the reduction of tritium content in wastes to a safe level [70]. This is generally performed by isotopic exchange [68], [71].

The second approach is based on the direct immobilization of tritiated oils into cementitious materials. In general, a preliminary step (aiming at solidifying the oil) is performed before incorporation. This can be achieved by absorption on different types of materials such as NOCHAR® polymers [72], zeolites, active alumina or activated ultrafine carbon [73], [74]. According to Sazonov et al. [73], the tritium diffusion coefficient in « oil – carbon – cement » compositions ranges from 10^{-15} to 10^{-16} $\text{m}^2.\text{s}^{-1}$, which is lower by 3 – 4 orders of magnitude compared to the diffusion coefficient of tritium in cement materials [74]. Preliminary microencapsulation in a phenol – formaldehyde polymer matrix was also considered [75].

3.2. Scientific issues and research strategy

In this introductory chapter, the issues of RLOW and tritiated wastes have been raised to understand the context of tritiated oil management. **The strategy adopted in this work is the direct conditioning of tritiated industrial oils in cementitious materials, additionally functionalized with a hydrogen/tritium getter.**

The first objective is to ensure that the solidification/stabilization (S/S) of industrial oils in cementitious materials is well controlled, with no oil leakage, while maintaining strong mechanical properties. In particular, alkali-activated materials (AAM) seem to be promising candidates. As mentioned earlier, industrial oils display varied compositions but most of them are of mineral origin, indicating the presence of several types of hydrocarbon species as shown in Figure 3 [7]. Predominant molecules are saturated long-chain hydrocarbons (paraffins) with straight or branched chains containing 15–30 carbon atoms, and saturated 5- or 6-membered hydrocarbon rings (naphthenic) with attached sidechains of up to 20 carbon atoms long. Aromatic components are also present but in small proportions.

As a major constituent of industrial oils [7], this work will mainly focus on the direct conditioning of pure paraffin-based mineral oils.

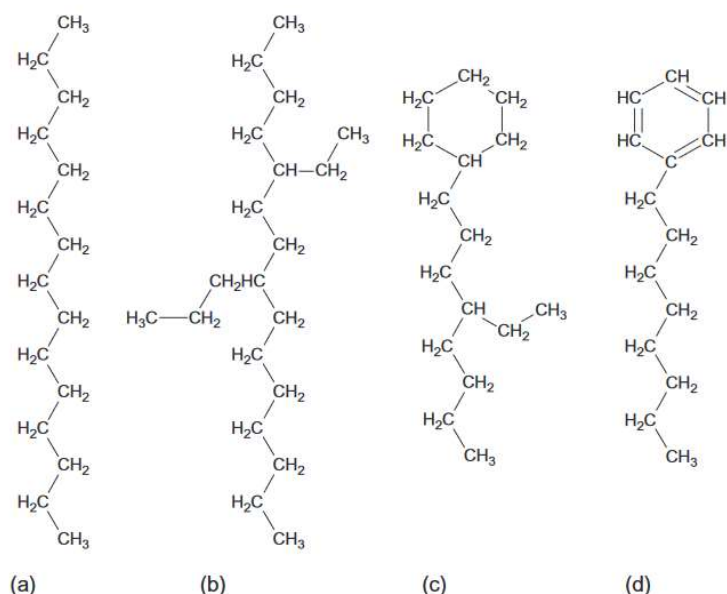


Figure 3: Examples of hydrocarbon molecules structures present in mineral oils: (a) paraffin (alkane); (b) branched paraffin (alkane); (c) naphthenic; (d) aromatic [7].

The second objective is the limitation of tritium release out of waste packages. Trials performed at CEA Marcoule evidenced that the tritium released from oily wastes is mainly in the form of tritiated water (HTO), but a significant amount of gaseous tritium (HT) is also observed [76]. **The HT form of tritium is particularly difficult to confine and will be the focus of the present work.** The strategy adopted to avoid HT release consists in functionalizing cementitious materials with a hydrogen/tritium getter. According to the literature, the preferred getter is made up of a mixture of MnO₂/Ag₂O proposed initially by [59] and studied more precisely in [61]. The trapping mechanism proposed by Galliez [61] will be discussed later in this work. **The release rate of HTO can be further controlled by formulating cementitious materials with low water permeability.**

To fulfill both objectives, two types of alkali-activated materials are considered in this work¹:

¹ Alkali activation is the generic term which is applied to the reaction of solid aluminosilicate precursors under alkaline conditions, to produce a hardened binder. Two types of alkali-activated materials can be distinguished, depending on the amount of calcium present in the aluminosilicate precursors. The term 'geopolymer' refers precisely to low-calcium alkali-activated aluminosilicate binders. For instance, blast furnace slags contain a high amount of calcium and do not fall into this category. More information about these materials are given in chapter III.

- **Geopolymers**, as they have shown very good effectiveness for RLOW immobilization. However, the limitation of tritium release might be an issue in this type of materials due the high amount of free water present in their structure.
- **Alkali-activated blast furnace slag cements**, in which the oil immobilization might be more difficult (due to their solid structure similar to that of Portland cements). However, the amount of free water present in these materials is known to be lower than in geopolymers, which could be an asset to avoid tritium release, in particular the HTO form.

In order to investigate the proposed objectives, this manuscript is divided in five independent chapters. Their aims are illustrated graphically in Figure 4.

Chapter I is a literature review on the incorporation of various organic liquids in alkali-activated materials, and more specifically geopolymer materials. The first part presents the different processing routes for the incorporation of organic liquids into fresh cementitious grouts. After discussing the limitations on the use of ordinary Portland cement for the immobilization of organic liquids, the second part describes the three main potential applications arising from the good compatibility between geopolymer materials and organic liquids.

Chapter II aims at understanding the mechanisms enhancing the fixation of mineral oils in reactive inorganic matrices, by emulsification. This requires using adequate surfactants to succeed in formulating the emulsion. Six common surfactants of different nature (cationic, anionic and non-ionic) are evaluated. All characterizations are performed in the fresh state, i.e. before hardening of the materials with the aim of formulating the best possible emulsion of mineral oil in fresh alkali-activated materials.

Chapter III aims at assessing the most adequate type of alkali-activated material (AAM) for the immobilization of mineral oil. The originality of this chapter is the direct comparison of two binders based on different raw materials, under the same processing conditions. Also, it aims at assessing how alkali-activated materials are impacted by incorporating mineral oils. In other words, it is a question of whether the impact on mechanical properties is due to physical reasons only (e.g. porosity increase due to oil incorporation) or chemical reasons as well (e.g. change in reaction products).

Chapter IV is dedicated to assessing and understanding the efficiency of the $\text{MnO}_2/\text{Ag}_2\text{O}$ hydrogen/tritium getter in alkali-activated materials, which has not yet been performed. In particular, the getter efficiency is known to be affected by the properties of its surrounding environment. In the case of cementitious-like materials, these can be the amount of free water, the sorption of ions, redox reactions, etc.

Chapter V aims at determining the long-term confinement of RLOW within geopolymer (GEO) matrices, in order to help allowing their acceptance in industrial disposal sites. In particular, environmental water seepage is usual and may dislodge RLOW from GEO with time. To this

purpose, the Surface Free Energy (SFE) of a typical GEO matrix is determined through wetting angles measurements. For instance, the knowledge of the SFE allows: 1) quantifying the affinity of any liquid for GEO materials and 2) drawing wetting envelopes to predict the wetting of any liquid on the GEO surface.

Despite being collectively connected by the issue of tritiated industrial oils conditioning, all chapters are completely independent and can be read separately. To facilitate their reading, Chapter II, III and IV are preceded by preamble sections aiming at providing basic knowledge.

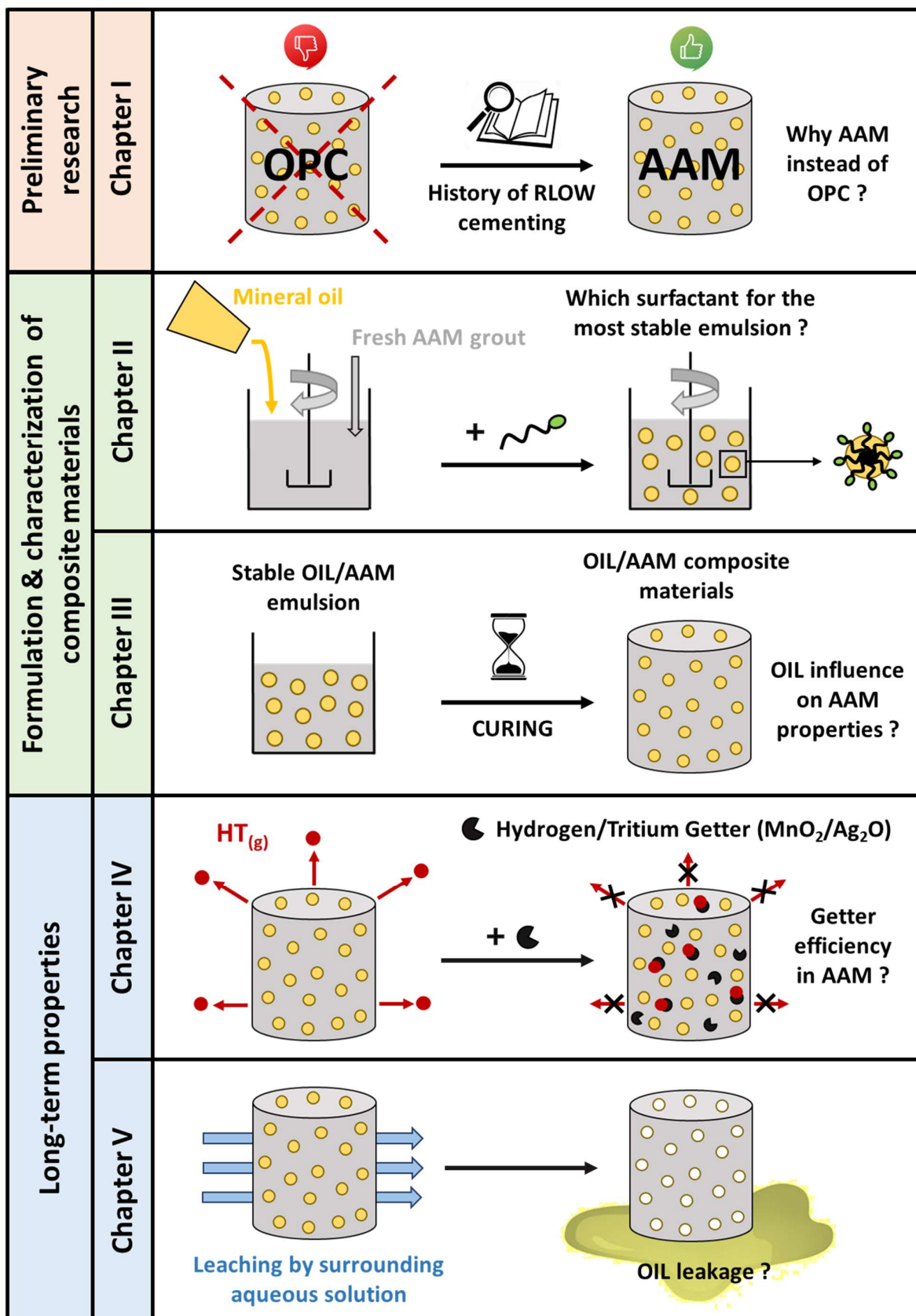


Figure 4: Schematic description of the main objectives of the present thesis manuscript.

References

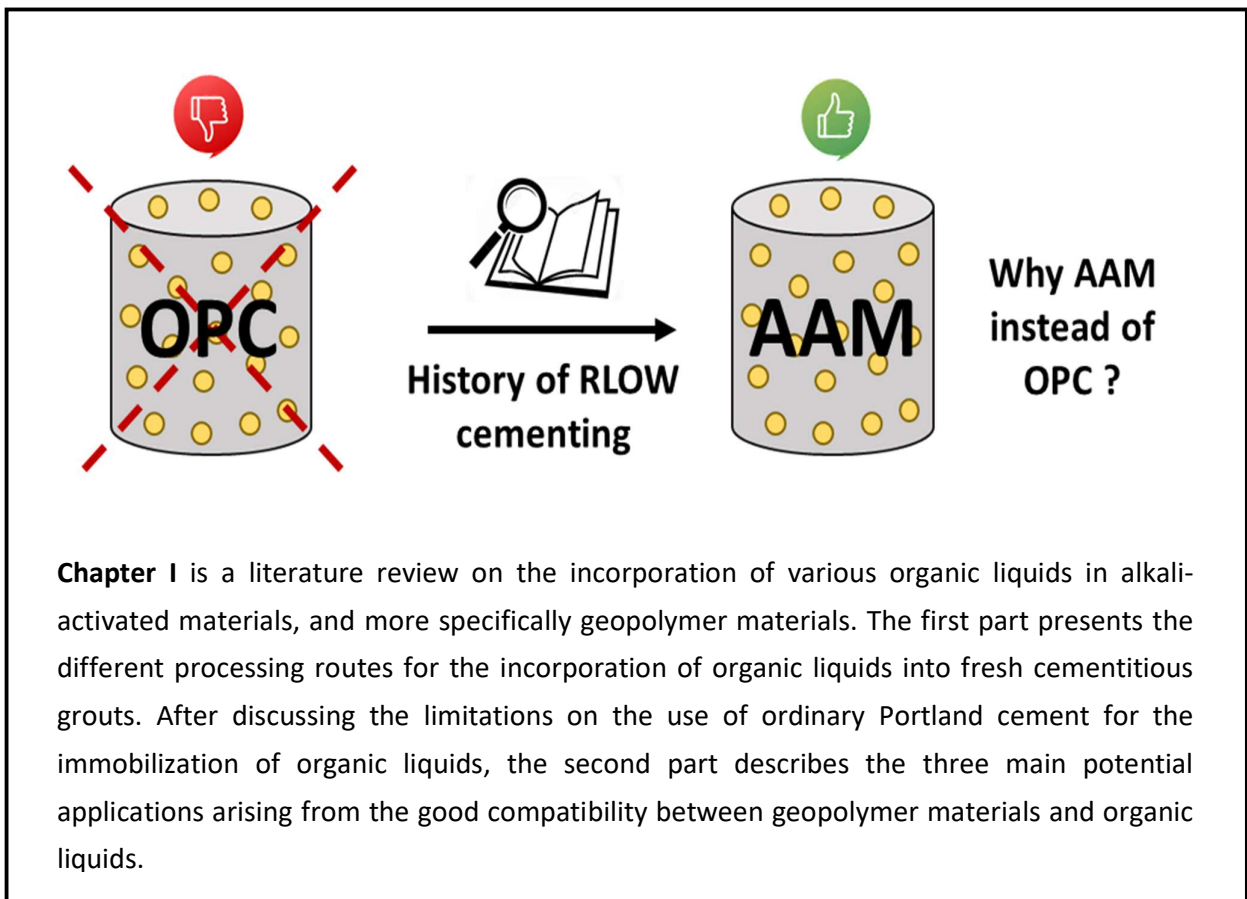
- [1] ANDRA, 'Catalogue descriptif des familles', 2009.
- [2] 'Inventaire national des matières et déchets radioactifs', ANDRA, 2018.
- [3] R. O. A. Rahman, H. A. Ibrahim, and Y.-T. Hung, 'Liquid Radioactive Wastes Treatment: A Review', *Water*, 2011, doi: 10.3390/w3020551.
- [4] PerkinElmer, 'Liquid Scintillation Cocktails'. <https://www.perkinelmer.com/fr/lab-products-and-services/application-support-knowledgebase/radiometric/liquid-scintillation-cocktails.html>
- [5] J. E. Birkett et al., 'Recent Developments in the Purex Process for Nuclear Fuel Reprocessing: Complexant Based Stripping for Uranium/Plutonium Separation', *Chim. Int. J. Chem.*, 2005, doi: 10.2533/000942905777675327.
- [6] International Atomic Energy Agency (IAEA), 'Treatment and conditioning of radioactive organic liquids', 1992.
- [7] I. Hutchings and P. Shipway, 'Lubricants and lubrication', *Tribology*, 2017, doi: doi.org/10.1016/B978-0-08-100910-9.00004-0.
- [8] 'Cyclife France'. <https://www.cyclife-edf.com/cyclife/organisation/cyclife-france>
- [9] R. V. de Pádua Ferreira et al., 'Treatment of radioactive liquid organic waste using bacteria community', *J. Radioanal. Nucl. Chem.*, 2012, doi: 10.1007/s10967-011-1564-2.
- [10] K. Liger, 'Le traitement des déchets d'assainissement-démantèlement', CEA, Les déchets tritités.
- [11] CEA, 'Rapport transparence et sécurité nucléaire'. 2020.
- [12] 'Appel à projet ANDRA: MILOR (Minéralisation de déchets liquides organiques radioactifs par voie plasma)', 2017.
- [13] ANDRA, 'MILOR, une solution pour traiter des déchets radioactifs liquides par plasma thermique', 2022. <https://www.andra.fr/milor-une-solution-pour-traiter-des-dechets-radioactifs-liquides-par-plasma-thermique>
- [14] M. Mabrouk, M. Marchand, A. Russello, J. M. Baronnet, and F. Lemont, 'Development of a Submerged Thermal Plasma Process for Combustion of Organic Liquid Waste', *Plasma Chem. Plasma Process.*, 2015, doi: 10.1007/s11090-014-9587-4.
- [15] D. Kelley and A. Gelis, 'Proven Technologies for the Solidification of Complex Liquid Radioactive Waste (LRW): Global Case Studies of Applications and Disposal Options', Shanghai, China, 2017.
- [16] H. Cassidy, 'Oil Immobilization Program at Sellafield: An Innovative Approach', 2007.
- [17] C.-E. Vaudey, S. Renou, J. Porco, D. Kelley, and R. Serrano, 'NOCHAR polymers: an aqueous and organic liquid solidification process for Cadarache LOR', 2013.
- [18] Yuu. Pokhitonov, V. Babain, and S. Strelkov, 'Radiation and Thermal Stability of Solid Radwaste after Immobilization in Polymer Matrix', Phoenix, USA, 2013.
- [19] M. Zilber, 'NOCHAR, a solution to answer to organic liquid storage stakes in France ?', PREDIS project, 2021.
- [20] P. Vejmelka, G. Rudolph, W. Kluger, and R. Köster, 'Le conditionnement par cimentation des déchets liquides radioactifs', 1992.
- [21] C. Cau Dit Coumes, N. Moulin, G. Ranc, P. Bouniol, C. Galle, and F. Frizon, 'Les ciments comme matériaux de confinement', CEA, 2008.
- [22] W.O. Greenhalgh, 'The Immobilization of organic liquid wastes', 1986.
- [23] D. M. Montgomery, C. J. Sollars, R. Perry, S. E. Tariingt, P. Barnes, and E. Henderson, 'Treatment of organic-contaminated industrial wastes using cement-based S/S - I. Microstructural analysis of cement-organic interactions', *Waste Manag. Res.*, 1991.
- [24] S. J. T. Pollard, D. M. Montgomery, C. J. Sollars, and R. Perry, 'Organic compounds in the cement-based stabilization/ solidification of hazardous mixed wastes—Mechanistic and process considerations', *J. Hazard. Mater.*, 1991, doi: 10.1016/0304-3894(91)87082-D.
- [25] I. Natali Sora, R. Pelosato, D. Botta, and G. Dotelli, 'Chemistry and microstructure of cement pastes admixed with organic liquids', *J. Eur. Ceram. Soc.*, 2002, doi: 10.1016/S0955-2219(01)00473-3.

- [26] D. E. Clark, P. Colombo, and R. M. Jr. Neilson, 'Solidification of oils and organic liquids', Nuclear Waste Management, 1982.
- [27] V. M. Hebatpuria, H. A. Arafat, H. S. Rho, P. L. Bishop, N. G. Pinto, and R. C. Buchanan, 'Immobilization of phenol in cement-based solidified-stabilized hazardous wastes using regenerated activated carbon: leaching studies', Journal of Hazardous Material, 1999.
- [28] L. Zhu, B. Chen, and X. Shen, 'Sorption of Phenol, p-Nitrophenol, and Aniline to Dual-Cation Organobentonites from Water', Environ. Sci. Technol., 2000, doi: 10.1021/es990177x.
- [29] J. L. Provis and S. A. Bernal, 'Geopolymers and Related Alkali-Activated Materials', Annu. Rev. Mater. Res., 2014, doi: 10.1146/annurev-matsci-070813-113515.
- [30] V. Cantarel, F. Nouaille, A. Rooses, D. Lambertin, A. Poulesquen, and F. Frizon, 'Solidification/stabilisation of liquid oil waste in metakaolin-based geopolymer', J. Nucl. Mater., 2015, doi: 10.1016/j.jnucmat.2015.04.036.
- [31] D. Lambertin, A. Rooses, and F. Frizon, 'Process for preparing a composite material from an organic liquid and resulting material', WO2014/044776 A1, 2014
- [32] C. A. Davy, G. Hauss, B. Planel, and D. Lambertin, '3D structure of oil droplets in hardened geopolymer emulsions', J. Am. Ceram. Soc., 2018, doi: 10.1111/jace.16142.
- [33] D. A. Geddes, X. Ke, S. A. Bernal, M. Hayes, and J. L. Provis, 'Metakaolin-Based Geopolymers for Nuclear Waste Encapsulation', Calcined Clays Sustain. Concr., 2018, doi: 10.1007/978-94-024-1207-9_29.
- [34] B. Planel et al., 'Water permeability of geopolymers emulsified with oil', Cem. Concr. Res., 2020, doi: 10.1016/j.cemconres.2020.106108.
- [35] V. Cantarel, D. Lambertin, A. Poulesquen, F. Leroux, G. Renaudin, and F. Frizon, 'Geopolymer assembly by emulsion templating: Emulsion stability and hardening mechanisms', Ceram. Int., 2018, doi: 10.1016/j.ceramint.2018.03.079.
- [36] 'EU-project PREDIS, WP5 - Innovations in liquid organic waste treatment and conditioning'. <https://predis-h2020.eu/work-packages/>
- [37] P. Calmon and J. Garnier-Laplace, 'Tritium and the environment', IRSN, 2001.
- [38] ASN (Autorité de sûreté nucléaire), Livre Blanc du Tritium. 2019.
- [39] 'Sources and effects of ionizing radiation', United Nations Scientific Committee on the Effects of Atomic Radiation, UNSCEAR 2000 Report, 2000.
- [40] 'ITER'. <https://www.iter.org/>
- [41] D. Canas, C. Decanis, K. Liger, D. Dall'ava, and J. Pamela, 'Classification Methodology for Tritiated Waste Requiring Interim Storage', Fusion Sci. Technol., 2015, doi: 10.13182/FST14-T13.
- [42] J. Pamela, J.-M. Bottereau, D. Canas, C. Decanis, K. Liger, and F. Gaune, 'ITER tritiated waste management by the Host state and first lessons learned for fusion development', Fusion Eng. Des., 2014, doi: 10.1016/j.fusengdes.2013.12.006.
- [43] J. Pamela, C. Decanis, D. Canas, K. Liger, and F. Gaune, 'Reducing the tritium inventory in waste produced by fusion devices', Fusion Eng. Des., 2015, doi: 10.1016/j.fusengdes.2015.02.043.
- [44] F. Mannone, 'Immobilization of tritiated waste water by hydraulic cements: a survey of the state of the art', Nuclear Science and Technology, 1987.
- [45] F. Mannone, 'Management of tritium contaminated wastes: a survey of alternative options', Nuclear Science and Technology, 1990.
- [46] A. Le Floch, 'Etude phénoménologique et modélisation du piégeage du tritium au sein de colis de déchets tritiés', 2017.
- [47] G. L. Powell, 'Hydriding kinetics of an organic hydrogen getter-DPB', J. Alloys Compd., 2007, doi: 10.1016/j.jallcom.2007.01.070.
- [48] R. L. Courtney and L. A. Harrah, 'Organic hydrogen getters: Part 1', J. Mater. Sci., 1977, doi: 10.1007/BF00738483.
- [49] H. Dong et al., 'Polymer Framework with Continuous Pores for Hydrogen Getters: Molding and a Boost in Getter Rate', ACS Appl. Polym. Mater., 2020, doi: 10.1021/acspapm.0c00391.
- [50] P. J. Nigrey, 'An issue paper on the use of hydrogen getters in transportation packaging', Sandia National Laboratories, 2000.

- [51] V. Chaudron, A. Laurent, F. Arnould, and C. Latge, 'Experimental evaluation of hydrogen getters as mitigation technique in a fusion reactor', 1997. doi: 10.1109/FUSION.1997.687022.
- [52] A. R. Kazanjian, 'Radiation stability of a hydrogen getter material (DPPE)'. 1976.
- [53] S. Thiebaut, 'Stockage des isotopes de l'hydrogène Etude du vieillissement des trituries métallique', 2010.
- [54] V. Chaudron, 'Etude de la mitigation du risque hydrogène dans un réacteur de fusion thermonucléaire par réduction d'un oxyde métallique', 1998.
- [55] F. Cuevas and M. Latroche, 'Intermetallic alloys as hydrogen getters', *J. Alloys Compd.*, 2022, doi: 10.1016/j.jallcom.2022.164173.
- [56] A. Schneemann et al., 'Nanostructured Metal Hydrides for Hydrogen Storage', *Chem. Rev.*, 2018, doi: 10.1021/acs.chemrev.8b00313.
- [57] A. Kozawa, 'Reaction mechanism of hydrogen absorbers made of manganese dioxide'. 1976.
- [58] A. Kozawa, 'Hydrogen gas absorber made of MnO₂ catalyzed with palladium or platinum salts'. 1978.
- [59] A. Kozawa and K. W. Kordesch, 'Silver Catalyzed Manganese Dioxide Hydrogen Gas Absorber', US4252666A, 1981
- [60] K. Galliez, P. Deniard, D. Lambertin, S. Jobic, and F. Bart, 'Influence of MnO₂ polymorphism form on MnO₂/Ag₂O hydrogen getter', *J. Nucl. Mater.*, 2013, doi: 10.1016/j.jnucmat.2013.03.053.
- [61] K. Galliez, 'Study and understanding of the irreversible trapping of hydrogen using a mixture of MnO/Ag₂O', PhD, University of Nantes, France, 2012.
- [62] X. Lefebvre, K. Liger, and M. Troulay, 'Procédé et dispositif de réduction du dégazage de déchets tritiés issus de l'industrie nucléaire', EP 2 605 249 B1, 2011.
- [63] K. Janberg and F. Petrucci, 'Dry storage in casks at the site of Super-Phenix - The special problem of the tritium getter-process within a transport and storage cask filled with absorber rods', 1995.
- [64] C. Chlique et al., 'Effect of gamma irradiation on MnO₂/Ag₂O hydrogen getter', *J. Nucl. Mater.*, 2015, doi: 10.1016/j.jnucmat.2014.11.128.
- [65] C. Chlique, D. Lambertin, F. Frizon, P. Deniard, and S. Jobic, 'Effect of temperature on the γ -MnO₂/"Ag₂O" hydrogen getter structure', *Fusion Eng. Des.*, 2016, doi: 10.1016/j.fusengdes.2016.06.014.
- [66] D. Lambertin and C. Cau Dit Coumes, 'Hydrogen-trapping material, method of preparation and uses', WO 2010/066811, 2010.
- [67] L. Dong et al., 'Isotope exchange reaction in tritium-contaminated vacuum pump oil: mechanism and HTO effect', *RSC Adv.*, 2017, doi: 10.1039/C6RA25404G.
- [68] A. B. Sazonov, É. P. Magomedbekov, G. V. Veretennikova, S. A. Samoilov, and A.V. Zharkov, 'Method for extracting tritium from tritium-containing vacuum-oil wastes', *At. Energy*, 2005, doi: 10.1007/s10512-005-0181-y.
- [69] J. P. Krasznai, D. F. Mullins, and R. A. Mowat, 'Tritiated Waste Management - Tritiated Oil Packaging and Decontamination', *Fusion Technol.*, 1995, doi: 10.13182/FST95-A30631.
- [70] A. Olejniczak, J. Fall, K. Olejniczak, M. V. Gustova, and A. G. Shostenko, 'Solid phase extraction of tritiated contaminants from tritium-containing waste oils', *J. Radioanal. Nucl. Chem.*, 2016, doi: 10.1007/s10967-016-4953-8.
- [71] É. P. Magomedbekov, V. A. Shalygin, O. A. Baranova, M. Yu. Isaeva, and A. V. Zharkov, 'Removal of tritium from vacuum oil by isotopic exchange', *At. Energy*, 2005, doi: 10.1007/s10512-005-0180-z.
- [72] U.S. Department of Energy, 'Nochar Petrobond - Absorbent polymer - Tritiated oil solidification', 2001.
- [73] A. B. Sazonov, A. D. Thun, E. P. Magomedbekov, A. V. Ponomarev, I. G. Tananaev, and B. F. Myasoedov, 'Carbon sorbents for immobilization of tritium-containing waste oils', *Russ. J. Gen. Chem.*, 2011, doi: 10.1134/S1070363211090465.
- [74] A. B. Sazonov, A. V. Aleshina, and E. P. Magomedbekov, 'Immobilization of tritium-containing oil wastes by their incorporation in a cement matrix', *Radiochemistry*, 2009, doi: 10.1134/S106636220904016X.
- [75] A. G. Mikhal'chenko and V. A. Starchenko, 'Polymeric matrices promising for immobilization of tritium radioactive wastes', *Radiochemistry*, 2012, doi: 10.1134/S1066362212040182.
- [76] CEA Marcoule, 'Internal Report about tritium outgassing from radioactive oily wastes', 2020.

Chapter I

Incorporation of organic liquids into geopolymer materials: A review of processing, properties and applications

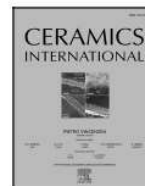




Contents lists available at ScienceDirect

Ceramics International

journal homepage: www.elsevier.com/locate/ceramint



Review article

Incorporation of organic liquids into geopolymer materials - A review of processing, properties and applications

Charles Reeb^{a,b}, Christel Pierlot^a, Catherine Davy^{a,*}, David Lambertin^b

^a Univ. Lille, CNRS, Centrale Lille, ENSCL, Univ. Artois, UMR 8181-UCSC-Unité de Catalyse et de Chimie Du Solide, F-59000, Lille, France

^b CEA, DES, ISEC, DE2D, SEAD, LCBC, Univ Montpellier, Marcoule, France

ARTICLE INFO

Keywords:

Geopolymers
Organic liquid
Incorporation
Emulsion
Impregnation

ABSTRACT

Geopolymers, composed of an amorphous three-dimensional inorganic network and synthesized by the activation of a solid aluminosilicate precursor with an alkaline activating solution, have attracted increasing attention because of their environmental benefits and favorable characteristics. This review deals with the development of organic/inorganic composite materials made by adding organic liquids into inorganic geopolymer matrices. Firstly, the incorporation processing approaches are presented and are divided into three categories: (i) Direct incorporation, (ii) Pre-emulsification (iii) Solid impregnation. Their main advantages and drawbacks are discussed in relation to the aimed properties. Secondly, this review highlights that geopolymers are low-cost candidates allowing technologically significant applications, through the incorporation of various organic liquids. Aside from the well-studied immobilization of industrial waste streams commonly known as stabilization/solidification (S/S), the development of highly porous geopolymer foams and the design of reinforced organic/inorganic composite matrices are being notably investigated. This review aims at summarizing the main published results, and fostering further investigations into innovative uses of organic liquids incorporated into geopolymers for a wide range of applications.

1. Introduction

Nowadays, the world production of Portland cement has reached about 4 billion tons [1], being one of the most produced merchandise worldwide (in volume). Such a significant production induces a high environmental impact; the production of Portland cement is responsible for about 0.8 tons of CO₂ equivalent per ton produced and contributes to about 8% of anthropogenic CO₂ emissions [2]. Therefore, there is an urgent need for alternatives to Portland cement, which are able to handle the increasing demand for infrastructure building while reducing the CO₂ emissions.

In the late 1970s, J. Davidovits drew the attention to Alkali Activated Materials (AAM) based on low calcium precursors, and named these materials geopolymers by analogy to their organic counterparts [3,4]. Geopolymers can be made from natural aluminosilicate minerals or industrial aluminosilicate wastes such as metakaolin, fly ash, blast furnace slag, rice husk ash, etc. mixed with aqueous solutions containing reactive ingredients (potassium/sodium hydroxide, phosphoric acid, potassium/sodium silicates, etc.) [5]. With a life cycle analysis

approach, the reductions in CO₂ emissions by replacing Portland cement with geopolymers strongly vary, but they are estimated to be of 30% at least [6], and can be as high as 80% [7]. Nowadays, geopolymers are one of the most promising material to replace Portland cement, because of their powerful characteristics including good mechanical properties, low permeability to liquids, resistance to high temperatures and acidic attack, etc. [8]. There has been a series of reviews related to geopolymer in the past few years testifying of the increasing interest for this material [8–18].

Incorporation of industrial wastes into cementing materials (by Stabilization and Solidification i.e. S/S¹) is well known, because it offers assurance of chemical stabilization of many compounds and produces a mechanically stable waste form [19–21]. However, the stabilization of organic liquids (OL) in Ordinary Portland Cement (OPC) strongly retards and interferes with cement setting, and organic liquids usually do not form strong chemical bonds within the cement as some inorganics do [22–24]. Due to these issues, geopolymers have been proposed instead of OPC for the treatment of OL wastes; the influence of OL on geopolymer properties has been observed as less important [25,26].

Hydration of OPC is based on dissolution-precipitation reactions. The

* Corresponding author.

E-mail address: catherine.davy@centraledelille.fr (C. Davy).

¹ Stabilization and solidification (S/S) is a process by which contaminants are immobilized and rendered immobile.

<https://doi.org/10.1016/j.ceramint.2020.11.239>

Received 18 September 2020; Received in revised form 25 November 2020; Accepted 29 November 2020

Available online 3 December 2020

0272-8842/© 2020 The Author(s).

Published by Elsevier Ltd.

This is an open access article under the CC BY-NC-ND license

<http://creativecommons.org/licenses/by-nc-nd/4.0/>

Glossary			
AAF	Alkali-activated Fly ash	NAF	Non-Aqueous drilling Fluid
AAM	Alkali-activated material	OBM	Oil-Based Mud
CTAB	Cetyl Trimethyl Ammonium Bromide or Cetrimonium bromide	OK	Odorless Kerosene
EDS	Energy-Dispersive X-ray Spectroscopy	OL	Organic Liquid
GEOIL	Composite made of Geopolymer and OIL, i.e. Oil-containing geopolymer	OPC	Ordinary Portland Cement
GP	GeoPolymer	PCM	Phase Changing Material
IAEA	International Atomic Energy Agency	PEG	Polyethylene Glycol
FT-IR	Fourier Transform Infrared Spectroscopy	QAS	Quaternary Ammonium Salt
MK	MetaKaolin	SBM	Synthetic-Based Mud
		SEM	Scanning Electron Microscopy
		S/S	Stabilization/Solidification
		TBP	TriButyl Phosphate

anhydrous phases dissolve in water until saturation at which the hydrates precipitate through a nucleation process. The main reacting phases in OPC² are Alite (C₃S), Belite (C₂S) and Celite (C₃A and C₄AF), which dissolution-precipitation reactions provide Calcium Aluminate and Silicate Hydrates (C-A-S-H); C-A-S-H are amorphous, with an atomic structure arrangement based on lamellar tobermorite models [27,28].

Geopolymers belong to alkali-activated materials (AAM). Unlike OPC, AAM (and geopolymers) require a strong alkaline (e.g. NaOH) source to accelerate the dissolution of various inorganic precursors [29]. Theoretically, any material composed of reactive silicates and aluminates can be alkali-activated. Two main types of AAM can be distinguished, depending on the amount of Ca present in the raw materials³ [12,30,31]. C-(N)-A-S-H type gels are formed in Ca-rich systems through hydration mechanisms similar to the formation of C-A-S-H in Portland cements [32]. N-A-S-(H) type gels are formed in Ca-poor systems through polycondensation reactions, also called geopolymerization [33]. It is noted that water is part of C-A-S-H structures (through hydration reactions). On the opposite, for N-A-S-(H) tridimensional aluminosilicate networks, water is only required as a dissolution medium and is released upon gel formation (i.e. after poly-condensation). These fundamental differences in raw materials, reactivity or structures are starting points to understand the distinct behavior of both systems in the presence of liquid organic species.

In this review, three methods for the incorporation of OL into cementing materials, and more specifically into geopolymers, are distinguished (Fig. 1):

(i) Direct incorporation into the reactive slurry, (ii) Pre-emulsification prior to the addition of the solid precursor, (iii) Solid impregnation prior to the addition into the reactive mixture. In the following, the processing features of these methods will be discussed and compared depending on the properties required for the end applications.

Aside from the S/S of industrial waste, the significant efficiency of geopolymers to incorporate OL offers the possibility to expand the use of these composite materials to a number of applications. Two of the main applications already under strong investigation (apart from S/S) will be presented in this paper. These are the preparation of geopolymer foams by emulsion templating of vegetable oils, and the incorporation of organic polymers to design composite materials with reinforced or emerging properties.

² The cementing nomenclature consists of abbreviating the oxides and to replace them by the following capital letters: CaO = C; SiO₂ = S; Al₂O₃ = A; Fe₂O₃ = F; H₂O = H; Na₂O₃ = N.

³ Systems for which the molar ratio Ca/(Si + Al) is higher than 1 are considered rich in Ca.

2. Processing routes

This section describes the main processing routes to introduce OL into cementing materials (OPC and AAM⁴). Usually, Portland cement powder is mixed with water, whereas AAM powders are activated with an alkaline silicate aqueous solution (or with water, in the case of “one part geopolymers” [30]). Therefore, the addition of an extra liquid (OL) which is non-miscible with water is adding complexity to the system, because it will be made up of two distinct liquid phases and of a high amount of solid particles. Contrarily to the obvious, the OL is not necessarily incorporated at the end of the process, i.e. directly into the reactive cement slurry, but it can be introduced at different stages of the composite manufacturing, using different approaches. Fig. 1 presents a simplified schematic description of the three main processing routes for the incorporation of OL into cementing materials:

- Route 1 represents the *direct* process. First, the cement paste slurry is produced by dispersing the solid precursors in the aqueous solution. The OL is then directly incorporated into the slurry under strong mechanical mixing before the cement hardens.
- Route 2 represents the *pre-emulsification* process. First, the OL is emulsified in the activating solution still free from any solid precursor. As soon as a stable emulsion of the OL in the aqueous activating solution (O/W⁵) is obtained, the solid precursor is added to the emulsion to initiate cement hardening.
- Route 3 represents the *solid impregnation* process. This process consists of impregnating the OL on a solid powder. It can be divided into two distinct paths depending on the type of powder that is impregnated:
 - 3.1: The OL is impregnated on the cementing precursor itself and then mixed with the activating solution.
 - 3.2: The organic liquid is impregnated on a dedicated adsorbing powder before being added to the cement slurry.

2.1. Direct incorporation

The direct incorporation is a common procedure because of its simplicity (Fig. 1, route 1). All the components are successively introduced into a single container, which is also called “one pot” mixing [34]; the order of addition is very important. As mentioned earlier, the reactive slurries leading to the formation of cementing materials are in fact aqueous solutions, highly loaded with solid particles. In such instance, the addition of a water-immiscible liquid (the OL) into the reactive

⁴ In order to simplify, OPC and AAM will be referred as cement throughout this document, unless stated otherwise.

⁵ W = Water and O = Oil.

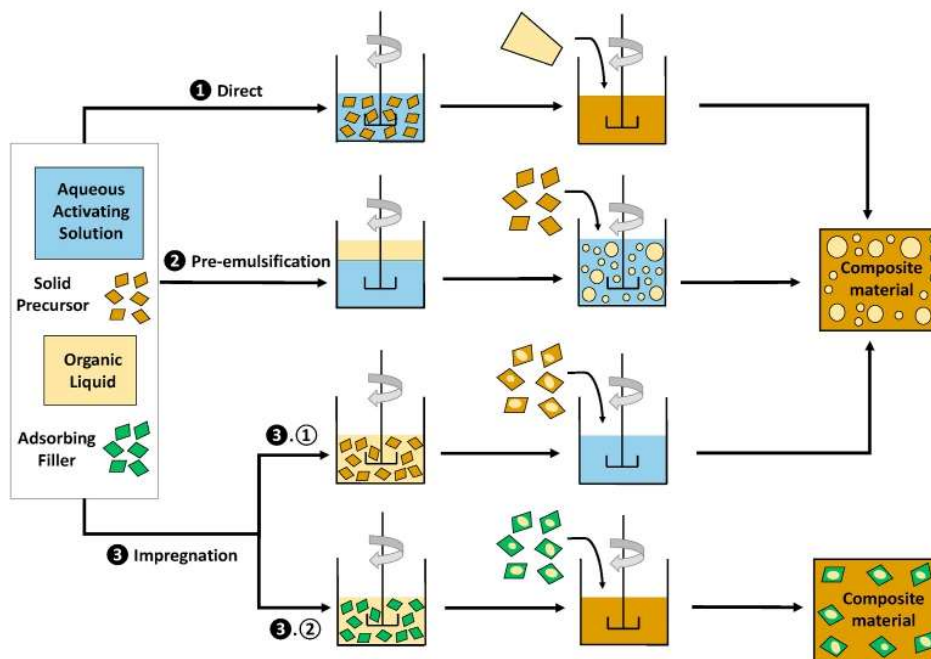


Fig. 1. Simplified schematic representation of the three main processing routes of incorporation of OL into Portland cement or alkali-activated materials. The sizes of the components are not scaled.

aqueous slurry resembles the formulation of an emulsion, in which the dispersed liquid is likely to undergo spontaneous coalescence to minimize the overall Gibbs free energy of the liquid-liquid interface [35]. An advantage of the direct route is the intrinsic high viscosity of the cement slurry, which increases the shear stress applied to the dispersed liquid, thus promoting the creation of smaller droplets. Viscosities of cementing slurries (OPC and AAM) are hundreds of times higher than that of water, depending on the formulation parameters [36,37]. In her study on emulsion fragmentation [38], Mabilie studied the influence of viscosity (η) of the continuous phase on the droplet size distribution. Keeping the fraction of dispersed phase (2.5 wt%) and the shear rate constant ($\dot{\gamma} = 500 \text{ s}^{-1}$), the author played with the viscous shear stress ($\sigma = \eta\dot{\gamma}$) by changing the viscosity of the continuous phase. The viscosity ratio between continuous and dispersed phase and the interfacial tension, both having an impact on emulsion formulation where also kept constant at 1.0 and 6.0 mN m^{-1} respectively. It was observed that the higher the viscosity of the continuous phase (i.e. the higher the viscous shear stress), the smaller and the more homogeneous the droplet size distribution. A gradually increasing shear stress (from 170 to 475 Pa) creates gradually decreasing droplet size distributions from 10 to $5 \mu\text{m}$. This was demonstrated for concentrated emulsions up to 75 wt% of the dispersed phase. Another advantage of having a higher viscosity of the continuous phase is that it hinders the coalescence of the formed droplets. To illustrate this latter point, sedimentation or creaming may occur over time, and are indirectly responsible for droplets coalescence. The velocity of coalescence and creaming is driven by several parameters, in particular the viscosity of the continuous phase. It is described using the Stokes equation [39]:

$$v = \frac{2(\rho_p - \rho_f)gr^2}{9\mu} \quad (1)$$

where v , ρ_p , ρ_f , g , r , μ are respectively the droplet velocity (m/s), the droplet density (kg/m^3), the density of the dispersing phase (kg/m^3), the gravity field (m/s^2), the spherical droplet radius (m) and the dynamic viscosity of the medium (Pa.s). This relationship shows that sedimentation or creaming are slowed down as the viscosity of the dispersing

phase increases, therefore decreasing flocculation and hence coalescence.

Several types of OL have been incorporated through the direct route. Masrullita et al. [40] incorporated 10 wt% of paraffin oil into OPC that way. Several works describe the easy direct incorporation of vegetable oils into geopolymer materials, even at high oil amounts [41–43]. Davy et al. [44] directly immobilized a mineral oil in geopolymer up to 60 vol%. Despite the viscosity of the geopolymer suspension, the phases can undergo separation, especially when the amount of incorporated liquid is high [45,46].

Another concern appears when the viscosity difference is high, i.e. for organic liquids with low viscosity [38]. If the viscosity difference is too pronounced, the droplets maintain an equilibrium state upon shearing and do not break [38], therefore keeping a broad size more likely to undergo coalescence. Grace [47] evidenced that the closer the viscosity ratio is to 1, the easier the incorporation of the second liquid; the incorporation becomes more difficult as the viscosity ratio diverges from 1 in either directions (bigger or smaller than 1). Composite organic/inorganic materials have been prepared through the direct route by mixing geopolymer slurries with curable epoxy resins by hand mixing only, hence testifying of the easiness of incorporation [45]. In this process, the key step is to perform the incorporation of the curable resin at the adequate polymerization rate in order to avoid phase separation. As an explanation, several authors mention a better chemical compatibility between the organic and the inorganic phases at an early stage of resin polymerization, but there may be a viscosity effect as well. The resin is initially very fluid and becomes more viscous over time (with the progression of its hardening), hence decreasing the viscosity difference between the two liquid phases.

Finally, it is worth noting that for most of the direct incorporation processes presented in this section, no additives (e.g. surfactants) have been necessary to reduce the interfacial tension and promote the OL incorporation, even at high amounts (up to 60 vol%). However, the counterpart of not adding any surfactant is the lack of control over droplet size distributions and homogeneity [44].

2.2. Pre-emulsification

When manufacturing OL/cement composites, it is crucial to avoid phase separation between the OL and the slurry until hardening of the cementing material. The higher the amount of OL, the most likely the emulsion is to undergo phase separation. Even if the OL incorporation is achieved, the droplet size distribution may be large and inhomogeneous [44]. To avoid these issues, the pre-emulsification process (Fig. 1, Route 2) was developed. It consists in emulsifying the OL into the activating solution (and make an oil-in-water system O/W) prior to the addition of solid precursors and fillers. It is reasonably assumed that if the emulsion shows a good stability over time, the cement material will have sufficient time to set before the system goes back to its thermodynamically most stable state, the latter being reached when the two liquids are separated. In addition, by proceeding that way, it is also easier to control the droplet size distribution and homogeneity. In return, that process requires an extra step and the use of additives promoting the stability of the emulsion (e.g. surfactants or polymers). Surfactants are required to both decrease the interfacial tension between the two liquids and stabilize the droplets. Without surfactant, the viscosity of the aqueous activating solution is not high enough to stabilize the emulsion for a sufficient time. However, during the emulsion step, the system is still free from any solid particles that might act as Pickering stabilizers as described by Cantarel et al. [25].

The International Atomic Energy Agency (IAEA) mentioned a significant increase in the waste proportion which can be incorporated when using the pre-emulsification technique [48]. In Ref. [48], only 12 vol% of waste could be incorporated using the direct route, whereas up to 35 vol% could be incorporated using the pre-emulsification technique, although the latter requires a huge amount of surfactant (30 vol %).

In particular, Zhang et al. [49] solidified a spent radioactive organic solvent (by about 10 wt%), namely Tri-Butyl Phosphate/Odorless Kerosene (TBP/OK), in Portland cement added with Zeolite, calcium hydroxide or non ionic MR-1 type emulsifier; they named this technique emulsification-solidification by analogy to the stabilization-solidification (S/S) process. Dong et al. [50] successfully immobilized up to 18 wt% of TBP/OK using 4 wt% of Tween 80 (i.e. Polyethylene glycol sorbitan monooleate, CAS Number: 9005-65-6) as an emulsifier in a phosphate acid-based geopolymer. Cantarel et al. [25, 36, 51] stabilized various organic liquids in geopolymer materials up to 70 vol% by using different surfactants; for instance, for highly fluid hexadecane, a CetylTrimethylAmmonium Bromide (CTAB) cationic surfactant is essential. Cantarel et al. focused on the incorporation of 20 vol % OL, and were able to obtain a small and homogeneous distribution of oil droplets ranging from a few micrometers to about 50 μm [36]. Although replacing OL by air, Glad and Kriven were able to synthesize highly porous geopolymers with tailored pore sizes ranging from 200 nm to 10 μm using hydrophobic polymers, i.e. alkoxy silanes such as dimethyldiethoxysilane (DIDE) $[(\text{CH}_3)_2(\text{OCH}_2\text{CH}_3)_2\text{Si}]$ [52].

Smitha et al. [53] went a step further, and prepared an emulsion of industrial lubricating oil by phase inversion in OPC. In practice, the aqueous solution is progressively added under strong mechanical stirring to the oil until a creamy emulsion is obtained; the optimal formulation is of 25%wt oil to cement ratio, i.e. about 10%vol; NaOH serves as both emulsifier and setting accelerator. Preparing an emulsion by catastrophic inversion (W/O to O/W or vice versa) is known to provide high stability because the droplets formed are very small. This is due to the fact that, at the point of phase inversion, the curvature radius of oil and water are equal to zero, allowing the formation of very small droplets (as small as 200 nm [54]); these are significantly more stable than bigger ones.

Skalle et al. [55] worked on an interesting hybrid mechanism combining both the direct and the pre-emulsification processing routes. First, a W/O emulsion is created (Fig. 1, Route 2) before being directly added to a reactive cement slurry (O/W) (Fig. 1, Route 1), providing a

double emulsion.

As mentioned earlier in this section, the use of surfactant is most of the time mandatory to create the emulsions in the presented examples, but by proceeding that way, the incorporation is controlled throughout the process.

2.3. Solid impregnation

Among the three main processing routes, the solid impregnation process (Fig. 1, Route 3) is not as obvious as the direct and pre-emulsification routes. The amount of OL that can be incorporated is low in comparison with the two aforementioned routes, i.e. generally not exceeding a few percent. The advantage of using this route lies in the fact that the organic liquid is adsorbed onto a solid material early in the process and it is added in the form of a solid in the cement slurry; additives such as surfactants are generally omitted. Therefore, there is no emulsion to be considered, and no risk of phase separation that may occur in the course of cementation. The incorporation of a solid in a cement material is easier than the incorporation of a liquid, and the properties of the final composites, especially mechanical performance, are expected to be less impacted.

Some authors are using the impregnation route in order to mimic oil polluted sands, and to understand in what conditions they can be used as fillers to produce concretes in particular areas of the world [56]. It has been evidenced that a quantity of diesel oil contamination as little as 2%, fixed to sand, causes a significant decrease in compressive strength of the resulting cement materials. Moreover, when following the evolution of compressive strength over time, the impact of contaminated sand is especially observed in the late hardening phase of the material, and less in the initial setting phase.

Other studies evidenced that hydration reactions of OPC are strongly affected by the addition of small amounts of organic compounds, leading to setting and hardening issues [20, 57–59]. However, by using the impregnation route, Almabrok et al. [60] successfully stabilized industrial 10 W mineral oil up to 10 wt% in OPC. They compared the preliminary wetting of the cement precursor or of the sand by the oil before adding water, but there was no significant difference; the compressive strength is divided by a factor 3 in both cases. By adding non swelling kaolinite clay, which acts as an oil adsorbent, the authors were able to lower the impact on mechanical properties to a factor of 2.5.

The IAEA studied the impregnation process of turbine and pump oils, and described it as the conversion of OL into dry particles prior to cementation in Portland cement, using a variety of adsorbents (e.g. natural or synthetic fibers, vermiculite, clays, diatomaceous earth, alkyl styrene polymer beads) [48]. According to the authors, this technique is more tolerant of batch-to-batch waste variability and higher waste incorporation of up to 56 vol% could be attained; this contrasts with other studies using the impregnation process, which generally allow the incorporation of a lower amount of liquid (below 10% and often at a few percent only). However, the IAEA also recognizes that a number of factors affect the efficiency of the process, including the OL viscosity. The associated mechanical performance of the composites is not provided.

The OL waste needing stabilization in cementing materials often contains toxic species, which must not leach out of the solidified material. Therefore, the oil impregnation on an appropriate adsorbent is helpful to avoid leaching and immobilize the toxic species. For instance, Sazonov et al. [61] decreased the tritium leaching rate by adsorbing tritiated oil on various adsorbents (zeolites, active alumina, activated carbon); the best results are achieved with activated carbon. Montgomery et al. [24] used a commercially available QAS-clay⁶ prior to

⁶ QAS-clay: Quaternary Ammonium Salt exchanged clay. These clays are modified beforehand in order to adsorb organic compounds, e.g. by being added with CTAB (CTAB: CetylTrimethylAmmonium Bromide).

incorporation. QAS-clays are specifically designed to strongly adsorb organic compounds. In Ref. [24], the cement-based solidification of organic effluent waste adsorbed on QAS-clays provides solid bodies, with unconfined compressive strength significantly higher than the standard requirement of 350 kPa. Moreover, due to the strong binding of organics to QAS-clay, their leaching from the stabilized products is very low. The total organic carbon (TOC) is reduced by over 90% for each of the tested waste compared with unsolidified ones; the release of heavy metals is similarly reduced.

El-Naggar et al. [62] impregnated an organic solvent extraction liquid (2 hydroxy-5-nonylacetophenon) on metakaolin, before adding the activating solution to achieve a geopolymer-solvent composite (Fig. 1, 3.1). Leaching tests, and other characterizations, of the formulations containing the solvent extraction liquid proved that the solvent did not move out of the solidified cement composite, even under severe acidic attack. The compressive strength was slightly impacted, as shown by the formulation containing 8%vol of solvent (28 MPa), only experiencing a 4 MPa decrease in comparison with the reference material (32 MPa). The strength of formulations containing 8%vol solvent could be further improved from 28 MPa to 54 MPa by increasing the SiO₂/Na₂O molar ratio. The authors evidenced the good compatibility of the solvent with the geopolymer network and its low impact on the hardened material, which contrasts with OPC.

Cuccia et al. [63,64] immobilized radioactive waste oils in geopolymers, by preliminary adsorbing the oil on a commercial polymer. The resulting composite material complies with local leaching rate regulations but does not fulfill mechanical strength criteria (its compressive strength is lower than 10 MPa). However, the compressive strength of the pure geopolymer formulation is of only about 19 MPa. This means that the poor mechanical properties of the waste containing sample is not necessarily attributed to a bad oil/geopolymer compatibility but rather to the low mechanical properties of the pure geopolymer formulation. Formulation parameters (especially the Si/Al molar ratio) have a strong impact on the connectivity of the aluminosilicate network formed during geopolymerization, and hence, on the mechanical properties of the geopolymer materials [65].

2.4. Summary

Although possible, the addition of an extra immiscible liquid into a cementing material generally increases the setting time, lowers the mechanical properties, disturbs the flow of reactive slurries, may induce leaching of the OL, etc. However, by using the most appropriate incorporation process in accordance with the end applications, these issues can be overcome. Unfortunately, studies comparing the different processing routes at the same time are scarce [66]. Table 1 compares the processing routes and aims to summarize the advantages and drawbacks of using one or another, in order to guide the decision of the most appropriate path for a specific application. Moreover, all the examples discussed in this section are generally at a laboratory scale. At the industrial scale, the pre-emulsification and impregnation processes would be more challenging because they involve an additional step, which, in some cases (e.g. when dealing with radioactive waste), might be an issue. Moreover, these two processing routes require the addition of costly surfactants or adsorbents, which might be a limiting factor as well. Other incorporation techniques exist, such as the incorporation through diffusion of the OL into the cement pore network after cement hardening, but they are less commonly used [67].

3. Aimed applications

In the past few years, an increasing interest for the incorporation of OL into inorganic geopolymers has been observed, because it offers a wide variety of unique applications. This section aims at presenting the three main applications of the incorporation of OL into geopolymers, as summarized in Fig. 2. The OL is introduced in the fresh geopolymer

mortar following one of the processes described previously (Fig. 1). Interestingly, the type of oil appears to dictate the corresponding application, as follows:

- Mineral oils → Immobilization of industrial waste by S/S
- Vegetable oils → Production of highly porous materials
- Organic polymers → Production of materials with improved and/or emerging properties

3.1. Immobilization of waste OL (mineral oils)

3.1.1. Background on oil immobilization into Ordinary Portland Cement (OPC)

Before detailing the immobilization of OL waste into geopolymers, it is useful to recall the use of Portland cement for that purpose, because it has been widely and successfully used for the immobilization of many compounds.

As detailed earlier, according to IAEA, the direct immobilization of radioactive OL waste by cementation (i.e. S/S) is one of the best options because it is simple and cost effective [48]. It offers assurance of chemical stabilization of many compounds by producing a mechanically stable waste form, and OPC has been widely studied for that purpose [68]. A varied but non-exhaustive list of examples is presented below.

Early studies on that topic were presented by Clark et al. [66]. Their work aimed to determine the most suitable solidification agent for the disposal of radioactively contaminated OL wastes. Initially, the immobilization of a lubricating oil (mineral oil) in pure OPC from 12 to 50 vol % was performed using the direct process (Fig. 1, Route 1). All the samples ended in soft appearing materials, indicating that OPC alone is not a very effective media to solidify oily wastes. Then, vermiculite, an adsorbent clay that can retain liquids within the pores of its particle aggregates, as well as between the clay particles themselves, was used to adsorb the oil prior to solidification in OPC (Fig. 1, Route 3). OPC samples prepared with oil-saturated vermiculite set in about three days, which provided convenient monolithic solids; however, all had an initial oily appearance on the surface with traces of free liquid, and were not considered suitable. This is why a third technique, developed by the Nuclear Technology Corporation (NUTEK) was used. It consists of a chemical process to solidify radioactive waste oils, by combining an emulsifying agent (Fig. 1, Route 2) and a setting time accelerator, both aiming at preventing coalescence of the liquid before solidification. Adequate solid monoliths were obtained with this procedure, and no free liquid was observed at oil incorporation rates up to 30 vol%. Being the best option for the lubricating oil, the NUTEK technology was then used in the same way to solidify a complex mixture of organic liquids, but it was not very efficient. The only acceptable sample contained only 6 wt% of the liquid mixture, and even at this low proportion, the smell of organic vapors was strong. The conclusion of this research is that the pre-emulsification process using the NUTEK procedure is the best option for stabilizing lubricating oil, but in the case of an organic mixture, OPC is not a suitable option.

Masrulita et al. [40] stabilized paraffin oil in OPC and observed that the more paraffin is added, the lower the compressive strength. According to the authors, this is because the cement cannot efficiently coalesce with the added hydrocarbon; instead, cavities are formed in the composite materials, resulting in lower densities and therefore lower compressive strength.

OPC has often been used for S/S of TBP/OK, which is a common mixture for extraction of radioactive waste [34,69]. However, the addition of TBP strongly decreases the compressive strength of the resulting solid materials [70]. In a recent study [49], about 10 wt% of simulated radioactive spent organic solvent (TBP/OK) was solidified with OPC by the emulsification–solidification method (Fig. 1, Route 2). X-Ray Diffraction (XRD) analysis illustrated that the incorporation of both TBP/OK and the emulsifier did not change the cement hydration

Table 1
Summary of advantages and drawbacks of the main incorporation processing routes.

	Advantages	Drawbacks
Direct	<ul style="list-style-type: none"> o Easy incorporation in one step o High amount of oil o No extra additives required 	<ul style="list-style-type: none"> o Phase separation before setting might occur
Pre-emulsification	<ul style="list-style-type: none"> o High amount of oil o Phase separation controlled by preliminary emulsification o Controlled size of oils droplets 	<ul style="list-style-type: none"> o Two steps process o Addition of surfactants required
Impregnation	<ul style="list-style-type: none"> o Useful for high leachable toxic compounds (adsorption on solid particles) o No phase separation because the liquid is solidified beforehand 	<ul style="list-style-type: none"> o Low amount of oil incorporated o Two step process o Requires the addition of a solid adsorbent (if not impregnated on the cementing precursor) o Cost of solid adsorbent

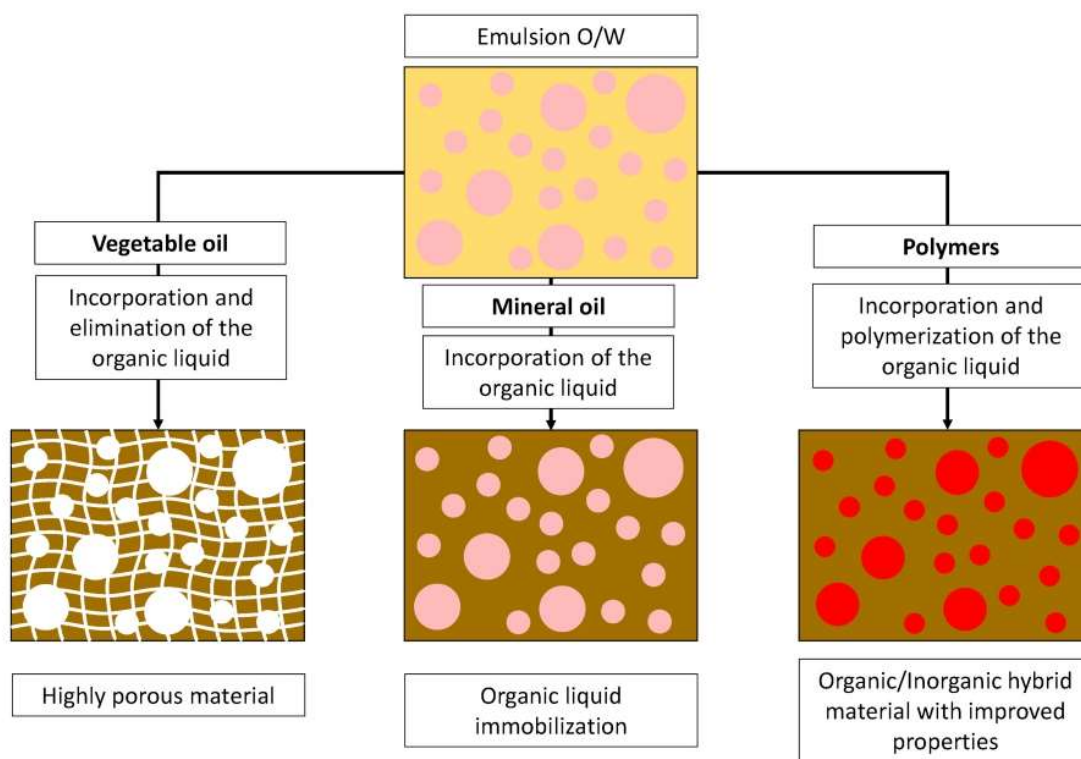


Fig. 2. Schematic representation of the three main application of incorporating OL into geopolymer materials: Incorporation of vegetable oil to produce geopolymer foams (left), stabilization of mineral waste oils (middle), addition of organic polymers to design reinforced materials (right).

products. The resulting compressive strength of the composite material is of about 19 MPa. Unfortunately, no comparison of mechanical properties with a liquid free cement was performed.

Several authors presented the impact of crude oil on compressive strength [71–73]. As discussed earlier, oil-contaminated sands used as additives in cement manufacturing strongly reduces the compressive strength of concretes. For instance, sands contaminated with crude oil at only 5 wt% reduces the compressive strength at 28 days of concretes by almost 50% (32–18 MPa) [71].

Almabrok et al. [60,74,75] studied the incorporation of various OL into Portland cement using the impregnation route (Fig. 1, Route 3), in order to avoid side effects on setting time and strength development. Despite impregnation, the addition of oil strongly affected cement setting and strength development, largely due to the perturbation of cement hydration. The addition of more than 10% of mineral oil led to unacceptable materials (compressive strength < 20 MPa) [60]. The addition of contaminated aggregates at 10 wt% with canola oil, refined mineral oil or crude oil, decreased the 28-day compressive strength by 71%, 75%

and 50%, respectively [74]. Moreover, calorimetric measurements highlight that the hydration of C_3S and C_3A is inhibited by the addition of oil, despite their adsorption prior to solidification. Hydration reactions are differently impacted by the type of oil; mineral oil is the most influencing one, whereas crude oil has only a slight impact. This testifies that inhibition is not due to the addition of oil-contaminated aggregates but rather to an interaction between the oils and the hydrating phases [74].

A recent study summarizes the issues faced by the use of Portland cement for gas well cementing, because of the intermixing of cement slurry and drilling mud⁷ that will almost inevitably occur [37]. In most

⁷ In wellbore processes, drilling muds cool the drill bit and carries the rock cuttings along back to the surface. Most of the muds are oil-based, using direct products of petroleum refining such as diesel oil or mineral oil. Sometimes, synthetic-based muds are prepared using highly refined fluid compounds that are more adapted to property specifications than traditional petroleum-based oils.

cases, the mud-contaminated cement undergoes failure, because it does not harden properly. As the cement slurry becomes more contaminated, it strongly thickens until it cannot flow anymore, which is also a major issue. According to the authors, a mud-to-cement conversion technique has not been successfully developed and applied for NAFs⁹ (Non-Aqueous drilling Fluids) so far. Contamination by NAFs is for instance detrimental to the strength development of Portland cement slurries, with as strong a drop as of 50% of the original compressive strength at 15 vol% of contamination [76]. Comparatively, alkali-activated fly ash (AAF) slurries exhibit superior performances against NAFs contamination compared to Portland cement [37]. According to the authors, this could be due to the breakdown of NAF emulsions, releasing an excess amount of water. In AAF containing a low Ca amount, water is not chemically bound to the N-A-S-(H) gel formed, i. e. it is only acting as the reaction medium, whereas in Portland cement water is part of the C-A-S-H structure. Therefore, changes in water amount might have less effect on the strength development of AAF than Portland cement. Unlike Portland cement slurries, AAF slurries develop sufficient compressive strength for cementation purposes at high levels of mud contamination. An incorporation rate of up to 40 vol% of Synthetic Based Mud (SBM)⁹ in AAF leads to materials with measurable compressive strength, while Portland cement loses the ability to harden with 30 vol% SBM contamination. Moreover, the incorporation of SBM into AAF provides flowable slurries (even at 40 vol%), whereas Portland cement slurries become too viscous. As for strength development, the excess of water released by the breakdown of the SBM emulsion could explain the decrease in viscosity observed in AAF slurries. On the contrary, the thickening of Portland cement slurries could be explained by capillary forces, which depend on the affinity of particles for both liquids [77–79]. In liquid-liquid-particle ternary systems, the addition of the second immiscible liquid to the particles suspension in the first liquid results in an increase in viscosity. In such systems driven by capillary forces, the second liquid stands between the particles leading to agglomerate formation, which is characterized by an increase in viscosity. Finally, AAF could efficiently solidify two types of SBMs and two types of Oil-Based Muds (OBMs)¹⁰, meaning that the mud-to-cement conversion in AAF is a versatile method. Likewise, AAF materials are more resistant than Portland cement to a contamination by water-based drilling [80]. The AAF solid precursor used in that study is class F¹¹ fly ash, containing a low amount of Ca, leading to the formation of N-A-S-H i. e. to a geopolymer.

3.1.2. Geopolymers: emerging materials as alternatives for OL immobilization

Table 2 below summarizes a number of works performed on the immobilization of OL into geopolymer materials and published in the recent years.

3.1.2.1. Waste immobilization. The immobilization of radioactive mineral oils in geopolymer materials, also named GEOIL (for GEopolymer/OIL) composites, has been extensively studied in the recent years [25, 36,44,51]. First, the feasibility of incorporating up to 70 vol% of a mineral oil in geopolymers was demonstrated, while maintaining the formation of strong monolithic solids [51]. Then, the influence of oil addition on the mechanical performance and leaching rate of GEOIL has

been studied [36]. For oils of viscosity on the order of 0.1–2 Pa s, an easy incorporation of up to 20 vol% in a geopolymer matrix was demonstrated, where the oil takes the form of an emulsion made of homogeneous and spherical droplets. The droplet size ranges from a few μm to 50 μm , with the diameter of the main population being about 5 μm , showing the good dispersion of the oil in the geopolymer material. As expected, the compressive strength decreases when the oil content increases, but the effect is not as pronounced as in OPC matrices. In particular, at 30 days, the decrease in compressive strength for GEOIL containing 20 vol% oil is about 35% (32–22 MPa) compared to the geopolymer without oil (reference GP); with 14 vol% oil, the compressive strength of GEOIL is smaller by only 12.5% when compared to the reference GP (32–28 MPa) [36]. Moreover, the cumulative quantity of oil compounds released in the leachate at 30 days does not exceed 0.19% of the organic material initially encapsulated in the sample, demonstrating the efficiency of the oil encapsulation in GEOIL composite. Unlike for Portland cement, rheological measurements and Fourier Transform InfraRed spectroscopy (FT-IR) have shown that there is no change in the geopolymerization kinetics (in particular in the setting time) [25]. The reason probably lies in the fact that geopolymers undergo polycondensation reactions to build their gel network, whereas Portland cement undergoes hydration mechanisms, which is fundamentally different.

Despite the fact that highly fluid OL (such as hexadecane) can be efficiently stabilized into geopolymer matrices, the addition of surfactants can be of use to better control the droplet size distribution, improve the incorporation quality and the rheology of the paste. In Ref. [25], CTAB and Pluronic L35¹² surfactants have been tested (respectively cationic and nonionic surfactant). Both surfactants provide GEOILs with rather homogeneous size distributions of oil droplets in the range of 10–100 μm (Fig. 3 [25]). Using surfactants also results in composite pastes with different rheological behaviors, thanks to the effect of the surfactant molecules at the intermolecular level.

At such scale, surfactants have the ability to position themselves at the surface of oil droplets through their polar head, leading to the formation of hydrophobic forces between droplets; the repulsive forces between these hydrophobically modified droplets are due to the interaction of the nonpolar tails of the surfactant molecules attached to the oil surface. The resulting system consists of a “shell” around each oil droplet, and induces an increase in viscosity. Several authors observed this phenomenon with cationic surfactants (for which it is strongest, owing to the strong adsorption on negatively charged particles) [83–85] and nonionic surfactants [86–88]. Cantarel et al. [25] also concluded that metakaolin particles surrounded oil droplets and acted as Pickering stabilizers (Fig. 4). Without mentioning the Pickering effect, Glad and Kriven present a similar behavior for metakaolin around oil droplets [52].

However, the quantity and type of surfactant should be chosen carefully when incorporating OL in geopolymers, particularly for systems with a high volume fraction of dispersed phase. In such context, 3D X-Ray micro-computed tomography quantifies the spatial distribution of the oil droplets in GEOIL (Fig. 5 [44]) and provides a connectivity analysis of the 3D oil emulsion. This allows to analyze whether the oil emulsion percolates (and may leach out of GEOIL). With an industrial gear oil immobilized at up to 60 vol%, the oil percolation threshold is reached from 27 vol% incorporation.

In order to overcome the undesirable leaching of OL with the direct immobilization technique as with Portland cement [89], El-Naggar et al. [62] have investigated geopolymers as an alternative to immobilize a solvent extraction liquid of interest in the nuclear industry, loaded with Cu²⁺ beforehand (LIX-84, made up of 2-hydroxy-5-nonylaceto-phenon). FT-IR analyses were performed after leaching tests to verify that the solvent was still present in the materials and proved the compatibility

⁹ NAFs are invert emulsions (water in oil) containing solids including organophilic clays, viscosity modifying polymers and dispersing agents.

⁹ SBM (Synthetic-Based Mud): Invert emulsion where synthetic oil (based on C₁₆–C₁₈ internal olefins) is the continuous phase and CaCl₂ brine is the dispersed phase. Also contains various additives.

¹⁰ OBM (Oil-Based Mud): Mineral oil-based mud.

¹¹ Several types of fly ashes exist and are classified according to their oxide contents. Class F fly ash is poor in CaO and contains a significant amount of Al₂O₃.

¹² Pluronic L35: Commercial nonionic surfactant.

Table 2

Immobilization of mineral waste oils in geopolymer materials; MK = Metakaolin, FA = Fly ash, vol% = volume percentage, wt.% = weight percentage, CTAB = CetylTrimethylAmmonium Bromide (cationic surfactant), SBM = Synthetic Based Mud, OBM = Oil Based Mud. Pluronic L35 and Tween 80 are non-ionic surfactants.

Alumino-silicates sources	Activating solution	Oil type	Amount	Surfactant	Incorporation process (Fig. 1)	Ref.
MK	Acid: H ₃ PO ₄	TriButyl Phosphate/odorless kerosene (TBP/OK)	6-18 wt%	Tween 80	① Pre-emulsification	[50]
FA	Alkaline: NaOH	Paraffin wax	8-15 wt%	None	②, ③. Impregnation on lightweight coarse aggregates	[81]
MK	NaOH	Dodecanol	About 3.5 wt %	CTAB	Impregnation after GP set ^a	[67]
MK	NaOH	Motor oil	5-60 vol%	None	① Direct	[44]
MK	NaOH	Motor oil (aliphatic compounds)	7-20 vol%	None	② Pre-emulsification	[36]
MK	NaOH	Hexadecane	20 vol%	CTAB or Pluronic L35 ^a	② Pre-emulsification	[25]
MK	NaOH	Lubricating oils	10 wt%	None	②, ③ Impregnation on commercial polymer	[63]
MK	NaOH	LIX84 (commercial solvent extraction liquid)	0–15%	None	③. Impregnation on MK	[62]
MK	NaOH	Dimethyldiethoxysilane (DIDE)	About 10 wt %	None	① Direct	[60]
FA	NaOH	SBM and OBM	10-40 vol%	None	① Direct	[37]
MK	NaOH, KOH	Hexadecane	20-70 wt%	None	① Direct	[82]

^a The solid geopolymer is left in touch with an excess of dodecanol at 60 °C for 30 min.

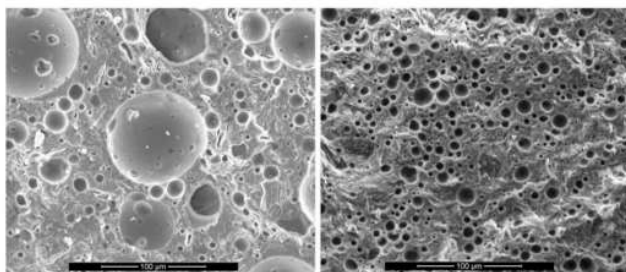


Fig. 3. Scanning electron micrograph of a calcinated GEOIL composite containing 20 vol% of hexadecane with CTAB (left) or L35 (right) surfactants [25].

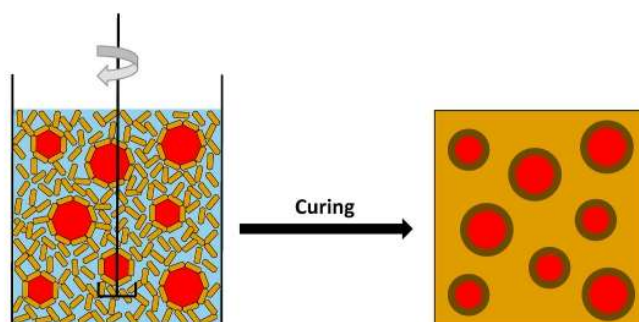


Fig. 4. Pickering-type stabilization of oil droplets in a fresh geopolymer mortar (left) providing encapsulated oil droplets after curing (right).

between geopolymers and LIX-84. Indeed, leaching experiments indicated that the formulations performed well, because most of the Cu²⁺ remained in the geopolymer material, even under severe acidic conditions (less than 5% of the total Cu²⁺ leached out).

Cuccia et al. [63] have studied the immobilization of radioactive waste oil in geopolymer materials with the impregnation process (Fig. 1, 3.2). They used two different types of adsorbents prior to solidification, i.e. bentonite and a commercial polymer (NOCHAR). For both kinds of adsorbents, the authors obtained geopolymer matrices with homogeneously distributed waste and leaching rates at 150 days compliant with local regulations.

Apart from alkaline activating conditions, geopolymers can also be

activated in acidic conditions. This is a valuable asset in specific applications where alkaline conditions are deleterious. In a recent study, phosphate acid-based geopolymers were investigated as a solidification technology for TBP/OK [50]. These acidic-synthesized geopolymers have reputed to have higher strength, durability, and thermal stability than alkali silicate-metakaolin geopolymers [90–93]. This is explained by the formation of berlinite (AlPO₄) resulting from the combination of Al³⁺ (from metakaolin) and PO₄³⁻ (from phosphoric acid). The presence of this crystalline phase reinforces the structure of geopolymers by filling air voids (porosity) [92,93]. In Ref. [50], the phosphate acid-based geopolymer has a high compressive strength of about 79 MPa, and that of solidified TBP/OK forms is up to 59 MPa. The compressive strength does not decrease drastically with increasing TBP/OK content. With 18 wt% of TBP/OK, the decrease in compressive strength is about 25%, which is significant but still more than acceptable considering the initial high value. Leaching tests demonstrate that a very limited amount of solidified TBP/OK is released from phosphate acid-based geopolymers, meaning that TBP/OK is physically well encapsulated within the solid body. The only drawback is with setting time, which significantly increases with the addition of TBP/OK.

3.1.2.2. Phase changing materials (PCM). The incorporation of phase changing materials (PCM) into geopolymers aims to produce smart materials, able to mitigate temperature changes in their vicinity. PCM are capable of changing phase from solid to liquid at a specific melting temperature (or vice versa), and it is usually low (i.e. below 100 °C). During the phase changing process, a certain amount of energy (i.e. heat) is captured from or released into the surrounding environment [94], retarding the change in temperature. Several studies have investigated the immobilization of PCM in building materials, such as thermal regulating panels [95]. More precisely, OL such as paraffin [81,96,97] or dodecanol [67], were incorporated into geopolymers to produce materials with smart thermal properties. A wall made-up of this type of material would be able to keep comfortable temperatures inside a building during daytime (by the endothermic melting of the PCM) and night-time (through the exothermic solidification of the PCM).

Using the direct incorporation (Fig. 1, Route 1), paraffin is distributed homogeneously in a geopolymer concrete, among voids and aggregates. However, after a number of temperature change cycles, a leakage of paraffin to the material surface is often encountered. In order to overcome that issue, paraffin can be pre-encapsulated or stored into small (inert and stable) closed polymer capsules to prevent leakage, before being mixed with concrete [96,97]. Shadnia et al. [97] studied

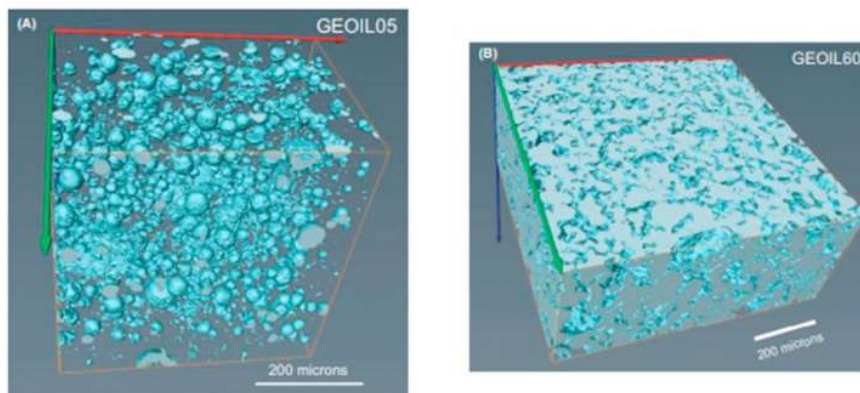


Fig. 5. Spatial representation obtained by X-ray micro-CT of the oil distribution (in light blue) in GEOIL composites containing 5 vol% (left) and 60 vol% (right) of oil. The oil volume is either not-percolating (left) or percolating (right) [44]. (For interpretation of the references to colour in this figure legend, the reader is referred to the Web version of this article.)

the incorporation of commercial micro-encapsulated PCM (paraffin) powder into geopolymer mortar. A decrease in mechanical properties is observed, but geopolymers with up to 20 vol% PCM incorporation are still convenient with compressive strength exceeding 15 MPa. The heat capacity curves of geopolymers added with PCM display endothermic peaks between 20 °C and 30 °C. This corresponds to the melting temperature range of the PCM material, which contrasts with the straight heat curve of the pure geopolymer material. The higher the amount of PCM, the higher the amplitude of the endothermic peak, meaning that incorporated PCM can effectively reduce the transport of heat through geopolymer bodies.

In a study by Sukontasukkul et al. [81], the PCM is impregnated on porous lightweight aggregates (Fig. 1, 3.2), which are then used as coarse aggregates in a geopolymer concrete mixture. The maximum incorporation is 60 vol% (40 vol% of PCM and 20 vol% of aggregates). As expected, the compressive strength decreases with the addition of pure lightweight aggregates (15–5 MPa with 60 vol% of aggregates), but it increases with the presence of paraffin in the aggregates, due to void filling by paraffin (5 MPa–7 MPa with aggregates loaded at 65 vol% of paraffin). The presence of paraffin significantly improves both thermal storage and heat insulation of geopolymer panels, as shown by the time delay of 22 min to reach the peak temperature (65 °C) and the ability to maintain the temperature higher than 55 °C inside the panel for more than 180 min after the end of heating.

Gasca-Tirado et al. [67] studied the use of dodecanol as PCM in geopolymers. The incorporation was performed after solidification of the geopolymer material, which is different from the incorporation routes presented earlier in this paper (Fig. 1). The solid bodies were immersed in an excess of liquid dodecanol at 60 °C, which then diffused into the material through its pore network. The effectiveness of CTAB is shown as a coupling agent between dodecanol and geopolymer; a surface treatment increases the maximum amount of incorporated dodecanol. However, the highest amount of dodecanol remains low (about 3 wt%) and further studies are needed to increase the incorporation capacity, in particular by modifying the geopolymer porosity. With the process involved, this method provides a percolating (connected) OL system.

3.2. Development of highly porous materials (mainly with vegetable oils)

Nowadays, porous geopolymers, also referred to as geopolymer foams, are becoming of interest because of their unique combination of properties, i.e. good thermal and chemical stability [15,98,99], high mechanical strength [100,101], low CO₂ emission and low energy use during their manufacture. They have been studied for a variety of applications, including membrane and membrane supports [102,103],

adsorbents and filters [104–109], catalysts [94,110–112] and acoustic and thermal insulators [17,18,113–115].

Over the last 10 years, the number of publications concerning geopolymer foams has increased significantly, bringing forth several reviews related to that topic [17,18,116]. For many of these applications, the porosity of geopolymer foams needs to be as high as possible and as open as possible, i.e. the porous network needs to be connected (or percolating) as much as possible to allow external species to flow in and out. A significant amount of meso- and macro-porosity¹³ is intrinsically present in geopolymers [117–119] and can be optimized simply by regulating the formulation and processing parameters of its bulk components [120,121]. The focus of the following studies is to promote the introduction of interconnected ultra-macro-porosity¹⁴ in addition to the meso- and macroporosity of geopolymers by combining a vegetable oil and a blowing agent, in general oxygen peroxide H₂O₂.

In pioneering studies [43,122,123], vegetable oils were used to produce highly porous and open geopolymers by emulsion templating (Fig. 6, Red pathway). First, vegetable oils are easily incorporated in the geopolymer slurries following the direct route (Fig. 1, route 1). Vegetable oils, mainly triglycerides, then undergo saponification in alkaline conditions [78], leading to water-soluble soap and glycerol species, which are easily extracted after GP curing; after removal, these species leave a large and connected pore network.¹⁵ The extraction is usually done by hot water exchange. In addition, the extraction allows to check the completion of geopolymerization, since non-fully condensed geopolymer materials are sensitive to water, would swell and disaggregate [41,42]. A very recent study [124] has investigated the influence of various surfactants on sunflower oil emulsification. It has highlighted that the pore network could be sized by the use of specific surfactants. However, vegetable oils mainly allow the formation of meso- or small macro-pores [125]. It is not the most efficient way to increase total porosity, but the advantage of vegetable oils is their ability to promote the connectivity of the pore network. Table 3 summarizes the main

¹³ In the IUPAC classification of pore sizes, the micropore width does not exceed 2 nm, the mesopore width is in the range 2–50 nm and the macropore width is above 50 nm (0.05 μm) [160].

¹⁴ The term “ultramacroporosity” refers to pores displaying a width of hundreds of microns, and generated on purpose by the use of a blowing agent, in contrast with macropores intrinsically present in geopolymers and generally having a width lower than 100 μm.

¹⁵ Portland cements could not be considered in this application because they are water-activated and would not provide the required alkalinity. Despite this drawback, some studies on the incorporation of vegetable oils in OPC for the purpose of making lightweight concrete have been performed [161].

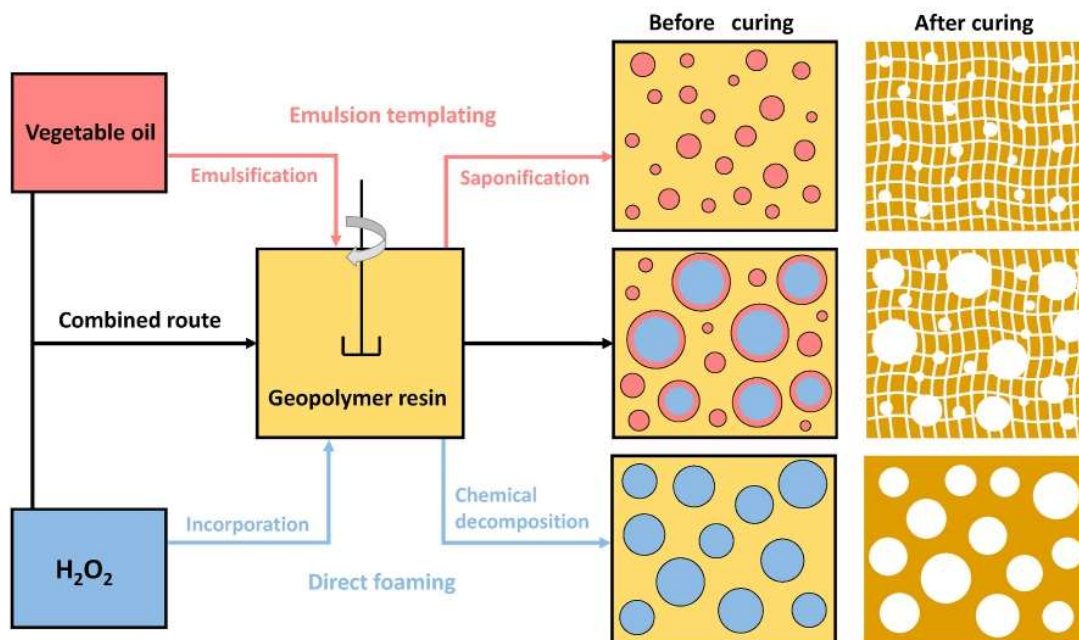


Fig. 6. Simplified schematic representation of synthetic routes to porous geopolymer, by emulsion templating of vegetable oils (red pathway), by direct foaming using H_2O_2 as a blowing agent (blue pathway), or through the combined route (black pathway). (For interpretation of the references to colour in this figure legend, the reader is referred to the Web version of this article.)

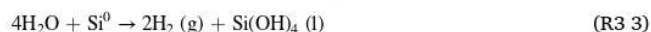
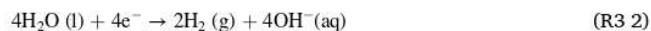
Table 3

Processing of highly porous geopolymers using vegetable oils; MK = Metakaolin, FA = Fly ash, vol% = volume percentage, wt.% = weight percentage.

Alumino-silicate sources	Alkali ions	Oil type	Amount incorporated	Amount of H_2O_2	Process of incorporation (Fig. 1)	Reference
FA	NaOH	Corn, Palm	4-12 wt%	/	● Direct	[43]
MK	KOH	Canola, Biodiesel, Paraffin	1:1 oil-to-water volume fraction	/	● Direct	[125]
MK	KOH	Olive	20-45 wt%	5-15 wt%	● Direct	[126]
MK	KOH	Sunflower, Canola, Olive	20-70 wt%	0-20 wt%	● Direct	[41]
MK	KOH	Sunflower, Canola, Olive	0-10 wt%	0-20 wt%	● Direct	[127]
MK	NaOH	Soy bean	20 wt%	About 6 wt%	● Pre-emulsification	[128]
MK and FA	KOH	Coconut, Babassu, Palm Stearin, Beef tallow, Olive, Castor, Sunflower, Soybean, Biodiesel	25 wt%	6 wt%	● Direct	[129]
MK	NaOH	Canola	2-6 wt%	0,5-1,5 wt%	● Direct	[130]
MK and FA	KOH	Sunflower	25 wt%	6 wt%	● Direct	[131]
MK	NaOH	Sunflower	20 wt%	/	● Pre-emulsification	[124]

research works on the development of highly porous geopolymers using vegetable oils for emulsion templating, with saponification reactions.

Without involving OL, the direct foaming processing route is the most widely used technique for producing highly porous geopolymers [17,132] (Fig. 6, Blue pathway). With this method, wet geopolymer foams are produced by incorporating air or gas into the homogeneous slurry, which sets subsequently by curing at a given temperature to obtain consolidated porous materials. To develop alkali-activated foams, several frequently selected blowing agents are H_2O_2 [42,101] (Equation R1), aluminum powder [133,134] (Equation R2), or silica fume [114,135,136] (Equations R3). These agents decompose in alkaline conditions and react inside the cement matrix, generating gas and resulting in the creation of macropores of different sizes and shapes, through the following decomposition reactions:



These foaming agents are very efficient in drastically increasing the total porosity, but they mainly form a closed pore network [101,133,131]. This is a drawback for a number of potential applications of geopolymer foams. Moreover, despite the high viscosity of geopolymer slurries, foaming is a thermodynamically unstable process, as the gas bubbles in the wet foams are likely to undergo spontaneous drainage, continuous Ostwald ripening and coalescence for minimizing the overall Gibbs free energy of the slurry/air system. Due to the instability of wet foams, large pores (of hundreds of micron size) and a wide range of pore sizes are typically present in the final foam. In order to avoid this phenomenon, the most frequently used approach is to add stabilizing agents such as surfactants, particles or fibers to the suspension or to the liquid

medium [103,131,137].

Several authors [41,42,127,128] have proposed to combine H₂O₂ (as a blowing agent) and vegetable oils, in order to benefit from both the high porosity generated by O₂ production (Equation (1)) and from the capacity of the oils to build connection between pores. The soap molecules generated through the oil saponification are in fact anionic surfactants, able to stabilize both the gas bubbles produced by the decomposition of H₂O₂ and the oil droplets (Fig. 6, Black pathway). For instance, Bai et al. [41] were able to produce a geopolymer foam with a total volume porosity of 89%, of which 86% is open. However, these highly porous materials have low compressive strengths, of less than 1.0 MPa.

Further studies have been dedicated to improving the mechanical strength of geopolymer foams by varying several parameters, such as vegetable oil and H₂O₂ contents [41,127] or the type of oil [129], while keeping a highly interconnected ultra-macro-porosity. Moreover, several authors [132,129,126] proposed a heat treatment up to 1200 °C once the material has hardened. In general, such heat treatment significantly increases the mechanical compressive strength while maintaining a highly interconnected ultra-macro-porosity. Heating above 1000 °C leads to the formation of crystalline phases (ceramic glasses) while samples heated below 800 °C remain amorphous (i.e. geopolymer) [138]. Table 4 summarizes the porous and mechanical properties of ultra-porous geopolymers synthesized with various processing parameters. It is observed that total porosity is generally very close to open porosity; this means that the porosity of these foams is almost fully interconnected. According to Bai et al. [41], 10 wt% H₂O₂ and 20 wt% olive oil is a favorable combination regarding final porosity and strength. As for the heat treatment, an optimal temperature is about 800 °C in order to avoid extensive dimensional changes [138]. Finally, in order to increase mechanical strength, composite materials are also added with ceramic particles (silicon carbide) or polyurethane resins in the geopolymer, as a complement to H₂O₂ and vegetable oils [126,130].

3.3. Improvement of existing properties or promotion of emerging ones (organic polymers)

Geopolymers, as ceramics, display a typical brittle mechanical behavior with low ductility and low fracture toughness. These properties might represent significant limits for structural applications. A number of studies aimed at overcoming this drawback by producing geopolymer composites, improved by the addition of liquid organic polymer compounds, such as water-soluble polymers, polymer emulsions, or water-immiscible (epoxy or polysiloxane) resins. Table 5 summarizes a number of research works performed to develop such composites.

3.3.1. Water-soluble organic polymers

The incorporation of functional organic polymers containing carboxyl groups, amino groups or hydroxide radicals into geopolymers

increases the compatibility between organic and inorganic phases, due to their interactions with the polar SiOH or Si-O- functions of the geopolymer N-A-S-H structure. For this reason, polyacrylic acid, sodium polyacrylate, polyethylene glycol (PEG), polyvinyl alcohol and polyacrylamide have been used as water-soluble polymer reactants into metakaolin-based concretes. High quantities of water-soluble polymers could probably be incorporated into fresh geopolymers. However, since the incorporation of only 1% of such polymer is already leading to a significant improvement (29%) of compressive strength, these polymers have not been tested at higher concentrations [144,145].

In [147], the addition of up to 6 wt% of polyethylene glycol (PEG) in metakaolin-based geopolymers shows a global increase in elastic strain, associated to a decrease in flexural and compressive strengths. Porosity increases as the percentage of PEG increases, due to cavities formed after removal of the polymer particles ranging from 1 to 10 μm and having a spherical shape. Others authors have studied the effect of PEG molecular weights. As observed in Ref. [146], the lowest compressive strengths are observed with the heaviest PEG (20 000 g mol⁻¹). Low molecular weights PEGs (400 g mol⁻¹), incorporated at up to 10 wt% contribute to an important increase in compressive strength, probably due to lower porosity [146].

Composites made of geopolymer and alginate spheres have been developed through ionotropic gelation [154,155]. Ionotropic gelation is based on the capability of polyelectrolytes to crosslink in the presence of multivalent counter ions, to form hydrogels [156]. Sodium alginate is dissolved in water and then directly added to the fresh geopolymer; the mix is added with CaCl₂ (Ca²⁺) to initiate the ionotropic gelation [154]. Alginate is a natural anionic polysaccharide containing many carboxyl groups, which are effective for binding metallic ions. However, the mechanical properties of alginate alone are insufficient and its range of application is therefore limited. The combination of alginate with a strong geopolymer network leads to the development of composite materials capable of adsorbing heavy metals, and useable for wastewater treatment. In Ge et al. [154], composite spheres with a geopolymer/alginate mass ratio of 1:(0.10–0.18) were developed; the sample at 1:0.16 displayed the highest efficiency for Cu(II) removal from water, with a value of about 70%.

3.3.2. Polymers in emulsions

To avoid the incompatibility between aqueous and organic phases, some authors [152] have used a resin emulsion of butyl acrylate and acrylic acid, which can be easily diluted with metakaolin in the activating solution. Even if the highest compressive and flexural strengths are obtained for geopolymer composites reinforced with only 1 wt% of organic resin, this pathway allows an incorporation up to 5 wt% of organic materials. Good compatibility between the two phases is ensured by the polycondensation reaction between carboxylic acid functions and hydroxyl groups from the aluminosilicate source, which creates an organic/inorganic continuous gel. Moreover, the water

Table 4
Porosity and mechanical strength of various geopolymers for different processing parameters.

Sample label and Ref.	Oil type	Oil wt%	H ₂ O ₂ wt%	Heat treatment	Total porosity ^a (vol%)	Open porosity ^b (vol%)	Compressive strength (MPa)
1 [41]	Olive	20	10	none	81.4	79.5	3.11
2 [41]	Olive	53	10	none	70.3	68.4	2.38
3 [41]	Olive	20	15	none	86.3	84.0	0.78
4 [41]	Sunflower	20	10	none	77.0	75.0	2.00
5 [131]	Sunflower	25	6	none	83.5	66.4	0.45
6 [129]	Sunflower	25	6	900 °C	81.0	73.0	0.60
7 [129]	Coconut	25	6	900 °C	82.0	79.0	0.70
8 [129]	Olive	25	6	900 °C	80.0	77.0	1.50
9 [129]	Olive	25	6	600 °C	86.0	80.0	0.50
10 [129]	Olive	25	6	1200 °C	76.0	73.0	1.90

^a The total porosity (TP) was obtained based on the relation $TP = 100 \times (1 - \rho/\rho_0)$, where ρ is the bulk density obtained by the ratio of weight over the geometrical volume and ρ_0 is the true density of the pore-free solid material, measured with a helium pycnometer.

^b The open porosity was estimated by the Archimedes principle using distilled water.

Table 5

Processing of reinforced hybrid organic/inorganic geopolymers using organic polymers; MK = Metakaolin, FA = Fly ash, BFS = Blast furnace slag, * = dry extract of 50%.

Alumino-silicate sources	Alkali ions	Organic polymer	Incorporated amount (%)	Incorporation process (Fig. 1)	Ref.
MK	NaOH	Epoxy resin	30	① Direct	[139]
FA	NaOH	Epoxy resin	20	① Direct	[140]
MK	NaOH	Epoxy resin	20	② Pre-emulsification	[38]
MK	NaOH	Epoxy resin	20	② Pre-emulsification	[39]
MK	NaOH	Epoxy resin	25	② Pre-emulsification	[141]
MK	NaOH	Epoxy resin	25	② Pre-emulsification	[142]
MK	NaOH	Polydimethylsiloxane	15	② Pre-emulsification	[143]
MK, K	NaOH	Sodium polyacrylate (PAANa), polyacrylamide (PAm), polyethylene glycol (PEG), polyvinyl alcohol (PVA)	1	① Direct	[144]
MK	NaOH	Sodium polyacrylate	1.2	① Direct	[145]
MK	NaOH	Polyethylene glycol	10	① Direct	[146]
MK	NaOH	Polyethylene glycol	6	① Direct	[147]
MK, BFS	NaOH	Waterborne bisphenol-A epoxy resin	25*	① Direct	[148]
MK, FA	NaOH	Waterborne bisphenol-A epoxy resin	4*	① Direct	[149]
FA, BFS	NaOH	Styrene-butadiene emulsion	10*	① Direct	[150]
MK, BFS	NaOH	Acrylic acid/butyl acrylate emulsion and ethylene-vinyl acetate copolymer (powder)	7.5*	① Direct	[151]
MK, BFS	NaOH	Acrylic acid/butyl acrylate emulsion and ethylene-vinyl acetate copolymer (powder)	2.5*	① Direct	[152]
BFS	NaOH	Acrylic emulsion	2.5*	① Direct	[153]

molecules generated by these reactions are stabilized by hydrogen bonding with acrylate ester groups, and their evaporation is inhibited in favor of the geopolymerization reaction [151].

Geopolymer samples have been synthesized with an incorporation rate from 0 to 5 wt% of polyacrylic resin emulsion [153]. The results show that an increase in polyacrylic resin content up to 1 wt% has a positive impact on compressive strength (it is increased by 36,3%) and flexural toughness (increased by 104,6%); beyond this concentration the mechanical properties decline. Further studies confirmed an increase by 50% in the flexural toughness coefficient of geopolymer with the incorporation of only 0.8 wt% of polyacrylate [145].

Finally, the dilution of Styrene-butadiene latex (as an emulsion) has been carried out into mixed fly ash/slag based geopolymers. This increases the flexural strength of geopolymer mortars thanks to the enhanced bonding interactions in the geopolymer cement [150].

3.3.3. Epoxy resins

The first blending tests between water-immiscible organic polymers and geopolymers have been carried out with an epoxy resin from diglycidyl ether of bisphenol-A (DGEBA) and diethyltoluene-diamine as a curing agent [157,158]. A 20 wt% aqueous suspension of kaolin mixed with potassium silicate and potassium hydroxide was simply added to a mixture of DGEBA and diamine. After simultaneous curing of both organic and inorganic parts, epoxy matrices with homogeneously distributed geopolymer parts were obtained. A composite epoxy material containing 20 wt% of dispersed geopolymer has shown improved thermal stability compared to epoxy alone. These first composite matrices have highlighted the possibility of combining organic epoxy resins and inorganic geopolymer cements.

Following these research, composite materials have been synthesized by dispersing fresh epoxy resins within geopolymers. By playing with the chemical composition of the components in the mixture, several types of materials have been developed. They present varied properties and their applications often depend on the ratio between organic and inorganic phases.

The first attempts to prepare composite materials with geopolymer as the continuous phase consisted in reversing the process developed by Hussain [157,158]. In other words, the organic epoxy phase (epoxypolyol and polyamine) is directly introduced into the geopolymer suspension but phase segregation is observed [142]. The issue was solved by modifying the process, so as to mix the epoxypolyol and the polyamine prior to their addition into the geopolymer suspension, to

initiate the polymerization of the epoxy resin. With that method, the partially cross-linked epoxy resin is efficiently added to the geopolymeric suspension without phase segregation. According to the authors, this is due to an improved compatibility between the organic and the aqueous inorganic phases, leading to a homogeneous and stable dispersion of organic micro domains into the inorganic continuous phase. The large number of hydroxyl tails formed during the epoxy ring opening reaction makes the organic phase “temporarily hydrophilic”, and hence increasing the compatibility with the aqueous inorganic phase [141]. If mixing is delayed, the compatibility between the phases reduces because the dispersed phase recovers its hydrophobic nature over time. By correctly monitoring the process, 25 wt% of epoxy resin can be mixed with the geopolymer suspension without needing external additives. Epoxy resins are easily observed by Scanning Electron Microscopy (SEM) in hardened geopolymers, in order to analyze their dispersion state. They are generally incorporated in well-defined

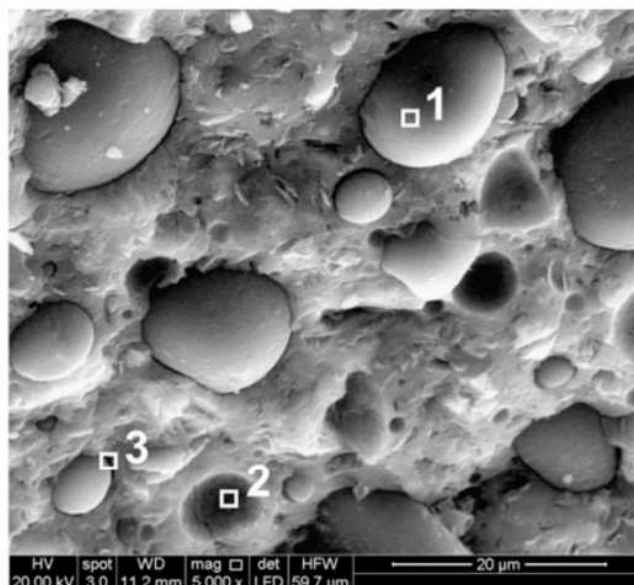


Fig. 7. SEM micrographs of a composite geopolymer material containing 20 wt% of epoxy resin cured at room temperature for 24 h [45].

microspheres with diameters in the range of 1–20 μm (Fig. 7 [45]). In order to evidence the organic-inorganic compatibility, Energy Dispersive Spectrometry (EDS) measurements have been performed at the organic-inorganic interface (Fig. 7, 3), showing the significant presence of both the elements of the inorganic phase (Na, Si, Al) and the organic phase (C,O) [45]. In contrast, EDS measurements on areas representing pure inorganic or organic phases (Fig. 7, 1 and 2 respectively) only present the respective elements of the phases. Such composite materials have been developed for different systems, namely the combination of N,N-diglycidyl-4-glycidyl-oxyaniline, bis-(2-aminoethyl)amine and 2,4-diamino-toluene [45] and several two-components commercial mixtures named Epojet® epoxy [142], Epojet® and EpojetLV® [46,141]. Both two-components Epojet® and EpojetLV® resins contain an aromatic amine that contributes to improve the thermal stability of the geopolymer [141]. Whatever the epoxy resin used, the highest amount that could be incorporated into the geopolymer without phase separation is about 25 wt% [141]. The main advantage of adding epoxy resins in geopolymer materials is the significant enhancement of their compressive strength and toughness compared to pure geopolymers.

Recently, Roviello et al. [143] have proposed a new class of epoxy resin, using both melamine as curing agent and aminopropyltrimethoxysilane as silicon source, to be introduced into geopolymers. The advantage of using melamine is the assurance of high thermal stability and fire resistance due to the presence of an azacyclic ring. Aminopropyltrimethoxysilane, which can be fixed to the organic resin via covalent bonds, ensure a high compatibility with the inorganic silicate matrix thanks to the silane groups. Such composite materials based on geopolymers are able to contain up to 25 wt% of epoxy melamine resin. They are particularly attractive for designing thermo-resistant and thermo-insulating wall panels.

Waterborne bisphenol-A epoxy resins have been used to formulate geopolymers by mold pressing [149]. The authors obtain an optimal compressive strength of 116 MPa at a molding pressure of 200 MPa. With an increasing epoxy resin content from 0 to 8 wt%, porosity gradually increases while the pore size distribution initially reduces and then increases. Waterborne bisphenol-A epoxy resin and waterborne polyamine epoxy curing agent have been used together to formulate geopolymers for in deep water oil well cementation applications [148]. The mixing of epoxy resin and curing agent with geopolymer needs to be performed after the initiation of both polymerization reactions. During the cross-linking process of the resin, the epoxy opening ring reaction initially makes the resin phase hydrophilic and compatible with the aqueous geopolymer suspension. The amount of organic phase could be as high as 50% while presenting an excellent dispersion quality up to a micrometric scale.

Epoxy resin has also been used without amino-organic curing agent. Direct mixing of 30 wt% of epoxy resin in a geopolymer solution was carried out in Ref. [139], in order to reduce drying shrinkage and easy cracking of green anti-corrosion coating applications. The compressive strength decreased at earlier age with an increasing amount of epoxy resin due to polycondensation slowdown, but after 28 days, the compressive strength of samples containing epoxy resin was almost as high as the resin-free reference. In Ref. [140], up to 20 wt% of epoxy resin have been added into fly ash based geopolymer suspensions in order to reinforce thermal and microstructural properties. Composites containing 5 to 10 wt% of epoxy resins are suitable as geothermal pipes because of enhanced fire resistance. This is especially the case of the formulation containing 5 wt% epoxy, which also has the highest tensile strength (3.33 MPa compared to 2.56 MPa for resin-free GP).

3.3.4. Polysiloxane resins

In order to obtain a closer interaction between organic and inorganic components within a geopolymer-based material, some authors exploited the chemical similarity between polysiloxanes and polysialates [142]. Polysiloxanes are inorganic polymers based on Si–O chains, containing alkyl or aryl groups bonded to Si atoms, therefore possessing

a backbone very similar to those characterizing geopolymers (polysialates).

In Roviello et al. [142], composite polysiloxane-geopolymer samples have been prepared by incorporating 15 wt% of a commercial oligomeric dimethylsiloxane resin into a freshly prepared geopolymeric suspension under mechanical stirring. Prior to the addition into the geopolymeric suspension, a Sn (IV) catalyst is added to initiate the organic polymerization. With this method, by mixing both organic and aqueous phases, the polycondensation reactions of geopolymer and dimethylsiloxane are already initiated, improving the compatibility between both phases. After the full curing of the two, the combination of SEM and EDS shows that the siloxane phase is well dispersed in the GP down to a nanometric scale (Fig. 8 [142]). This indicates a very close interaction between the phases, characterized by the scattered mapping of carbon. An interpenetrated network between geopolymeric and siloxane components is probably formed, in which chemical bonds between aluminosilicate and siloxane species could be present. The enhanced mechanical properties, along with the high fire resistance of the resulting composite materials, suggest their usefulness for building applications and for the production of heat-resistant protective coatings and adhesives.

4. Summary

Driven by the need for low-cost, eco-friendly engineering parts, tremendous efforts have been recently devoted to develop varied and novel processing technologies for the design of geopolymers. More specifically, the incorporation of OL into geopolymers to create composite organic/inorganic materials has gained significant interest in the past few years, with a range of possible applications depending on the type of organic liquid incorporated:

- Mineral oils are efficiently immobilized in geopolymers to treat various OL waste streams or to produce materials with improved thermal properties (PCM). The durability of these systems over a long period is still under investigation, because they are quite recent in the field when compared to traditional Portland cements, for which a number of durability studies has been reported.
- Vegetable oils, mainly made up of triglycerides, are used as such or in combination with blowing agents to produce geopolymer foams with better understanding and control of the pore network design (pore size distribution and connectivity/percolation).
- The possibility of blending organic polymers and inorganic geopolymer materials is used for the development of composite materials with improved or emerging properties.

Unfortunately, studies dealing with the direct comparison between geopolymers and Portland cements regarding the incorporation of organic liquids are still scarce, so that it may be difficult to fully testify of the technical benefits of using geopolymers instead of traditional Portland cements.

This review also aimed at highlighting that the method of OL incorporation into geopolymers needs to be carefully chosen depending on the end application, which determines the required properties of the resulting materials. In addition, the industrial feasibility of these processes has to be taken into account. In particular, the cost of additives (e.g. surfactants, adsorbents) or the extra handling of toxic OL may be practical issues. Following research on S/S of OL in inorganic geopolymers, the favorable compatibility between inorganic and organic phases can be used to broaden the application range of these composite materials. Among them, this review presents both the production of highly porous geopolymer foams and the development of polymer-reinforced materials, which have already been widely investigated. In the future, other types of OL could be stabilized in geopolymers in order to develop geopolymer composite materials with emerging properties, such as geopolymer composites with high corrosion resistance [139] or

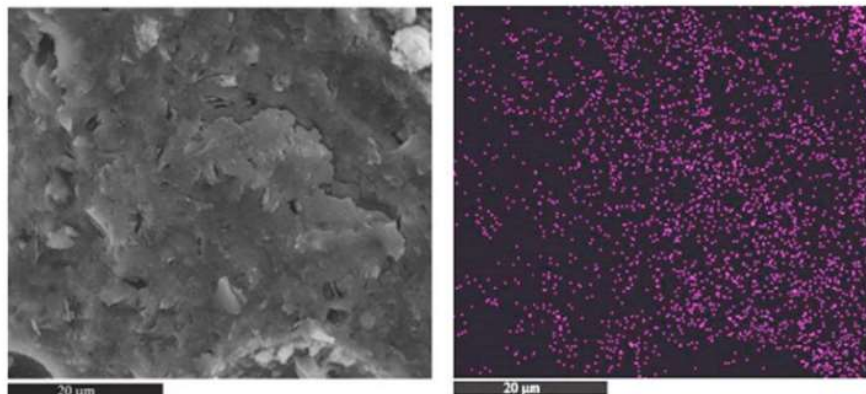


Fig. 8. SEM micrograph at 5000 magnification (left) and EDS mapping at the same magnification of carbon (right) of a geopolymer composite material containing 10 wt% of dimethylsiloxane [142].

biomimetic properties [159], besides possessing a reasonable carbon footprint.

Declaration of competing interest

The authors declare that they have no known competing financial interests or personal relationships that could have appeared to influence the work reported in this paper.

Acknowledgments

This project has received funding from the European Union's Horizon 2020 research and innovation programme for Nuclear Fission and Radiation Protection Research (Call NFRP-2019-2020) under grant agreement No. 945098 (PREDIS).

Chevreul Institute (FR 2638), Ministère de l'Enseignement Supérieur et de la Recherche, Région Hauts de France, and FEDER are acknowledged for supporting and funding part of this work.

References

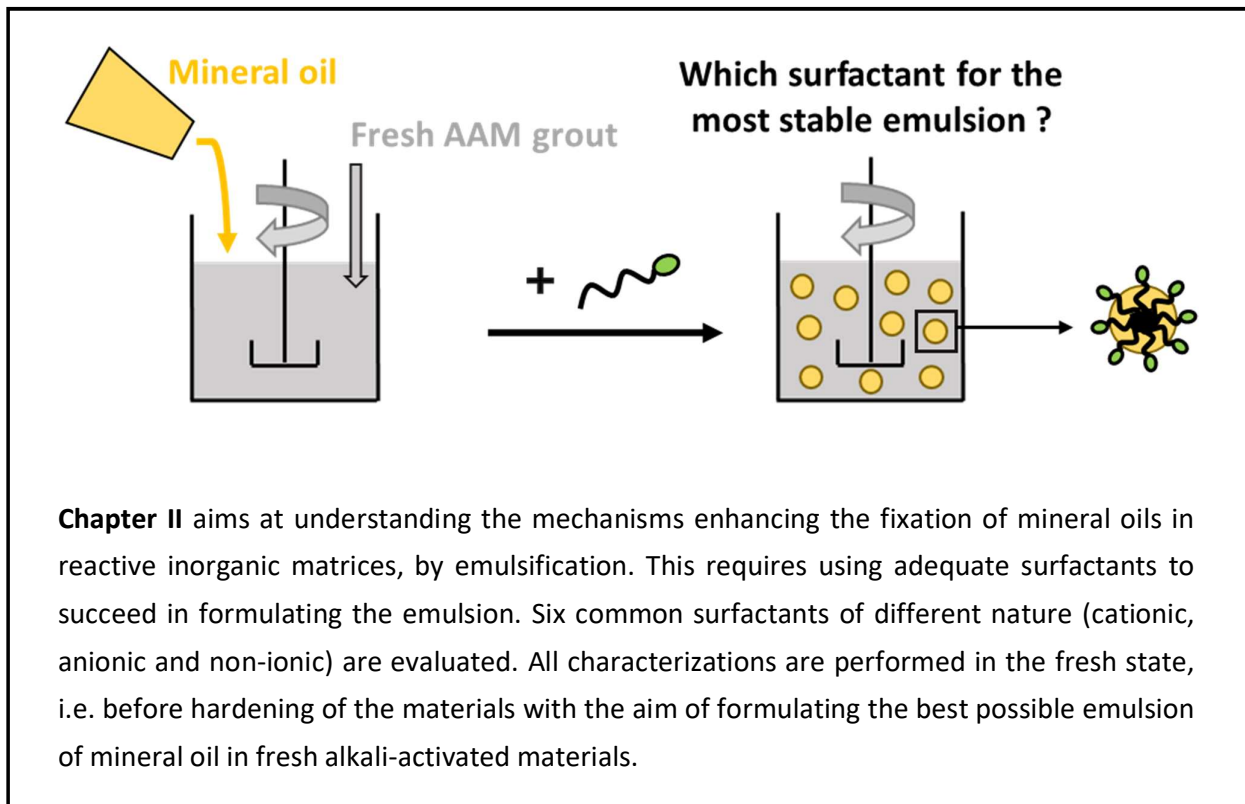
- [1] A. Naqi, J. Jang, Recent progress in green cement technology utilizing low-carbon emission fuels and raw materials: a review, *Sustainability*-Basel 11 (2) (2019) 537, <https://doi.org/10.3390/sul1020537>.
- [2] R.M. Andrew, Global CO₂ emissions from cement production, 1928–2018, *Earth Syst. Sci. Data* 11 (4) (2019) 1675–1710, <https://doi.org/10.5194/essd-11-1675-2019>.
- [3] J. Davidovits, Geopolymers of the first generation: SILIFACE -process, in: *Proceedings of the Geopolymer '88 First International Conference on Soft Mineralogy*, vol. 1, 1988, pp. 49–67.
- [4] J. Davidovits, *Geopolymer Chemistry and Applications*, fifth ed., GEOPOLYMER Institute, 2020, ISBN 978-2-9544531-1-8.
- [5] J.L. Provis, J.S.J. van Deventer, *Geopolymers: Structure, Processing, Properties and Industrial Applications*, 2009, ISBN 978-1-4398-0970-9.
- [6] B. Tempest, O. Sanusi, J. Gergely, V. Ogunro, D. Weggel, 'Compressive Strength and Embodied Energy Optimization of Fly Ash Based Geopolymer Concrete', Presented at the World of Coal Ash, WOCA, 2009 ([Online access]).
- [7] U. Ernst, von Weizsäcker, Factor five: transforming the global economy through 80% improvements in resource productivity, *Earthscan/The Natural Edge Project*, 2009.
- [8] P. Duxson, A. Fernández-Jiménez, J.L. Provis, G.C. Lukey, A. Palomo, J.S.J. van Deventer, Geopolymer technology: the current state of the art, *J. Mater. Sci.* 42 (9) (May 2007) 2917–2933, <https://doi.org/10.1007/s10853-006-0637-z>.
- [9] D. Khale, R. Chaudhary, Mechanism of geopolymerization and factors influencing its development: a review, *J. Mater. Sci.* 42 (3) (Feb. 2007) 729–746, <https://doi.org/10.1007/s10853-006-0401-4>.
- [10] J.L. Provis, G.C. Lukey, J.S.J. van Deventer, Do geopolymers actually contain nanocrystalline zeolites? A Reexamination of Existing Results, *Chem. Mater.* 17 (12) (Jun. 2005) 3075–3085, <https://doi.org/10.1021/cm050230i>.
- [11] K. Komnitsas, D. Zaharaki, Geopolymerisation: a review and prospects for the minerals industry, *Miner. Eng.* 20 (14) (Nov. 2007) 1261–1277, <https://doi.org/10.1016/j.mineng.2007.07.011>.
- [12] J.L. Provis, S.A. Bernal, Geopolymers and related alkali-activated materials, *Annu. Rev. Mater. Res.* 44 (1) (2014) 299–327, <https://doi.org/10.1146/annurev-matsci-070813-113515>.
- [13] P.N. Lemougna, K. Wang, Q. Tang, U.C. Melo, X. Cui, Recent developments on inorganic polymers synthesis and applications, *Ceram. Int.* 42 (14) (Nov. 2016) 15142–15159, <https://doi.org/10.1016/j.ceramint.2016.07.027>.
- [14] Y.-M. Liew, C.-Y. Heah, A.B. Mohd Mustafa, H. Kamarudin, Structure and properties of clay-based geopolymer cements: a review, *Prog. Mater. Sci.* 83 (Oct. 2016) 595–629, <https://doi.org/10.1016/j.pmatsci.2016.08.002>.
- [15] B. Singh, G. Ishwarya, M. Gupta, S.K. Bhattacharyya, Geopolymer concrete: a review of some recent developments, *Constr. Build. Mater.* 85 (Jun. 2015) 78–90, <https://doi.org/10.1016/j.conbuildmat.2015.03.036>.
- [16] Y.H.M. Amran, N. Farzadnia, A.A. Abang Ali, Properties and applications of foamed concrete; a review, *Constr. Build. Mater.* 101 (Dec. 2015) 990–1005, <https://doi.org/10.1016/j.conbuildmat.2015.10.112>.
- [17] C. Bai, P. Colombo, Processing, properties and applications of highly porous geopolymers: a review, *Ceram. Int.* 44 (14) (Oct. 2018) 16103–16118, <https://doi.org/10.1016/j.ceramint.2018.05.219>.
- [18] Z. Zhang, J.L. Provis, A. Reid, H. Wang, Geopolymer foam concrete: an emerging material for sustainable construction, *Constr. Build. Mater.* 56 (Apr. 2014) 113–127, <https://doi.org/10.1016/j.conbuildmat.2014.01.081>.
- [19] A.K. Karamalidis, E.A. Voudrias, Cement-based stabilization/solidification of oil refinery sludge: leaching behavior of alkanes and PAHs, *J. Hazard Mater.* 148 (1–2) (Sep. 2007) 122–135, <https://doi.org/10.1016/j.jhazmat.2007.02.032>.
- [20] S. Trussell, R.D. Spence, A review of solidification/stabilization interferences, *Waste Manag.* 14 (6) (1994) 507–519.
- [21] S. Paria, P.K. Yuet, 'Solidification-stabilization of organic and inorganic contaminants using portland cement: a literature review', *Environ. Rev.* 14 (4) (Dec. 2006) 217–255, <https://doi.org/10.1139/a06-004>.
- [22] N. Nestle, C. Zimmermann, M. Dakkouri, R. Niessner, Action and distribution of organic solvent contaminations in hydrating cement: time-resolved insights into solidification of organic waste, *Environ. Sci. Technol.* 35 (24) (Dec. 2001) 4953–4956, <https://doi.org/10.1021/es015528n>.
- [23] S.J.T. Pollard, D.M. Montgomery, C.J. Sollars, R. Perry, 'Organic compounds in the cement-based stabilisation/solidification of hazardous mixed wastes—mechanistic and process considerations', *J. Hazard Mater.* 28 (3) (Nov. 1991) 313–327, [https://doi.org/10.1016/0304-3894\(91\)87082-D](https://doi.org/10.1016/0304-3894(91)87082-D).
- [24] D.M. Montgomery, C.J. Sollars, R. Perry, Optimization of cement-based S/S of organic-containing industrial wastes using organophilic clays.pdf, *Waste Manag.* 9 (1991) 21–34.
- [25] V. Cantarel, D. Lambertin, A. Poulesquen, F. Leroux, G. Renaudin, F. Frizon, Geopolymer assembly by emulsion templating: emulsion stability and hardening mechanisms, *Ceram. Int.* 44 (9) (Jun. 2018) 10558–10568, <https://doi.org/10.1016/j.ceramint.2018.03.079>.
- [26] C. Shi, A. Fernández-Jiménez, Stabilization/solidification of hazardous and radioactive wastes with alkali-activated cements, *J. Hazard Mater.* 137 (3) (Oct. 2006) 1656–1663, <https://doi.org/10.1016/j.jhazmat.2006.05.008>.
- [27] I.G. Richardson, The calcium silicate hydrates, *Cem. Concr. Res.* 38 (2) (Feb. 2008) 137–158, <https://doi.org/10.1016/j.cemconres.2007.11.005>.
- [28] R.J. Myers, S.A. Bernal, R. San Nicolas, J.L. Provis, 'Generalized structural description of calcium-sodium aluminosilicate hydrate gels: the cross-linked substituted tobermorite model', *Langmuir* 29 (17) (Apr. 2013) 5294–5306, <https://doi.org/10.1021/la4000473>.
- [29] J.L. Provis, Activating solution chemistry for geopolymers, in: *Geopolymers, Structures, Processing, Properties and Industrial Applications*, Elsevier, 2009, ISBN 978-1-84569-449-4, pp. 50–71.
- [30] C. Shi, B. Qu, J.L. Provis, Recent progress in low-carbon binders, *Cem. Concr. Res.* 122 (2019) 227–250, <https://doi.org/10.1016/j.cemconres.2019.05.009>.
- [31] C. Li, H. Sun, L. Li, A review: the comparison between alkali-activated slag (Si+Ca) and metakaolin (Si+Al) cements, *Cem. Concr. Res.* 40 (9) (Sep. 2010) 1341–1349, <https://doi.org/10.1016/j.cemconres.2010.03.020>.
- [32] F. Puertas, M. Palacios, H. Manzano, J.S. Dolado, A. Rico, J. Rodríguez, A model for the C-A-S-H gel formed in alkali-activated slag cements, *J. Eur. Ceram. Soc.* 31

- (12) (Oct. 2011) 2043–2056, <https://doi.org/10.1016/j.jeurceramsoc.2011.04.036>.
- [33] V.F.F. Barbosa, K.J.D. MacKenzie, C. Thaumaturgo, Synthesis and characterisation of materials based on inorganic polymers of alumina and silica: sodium polysialate polymers, *Int. J. Inorg. Mater.* 2 (4) (Sep. 2000) 309–317, [https://doi.org/10.1016/S1466-6049\(00\)00041-6](https://doi.org/10.1016/S1466-6049(00)00041-6).
- [34] W.O. Greenhalgh, The Immobilization of organic liquid wastes, in: Presented at the Waste Management '86, 1986 ([Online access]).
- [35] C. Costa, Emulsion formation and stabilization by biomolecules: the leading role of cellulose, *Polymers* 11 (10) (2019) 1570, <https://doi.org/10.3390/polym11101570>, al.
- [36] V. Cantarel, F. Nouaille, A. Rooses, D. Lambertin, A. Poulesquen, F. Frizon, Solidification/stabilisation of liquid oil waste in metakaolin-based geopolymer, *J. Nucl. Mater.* 464 (Sep. 2015) 16–19, <https://doi.org/10.1016/j.jnucmat.2015.04.036>.
- [37] X. Liu, S. Nair, K. Aughenbaugh, E. van Oort, Mud-to-cement conversion of non-aqueous drilling fluids using alkali-activated fly ash, *J. Pet. Sci. Eng.* 182 (Nov. 2019) 106242, <https://doi.org/10.1016/j.petrol.2019.106242>.
- [38] C. Mabilie, Fragmentation of Emulsions in a Simple Shear Stress Flow, PhD, University of Bordeaux, France, 2013.
- [39] G. G. Stokes, 'On the Effect of the Internal Friction of Fluids on the Motion of Pendulums', Cambridge Philosophical Society, vol. vol. 9, 1850.
- [40] M. Masrullita, P. Burhan, Y. Trihadiningrum, Stabilization/solidification of waste containing heavy metals and hydrocarbons using OPC and land tras cement, *J. Ecol. Eng.* 19 (6) (Nov. 2018) 88–96, <https://doi.org/10.12911/22998993/92926>.
- [41] C. Bai, G. Franchin, H. Elsayed, A. Conte, P. Colombo, High strength metakaolin-based geopolymer foams with variable macroporous structure, *J. Eur. Ceram. Soc.* 36 (16) (Dec. 2016) 4243–4249, <https://doi.org/10.1016/j.jeurceramsoc.2016.06.045>.
- [42] M.S. Cilla, M.R. Morelli, P. Colombo, Open cell geopolymer foams by a novel saponification/peroxide/gelcasting combined route, *J. Eur. Ceram. Soc.* 34 (12) (Oct. 2014) 3133–3137, <https://doi.org/10.1016/j.jeurceramsoc.2014.04.001>.
- [43] S.K. Kaliappan, A.A. Siyal, Z. Man, M. Lay, R. Shamsuddin, Effect of pore forming agents on geopolymer porosity and mechanical properties, in: Presented at the 3rd International Conference on Applied Science and Technology, Penang, Malaysia, 2018, <https://doi.org/10.1063/1.5055468>.
- [44] C.A. Davy, G. Hauss, B. Planel, D. Lambertin, 3D structure of oil droplets in hardened geopolymer emulsions, *J. Am. Ceram. Soc.*, p. jace (Oct. 2018) 16142, <https://doi.org/10.1111/jace.16142>.
- [45] C. Ferone, G. Roviello, F. Colangelo, R. Cioffi, O. Tarallo, Novel hybrid organic-geopolymer materials, *Appl. Clay Sci.* 73 (Mar. 2013) 42–50, <https://doi.org/10.1016/j.clay.2012.11.001>.
- [46] F. Colangelo, G. Roviello, L. Ricciotti, C. Ferone, R. Cioffi, Preparation and characterization of new geopolymer-epoxy resin hybrid mortars, *Materials* 6 (7) (Jul. 2013) 2989–3006, <https://doi.org/10.3390/ma6072989>.
- [47] H.P. Grace, Dispersion phenomena in high viscosity immiscible fluid systems and applications of static mixers as dispersion devices in such systems, *Chem. Eng. Commun.* 14 (3–6) (Mar. 1982) 225–277, <https://doi.org/10.1080/00986448208911047>.
- [48] International Atomic Energy Agency (IAEA), Treatment and Conditioning of Radioactive Organic Liquids, 1992. Accessed: May 05, 2020. [Online]. Available: https://www-pub.iaea.org/MTCD/publications/pdf/te_656_web.pdf.
- [49] W. Zhang, J. Li, J. Wang, Solidification of spent radioactive organic solvent by sulfoaluminate and Portland cements, *J. Nucl. Sci. Technol.* 52 (11) (Nov. 2015) 1362–1368, <https://doi.org/10.1080/00223131.2015.1076747>.
- [50] T. Dong, S. Xie, J. Wang, G. Zhao, Q. Song, Solidification and stabilization of spent TBP/OK organic liquids in a phosphate acid-based geopolymer, *Sci. Technol. Nucl. Install.* 2020 (Jan. 2020) 1–7, <https://doi.org/10.1155/2020/8094205>.
- [51] D. Lambertin, A. Rooses, F. Frizon, Process for Preparing a Composite Material from an Organic Liquid and Resulting Material, 2014 patent n° WO2014/04776 A1.
- [52] B.E. Glad, W.M. Kriven, Highly porous geopolymers through templating and surface interactions, *J. Am. Ceram. Soc.* 98 (7) (Jul. 2015) 2052–2059, <https://doi.org/10.1111/jace.13584>.
- [53] M. Smitha, N. Sathi Sasidharan, P.K. Watal, Immobilisation of Alpha Contaminated Lubricating Oils in Cement Matrix, Technical report, Atomic research center, Mumbai, India, 2000.
- [54] C. Pierlot, J.F. Ontiveros, M. Royer, M. Catté, J.-L. Salager, Emulsification of viscous alkyd resin by catastrophic phase inversion with nonionic surfactant, *Colloids Surf. Physicochem. Eng. Asp.* 536 (Jan. 2018) 113–124, <https://doi.org/10.1016/j.colsurfa.2017.07.030>.
- [55] P. Skalle, J. Sveen, Emulsion cement, Technical report, in: Presented at the Offshore Europe Conference, 1991.
- [56] G.M. Ayininuola, Influence of diesel oil and bitumen on compressive strength of concrete, *J. Civ. Eng.* 37 (2009) 65–71.
- [57] D.M. Montgomery, C.J. Sollars, R. Perry, S.E. Tariingt, P. Barnes, E. Henderson, Treatment of organic-contaminated industrial wastes using cement-based S/S - I. Microstructural analysis of cement-organic interactions, *Waste Manag. Res.* 9 (1991) 103–111.
- [58] S.A. Wilson, N.J. Langdon, P.J. Walden, The effects of hydrocarbon contamination on concrete strength, *Geotech. Eng.* (3) (2001) 189–193.
- [59] S. Chandra, P. Flodin, Interactions of polymers and organic admixtures on portland cement hydration, *Cem. Concr. Res.* 17 (6) (1987) 875–890, [https://doi.org/10.1016/0008-8846\(87\)90076-7](https://doi.org/10.1016/0008-8846(87)90076-7).
- [60] M.H. Almabrok, R. McLaughlan, K. Vessalas, Investigation of oil solidification using direct immobilization method, in: Presented at the Environmental Research Event, Sydney, Australia, 2011 ([Online access]).
- [61] A.B. Sazonov, A.V. Aleshina, E.P. Magomedbekov, Immobilization of tritium-containing oil wastes by their incorporation in a cement matrix, *Radiochemistry* 51 (4) (2009) 412–414, <https://doi.org/10.1134/S106636220904016X>.
- [62] M.R. El-Naggar, E.A. El-Sherief, H.S. Mekhemar, Performance of geopolymers for direct immobilization of solvent extraction liquids: metakaolin/LIX-84 formulations, *J. Hazard Mater.* 360 (Oct. 2018) 670–680, <https://doi.org/10.1016/j.jhazmat.2018.08.057>.
- [63] V. Cuccia, C.B. Freire, A.C.Q. Ladeira, Radwaste oil immobilization in geopolymer after non-destructive treatment, *Prog. Nucl. Energy* 122 (Apr. 2020) 103246, <https://doi.org/10.1016/j.pnucene.2020.103246>.
- [64] Y Tech Tech, Fiche technique NOCHAR [Online]. Available at: <https://www.tech-y-tech.fr/nochar/>.
- [65] P. Duxson, J.L. Provis, G.C. Lukey, S.W. Mallicoate, W.M. Kriven, J.S.J. van Deventer, Understanding the relationship between geopolymer composition, microstructure and mechanical properties, *Colloids Surf. Physicochem. Eng. Asp.* 269 (1–3) (2005) 47–58, <https://doi.org/10.1016/j.colsurfa.2005.06.060>.
- [66] D.E. Clark, P. Colombo, R.M. Neilson Jr., Solidification of Oils and Organic Liquids, BNL-51612, Nuclear Waste Management, 1982, <https://doi.org/10.2172/6462993>.
- [67] J.R. Gasca-Tirado, Porous geopolymer as a possible template for a phase change material, *Mater. Chem. Phys.* 236 (2019) 121785, <https://doi.org/10.1016/j.matchemphys.2019.121785>.
- [68] J.R. Conner, S.L. Hoeffner, A critical review of stabilisation/solidification technology, *Crit Rev. Env. Sci Technol* 28 (1998) 397–462, <https://doi.org/10.1080/10643389891254250>.
- [69] C. Zhuying, W. Huang, G. Zhang, Y. Zhang, J. Zhang, Study on the formulation of cement solidification of 30% TBP-OK organic liquid waste, *At. Energy Sci. Technol.* 2 (4) (1991) 74–78.
- [70] Z.Z. Hua Rong Liu Shu-juan, Luo Ming-biao, Solidification of spent TBP by alkali-activated slag, *At. Energy Sci. Technol.* 47 (2013) 11, <https://doi.org/10.7538/yzk.2013.47.11.1956>.
- [71] W.O. Ajagbe, O.S. Omokehinde, G.A. Alade, O.A. Agbde, Effect of crude oil impacted sand on compressive strength of concrete, *Constr. Build. Mater.* 26 (1) (2012) 9–12, <https://doi.org/10.1016/j.conbuildmat.2011.06.028>.
- [72] R.B. Abdul-Ahad, A.A. Mohammed, Compressive and tensile strength of concrete loaded and soaked in crude oil, *Eng. J. Univ. Qatar* 13 (2000).
- [73] S.P. Ejeh, O.A.U. Uche, Effect of crude oil spill on compressive strength of concrete materials, *J. Appl. Sci. Res.* 5 (10) (2009) 1756–1761.
- [74] M.H. Almabrok, R.G. McLaughlan, K. Vessalas, P. Thomas, Effect of oil contaminated aggregates on cement hydration, *Am. J. Eng. Res.* 8 (5) (2019) 81–89.
- [75] Characterisation of cement mortar containing oil-contaminated aggregates, in: C. M.H. Almabrok, R.G. McLaughlan, K. Vessalas (Eds.), *From Materials to Structures: Advancement through Innovation*, 2013, ISBN 978-0-415-63318-5, pp. 1091–1096.
- [76] K. Aughenbaugh, S.D. Nair, K. Cowan, E. van Oort, Contamination of Deepwater Well Cementations by Synthetic-Based Drilling Fluids, Galveston, Texas, USA, 2014, <https://doi.org/10.2118/170325-MS>.
- [77] E. Koo, J. Johannsmeier, L. Schwebler, N. Willenbacher, Tuning suspension rheology using capillary forces, *Soft Matter* 8 (24) (2012) 6620, <https://doi.org/10.1039/c2sm25681a>.
- [78] F. Bossler, E. Koo, Structure of particle networks in capillary suspensions with wetting and nonwetting fluids, *Langmuir* 32 (6) (Feb. 2016) 1489–1501, <https://doi.org/10.1021/acs.langmuir.5b04246>.
- [79] F. Bossler, L. Weyrauch, R. Schmidt, E. Koo, Influence of mixing conditions on the rheological properties and structure of capillary suspensions, *Colloids Surf. Physicochem. Eng. Asp.* 518 (Apr. 2017) 85–97, <https://doi.org/10.1016/j.colsurfa.2017.01.026>.
- [80] M. Ahdaya, A. Imqam, Investigating geopolymer cement performance in presence of water based drilling fluid, *J. Pet. Sci. Eng.* 176 (May 2019) 934–942, <https://doi.org/10.1016/j.petrol.2019.02.010>.
- [81] P. Sukontasukkul, N. Nontiyutirikul, S. Songpiriyakij, K. Sakai, P. Chindaprasirt, Use of phase change material to improve thermal properties of lightweight geopolymer panel, *Mater. Struct.* 49 (11) (Nov. 2016) 4637–4645, <https://doi.org/10.1617/s11527-016-0812-x>.
- [82] A. Barneoud-Chapelier, J. Causse, A. Poulesquen, Synthesis of geopolymer emulsions, *Mater. Lett.* 276 (Oct. 2020) 128188, <https://doi.org/10.1016/j.matlet.2020.128188>.
- [83] P. Panya, E.J. Wanless, O. Arquero, G.V. Franks, The effect of ionic surfactant adsorption on the rheology of ceramic glaze suspensions, *J. Am. Ceram. Soc.* 88 (3) (Mar. 2005) 540–546, <https://doi.org/10.1111/j.1551-2916.2005.00121.x>.
- [84] Y.K. Leong, D.V. Boger, P.J. Scales, T.W. Healy, Interparticle forces arising from adsorbed surfactants in colloidal suspensions: an additional attractive force, *J. Colloid Interface Sci.* 181 (2) (Aug. 1996) 605–612, <https://doi.org/10.1006/jcis.1996.0418>.
- [85] M. Sakamoto, Y. Kanda, M. Miyahara, K. Higashitani, Origin of long-range attractive force between surfaces hydrophobized by surfactant adsorption, *Langmuir* 18 (15) (Jul. 2002) 5713–5719, <https://doi.org/10.1021/la025701j>.
- [86] A. Suzzoni, L. Barre, E. Kohler, P. Levitz, L.J. Michot, J. M'Hamdi, Interactions between kaolinite clay and AOT, *Colloids Surf. Physicochem. Eng. Asp.* 556 (Nov. 2018) 309–315, <https://doi.org/10.1016/j.colsurfa.2018.07.049>.

- [87] Y. Deng, J.B. Dixon, G.N. White, Bonding mechanisms and conformation of poly (ethylene oxide)-based surfactants in interlayer of smectite, *Colloid Polym. Sci.* 284 (4) (Jan. 2006) 347–356, <https://doi.org/10.1007/s00396-005-1388-0>.
- [88] R.A. Kennedy, M.L. Kennedy, Effect of selected non-ionic surfactants on the flow behavior of aqueous veegum suspensions, *AAPS PharmSciTech* 8 (1) (Mar. 2007) E171–E176, <https://doi.org/10.1208/pt0801025>.
- [89] I. Natali Sora, R. Pelosato, D. Botta, G. Dotelli, Chemistry and microstructure of cement pastes admixed with organic liquids, *J. Eur. Ceram. Soc.* 22 (9–10) (2002) 1463–1473, [https://doi.org/10.1016/S0955-2219\(01\)00473-3](https://doi.org/10.1016/S0955-2219(01)00473-3).
- [90] D.S. Perera, Relative strengths of phosphoric acid-reacted and alkali-reacted metakaolin materials, *J. Mater. Sci.* 43 (19) (Oct. 2008) 6562–6566, <https://doi.org/10.1007/s10853-008-2913-6>.
- [91] M. Sellami, M. Barre, M. Toumi, Synthesis, thermal properties and electrical conductivity of phosphoric acid-based geopolymer with metakaolin, *Appl. Clay Sci.* 180 (Nov. 2019) 105192, <https://doi.org/10.1016/j.clay.2019.105192>.
- [92] H.K. Tchakouté, C.H. Rüschler, E. Kamseu, F. Andreola, C. Leonelli, Influence of the molar concentration of phosphoric acid solution on the properties of metakaolin-phosphate-based geopolymer cements, *Appl. Clay Sci.* 147 (Oct. 2017) 184–194, <https://doi.org/10.1016/j.clay.2017.07.036>.
- [93] H.K. Tchakouté, C.H. Rüschler, Mechanical and microstructural properties of metakaolin-based geopolymer cements from sodium waterglass and phosphoric acid solution as hardeners: a comparative study, *Appl. Clay Sci.* 140 (May 2017) 81–87, <https://doi.org/10.1016/j.clay.2017.02.002>.
- [94] S. Sharma, D. Medpelli, S. Chen, D.-K. Seo, Calcium-modified hierarchically porous aluminosilicate geopolymer as a highly efficient regenerable catalyst for biodiesel production, *RSC Adv.* 5 (80) (2015) 65454–65461, <https://doi.org/10.1039/C5RA01823D>.
- [95] A. Marani, M.L. Nehdi, Integrating phase change materials in construction materials: critical review, *Constr. Build. Mater.* 217 (Aug. 2019) 36–49, <https://doi.org/10.1016/j.conbuildmat.2019.05.064>.
- [96] D. Frattini, G. Roviello, L. Ricciotti, C. Ferone, F. Colangelo, O. Tarallo, Geopolymer-based composite materials containing pcm for thermal energy storage, *Cem. Concr. Compos.* 59 (May 2015) 89–99, <https://doi.org/10.1016/j.cemconcomp.2015.03.007>.
- [97] R. Shadnia, L. Zhang, P. Li, Experimental study of geopolymer mortar with incorporated PCM, *Constr. Build. Mater.* 84 (Jun. 2015) 95–102, <https://doi.org/10.1016/j.conbuildmat.2015.03.066>.
- [98] W.D.A. Rickard, A. van Riessen, Performance of solid and cellular structured fly ash geopolymers exposed to a simulated fire, *Cem. Concr. Compos.* 48 (Apr. 2014) 75–82, <https://doi.org/10.1016/j.cemconcomp.2013.09.002>.
- [99] T. Bakharev, Resistance of geopolymer materials to acid attack, *Cem. Concr. Res.* 35 (4) (Apr. 2005) 658–670, <https://doi.org/10.1016/j.cemconres.2004.06.005>.
- [100] P. Palermo, A. Formia, P. Antonaci, S. Brini, J.-M. Tulliani, Geopolymer technology for application-oriented dense and lightened materials, Elaboration and characterization, *Ceram. Int.* 41 (10) (Dec. 2015) 12967–12979, <https://doi.org/10.1016/j.ceramint.2015.06.140>.
- [101] R.M. Novais, L.H. Buruberri, G. Ascensão, M.P. Seabra, J.A. Labrincha, Porous biomass fly ash-based geopolymers with tailored thermal conductivity, *J. Clean. Prod.* 119 (Apr. 2016) 99–107, <https://doi.org/10.1016/j.jclepro.2016.01.083>.
- [102] Y. Ge, Y. Yuan, K. Wang, Y. He, X. Cui, Preparation of geopolymer-based inorganic membrane for removing Ni²⁺ from wastewater, *J. Hazard Mater.* 299 (Dec. 2015) 711–718, <https://doi.org/10.1016/j.jhazmat.2015.08.006>.
- [103] C. Bai, High-porosity geopolymer foams with tailored porosity for thermal insulation and wastewater treatment, *J. Mater. Res.* 32 (17) (Sep. 2017) 3251–3259, <https://doi.org/10.1557/jmr.2017.127>.
- [104] M. Minelli, V. Medri, E. Papa, F. Miccio, E. Landi, F. Doghieri, Geopolymers as solid adsorbent for CO₂ capture, *Chem. Eng. Sci.* 148 (Jul. 2016) 267–274, <https://doi.org/10.1016/j.ces.2016.04.013>.
- [105] M. Minelli, Characterization of novel geopolymer – Zeolite composites as solid adsorbents for CO₂ capture, *Chem. Eng. J.* 341 (Jun. 2018) 505–515, <https://doi.org/10.1016/j.cej.2018.02.050>.
- [106] R.M. Novais, L.H. Buruberri, M.P. Seabra, J.A. Labrincha, Novel porous fly-ash containing geopolymer monoliths for lead adsorption from wastewaters, *J. Hazard Mater.* 318 (Nov. 2016) 631–640, <https://doi.org/10.1016/j.jhazmat.2016.07.059>.
- [107] Y. Ge, X. Cui, Y. Kong, Z. Li, Y. He, Q. Zhou, Porous geopolymeric spheres for removal of Cu(II) from aqueous solution: synthesis and evaluation, *J. Hazard Mater.* 283 (Feb. 2015) 244–251, <https://doi.org/10.1016/j.jhazmat.2014.09.038>.
- [108] D. Medpelli, R. Sandoval, L. Sherrill, K. Hristovski, D.-K. Seo, Iron oxide-modified nanoporous geopolymers for arsenic removal from ground water, *Resour.-Effic. Technol.* 1 (1) (Jul. 2015) 19–27, <https://doi.org/10.1016/j.refit.2015.06.007>.
- [109] K. Okada, A. Ooyama, T. Isoe, Y. Kameshima, A. Nakajima, K.J.D. MacKenzie, Water retention properties of porous geopolymers for use in cooling applications, *J. Eur. Ceram. Soc.* 29 (10) (Jul. 2009) 1917–1923, <https://doi.org/10.1016/j.jeurceramsoc.2008.11.006>.
- [110] M.I.M. Alzeer, K.J.D. MacKenzie, R.A. Keyzers, Facile synthesis of new hierarchical aluminosilicate inorganic polymer solid acids and their catalytic performance in alkylation reactions, *Microporous Mesoporous Mater.* 241 (Mar. 2017) 316–325, <https://doi.org/10.1016/j.micromeso.2016.12.018>.
- [111] P. Sazama, O. Bortnovsky, J. Dědeček, Z. Tvarůzková, Z. Sobalík, Geopolymer based catalysts—new group of catalytic materials, *Catal. Today* 164 (1) (Apr. 2011) 92–99, <https://doi.org/10.1016/j.cattod.2010.09.008>.
- [112] M.I.M. Al-Zeer, K.J.D. MacKenzie, Fly ash-based geopolymers as sustainable bifunctional heterogeneous catalysts and their reactivity in friedel-crafts acylation reactions, *Catalysts* 9 (4) (Apr. 2019) 372, <https://doi.org/10.3390/catal9040372>.
- [113] Z. Zhang, J.L. Provis, A. Reid, H. Wang, Mechanical, thermal insulation, thermal resistance and acoustic absorption properties of geopolymer foam concrete, *Cem. Concr. Compos.* 62 (Sep. 2015) 97–105, <https://doi.org/10.1016/j.cemconcomp.2015.03.013>.
- [114] Y. Luna-Galiano, C. Leiva, C. Arenas, C. Fernández-Pereira, Fly ash based geopolymeric foams using silica fume as pore generation agent. Physical, mechanical and acoustic properties, *J. Non-Cryst. Solids* 500 (Nov. 2018) 196–204, <https://doi.org/10.1016/j.jnoncrysol.2018.07.069>.
- [115] J. Feng, R. Zhang, L. Gong, Y. Li, W. Cao, X. Cheng, Development of porous fly ash-based geopolymer with low thermal conductivity, *Mater. Des.* 1980–2015 65 (Jan. 2015) 529–533, <https://doi.org/10.1016/j.matdes.2014.09.024>.
- [116] R.M. Novais, Robert C. Pullar, J.A. Labrincha, Geopolymer foams: an overview of recent advancements, *Prog. Mater. Sci.* 109 (Apr. 2020) 100621, <https://doi.org/10.1016/j.pmatsci.2019.100621>.
- [117] F.G.M. Aredes, T.M.B. Campos, J.P.B. Machado, K.K. Sakane, G.P. Thim, D. Brunelli, Effect of cure temperature on the formation of metakaolinite-based geopolymer, *Ceram. Int.* (2015) 10, <https://doi.org/10.1016/j.ceramint.2015.02.022>.
- [118] P. Risdanareni, J.J. Ekaputri, M.M.A.B. Abdullah, Effect of alkaline activator ratio to mechanical properties of geopolymer concrete with trass as filler, *Appl. Mech. Mater.* 754–755 (2015), <https://doi.org/10.4028/www.scientific.net/AMM.754-755.406>.
- [119] V. Benavent, F. Frizon, A. Poulesquen, Effect of composition and aging on the porous structure of metakaolin-based geopolymers, *J. Appl. Crystallogr.* 49 (6) (Dec. 2016) 2116–2128, <https://doi.org/10.1107/S1600576716014618>.
- [120] Y. Ma, J. Hu, G. Ye, The pore structure and permeability of alkali activated fly ash, *Fuel* 104 (Feb. 2013) 771–780, <https://doi.org/10.1016/j.fuel.2012.05.034>.
- [121] E. Jämstorp, M. Strømme, G. Frenning, Modeling structure–function relationships for diffusive drug transport in inert porous geopolymer matrices, *J. Pharm. Sci.* 100 (10) (Oct. 2011) 4338–4348, <https://doi.org/10.1002/jps.22636>.
- [122] D.K. Seo, D. Medpelli, J. Seo, Porous Geopolymer Materials, 2013. Patent n° US 2013/0055924 A1.
- [123] A. Thomas, Fats and fatty oils, in: *Ullmann's Encyclopedia of Industrial Chemistry*, 2000.
- [124] Z. Wang, D. Lu, Study on the effect of emulsifiers on the pore structures of geopolymer prepared by emulsion templating, *Mater. Res. Express* (May 2020), <https://doi.org/10.1088/2053-1591/ab94f9>.
- [125] D. Medpelli, J.-M. Seo, D.-K. Seo, Geopolymer with hierarchically meso-/macro-porous structures from reactive emulsion templating, *J. Am. Ceram. Soc.* 97 (1) (Jan. 2014) 70–73, <https://doi.org/10.1111/jace.12724>.
- [126] C. Bai, J. Zheng, G.A. Rizzi, P. Colombo, Low-temperature fabrication of SiC/geopolymer cellular composites, *Compos. Part B Eng.* 137 (Mar. 2018) 23–30, <https://doi.org/10.1016/j.compositesb.2017.11.013>.
- [127] C. Bai, T. Ni, Q. Wang, H. Li, P. Colombo, Porosity, mechanical and insulating properties of geopolymer foams using vegetable oil as the stabilizing agent, *J. Eur. Ceram. Soc.* 38 (2) (Feb. 2018) 799–805, <https://doi.org/10.1016/j.jeurceramsoc.2017.09.021>.
- [128] P. Hua, Adsorption of acid green and procion red on a magnetic geopolymer based adsorbent: experiments, characterization and theoretical treatment, *Chem. Eng. J.* 383 (Mar. 2020) 123113, <https://doi.org/10.1016/j.cej.2019.123113>.
- [129] M.S. Cilla, M.D. de Mello Innocentini, M.R. Morelli, P. Colombo, Geopolymer foams obtained by the saponification/peroxide/gelcasting combined route using different soap foam precursors, *J. Am. Ceram. Soc.* 100 (8) (Aug. 2017) 3440–3450, <https://doi.org/10.1111/jace.14902>.
- [130] J. Fiset, M. Cellier, P.Y. Vuillaume, Macroporous geopolymers designed for facile polymers post-infusion, *Cem. Concr. Compos.* 110 (Jul. 2020) 103591, <https://doi.org/10.1016/j.cemconcomp.2020.103591>.
- [131] M. Strozi Cilla, M. Raymundo Morelli, P. Colombo, Effect of process parameters on the physical properties of porous geopolymers obtained by gelcasting, *Ceram. Int.* 40 (8) (Sep. 2014) 13585–13590, <https://doi.org/10.1016/j.ceramint.2014.05.074>.
- [132] E. Landi, Alkali-bonded ceramics with hierarchical tailored porosity, *Appl. Clay Sci.* 73 (Mar. 2013) 56–64, <https://doi.org/10.1016/j.clay.2012.09.027>.
- [133] P. Hlaváček, V. Šmilauer, F. Škvárab, L. Kopecký, R. Šulc, Inorganic foams made from alkali-activated fly ash: mechanical, chemical and physical properties, *J. Eur. Ceram. Soc.* (2015), <https://doi.org/10.1016/j.jeurceramsoc.2014.08.024>.
- [134] R. Arellano Aguilar, O. Burciaga Díaz, J.I. Escalante García, Lightweight concretes of activated metakaolin-fly ash binders, with blast furnace slag aggregates, *Constr. Build. Mater.* 24 (7) (Jul. 2010) 1166–1175, <https://doi.org/10.1016/j.conbuildmat.2009.12.024>.
- [135] E. Prud'homme, Silica fume as porogen agent in geo-materials at low temperature, *J. Eur. Ceram. Soc.* (2010), <https://doi.org/10.1016/j.jeurceramsoc.2010.01.014>.
- [136] E. Prud'homme, P. Michaud, E. Joussein, C. Peyratout, A. Smith, S. Rossignol, In situ inorganic foams prepared from various clays at low temperature, *Appl. Clay Sci.* 51 (1–2) (Jan. 2011) 15–22, <https://doi.org/10.1016/j.clay.2010.10.016>.
- [137] L. Korat, V. Ducman, The influence of the stabilizing agent SDS on porosity development in alkali-activated fly-ash based foams, *Cem. Concr. Compos.* 80 (Jul. 2017) 168–174, <https://doi.org/10.1016/j.cemconcomp.2017.03.010>.
- [138] C. Bai, P. Colombo, High-porosity geopolymer membrane supports by peroxide route with the addition of egg white as surfactant, *Ceram. Int.* 43 (2) (Feb. 2017) 2267–2273, <https://doi.org/10.1016/j.ceramint.2016.10.205>.

Chapter II

Emulsification of low viscosity oil in AAM materials



Mineral oil
Fresh AAM grout

Which surfactant for the most stable emulsion ?

Chapter II aims at understanding the mechanisms enhancing the fixation of mineral oils in reactive inorganic matrices, by emulsification. This requires using adequate surfactants to succeed in formulating the emulsion. Six common surfactants of different nature (cationic, anionic and non-ionic) are evaluated. All characterizations are performed in the fresh state, i.e. before hardening of the materials with the aim of formulating the best possible emulsion of mineral oil in fresh alkali-activated materials.

Summary Chapter II

PREAMBLE CHAPTER II	49
1. EMULSIONS.....	50
2. SURFACTANTS.....	51
3. PICKERING EMULSIONS.....	53
4. SURFACTANTS AND SOLID PARTICLES	55
5. CONCLUSION.....	56
REFERENCES	57
CHAPTER II: EMULSIFICATION OF LOW VISCOSITY OIL IN ALKALI-ACTIVATED MATERIALS	59
ABSTRACT	59
1. INTRODUCTION.....	60
1.1. INDUSTRIAL CONTEXT.....	60
1.2. SCIENTIFIC BACKGROUND.....	60
1.3. AIMS AND SCOPES.....	63
2. EXPERIMENTAL	63
2.1. RAW MATERIALS.....	63
2.2. PREPARATION OF COMPOSITE MATERIALS	65
2.3. RHEOLOGY.....	65
2.4. DROPLET SIZE MEASUREMENTS	66
2.5. INTERFACIAL TENSION	67
2.6. DILUTED TERNARY SUSPENSIONS	67
3. RESULTS AND ANALYSIS	68
3.1. FORMATION OF THE AAM-OIL EMULSIONS	68
3.1.1. <i>Macroscopic observations</i>	68
3.1.2. <i>Rheology of fresh AAM</i>	69
3.1.3. <i>Analysis: formation of the emulsion</i>	72
3.2. PERFORMANCE OF AAM-OIL EMULSIONS THROUGH DROPLET SIZE MEASUREMENTS.....	73
3.2.1. <i>Droplet size measurements</i>	73
3.2.2. <i>Droplets velocity as an indicator for emulsion stability</i>	76
3.3. FORMATION AND STABILITY OF AAM-OIL EMULSIONS: EFFECT OF THE INTERFACIAL TENSION	77
3.3.1. <i>Direct measurement of the interfacial tension</i>	77
3.3.2. <i>Relationship between interfacial tension and OL droplet size</i>	79
3.4. FORMATION AND STABILITY OF AAM-OIL EMULSIONS: ROLE OF SOLID PARTICLES.....	80
3.4.1. <i>Influence of surfactants in the absence of particles</i>	80
3.4.2. <i>Influence of particles in the absence of surfactants</i>	80
3.4.3. <i>Influence of surfactants on the interaction between MK particles and both liquid phases</i>	82
3.4.4. <i>Influence of surfactants on the interaction between BFS particles and both liquid phases</i>	83
3.4.5. <i>Comparison and analysis of the diluted ternary suspensions</i>	83

3.5. DISCUSSION: TWO DISTINCT PATTERNS CONCERNING THE EFFECT OF SURFACTANTS DESCRIBE THE EMULSION FORMATION AND STABILITY.....	84
4. CONCLUSIONS.....	88
ACKNOWLEDGMENTS	89
APPENDIX A	90
APPENDIX B.....	92
REFERENCES	95

Preamble chapter II

The main objective of this chapter is to control the incorporation of industrial oils in fresh AAM grouts. In the interest of industrial simplicity, the selected incorporation process is the direct incorporation (Figure 1) of oil in fresh AAM slurries, as described in [1]. First, solid precursor particles (metakaolin or blast furnace slag) are introduced in the alkaline activating solution to prepare fresh AAM grouts. The dissolution of all solid particles is not immediate and AAM grouts can be considered as highly concentrated suspensions of solid particles dispersed in aqueous solutions. It is within this complex environment that the oil is introduced, forming an emulsion due to its lipophilic nature, which contrasts with the hydrophilic nature of the activating solution. In the absence of additives facilitating the emulsion formation and stability (Figure 1, 1), the formed emulsion is of poor quality and might be unstable, resulting in (partial) phase separation. On the contrary, **the addition of surfactants (Figure 1, 2) helps promoting the formation of stable emulsions, displaying much smaller and homogenous oil droplets.**

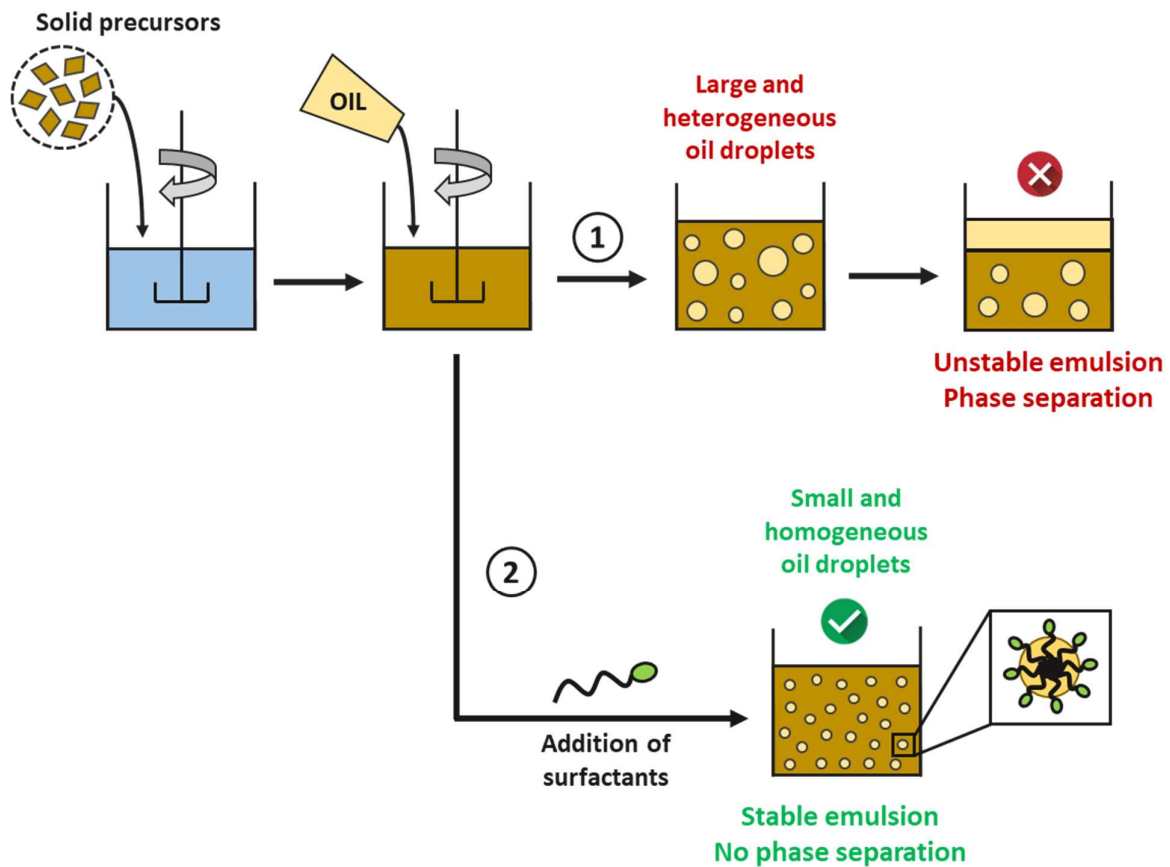


Figure 1: Description of the system under investigation.

1. Emulsions

Emulsions are multiphasic systems composed of at least two non-miscible liquids. One of the liquids is suspended in the other one in the form of spherical droplets of varying sizes ranging from several dozen nanometers to hundreds of microns. The suspended liquid is called the dispersed phase and the dispersing liquid is called the continuous phase. In general, the most hydrophilic liquid is written « W » for water and the most lipophilic liquid is written « O » for oil. Accordingly, direct emulsions in which oil is dispersed in water (O/W) are distinguished from indirect emulsions in which water is dispersed in oil (W/O). The formation of an emulsion is in fact the creation of an interface between two immiscible liquids with the change in free energy written as follows [2]:

$$\Delta G = \Delta A \cdot \gamma - T \cdot \Delta S \quad (1)$$

With ΔG the free enthalpy difference at constant T, P and n, ΔA the interfacial surface area variation between the two liquids, γ the interfacial tension and ΔS the entropy difference. During the formation of an emulsion, disorder and entropy increase but the interfacial tension is stronger and counterbalances the entropic factor ($\Delta G > 0$). Emulsions are therefore non-spontaneously created and require an external energy supply. Most of the time, this energy supply is in the form of mechanical shearing provided by several types of agitators. This is also why emulsions are kinetically stable (metastable) but thermodynamically unstable. It can be understood from Eq. 1 that the lower the interfacial tension, the more stable an emulsion and the slower the phase separation. In the absence of any stabilization mechanism, emulsions break down to go back to their thermodynamic stable state. This happens when the interfacial area between the two phases is minimal, i.e. when both phases are macroscopically separated. Figure 2 below represents the destabilization mechanisms that can be encountered (creaming, flocculation, Ostwald ripening, coalescence) [3]:

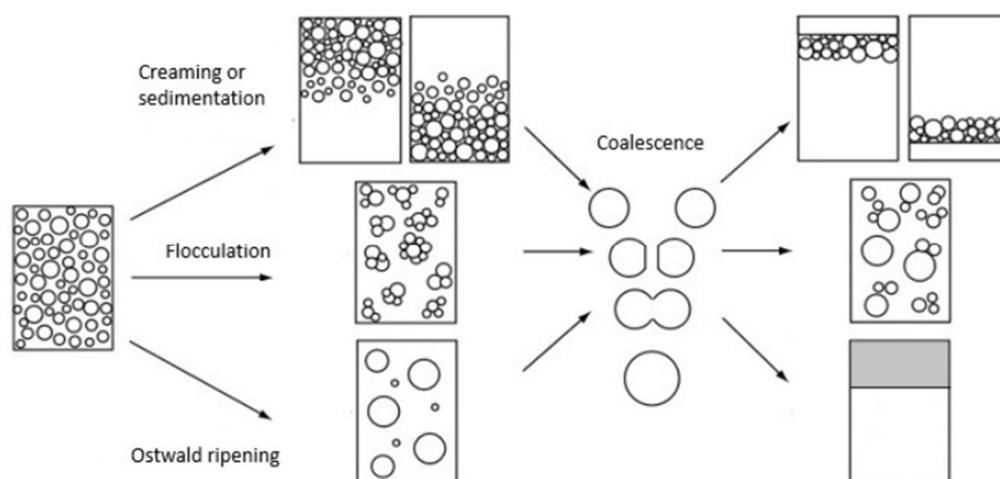


Figure 2: Schematic representation of emulsions destabilization mechanisms [3].

Sedimentation or creaming find their origin in the density difference between the two liquids: if the dispersed phase is the lightest, creaming will be observed, whereas if the dispersed phase is the heaviest, sedimentation will be observed. The droplets migration, caused by gravity, is described by the Stokes relation [4]:

$$v = \frac{2(\rho_p - \rho_f)gr^2}{9\mu} \quad (2)$$

With v the speed limit of moving droplets, ρ_p the droplets density, ρ_f the density of the dispersing phase, g the gravity field, r the radius of spherical droplets and μ the dynamic viscosity of the continuous phase. It is deduced that the kinetics of sedimentation/creaming decrease with increasing viscosity of the continuous phase. Consequently, this decreases the rate of flocculation and coalescence due to the fact that sedimentation/creaming partially contribute to these destabilization mechanisms.

Interestingly, the advantage of oil emulsions in AAM grouts is the intrinsic high viscosity of the dispersing phase, i.e. the AAM grout. Thanks to this high viscosity, most of the destabilization mechanisms are slowed down. However, if the emulsion is concentrated and poorly formulated with the presence of large and heterogeneous oil droplets, it might break down anyway (at least partially). Emulsifiers (surfactants) are generally used to improve emulsions quality and stability.

2. Surfactants

The primary role of surfactants when formulating emulsions is to reduce the interfacial tension γ between the two liquids, allowing the formation of smaller and more homogeneous droplets. The interfacial tension can be defined considering a container filled with water (Figure 3). Within the liquid, water molecules benefit from homogeneous attractive interactions with all their neighboring water molecules: hydrogen bonding, van der Waals bonding, dipole-dipole interactions. The balance of forces is therefore zero. On the contrary, water molecules present at the surface lose part of their cohesive interactions with neighboring molecules. The balance of forces is therefore non-zero and molecules at the surface are subjected to a pendular force (tension), which attracts them towards the liquid. This is the interfacial tension, which was first defined by Gibbs as follows [5]-[7]:

$$\gamma = \left(\frac{\partial G}{\partial A} \right)_{T,V,n}$$

It characterizes the amount of free energy (G) required to form an interface of surface (A) between two distinct phases, at constant T , V and n . The interfacial tension is expressed in $N.m^{-1}$ and is equivalent to a unit of energy per area in $J.m^{-2}$.

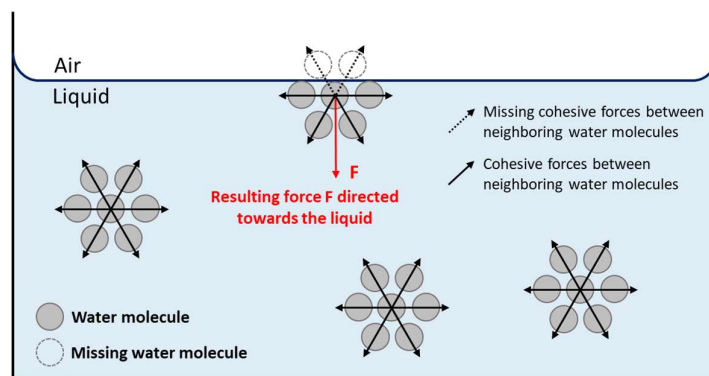


Figure 3: The physical origin of the interfacial tension: water molecules present at the surface are missing attractive interactions and are seeking to move back within the liquid [8].

Surfactants are amphiphilic molecules, composed of a hydrophilic part (polar head) and a hydrophobic part (unpolar tail). This property provides surfactant molecules the ability to adsorb at interfaces between two liquids of distinct polarity, hence reducing the interfacial tension. Thus, they facilitate the possibility of creating smaller droplets when formulating emulsions. Surfactants are generally classified in four distinct categories depending on their polar head nature [9]:

- **Anionic:** sulfates, sulfonates, organophosphorus, etc.
- **Cationic:** quaternary ammonium salt, alkylamine salts, amine oxides, etc.
- **Zwitterionic:** alkyl betaines, imidazole and amino acids derivatives, etc.
- **Non-ionic:** with ester, ether or amide bonds, amines, etc.

The selection of the appropriate surfactant in the preparation of emulsions is still often based on the semi-empirical Hydrophilic Lipophilic Balance (HLB) [10]. It was defined by Griffin in 1949 and is a way of ranking surfactants depending on their hydrophilic-lipophilic nature [11]. Each surfactant can be attributed an empirical HLB value, comprised between 0 and 20:

- If $HLB < 8$, the surfactant is rather lipophilic: W/O emulsion are favored.
- If $HLB > 12$, the surfactant is rather hydrophilic: O/W emulsions are favored.
- If $8 < HLB < 12$, the surfactant is considered equilibrated.

It is noted that the above-mentioned considerations are only valid for equilibrated volume fractions of liquids (50/50 v/v). Indeed, the volume ratio has an impact on the type of emulsion that is formed, the major phase having a tendency to be the dispersing phase. Among others, a good way of calculating the HLB value of surfactants is the empirical scale of David [12]. It is based on the surfactant chemical structures, and more specifically on the mass percentage of each hydrophilic/lipophilic groups:

$$HLB = 7 + \sum (HLB \text{ associated to each of the molecule groups}) \quad (3)$$

The HLB provides an empirical assessment of the most adapted surfactant for a given application [13] but it should not be used thoughtlessly as it contains numerous limitations.

In addition to improving emulsions quality by decreasing the size of dispersed droplets, surfactants also improve emulsions stability by preventing coalescence from occurring.

When two droplets come into close contact, van der Waals attractive interactions become very strong and tend to bring droplets together until disruption of the liquid film, resulting in coalescence and phase separation. Depending on the chemical nature of the surfactant present at the interface, van der Waals attractions might be overcome by steric repulsion (non-ionic) and/or electrostatic repulsion (ionic) [10].

3. Pickering emulsions

Rather than being stabilized by surfactant molecules, Pickering emulsions characterize mixtures of immiscible liquids stabilized using solid particles [14]. The concept of wetting, describing the ability of a liquid to spread over a solid surface is the base of Pickering emulsions. At equilibrium, a drop of liquid on a solid substrate produces a contact angle θ , which is the angle formed between planes tangent to the surfaces of solid and liquid at the wetting perimeter (Figure 4) [10].

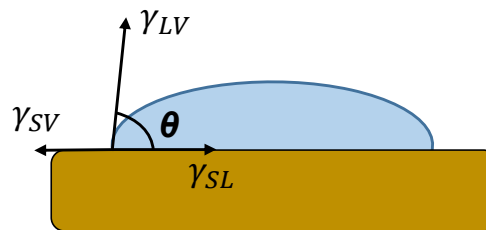


Figure 4: Graphical representation of the Young-Dupré relation, relating the wetting angle (θ) to the interfacial tensions (γ_{LV} , γ_{SL} , γ_{SV}).

Theoretically, it is possible to predict the wetting from the interfacial tensions respective of the phases in presence (solid, liquid, vapor). It just requires writing the balance of capillary forces presented in Figure 5, by projection on the solid plane, as:

$$\gamma_{LG} \cdot \cos \theta = \gamma_{SG} - \gamma_{LS} \quad (4)$$

The Young-Dupré relation is deduced, allowing to predict the contact angle from interfacial tensions:

$$\cos \theta = \frac{\gamma_{SG} - \gamma_{LS}}{\gamma_{LG}} = \frac{\gamma_S - \gamma_{LS}}{\gamma_L} \quad (5)$$

It is noted that the lower the superficial tension of the liquid (γ_L), the higher its ability to wet a solid surface. By contrast, the higher the surface energy of the solid (γ_S), the higher its ability

to be wet by a liquid. When a drop of liquid is placed onto a solid, the liquid either spreads to form a thin (uniform) film ($\theta = 0^\circ$) or remains as a discrete drop. In practice, good wetting is considered if $\theta < 90^\circ$ and poor wetting is considered if $\theta > 90^\circ$.

Considering Pickering emulsions, the attachment energy of a solid particle at the O/W interface depends on the contact angle θ and the interfacial tension γ . Considering a spherical solid particle of radius r with negligible gravity due to its small size, the energy required to remove such a particle from the interface between two liquids is given by [2]:

$$\Delta E = \gamma\pi r^2(1 \pm \cos \theta)^2 \quad (6)$$

The positive sign corresponds to the extraction of particles towards the oil phase and the negative sign corresponds to the extraction of particles towards the water phase. This equation shows that absorption is low for contact angles ranging from 0° to 20° and 160° to 180° . The closer the contact angle to 90° , the higher the attachment energy [15], [16]. The consequence of a high attachment energy is that once attached at the interface, solid particles are very difficult to remove. This is why Pickering emulsions are considered as more stable than classical emulsions stabilized by surfactants. Few additional remarks can be addressed:

- The initial location of particles is important for the stability of Pickering emulsions. Yan et al. [17] demonstrated that particles need to be present in the continuous phase before the introduction of the second liquid to form the emulsion.
- The size of particles is a key parameter of Pickering emulsions. It determines their ability to remain in solution or to position themselves at the interface. Accordingly, the lower the particle size, the higher the emulsion stability [18]. To facilitate the understanding of Pickering emulsions, particles are generally considered as spherical. However, their shape and roughness also determine their wettability and play a role in their stabilizing effect.
- The size of dispersed droplets decreases when the amount of solid particles increases [18], [19]. In addition, when the amount of particles is high, the formation of tridimensional flocculated particles has been observed, stabilizing even more the emulsion as the contact between two droplets becomes more difficult [20].

As it was illustrated in Figure 1, the objective of this work is to immobilize industrial oils in fresh AAM grouts. It is therefore important to take solid particles (metakaolin and blast furnace slag) into account, especially because they are present in high quantity (> 40 wt. %). The presence of particles in such a high quantity is expected to impact the emulsion stability as in the case of Pickering emulsions. For instance, Cantarel et al. [21] proposed a stabilization mechanism for hexadecane emulsions in fresh geopolymer grouts, based on hexadecane droplets surrounded by metakaolin particles (Figure 5).

naturally or be induced by adsorbed hydrophobic species [27]. Graphite and coal are a few of the solids possessing natural hydrophobicity and their aggregation is observed in polar solvents. However, surface hydrophobicity of solid particles is often induced by the adsorption of surfactants. For instance, Pitois et al. [28] highlighted the effect of surfactants on increasing the yield stress of fresh cement pastes owing to hydrophobic forces.

5. Conclusion

This preamble section aimed at pointing out that the studied systems are quite complex. Many parameters might impact the mineral oil emulsification in AAM. First, two distinct types of AAM are considered, implying many differences: 1) the type of solid precursor particles (chemical nature, size, shape, roughness), 2) the amount of suspended particles (higher in blast furnace slag system), and 3) the composition of the activating solutions, which impacts the interfacial tension. Also, the positioning of surfactants in these complex quaternary systems (aqueous activating solution, mineral oil, solid particles, and surfactants) is not straightforward. Surfactants are added to improve the emulsion quality and stability by positioning themselves at the interface between the two liquids. However, they might as well adsorb at the surface of solid precursor particles, hence modifying the rheology of final mixtures. Finally, the affinity of solid precursor particles (present in large quantities) for the mineral oil is a question on hold. Solid particles could interact with the oil and even participate to the emulsion stability as in Pickering emulsions.

All these questions will be the topic of the following chapter with the aim of assessing the best surfactant(s) for the incorporation of mineral oils in AAM, either based on metakaolin or on blast furnace slag. The stability of emulsions is only required until hardening of the AAM but formulating emulsions with oil droplets as small as possible is an objective as they will be more efficiently encapsulated within AAM and also less detrimental to final mechanical properties. To this purpose, several surfactants will be studied in this chapter to improve the emulsion of a mineral oil in fresh AAM slurries.

References

- [1] C. Reeb, C. Pierlot, C. Davy, and D. Lambertin, « Incorporation of organic liquids into geopolymer materials - A review of processing, properties and applications », *Ceram. Int.*, 2021, doi: 10.1016/j.ceramint.2020.11.239.
- [2] T. F. Tadros, « Emulsion Formation, Stability, and Rheology », 2013. doi: 10.1002/9783527647941.ch1.
- [3] Costa C. et al., « Emulsion Formation and Stabilization by Biomolecules: The Leading Role of Cellulose », *Polymers*, 2019, doi: 10.3390/polym11101570.
- [4] G.G. Stokes, « On the effect of the internal friction of fluids on the motion of pendulums », *Philos. Mag.*, 1851.
- [5] J. W. Gibbs, « On the Equilibrium of Heterogeneous Substances », *Am. J. Sci.*, 1878.
- [6] L. Courard and F. Michel, « Energies libres de surface des liquides et des solides: une approche de la comprehension des phenomenes interfaciaux », Liège University, 2003.
- [7] S. Le Roux, « Effet Marangoni aux interfaces fluides », PhD, Rennes University, 2015.
- [8] « Process parameter surface tension ». <https://www.sita-process.com/information-service/process-parameter-surface-tension/overview/>
- [9] J. H. Clint, « Nature of surfactants », in *Surfactant Aggregation*, 1992. doi: 10.1007/978-94-011-2272-6_1.
- [10] T. F. Tadros, « An Introduction to Surfactants », 1st Ed. Berlin: De Gruyter, 2014.
- [11] Griffin, W.C., « Classification of Surface-Active Agents by "HLB" », *J. Soc. Cosmet. Chem.*, 1949.
- [12] J. T. Davies, « A quantitative kinetic of emulsion type. I. Physical chemistry of the emulsifying agent », *Gas-liquid and liquid-liquid interfaces: Proceedings of 2nd international congress surface activity*, 1957.
- [13] E. Ruckenstein, « Microemulsions, Macroemulsions, and the Bancroft Rule », *Langmuir*, 1996, doi: 10.1021/la960849m.
- [14] S. U. Pickering, « Pickering: Emulsions », *J. Chem. Soc. Trans.*, 1907, doi: 10.1039/CT9079102001.
- [15] S. Tarimala, « Self-assembled structure and dynamics of solid particles at pickering emulsion interfaces », PhD, Texas Tech University, 2006.
- [16] N. Popp, S. Kutuzov, and A. Böker, « Various Aspects of the Interfacial Self-Assembly of Nanoparticles », *Adv. Polym. Sci.*, 2010, doi: 10.1007/12_2010_52.
- [17] Y. Yan and J. H. Masliyah, « Solids-stabilized oil-in-water emulsions: Scavenging of emulsion droplets by fresh oil addition », *Colloids Surf. Physicochem. Eng. Asp.*, 1993, doi: 10.1016/0927-7757(93)80423-C.
- [18] D. E. Tambe and M. M. Sharma, « The effect of colloidal particles on fluid-fluid interfacial properties and emulsion stability », *Adv. Colloid Interface Sci.*, 1994.
- [19] B. P. Binks and C. P. Whitby, « Silica Particle-Stabilized Emulsions of Silicone Oil and Water: Aspects of Emulsification », *Langmuir*, 2004, doi: 10.1021/la0303557.
- [20] S. Abend and G. Lagaly, « Bentonite and double hydroxides as emulsifying agents », *Clay Miner.*, 2001, doi: 10.1180/0009855013640009.
- [21] V. Cantarel, D. Lambertin, A. Poulesquen, F. Leroux, G. Renaudin, and F. Frizon, « Geopolymer assembly by emulsion templating: Emulsion stability and hardening mechanisms », *Ceram. Int.*, 2018, doi: 10.1016/j.ceramint.2018.03.079.
- [22] C. Wang, O. Kayali, and J.-L. Liow, « Effect of electrostatic repulsion induced by superplasticizers on the flow behaviour of fly ash pastes », presented à Fifth International Conference on Sustainable Construction Materials and Technologies, 2019.
- [23] Y. Hu, Q. Yang, J. Kou, C. Sun, and H. Li, « Aggregation mechanism of colloidal kaolinite in aqueous solutions with electrolyte and surfactants », *PLOS ONE*, 2020, doi: 10.1371/journal.pone.0238350.
- [24] X. Zhang, Y. Hu, and R. Liu, « Hydrophobic aggregation of ultrafine kaolinite », *J. Cent. South Univ. Technol.*, 2008, doi: 10.1007/s11771-008-0069-9.

- [25] Y. K. Leong, D. V. Boger, P. J. Scales, and T. W. Healy, « Interparticle Forces Arising from Adsorbed Surfactants in Colloidal Suspensions: An Additional Attractive Force », *J. Colloid Interface Sci.*, 1996, doi: 10.1006/jcis.1996.0418.
- [26] F. M. Fowkes, « Attractive forces at interfaces », *Ind. Eng. Chem.*, 1964, doi: 10.1021/ie50660a008.
- [27] P. Somasundaran, S. C. Mehta, X. Yu, and S. Krishnakumar, « Colloid Systems and Interfaces Stability of Dispersions through Polymer and Surfactant Adsorption », in *Handbook of Surface and Colloid Chemistry*, 2009.
- [28] B. Feneuil, O. Pitois, and N. Roussel, « Effect of surfactants on the yield stress of cement paste », *Cem. Concr. Res.*, 2017, doi: 10.1016/j.cemconres.2017.04.015

Chapter II: Emulsification of low viscosity oil in alkali-activated materials (Published in *Cement and Concrete Research*)

Charles Reeb^{1,2}, Christel Pierlot¹, Catherine A. Davy¹, Matthieu Bertin², Vincent Cantarel³,
David Lambertin²

¹Univ. Lille, CNRS, Centrale Lille, ENSCL, Univ. Artois, UMR 8181-UCCS-Unité de Catalyse et de Chimie du Solide – F-59000 Lille, France

²CEA, DES, ISEC, DE2D, SEAD, LCBC, Univ Montpellier, Marcoule, France

³Japan Atomic Energy Agency, CLADS, Waste Management Division, Storage Equipment Soundness Evaluation Group, Tokai-mura, Ibaraki-ken, Japan

Abstract

This research aims to understand the mechanisms enhancing the fixation of low viscosity mineral oils, including tailings, in reactive inorganic matrices, by emulsification. To this purpose, significant amounts of a model low viscosity pure mineral oil (20%vol) are immobilized in alkali-activated materials (AAM), either based on metakaolin or blast furnace slag. In such case, Portland cement-based matrices are not adequate (emulsification delicate to manage and excessive setting retardation). Various surfactants are used to ease the oil emulsion.

Visual observation and rheology evidence two distinct groups of surfactants. One contributes to structuring the oil/AAM fresh mix, with greater viscosity than without surfactant; the other includes non-structuring surfactants, without change in viscosity. Each group depends on the AAM considered. Characterization of diluted ternary suspensions (solid particles – oil – activating solution) relates the structuring effect to interactions between oil and solid particles, through the surfactants non-polar hydrocarbon tails.

Whatever the AAM and the surfactant, the oil droplet size decreases significantly, without consistent correlation with the interfacial tension between oil/activating solution. Surfactants exhibit different efficiency depending on their solubility in the continuous phase and interfacial tension alone does not explain the reduction in oil droplet size.

A detailed discussion featuring two distinct surfactant mechanisms for the stabilization of oil emulsions in AAM is undertaken.

Keywords: Alkali-activated cement (D), BFS, Composite (E), Geopolymer, Surfactant, Emulsion

1. Introduction

1.1. Industrial context

The immobilization of varied wastes into cement-based materials by solidification/stabilization (S/S) is a common procedure, because it ensures a chemical stabilization of many compounds and produces a mechanically stable waste form [1], [2].

For immobilizing organic liquids (OL), although heat treatment and calcination are common industrial procedures, it is a delicate option for radioactive OL waste, due to current regulations limiting radiologic activity and due to the composition of the waste in specific (heavy) chemical compounds. Currently, large amounts of radioactive organic wastes are stored temporarily in the vicinity of nuclear facilities, awaiting further and longer-term treatment. For these reasons, the S/S of radioactive OL has been investigated, particularly in cement matrices; see for instance [3]. More recently, a number of studies has been published on the conditioning of organic liquids in geopolymer cements; these are referred to in the review paper by Reeb and al. [4].

In the case of organic liquids (OL), their incorporation in cement-based materials is also of interest for various applications, e.g. the formation of porous materials (through emulsion templating and removal of the dispersed phase [5], [6], the design of composite materials with improved and/or combined properties [7] or the immobilization of industrial wastes [8], [9]. The process is similar to that of cement paste foaming, although specific phenomena might occur with OL [10], [11], such as saponification of vegetable oils [6].

Several methods to incorporate OL into cement-based materials are distinguished [4]. These are 1) the direct incorporation into a reactive cement slurry, 2) the pre-emulsification prior to the addition of a solid cement precursor or 3) the impregnation into solids prior to the addition into the cement slurry. The micro-encapsulation of organic liquids into polymer shells prior to their incorporation into a cement slurry has also been proposed, but it is expensive and technically challenging [12]. The direct process is particularly interesting because it offers the possibility to incorporate large amounts of OL. However, practical issues remain for the adequate incorporation of low viscosity OL into cement matrices, mainly due to the instability of the mix [4].

1.2. Scientific background

Cement matrices for waste immobilization. Portland cements have been widely studied to immobilize organic compounds, but issues exist regarding cement setting and strength development in presence of OL [13]-[15]. Comparatively, alkali-activated materials (AAM) display better performance for OL immobilization [16]-[18]. Nowadays, AAM are also of

interest because of their lower environmental impact, their reasonable cost and their use in various applications such as insulation, catalysis or filtration [19]. AAM require a strong alkaline source (e.g. NaOH) to accelerate the dissolution of inorganic solid precursors composed of reactive silicates and aluminates [20].

Depending on the amount of Ca present in the raw materials, two main types of solid phases are obtained [21]-[23]. C-(N)-A-S-H⁺ type gels are formed in Ca-rich systems through hydration mechanisms similar to the formation of C-A-S-H in Portland cements [24]. N-A-S-(H) type solids are formed in Ca-poor systems through polycondensation reactions, also called geopolymerization [25]. The main distinction between these two solid types is that water is part of the C-(N)-A-S-H tobermorite-like structures (through hydration reactions) [26], whereas water is not part of the N-A-S-(H) tridimensional aluminosilicate networks, being only required as a dissolution medium and being released upon solid formation (through polycondensation reactions) [27]. These fundamental differences in raw materials, reactivity and solid structures explain the distinct behaviors of both systems in presence of OL species. More specifically, while the presence of organic compounds generally disturbs the setting and hardening of C-(N)-A-S-H binders [28]-[30], the mechanism of geopolymer formation is such that liquid/liquid interactions are not damageable for the synthesis of composite organic/inorganic materials [9],[31].

Emulsification processes. The immobilization of an OL in a cement matrix is performed by emulsifying the OL using a mechanical stirring apparatus (rotating blade and container). The external stirring energy brought to the system allows forming smaller droplets by progressive break-up of the OL phase. The formation of a stable emulsion requires to control the droplet size distribution, and ideally to form uniform droplets smaller than 1 μm . The droplet break-up processes are critical in this regard. The main parameters driving these phenomena are presented in Appendix A1. They are the capillary number (under laminar flow or turbulent flow driven by viscous forces, as used in the pioneering works of Grace [32]) and the Weber number (under turbulent flow driven by inertial forces).

Emulsion stability. Emulsions require an energy input because they are *thermodynamically unstable*. Even after production, they tend to go back to their thermodynamically most favored state, i.e. when the two liquids are separated in distinct phases. One of the most problematic emulsion breakdown process is *coalescence* (i.e. the fusion of two or more droplets into larger ones). This mechanism is driven by the disjoining pressure. It is described in more details in Appendix A1.

[†]In cement chemistry, C stands for CaO, N for Na₂O, A for Al₂O₃, S for SiO₂ and H for H₂O.

Moreover, for a given emulsion, gravitational forces imply that larger droplets move faster than smaller ones to the top of the mixing container (if their density is lower than that of the medium – it is *creaming*) or to the bottom (if their density is larger than that of the medium – it is *sedimentation*); this is described by Stokes equation, modified for concentrated emulsions [33]. It is usually considered that stable emulsions, i.e. emulsions with negligible creaming, correspond to droplet velocities below 1 mm/j [31].

Effect of surfactants. In order to allow droplets deformation until break-up, surfactants are used to lower the interfacial tension, by positioning themselves at the interface between the two immiscible liquids [34]. More specifically, they allow the formation of finer and more homogeneous droplet size distributions [11].

Surfactants also play a major role in emulsion stability by limiting coalescence through various mechanisms: 1) smaller droplets, which are formed by adding surfactants, are generally less susceptible to surface fluctuations, 2) surfactants enhance the Gibbs elasticity of the droplets, and this dampens the interface fluctuation due to the Marangoni effect [33], 3) surfactants increase electrostatic and/or steric repulsions, which in turn increases the disjoining pressure.

The purpose of adding surfactant is therefore twofold - decrease the interfacial tension to improve the emulsion quality, and limit the coalescence of droplets.

Effect of the presence of solid particles. AAM matrices are made by stirring an aqueous alkaline solution with solid alumino-silicate particles made of blast furnace slag (BFS), metakaolin (MK) or else, until obtaining a homogeneous slurry (i.e. a fresh paste). Therefore, the addition of OL into AAM slurries leads to the formation of **complex ternary systems**, being simultaneously emulsions (due to the presence of OL) and suspensions (due to the presence of solid particles).

For instance, Cantarel et al. [9] have proposed that the solid particles could act as oil stabilizers, as observed in Pickering emulsions. In specific conditions, the addition of an immiscible liquid to a suspension of solid particles leads to the formation of so called “capillary systems”, characterized by a strong structuration of the medium [35],[36]. In such capillary systems, the oil positions itself in between particles thanks to capillary forces, hence creating agglomerates of particles, which strongly increases the viscosity of the initial suspension.

In these ternary systems, surfactants also interact with solid alumino-silicate particles. For instance, the adsorption of surfactant polar heads at the surface of solid particles could occur either *via* hydrogen bonding [37] or *via* electrostatic interactions [38]–[40]. It has been observed that the adsorption of surfactants at the surface of suspended solid particles could lead to the formation of “hydrophobic forces” with strong impact on the rheology of the suspensions [37],[39],[41],[42]. Some authors have highlighted different behaviors for

surfactants in cement paste, such as precipitation [43], interaction with cement grains or no interaction with cement grains [44], which lead to contrasting impact on the properties of the fresh mix (rheology, surface tension, stability).

1.3. Aims and scopes

The present study aims at understanding the formation and stability mechanisms occurring when emulsifying a mineral oil (an alkane) into two distinct types of fresh AAM pastes. Various surfactants (cationic, anionic, and non-ionic) are added to the fresh AAM paste containing oil, and contribute to the emulsion quality and stability. The AAM are either alkali-activated BFS (AABFS), leading to a C-(N)-A-S-H gel, with a high Ca content, or MK-based geopolymer (GP), leading to N-A-S-(H) solids, with a low Ca content. The incorporation consists in adding 20%vol. of a model low viscosity organic liquid, i.e. a non-reactive mineral oil, which cannot be immobilized without surfactant addition.

In the following, the consistency of the fresh slurries is determined by combining visual observations and rheology. These elements are used to determine whether the usual conditions for droplets breakup and small droplets formation are reached, following the work initially proposed by Grace [32]. Two different behaviors (structuring/non-structuring) of the fresh emulsions are also discussed.

Once the conditions for the formation of an emulsion are reached, different mechanisms tend to destabilize it. In order to discuss gravitational effects as destabilizing factors, oil droplet size distributions are quantified, and the average droplets velocity is determined using the modified Stokes law for concentrated suspensions.

The contribution of interfacial forces to the formation and stability of the emulsions is discussed after measuring the interfacial tension between the oil and the activating solution added with different surfactants. Interfacial tension and mean droplet size are correlated, in order to highlight the two different surfactant behaviors.

Finally, the effect of solid MK or BFS particles on the emulsion stability is assessed by determining the behavior of diluted ternary suspensions (solid particles-oil-activating solution). Mechanisms explaining the emulsion formation and stability, depending on the surfactant involved, are discussed.

2. Experimental

2.1. Raw materials

An aqueous sodium silicate solution (Betol 39T) was obtained from Woellner (Germany). Sodium hydroxide (purity > 99%) was purchased from VWR International (USA). A commercial

pure mineral oil (Finavestan A360B) was obtained from Total (France); its density is of 0.87 g/cm³ (+/- 0.01). This oil is chosen due to its absence of additives, to its absence of reactivity in alkaline media, and to its low viscosity (of about 0.1 Pa.s at a shear rate of 100 s⁻¹). Metakaolin (MK) powder of M1000 grade was obtained from Imerys (France) and blast furnace slag (BFS) particles were purchased from Ecocem (France). The density, the median diameter (d₅₀) and the Specific Surface Area (given by the provider) for MK and BFS particles are given in Table 1.

Table 1: Properties of MK and BFS particles.

	Density (g/cm³)	d₅₀ (μm)	Specific Surface Area (m²/g)
MK	2.40	15.0	17.00
BFS	2.90	11.0	0.45

Two dyes adapted to staining organic liquids, namely Sudan blue II and Sudan red III, were obtained from Sigma Aldrich (USA). The surfactants used in this work are listed in Table 2. SDS, Brij O10, Tween 80 and Span 80 were purchased from Acros Organics (USA). CTAB and Glucocon 225DK (hereafter referred to as Glucocon) were obtained from Sigma Aldrich and BASF (Germany), respectively. Owing to their HLB, all surfactants (except Span 80) are predominantly hydrophilic, so that they are added to the aqueous activating solution of MK or BFS. Preliminary investigations show that all surfactants (including Span 80) are partly to fully soluble in these solutions. Xanthan gum (Sigma Aldrich, USA) was obtained from Sigma Aldrich (USA).

Table 2: Denomination and chemical description of surfactants tested in this study.

Chemical description	Commercial name	Category	HLB ^a
Cetyl Trimethyl Ammonium Bromide	CTAB	Cationic (+)	10
Sodium Dodecyl Sulfate	SDS	Anionic (-)	40
Polyoxyethylene (10) oleyl ether	Brij O10	Non-ionic (∅)	12.4
C8-C10-alkyl polyglucoside	Glucopon 225DK	Non-ionic (∅)	13.5
Polyoxyethylene (20) sorbitan monooleate	Tween 80	Non-ionic (∅)	15
Sorbitan monooleate	Span 80	Non-ionic (∅)	4.3

^aHLB = Hydrophilic Lipophilic Balance. Surfactant are hydrophilic if HLB > 10; Surfactants are lipophilic if HLB < 10; Surfactants are equilibrated if HLB = 10.

2.2. Preparation of composite materials

In order to obtain a MK-based GP paste, the components (sodium silicate, sodium hydroxide, water and MK) are weighed with a molar composition of 3.5 SiO₂ : 1.0 Al₂O₃ : 1.0 Na₂O : 14.0 H₂O.

For the AABFS paste, the components (sodium silicate, sodium hydroxide, water and BFS) are weighed with a water/BFS mass ratio equal to 0.45 and a mass concentration of sodium hydroxide of 10%. This allows a good workability of the paste and reasonable hardening of the material [45].

In both cases, the molar concentration of surfactant with respect to the volume of activating solution (sodium silicate, sodium hydroxide and water) is 3.10⁻³ mol.L⁻¹, allowing a good incorporation of the oil.

Further details on AAM slurry manufacturing, dyeing and density are given in Appendix A2.

2.3. Rheology

The viscosities of fresh materials were measured on an AR1000 rheometer (TA Instruments) at 25°C and using a vane geometry. A gradually increasing shear rate from 10⁻² to 100 s⁻¹ was applied to the fresh mixtures over a period of 3 min, followed by a gradually decreasing shear rate in the same conditions. Flow curves (shear stress τ as a function of shear rate $\dot{\gamma}$) were plotted, from which viscosity η is deduced ($\eta = \tau/\dot{\gamma}$).

Flow curves were also modeled using the Herschel-Bulkley relationship, which appears as a suitable candidate to describe AAM rheological behavior [46],[47]. This relationship involves three varying parameters, and is applicable to fluids with non-linear evolution as follows [48]:

$$\sigma = \sigma_0 + K\dot{\gamma}^n \quad (1)$$

where σ_0 is the yield stress (Pa), K is the consistency index (Pa.s) and n is the flow index. Comparing K values is possible for fluids with similar n values. Shear thinning is observed when $n < 1$, and shear thickening for $n > 1$.

2.4. Droplet size measurements

The sample preparation consists in carefully diluting a droplet of an alkali-activated paste containing oil with an aqueous gel of xanthan gum at 0.5 wt.% prepared beforehand (Figure 1). The dilution prevents cement hardening and freezes the oil droplets thanks to the high viscosity of the gel. A drop of the dilution is then placed on a glass slide and observed with an optical microscope (Keyence VHX-5000) in reflexing mode.

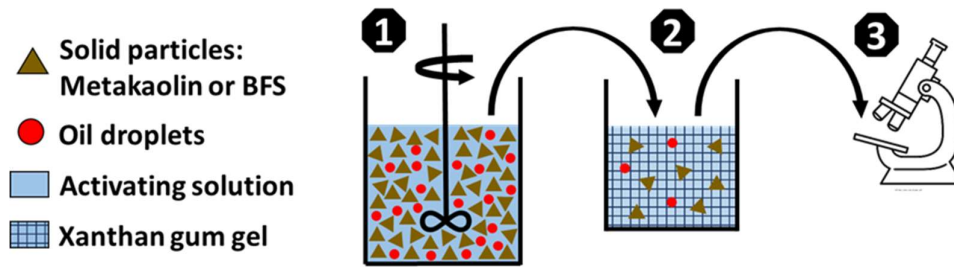


Figure 1: Schematic representation of the dilution of fresh alkali-activated slurries containing oil (1) in a xanthan gum gel (2) followed by microscopic observations (3).

For each sample, diameters of at least 100 droplets were measured manually using the ImageJ software to determine droplet size distributions. The median diameter d_{50} is the diameter for which the cumulative volume fraction is equal to 50%. In addition, the mean volume diameter ($d[4,3]$) and the standard deviation, as an indicator for polydispersity (P), were calculated as follows:

- Mean volume diameter from De Brouckere [49]:

$$d[4,3] = \frac{\sum_1^n d_i^4 \sigma_i}{\sum_1^n d_i^3 \sigma_i} \quad (2)$$

- Polydispersity index:

$$P = \frac{1}{n-1} \times \sqrt{\sum_i^n (d_i - d_{50})^2} \quad (3)$$

where σ_i is the total number of droplets with diameter d_i (μm) and n the total number of droplets analyzed.

2.5. Interfacial tension

For a spherical droplet of radius R , made of fluid 1 and located inside fluid 2, Young Laplace's equation [50] reads:

$$\Delta P = \frac{2\gamma_{12}}{R} \quad (4)$$

Where ΔP is the pressure difference at the interface and γ_{12} is the interfacial tension between the two immiscible fluids. γ_{12} is interpreted as the force by unit length, which holds the surface between fluid 1 and fluid 2.

γ_{12} is measured for an oil droplet placed inside a solution, which is either deionized water or one of the two alkaline activating solutions of the AAM of this research. For each surfactant considered individually, each solution is prepared with a concentration of $3 \cdot 10^{-3} \text{ mol} \cdot \text{L}^{-1}$ and let under mechanical stirring for several hours.

The interfacial tension is determined at 25°C using an automatic drop tensiometer TRACKER™ (Teclis scientific) in the rising drop configuration. First, a droplet of oil is produced from a needle in the mix of activating solution and surfactant contained in a tank. Then, a camera follows the drop formation and a photograph is recorded once the drop is stable. Finally, thanks to the TRACKER™ software and by using models based on Young-Laplace's equation, the droplet size and shape are analyzed automatically to determine the interfacial tension γ_{12} .

2.6. Diluted ternary suspensions

In order to observe the effect of each surfactant on the interactions between solid particles and both liquid phases (activating solution (AS) and oil), diluted ternary mixtures were formulated with a low amount of solid particles (5%vol.). Except for that strong reduction in particle content, the other formulation parameters have been chosen in order to be as close as possible to actual pastes. In practice, all components were weighted and poured in 20 mL flasks, and mixtures were homogenized for 1 min using an Ultraturrax® stirrer (10000 rpm). The oil was colored in blue using a Sudan blue II organic dye in order to be easily traceable. Table 3 below summarizes the formulated compositions. After mixing, samples were left to

rest during 3 days until stabilization to an equilibrium state, after which pictures of each sample were taken (see Results section).

Table 3: Summary of formulated ternary mixtures. The volume of oil is 20%vol. The volume of particles (MK and BFS) is 5%vol. The concentration of surfactants is 3.10^{-3} mol.L⁻¹. The mixtures G1 to G14 were formulated with the AS of a MK-based GP as aqueous phase. The mixtures L1 to L14 were formulated with the AS of an AABFS as aqueous phase.

MK-based GP activating solution		AABFS activating solution		Surfactants
Sample N°	MK amount	Sample N°	BFS amount	
G1	-	L1	-	None
G2	-	L2	-	CTAB
G3	-	L3	-	Brij O10
G4	-	L4	-	Glucopon
G5	-	L5	-	SDS
G6	-	L6	-	Span 80
G7	-	L7	-	Tween 80
G8	5%vol.	L8	5%vol.	None
G9	5%vol.	L9	5%vol.	CTAB
G10	5%vol.	L10	5%vol.	Brij O10
G11	5%vol.	L11	5%vol.	Glucopon
G12	5%vol.	L12	5%vol.	SDS
G13	5%vol.	L13	5%vol.	Span 80
G14	5%vol.	L14	5%vol.	Tween 80

3. Results and analysis

3.1. Formation of the AAM-oil emulsions

3.1.1. Macroscopic observations

Without surfactant, in the MK-based GP paste, a small fraction of oil coalesces at the surface and oil droplets are visible to the naked eye (Figure 2, red dots). For the AABFS paste, a significant amount of oil quickly coalesces at the surface (Figure 2, red spots). The incorporation of the oil is slightly more efficient in MK-based GP than in AABFS, but it is not sufficient for oil immobilization; without surfactant, the emulsions are not properly formulated and not stable.

Comparatively, Figure 2 shows that all tested surfactants improve significantly the incorporation of the oil in both AAM, with homogeneous mixtures and no coalescence. Oil droplets are no longer visible to the naked eye; thanks to the use of surfactants, the emulsions are properly formulated and stable.

From these macroscopic observations alone, two distinct effects of surfactants are noted. A number of surfactants lead to flowable mixtures with an aspect similar to the paste without surfactant. These are called “non-structuring” surfactants. They are SDS and Glucocon for MK-based GP, or CTAB, SDS, Glucocon, Brij O10 and Tween 80 for AABFS. In contrast, the other surfactants lead to thick pastes, which are viscous and non-flowable mixtures. They are described as “structuring” surfactants. These are CTAB, Brij O10, Span 80 and Tween 80 for MK-based GP, or Span 80 for AABFS. It is to be noticed that the surfactants corresponding to each type differ, depending on the AAM considered. The structuration of the paste is attributed to an agglomeration of solid particles in presence of certain surfactants [51]; it is investigated further in this research.

First, the mechanisms of structuration or non-structuration of the pastes are investigated below, by *quantifying* the macroscopic observations through rheology measurements.







	Reference without surfactants	Non-structuring surfactants (stable viscosity)		Structuring surfactants (higher viscosity)	
MK-based GP			SDS Glucocon		CTAB Brij O10 Span 80 Tween 80
AABFS			CTAB SDS Glucocon Brij O10 Tween 80		Span 80

Figure 2: Macroscopic observations highlighting the influence of surfactants on the incorporation of oil (colored with organic red dye) in fresh AAM.

3.1.2. Rheology of fresh AAM

Flow curves obtained for AAM slurries with different surfactants are presented in Figure 3 (for MK-based GP) and Figure 4 (for AABFS) respectively. Back and forth evolutions (from 10^{-2} to 100 s^{-1} and from 100 to 10^{-2} s^{-1}) are nearly stackable for all the samples. Therefore, only back

measurements are presented, in order to have a better readability and to avoid the plastic effect observed at low shear rates when moving forth.

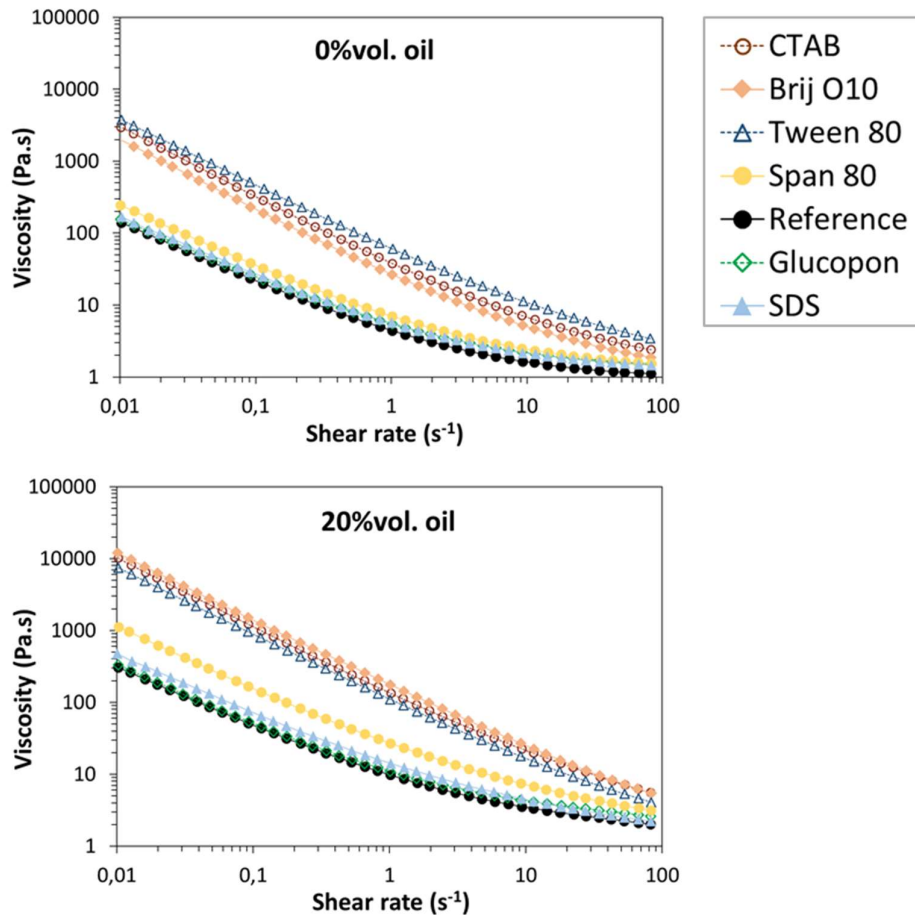


Figure 3: Influence of surfactants on the evolution of flow curves in MK-based GP paste: without oil (top), with 20%vol. of oil (down).

For MK-based GP pastes without oil (Figure 3, top), Glucopton and SDS do not significantly influence the viscosity of MK-based GP pastes, as observed earlier by Kaddami and Pitois [52]. Span 80 only slightly increases viscosity in the absence of oil. On the opposite, the addition of Tween 80, CTAB or Brij O10 induces a strong viscosity increase, by one order of magnitude at low shear rate. This indicates a structuration of the solid particles suspensions.

For MK-based GP pastes added with oil (Figure 3, down), the impact of surfactants, which is observed without oil, is confirmed and strongly amplified. Tween 80, CTAB and Brij O10 all induce a similar and significant structuration of the paste, with a viscosity increase by more than one order of magnitude at low shear rate. The effect of Span 80, leading to a viscosity increase, is more pronounced in presence of oil (with an increase by a factor of 2 at low shear rate). Despite the incorporation of oil, SDS and Glucopton do not have a significant impact on the rheology of the system.

For the AABFS pastes without oil (Figure 4, top), except for Span 80, all flow curves are superposed, with no significant influence of the surfactants on the viscosity of the fresh materials. Span 80 is the only surfactant leading to a significant increase in viscosity (by 50% at low shear rate). For AABFS pastes containing oil (Figure 4, down), flow curves are not exactly superposed anymore, but the influence of surfactants is limited in comparison with the observations made on MK-based GP pastes. Except for Span 80, which causes a significant increase in viscosity by a factor of 2, none of the tested surfactants significantly affects the rheology of AABFS pastes containing oil, especially at high shear rates.

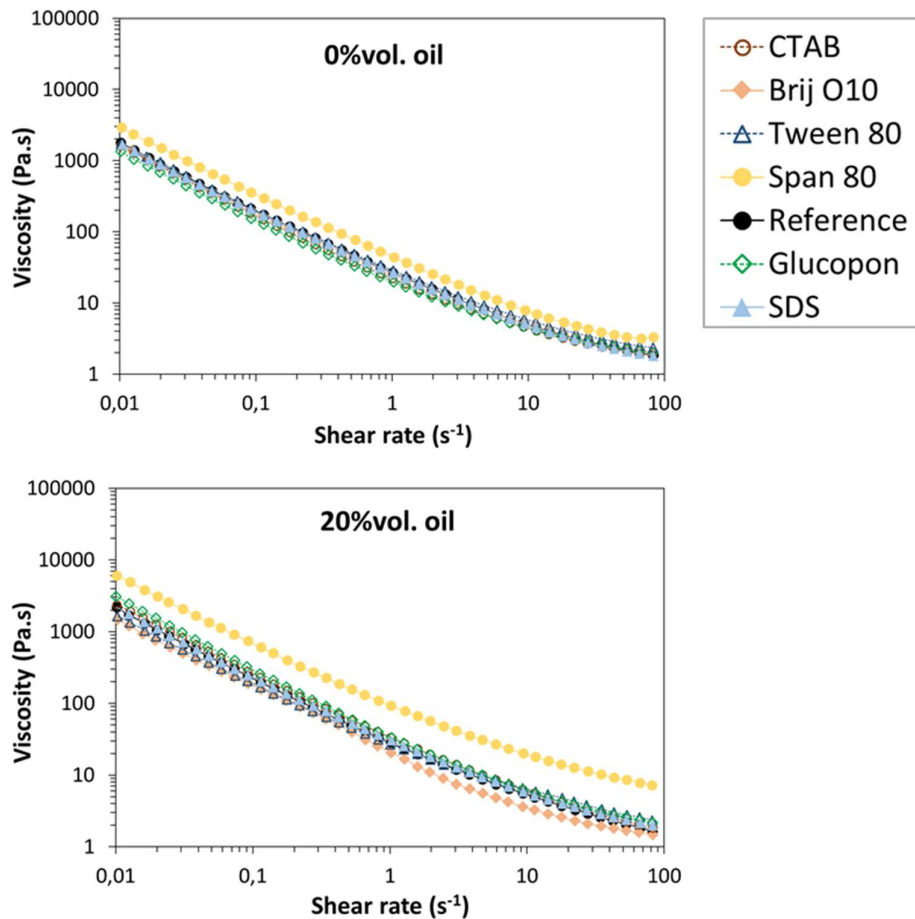


Figure 4: Influence of surfactants on the evolution of flow curves in AABFS pastes without oil (top), or with 20%vol. oil (down)

Finally, the flow curves from Figures. 3 and 4 were fitted using the Herschel-Bulkley model. Although not shown, it is noted that all pastes have a flow index n smaller than one. As expected from the literature [46],[47], this indicates that AAM have a shear-thinning behavior. Shear thinning mixtures display high viscosities when they are not subjected to any shearing other than gravitational shearing (i.e. at rest); in such case, oil droplets are stable because no significant droplet movement is expected. This is investigated further in Sub-section 3.2.2.

Moreover, yield stress σ_0 is a useful parameter to confirm the structuration, because the higher the structuration, the greater σ_0 . Yield stress values σ_0 are presented in Table 4. The yield stress of MK-based GP pastes is strongly impacted by CTAB, Brij O10 and Tween 80 surfactants, leading to non-flowable slurries, especially in presence of oil ($\sigma_0 \geq 80$ Pa), whereas Glucocon and SDS provide similar yield stress to that of the reference paste. As for viscosity, Span 80 only increases significantly σ_0 in presence of oil, in good correlation with the structuring behavior of the paste (Figure 2). In AABFS pastes, yield stress variations are limited, except with Span 80. Most of the surfactants provide a similar yield stress to the reference paste. Span 80 is the only surfactant significantly affecting the yield stress (and the flowability) of AABFS pastes; it is also the only surfactant leading to a structuration of AABFS paste.

Table 4: Yield stress values σ_0 obtained with the Herschel-Bulkley model of the experimental flow curves

Yield stress σ_0 (Pa)	MK-based GP		AABFS	
	0%vol.	20%vol.	0%vol.	20%vol.
Reference	2.2	4.1	24.9	20.1
Glucocon	2.4	4.2	13.9	28.9
CTAB	30.8	103.5	16.7	23.9
Brij O10	20.6	119.4	18.1	17.1
Tween 80	42.0	79.8	19.6	16.0
Span 80	3.5	13.3	35.1	63.0
SDS	2.6	6.0	18.7	22.2

3.1.3. Analysis: formation of the emulsion

In order to determine if the viscosity ratio p is in the good range for easy droplet break-up (see Appendix A), the latter was calculated between the AAM slurries (i.e. continuous phase) and the oil (i.e. dispersed phase) for a given shear rate of 100 s^{-1} (Table 5). Only extreme cases are presented; reference slurries (without surfactant) represent the lowest viscosity of the continuous phase, whereas slurries containing Tween 80 and Span 80 represent the highest viscosity of the continuous phase in MK-based GP and AABFS slurries respectively. According to the correlation between Ca_c and p proposed by Grace [32], all the formulated slurries display a viscosity ratio p in the adequate range to have a low critical capillary number Ca_c (i.e. Ca_c quite close to 1). This is indicative of an easier break-up of the OL droplets and a good incorporation of the OL.

Table 5: Viscosity ratios $p (= \eta_d/\eta_c)$ calculated based on viscosity measurements at a given shear rate of 100 s^{-1} and a temperature of 25°C for MK-based GP or AABFS pastes with 20%vol oil (reference: without surfactant, or with most influential surfactants)

Phase considered		Viscosity at 100 s^{-1}	Viscosity ratio ($p = \eta_d/\eta_c$)
Dispersed	Mineral oil (Finavestan)	0.130	-
Continuous	MK-based GP (reference)	1.119	1.16×10^{-1}
	AABFS (reference)	1.854	7.0×10^{-2}
	MK-based GP (Tween 80)	3.434	3.8×10^{-2}
	AABFS (Span 80)	3.314	3.9×10^{-2}

3.2. Performance of AAM-oil emulsions through droplet size measurements

This part investigates the droplet size distributions of the OL dispersed in the fresh AAM slurries, in order to determine whether creaming and coalescence (i.e. emulsion instability) can occur.

3.2.1. Droplet size measurements

Examples of microscopic observations of fresh materials are given in Figure 5 with their corresponding droplet size distributions. The complete set of microscopic observations and their corresponding droplet size distributions are given in Appendix B1 (MK-based GP samples) and Appendix B2 (AABFS samples).

It is to be noticed that when using Tween 80 in MK-based GP (Figure 5, b), agglomerates of particles are observed despite the dilution. Moreover, these agglomerates surround very small oil droplets.

Figure 5 also shows that without surfactants, large droplets are present in both types of AAM. The majority have a diameter lower than $100 \mu\text{m}$ in MK-based GP, whereas the majority have a diameter higher than $100 \mu\text{m}$ in AABFS. These droplet sizes are in accordance with macroscopic observations previously discussed (Figure 2). This confirms that without surfactants, the oil droplets are observable to the naked eye in both matrices, the resolution capability of human eye being about $100 \mu\text{m}$.

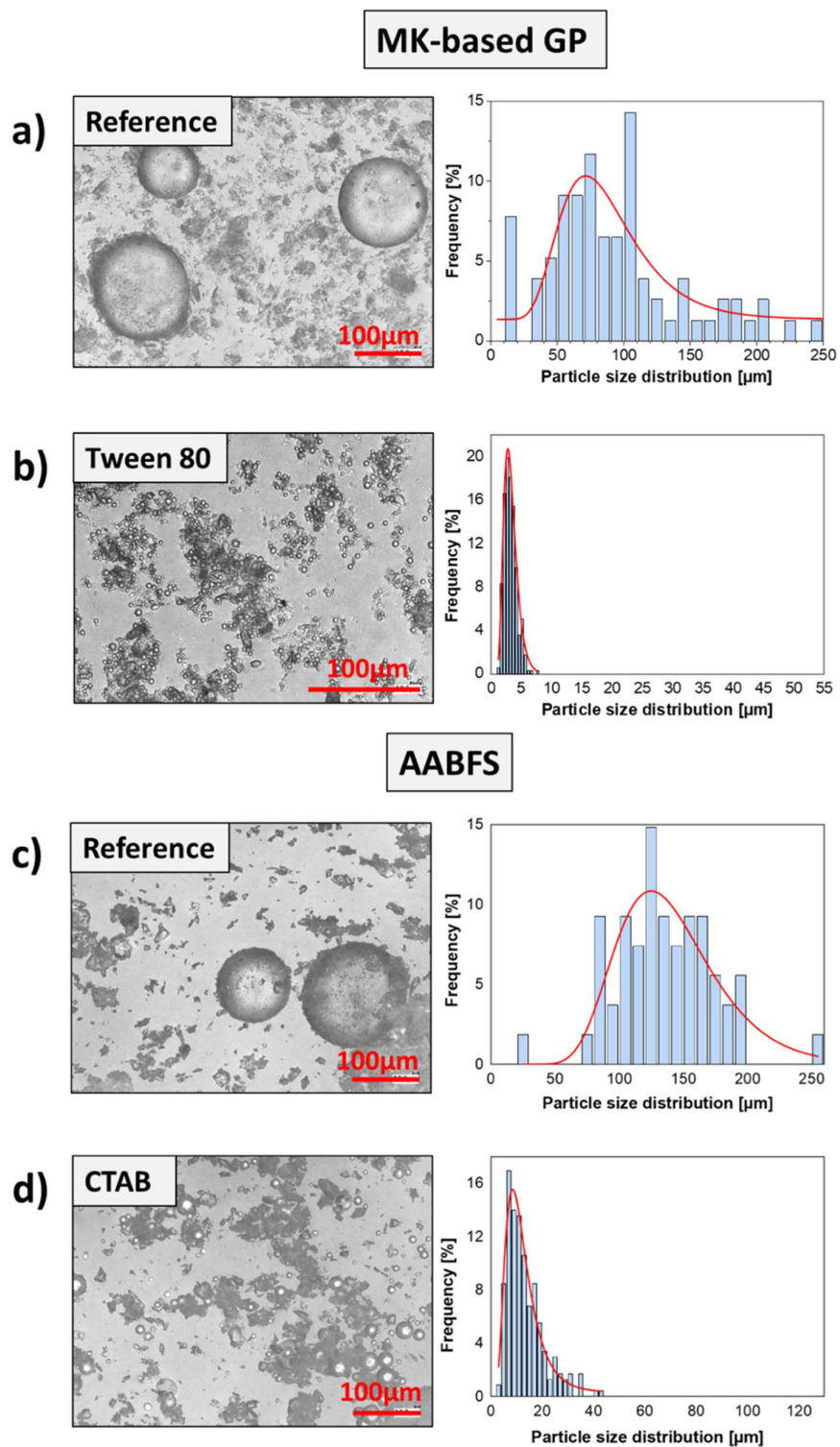


Figure 5: Microscopic observations of fresh AAM containing 20%vol. of oil after dilution in a xanthan gum gel: MK-based GP without surfactant (a), AABFS without surfactant (c), MK-based GP + Tween 80 (b) and AABFS + CTAB (d).

The median diameters (d_{50}), the mean volume diameter ($d[4,3]$) and the standard deviation (P) have also been quantified (Table 6).

Table 6: Influence of surfactants on the statistical parameters determined from the droplets size measurements. Structuring surfactants are highlighted with a grey background; Non-structuring surfactants appear without background.

Surfactants	MK-based GP			AABFS		
	d_{50} (μm)	$d[4,3]$ (μm)	P	d_{50} (μm)	$d[4,3]$ (μm)	P
Reference	82.18	169.03	6.15	135.66	165.42	5.30
SDS	4.60	32.11	0.81	66.38	85.67	2.45
Glucopon	4.83	17.77	0.32	22.83	43.78	1.28
CTAB	3.40	11.81	0.23	10.99	25.82	0.46
Brij O10	2.64	4.41	0.07	32.16	72.04	1.71
Tween 80	3.16	4.30	0.05	35.28	52.41	1.43
Span 80	3.62	10.67	0.16	21.51	42.34	0.83

Without surfactant, the comparison of d_{50} evidences the better incorporation of oil in MK-based GP paste ($d_{50} = 82 \mu\text{m}$) than in AABFS paste ($d_{50} = 136 \mu\text{m}$), as observed in Figure 2. A huge impact of surfactants is noted with significantly smaller droplet sizes in both AAM. In MK-based GP slurries, d_{50} is lower than $5 \mu\text{m}$ whatever the surfactant used. In AABFS slurries, the impact is smaller, with d_{50} comprised between 10 and $66 \mu\text{m}$. The addition of surfactant does not change the fact that the oil is more efficiently dispersed in MK-based GP slurries than in AABFS slurries. However, d_{50} does not take proper account of large droplets.

The comparison of surfactant efficiency is more adequate when using the mean volume diameter $d[4,3]$, which is more sensitive to the presence of large droplets. The latter is indeed an important parameter, because even if large droplets are present in a limited number, they represent an important volume proportion of oil. Mean volume diameter $d[4,3]$ values show that without surfactant, significant amounts of large oil droplets are present in both MK-based GP slurries ($d[4,3] = 169 \mu\text{m}$) and AABFS slurries ($d[4,3] = 165 \mu\text{m}$).

In MK-based GP pastes, structuring surfactants (CTAB, Brij O10, Span 80 and Tween 80) are consistently more efficient to reduce droplet size than non-structuring surfactants (SDS and Glucopon). Tween 80 and Brij O10 are the most effective ones ($d[4,3] < 5 \mu\text{m}$). In AABFS pastes, no trend for droplet sizes, related to structuring or non-structuring surfactants, is observed. CTAB is the most efficient, while SDS, Tween 80 and Brij O10 are the least effective surfactants

to reduce oil droplet sizes. More importantly, in presence of surfactants, fewer large droplets are present in MK-based GP than in AABFS matrices.

A homogeneous droplet size distribution expresses an effective emulsion formulation. It is for instance an asset to avoid Ostwald ripening[‡] [33]. Homogeneity of the droplet size distribution is assessed through the polydispersity index P (Table 6).

Without surfactant, the polydispersity index P is very high in both matrices ($P > 5$). With surfactants, for MK-based GP pastes, P is smaller than one, with a value as low as 0.05 (with Tween 80). For AABFS pastes, P ranges from 0.46 (with CTAB) to 2.45 (with SDS). This is consistently smaller than the paste without surfactant ($P=5.30$). Again, this confirms the better incorporation of oil in MK-based GP than AABFS, here in terms of emulsion homogeneity.

3.2.2. Droplets velocity as an indicator for emulsion stability

After mixing, oil droplets migrate with a certain velocity, which depends on the balance between gravitational forces and hydrodynamic forces. For an emulsion of an organic liquid (OL) into a given continuous phase (here, the GP or AABFS paste), the modified Stokes law for concentrated suspensions reads [53]:

$$v = \frac{2\Delta\rho g r^2}{9} \left(\frac{1 + \frac{4.6\varphi}{(1-\varphi)^3}}{\eta_c(1-\varphi)} \right) \quad (5)$$

Where v is the droplet migration velocity (in $\text{m}\cdot\text{s}^{-1}$), g is gravitational acceleration (in $\text{m}\cdot\text{s}^{-2}$), $\Delta\rho$ is the density difference between the continuous phase and the droplet (in $\text{g}\cdot\text{cm}^{-3}$; it is positive for ascending droplets, and negative for descending ones), r is the droplet radius (in m), η_c is the dynamic viscosity of the continuous phase (in Pa.s), and φ is the volume fraction of oil (here, 20%).

The density difference $\Delta\rho$ between the paste and the droplet is $0.88 \text{ g}\cdot\text{cm}^{-3}$ for MK-based GP and $1.13 \text{ g}\cdot\text{cm}^{-3}$ for AABFS paste, meaning, in both cases, an ascending motion for the oil droplets, i.e. a potential for creaming. The viscosity η_c of the continuous phase is taken at a low shear rate value of 10^{-2} s^{-1} ; it ranges between 308 and 7460 Pa.s (MK-based GP, without surfactant or with the most viscosifying surfactant Tween 80), or between 2190 and 6070 Pa.s (AABFS paste without surfactant or with the most viscosifying surfactant Span 80). The average droplet radius r is taken as half the value of d_{50} (see Table 6 for values without and with surfactants).

[‡]Ostwald ripening is due to the diffusion of individual molecules (here, of oil) from smaller droplets to larger droplets because of the difference in Laplace's capillary pressure between small and large droplets. Therefore, Ostwald ripening can be inhibited by homogenizing the oil droplet sizes.

From these values, the droplet migration velocity is calculated as 13 nm.j^{-1} for MK-based GP, and 6.3 nm.j^{-1} for AABFS paste. With surfactant, the droplet velocity becomes close to zero, with values on the order of 10^{-10} - $10^{-8} \text{ mm.j}^{-1}$. It is usually considered that stable emulsions, i.e. emulsions with negligible creaming, correspond to droplet velocities below 1 mm.j^{-1} [53]. With that criterion, it is clear that all emulsions are stable and hydrodynamic effects may be neglected.

3.3. Formation and stability of AAM-oil emulsions: effect of the interfacial tension

3.3.1. Direct measurement of the interfacial tension

An important parameter characterizing the influence of surfactants on the formation and stability of emulsions is their capacity to reduce the interfacial tension between two liquids. The lower the interfacial tension, the smaller the size of the dispersed droplets and the better the formation of the emulsion. Smaller droplets also improve the stability of the emulsion.

The mean interfacial tension between Finavestan oil and deionized water, or each of the two activating solutions (AS), is given in Table 7. In addition to the interfacial tension, the solubility of the surfactants in aqueous solutions was visually assessed; it is also indicated in Table 7. Surfactants are categorized as soluble if the solution is perfectly clear, and categorized as (partly or fully) insoluble otherwise.

Table 7: Influence of surfactants on the interfacial tension (γ) between Finavestan A360B and the aqueous solutions of GP and AABFS pastes.

Aqueous solutions	Surfactant	\emptyset	CTAB	SDS	Brij O10	Glucopon	Span 80	Tween 80
Deionized water	γ (mN.m^{-1})	48.81 ± 0.58	7.72 ± 0.14	19.32 ± 1.67	5.22 ± 0.08	8.18 ± 0.49	21.05 ± 0.49	10.17 ± 0.53
	Solubility ^a	-	S	S	S	S	PS	S
AS of MK-based GP	γ (mN.m^{-1})	54.61 ± 2.16	26.57 ± 1.39	15.51 ± 0.61	52.73 ± 1.05	6.40 ± 1.04	24.64 ± 1.30	10.37 ± 2.11
	Solubility	-	PS	PS	PS	S	PS	PS
AS of AABFS	γ (mN.m^{-1})	61.50 ± 0.38	4.83 ± 0.12	20.93 ± 0.91	32.20 ± 2.91	6.87 ± 0.09	43.17 ± 2.31	17.53 ± 0.66
	Solubility	-	S	PS	PS	S	PS	PS

^a S = soluble ; PS = partially soluble or insoluble.

Surfactant solubility. Despite being mostly hydrophilic, the majority of the surfactants is only partly soluble in the activating solutions. They are therefore unable to fulfill properly their surface-active function. This is explained by the very high ionic strength of the activating solutions, which drastically lowers the activity of water. Concerning nonionic surfactants, the activity of water is not strong enough to create the hydrogen bonding necessary for their solubility. For ionic surfactants, the low activity of water inhibits the solvation of newly formed ions, and therefore hinders the surfactant dissociation. Moreover, some dissolved polar heads might recombine with ions present in the activating solutions, forming a precipitate like in the case of CTAB [43].

Interfacial tension. Without surfactants, the presence of sodium hydroxide (in both activating solutions) increases the interfacial tension in comparison with deionized water, in accordance with the literature [54],[55].

In deionized water, despite its lipophilic nature, a sufficient amount of Span 80 is solubilized in water, as the decrease in the interfacial tension shows. As expected from their HLB values, CTAB, Brij O10, Tween 80 and Glucocon are soluble and lead to interfacial tensions lower than 10 mN.m^{-1} . SDS is also soluble but does not decrease the interfacial tension as efficiently as the previously mentioned surfactants.

In the activating solutions, Glucocon is fully soluble in both activating solutions and therefore efficiently reduces the interfacial tension.

SDS reduces the interfacial tension with a nearly equivalent efficiency in water and both activating solutions. This indicates that despite the visual insolubility of SDS in the activating solutions, the solubilized amount is high enough for SDS to exert its surface-active function. The precipitation of SDS is in agreement with the results reported by Feneuil et al. [44].

CTAB, which is fully soluble in the AABFS activating solution, reduces effectively the interfacial tension in this system. However, CTAB only slightly reduces the interfacial tension in the MK-based GP activating solution. This is probably due to the fact that the quaternary ammonium polar heads of CTAB precipitate with anionic silicate ions present in the activation solution and form a white precipitate [43],[56].

Brij O10 is almost insoluble in the GP activating solution, as confirmed by its limited impact on the interfacial tension. On the opposite, in the AABFS activating solution, Brij O10 decreases the interfacial tension by a factor of about 2 compared to the solution without surfactant. However, the obtained value ($32.20 \pm 2.91 \text{ mN.m}^{-1}$) is 6 times bigger than in deionized water.

Tween 80 and Span 80 both have the same lipophilic tail but differ by their polar heads. They are mainly insoluble in the activating solutions. Despite this, with water and with the MK-based GP activating solution, they significantly reduce the interfacial tension with a

comparable efficiency. They are less efficient to reduce the interfacial tension with the AABFS activating solution, especially Span 80. Indeed, Span 80 is less soluble than Tween 80, as shown by their HLB values.

3.3.2. Relationship between interfacial tension and OL droplet size

In an attempt to relate the structuring or non-structuring behavior of surfactants to the effect of interfacial tension, the mean volume diameter $d[4,3]$ was plotted as a function of interfacial tension (Figure 6).

For non-structuring surfactants, droplet size and interfacial tension follow a linear relationship. In their case, the lower the interfacial tension (allowed by the surfactant), the smaller the droplet size.

For structuring surfactants, however, droplet size and interfacial tension do not follow a particular trend. Moreover, the surfactants with a low impact on interfacial tension (Tween 80 and Brij O10) are the most efficient to decrease the droplet size.

This confirms that the interfacial tension is not the only driving force controlling the oil emulsification. It justifies the following study on diluted ternary suspensions.

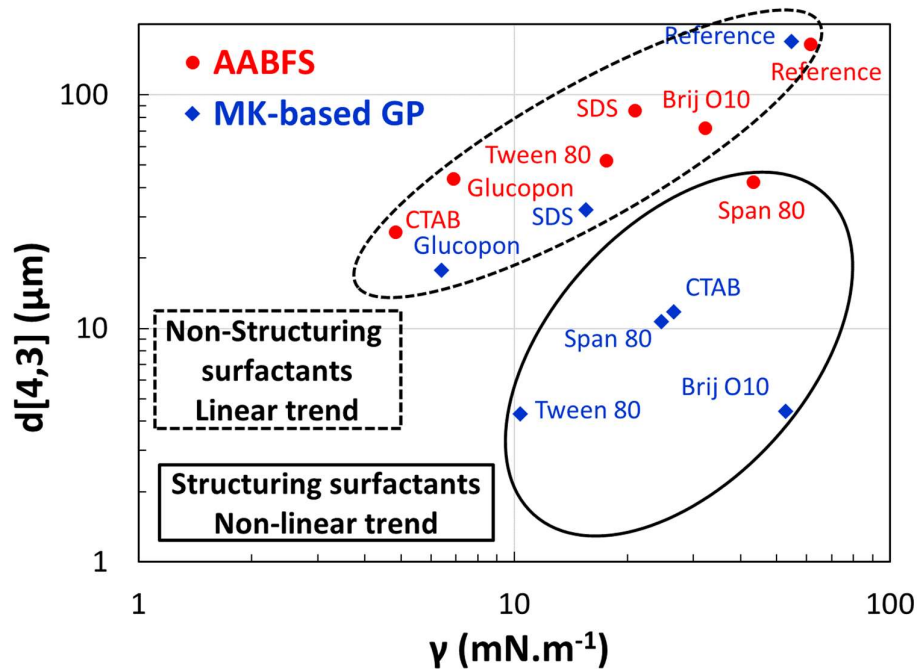


Figure 6: Influence of the surfactants on the evolution of mean volume diameter in function of interfacial tension.

3.4. Formation and stability of AAM-oil emulsions: role of solid particles

In this section, diluted ternary systems added with surfactants are investigated in order to better understand the mechanisms of AAM-oil emulsion stability. Fresh AAM containing oil are ternary systems made up of two immiscible liquid phases (aqueous activating solution and oil) and one solid phase (MK or BFS particles), added with surfactant (as a 4th component).

For MK-based GP or AABFS, Figure 7 shows emulsions of oil in activating solution added with each surfactant (Figures 7a and 7c), and the same emulsions added with solid particles (Figures 7b and 7d). All these mixtures are presented after thorough mixing and 3 days of stabilization to reach an equilibrium state. This method allows to compare the effect of each surfactant on the emulsification of oil, either without particles (Figures 7a and 7c) or in presence of solid particles (Figures 7b and 7d).

3.4.1. Influence of surfactants in the absence of particles (G1-G7 & L1-L7)

As expected, samples without surfactants and particles (G1 & L1) undergo oil creaming and coalescence. Whatever the surfactant added, oil creaming persists after decanting (Fig. 7a and c). However, observations of upper phases (i.e. oily phases) using an optical microscope evidence a resistance to coalescence thanks to the use of surfactants, with still visible oil droplets (Supplementary Materials - Appendix B3). Moreover, most of the oily phases in presence of surfactants (Figure 7, G2 to G7 and L2 to L7) are less translucent and display a higher volume than the references (G1 and L1). In particular, Glucopon is the best surfactant to increase the oil volume, i.e. to limit coalescence, in both AAM.

3.4.2. Influence of particles in the absence of surfactants (G8 & L8)

For MK-based GP without surfactant (G8, Figure 7b), a significant amount of MK particles is present in the oil, as shown by the greater volume of the oily phase in comparison with G1. This means that oil and MK particles interact, i.e. that they have good chemical affinity. However, a significant amount of MK particles is settling, indicating that the interactions between MK and oil are partial.

For AABFS without surfactant (L8), some BFS particles remain in the oil but the volume of the oily phase is almost identical to reference L1, meaning that the majority of BFS particles has actually settled.

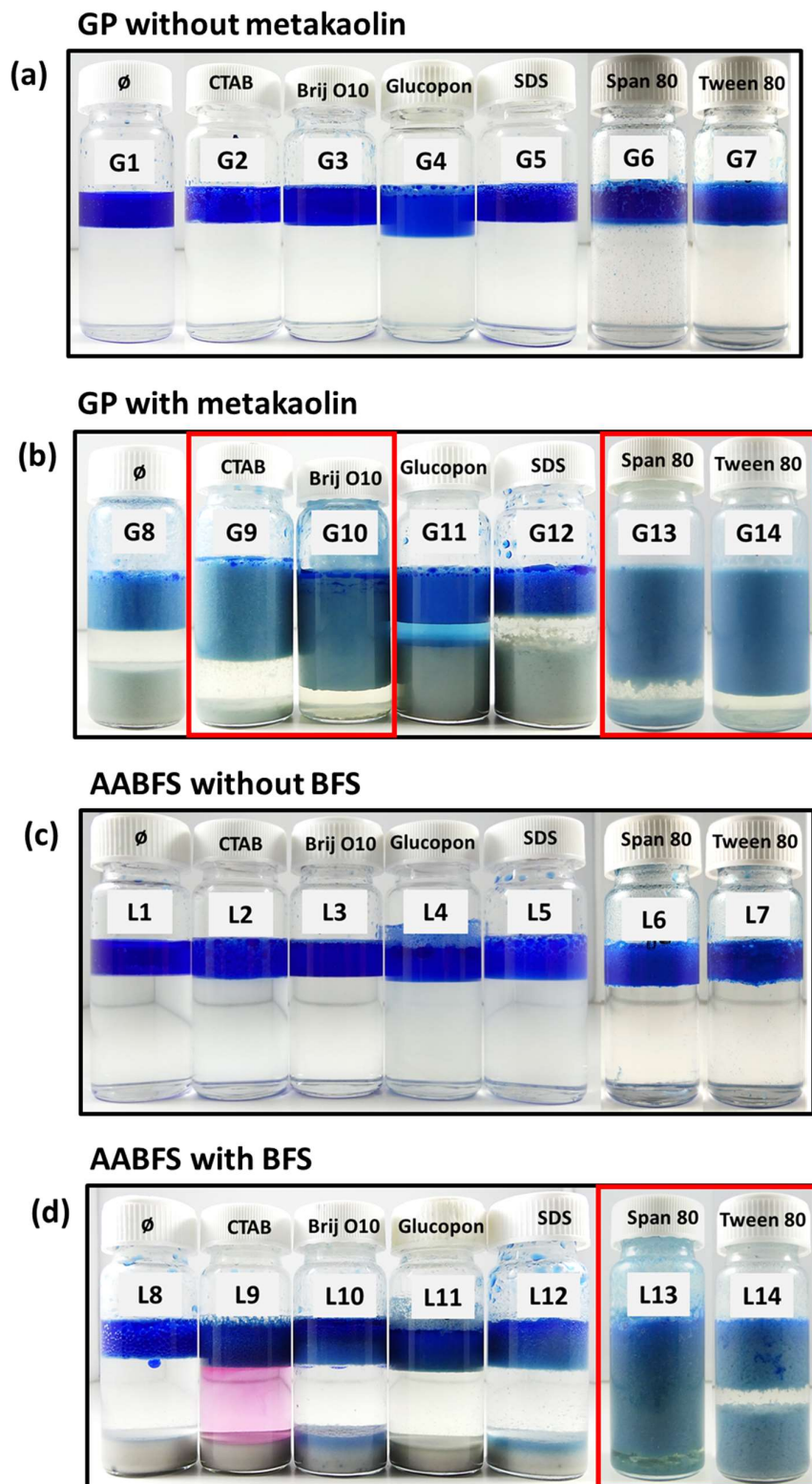


Figure 7: Pictures of diluted ternary mixtures taken after thorough mixing and 3 days stabilization. The oil is dyed in blue. Each system (GP or AABFS) uses a different composition of AS. Top pictures (a and c) are without solid particles, while bottom pictures (b and d) are with solid particles. The tubes framed in red correspond to the surfactants promoting attractive forces between the oil and the solid particles.

Unfortunately, it is impossible to quantify the amount of particles in both phases because the effective volume of particles is much bigger than the initially introduced volume (5%vol). This means that the particles are “swollen” by the activating solutions, which is in accordance with their high water demand. By comparing G8 and L8, it appears that MK particles have more affinity for the oil than BFS particles. The exact origin of this observation is delicate to determine because on the one hand, MK and BFS particles differ e.g. in their chemical nature, size and shape and on the other hand, activating solutions differ e.g. in their density and viscosity. Samples G8 and L8 were formulated by inverting the activating solutions and the same observations were made. This allows ruling out the fact that MK particles settle less than BFS particles due to distinct properties of the activating solutions. In comparison with the low density of the activating solutions, the density difference between solid particles, respectively 2.4 g/cm^3 and 2.9 g/cm^3 for MK and BFS particles, is not high enough to explain the observed variations. Another interpretation is that finer particles remain in the oily phase, whereas larger particles settle due to their weight. However, the median diameters of MK ($15 \mu\text{m}$) and BFS ($11 \mu\text{m}$) particles are close, and do not support this hypothesis. The significantly higher specific surface area (see Table 1), and possibly a higher chemical affinity of MK particles for the oil (compared to BFS) are considered adequate explanations for this phenomenon. Whatever the exact phenomenon involved, a better wetting of the MK particles by the oil is obtained, which explains the higher amount of MK particles in the oil phase.

3.4.3. Influence of surfactants on the interaction between MK particles and both liquid phases (G9-G14)

Two distinct effects of the surfactants are observed. With CTAB, Brij O10, Span 80 and Tween 80, corresponding respectively to samples G9, G10, G13 and G14, a coexistence of the three components occurs in one single phase, with almost no remaining MK particles at the bottom of the flask. These surfactants lead to attractive forces between oil droplets and solid particles, allowing the ternary systems to become almost monophasic, with a major upper phase composed of a tri-phasic network (activating solution–oil–MK particles), while the bottom phase is mainly an excess of the activating solution. These upper phases differ in their structuration, being for example gelled (with CTAB) or rather fluid (with Tween 80). This gelled or fluid consistency indicates that the stabilization of the suspension is not related to the alkali-activation of MK particles. On the contrary, Glucocon and SDS (samples G11 and G12) do not promote interactions of MK particles with oil. These surfactants induce a settling of MK particles, which is even more important than without surfactant (see reference sample G8).

Being related to the same surfactants, a correlation is done between the strong interactions of MK particles and oil mixed with CTAB, Brij O10, Span 80 or Tween 80 and the structuring behavior observed in Figure 2.

3.4.4. Influence of surfactants on the interaction between BFS particles and both liquid phases (L9-L14)

The influence of surfactants on the interactions between the three components (BFS particles-oil-activating solution) strongly differs in the AABFS system compared to MK-based GP. In presence of CTAB, Brij O10, GlucoPON or SDS, respectively samples L9, L10, L11 and L12, the majority of BFS particles have settled and the oily phase is creaming; volume variations are limited from one mixture to another. In other words, the volumes of particles and liquid phases are similar to the sample without surfactant (sample L8). These surfactants do not promote the coexistence of the three components in one single phase. Span 80 is the only surfactant promoting a total interaction between the three components, with almost one single phase remaining and a slight excess of activating solution at the bottom. This behavior is directly correlated to the structuring behavior observed previously on the corresponding paste (Figure 2). Tween 80 has a similar effect to Span 80, but the three components coexist in two distinct phases. The bottom phase contains less oil (i.e. it is less blue) in comparison with the upper phase; the bottom phase corresponds to settled material, while the upper phase floats above the mix, due to density differences. This is not sufficient to promote structuring of the corresponding paste.

3.4.5. Comparison and analysis of the diluted ternary suspensions

In order to quantify the results for the samples with particles (G8-G14 and L8-L14), each mix is considered as the assembly of three distinct phases (Figure 8, top left). The upper phase is called “oil emulsion”, because it corresponds to the emulsion of oil in the activating solution, together with a fraction of solid particles (oil emulsion); the middle phase or “aqueous phase” represents the activating solution, and the bottom phase or “solid suspension” represents the settled solid particles.

With this convention, the relative thickness of each phases was measured using the software ImageJ, assuming that the total thickness of the mix is equal to 1. As all the phases have the same horizontal dimensions (i.e. that of the tube inner diameter), the thickness is directly proportional to the phase volume fraction. Results are plotted on a ternary diagram (Figure 8) depending on their phase volume fractions. This diagram shows the presence of two distinct groups of surfactants.

The first group of surfactants (Figure 8, red zone) represents those, which do not promote the coexistence of the three components in one single phase; they also include the samples without surfactants in the diagram. The second group (Figure 8, green zone) represents surfactants promoting the coexistence of the three components in one single phase (oil emulsion). In the MK-based GP system, surfactants mainly belong to the second group,

whereas in the AABFS system, surfactants mainly belong to the first group. Those two groups, identified from the study on diluted suspensions, match exactly those identified visually in Figure 2. This means that the interactions between solid particles-oil-surfactant directly explain the rheological behavior of AAM paste (i.e. structuring or non-structuring).

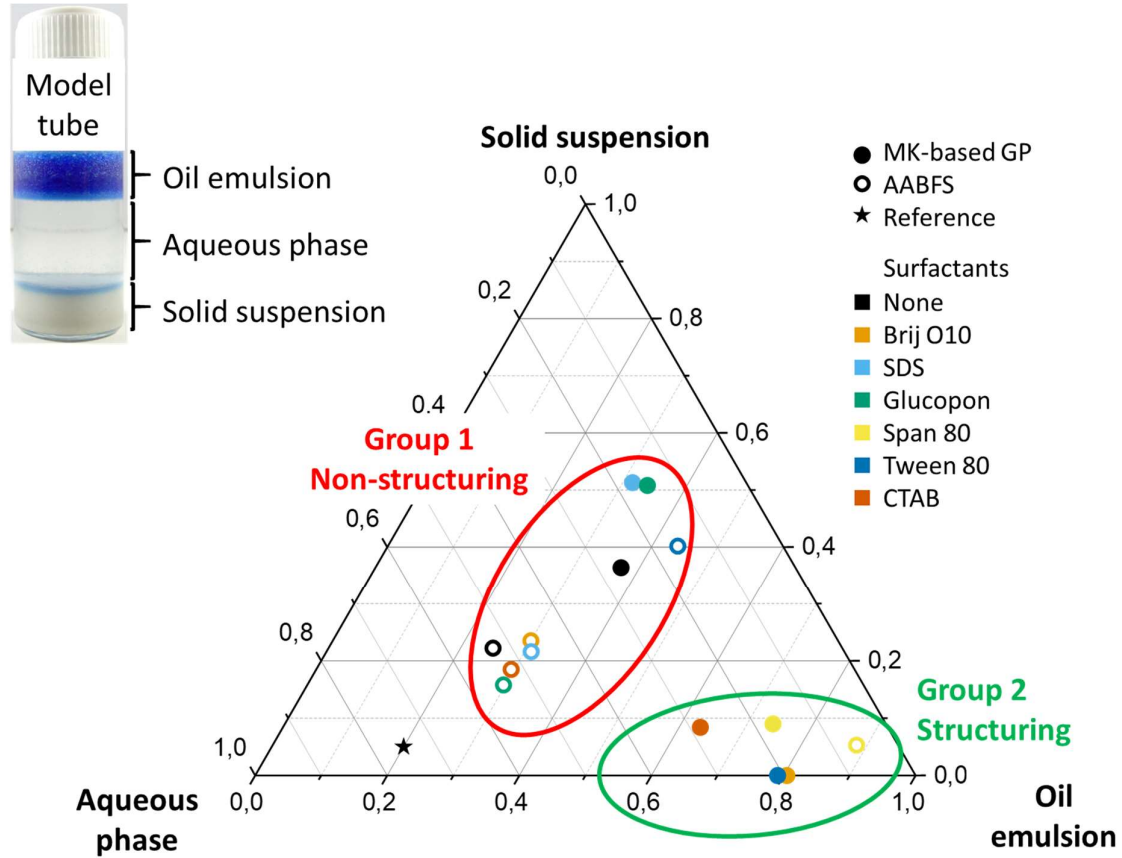


Figure 8: Ternary diagram representing the volume fractions of the three phases in tube G8 to G14 and L8 to L14. The black star corresponds to the volume fractions initially added (75%vol. activating solution, 20%vol. oil, 5%vol. solid particles).

3.5. Discussion: two distinct patterns concerning the effect of surfactants describe the emulsion formation and stability

All the results presented in this study evidence that surfactants have different impacts on the properties of fresh AAM throughout the incorporation of mineral oil.

- Rheological measurements (flow curves) along with macroscopic observations highlight the presence of “structuring” and “non-structuring” surfactants.
- Interfacial tension measurements evidence variations in the ability of surfactants to act as surface-active agents due to solubility variations in the activating solutions.

- Droplet size quantification confirms the efficiency of all surfactants to incorporate oil in AAM, meaning that the interfacial tension is not the only driving force improving the quality of emulsions.
- The study of ternary systems (activating solution – oil – solid particles) shows that some surfactants allow the coexistence of the three components in one single phase, while others do not.

These observations lead to the conclusion that surfactants contribute to the incorporation of oil in AAM *via* two distinct mechanisms. These can occur simultaneously or not. They are summarized in Figure 9.

In the classical mechanism or mechanism of action 1 (Figure 9, left), the surfactant simply reduces the oil droplet size by decreasing the interfacial tension. This is actually the classical way by which emulsions are formulated. In that case, the particles do not have a direct role on the stability of oil droplets. In order to allow Mechanism 1, surfactants need to be sufficiently soluble in the continuous phase to reduce effectively the interfacial tension, by positioning themselves at the interface between both liquid phases.

The singular mechanism or mechanism of action 2 (Figure 9, right) is more complex and involves the solid particles. For instance, it has been shown that clay modified by surfactants are good candidates to form Pickering emulsion [58]. However, the stabilization of the ternary systems in our research cannot be directly considered as a Pickering emulsion [9], because Pickering systems are characterized by oil droplets at least ten times bigger than stabilizing particles [59]. In our case, the sizes of oil droplets are of the same order of magnitude as BFS and MK particles (i.e. a few microns). For instance, the mean size of oil droplets in MK-based GP pastes containing Brij O10 is below 10 μm , which is smaller than the mean particle size of MK (> 10 μm).

The viscosity increase of fresh AAM in the presence of structuring surfactants and oil also recalls capillary systems studied by Koos [35],[36],[60]. In these ternary systems, oil droplets place themselves between solid particles, hence creating aggregates that are leading to a strong structuration of the mixture. However, in these systems controlled by capillary forces, the addition of surfactants tends to decrease the structuration of the medium, because the amplitude of capillary forces is proportional to the interfacial tension.

In our case, the viscosity increase of AAM pastes due to structuring surfactants, even in the absence of oil, indicates the formation of *particle aggregates*. They have been observed in this study in Figure 5b. This occurs very probably via the interactions of surfactant polar heads with MK or BFS hydrophilic surfaces. In such instance, the lipophilic chains of the surfactant remain vacant and available to interact with each other, creating aggregates of particles. A wide range of studies evidenced the formation of these “hydrophobic forces” due to the presence of

surfactants at the surface of suspended solid particles, with strong impacts on the viscosity of the corresponding suspensions [42], [44],[51].

In particular, the presence of the aggregates induces an important increase in the effective volume fraction of solid particles, when compared to suspensions containing individualized particles [61]. The well-known Krieger and Dougherty equation describes that the apparent viscosity depends on the effective solid volume fraction [62]. According to Sakamoto et al. [63], these attractive forces might be due to air bridges formed between particles, created by the coalescence of micrometric air bubbles stabilized by surfactants and introduced in the mixture upon mechanical stirring. The parallel between air bubbles and oil droplets, which are incorporated in AAM, could explain the presence of attractive forces and higher viscosities. In Mechanism 2, as the mineral oil (an alkane) is chemically similar to the lipophilic chains of the surfactants, it is thought that the oil positions itself between solid aggregates in the form of droplets. This causes an even greater increase in viscosity. From an energy point of view, it is less costly for the oil to interact with the lipophilic chains of the surfactant than directly with the continuous aqueous phase.

To fulfill Mechanism 2, surfactants need to be insoluble in the continuous phase and able to adsorb at the surface of solid particles via their polar heads. For example, it has been shown that alkyl poly-glucosides are unlikely to adsorb at the surface of kaolinite particles [64]; anionic surfactants are incapable of adsorbing at the surface of smectite particles in alkaline conditions because of electrical repulsion [42]. With this interpretation, it is clear that Glucopon and SDS surfactants cannot act via Mechanism 2 in fresh AAM.

Moreover, the two mechanisms described in Figure 9 are extreme cases, in which surfactants are whether perfectly soluble or completely insoluble. In such case, they are purely acting via only one of the two mechanisms. In practice, most surfactants are at least partially soluble in the activating solutions and probably act via a combination of both mechanisms, as it was inferred when measuring the interfacial tension. For instance, Tween 80 is soluble enough in MK-based GP pastes to effectively reduce the interfacial tension (Mechanism 1) and it also adsorbs at the surface of MK particles, causing a strong increase in viscosity (Mechanism 2). With these two mechanisms in mind, a surfactant would be inefficient if it was simultaneously insoluble in the activating solution and incapable of adsorbing at the surface of solid particles. This could be the case of Brij O10, which is almost insoluble in AABFS pastes, and does not anchor at the surface of BFS particles as shown by interfacial tension and rheological measurements.

Finally, it is easier to promote the agglomeration of particles in MK-based GP mixes than in AABFS mixes (Figure 7). In other words, the classical mechanism seems to be favored in AABFS and the singular mechanism seems to be favored in MK-based GP. This might be due to the

higher surface area of MK ($17 \text{ m}^2.\text{g}^{-1}$) in comparison with BFS particles ($0.45 \text{ m}^2.\text{g}^{-1}$) [65], which promotes surface interactions significantly higher in MK pastes.

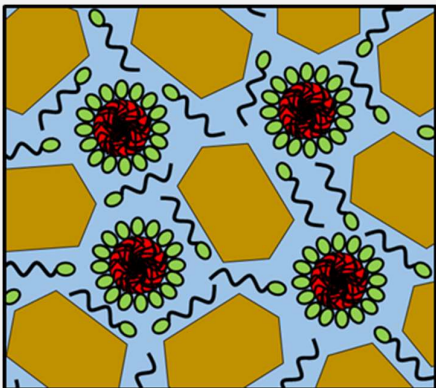
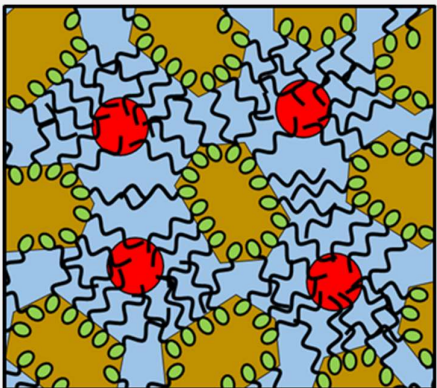
	Mechanism 1 (M1)	Mechanism 2 (M2)
Rheology	Non-structuring	Structuring
Surface active property	Efficient	Poor or Moderate
Oil-solid particles interaction	Low	High
Oil droplet size distribution	Finer and more homogeneous than without surfactant	Finer and more homogeneous than without surfactant
Concept mapping		
MK-based GP	Glucopon SDS	Span 80 CTAB Tween 80 Brij O10
AABFS	Glucopon SDS CTAB Tween 80	Span 80

Figure 9: Schematic representation of the two action mechanisms of surfactants for the incorporation of mineral oil in AAM. Classical mechanism 1 (left) and singular mechanism 2 (right). The light blue background represents the AS, the red circles represent the oil droplets and the brown hexagons correspond to the particles (BFS or MK). The green circles and the black lines correspond to the surfactant heads and tails respectively.

4. Conclusions

A low viscosity and non-reactive mineral oil was successfully incorporated in a proportion of 20%vol. in alkali-activated pastes made of MK or BFS particles, in order to form stable composite materials (oil immobilization). In both types of AAM, the oil incorporation is insufficient without surfactant, because heterogeneous and large visible droplets are observed. The use of cationic (CTAB), anionic (SDS) or non-ionic (Brij O10, Tween 80, Span 80 or Glucocon) surfactants successfully improves the incorporation of the oil in fresh AAM.

Rheological investigations, interfacial tension measurements and the analysis of diluted ternary suspensions show that surfactants proceed in two distinct behavior patterns to improve the incorporation of oil in AAM. The classical mechanism (Mechanism 1 or M1) reduces the interfacial tension to stabilize the emulsion of oil; it is the main surfactant mechanism in AABFS slurries. The singular mechanism (Mechanism 2 or M2) promotes the interaction of solid particles with the oil to stabilize the emulsion of oil; it is the main mechanism of action in MK-based GP slurries. These behavior patterns depend on the solubility of surfactants in the activating solutions and are valid for any alkane-type oil incorporated in AAM.

According to droplet size measurements, the incorporation of mineral oil exhibits higher performance in MK-based GP than in AABFS.

Finally, from an applicative point of view, M1 should be favored if a good workability of fresh AAM is required, whereas M2 should be targeted if the stability of the hardened composite AAM over time is the most crucial feature, in particular to potentially provide a better resistance to leaching (owing to greater oil-particles interactions).

Only a few surfactants will be considered in chapter III as described below:

AABFS	MK-based GEO
<ul style="list-style-type: none"> • Glucocon (M1) • CTAB (M1) • Span 80 (M2) 	<ul style="list-style-type: none"> • Glucocon (M1) • CTAB (M2) • Brij O10 (M2)

Tween 80 is not considered as its behavior is similar to Brij O10 and SDS is not considered because of its poor efficiency. Span 80 is considered in AABFS only because it is the sole surfactant acting under M2 in this material. Brij O10 is considered in GEO only because it is less efficient in AABFS.

Acknowledgments

This project has received funding from the European Union's Horizon 2020 research and innovation program for Nuclear Fission and Radiation Protection Research (Call NFRP-2019-2020) under grant agreement No. 945098 (PREDIS). Chevreul Institute (FR 2638), Ministère de l'Enseignement Supérieur et de la Recherche, Région Hauts de France, and FEDER are acknowledged for supporting and funding part of this work.

Appendix A

A1- State-of-the-art on emulsions

Emulsification processes. In order to create an emulsion, e.g. of an OL into a cement slurry, stirring occurs first under a laminar fluid flow (at low blade speed), and then under turbulent flow at greater blade velocity. The main driving parameters of the process are the capillary number Ca (in laminar regime) and the Weber number We (in turbulent regime).

The capillary number is defined as the ratio between the shear stress and the capillary pressure, and it is written as [66]:

$$Ca = \frac{\eta_c \cdot R \cdot \dot{\gamma}}{\gamma} \quad (6)$$

where η_c is the dynamic viscosity of the continuous phase (in Pa.s), $\dot{\gamma}$ is the applied shear rate (in s^{-1}), γ is the interfacial tension (in $N.m^{-1}$) and R is the droplet radius (in m). The critical capillary number Ca_c is the value above which a droplet of radius R breaks (due to viscous forces overcoming surface tensions), creating smaller droplets.

The pioneering works of Grace [32] have shown experimentally that the Ca_c depends on the viscosity ratio p , defined as: $p = \eta_d/\eta_c$, where η_d is the dynamic viscosity of the dispersed phase and η_c is the dynamic viscosity of the continuous phase. In the viscosity ratio p range between 0.01 - 1.0, Ca_c is minimal and on the order of 1, meaning that droplet break-up is easy, whereas at lower or higher viscosity ratios, the value of Ca_c increases very quickly.

In a turbulent flow regime, the break-up of an OL droplet is due to both viscous forces and inertial forces within the scales of macro-turbulence and Kolmogorov micro-turbulence (i.e. for a droplet Reynolds number $Re = \rho_c \dot{\gamma} R^2 / 4\eta_c$ greater than 5, where ρ_c is the density of the continuous phase), the inertial forces are predominant [67]. In such case, a Weber number We is defined as the ratio between the kinetic energy of a droplet due to turbulent fluctuations (ε_c) and the energy related to the interfacial tension (ε_s). The break-up of a droplet occurs for a critical Weber number on the order of 1.

In the vicinity of the mixing blade, the turbulent flow regime corresponds to droplet sizes on the order or below the scale of Kolmogorov micro-turbulence. In such case, the droplet break-up is mainly due to viscous forces (and not to inertial forces), and the capillary number Ca is considered again.

Stability of the emulsion. A major destabilizing process for emulsions is coalescence, i.e. the fusion of two or more droplets into larger ones.

The coalescence of two neighboring droplets is driven by disjoining pressure π . The latter depends on the distance h between the two droplets; it is described as the sum of an electrostatic repulsion π_E (negative value), a steric repulsion π_S (negative value), and the Van der Waals attraction π_A (positive value) [33]:

$$\pi(h) = \pi_E + \pi_S + \pi_A \quad (7)$$

The interfacial film is stable if $|\pi_E + \pi_S| > \pi_A$.

A2- Preparation of the AAM slurries

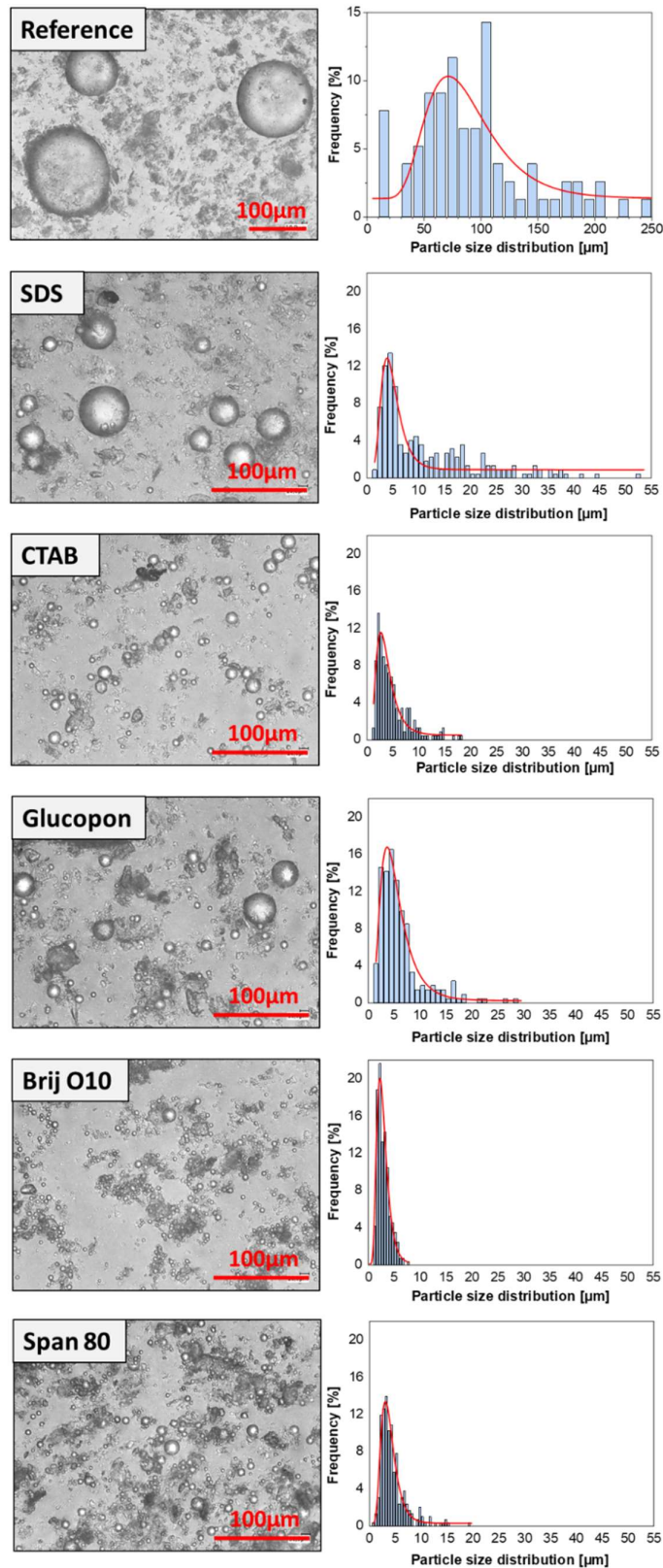
For both materials, the first step consists in preparing the alkali-activating solution. Sodium hydroxide pellets are dissolved in water purified by reverse osmosis. In the case of MK-based GP, sodium silicate solution (Betol 39T) is also added. The blend is left to cool down to room temperature for several hours. After cooling, the surfactant is added to the activating solution, and the mix is stirred mechanically at 800 rpm with a helical blade. At this stage, the solid precursor powder (MK or BFS) is quickly added to the activating solution and the mixing is carried out for 5 minutes until stabilization. Finally, the mineral oil is introduced in the cement paste at a constant flow rate of 4 mL.mm⁻¹ in order to obtain a composite material with an oil volume concentration of 20%vol (% of the total cement paste + oil volume).

Visual inspection of all pastes is performed, and photographs are taken (see Results section). For these observations, the oil was colored in red using an organic dye (Sudan III red) to create a stronger contrast between both liquid phases.

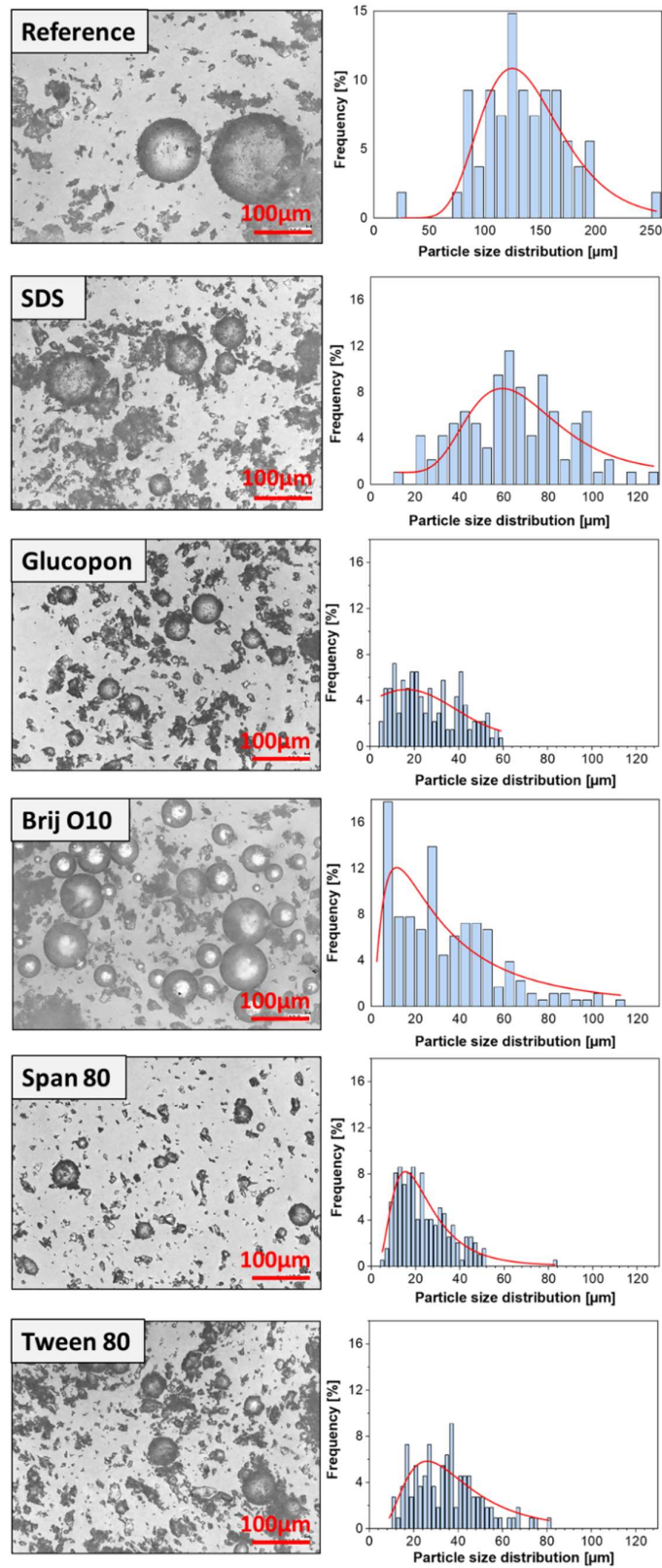
Pastes without coloring dye are used for rheology measurements (see Sub-section 2.3).

After hardening, the densities of pure AAM pastes (i.e. without oil) are 1.75 g.cm⁻³ (+/-0.02) and 2.00 g.cm⁻³ (+/-0.02) for MK-based GP and AABFS respectively.

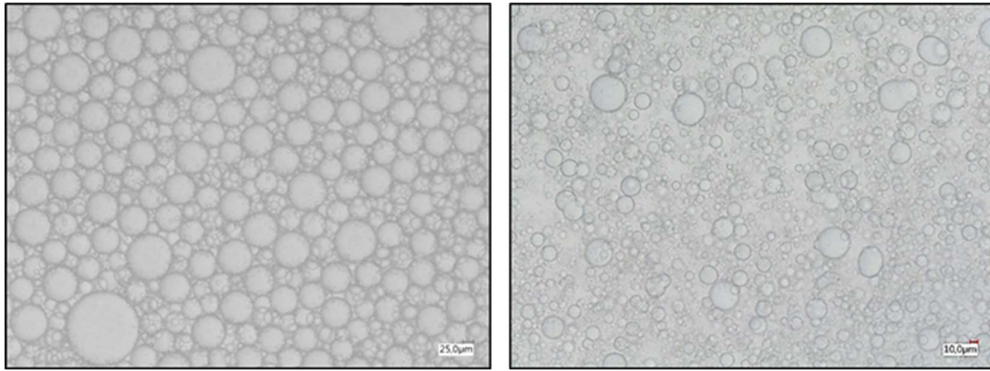
Appendix B



Appendix B1: Influence of surfactants on the size of oil droplets in MK-based GP: microscopic observations and corresponding droplet size distributions.



Appendix B2: Influence of surfactants on the size of oil droplets in AABFS: microscopic observations and corresponding droplet size distributions.



Appendix B3: Microscopic observations of upper phases of samples G2 x500 (left) and S4 x300 (right)

References

- [1] S. Trussell and R. D. Spence, 'A review of solidification/stabilization interferences', *Waste Manag.*, 1994.
- [2] S. Paria and P. K. Yuet, 'Solidification–stabilization of organic and inorganic contaminants using portland cement: a literature review', *Environ. Rev.* 2006, doi: 10.1139/a06-004.
- [3] International Atomic Energy Agency (IAEA), 'Treatment and conditioning of radioactive organic liquids', 1992.
- [4] C. Reeb, C. Pierlot, C. Davy, and D. Lambertin, 'Incorporation of organic liquids into geopolymer materials - A review of processing, properties and applications', *Ceram. Int.*, 2020, doi: 10.1016/j.ceramint.2020.11.239.
- [5] M. Rutkevičius et al., 'Fabrication of novel lightweight composites by a hydrogel templating technique', *Mater. Res. Bull.*, 2012, doi: 10.1016/j.materresbull.2012.01.014.
- [6] C. Bai, G. Franchin, H. Elsayed, A. Conte, and P. Colombo, 'High strength metakaolin-based geopolymer foams with variable macroporous structure', *J. Eur. Ceram. Soc.*, 2016, doi: 10.1016/j.jeurceramsoc.2016.06.045.
- [7] S.-Y. Guo et al., 'Mechanical and interface bonding properties of epoxy resin reinforced Portland cement repairing mortar', *Constr. Build. Mater.*, 2020, doi: 10.1016/j.conbuildmat.2020.120715.
- [8] A. K. Karamalidis and E. A. Voudrias, 'Cement-based stabilization/solidification of oil refinery sludge: Leaching behavior of alkanes and PAHs', *J Hazard Mater*, 2007, doi: 10.1016/j.jhazmat.2007.02.032.
- [9] V. Cantarel, D. Lambertin, A. Poulesquen, F. Leroux, G. Renaudin, and F. Frizon, 'Geopolymer assembly by emulsion templating: Emulsion stability and hardening mechanisms', *Ceram. Int.*, 2018, doi: 10.1016/j.ceramint.2018.03.079.
- [10] Z. Zhang, J. L. Provis, A. Reid, and H. Wang, 'Geopolymer foam concrete: An emerging material for sustainable construction', *Constr. Build. Mater.*, 2014, doi: 10.1016/j.conbuildmat.2014.01.081.
- [11] S. Petlitskaia and A. Poulesquen, 'Design of lightweight metakaolin based geopolymer foamed with hydrogen peroxide', *Ceram. Int.*, 2019, doi: 10.1016/j.ceramint.2018.10.021.
- [12] Cao Vinh Duy et al., 'Microencapsulated phase change materials for enhancing the thermal performance of Portland cement concrete and geopolymer concrete for passive building applications', *Energy Convers. Manag.*, 2017, doi: 10.1016/j.enconman.2016.11.061.
- [13] M. Masrulita, P. Burhan, and Y. Trihadiningrum, 'Stabilization / Solidification of Waste Containing Heavy Metals and Hydrocarbons Using OPC and Land Tras Cement', *J. Ecol. Eng.*, 2018, doi: 10.12911/22998993/92926.
- [14] D. E. Clark, P. Colombo, and R. M. Jr. Neilson, 'Solidification of oils and organic liquids', *Nuclear Waste Management*, 1982. doi: 10.2172/6462993.
- [15] M. H. Almabrok, R. G. McLaughlan, K. Vessalas, and P. Thomas, 'Effect of oil contaminated aggregates on cement hydration', *Am. J. Eng. Res.*, 2019.
- [16] X. Liu, S. Nair, K. Aughenbaugh, and E. van Oort, 'Mud-to-cement conversion of non-aqueous drilling fluids using alkali-activated fly ash', *J. Pet. Sci. Eng.*, 2019, doi: 10.1016/j.petrol.2019.106242.
- [17] C. Shi and A. Fernández-Jiménez, 'Stabilization/solidification of hazardous and radioactive wastes with alkali-activated cements', *J. Hazard. Mater.*, 2006, doi: 10.1016/j.jhazmat.2006.05.008.
- [18] M. H. Almabrok, R. McLaughlan, and K. Vessalas, 'Investigation of oil solidification using direct immobilization method', presented at the Environmental Research Event, Sydney, Australia, 2011.
- [19] J. L. Provis and J. S. J. van Deventer, *Alkali Activated Materials, State-of-the-Art Report*, RILEM TC 224-AAM. 2014.
- [20] J. L. Provis, 'Activating solution chemistry for geopolymers', in *Geopolymers, Structures, Processing, Properties and Industrial Applications*, Elsevier, 2009, doi: 10.1533/9781845696382.1.50.
- [21] K. Komnitsas and D. Zaharaki, 'Geopolymerisation: A review and prospects for the minerals industry', *Miner. Eng.*, 2007, doi: 10.1016/j.mineng.2007.07.011.

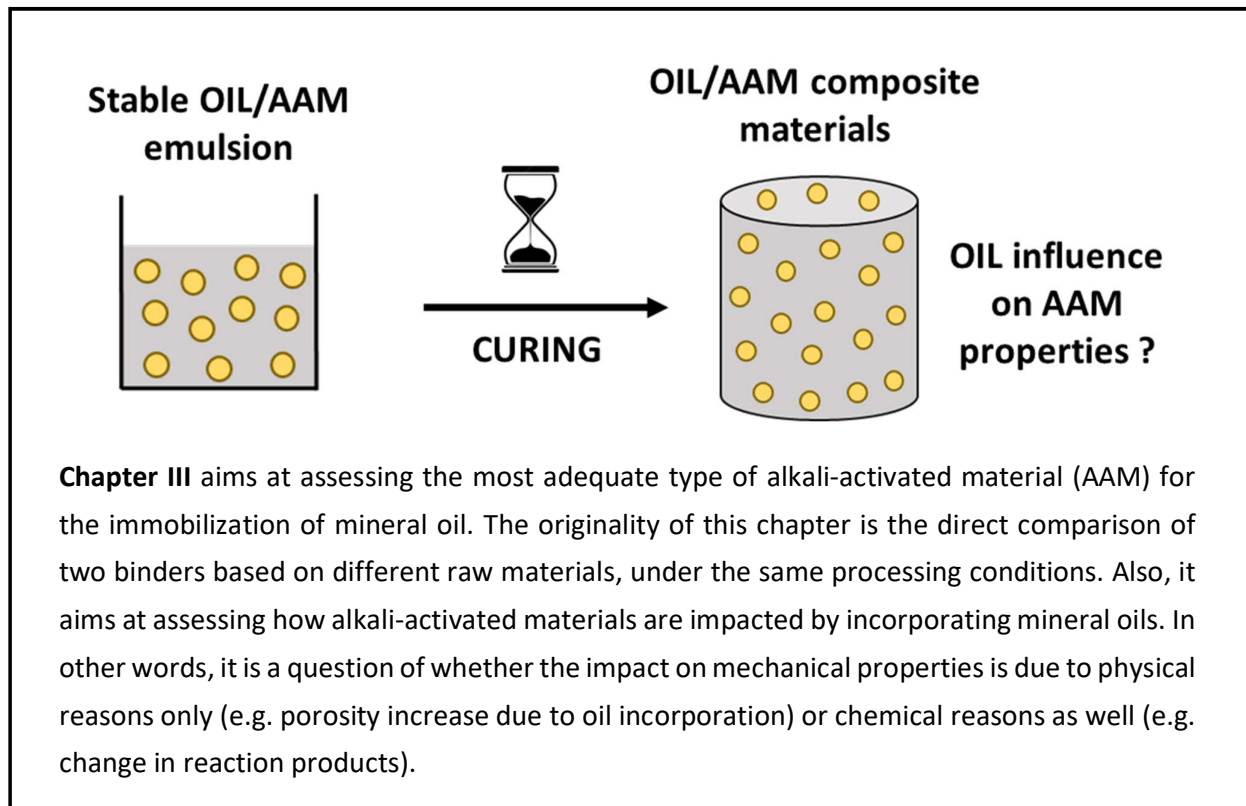
- [22] C. Shi, B. Qu, and J. L. Provis, 'Recent progress in low-carbon binders', *Cem. Concr. Res.*, 2019, doi: 10.1016/j.cemconres.2019.05.009.
- [23] C. Li, H. Sun, and L. Li, 'A review: The comparison between alkali-activated slag (Si+Ca) and metakaolin (Si+Al) cements', *Cem. Concr. Res.*, 2010, doi: 10.1016/j.cemconres.2010.03.020.
- [24] F. Puertas, M. Palacios, H. Manzano, J. S. Dolado, A. Rico, and J. Rodríguez, 'A model for the C-A-S-H gel formed in alkali-activated slag cements', *J. Eur. Ceram. Soc.*, 2011, doi: 10.1016/j.jeurceramsoc.2011.04.036.
- [25] V. F. F. Barbosa, K. J. D. MacKenzie, and C. Thaumaturgo, 'Synthesis and characterisation of materials based on inorganic polymers of alumina and silica: sodium polysialate polymers', *Int. J. Inorg. Mater.*, 2000, doi: 10.1016/S1466-6049(00)00041-6.
- [26] R. J. Myers, S. A. Bernal, J. D. Gehman, J. S. J. van Deventer, and J. L. Provis, 'The Role of Al in Cross-Linking of Alkali-Activated Slag Cements', *J. Am. Ceram. Soc.*, 2015, doi: 10.1111/jace.13360.
- [27] P. Duxson, A. Fernández-Jiménez, J. L. Provis, G. C. Lukey, A. Palomo, and J. S. J. van Deventer, 'Geopolymer technology: the current state of the art', *J. Mater. Sci.*, 2007, doi: 10.1007/s10853-006-0637-z.
- [28] N. Nestle, C. Zimmermann, M. Dakkouri, and R. Niessner, 'Action and Distribution of Organic Solvent Contaminations in Hydrating Cement: Time-Resolved Insights into Solidification of Organic Waste', *Environ. Sci. Technol.*, 2001, doi: 10.1021/es015528y.
- [29] S. J. T. Pollard, D. M. Montgomery, C. J. Sollars, and R. Perry, 'Organic compounds in the cement-based stabilisation/ solidification of hazardous mixed wastes—Mechanistic and process considerations', *J. Hazard. Mater.*, 1991, doi: 10.1016/0304-3894(91)87082-D.
- [30] D. M. Montgomery, C. J. Sollars, and R. Perry, 'Optimization of cement-based S/S of organic-containing industrial wastes using organophilic clays', *Waste Manag.*, 1991.
- [31] M. Ahdaya and A. Imqam, 'Investigating geopolymer cement performance in presence of water based drilling fluid', *J. Pet. Sci. Eng.*, 2019, doi: 10.1016/j.petrol.2019.02.010.
- [32] H. P. Grace, 'Dispersion phenomena in high viscosity immiscible fluid systems and applications of static mixers as dispersion devices in such systems', *Chem. Eng. Commun.*, 1982, doi: 10.1080/00986448208911047.
- [33] T. F. Tadros, 'Emulsion Formation, Stability, and Rheology', in *Emulsion Formation and Stability*, 2013, doi: 10.1002/9783527647941.ch1.
- [34] S. N. Kale and S. L. Deore, 'Emulsion Micro Emulsion and Nano Emulsion: A Review', *Syst. Rev. Pharm.*, 2016, doi: 10.5530/srp.2017.1.8.
- [35] F. Bossler and E. Koos, 'Structure of Particle Networks in Capillary Suspensions with Wetting and Nonwetting Fluids', *Langmuir*, 2016, doi: 10.1021/acs.langmuir.5b04246.
- [36] F. Bossler, L. Weyrauch, R. Schmidt, and E. Koos, 'Influence of mixing conditions on the rheological properties and structure of capillary suspensions', *Colloids Surf. Physicochem. Eng. Asp.*, 2017, doi: 10.1016/j.colsurfa.2017.01.026.
- [37] Y. Deng, J. B. Dixon, and G. N. White, 'Bonding mechanisms and conformation of poly(ethylene oxide)-based surfactants in interlayer of smectite', *Colloid Polym. Sci.*, 2006, doi: 10.1007/s00396-005-1388-0.
- [38] P. Panya, E. J. Wanless, O. Arquero, and G. V. Franks, 'The Effect of Ionic Surfactant Adsorption on the Rheology of Ceramic Glaze Suspensions', *J. Am. Ceram. Soc.*, 2005, doi: 10.1111/j.1551-2916.2005.00121.x.
- [39] E. Günister, S. İşçi, N. Öztekin, F. B. Erim, Ö. I. Ece, and N. Güngör, 'Effect of cationic surfactant adsorption on the rheological and surface properties of bentonite dispersions', *J. Colloid Interface Sci.*, 2006, doi: 10.1016/j.jcis.2006.07.021.
- [40] E. Günister, S. A. Alemdar, and N. Güngör, 'Effect of sodium dodecyl sulfate on flow and electrokinetic properties of Na-activated bentonite dispersions', *Bull. Mater. Sci.*, 2004, doi: 10.1007/BF02708522.
- [41] S. R. Derkach, 'Rheology of emulsions', *Adv. Colloid Interface Sci.*, 2009, doi: 10.1016/j.cis.2009.07.001.
- [42] A. Suzzoni, L. Barre, E. Kohler, P. Levitz, L. J. Michot, and J. M'Hamdi, 'Interactions between kaolinite clay and AOT', *Colloids Surf. Physicochem. Eng. Asp.*, 2018, doi: 10.1016/j.colsurfa.2018.07.049.

- [43] M. Bertin et al., 'Influence of cetyltrimethylammonium bromide and hydroxide ions on the interfacial tension and stability of emulsions of dodecane in aqueous silicate solutions', *Colloids Surf. Physicochem. Eng. Asp.*, 2021, doi: 10.1016/j.colsurfa.2021.127306.
- [44] B. Feneuil, O. Pitois, and N. Roussel, 'Effect of surfactants on the yield stress of cement paste', *Cem. Concr. Res.*, 2017, doi: 10.1016/j.cemconres.2017.04.015.
- [45] M. Ben Haha, G. Le Saout, F. Winnefeld, and B. Lothenbach, 'Influence of activator type on hydration kinetics, hydrate assemblage and microstructural development of alkali activated blast-furnace slags', *Cem. Concr. Res.*, 2011, doi: 10.1016/j.cemconres.2010.11.016.
- [46] M. Romagnoli, C. Leonelli, E. Kamse, and M. Lassinantti Gualtieri, 'Rheology of geopolymer by DOE approach', *Constr. Build. Mater.*, 2012, doi: 10.1016/j.conbuildmat.2012.04.122.
- [47] F. Puertas et al., 'Alkali-activated slag concrete: Fresh and hardened behaviour', *Cem. Concr. Compos.*, 2018, doi: 10.1016/j.cemconcomp.2017.10.003.
- [48] A. Pevere, G. Guibaud, E. van Hullebusch, P. Lens, and M. Baudu, 'Viscosity evolution of anaerobic granular sludge', *Biochem. Eng. J.*, 2006, doi: 10.1016/j.bej.2005.08.008.
- [49] S. M. Jafari, P. Beheshti, and E. Assadpoor, 'Rheological behavior and stability of d-limonene emulsions made by a novel hydrocolloid (Angum gum) compared with Arabic gum', *J. Food Eng.*, 2012, doi: 10.1016/j.jfoodeng.2011.10.016.
- [50] P.-G. de Gennes, F. Brochard-Wyart, and D. Quéré, 'Gouttes, bulles, perles et ondes', 2002.
- [51] S. Rossi, P. F. Luckham, and Th. F. Tadros, 'Influence of non-ionic polymers on the rheological behaviour of Na⁺-montmorillonite clay suspensions—I Nonylphenol-polypropylene oxide-polyethylene oxide copolymers', *Colloids Surf. Physicochem. Eng. Asp.*, 2002, doi: 10.1016/S0927-7757(01)00792-0.
- [52] A. Kaddami and O. Pitois, 'A physical approach towards controlling the microstructure of metakaolin-based geopolymer foams', *Cem. Concr. Res.*, 2019, doi: 10.1016/j.cemconres.2019.105807.
- [53] P. Mills and P. Snabre, 'Settling of a Suspension of Hard Spheres', *Europhys. Lett. EPL*, 1994, doi: 10.1209/0295-5075/25/9/003.
- [54] Y. Marcus, 'Surface Tension of Aqueous Electrolytes and Ions', *J. Chem. Eng. Data*, 2010, doi: 10.1021/je1002175.
- [55] Z. Li and B. C.-Y. Lu, 'Surface tension of aqueous electrolyte solutions at high concentrations — representation and prediction', *Chem. Eng. Sci.*, 2001, doi: 10.1016/S0009-2509(00)00525-X.
- [56] A. Albuquerque, C. Vautier-Giongo, and H. O. Pastore, 'Physical chemistry of nanostructured molecular sieves by the study of phase diagrams: the case of the cetyltrimethylammonium bromide-tetramethylammonium silicate-water system', *J. Colloid Interface Sci.*, 2005, doi: 10.1016/j.jcis.2004.10.065.
- [57] J. K. Mitchell and K. Soga, 'Fundamentals of Soil Behavior', 2005.
- [58] Y. Yang et al., 'An Overview of Pickering Emulsions: Solid-Particle Materials, Classification, Morphology, and Applications', *Front. Pharmacol.*, 2017, doi: 10.3389/fphar.2017.00287.
- [59] M. Destribats et al., 'Pickering Emulsions: What Are the Main Parameters Determining the Emulsion Type and Interfacial Properties?', *Langmuir*, 2014, doi: 10.1021/la501299u.
- [60] E. Koos, J. Johannsmeier, L. Schwebler, and N. Willenbacher, 'Tuning suspension rheology using capillary forces', *Soft Matter*, 2012, doi: 10.1039/c2sm25681a.
- [61] V. Cantarel, 'Synthesis of organic liquid-geopolymer composites in view of nuclear wastes conditioning', PhD, Blaise Pascal University, 2016.
- [62] I. M. Krieger and T. J. Dougherty, 'A Mechanism for Non-Newtonian Flow in Suspensions of Rigid Spheres', *Trans. Soc. Rheol.*, 1959, doi: 10.1122/1.548848.
- [63] M. Sakamoto, Y. Kanda, M. Miyahara, and K. Higashitani, 'Origin of Long-Range Attractive Force between Surfaces Hydrophobized by Surfactant Adsorption', *Langmuir*, 2002, doi: 10.1021/la025701j.
- [64] Y. Wu, S. Iglauer, P. Shuler, Y. Tang, and W. Goddard, 'Experimental Study of Surfactant Retention on Kaolinite Clay', *Tenside Surfactants Deterg.*, 2011, doi: 10.3139/113.110139.

- [65] A. Ya. Malkin, S. O. Ilyin, M. P. Arinina, and V. G. Kulichikhin, 'The rheological state of suspensions in varying the surface area of nano-silica particles and molecular weight of the poly(ethylene oxide) matrix', *Colloid Polym. Sci.*, 2017, doi: 10.1007/s00396-017-4046-4.
- [66] K. M. B. Jansen, W. G. M. Agterof, and J. Mellema, 'Droplet breakup in concentrated emulsions', *J. Rheol.*, 2001, doi: 10.1122/1.1333001.
- [67] J.-P. Canselier and M. Poux, 'Procédés d'émulsification – Mécanismes de formation des émulsions', *Techniques de l'ingénieur*, 2021.

Chapter III

How are alkali-activated materials impacted by incorporating low viscosity organic liquids?



Summary Chapter III

PREAMBLE CHAPTER III	103
1. CLASSIFICATION OF ALKALI-ACTIVATED MATERIALS	103
2. AAM WITH LOW CA CONTENT: GEOPOLYMERS.....	104
2.1. STRUCTURE.....	104
2.2. FORMULATION	105
3. AAM WITH HIGH CA CONTENT: C-A-S-H	106
3.1. STRUCTURE.....	106
3.2. FORMULATION	107
4. WATER PERMEABILITY OF AAM	108
REFERENCES	110
CHAPTER III: HOW ARE ALKALI-ACTIVATED MATERIALS IMPACTED BY INCORPORATING LOW VISCOSITY ORGANIC LIQUIDS?	113
ABSTRACT	113
1. INTRODUCTION.....	114
1.1. INDUSTRIAL CONTEXT.....	114
1.2. SCIENTIFIC BACKGROUND.....	114
1.3. AIMS AND SCOPES.....	115
2. MATERIALS AND METHODS	116
2.1. RAW MATERIALS	116
2.2. PREPARATION OF COMPOSITE MATERIALS	117
2.3. CHARACTERIZATION OF COMPOSITE MATERIALS.....	118
2.3.1. <i>Physical characterization</i>	118
2.3.1.1 Density and porosity measurement	118
2.3.1.2 Compressive strength measurements.....	119
2.3.1.3 2D SEM	120
2.3.1.4 3D X Ray micro-Computed Tomography (3D X Ray micro-CT).....	120
2.3.2. <i>Chemical characterization</i>	122
2.3.2.1 Micro-calorimetry.....	122
2.3.2.2 X Ray Diffraction (XRD).....	122
2.3.2.3 Solid state Magic Angle Spinning Nuclear Magnetic Resonance (MAS NMR)	122
3. RESULTS AND DISCUSSION	123
3.1. PHYSICAL CHARACTERIZATION	123
3.1.1. <i>Visual assessment of the incorporation of LVOL in hardened AAM</i>	123
3.1.2. <i>Influence of LVOL and surfactants on the mechanical strength and pore structure of AAM</i>	125
3.1.2.1 Effect of surfactant.....	126
3.1.2.2 Effect of 20%vol LVOL.....	127
3.1.2.3 Effect of 40%vol LVOL.....	128
3.1.3. <i>Influence of surfactants on the emulsion in hardened AAM</i>	132

3.1.3.1	Qualitative emulsion droplet analysis	132
3.1.3.2	3D representation and analysis of emulsion coalescence	134
3.1.3.3	Quantitative analysis	136
3.1.4.	<i>Chemical characterization</i>	137
3.1.4.1	Influence of LVOL or surfactants on the heat evolution of fresh AAM	137
3.1.4.2	Influence of LVOL or surfactants on the crystalline reaction products of AAM	138
3.1.4.3	Influence of LVOL or surfactants on the amorphous reaction products of AAM	141
4.	CONCLUSIONS	144
	ACKNOWLEDGMENTS	145
	APPENDIX	146
	REFERENCES	152

Preamble Chapter III

This chapter compares the two main types of alkali-activated material (AAM) for the immobilization of mineral oil. Despite being part of the same family, they strongly differ in terms of raw materials, reaction products, activating solutions, etc. This preamble section aims at shortly describing these two types of materials.

1. Classification of alkali-activated materials

The most apparent difference between alkali-activated binders and a traditional Portland cement is that the hardening of Portland cement is induced simply by mixing dry cement powder with water, whereas alkali-activated materials (AAM) are generally obtained by the activation of solid powdered precursors by an alkaline source [1].

AAM are obtained through the chemical reactions between two components, the alkaline activator (generally an aqueous liquid), and an aluminosilicate reactive solid precursor (generally a fine powder). Alkali activators are composed of alkali metals, in the form of hydroxides and/or silicates, dissolved in an aqueous solution. Materials used as solid precursors, mainly composed of aluminosilicates, are usually in a powdered and amorphous (reactive) mineralogical state. Figure 1 (left) presents the main raw materials used to prepare AAM in a ternary diagram $\text{CaO-SiO}_2\text{-Al}_2\text{O}_3$, into perspective with conventional Portland cement.

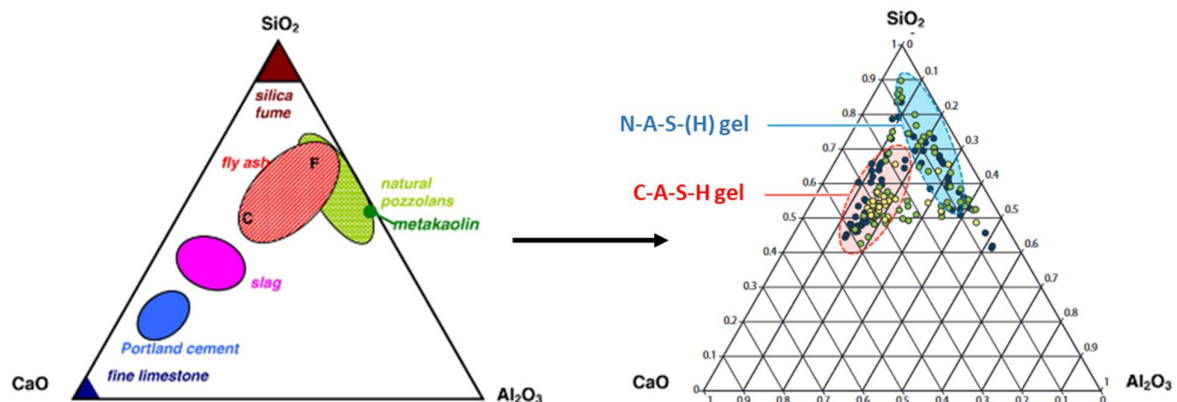


Figure 1: Ternary diagram $\text{CaO-Al}_2\text{O}_3\text{-SiO}_2$ of (left) raw materials used to prepare AAM [2] and (right) reaction products formed after alkali activation [1].

In discussing the chemistry of AAM, it is necessary to classify these systems as a function of the gel network that dominates their structure. This distinction is drawn based on the amount of calcium present in raw materials as seen in Figure 1. Ca-rich systems are generally considered when the molar ratio $\text{Ca}/(\text{Si} + \text{Al})$ is greater than 1. Two main gel types are distinguished:

- In Ca-rich systems, the major phase is a hydrated calcium aluminosilicate gel noted “**C-A-S-H**” (in the cement industry, C is for CaO, A for Al₂O₃, S for SiO₂ and H for H₂O). Raw materials leading to the formation of C-A-S-H gels are generally blast furnace slags (BFS) or class C fly ashes.
- In Ca-poor systems, the major phase is a sodium (or potassium, lithium or a mix of these) aluminosilicate gel noted “**N-A-S-(H)**” (or M-A-S-(H) with M=Na₂O, K₂O or Li₂O or a mix of these, and N=Na₂O). Raw materials leading to the formation of N-A-S-(H) gels are generally metakaolin or class F fly ashes. The N-A-S-(H) gel is an amorphous reticulated 3D aluminosilicate framework.

The Qⁿ(mAl) notation is often used to describe the local environment of silica atoms in the C-A-S-H and N-A-S-(H) aluminosilicate networks. Q represents a Si atom, n its degree of connectivity with neighboring oxygen atoms and m the number of second neighboring aluminum atoms [3]. This notation is illustrated in Figure 2 for n = 4 and 0 ≤ m ≤ 4.

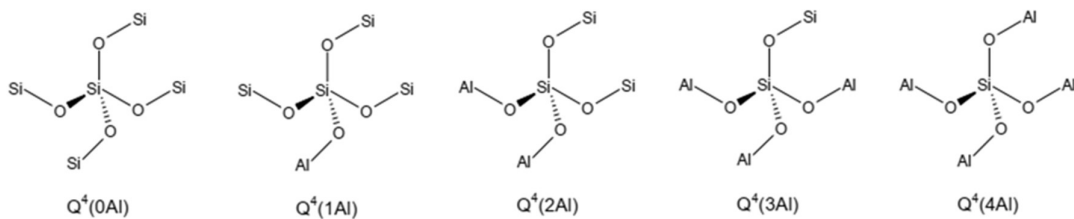


Figure 2: Coordination of Si atoms described in the Qⁿ(mAl) notation, for n = 4 and 0 ≤ m ≤ 4 [3].

2. AAM with low Ca content: geopolymers

2.1. Structure

In the late 70s, J. Davidovits drew the attention to Ca-poor AAM based on metakaolin and named these materials geopolymers by analogy with organic polymers [4].

N-A-S-(H) gels are formed by poly-condensation reactions using water as a solvent, after which water is released. Hence, water is not part of the final N-A-S-(H) framework and is presented into brackets. It is said that water is free and mainly present in pores whose sizes and proportions depend on the formulation conditions. Provis et al. [5] proposed that N-A-S-(H) gels and zeolites structures are locally similar. However, although N-A-S-(H) gels are very similar to zeolite-like crystalline structures, they appear as disordered (amorphous) when the scale of observation is higher than a few Angströms and are therefore difficult to observe using analytical techniques based on diffraction. Figure 3 represents the N-A-S-(H) structure as proposed by Barbosa et al. [6]. It is comprised of Si⁴⁺ and Al³⁺ cations in tetrahedral coordination (Q⁴), which are linked together by oxygen bridges. This provides a tridimensional

solid framework in which the negative charges from each tetrahedral Al (AlO_4^-) are counterbalanced by alkali cations (e.g. Na^+).

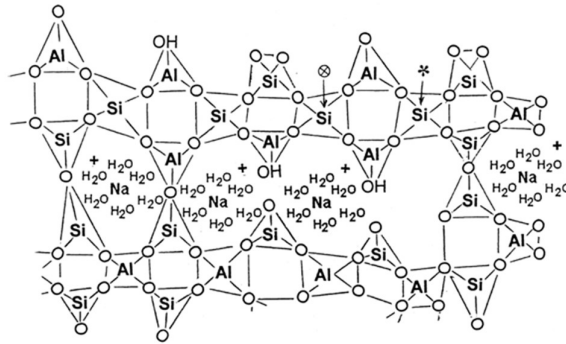


Figure 3: Schematic representation of the three-dimensional N-A-S-(H) structure as proposed by Barbosa et al. [6].

2.2. Formulation

The following information are given for Na-based geopolymers, but they are also useful for K- and Li-based geopolymers. Acid-activated geopolymers also exist, but they are not considered in this research due to a very limited knowledge of their durability.

The composition of a sodium-based geopolymer is generally defined by three molar ratios: **1) $\text{SiO}_2/\text{Al}_2\text{O}_3$; 2) $\text{H}_2\text{O}/\text{Na}_2\text{O}$; 3) $\text{Na}_2\text{O}/\text{Al}_2\text{O}_3$** . These parameters influence the microstructural arrangement of the N-A-S-(H) gel and, as a consequence, the macroscopic properties of the final solid material. In general, the Al content is fixed by the solid aluminosilicate precursor, which is the only source of Al. Other species are adapted in the alkali-activating solution to meet the desired molar ratio. Accordingly, the activating solution is generally a mixture of alkali silicates and alkali hydroxides.

$\text{SiO}_2/\text{Al}_2\text{SiO}_3$ (Si/Al): The molar ratio Si/Al is the most important parameter in formulating geopolymers. For instance, Duxson et al. [7] have shown that mechanical properties are improved with increasing Si/Al in the range 1.15 to 1.90. This is explained by the Loewenstein principle, which states that Al-O-Al bindings are not favored thermodynamically [8]. Hence, if the amount of Si is not sufficient, aluminosilicate chains will be shorter and not fully interconnected, whereas in Si-rich systems the formation of widely interconnected frameworks is possible. The pore structure is also impacted by the Si/Al ratio. For formulations with $\text{Si/Al} < 1.4$, the microstructure comprises large interconnected pores, while formulations with $\text{Si/Al} \geq 1.65$ display a fine, homogenous and non-connected pore network [7]. It is noted that high Si contents lead to the presence of Q^3 coordinated Si, which reduces the polymerization degree and the mechanical performances of the final materials [1], [7].

H₂O/Na₂O: The molar ratio H₂O/Na₂O is also important. Indeed, on the one hand, the amount of water must be sufficient to allow an effective mixing of the reactants and ensure a good mobility of the ionic species. This is associated with a good workability of the fresh grout. On another hand, the amount of water should not be too high to avoid diluting the reactants, which would lead to increased setting times. As it is not part of the final structure, a high amount of water also drastically decreases mechanical properties by creating more numerous and larger pores. This was for instance shown by Barbosa et al. [6].

Na₂O/Al₂O₃ (Na/Al): A molar ratio Na/Al close to 1 seems to be the optimum concerning mechanical performances of geopolymer materials [9]. Hydroxide (HO⁻) ions contribute to dissolving Al³⁺ and Si⁴⁺ cations from the solid precursor, whereas Na⁺ ions contribute to forming the N-A-S-(H) network by counterbalancing negatives charges arising from the [AlO₄⁻] species.

3. AAM with high Ca content: C-A-S-H

3.1. Structure

There is a consensus on the main hydrated product formed during the activation of Ca-rich systems. This is a poorly crystalline calcium aluminosilicate gel, noted **C-A-S-H** and similar to the C-S-H gel formed in Portland cement but with a lower Ca/Si ratio and the incorporation of Al [10]. C-A-S-H gels are made from hydration reactions, meaning that water is part of the final solid framework. A significant part of the water is therefore chemically bound, contrasting with the free water present in the N-A-S-(H) structure. However, free water is also present in C-A-S-H systems, owing to the excess of water required to have workable fresh grouts. In general, it is considered that C-A-S-H gels have a weakly organized structure similar to the tobermorite 14Å arrangement. The tobermorite architecture is composed of silicate chains (Q² or Q³) along which repeating units called “dreierketten” follow one another. Some additional rules are acknowledged:

- Aluminum is present only in bridging sites [11].
- According to the Loewenstein principle, Al-O-Al bindings are not favored thermodynamically [12].
- There are no Q⁰ or Q¹(1Al) in the structure of a C-A-S-H.
- C-A-S-H might be written C-(N)-A-S-H due to the fact that Na⁺ could replace Ca²⁺ in the gel structure even if it is not favored [13].

A schematic representation of the C-A-S-H structure taking into account the above-mentioned information is given in Figure 4 [1].

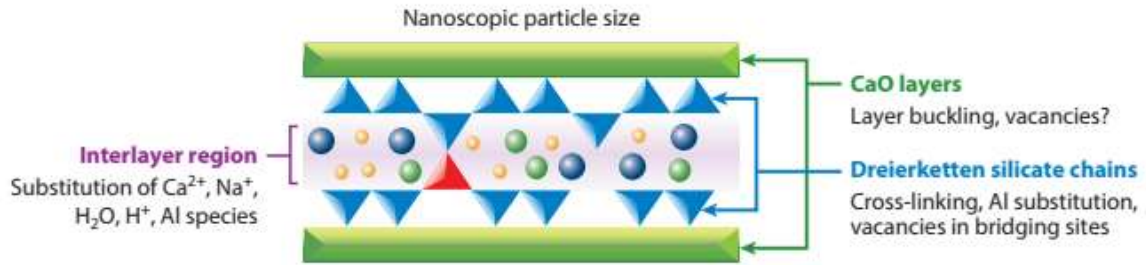


Figure 4: Tobermorite-like C-A-S-H structure. Blue triangles represent tetrahedral silicates, red triangles represent Al substitution at bridging sites, green bands represent CaO layers and circles represent various ionic species present in the aqueous intermediate layer (Ca^{2+} , Na^+ , HO^- , ...) [1].

3.2. Formulation

Although numerous generalities are widely accepted about the C-A-S-H structure, several parameters can affect their microstructure and hence modify the macroscopic properties of the final solid materials. The formulation of Ca-rich systems is generally controlled by two parameters: **1) The type of activation; 2) The water to solid precursor mass ratio (W/S)**. The Ca content is fixed by the solid aluminosilicate precursor, which is the only source of Ca.

Type of activation: Contrarily to Ca-poor systems, Ca-rich precursors can be effectively activated by alkali hydroxides, silicates, carbonates or sulfates [14]. Alkali metal hydroxides and silicates are the most widely used [13]. In general, the hydroxide activation accelerates the reactivity, which leads to an early decrease in the mobility of the ionic species in the system. On the contrary, the activation by silicates leads to a slower reactivity, allowing a uniform precipitation and a higher degree of reaction. This difference results in materials with larger and more numerous pores in hydroxide-activated materials. The type of activation also modifies the $\text{Ca}/(\text{Si}+\text{Al})$ molar ratio.

Ca/(Si+Al): The $\text{Ca}/(\text{Si}+\text{Al})$ molar ratio varies depending on the type of activation (i.e. on the Si supply) and the composition of solid precursors (i.e. on the Ca supply). Hydroxide-activation leads to a higher $\text{Ca}/(\text{Si}+\text{Al})$ than silicate-activation. Consequently, studies conducted by Puertas et al. [10] and Jiménez et al. [15] highlighted that hydroxide activation results in the formation of Q^2 species mainly, while the amount of Q^3 species is low. This indicates that linear aluminosilicate chains are hardly connected, leading to the formation of an open microstructure with a higher porosity and lower mechanical performances. On the contrary, silicate activation generates a high number of Q^3 species, implying a higher connectivity between aluminosilicate chains. The resulting microstructure is denser, more compact with a lower porosity and higher mechanical performances. Other than the type of activation, the amount of Ca present in the solid precursor also affects the $\text{Ca}/(\text{Si} + \text{Al})$ ratio. It has been

observed that the gel connectivity, irrespective of the type of activation, increases with decreasing amount of calcium, which is in accordance with previously discussed observations [16].

Water/Slag (W/S): In terms of reactivity and workability, the importance of water is similar in Ca-rich systems as is Ca-poor systems. It is well known that increasing the amount of water in Ca-rich AAM decreases the mechanical performances of the final solid material [17]. However, Yang et al. [18] also highlighted that if the amount of water is too low, mechanical performances decrease as well. This can be understood by the fact that in Ca-rich AAM, water is part of the formed C-A-S-H framework.

Solid precursor composition: Ca-rich AAM may be obtained from the activation of blast furnace slag (BFS). The composition of BFS varies significantly depending on its origin but it can be simplified in a quaternary system: $\text{MgO-CaO-SiO}_2\text{-Al}_2\text{O}_3$, with other components considered as negligible [14]. Due to structural restrictions in the tobermorite-like structure, the presence of high amounts of Al and/or Mg lead to the formation of secondary phases, impacting the final properties [14]. For instance, some authors mention hydrotalcite as a second main phase intertwined with the C-A-S-H gel [13] and systems activated with alkali hydroxides generally lead to the formation of AFm secondary phases [19].

4. Water permeability of AAM

The above-mentioned formulation parameters affect the percolating pore network of AAM binders, which has a direct impact on the ability of AAM to resist fluid mass transport and degradation.

In particular, water permeability of AAM is one of the key transport properties (besides diffusivity) to assess their durability [20] and their ability to confine HTO. Water permeability is driven by the pore volume, size and morphology (succession of small and bigger pores, presence of non-percolating pores, etc.). The type of precursor and the amount of water are the two main factors influencing the gel structure of AAM and thereby their water permeability. This is summarized by Nguyen et al. in Figure 5 [21]. In terms of precursor type, N-A-S-(H) gels result in a much higher water permeability ($10^{-8} \text{ m}\cdot\text{s}^{-1}$) compared to C-A-S-H gels ($10^{-13} \text{ m}\cdot\text{s}^{-1}$) [21]. This is generally attributed to the intrinsic higher porosity of N-A-S-(H) gels [21], but it is mainly due to the easiness to generate cracks in N-A-S-(H) solids [22], [23], which are significant fluid pathways. For both types of gels, a higher amount of water leads to a greater permeability due to the larger pore volume and pore sizes.

Among the C-A-S-H, the type of activation (hydroxides or silicates) also influences the pore structure. Blyth et al. [21] highlighted that silicate-activated BFS possesses lower permeability than ordinary Portland cement (OPC) paste at similar water content. On the contrary,

hydroxide-activated BFS are three orders of magnitude more permeable. This is explained by the smaller pore volume and the finer pore size distribution of silicate-activated BFS in comparison with hydroxide-activated BFS [20], [24].

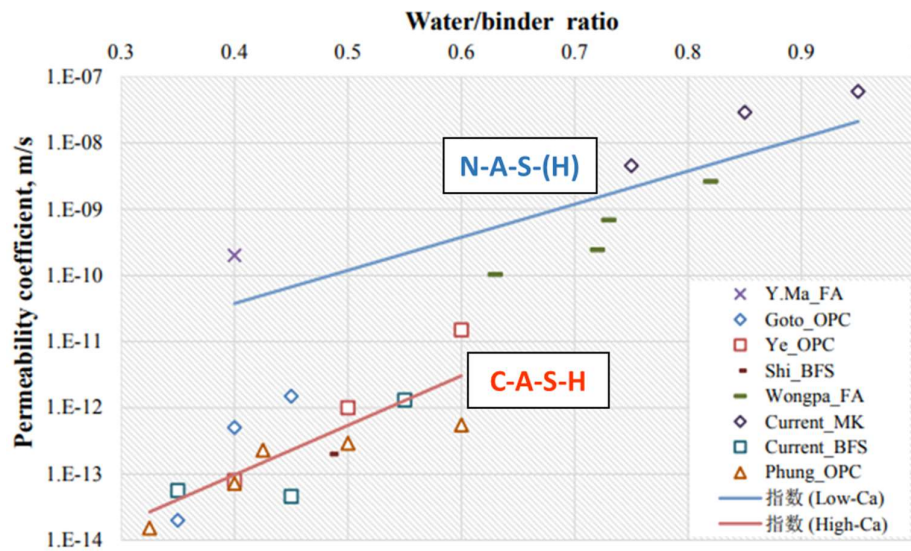


Figure 5: Water permeability of AAM depending on the type of solid precursors and the amount of water [21].

References

- [1] J. L. Provis and S. A. Bernal, « Geopolymers and Related Alkali-Activated Materials », *Annu. Rev. Mater. Res.*, 2014, doi: 10.1146/annurev-matsci-070813-113515.
- [2] B. Lothenbach, K. Scrivener, and R. D. Hooton, « Supplementary cementitious materials », *Cem. Concr. Res.*, 2011, doi: 10.1016/j.cemconres.2010.12.001.
- [3] A. C. E. Idrissi, « Géopolymérisation et activation alcaline des coulis d'injection: structuration, micromécanique et résistance aux sollicitations physico-chimiques », PhD, University of Nantes, 2016.
- [4] J. Davidovits, « Geopolymers of the First Generation: SILIFACE-process », 1st European conference on soft mineralurgy, 1988.
- [5] J. L. Provis, G. C. Lukey, and J. S. J. van Deventer, « Do Geopolymers Actually Contain Nanocrystalline Zeolites? A Reexamination of Existing Results », *Chem. Mater.*, 2005, doi: 10.1021/cm050230i.
- [6] V. F. F. Barbosa, K. J. D. MacKenzie, and C. Thaumaturgo, « Synthesis and characterisation of materials based on inorganic polymers of alumina and silica: sodium polysialate polymers », *Int. J. Inorg. Mater.*, 2000, doi: 10.1016/S1466-6049(00)00041-6.
- [7] P. Duxson, J. L. Provis, G. C. Lukey, S. W. Mallicoat, W. M. Kriven, and J. S. J. van Deventer, « Understanding the relationship between geopolymer composition, microstructure and mechanical properties », *Colloids Surf. Physicochem. Eng. Asp.*, 2005, doi: 10.1016/j.colsurfa.2005.06.060.
- [8] M. Jeffroy, C. Nieto-Draghi, and A. Boutin, « New Molecular Simulation Method To Determine Both Aluminum and Cation Location in Cationic Zeolites », *Chem. Mater.*, 2017, doi: 10.1021/acs.chemmater.6b03011.
- [9] M. Rowles and B. O'Connor, « Chemical optimisation of the compressive strength of aluminosilicate geopolymers synthesised by sodium silicate activation of metakaolinite », *J. Mater. Chem.*, 2003, doi: 10.1039/b212629j.
- [10] F. Puertas, M. Palacios, H. Manzano, J. S. Dolado, A. Rico, and J. Rodríguez, « A model for the C-A-S-H gel formed in alkali-activated slag cements », *J. Eur. Ceram. Soc.*, 2011, doi: 10.1016/j.jeurceramsoc.2011.04.036.
- [11] R. J. Myers, S. A. Bernal, R. San Nicolas, and J. L. Provis, « Generalized Structural Description of Calcium-Sodium Aluminosilicate Hydrate Gels: The Cross-Linked Substituted Tobermorite Model », *Langmuir*, 2013, doi: 10.1021/la4000473.
- [12] W. Loewenstein, « The distribution of aluminum in the tetrahedra of silicates and aluminates », *Am. Mineral.*, 1954.
- [13] M. Ben Haha, G. Le Saout, F. Winnefeld, and B. Lothenbach, « Influence of activator type on hydration kinetics, hydrate assemblage and microstructural development of alkali activated blast-furnace slags », *Cem. Concr. Res.*, 2011, doi: 10.1016/j.cemconres.2010.11.016.
- [14] S. A. Bernal, « Advances in near-neutral salts activation of blast furnace slags », *RILEM Tech. Lett.*, 2016.
- [15] A. Fernández-Jiménez, F. Puertas, I. Sobrados, and J. Sanz, « Structure of Calcium Silicate Hydrates Formed in Alkaline-Activated Slag: Influence of the Type of Alkaline Activator », *J. Am. Ceram. Soc.*, 2003, doi: 10.1111/j.1151-2916.2003.tb03481.x.
- [16] K. Gong and C. E. White, « Impact of chemical variability of ground granulated blast-furnace slag on the phase formation in alkali-activated slag pastes », *Cem. Concr. Res.*, 2016, doi: 10.1016/j.cemconres.2016.09.003.
- [17] C. Bilim, C. D. Atiş, H. Tanyildizi and O. Karahan, « Predicting the compressive strength of ground granulated blast furnace slag concrete using artificial neural network », *Adv. Eng. Softw.*, 2009, doi: 10.1016/j.advengsoft.2008.05.005.
- [18] T.-R. Yang, T.-P. Chang, B.-T. Chen, J.-Y. Shih, and W.-L. Lin, « Effect of alkaline solutions on engineering properties of alkali-activated ggbs paste », *J. Mar. Sci. Technol.*, 2012.
- [19] J.I. Escalante-Garcia, A.F. Fuentes, A. Gorokhovskiy, P.E. Fraire-Luna and G. Mendoza-Suarez, « Hydration Products and Reactivity of Blast-Furnace Slag Activated by Various Alkalis », *J. Am. Ceram. Soc.*, 2003.

- [20] A. Blyth, C. A. Eiben, G. W. Scherer, and C. E. White, « Impact of activator chemistry on permeability of alkali-activated slags », *J. Am. Ceram. Soc.*, 2017, doi: 10.1111/jace.14996.
- [21] T. N. Nguyen and al., « Effect of precursors and water to binder ratios on the water permeability of alkali-activated mortars », 4th Int. RILEM conference on microstructure related durability of cementitious composites, 2020.
- [22] H. Lahalle, V. Benavent, V. Trincal, T. Watzel, R. Bucher, et al. « Robustness to water and temperature, and activation energies of metakaolin-based geopolymer and alkali-activated slag binders. », *Const. and Buil. Mat.*, 2021; doi: 10.1016/j.conbuildmat.2021.124066
- [23] V Trincal, V Benavent, H Lahalle, B Balsamo, « Effect of drying temperature on the properties of alkali-activated binders-Recommendations for sample preconditioning », *Cem. and Concr. Res.*, 2022
- [24] Z. Zhang and H. Wang, « Analysing the relation between pore structure and permeability of alkali-activated concrete binders », in *Handbook of Alkali-Activated Cements, Mortars and Concretes*, 2015. doi: 10.1533/9781782422884.2.235.

Chapter III: How are alkali-activated materials impacted by incorporating low viscosity organic liquids? *(Published in Materials and Structures)*

Charles Reeb^{1,2}, Catherine A. Davy¹, Matthieu De Campos², Jérôme Hosdez³, Christel Pierlot¹, Cyrille Albert-Mercier⁴, David Lambertin²

¹ Univ. Lille, CNRS, Centrale Lille, ENSCL, Univ, Artois, UMR 8181-UCCS-Unité de Catalyse et de Chimie du Solide – F-59000 Lille, France

² CEA, DES, ISEC, DE2D, SEAD, LCBC, Univ Montpellier, Marcoule, France

³ Univ. Lille, CNRS, Centrale Lille, Laboratoire de Mécanique, Multiphysique et Multiéchelle (LaMcube) UMR CNRS 9013, Lille, 59000, France

⁴ Université Polytechnique Hauts-de-France, CERAMATHS, 59600 Maubeuge, France

Abstract

This research determines an adequate alkali-activated material (AAM) for the incorporation of huge amounts (20 or 40%vol) of low viscosity organic liquids (LVOL), e.g. for waste stabilization/solidification. The selected AAM are either based on high-Ca content blast furnace slag, or on low Ca-content metakaolin, i.e. on a geopolymer matrix.

First, the selection of the AAM is performed to ensure no LVOL leakage and a sufficient compressive strength f_c (> 8 MPa). Surfactants are compulsory to allow incorporation. After 90 days curing, for slag pastes, f_c ranges between 10-20 MPa at 20%vol LVOL, but it is zero at 40% LVOL, whatever the surfactant. For geopolymer pastes, the AAM-LVOL composites have an average f_c of 25 MPa at 20%vol LVOL, and of 15 MPa at 40% LVOL.

With surfactant, the AAM solid pore structure of slag pastes is denser (with smaller specific surface area and micropore amount); it is unchanged for geopolymer pastes. Whatever the surfactant, air entrained bubbles are present. Their proportion is maximal with Glucocon. Together with LVOL presence, this generally contributes to decreasing f_c .

The emulsion (entrained air+LVOL droplets) is characterized in hardened AAM by combining 2D Scanning Electron Microscopy and 3D X-Ray micro-computed tomography. Surfactants significantly decrease the emulsion droplet size distribution. For geopolymer pastes up to 40%vol LVOL, the most adequate surfactants are Brij O10 and CTAB; for slag paste up to 20% vol LVOL, it is CTAB.

Moreover, the setting reactions are not impacted by LVOL or surfactants, and neither are the reaction products. It is concluded that the decrease in mechanical performance of AAM-LVOL composites is only due to physical reasons, particularly the decrease in AAM proportion, the emulsion quality (coalescence, droplet size and shape) and air entrained bubbles.

Keywords: Alkali-activated materials (AAM), geopolymer (GEO), blast furnace slag (BFS), surfactants, low viscosity oil.

1. Introduction

1.1. Industrial context

The incorporation of organic liquids (OL) into cementing materials has several significant benefits. These include the immobilization of radioactive waste from the nuclear industry or from medical uses [1]-[3], the design of composite materials with increased thermal inertia by incorporating phase changing materials (PCM) [4]-[7], the formulation of ultra-porous materials (i.e. foams) by OL extraction [8]-[10], or the development of materials with reinforced and/or emerging properties [11]-[13].

Although significant research has been conducted on incorporating OL into ordinary Portland cement (OPC), it is not of practical use, due to the difficulty of incorporation and consequent unfavorable characteristics, such as delayed setting time, loss of strength and uncertain long-term stability, all of which are increased with increasing OL content [14]-[18].

The issues of the incorporation of OL can be addressed by using alkali-activated materials (AAM) instead of OPC. AAM do not only provide performances comparable to conventional OPC concretes, but also additional advantages, including high OL incorporation rates (up to 20-60%vol) [19]-[21], rapid development of mechanical strength, small drying shrinkage, high fire resistance and superior acid resistance [22]-[24].

1.2. Scientific background

Two main types of AAM are distinguished, depending on the selected raw materials [25]. The alkali-activation of solid precursors with low calcium contents (e.g. class F fly ash or metakaolin MK) results in N-A-S-(H) gels through poly-condensation. N-A-S-(H) possess a three-dimensional imperfect (amorphous) aluminosilicate structure with predominant Q^4 silica structural units. On the other hand, alkali-activated solid precursors with high calcium contents (more than 10% Ca, e. g. blast furnace slag BFS or class C fly ash) result in C-(N)-A-S-H gels through hydration reactions. C-(N)-A-S-H consist of a partially polymerized chain-like silica structure with mainly Q^1 and Q^2 silica structural units, and minor proportions of Q^3 and Q^4 units. They are of very similar structure to the main solids present in Portland cements. Since these two families of AAM (based on N-A-S-H or C-A-S-H) have such different solid structures, it is useful to check their adequacy for encapsulating low viscosity organic liquids (LVOL).

With AAM, several strategies exist for the incorporation of OL [26]. The direct route (where the OL is directly poured into the fresh GP slurry) is easy to implement, and large amounts of OL can be incorporated [21], [27], [28]. After the formation of OL droplets by mechanical

stirring, the intrinsic viscosity of AAM-slurries generally helps to prevent OL coalescence until hardening of the paste.

However, at high incorporation rates (more than 10%vol) and for low viscosity OL (below 1 Pa.s, [29]), coalescence of OL droplets becomes more favorable, and this leads to phase separation i.e., to the loss of the OL emulsion. In such cases, the addition of surfactants is compulsory to maintain emulsion stability. Surfactants can reduce the size of dispersed droplets by decreasing the interfacial tension, which stabilizes the emulsion. Several types of surfactants have proven their efficiency for the incorporation of OL in AAM, especially cationic [30] and non-ionic ones [31]. Surfactants are also organic molecules with versatile chemical structures; they can adsorb at the surface of solid precursors. In particular, [2] proposed that complementarily to decreasing the surface tension, the addition of surfactant promotes the agglomeration of solid particles at the surface of the OL droplets, similar to a Pickering-like stabilization mechanism. Surfactants also promote the stabilization of air bubbles introduced during the mixing of the fresh cement slurry. This may enhance the total porosity of the material and reduce its mechanical strength and long-term stability [32]-[34].

1.3. Aims and scopes

This research determines the most appropriate AAM for the immobilization of high amounts (up to 20 or 40%vol) of low viscosity OL (LVOL). The two main types of AAM are tested. They are either made of N-A-S-(H) solids (i.e. of geopolymers GP, based on a MK solid precursor) or made of C-(N)-A-S-H solids (based on BFS, and similar to Portland cements). Two typical formulations are selected from the literature for their excellent mechanical performance, one for MK-based AAM [1], [2], [22], [27], [28] and the other for BFS-based AAM [35]. MK is alkali-activated with sodium silicates (to get a typical stoichiometry with excellent mechanical strength) and BFS with sodium hydroxide because the LVOL emulsion is easier with this activator. Surfactants are used and compared to assess their effect on the LVOL emulsion, and to choose the most adequate one.

The adequacy of the AAM-surfactant pair for LVOL immobilization is determined mainly in the hardened state, for durations of up to 90 days, firstly from the physical viewpoint, and secondly from the chemical viewpoint.

The physical characterization aims to ensure the absence of LVOL leakage, a minimal compressive strength ($f_c \geq 8\text{MPa}$ according to industrial specifications [36]), and to correlate the emulsion morphology to the density, pore structure and mechanical performance of the AAM+surfactant+LVOL composites. Each OL emulsion is characterized in 2D, by Scanning Electron Microscopy (SEM), and in 3D, in a non-destructive manner, by X Ray micro-computed tomography (X Ray micro-CT).

The chemical assessment combines isothermal micro-calorimetry, X Ray Diffraction (XRD) and ^{29}Si , ^{27}Al solid state MAS NMR to determine whether the presence of surfactant or LVOL impacts significantly the AAM structure. Moreover, the different chemical nature of the solid precursors and the reactivity differences (hydration for slag vs. condensation with MK) may lead to distinct interferences. In particular, a smaller degree of polymerization, due to OL presence or to surfactant adsorption at the interface of the solid precursors, could be responsible for poorer mechanical properties.

Investigating both physical and chemical aspects is favorable from a *durability* perspective.

2. Materials and methods

2.1. Raw materials

A pure mineral oil (Finavestan A360B) with a density of 0.864 g.cm^{-3} is obtained from Total (France). This oil is chosen for its purity (i.e. its absence of additives), for its low viscosity of 0.13 Pa.s at 100 s^{-1} at 25°C [29], and, as a linear alkane, for its absence of reactivity in alkaline media.

An aqueous sodium silicate solution (Betol 39T) is obtained from Woellner (Germany). Sodium hydroxide (purity > 99%) is purchased from VWR International (USA). A metakaolin (MK) powder of M1000 grade is obtained from Imerys (France) and blast furnace slag (BFS) powder is purchased from Ecocem (France). MK powder is characterized by X Ray fluorescence (XRF) as composed of 54%wt SiO_2 (+/- 1%), 39.5%wt Al_2O_3 (+/-1%), 1.7%wt TiO_2 (+/-0.1%), 1.4%wt Fe_2O_3 (+/-0.1%) and other oxides present in less than 1%wt. BFS is characterized by XRF as composed of 34.9%wt SiO_2 (+/-1.8%), 10.0%wt Al_2O_3 (+/- 1.3%), 43.2%wt CaO (+/-0.5), 8.8%wt MgO (+/- 1.8%), and other oxides present in less than 1%wt. The apparent density is of 2.23 g.cm^{-3} for MK powder and 2.9 g.cm^{-3} for BFS.

Following preliminary research (see conclusions chapter II), four different surfactants are compared (Table 1). Brij O10 and Span 80 are purchased from Acros Organics (USA); Brij O10 is more suited to MK-based AAM, while Span 80 is more adequate for alkali-activated BFS paste. CTAB and GlucoPON 225DK (hereafter referred to as GlucoPON) are obtained from Sigma Aldrich and BASF (Germany), respectively.

Table 1: Denomination and chemical description of surfactants tested in this study.

Chemical description	Commercial name	Category	HLB
Sorbitan monooleate	Span 80	Non-ionic (\emptyset)	4.3
Cetyl Trimethyl Ammonium Bromide	CTAB	Cationic (+)	10
Polyoxyethylene (10) oleyl ether	Brij O10	Non-ionic (\emptyset)	12.4
C ₈ -C ₁₀ -alkyl polyglucoside	Glucopon 225DK	Non-ionic (\emptyset)	13.5

2.2. Preparation of composite materials

Two typical formulations of AAM cements are selected from the literature for their excellent mechanical performance, one for MK-based AAM [1], [2], [22], [27], [28] and the other for slag-based AAM [35]. The choice is made of an alkali-activation with sodium silicate for MK in order to obtain an adequate stoichiometry for good mechanical performance, and sodium hydroxide for BFS. In the latter case, the activator choice is due to a preliminary study in our lab, showing that the OL emulsification is better (with smaller and more homogeneously distributed droplets) in sodium hydroxide activated BFS than in sodium silicate activated BFS (see Figure S1 in the Appendix).

In practice, the MK-based geopolymer (GEO) fresh paste (or slurry) is obtained as follows. The components (sodium silicate solution, sodium hydroxide, water and MK) are weighed in order to obtain a molar composition of $3.5 \text{ SiO}_2 : 1.0 \text{ Al}_2\text{O}_3 : 1.0 \text{ Na}_2\text{O} : 14.0 \text{ H}_2\text{O}$. For the alkali activated BFS (AABFS) paste, the components (sodium hydroxide, water and BFS) are weighed with a water/BFS mass ratio equal to 0.45 and a mass concentration of sodium hydroxide of 10%. This allows a good workability of the paste and reasonable hardening of the material [37].

For both materials, the first step consists in preparing the alkali-activating solution. Sodium hydroxide pellets are dissolved in water (purified by reverse osmosis). In the case of MK-based GEO, the sodium silicate solution (Betol 39T) is also added. The blend is left to cool down to room temperature for several hours. After cooling, the surfactant is added to the activating solution, and the mix is stirred mechanically at 800 rpm with a helical blade. The molar concentration of surfactant with respect to the volume of activating solution (sodium silicate, sodium hydroxide and water) is $3 \cdot 10^{-3} \text{ mol.L}^{-1}$, allowing a good incorporation of the oil. At this stage, the solid precursor powder (MK or BFS) is quickly added to the activating solution and

the mixing is carried out for 3 minutes until stabilization. Finally, the Finavestan LVOL is quickly introduced in the cement paste and the mixing is carried for 2 additional minutes to obtain composite materials with a LVOL volume concentration of 0, 20 or 40% (% of the total AAM paste + LVOL volume).

The formulated materials are named as follows: GEO-X-Y or BFS-X-Y, with X = 0, 20 or 40 the %vol of LVOL and Y = 0, C, G or B accounting for, respectively, no surfactant, CTAB, Glucopon 225DK or Brij O10. Table 2 describes all the tested formulations. For micro-calorimetry only, an AABFS sample is formulated using 10 times (i.e. $3 \cdot 10^{-2} \text{ mol.L}^{-1}$) the amount of Glucopon required for stabilizing the emulsion; this sample is named BFS-0-G10.

2.3. Characterization of composite materials

2.3.1. Physical characterization

2.3.1.1 Density and porosity measurement

These measurements are only feasible for AAM pastes, with or without surfactant, but free of LVOL. All samples are matured in endogenous conditions at 25°C for 90 days. The bulk density ρ is assessed as the ratio of the weight to the geometrical volume. The true (absolute) density ρ_0 of the “pore-free” solid material is measured with a helium pycnometer (all pores are considered open). The “pore-free” materials are obtained through freeze-drying; to this purpose, centimetric hardened paste samples are poured into liquid nitrogen and dehydrated in vacuum during at least 48h. The open porosity (OP) of each sample is measured based on the following relationship: $OP (\%) = 100 \times (1 - \rho/\rho_0)$.

Nitrogen sorption-desorption isotherms are performed to quantify the pore structure up to a size of about 200 nm. Experiments are conducted on freeze-dried samples at 77 K on a Micromeritics ASAP 2020 device. Classical BET and BJH models are used to derive the material specific surface area [38], [39]. The micropore amount is calculated as the adsorbed quantity of nitrogen for $(P/P_0) \leq 0.1$ (in $\text{cm}^3 \cdot \text{g}^{-1}$); it is the amount of pores smaller than 2 nm present per gram of AAM [39]. All bigger pores (mesopores between 2 and 50 nm and macropores bigger than 50 nm) are characterized on the isotherms for $(P/P_0) \geq 0.1$.

Table 2: Description of the different formulations investigated in this research

Formulation	Cement type	Surfactant type	Oil (%vol)
GEO-0-0	Na-metasilicate activated MK geopolymer	none	0
GEO-20-0			20
GEO-40-0			40
GEO-0-G		Glucopon 225DK	0
GEO-20-G			20
GEO-40-G			40
GEO-0-C		CTAB	0
GEO-20-C			20
GEO-40-C			40
GEO-0-B		Brij O10	0
GEO-20-B			20
GEO-40-B			40
BFS-0-0	NaOH activated Blast Furnace Slag	none	0
BFS-20-0			20
BFS-40-0			40
BFS-0-G		Glucopon 225DK	0
BFS-20-G			20
BFS-40-G			40
BFS-0-C		CTAB	0
BF-20-C			20
BFS-40-C			40
BFS-0-S		Span 80	0
BFS-20-S			20
BFS-40-S			40

2.3.1.2 Compressive strength measurements

The compressive strength of the AAM pastes is measured using a hydraulic press (3R RP 40/400 N) according to the method recommended in the European EN 196–1 standard. This uses 40 x 40 x 160 mm³ parallelepipedal samples, obtained by pouring fresh AAM pastes into PTFE molds, and cured at 20°C under 100% relative humidity (RH) and atmospheric pressure. AAM pastes are made either without or with LVOL (Table 2). After demolding (at 48h after manufacturing), the samples are kept at (20°C; 100%RH; atmospheric pressure) until testing.

Each parallelepipedal sample is broken into two pieces under three points bending before compressive strength measurement. Compressive strength is measured after 7, 14, 28 and 90 days maturation. After bending test (and before compressive strength measurement), a picture of the fracture area is taken in order to visually assess the influence of the surfactant on the incorporation of the LVOL. Moreover, the fracture area is applied on an absorbent paper to observe any potential LVOL leakage.

2.3.1.3 2D SEM

Microscopic observations of samples free of LVOL are performed by Scanning Electron Microscopy (SEM) (FEI Inspect S50, high vacuum mode, acceleration voltage of 15 kV, current intensity of 50 nA, and working distance of 10 mm) on fractured samples dried by lyophilization.

Microscopic observations of samples containing LVOL, without drying, are performed by Environmental Scanning Electron Microscopy (ESEM) with an FEI Quanta 200 ESEM equipped with a Field Emission Gun. Sample observations are performed at 23°C with 300 Pa water vapor in the ESEM chamber at a high electron beam voltage of 8 kV. A dedicated Gaseous Secondary Electron Detector (GSED) is used to produce the images.

2.3.1.4 3D X Ray micro-Computed Tomography (3D X Ray micro-CT)

With this observation method, the samples do not require fracturing, drying or polishing, or even resin impregnation. Their edges are simply carefully cut to a 1 cm³ size using a diamond saw. Eight image series are acquired in less than 30 minutes each and processed by X ray micro-CT at the ISIS4D platform (Lille, France) [40]-[43]. Each image series corresponds to one different sample of AAM paste (either MK-based GEO or AA-BFS) incorporating 40 %vol LVOL, without or with a given surfactant (Table 3). For all of them, an identical voxel size of 5 microns is used.

The X Ray micro-CT apparatus is equipped with a nano focus tube operated at a 60 kV tension and 35 μA current, with a flat detector panel of 1874x1496 pixels². At each given angular position of the sample, the projection image is the average of four images in order to limit noise. After the reconstruction procedure (along the Z axis, with a filtered retro-projection algorithm [43], [44] and acquisition artifacts removal, an output volume is computed, composed of 1094-1146 images in a (X, Y) plane (at 1.24-2.76 x 10⁶ pixels² each) regularly spaced from one another by one voxel size (5 microns). Each sample corresponds to huge datasets of 1.42-3.16 x 10⁹ voxels³, linearly scaled into a 16-bit format.

Before quantitative analysis, all images are cropped in a (X, Y) plane so that sample boundaries and exterior are removed. The remaining image volumes, ranging between 6.10 and 23.0

mm³, are given in Table 3. For each given formulation, the biggest possible volumes are selected, to be able to consider them as representative of the emulsion morphology, with a number of segmented droplets of several thousands and more.

The images are filtered and segmented with the ImageJ software [45], in a minimal manner to avoid information loss. To this purpose, the grey level histogram of the whole image stack is spread over the whole 0-255 available range. Contrast is enhanced and a limited Gaussian Blur filter (0.8 pixel radius) is applied. Thresholding is then performed using the image stack histogram, by selecting the local minimum grey level value between darker pores and lighter solids. This provides realistic binary images (with pores in black and the solids in white).

Further, the droplet size distribution is quantified as in [28], with the Beat plugin [46] for 3D Continuous Particle Size Distributions (3D CPSD); this process simulates mercury intrusion and provides a particle size corresponding to the biggest sphere able to intrude a given volume.

Finally, the assessment of the connected (continuous) droplet volume is performed using the 3D dedicated tools of the Avizo Fire software (Thermo Scientific, USA). Although it is continuous, this droplet volume may correspond to *partially coalesced droplets*, where the connected droplets are still of spherical shape. In such instance, the image analysis is able to provide a 3D CPSD (see above).

Table 3: Main characteristics of the samples investigated by 3D X Ray micro-CT (voxel size = 5 microns)

Material type	BFS-40-0	BFS-40-G	BFS-40-C	BFS-40-S
Size of the raw image stack (pixels ³)	1201x1310 x1146	1662x1662 x1146	1296x1326 x1146	1144x1315 x1094
Size of the cropped image stack (pixels ³)	316x372x1146	516x759x342	422x348x940	418x392x344
Size of the cropped image stack (mm ³)	16.8	16.7	17.2	7.04
Manual threshold (grey level)	83	95	82	76
Observed relative volume of the OL emulsion (%) in a given object size range (microns)	28.1 (10-520 microns)	39.8 (10-570 microns)	32.7 (10-580 microns)	20.3 (10-570 microns)
Connected part of the OL emulsion (%)	15.9	39.8	32.7	19.8

Material type	GEO-40-0	GEO-40-G	GEO-40-C	GEO-40-B
Size of the raw image stack (pixels ³)	974x1280 x1146	1347x1089 x1146	1140x1091 x1146	1367x1367 x1146
Size of the cropped image stack (pixels ³)	302x476x730	500x279x1146	307x274x580	510x452x800
Size of the cropped image stack (mm ³)	13.1	20.0	6.10	23.0
Manual threshold (grey level)	95	154	72	119
Observed relative volume of the OL emulsion (%) in a given object size range (microns)	42.3 (10-500 microns)	23.7 (10-465 microns)	29.1 (10-456 microns)	12.9 (10-753 microns)
Connected part of the OL emulsion (%)	26.5	22.4	24.2	8.6

2.3.2. Chemical characterization

2.3.2.1 Micro-calorimetry

The reactivity of the AAM pastes is followed using a TAM AIR calorimeter (from TA instruments) under isothermal conditions at 25.0 ± 0.001 °C. The preparation of alkali-activated slurries is performed outside the calorimeter. About 2 g of each fresh mixture is cast in a dedicated glass container and introduced in the calorimeter. The heat flow is recorded versus time at a stable temperature of 25 °C. The first 30 min are omitted for the calculation of the cumulative heat due to extra undesirable heat resulting from the introduction of the container in the calorimetric chamber.

2.3.2.2 X Ray Diffraction (XRD)

XRD patterns of the AAM are obtained with a Bragg Brentano geometry on a PANalytical X'Pert PRO MPD apparatus (with a copper anode $\lambda K\alpha_1 = 1.54056$ Å generated at 45 mA and 40 kV and an X'celerator detector) on pastes ground by hand to a particle size below 100 µm size. The XRD patterns are collected in the 2θ range 5–70° with 0.017° steps, corresponding to 0.625 s measurement time per step.

2.3.2.3 Solid state Magic Angle Spinning Nuclear Magnetic Resonance (MAS NMR)

Solid structure characterizations adapted to amorphous solids are performed by ²⁷Al MAS NMR and by ²⁹Si MAS NMR. The tilt angles are $\pi/6$ and $\pi/2$ respectively. The ²⁷Al MAS spectra are recorded at a Larmor frequency of 208.5 MHz using a Bruker Avance II 800 MHz (18.8 T) spectrometer. The spectra are made up of 2048 free induction decays with a pulse length of

1 μs and a relaxation delay of 1 s to ensure quantitative reliability of the intensities observed for the ^{27}Al central transition for sites experiencing different quadrupole couplings. The samples are spun at 22 kHz in a 3.2 mm probe, and the chemical shifts are referred to $\text{Al}(\text{H}_2\text{O})_6^{3+}$. The ^{29}Si MAS spectra are recorded at a Larmor frequency of 79.5 MHz using a Bruker Avance 400 MHz (9.4T) spectrometer. The spectra are obtained with 256 scans (pulse length of 5 μs and optimized relaxation delay from 1 to 120 s according to the sample). The samples are spun at 5 kHz in a 7 mm probe, and the chemical shifts are referred to trimethylsilylsilane (TMS). Spectral decomposition is performed with the DMFit software [47].

3. Results and discussion

3.1. Physical characterization

3.1.1. Visual assessment of the incorporation of LVOL in hardened AAM

All the formulated samples harden in reasonable time (i.e., less than 48h), yielding solid AAM+LVOL composites.

At 28 days, fractured areas of prismatic samples (broken by three points bending) are placed on an adsorbent paper to assess visually the incorporation of LVOL into the AAM matrices. Figure 1 shows a photograph of the fractured areas with the binary image of the adsorbent paper surface, where the oil is in black and the dry paper in white.

The analysis is performed either for the GEO paste (top)[§] or the BFS paste (bottom). The pastes are without oil (top row), or with 20 or 40vol% oil (second and third row), and without surfactant (left column) or with the most efficient surfactant (right columns).

Without surfactant, whatever the AAM and the oil proportion, a significant amount of LVOL is visibly adsorbed on the paper. Following earlier statements, this proves that the use of surfactant is compulsory for adequate LVOL incorporation in AAM.

For both BFS pastes (20 or 40vol% LVOL) with surfactant, the yellow areas at the rim possibly indicate a carbonated area, or sulfur oxidation in the highly alkaline porewater [48]. This is attributed to the presence of surfactant, which has the ability to stabilize air bubbles inside the cement matrix. The material is therefore more permeable to ambient air and particularly to CO_2 [49], [50]. This may promote carbonation and potentially reduce compressive strength and long-term stability [51].

[§]A macroscopic void is observed in the GEO paste containing 40%vol. of LVOL + surfactant, due to air incorporation during mixing. For this paste, the addition of surfactant leads to a strong increase in viscosity. For further composite manufacturing, this will require vibrating the mold, to remove any such void.

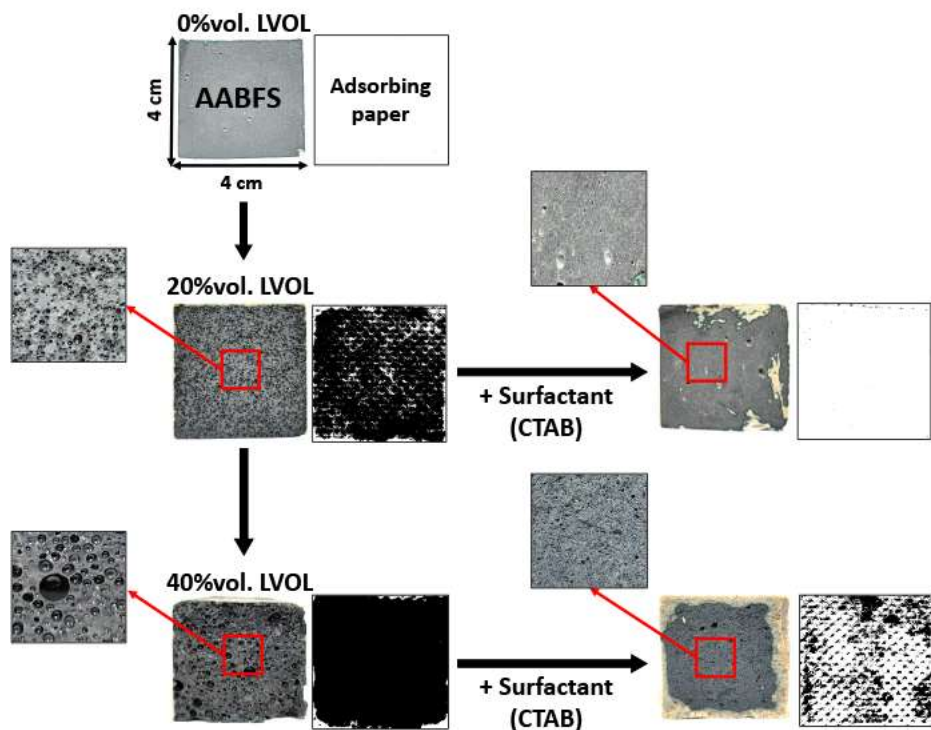
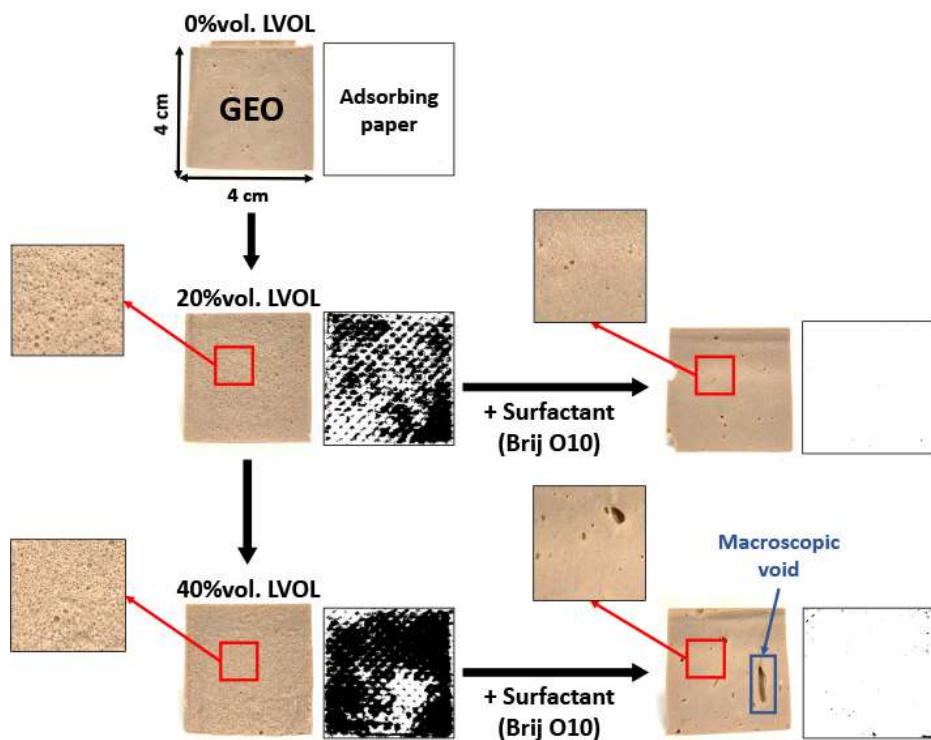


Figure 1: Photographs of fractured areas and impregnation patterns on adsorbent paper for (top) MK-based GEO at 0, 20 or 40%vol LVOL, without and with surfactant, and (bottom) AABFS at 0, 20 or 40%vol LVOL, with or without surfactant, all at 28 days. On the adsorbent paper surface, the oil is in black and the dry paper in white.

In the absence of surfactant, in both GEO and BFS-LVOL composites, the LVOL droplets are visible to the naked eye. This indicates that the droplets are bigger than 100 microns. After surfactant addition, LVOL droplets only remain clearly visible in the BFS paste with 40%vol LVOL. In all other cases, the adsorbent paper shows very limited sign of LVOL leakage.

3.1.2. Influence of LVOL and surfactants on the mechanical strength and pore structure of AAM

The compressive strength f_c of all the AAM-LVOL composites is measured at 7, 14, 28 and 90 days after curing under 100% RH at 20°C (see Figure S2 in Appendix). It is also plotted at 90 days as a function of oil proportion for GEO pastes (Figure 2 top) and BFS pastes (Figure 2 bottom), without or with surfactant.

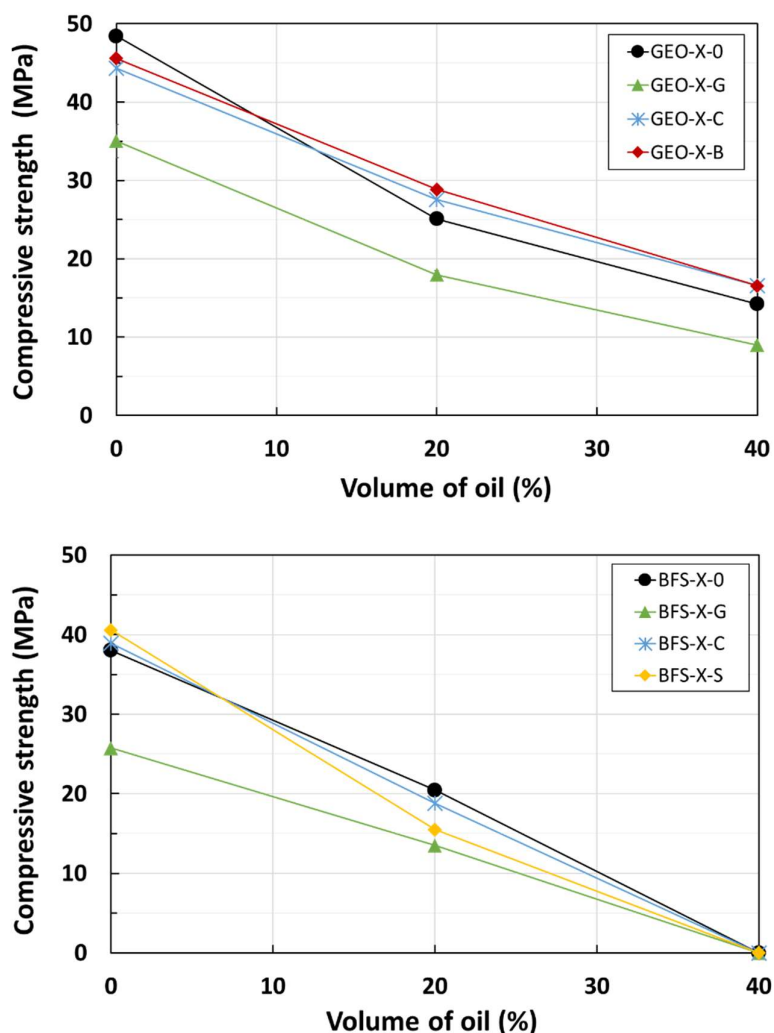


Figure 2: Average compressive strength f_c (in MPa) of AAM and AAM-LVOL mortar composites after 90 days curing under 100% relative humidity at 20°C, as a function of LVOL proportion: (top) for MK-based GEO pastes and (bottom) for AABFS pastes.

3.1.2.1 Effect of surfactant

Without LVOL, the presence of surfactant affects f_c in all GEO pastes (Figure 2 top), but in BFS pastes, f_c is only reduced in the paste prepared with Glucocon (Figure 2 bottom). However, the effect of CTAB or Brij O10 is limited for GEO pastes. The greatest decrease in f_c is obtained with Glucocon for both AAM matrices, with an average of 35.0 MPa +/- 2 for GEO-0-G compared to 48.4 MPa +/-0.3 for GEO-0-0 (i.e. 28% loss), and an average of 25.8 MPa +/- 2.8 for BFS-0-G compared to 38.0 MPa +/- 0.3 for BFS-0-0 (i.e. 32% loss). This is attributed to the presence of air-entrained bubbles. They are visible in the SEM images of fractured surfaces in Figure 3.

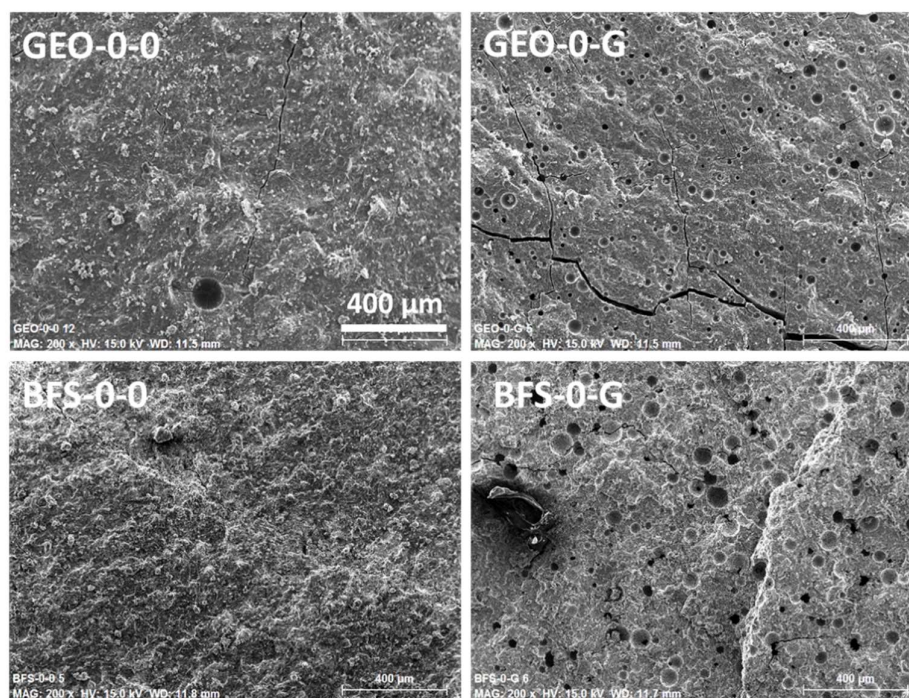


Figure 3: SEM micrographs of fracture surfaces of GEO-0-0, GEO-0-G, BFS-0-0 and BFS-0-G at x200 magnification, highlighting the presence of a significant number of entrained air bubbles (dark circles) when Glucocon (G) is added to each paste.

Complementary measurements (Fig. 4a and Table 4) also show a significant increase in porosity, and a decrease in apparent density, whatever the AAM and whatever the surfactant. All surfactants contribute to increase open porosity, i.e., they all add entrained air bubbles into the AAM cement. In good correlation with the decrease in f_c , for both AAM, the most air-entraining surfactant is Glucocon. This also affects the deviation of apparent density measurements, with values greater than 10% (and of almost 20% in some cases), whatever the LVOL % and whatever the AAM (Table 4). In earlier research [52], Glucocon has been described as an efficient foaming agent in alkaline conditions. Contrarily to Glucocon, the other surfactants all induce a significant increase in viscosity, as observed in [53]. This leads to

the stabilization of entrained air bubbles, and these are of smaller sizes than with Glucocon (see X Ray microCT results below).

For GEO pastes however, the nitrogen sorption-desorption isotherms are identical in presence of surfactant or not (see Figure S3 in the Appendix). This means that the pore structure is identical, particularly in terms of specific surface area (Figure 4b) and micropore amount (Figure 4c).

For BFS with CTAB or Span 80 (i.e., BFS-0-C and BFS-0-S), f_c is slightly greater than the reference case without surfactant, although BFS-0-C and BFS-0-S have an open porosity twice or four times greater than for BFS-0-0, respectively. This is attributed to denser BFS pastes with surfactants, as shows the smaller specific surface area in Figure 4b and the smaller micropore amount in Figure 4c. In presence of surfactant, the nitrogen sorption-desorption isotherms of BFS pastes are affected, with a generally smaller total adsorbed volume (see Figure S3 in the Appendix). At this stage, it is also possible that surfactant presence may accelerate the BFS setting reactions and strengthen the cement matrix. This is investigated in Sub-Section 3.2.1.

3.1.2.2 Effect of 20%vol LVOL

With 20%vol LVOL, for GEO pastes, two surfactants (CTAB and Brij O10) improve the compressive strength f_c compared to the reference without surfactant, whereas Glucocon reduces f_c (Figure 2, top). However, with all surfactants, the apparent density is smaller than if taking into account only the presence of LVOL (Table 4), meaning that air entrained bubbles are present together with the LVOL emulsion. The improvement in f_c with CTAB or Brij O10, compared to the case without surfactant, is attributed to smaller LVOL droplet sizes achieved by surfactant action. Small size droplets mean that during loading, the mechanical forces can more easily transfer through the cement matrix, with smaller obstacles and more straightforward routes. Droplet sizes are identified in a qualitative manner by 2D SEM (Figure 5, middle columns). For GEO pastes, the smallest droplet sizes are obtained with Brij O10. They are significantly smaller than 100 microns (which is the image scale), and on the order of a few microns. Comparatively, the GEO paste with 20%vol LVOL and no surfactant (GEO-20-0) presents droplet sizes visible to the naked eye (Figure 1, top) i.e., droplets bigger than 100 microns.

For BFS pastes at 20%vol LVOL, all surfactants reduce f_c compared to the BFS-20-0 paste without surfactant (Figure 2, bottom). The smallest decrease is obtained with CTAB (average $f_c = 18.8 \text{ MPa} \pm 0.7$ instead of $20.5 \text{ MPa} \pm 0.8$ for BFS-20-0). Apparent density is on the order of the theoretical value (accounting only for LVOL presence) except with Glucocon, due to entrained air bubbles (Table 4). Glucocon has the strongest detrimental effect, with an

average f_c of 13.5 MPa \pm 0.6 compared to the average of 20.5 MPa \pm 0.8 without oil (i.e. 48% decrease).

The presence of LVOL is most detrimental with BFS pastes, with an average f_c of 13.5-18.8 MPa (i.e., a 46-62% decrease) depending on the surfactant considered. As a matter of comparison, with GEO pastes, average f_c is between 18.0 and 28.9 MPa on average (i.e., 37-49% decrease), depending on the surfactant considered.

2D SEM (Figure 5 bottom, middle column) of BFS pastes with 20%vol LVOL show that the droplet sizes with CTAB or Glucocon are bigger than for GEO pastes at 20%vol LVOL. With Span 80, no clear spherical droplets are visible, meaning that the LVOL is not forming a typical and adequate emulsion, but rather elongated, sheared, LVOL droplets (more likely to induce stress concentrations and reduce mechanical strength).

3.1.2.3 Effect of 40%vol LVOL

At 40%vol LVOL, the GEO pastes display sufficient strength, with average values of 16.6 MPa \pm 0.11 with CTAB or Brij O10, which is slightly above the average of 14.2 MPa \pm 0.6 obtained without surfactant. Glucocon only provides an average strength of 9.0 MPa \pm 0.4. The industrial storage specifications for a minimal compressive strength of 8 MPa are respected [36]. 2D SEM (Figure 5 top, right column) shows that all surfactants in GEO pastes provide spherical droplets, the smallest being obtained with Brij O10, at sizes significantly below 100 microns.

For the BFS pastes added with 40%vol LVOL, either with or without surfactant, the measured strength is negligible after 90 days curing. According to the literature [54], no compressive strength evolution is expected for alkali activated BFS after 90 days. This means that the AABFS-LVOL composites incorporating 40%vol. LVOL will not have a measurable strength, even after 90 days. With 2D SEM (Figure 5 bottom, right column), it is visible that with CTAB and Span 80, the LVOL forms a highly coalesced, continuous, sub-volume, which is not favorable for mechanical loading. This may however be partly due to the partial ESEM vacuum. On the opposite, with Glucocon, spherical LVOL droplets are obtained (they are possibly partially coalesced), but it is insufficient for mechanical strength.

The quantification of LVOL droplet sizes is performed by X Ray micro-CT, without requiring any partial pressure as with the ESEM (see Sub-Section 3.1.3).

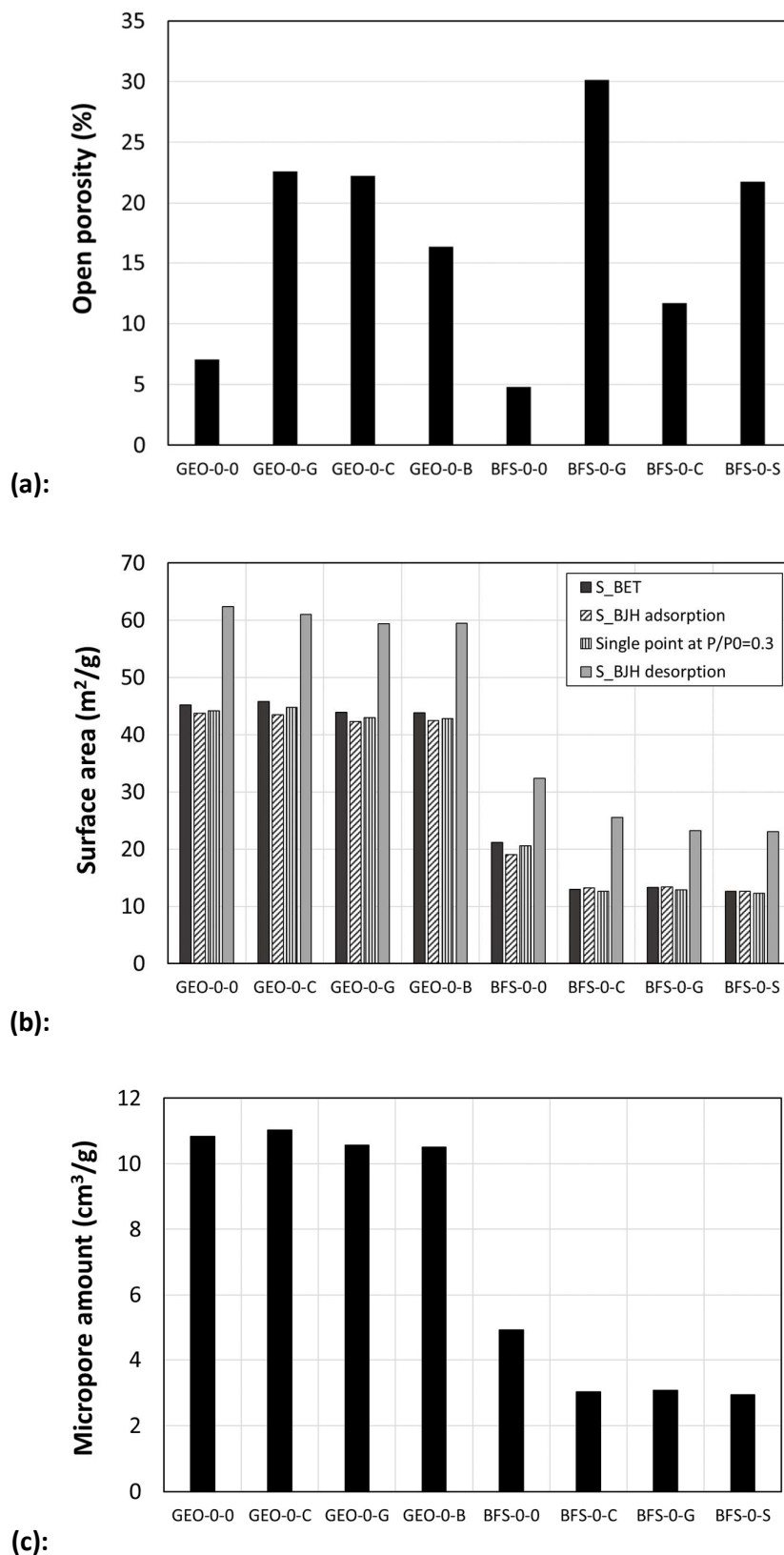


Figure 4: (a): Open porosity, (b): Specific surface and (c): micropore amounts of AAM pastes, without or with each individual surfactant, and without oil.

Table 4: Apparent density and open porosity characterizations at 90 days under endogenous conditions at 20°C.

Samples	Apparent density (g.cm ⁻³)	Density theoretical (g.cm ⁻³) ^a	Density deviation (%) ^b	Open porosity (%)
GEO-0-0	1.79	-	-	7.05
GEO-20-0	1.64	1.60	2.14	-
GEO-40-0	1.45	1.42	2.22	-
GEO-0-G	1.56	1.79	14.66	22.59
GEO-20-G	1.35	1.60	18.50	-
GEO-40-G	1.25	1.42	13.31	-
GEO-0-C	1.74	1.79	2.85	22.22
GEO-20-C	1.57	1.60	1.77	-
GEO-40-C	1.42	1.42	0.11	-
GEO-0-B	1.71	1.79	4.21	16.40
GEO-20-B	1.55	1.60	3.05	-
GEO-40-B	1.40	1.42	1.17	-
BFS-0-0	2.01	-	-	4.80
BFS-20-0	1.79	1.78	0.81	-
BFS-40-0	1.72	1.55	9.93	-
BFS-0-G	1.70	2.01	18.38	30.15
BFS-20-G	1.51	1.78	18.09	-
BFS-40-G	1.30	1.55	19.32	-
BFS-0-C	1.92	2.01	4.50	11.70
BFS-20-C	1.75	1.78	1.65	-
BFS-40-C	1.53	1.55	1.69	-
BFS-0-S	1.95	2.01	2.88	21.76
BFS-20-S	1.74	1.78	2.07	-
BFS-40-S	1.54	1.55	0.57	-

^aThe theoretical density ρ_{theo} is calculated based on the relation $\rho_{theo} = \rho_{oil} \cdot \%vol_{oil} + \rho_{AAM} \cdot (1 - \%vol_{oil})$ with ρ_{AAM} the density measured for pure alkali-activated materials (i.e. GEO-0-0 and BFS-0-0).

^bThe density deviation is calculated based on the following relation: $[(|\rho_{measured} - \rho_{theo}|) / \rho_{measured}] \times 100$

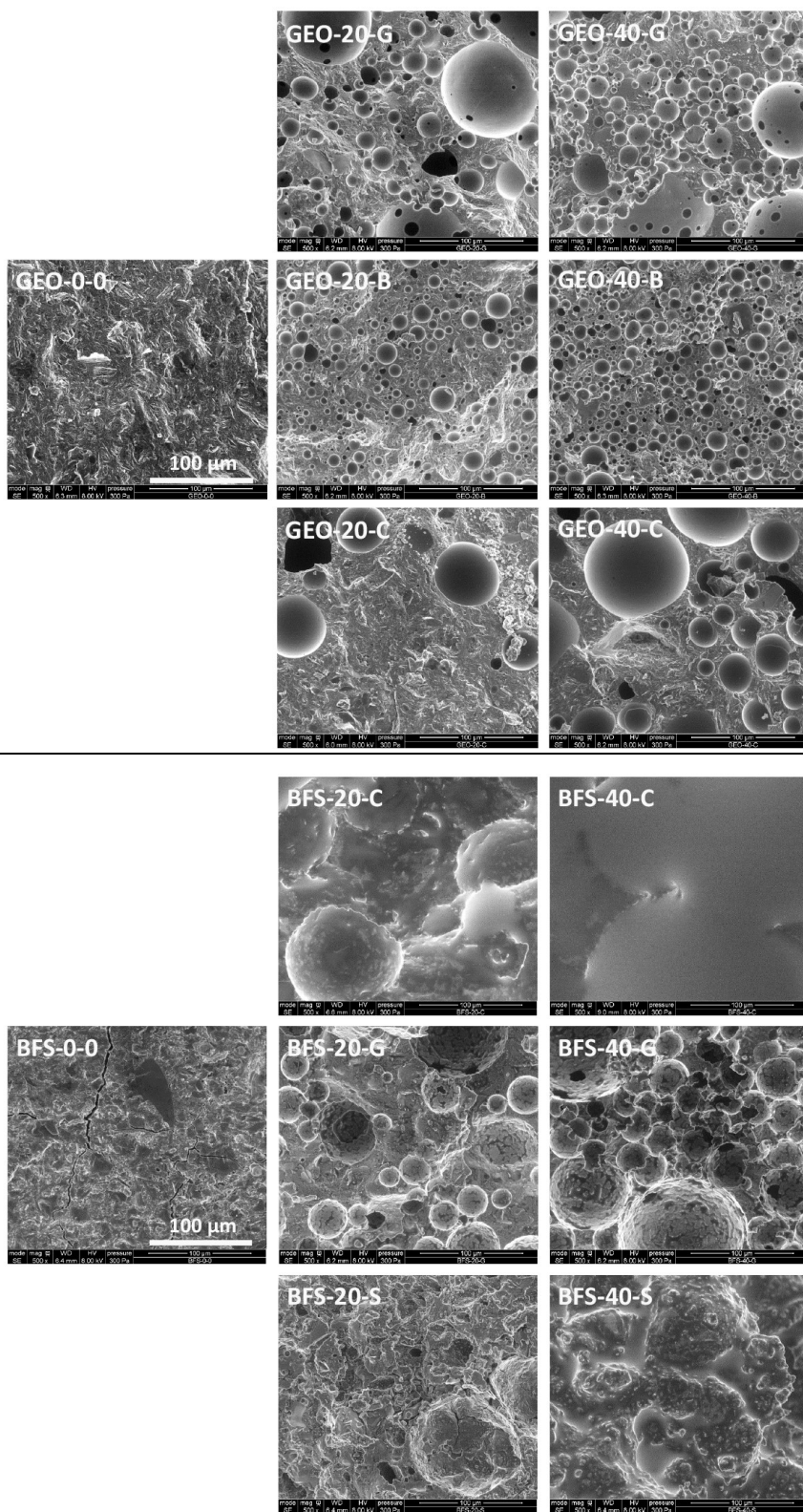


Figure 5: 2D Scanning Electron Microscopy (SEM) images of GEO (top) and BFS (bottom) pastes without oil or surfactant (left) or with 20%vol LVOL and surfactant (middle column), or with 40%vol LVOL and surfactant (right column). Surfactants are Glucopton, Brij O10 and CTAB for GEO pastes, CTAB, Glucopton and Span 80 for BFS pastes. All images are at the same magnification (x500) and scale.

3.1.3. Influence of surfactants on the emulsion in hardened AAM

This part is only performed on cement matrices added with 40%vol LVOL.

3.1.3.1 Qualitative emulsion droplet analysis

Figure 6 provides examples of raw X Ray micro-CT images of GEO pastes incorporating 40%vol LVOL (Figure 6a), or BFS pastes incorporating 40%vol LVOL (Figure 6b), either without or with each of the three surfactants tested per cement matrix. For comparison purposes, each image is at the same size and scale.

For both cement matrices, it is observed that in the absence of surfactant, the LVOL droplets are significantly bigger than with surfactant.

For GEO pastes, all surfactants decrease the LVOL droplet size. Air voids and LVOL droplets are hardly distinguished from one another (both are the darkest grey shade). The smallest LVOL droplets appear to be obtained with Brij O10.

For BFS pastes, only Glucopon and CTAB provide smaller LVOL droplets. Glucopon displays air entrained voids (they appear as bigger and darker spheres than the LVOL). CTAB provides coalesced droplets, but air and LVOL are not easily distinguished (meaning that air is not present in large proportions). Despite the presence of these two surfactants and of spherical droplets, the compressive strength of the BFS+LVOL composite is not measurable. With Span 80, the LVOL is present as coalesced and irregular, elongated and non-spherical droplets. This is clearly bound to limit the compressive strength of the BFS+LVOL composite, as observed in Figure 2. In all cases, the coalescence of the LVOL droplets appears a key factor to explain the non-measurable mechanical strength, whether it is partial (with spherical droplets still visible) or more complete (as with Span 80).

Finally, Figure 6 shows that the incorporation of LVOL is much better in GEO pastes than in BFS pastes, with much smaller and more homogeneous droplets, well encapsulated in a hard aluminosilicate network. The reasons are multiple: a) sodium hydroxide, more concentrated in BFS paste, increases the interfacial tension between the LVOL and the activating solutions [53]; this results in a higher energy required to produce smaller droplets, b) the viscosity ratio between the main and the dispersed phases plays a role in the formation of an emulsion [54], and the viscosity of the two AAM slurries are different, c) MK and BFS solid particles have different chemical and physical properties, and their concentration in the AAM is different. Therefore, the LVOL is initially less well emulsified in fresh BFS paste so that coalescence of oil droplets is favored before hardening.

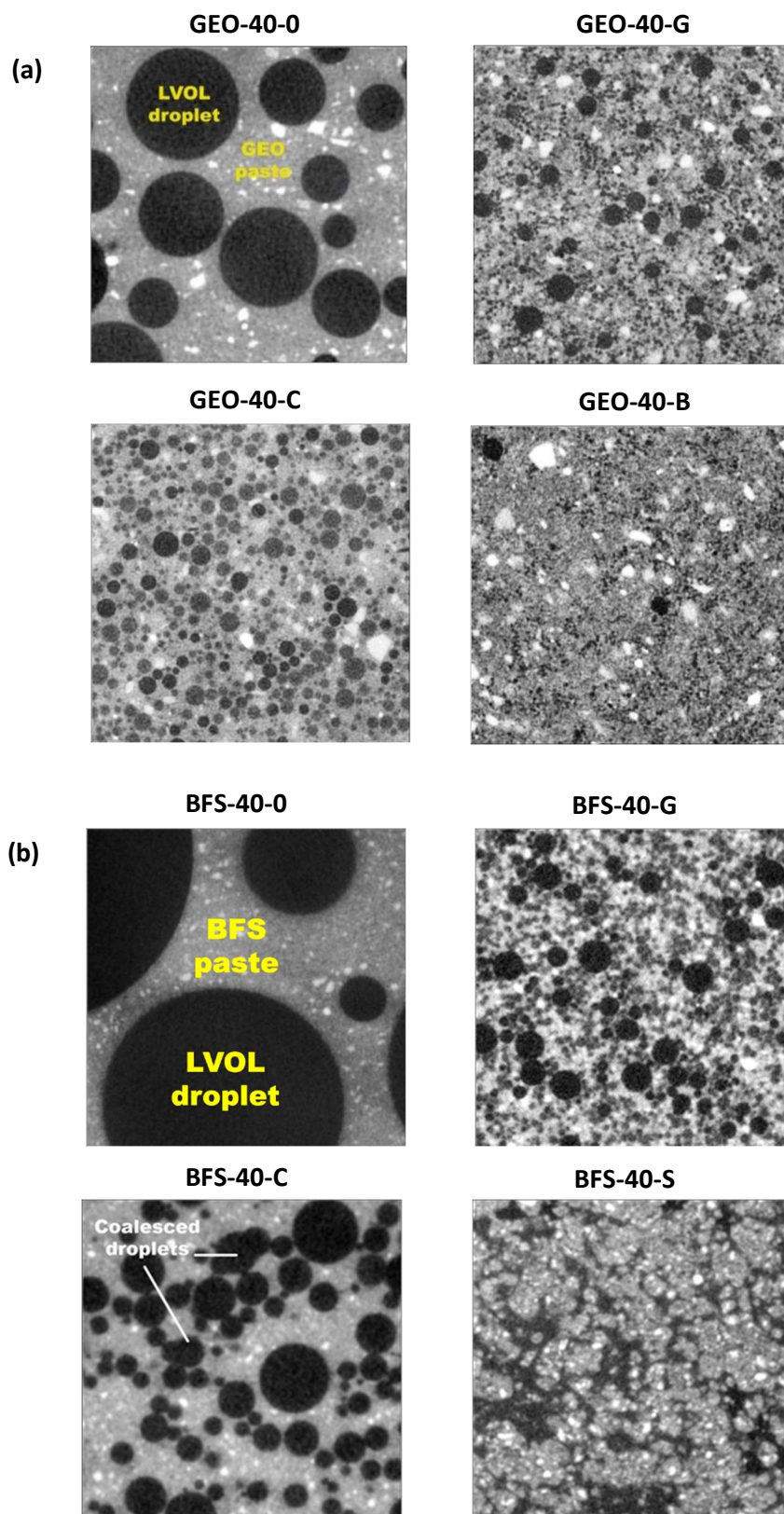


Figure 6: Examples of raw 2D images of X Ray micro-tomography for (a) GEO pastes and (b) AABFS pastes, all at 40%vol oil, without surfactant, or with Glucopon, or CTAB or BrijO10 (GEO only) or Span 80 (AABFS only). For comparison purposes, each image has an identical size of 1.37 mm x 1.37 mm.

3.1.3.2 3D representation and analysis of emulsion coalescence

After qualitative observations, binary thresholding of the LVOL emulsion is performed. This provides 3D representation of the emulsions and coalescence analysis (Figure 7).

The 3D representations allow to determine the 3D connectivity of LVOL in each cement matrix. Each 3D connected LVOL volume is represented in a single color. If spherical droplets are present, despite their connectivity, the coalescence is considered partial.

In GEO paste without surfactant (GEO-40-0), the LVOL emulsion is made of relatively unconnected (non-coalesced) spherical droplets, although their size is the biggest of the four cases. With Brij O10, distinct LVOL droplets are obtained, of a rather elongated shape, i.e., coalescence is partial and limited; the droplets are remarkably smaller than without surfactant. With CTAB, two main connected LVOL zones are observed; the spherical shape of the droplets is clearly visible, meaning that coalescence is only partial. With Glucocon, all the LVOL is connected, but again, distinct spherical droplets are present, meaning that coalescence is partial. For limiting connectivity and droplet size, and hence, best contributing to mechanical loading and strength, the best surfactant is therefore Brij O10; CTAB also provides interesting properties regarding the limitation of coalescence.

In BFS pastes, the LVOL emulsion is partly connected without surfactant, but the droplets are of large size (and the sample itself displays LVOL creaming at its surface, i.e., the LVOL is distributed in a highly heterogeneous manner). With CTAB or Glucocon, the LVOL emulsion is fully connected, but with spherical shaped droplets (partial coalescence). With Span 80, the main part of the LVOL volume is also connected, despite small isolated LVOL zones; the emulsion does not display spherical droplets, i.e., the emulsion is coalesced. In brief, with BFS paste, no surfactant is able to limit LVOL connectivity (Span 80 is not either able to limit coalescence), and hence, to provide minimal compressive strength to the cement matrix.

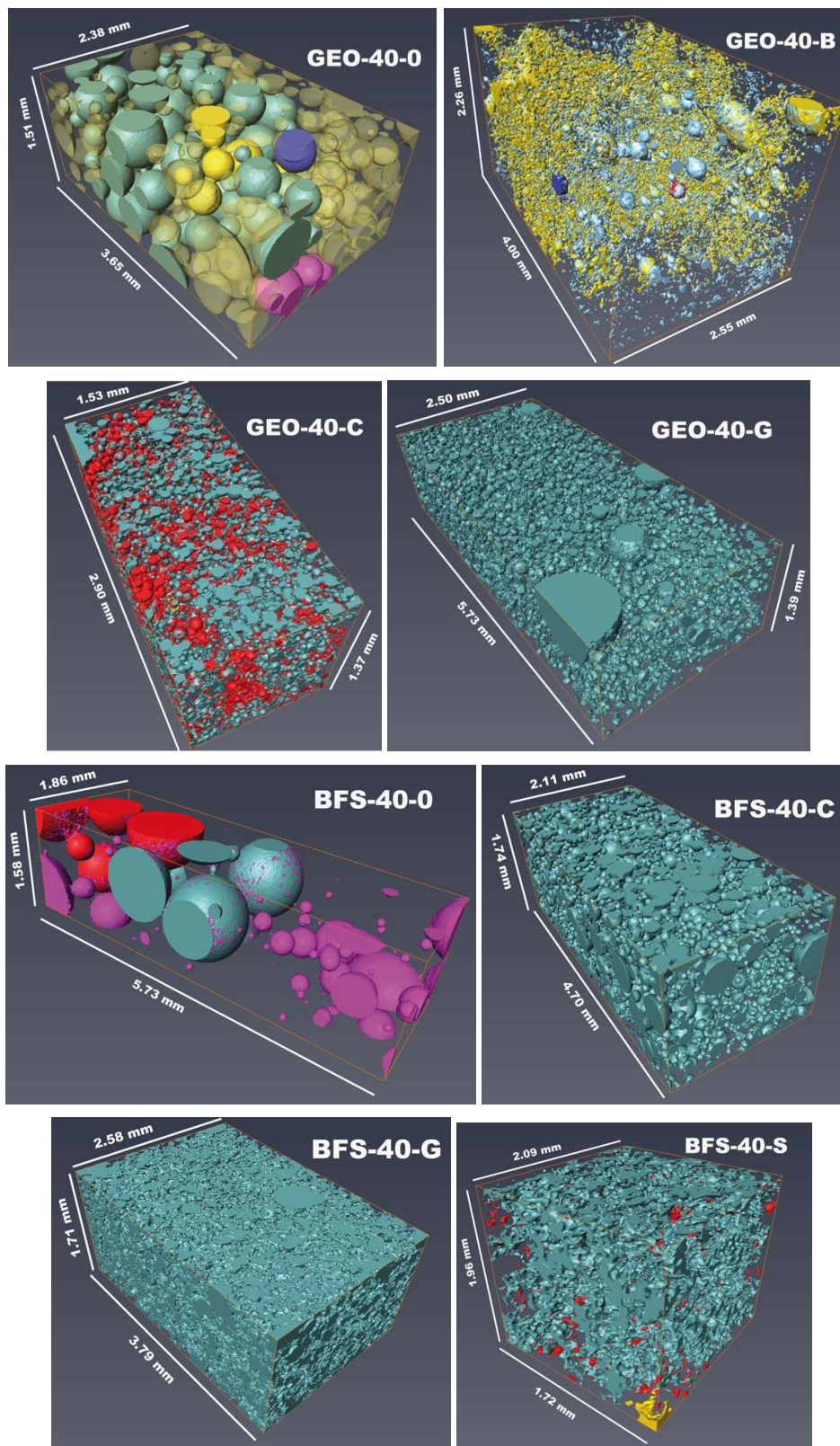


Figure 7: 3D X Ray micro-tomography image analysis - 3D representation of the emulsions after image thresholding: GEO-40-0, GEO-40-B, GEO-40-C, GEO-40-G and BFS-40-0, BFS-40-C, BFS-40-G, BFS-40-S. Each different color corresponds to a different connected object between at least two adjacent faces of the sample volume.

3.1.3.3 Quantitative analysis

Because coalescence is partial in all cases but one, the LVOL droplet size distributions are quantified in Figure 8. The analysis uses a modelling of the LVOL 3D volumes to derive the biggest spheres that can be included in all its different zones [46].

For GEO pastes, the droplet size at half the distribution (i.e., at 50%vol), labelled d_{50} , is of 410 microns without surfactant, but this value decreases below 100 microns with any of the three surfactants. As expected, the smallest droplet size distribution and the minimum d_{50} are obtained with Brij O10, with $d_{50} = 10$ microns. With Glucocon, $d_{50} = 30$ microns, and with CTAB, $d_{50} = 54$ microns.

For BFS pastes, d_{50} is of 1 mm +/-0.08 on average without surfactant. This value decreases down to 140 microns with CTAB and 50 microns with Glucocon (an identical value is predicted for Span 80). All surfactants provide significantly smaller droplet sizes, although none matches the efficiency of Brij O10 in GEO paste ($d_{50} = 10$ microns). CTAB and Glucocon are not as efficient in BFS as in GEO pastes.

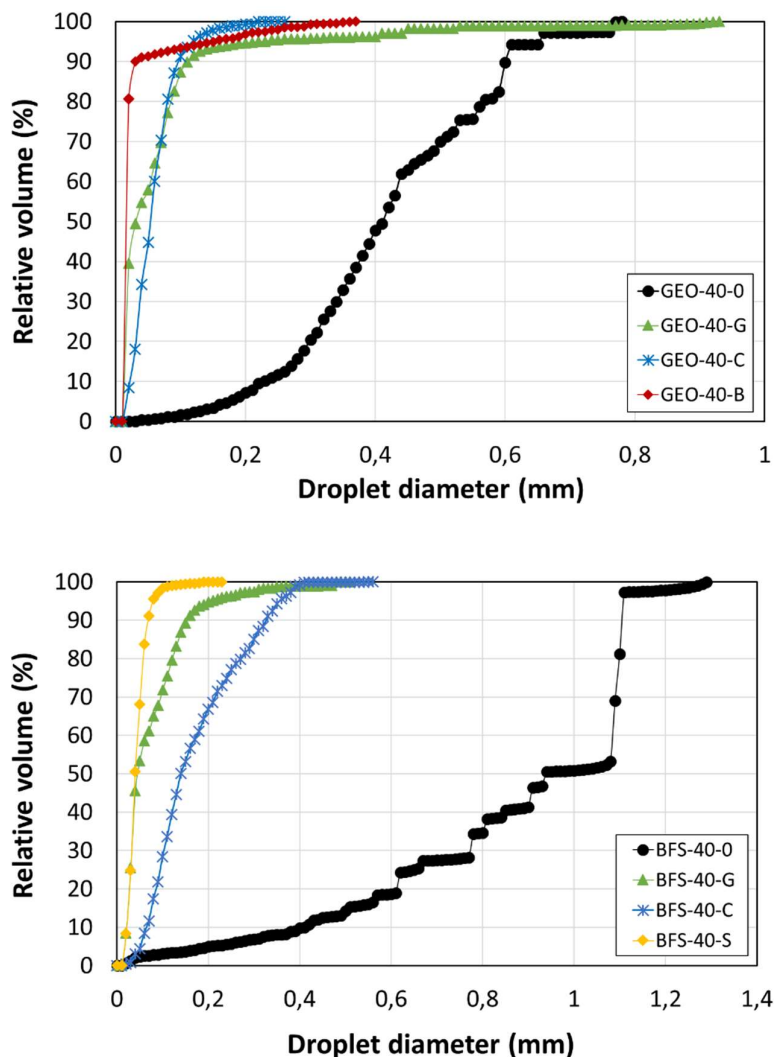


Figure 8: 3D X Ray micro-tomography image analysis - 3D Continuous droplet size distribution of (a) GEO pastes and (b) AABFS pastes, all at 40%vol oil, without surfactant, or with Glucocon (G), or CTAB (C) or BrijO10 (B, GEO only) or Span 80 (S, AABFS only).

3.1.4. Chemical characterization

3.1.4.1 Influence of LVOL or surfactants on the heat evolution of fresh AAM

The early-stage heat evolution results of AAM are shown in Figure 9. Time zero on the plots represents the time at which each freshly mixed paste sample is placed in the instrument, i.e. approximately 5 min after the start of mixing.

For both BFS and GEO, an exothermic peak appears immediately, which is attributed to the wetting and dissolution of solid particles [55]-[58]. As widely accepted, the formation and polymerization of gels are responsible for the noticeable second heat peaks following the initial dissolution period [55], [56].

For GEO slurries, the initial dissolution peak is followed by a short dormant period and another broad exothermic peak. After the initial dissolution process, the concentrations of dissolved ionic species reach a threshold for the outset of the following reactions. The dormant period, which is considered as an induction period for Ordinary Portland Cement (OPC) hydration, is supposed to be the time needed for concentration increase, mainly in silicate and aluminate species [55]. Both polymerization and condensation of N-A-S-(H) gels are exothermic and explain the main contribution to the second peak [58], [59].

A second exothermic peak is also observed in the heat evolution curve of NaOH-activated BFS. The extensive precipitation of reaction products, such as C-A-S-H, is reported to be responsible for this broad peak [23], [60]. The higher alkaline concentration in NaOH-activated BFS contributes to the early rising of the second narrow peak (1 h) in comparison with the second wide peak of GEO slurries (10 h) [55].

It is observed that the reactivity of both types of materials is not affected by the presence of LVOL. At the chosen concentration ($3 \cdot 10^{-3} \text{ mol.L}^{-1}$), surfactants do not have an impact on GEO condensation and polymerization. This observation is also true in the case of BFS, except for Glucocon, which delays the start of gel formation. To confirm this statement, a sample containing 10 times ($3 \cdot 10^{-2} \text{ mol.L}^{-1}$) the amount of Glucocon required for emulsion stabilization was formulated. As expected, the hydration of that sample is strongly delayed and only starts after 40 h, but the cumulative heat then seems to quickly catch up its original value. In fact, Glucocon has a carbohydrate polar head, which is known to delay hardening of OPC cements [61], [62] or of AABFS [63].

3.1.4.2 Influence of LVOL or surfactants on the crystalline reaction products of AAM

The XRD patterns of the AAM composites are collected and identified in order to characterize the influence of LVOL or surfactant on the reaction products (Figure 10).

The XRD patterns of NaOH-activated BFS samples reveal the presence of three phases: two poorly crystalline tobermorite-like phases, denoted C-S-H gel ($2\theta = 27^\circ$ and 50°) and C-A-S-H gel ($2\theta = 7^\circ$); and also a hydrotalcite-like phase ($2\theta = 10\text{-}12^\circ$) [37].

Except for the presence of quartz, all XRD patterns of the GEO samples show the typical amorphous structure of MK-based GEO, with a wide diffraction hump in the range $2\theta = 20^\circ$ to 35° . This broad hump is attributed to the amorphous N-A-S-(H) aluminosilicate gel, which is the primary binder phase present in GEO materials. Quartz, initially present in MK, holds a crystalline structure that makes its dissolution rate in alkaline media very low. Quartz is therefore non-reactive and remains after geopolymerization [64], [65].

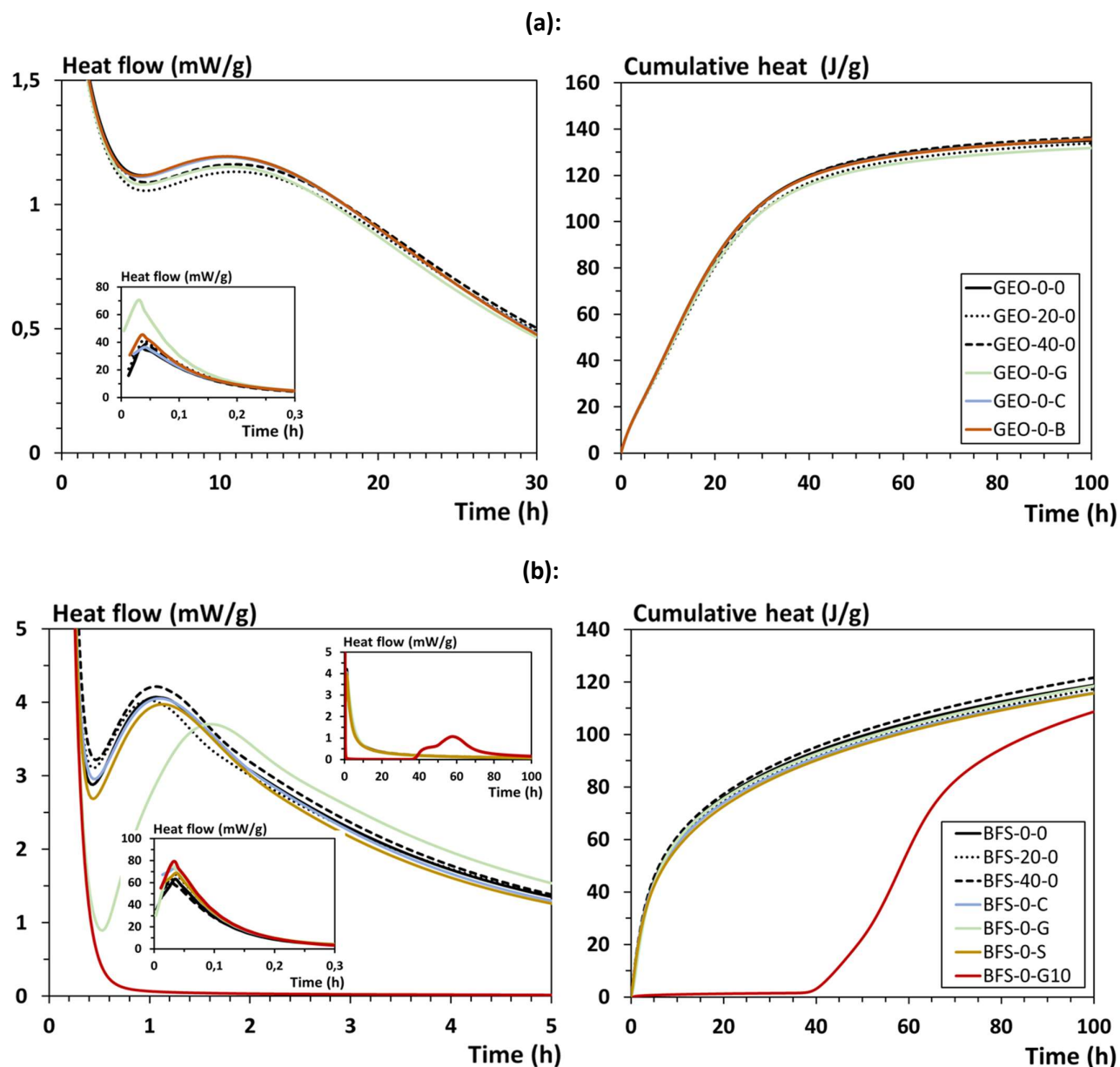


Figure 9: Influence of mineral oil and surfactants on the heat evolution of (a): MK-based GEO slurries; (b): AABFS slurries, with with 0, 20 or 40vol% LVOL and no surfactant, or no oil and each individual surfactant. BFS-0-G10 is for Glucopton used at 10 times the concentration of all other mixes, to confirm the effect of Glucopton on AABFS setting.

The characteristic humps of the poorly crystalline C-A-S-H gel and of the amorphous N-A-S-(H) gel might shift due to different polymerization degrees. This can be (for example) induced by changing the composition of the raw materials or the alkaline concentration in the activating solution. In this study, the XRD patterns of AAM are neither influenced by the addition of LVOL nor by the presence of surfactants. It is therefore concluded that these additives do not impact the formed reaction products. This is further discussed below, through more adequate NMR analyses for characterizing the C-A-S-H and N-A-S-(H) amorphous gels [66].

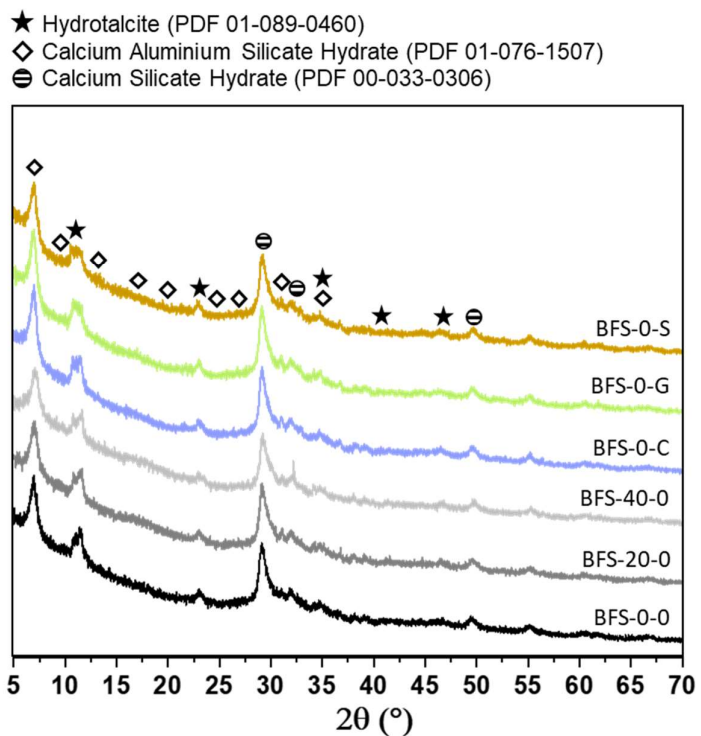
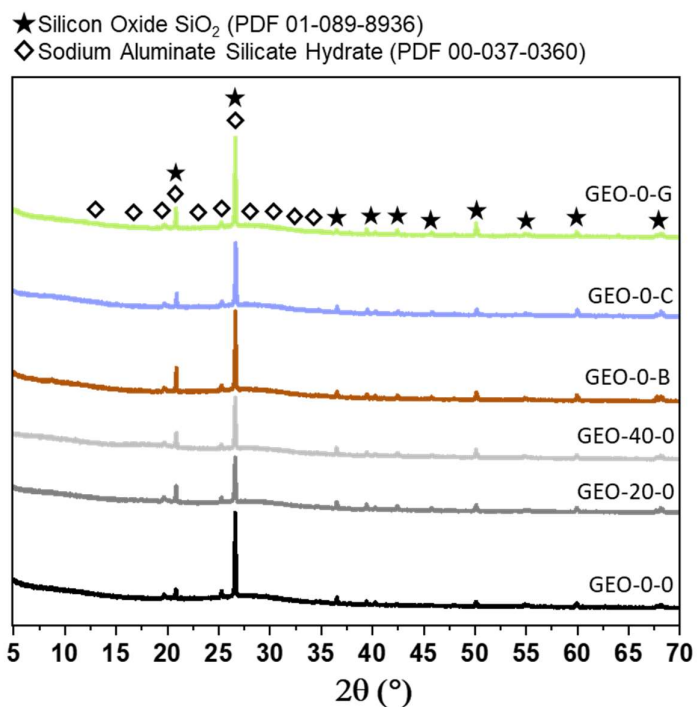


Figure 10: XRD patterns at 28 days of MK-based GEO (top) and AABFS (bottom), with no LVOL and each individual surfactant, or with 0, 20 or 40%vol LVOL and no surfactant.

3.1.4.3 Influence of LVOL or surfactants on the amorphous reaction products of AAM

The ^{29}Si and ^{27}Al MAS NMR spectra of AAM and AAM-LVOL composites are presented in Figure 11. The ^{29}Si and ^{27}Al MAS NMR spectra of the MK and BFS solid powders are given in Appendix (Figure S4). The deconvolution of ^{29}Si and ^{27}Al MAS NMR spectra are presented in Appendix (Figures S5 and S6). Deconvolution results are given in Table 5 for ^{29}Si and Table 6 for ^{27}Al .

The ^{29}Si MAS NMR spectra of MK-based GEO materials exhibit a typical broad resonance centered at -90 ppm (Figure 11a and Table 5), consistent with previous observations [67]. A low intensity level at -100 ppm suggests that the $\text{Q}^4(1\text{Al})$ component of the spectra present in the specimens is low, implying that the signal resulting from MK has been largely diminished (Figure S4). The low intensity in the region attributed to MK is probably a result of MK being almost completely consumed during synthesis. Moreover, the Si/Al molar ratio of MK-based GEO formulated in this study is 1.75; for such Si/Al, the ^{29}Si spectra are in accordance with [67], [68], with high amounts of $\text{Q}^4(2\text{Al})$ and $\text{Q}^4(3\text{Al})$ species and lower amounts of $\text{Q}^4(1\text{Al})$, $\text{Q}^4(0\text{Al})$ and $\text{Q}^4(4\text{Al})$.

The ^{27}Al MAS NMR spectra of MK-based GEO exhibit two resonances, dominated by a peak centered at 60 ppm (Figure 11b and Table 6), indicating tetrahedrally coordinated aluminum [69]. The dominance of Al(IV) has been widely reported and confirms that geopolymerization converts Al(V) and Al(VI) present in MK into Al(IV). Although the ^{27}Al MAS NMR spectra are dominated by the resonance associated with Al(IV), a small resonance at about 5 ppm (Table 6) indicates the presence of remaining Al(VI). It is well known that Al(VI) is more stable than Al(V) and will be the last geometric form of aluminum to be completely consumed during reaction [70]. It is also in accordance with the suggestion made after observation of ^{29}Si spectra, that some unreacted MK is still present.

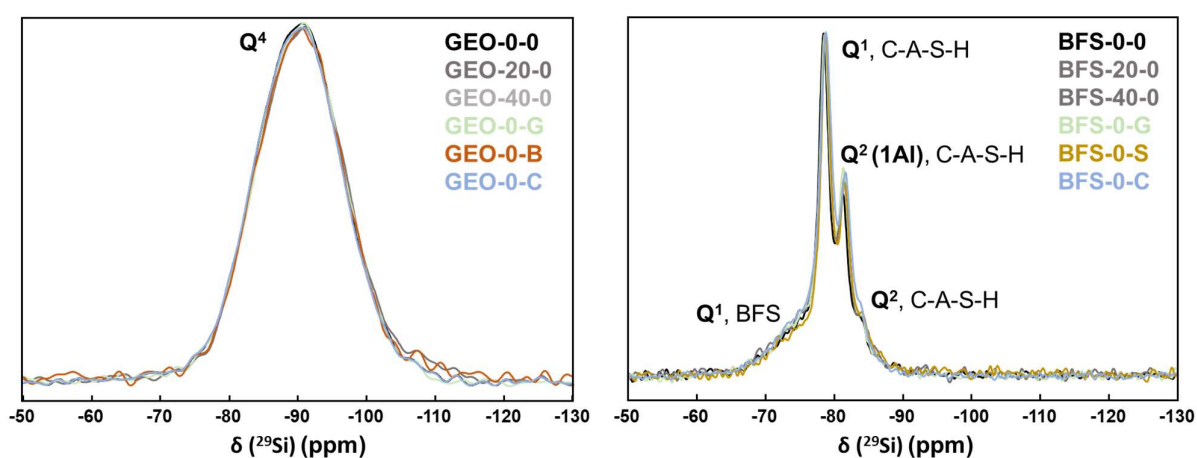
The ^{29}Si MAS NMR spectra of BFS pastes are dominated by two main peaks centered at -79 and -81 ppm (Figure 11a and Table 5). These are attributed to silicate groups in the C-A-S-H tobermorite-like structure with different degrees of connectivity, Q^1 and $\text{Q}^2(1\text{Al})$ respectively [71]-[74]. Q^1 species represent in general the end chain of the tobermorite structure and Q^2 species are chain mid-members. Two other peaks with weaker intensities, centered at -74 and -84 ppm are observed, and attributed to Q^1 silicates in unreacted BFS and $\text{Q}^2(0\text{Al})$ in C-A-S-H, respectively. The weak peak corresponding to silicates in BFS indicates the good hydration progress. It has to be noted that the amount of $\text{Q}^2(0\text{Al})$ is low and no Q^3 are detected, which is due to the sodium hydroxide activation, which does not allow formation of these silicates. The amount of Q^1 in C-A-S-H is quite high, which is probably due to the high concentration of sodium hydroxide in the activating solution [75].

The ^{27}Al MAS NMR spectra of BFS pastes are dominated by two main peaks centered at 10 and 72 ppm (Figure 11b and Table 6). The peak at 72 ppm corresponds to 4-coordinated Al atoms

(tetrahedral) in C-A-S-H gels. The peak at 10 ppm corresponds to 6-coordinated Al atoms (octahedral), most probably located in the hydrotalcite phase observed with XRD (Figure 9) [76]. There is also a shoulder between 50 and 70 ppm, which is attributed to 4-coordinated and 5-coordinated Al atoms initially present in BFS, in accordance with ^{29}Si spectra.

The key point here lies in the fact that all the ^{29}Si and ^{27}Al MAS NMR spectra are almost perfectly stackable. This means that neither the LVOL nor the surfactants have an impact on the reaction products that are formed in the AAM composites. Mechanical properties variations observed in the previous section are therefore only attributed to the increase in porosity (LVOL and air), i.e. exclusively to physical effects.

(a):



(b):

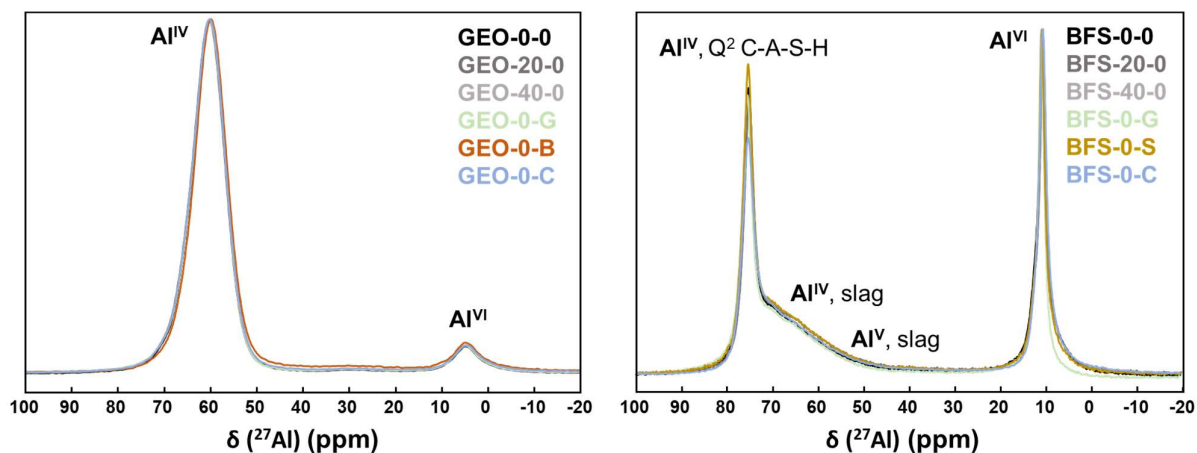


Figure 11: Influence of LVOL and surfactants on (a): ^{29}Si MAS NMR spectra and (b): ^{27}Al MAS NMR spectra, for MK-based GEO (left) and AABFS (right), with 0, 20 or 40%vol LVOL or no LVOL and each individual surfactant, at 28 days.

Table 5: Deconvolution results for ^{29}Si MAS NMR spectra of MK-based GEO and AABFS.

MK-based GEO			AABFS		
δ (ppm)	Connectivity	%	δ (ppm)	Connectivity	%
-101.7	Q ⁴ (0Al)	5.7	-73.9	Q ¹ BFS	23
-96.9	Q ⁴ (1Al)	13.2	-78.3	Q ¹	46.7
-91.8	Q ⁴ (2Al)	37.6	-81.1	Q ² (1Al)	23.3
-86.6	Q ⁴ (3Al)	28.8	-83.9	Q ²	7
-81.5	Q ⁴ (4Al)	13			
-75	MK	1.6			

Table 6: Deconvolution results for ^{27}Al MAS NMR spectra of MK-based GEO and AABFS.

MK-based GEO			AABFS		
δ (ppm)	Connectivity	%	δ (ppm)	Connectivity	%
68.1	Al ^{IV}	8.8	75.3	Al ^{IV}	35.1
60.1	Al ^{IV}	83.0	70.2	Al ^{IV} BFS	8.0
50.2	Al ^{IV}	1.6	63.1	Al ^{IV} BFS	17.7
4.7	Al ^{VI}	6.6	49.3	A ^V BFS	2.8
			12.5	Al ^{VI}	6.9
			10.6	Al ^{VI}	22.6
			7.9	Al ^{VI}	6.9

4. Conclusions

In order to determine the optimal conditions for low viscosity organic liquid (LVOL) in alkali activated matrices (AAM), a pure mineral oil was successfully immobilized in MK-based GEO and alkali-activated BFS (AABFS) in a proportion up to 40%vol. The main conclusions and guidelines of the study are as follows:

- The preparation of AAM-LVOL composite materials containing up to 40%vol of LVOL is possible with both GEO and AABFS pastes. The advantage of using surfactants allows (1) stabilizing fine and homogenous LVOL droplets, and (2) avoiding LVOL leaking out of the materials.
- The AAM-LVOL composites immobilizing 20%vol LVOL all have a measurable compressive strength, of 25 MPa on average for GEO-LVOL composites and 20 MPa on average for AABFS-LVOL composites. The GEO-LVOL composites containing 40%vol LVOL have an average compressive strength of 15 MPa, while the AABFS-LVOL composites containing 40%vol of LVOL do not have a measurable compressive strength, even those containing surfactants.
- The addition of surfactants, with the aim of improving LVOL incorporation, leads to the side effect of increasing the porosity of AAM. For GEO pastes, this negatively impacts compressive strength f_c ; for AABFS pastes, f_c is only reduced with Glucocon, otherwise the presence of CTAB or Span 80 densifies the reaction products, so that f_c is slightly improved. In both types of AAM, Glucocon is the surfactant incorporating and stabilizing the highest amount of air bubbles.
- For GEO pastes at 20%vol LVOL, f_c is increased thanks to CTAB or Brij O10 (compared to the paste without surfactant). This is attributed to smaller LVOL droplets. At 40%vol., the connectivity of the LVOL emulsion is detrimental to mechanical strength; this is particularly observed for AABFS pastes.
- There is no influence of the LVOL on the setting time and strength development of AAM materials. Moreover, at the low concentration of that study ($3 \cdot 10^{-3} \text{ mol} \cdot \text{L}^{-1}$), surfactants do not influence the setting time and strength development of AAM materials, except for Glucocon, which slightly retards AABFS hydration, and more so at higher concentrations.
- The main reaction products of AAM (C-A-S-H in AABFS and N-A-S-(H) in GEO) are not impacted by the addition of LVOL or surfactants. The impact on mechanical properties is therefore only attributed to the increase in porosity (LVOL and air).

With the chosen AAM formulations, it is concluded that the use of MK-based GEO is more favorable for the immobilization of high amounts (40%vol) LVOL than AABFS. However, for 20%vol incorporation, both MK-based GEO and AABFS pastes are suitable with a surfactant (CTAB for both, or Brij O10 for GEO). The type and concentration of surfactant must be carefully chosen, not only for the purpose of stabilizing the LVOL emulsion but also to avoid side effects, such as an excessive increase in porosity, influencing mechanical and long-term properties of the AAM-LVOL composites.

Acknowledgments

This project has received technical support from:

- Renaud Podor working at the Institut de Chimie Séparative de Marcoule, UMR 5257 CEA-CNRS-UM2-ENSCM, Site de Marcoule, BP17171, F-30207 Bagnols sur Cèze Cedex, France for Environmental Scanning Electron Microscopy observations.
- Bertrand Revel working at the University of Lille for solid-state NMR measurements.

This research did not receive any specific grant from funding agencies in the public, commercial, or not-for-profit sectors.

Appendix

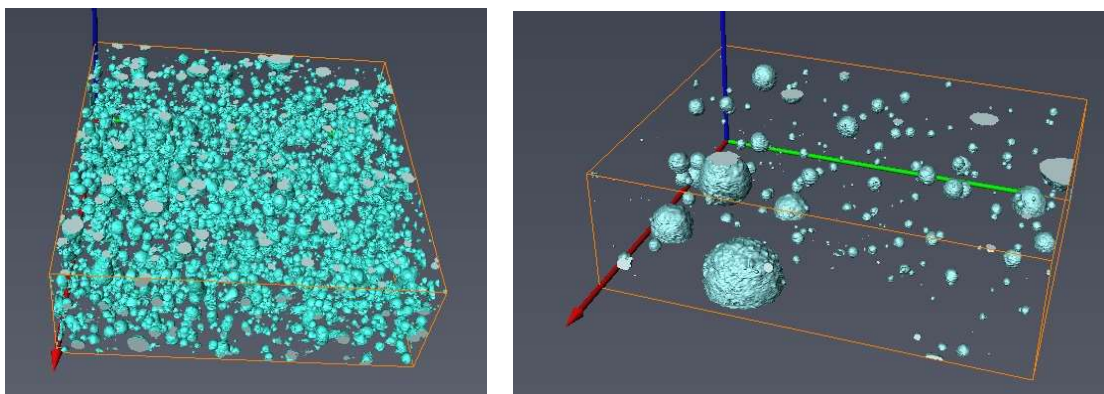


Figure S1: Results from preliminary LVOL incorporation study - 3D representation of the oil emulsion (20%vol) encapsulated inside an alkali activated BFS material, obtained by (left) 10%wt sodium hydroxide activation (voxel size = 1 micron, sample size $0.85 \times 0.87 \times 0.3 \text{ mm}^3$) and (right) 10%wt sodium silicate activation (voxel size = 1 micron, sample size $0.75 \times 0.99 \times 0.3 \text{ mm}^3$). The oil is an industrial mineral oil Mobil DTE 26 (mainly composed of linear alkanes, with a low viscosity of 0.045 Pa.s). The water-to-BFS ratio is of 0.40.

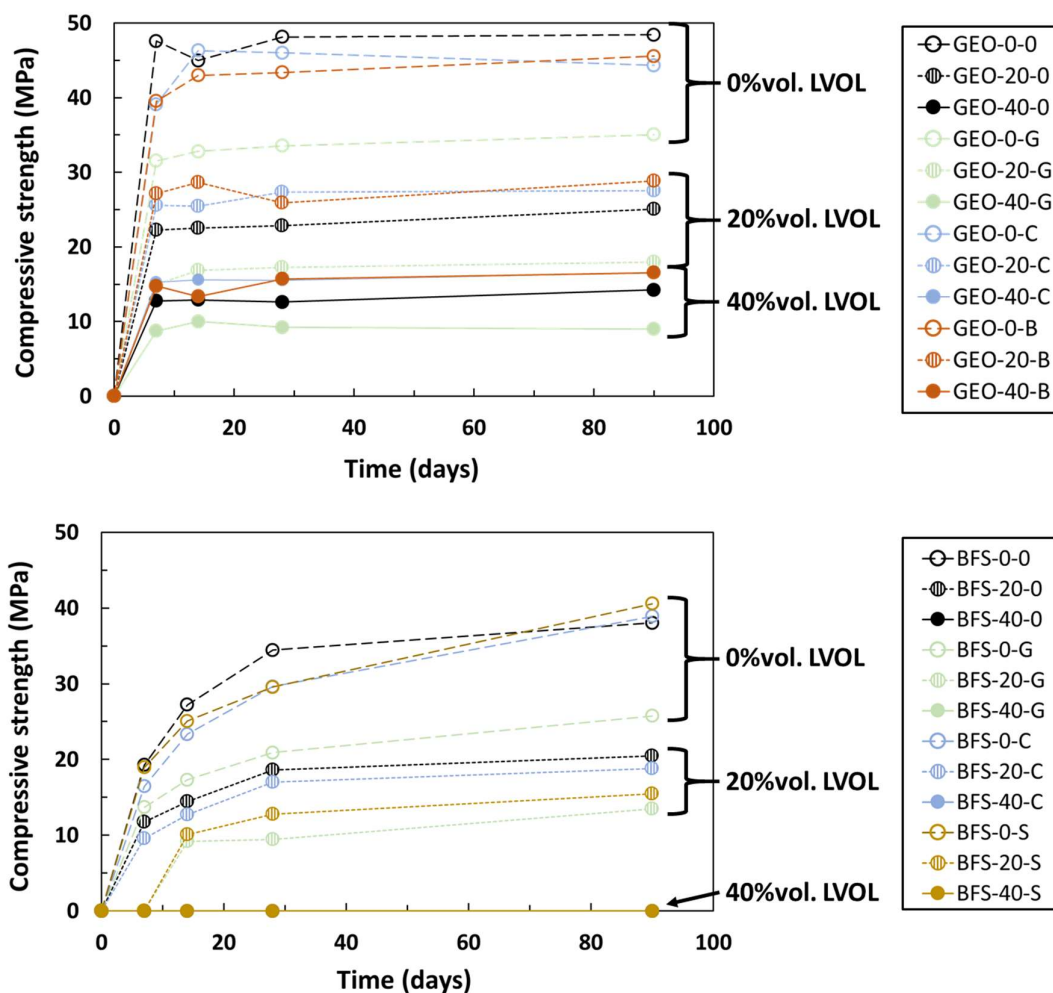


Figure S2: Compressive strength f_c (MPa) of AAM and AAM-LVOL composites at 7, 14, 28 and 90 days under 100% relative humidity at 20°C: (top) is for GEO pastes and (bottom) is for AABFS pastes.

The GEO-LVOL composites rapidly develop their compressive strength with a nearly constant compressive strength after 7 days (Figure S2, top). This is typical for GEO materials and in accordance with isothermal calorimetry (Figure 9a). The latter shows that after 60 hours, the heat flow is almost zero and the cumulative heat constant [77], [78].

In contrast with the GEO pastes, BFS-LVOL composites display a more progressive development of their compressive strength (Figure S2, down). This is also typical for this kind of material and in accordance with isothermal calorimetry (Figure 9b). The latter shows that after 100 hours analysis, the heat flow is still non-zero and the cumulative heat still increases [79], [80].

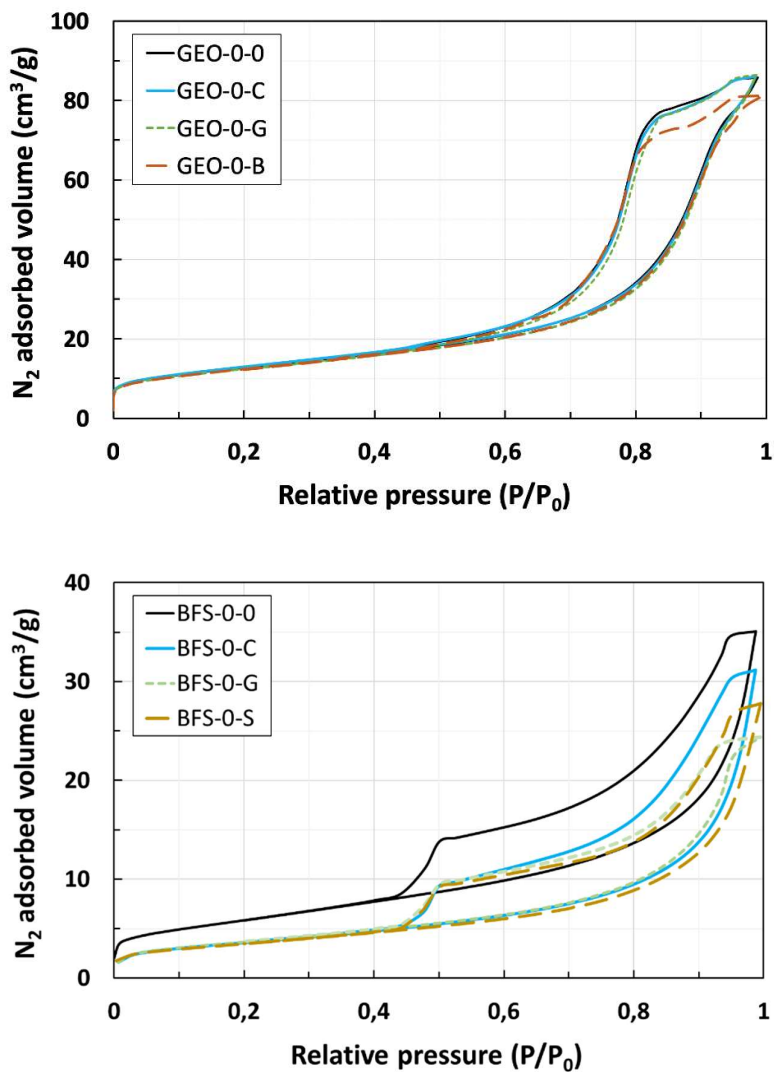


Figure S3: Nitrogen sorption-desorption isotherms of the AAM pastes, either MK-based ones (top) or BFS-based ones (bottom).

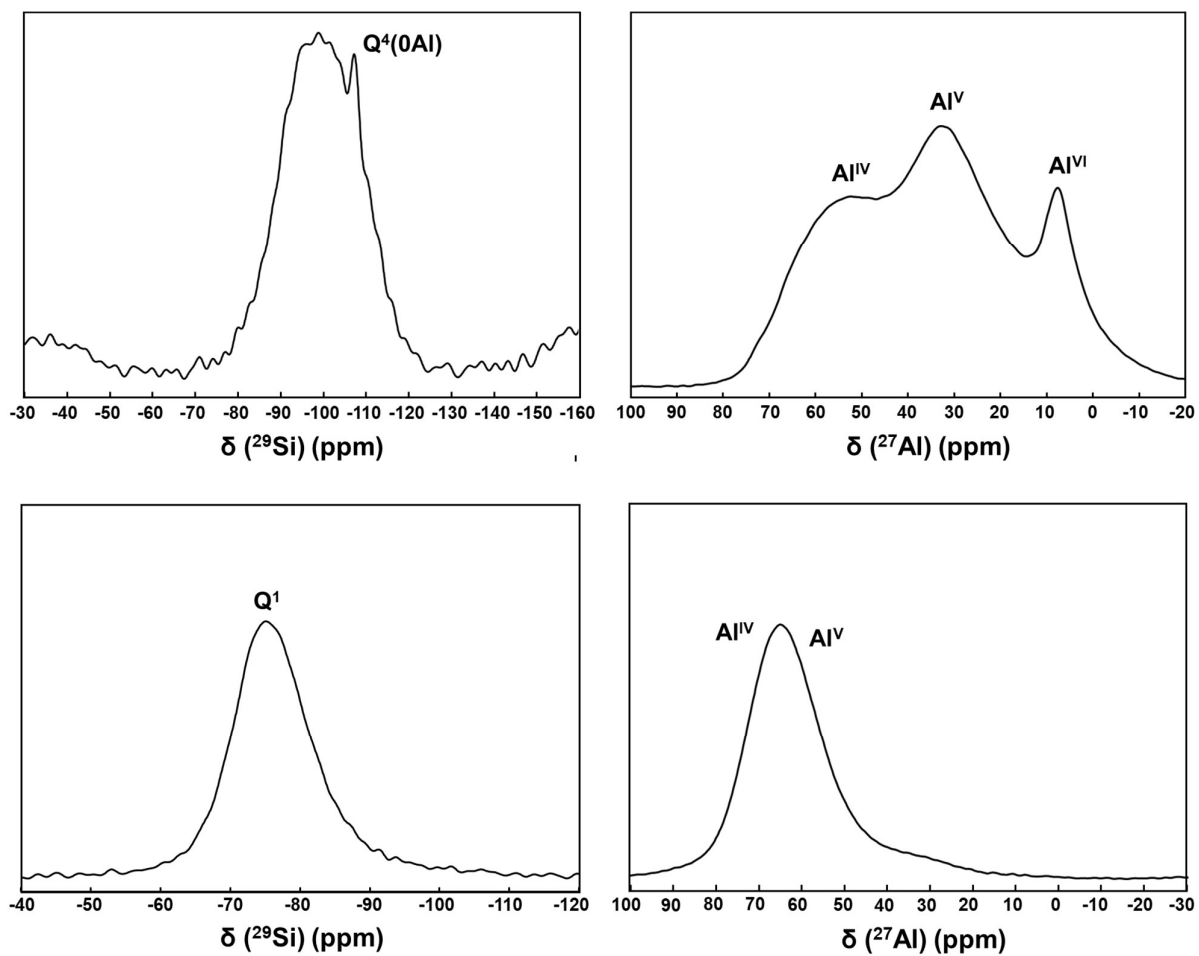


Figure S4: ^{29}Si (left) and ^{27}Al (right) MAS NMR spectra of (top): metakaolin powder and (bottom): BFS powder.

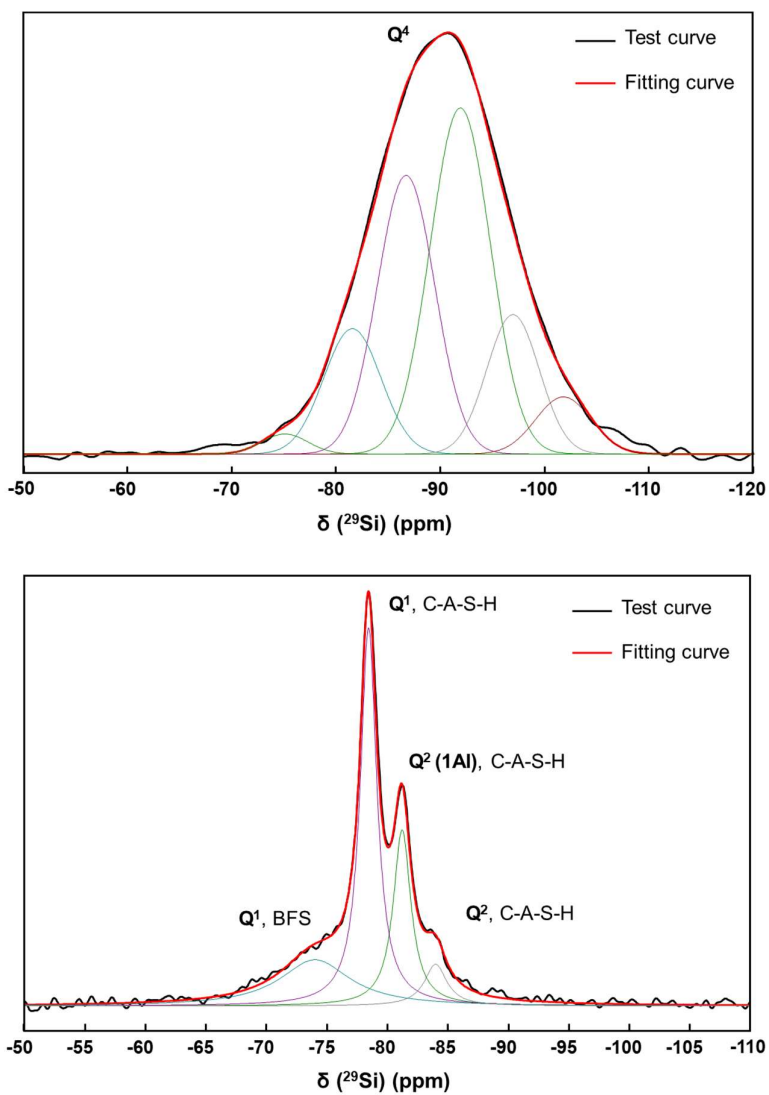


Figure S5: Deconvolution results for ^{29}Si MAS NMR spectra of (top) GEO samples and (bottom) AABFS samples.

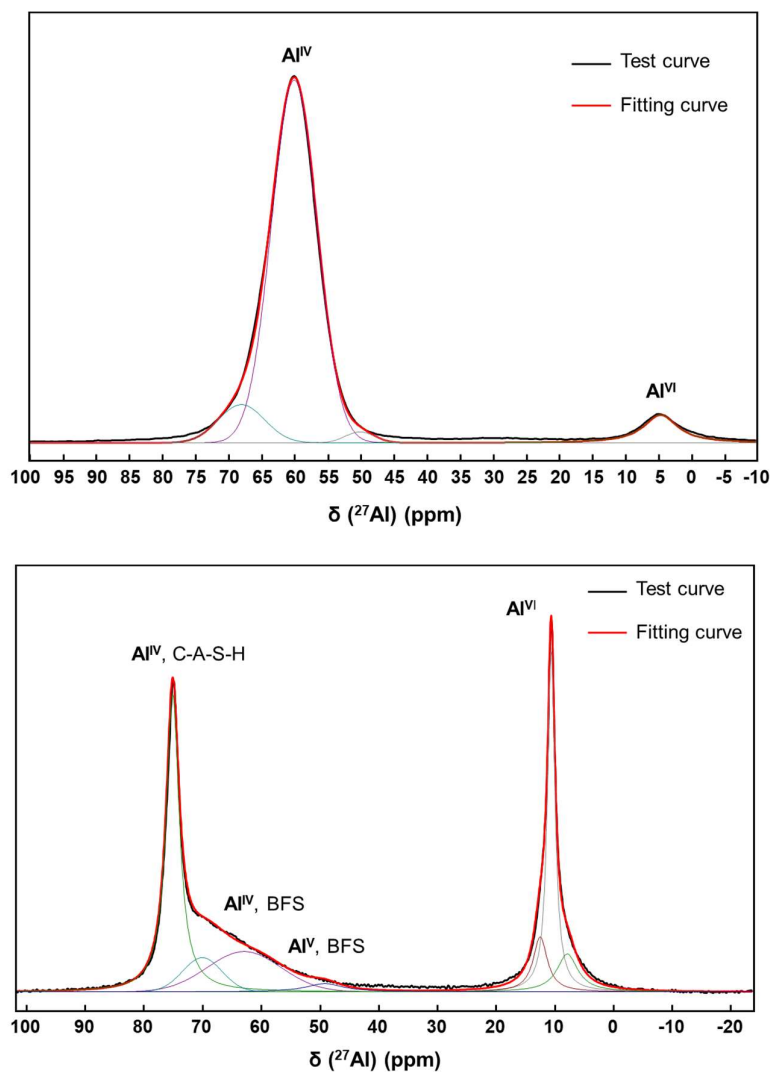


Figure S6: Deconvolution results for ^{27}Al MAS NMR spectra of (top) GEO samples and (bottom) AABFS samples.

References

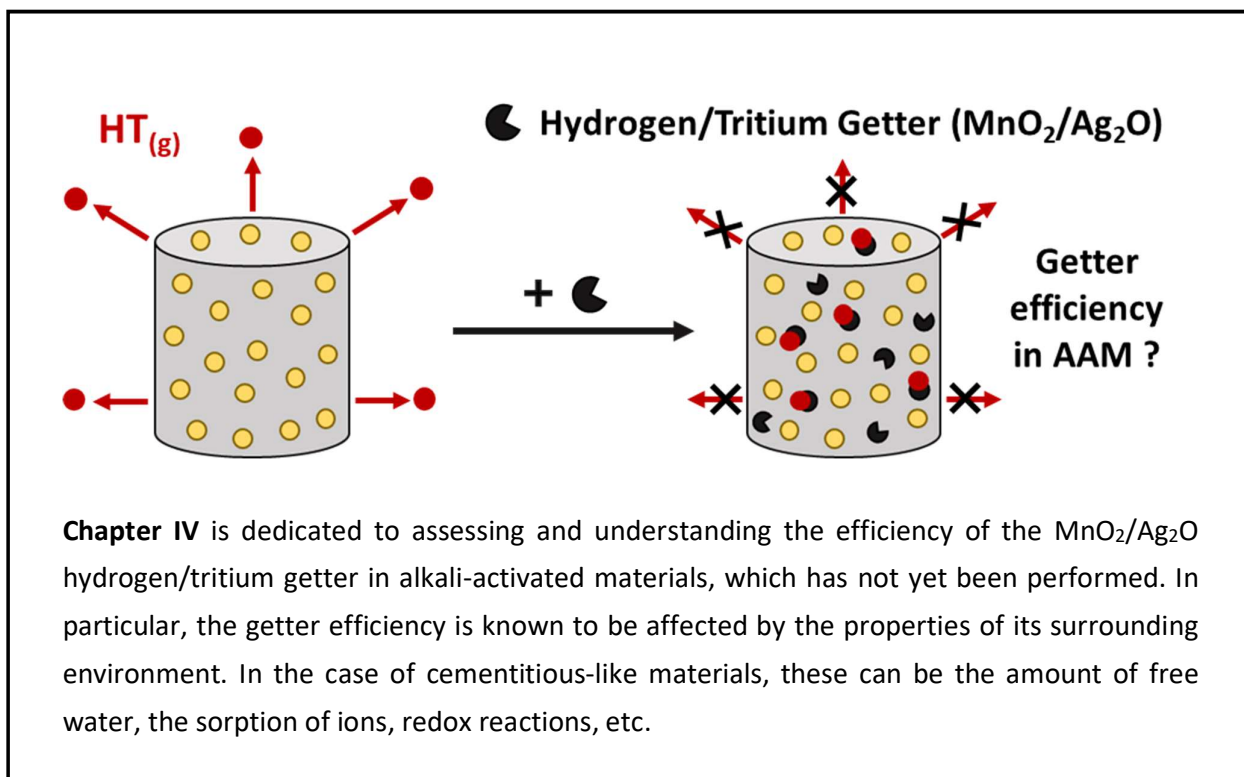
- [1] V. Cantarel, F. Nouaille, A. Rooses, D. Lambertin, A. Poulesquen, and F. Frizon, 'Solidification/stabilisation of liquid oil waste in metakaolin-based geopolymer', *J. Nucl. Mater.*, 2015, doi: 10.1016/j.jnucmat.2015.04.036.
- [2] V. Cantarel, D. Lambertin, A. Poulesquen, F. Leroux, G. Renaudin, and F. Frizon, 'Geopolymer assembly by emulsion templating: Emulsion stability and hardening mechanisms', *Ceram. Int.*, 2018, doi: 10.1016/j.ceramint.2018.03.079.
- [3] V. Cuccia, C. B. Freire, and A. C. Q. Ladeira, 'Radwaste oil immobilization in geopolymer after non-destructive treatment', *Prog. Nucl. Energy*, 2020, doi: 10.1016/j.pnucene.2020.103246.
- [4] D. Frattini, G. Roviello, L. Ricciotti, C. Ferone, F. Colangelo, and O. Tarallo, 'Geopolymer-based composite materials containing pcm for thermal energy storage', *Cem. Concr. Compos.*, 2015, doi: 10.1016/j.cemconcomp.2015.03.007.
- [5] R. Shadnia, L. Zhang, and P. Li, 'Experimental study of geopolymer mortar with incorporated PCM', *Constr. Build. Mater.*, 2015, doi: 10.1016/j.conbuildmat.2015.03.066.
- [6] P. Sukontasukkul, N. Nontiyutsirikul, S. Songpiriyakij, K. Sakai, and P. Chindaprasirt, 'Use of phase change material to improve thermal properties of lightweight geopolymer panel', *Mater. Struct.*, 2016, doi: 10.1617/s11527-016-0812-x.
- [7] V. D. Cao, S. Pilehvar, C. Salas-Bringas, A. M. Szczotok, J. F. Rodriguez, M. Carmona, N. Al-Manasir, A.L. Kjoniksen, 'Microencapsulated phase change materials for enhancing the thermal performance of Portland cement concrete and geopolymer concrete for passive building applications', *Energy Convers. Manag.*, 2017, doi: 10.1016/j.enconman.2016.11.061.
- [8] D. Medpelli, J. M. Seo, and D. K. Seo, 'Geopolymer with Hierarchically Meso-/Macroporous Structures from Reactive Emulsion Templating', *J. Am. Ceram. Soc.*, 2014, doi: 10.1111/jace.12724.
- [9] Z. Wang and D. Lu, 'Study on the effect of emulsifiers on the pore structures of geopolymer prepared by emulsion templating', *Mater. Res. Express*, 2020, doi: 10.1088/2053-1591/ab94f9.
- [10] C. Bai, T. Ni, Q. Wang, H. Li, and P. Colombo, 'Porosity, mechanical and insulating properties of geopolymer foams using vegetable oil as the stabilizing agent', *J. Eur. Ceram. Soc.*, 2018, doi: 10.1016/j.jeurceramsoc.2017.09.021.
- [11] M. Hussain, R. Varely, Y. B. Cheng, Z. Mathys, and G. P. Simon, 'Synthesis and thermal behavior of inorganic-organic hybrid geopolymer composites', *J. Appl. Polym. Sci.*, 2005, doi: 10.1002/app.21413.
- [12] G. Roviello, L. Ricciotti, C. Ferone, F. Colangelo, R. Cioffi, and O. Tarallo, 'Synthesis and Characterization of Novel Epoxy Geopolymer Hybrid Composites', *Materials*, 2013, doi: 10.3390/ma6093943.
- [13] G. Roviello, C. Menna, O. Tarallo, L. Ricciotti, C. Ferone, F. Colangelo, D. Asprone, R. di Maggio, E. Cappelletto, A. Prota and R. Cioffi 'Preparation, structure and properties of hybrid materials based on geopolymers and polysiloxanes', *Mater. Des.*, 2015, doi: 10.1016/j.matdes.2015.08.006.
- [14] A. Eddhahak, S. Drissi, J. Colin, S. Caré, and J. Neji, 'Effect of phase change materials on the hydration reaction and kinetic of PCM-mortars', *J. Therm. Anal. Calorim.*, 2014, doi: 10.1007/s10973-014-3844-x.
- [15] D. E. Clark, P. Colombo, and R. M. Jr. Neilson, 'Solidification of oils and organic liquids', *Nuclear Waste Management*, 1982. doi: 10.2172/6462993.
- [16] M. Masrulita, P. Burhan, and Y. Trihadiningrum, 'Stabilization/Solidification of Waste Containing Heavy Metals and Hydrocarbons using OPC and Land Trass Cement', *J. Ecol. Eng.*, 2018, doi: 10.12911/22998993/92926.
- [17] M. H. Almabrok, R. McLaughlan, and K. Vessalas, 'Investigation of oil solidification using direct immobilization method', presented at the Environmental Research Event, Sydney, Australia, 2011.
- [18] M. H. Almabrok, R. G. McLaughlan, K. Vessalas, and P. Thomas, 'Effect of oil contaminated aggregates on cement hydration', *Am. J. Eng. Res.*, 2019.
- [19] M. R. El-Naggar, E. A. El-Sherief, and H. S. Mekhemar, 'Performance of geopolymers for direct immobilization of solvent extraction liquids: Metakaolin/LIX-84 formulations', *J. Hazard. Mater.*, 2018, doi: 10.1016/j.jhazmat.2018.08.057.

- [20] M. Ahdaya and A. Imqam, 'Investigating geopolimer cement performance in presence of water based drilling fluid', *J. Pet. Sci. Eng.*, 2019, doi: 10.1016/j.petrol.2019.02.010.
- [21] B. Planel, C. A. Davy, P. M. Adler, G. Hauss, M. Bertin, V. Cantarel, D. Lambertin, 'Water permeability of geopolymers emulsified with oil', *Cem. Concr. Res.*, 2020, doi: 10.1016/j.cemconres.2020.106108
- [22] P. Duxson, A. Fernández-Jiménez, J. L. Provis, G. C. Lukey, A. Palomo, and J. S. J. van Deventer, 'Geopolymer technology: the current state of the art', *J. Mater. Sci.*, 2007, doi: 10.1007/s10853-006-0637-z.
- [23] J. L. Provis and J. S. J. van Deventer, 'Alkali Activated Materials: State-of-the-Art Report', RILEM TC 224-AAM. 2014.
- [24] B. Singh, G. Ishwarya, M. Gupta, and S. K. Bhattacharyya, 'Geopolymer concrete: A review of some recent developments', *Constr. Build. Mater.*, 2015, doi: 10.1016/j.conbuildmat.2015.03.036.
- [25] J. L. Provis and S. A. Bernal, 'Geopolymers and Related Alkali-Activated Materials', *Annu. Rev. Mater. Res.*, 2014, doi: 10.1146/annurev-matsci-070813-113515.
- [26] C. Reeb, C. Pierlot, C. Davy, and D. Lambertin, 'Incorporation of organic liquids into geopolymer materials - A review of processing, properties and applications', *Ceram. Int.*, 2020, doi: 10.1016/j.ceramint.2020.11.239.
- [27] D. Lambertin, A. Roosees, and F. Frizon, 'Process for preparing a composite material from an organic liquid and resulting material', WO2014/044776 A1, 2014
- [28] C. A. Davy, G. Hauss, B. Planel, D. Lambertin, '3D structure of oil droplets in hardened geopolymer emulsions', *J. Am. Ceram. Soc.*, 2018, 1–6, doi: 10.1111/jace.16142
- [29] C. Pierlot, H. Hu, C. Reeb, J. Bassetti, M. Bertin, D. Lambertin, C. Davy, V. Nardello-Rataj, 'Selection of suitable surfactants for the incorporation of organic liquids into fresh geopolymer pastes', *Chem. Eng. Sci.*, 2022, doi: 10.1016/j.ces.2022.117635x
- [30] S. Petlitskaia, A. Poulesquen, 'Design of lightweight metakaolin based geopolymer foamed with hydrogen peroxide', *Ceramics International*, 2018, doi: 10.1016/j.ceramint.2018.10.021
- [31] T. Dong, S. Xie, J. Wang, G. Zhao, and Q. Song, 'Solidification and Stabilization of Spent TBP/OK Organic Liquids in a Phosphate Acid-Based Geopolymer', *Sci. Technol. Nucl. Install.*, 2020, doi: 10.1155/2020/8094205.
- [32] M. Kligys, A. Laukaitis, M. Sinica, and G. Sezemanas, 'The Influence of Some Surfactants on Porous Concrete Properties', *Materials Science*, 2007.
- [33] X. Ouyang, Y. Guo, and X. Qiu, 'The feasibility of synthetic surfactant as an air entraining agent for the cement matrix', *Constr. Build. Mater.*, 2008, doi: 10.1016/j.conbuildmat.2007.05.002.
- [34] D. Yan et al., 'Effects and mechanisms of surfactants on physical properties and microstructures of metakaolin-based geopolymer', *J. Zhejiang Univ.-Sci. A*, 2021, doi: 10.1631/jzus.A2000059.
- [35] A. Blyth, C. A. Eiben, G. W. Scherer, C. E. White, Impact of activator chemistry on permeability of alkali-activated slags, *J. Am. Ceram. Soc.* 2017, doi: 10.1111/jace.14996
- [36] IAEA, International Atomic Energy Agency, « Treatment and Conditioning of Radioactive Organic Liquids », 1992
- [37] M. Ben Haha, B. Lothenbach, G. Le Saout, and F. Winnefeld, 'Influence of slag chemistry on the hydration of alkali-activated blast-furnace slag — Part I: Effect of MgO', *Cem. Concr. Res.*, 2011, doi: 10.1016/j.cemconres.2011.05.002.
- [38] J. Rouquerol, F. Rouquerol, P. Llewellyn, G. Maurin, K.S. Sing, 'Adsorption by Powders and Porous Solids: Principles, Methodology and Applications', 2014.
- [39] M. Thommes, K. Kaneko, A.V. Neimark, J.P. Olivier, F-R. Reinoso, J. Rouquerol, K.S.W. Sing, 'Physisorption of gases, with special reference to the evaluation of surface area and pore size distribution', IUPAC Technical Report, 2015.
- [40] G. Peix, P. Duvauchelle, N. Freud, in *X-Ray Tomography in Material Science* (Hermes Science, London), 2000, Chap. 1:15–27.
- [41] N. Limodin, T. Rougelot, J. Hosdez, 2013, <http://isis4d.univ-lille.fr/>.

- [42] Y. Song, C. A. Davy, D. Troadec, A.-M. Blanchenet, F. Skoczylas, J. Talandier, J. C. Robinet, 'Multi-scale pore structure of COx claystone: Towards the prediction of fluid transport', *Marine and Petroleum Geology*, 2015, doi: 10.1016/j.marpetgeo.2015.04.004.
- [43] A. C. Kak, M. Slaney, 'Principles of Computerized Tomographic Imaging', IEEE Press, Piscataway, NJ, 1988.
- [44] A. C. Kak, M. Slaney, 'Principles of Computerized Tomographic Imaging', Society of Industrial and Applied Mathematics, Philadelphia, 2001. doi:10.1137/1.9780898719277.
- [45] J. Schindelin, I. Arganda-Carreras, E. Frise, V. Kaynig, M. Longair, T. Pietzsch T, Fiji: an open-source platform for biological-image analysis, *Nat Methods* 9(7) (2012) 676.
- [46] B. Münch, L. Holzer, 'Contradicting geometrical concepts in pore size analysis attained with electron microscopy and mercury intrusion', *J. Am. Ceram. Soc.* 2008, doi: 10.1111/j.1551-2916.2008.02736.x.
- [47] D. Massiot et al., 'Modelling one- and two-dimensional solid-state NMR spectra', *Magn. Reson. Chem.*, 2002, doi: 10.1002/mrc.984.
- [48] Stephant, Etude de l'influence de l'hydratation de laitiers sur les propriétés de transfert gazeux dans les matériaux cimentaires, PhD thesis (in French), Bourgogne University, 2015.
- [49] P. Bulejko and V. Bílek, 'Influence of chemical additives and curing conditions on the mechanical properties and carbonation resistance of alkali-activated slag composites', *Materials and Technology*, 2017, doi: 10.17222/mit.2015.185.
- [50] K. Behfarnia and M. Rostami, 'An assessment on parameters affecting the carbonation of alkali-activated slag concrete', *Journal of Cleaner Production*, 2017, doi: 10.1016/j.jclepro.2017.04.097.
- [51] K.-I. Song, J.-K. Song, B. Y. Lee, and K.-H. Yang, 'Carbonation Characteristics of Alkali-Activated Blast-Furnace Slag Mortar', *Adv. Mater. Sci. Eng.*, 2014, doi: 10.1155/2014/326458.
- [52] A. Kaddami and O. Pitois, 'A physical approach towards controlling the microstructure of metakaolin-based geopolymer foams', *Cem. Concr. Res.*, 2019, doi: 10.1016/j.cemconres.2019.105807.
- [53] C. Reeb, C. A. Davy, C. Pierlot, M. Bertin, V. Cantarel, D. Lambertin, 'Emulsification of low viscosity oil in alkali-activated materials', *Cement and Concrete Research*, *under revision*, March 2022.
- [54] M. Ben Haha, G. Le Saout, F. Winnefeld, and B. Lothenbach, 'Influence of activator type on hydration kinetics, hydrate assemblage and microstructural development of alkali activated blast-furnace slags', *Cem. Concr. Res.*, 2011, doi: 10.1016/j.cemconres.2010.11.016
- [55] Z. Sun and A. Vollpracht, 'Isothermal calorimetry and *in-situ* XRD study of the NaOH activated fly ash, metakaolin and slag', *Cem. Concr. Res.*, 2018, doi: 10.1016/j.cemconres.2017.10.004.
- [56] J. Cai, L. Xiaopeng, T. Jiawei, and V. Brecht, 'Thermal and compressive behaviors of fly ash and metakaolin-based geopolymer', *J. Build. Eng.*, 2020, doi: 10.1016/j.jobe.2020.101307.
- [57] Z. Zhang, W. Hao, Z. Yingcan, R. Andrew, J. L. Provis, and F. Bullen, 'Using fly ash to partially substitute metakaolin in geopolymer synthesis', *Appl. Clay Sci.*, 2014, doi: 10.1016/j.clay.2013.12.025.
- [58] X. Yao, Z. Zhang, H. Zhu, and Y. Chen, 'Geopolymerization process of alkali-metakaolinite characterized by isothermal calorimetry', *Thermochimica Acta*, 2009, doi: 10.1016/j.tca.2009.04.002.
- [59] S. A. Bernal, J. L. Provis, R. Volker, and R. Mejia de Gutierrez, 'Evolution of binder structure in sodium silicate-activated slag-metakaolin blends', *Cem. and Concr. Compos.*, 2011, doi: 10.1016/j.cemconcomp.2010.09.004.
- [60] S. Chithiraputhiran and N. Narayanan, 'Isothermal reaction kinetics and temperature dependence of alkali activation of slag, fly ash and their blends', *Constr. Build. Mater.*, 2013, doi: 10.1016/j.conbuildmat.2013.03.061.
- [61] L. Lei, R. Li, and A. Fuddin, 'Influence of maltodextrin retarder on the hydration kinetics and mechanical properties of Portland cement', *Cem. Concr. Compos.*, 2020, doi: 10.1016/j.cemconcomp.2020.103774.
- [62] K. Kochova, K. Schollbach, F. Gauvin, and H. J. H. Brouwers, 'Effect of saccharides on the hydration of ordinary Portland cement', *Construction and Building Materials*, 2017, doi: 10.1016/j.conbuildmat.2017.05.149.
- [63] N. Schneider and D. Stephan, 'The effect of d-gluconic acid as a retarder of ground granulated blast-furnace slag pastes', *Constr. Build. Mater.*, 2016, doi: 10.1016/j.conbuildmat.2016.06.127.

- [64] L. Chen, Z. Wang, Y. Wang, and J. Feng, 'Preparation and Properties of Alkali Activated Metakaolin-Based Geopolymer', *Materials*, 2016, doi: 10.3390/ma9090767.
- [65] P. Palmero, A. Formia, P. Antonaci, S. Brini, and J. M. Tulliani, 'Geopolymer technology for application-oriented dense and lightened materials. Elaboration and characterization', *Ceram. Int.*, 2015, doi: 10.1016/j.ceramint.2015.06.140.
- [66] P. He et al., 'Effects of Si/Al ratio on the structure and properties of metakaolin based geopolymer', *Ceram. Int.*, 2016, doi: 10.1016/j.ceramint.2016.06.033.
- [67] P. Duxson, J. L. Provis, G. C. Lukey, F. Separovic, and J. S. J. van Deventer, 'Si NMR Study of Structural Ordering in Aluminosilicate Geopolymer Gels', *Langmuir*, 2005, doi: 10.1021/la047336x.
- [68] Q. Wan, F. Rao, S. Song, R. E. Garcia, R. M. Estrella, C. L. Patino and Y. Zhang, 'Geopolymerization reaction, microstructure and simulation of metakaolin-based geopolymers at extended Si/Al ratios', *Cem. Concr. Compos.*, 2017, doi: 10.1016/j.cemconcomp.2017.01.014.
- [69] P. Duxson, G. C. Lukey, F. Separovic, and J. S. J. van Deventer, 'Effect of Alkali Cations on Aluminum Incorporation in Geopolymeric Gels', *Ind. Eng. Chem. Res.*, 2005, doi: 10.1021/ie0494216.
- [70] C. Kuenzel, T. P. Neville, S. Donatello, L. Vandeperre, A. R. Boccaccini, and C. R. Cheeseman, 'Influence of metakaolin characteristics on the mechanical properties of geopolymers', *Appl. Clay Sci.*, 2013, doi: 10.1016/j.clay.2013.08.023.
- [71] F. Bonk, J. Schneider, M. Alba Cincotto, and H. Panepucci, 'Characterization by multinuclear high-resolution NMR of hydration products in activated blast furnace slag pastes', *J. Am. Ceram. Soc.*, 2003, doi: 10.1111/j.1151-2916.2003.tb03545.x.
- [72] P. J. Schilling, L. G. Butler, A. Roy, and H. C. Eaton, '29Si and 27Al MAS-NMR of NaOH-Activated Blast-Furnace Slag', *J. Am. Ceram. Soc.*, 1994, doi: 10.1111/j.1151-2916.1994.tb04606.x.
- [73] J. Schneider, M. A. Cincotto, and H. Panepucci, '29Si and 27Al high-resolution NMR characterization of calcium silicate hydrate phases in activated blast-furnace slag pastes', *Cem. Concr. Res.*, 2001, doi: 10.1016/S0008-8846(01)00530-0.
- [74] S. D. Wang and K. L. Scrivener, '29Si and 27Al NMR study of alkali-activated slag', *Cem. Concr. Res.*, 2003, doi: 10.1016/S0008-8846(02)01044-X.
- [75] H. Hilbig and A. Buchwald, 'The effect of activator concentration on reaction degree and structure formation of alkali-activated ground granulated blast furnace slag', *J. Mater. Sci.*, 2006, doi: 10.1007/s10853-006-0755-7.
- [76] K. J. D. MacKenzie, R. H. Meinhold, B. L. Sherriffb, and Z. Xub, '27Al and 25Mg Solid-state Magic-angle Spinning Nuclear Magnetic Resonance Study of Hydrotalcite and its Thermal Decomposition Sequence', *J. Mater. Chem.*, 1993, doi: 10.1039/JM9930301263.
- [77] A. Albidah, M. Alghannam, H. Abbas, T. Almusallam, and Y. Al-Salloum, 'Characteristics of metakaolin-based geopolymer concrete for different mix design parameters', *J. Mater. Res. Technol.*, 2021, doi: 10.1016/j.jmrt.2020.11.104.
- [78] Z. Sun and A. Vollpracht, 'One year geopolymerisation of sodium silicate activated fly ash and metakaolin geopolymers', *Cem. Concr. Compos.*, 2019, doi: 10.1016/j.cemconcomp.2018.10.014.
- [79] A. Fernández-Jiménez, J. G. Palomo, and F. Puertas, 'Alkali-activated slag mortars Mechanical strength behaviour', *Cement and Concrete Research*, 1999, doi: 10.1016/S0008-8846(99)00154-4.
- [80] C. Bilim, C. D. Atiş, H. Tanyildizi, and O. Karahan, 'Predicting the compressive strength of ground granulated blast furnace slag concrete using artificial neural network', *Adv. Eng. Softw.*, 2009, doi: 10.1016/j.advengsoft.2008.05.005.

Chapter IV



Summary Chapter IV

PREAMBLE CHAPTER IV	161
1. MANGANESE OXIDES	161
2. THE COMPLEX Γ -MNO ₂ STRUCTURE AND ITS IMPACT ON GETTER EFFICIENCY	162
3. THE GETTER TRAPPING MECHANISM	164
4. APPLICATION IN CEMENTITIOUS MATERIALS	165
REFERENCES	168
CHAPTER IV: TRAPPING PERFORMANCE OF ALKALI-ACTIVATED MATERIALS INCORPORATING A HYDROGEN/TRITIUM GETTER FOR THE CONDITIONING OF TRITIATED ORGANIC LIQUIDS	171
ABSTRACT	171
1. INTRODUCTION	172
1.1. INDUSTRIAL CONTEXT	172
1.2. SCIENTIFIC BACKGROUND	172
1.3. AIMS AND SCOPES	173
2. MATERIALS AND METHODS	174
2.1. RAW MATERIALS	174
2.2. MATERIALS PREPARATION	174
2.3. HYDROGEN TRAPPING PERFORMANCE	178
2.3.1. <i>Gamma irradiation experiments</i>	178
2.3.2. <i>Magnesium corrosion</i>	180
2.4. INTERACTIONS BETWEEN THE AAM POREWATERS AND THE GETTER	181
3. RESULTS AND ANALYSIS	181
3.1. H ₂ TRAPPING PERFORMANCE OF HARDENED AAM IN PRESENCE OF GETTER AND OL (MATERIALS B AND C)	181
3.2. CONTINUOUS H ₂ TRAPPING PERFORMANCE OF AAM IN PRESENCE OF GETTER (MATERIALS D)	183
3.2.1. <i>Trapping kinetics</i>	184
3.2.2. <i>Trapping efficiency</i>	184
3.3. INFLUENCE OF THE POREWATER CHEMISTRY ON THE Γ -MNO ₂ /AG ₂ O GETTER	187
3.3.1. <i>Interactions between porewaters and γ-MnO₂/Ag₂O getter</i>	187
3.3.1.1 Ion sorption at the surface of the γ -MnO ₂ /Ag ₂ O getter	188
3.3.1.2 XRD results	188
3.3.1.3 Hydrogen trapping capacity of γ -MnO ₂ /Ag ₂ O getter powder	190
3.3.2. <i>Interaction between sulfides and γ-MnO₂/Ag₂O hydrogen getter</i>	191
3.3.2.1 SEM observations of the γ -MnO ₂ /Ag ₂ O getter powder	191
3.3.2.2 XRD results	191
3.3.2.3 Hydrogen trapping capacity of γ -MnO ₂ /Ag ₂ O getter	191
4. CONCLUSION	194
APPENDIX: INTERACTIONS BETWEEN THE AAM POREWATERS AND THE GETTER	195
REFERENCES	197

Preamble Chapter IV

Due to its widely accepted effectiveness [1]-[5], the hydrogen/tritium getter studied in this work is a blend of γ -manganese dioxide (γ -MnO₂) and silver oxide (Ag₂O) written **γ -MnO₂/Ag₂O**. According to Galliez [6], the greatest trapping efficiency is reached when manganese oxide and silver oxide powders are weighed in proportions such that the mass ratio γ -MnO₂/Ag₂O = 87/13. The getter preparation process described by [2] involves a grinding step, which promotes the granulation of Ag₂O particles at the surface of γ -MnO₂. In the following, the structure of γ -MnO₂ and the trapping mechanisms will be described. A brief state of the art on the use of this getter in cementitious materials will also be discussed.

1. Manganese oxides

The interesting chemistry of manganese is due to its various oxidation states. Among the possible oxidation states of manganese (in the range of -III to +VII), the +II, +III, and +IV oxidation states are the most prevalent [7]. Manganese possesses the ability to form multiple bonds with oxygen through spontaneous oxidation to a variety of stoichiometric oxides/hydroxides/oxyhydroxides. Galliez [2] focused his work on the efficiency of hydrogen getters made up of manganese dioxides (MnO₂) of mixed oxidation states +III-IV or oxidation state +IV. Figure 1 summarizes the structures of MnO₂ polymorphs [8]. Two types of structures are distinguished:

- **Lamellar structures:** They consist of MnO₆ octahedrons connected together by their edges. An example of this type of structure is birnessite δ -MnO₂ (Figure 1).
- **Tunnel structures:** They consist of MnO₆ octahedrons linked together by their corners. An example of this type of structure is cryptomelane α -MnO₂ (Figure 1).

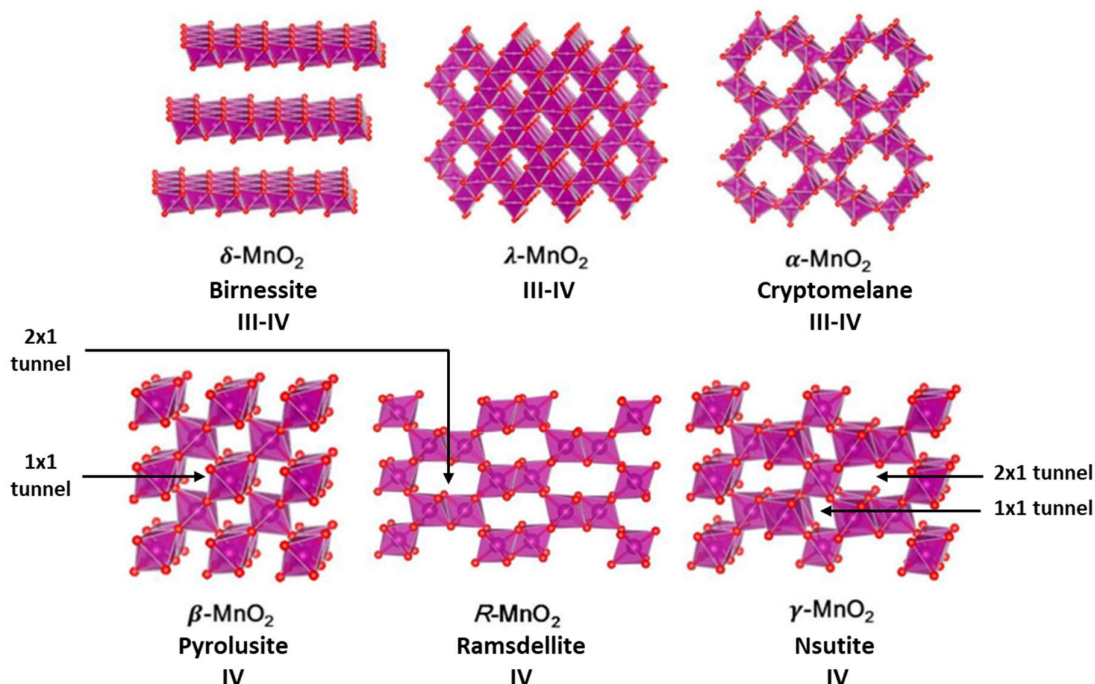


Figure 1: Structures of MnO_2 polymorphs (Mn: magenta and O: red). The structure of $\gamma\text{-MnO}_2$ consists of an intergrowth between 1×1 and 2×1 tunnels. The ratio of 1×1 tunnel over 1×1 and 2×1 tunnels is called Pr ($0\% < \text{Pr} < 100\%$). The shown $\gamma\text{-MnO}_2$ structure displays a Pr = 50%. Water molecules and guest cations are omitted for clarity [8].

The results of Galliez [6] highlighted that the dense and compact 3D structure of the $\lambda\text{-MnO}_2$ has a low trapping efficiency due to the difficult access of hydrogen atoms to reactive sites. In the case of birnessite, the lamellar structure has a strong tendency to interact with water, which is interfering with the trapping of H_2 . Cryptomelane displays good hydrogen trapping efficiency. Overall, the most effective manganese dioxide polymorph is $\gamma\text{-MnO}_2$, i.e. nsutite [6].

2. The complex $\gamma\text{-MnO}_2$ structure and its impact on getter efficiency

Pyrolusite or $\beta\text{-MnO}_2$ is the most thermodynamically stable manganese dioxide form. It is composed of MnO_6 octahedrons linked together by their corners forming 1×1 tunnels (Figure 1). Ramsdellite or $R\text{-MnO}_2$ is composed of MnO_6 octahedron linked together by their corners and edges forming 2×1 tunnels (Figure 1). Nsutite or $\gamma\text{-MnO}_2$ is a mixture of pyrolusite and ramsdellite manganese dioxide species [9]. It is considered as an irregular intergrowth of pyrolusite and ramsdellite blocks, hence composed of 1×1 and 2×1 tunnels and first identified by De Wolf [10]. This irregular assembly is therefore called the De Wolf defect. Another specificity of the nsutite structure is the presence of microtwinning defects. This occurs when two adjacent MnO_6 octahedron are oriented so that they share the same crystal lattice points

in a symmetrical manner. The result is an intergrowth of two-separated MnO_6 octahedron that are tightly bonded to each other.

Due to these defects, the structure of nsutite is difficult to characterize by XRD. The random sequencing of R-MnO_2 and $\beta\text{-MnO}_2$ depends on the nsutite synthesis conditions and the resulting defects actually have a strong impact on the getter efficiency. The amount of 1×1 tunnels in the structure, i.e. the amount of pyrolusite units, is referred to as Pr. The amount of microtwinning defects is referred to as Tw. Both Pr and Tw are expressed in %.

Chabre and Parmentier [5] developed an empirical method allowing the determination of these two parameters based on peaks shifting along diffraction patterns. Accordingly, Figure 2 compares the trapping efficiency of getters made up of nsutites with varying Pr and Tw in their structure. It confirms that pyrolusite and ramsdellite alone display a poor hydrogen trapping efficiency. On the contrary, all nsutites that have been tried are efficiently trapping hydrogen gas. However, Galliez [2] evidenced that the higher the microtwinning rate (high Tw) and the lower the amount of 1×1 tunnel (low Pr), the higher the hydrogen trapping kinetics. Indeed, the reactive sites are more easily accessible for hydrogen atoms in a highly disordered structure (high Tw) and in 2×1 tunnels (low Pr). Finally, the specific surface area also plays an important role with higher specific surface area promoting trapping efficiency.

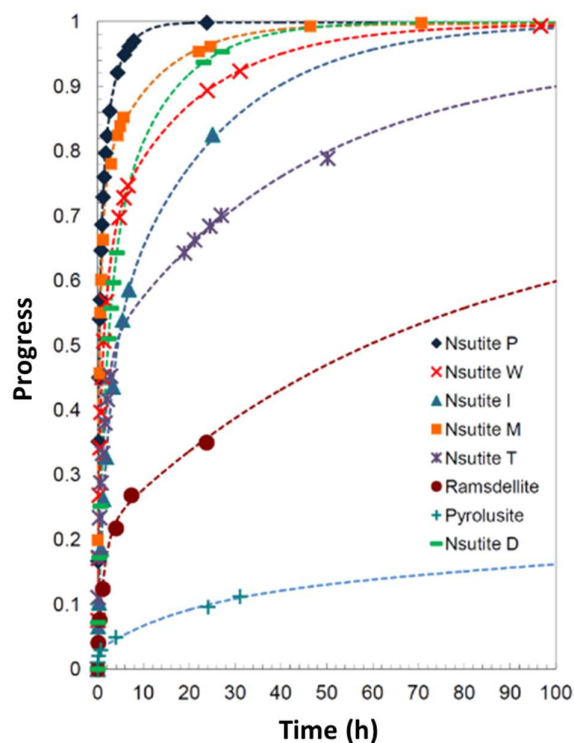


Figure 2: Influence of the $\gamma\text{-MnO}_2$ form used in the preparation of $\text{MnO}_2/\text{Ag}_2\text{O}$ hydrogen getters on the hydrogen trapping efficiency with the progress = $n(\text{H}_2)_{\text{trapped}}/n(\text{H}_2)_{\text{initial}}$ [2].

3. The getter trapping mechanism

In their reaction with hydrogen atoms, manganese dioxides are reduced and transformed in manganese oxyhydroxides.

Figure 3 presents the structures of groutite (α -MnOOH) and manganite (γ -MnOOH) oxyhydroxides in order to visualize the hydrogen insertion sites [2]. Groutite is formed by the reduction of ramsdellite and has the same 2x1 tunnel structure. Manganite is formed by the reduction of pyrolusite and has the same 1x1 tunnel structure. In both groutite and manganite, hydrogens are linked to pyramidal oxygen atoms and manganese is in oxidation state +III. The presence of manganese atoms in oxidation state +III leads to the presence of Jahn-Teller effect, which is a deformation of MnO_6 octahedrons [11]. Finally, δ -MnOOH is considered as the oxyhydroxide form of nsutite [12]. As well as γ - MnO_2 is an intergrowth of ramsdellite and pyrolusite, δ -MnOOH is an intergrowth of groutite and manganite. However, the microtwinning defects present in the nsutite form are no longer present in the δ -MnOOH form [13].

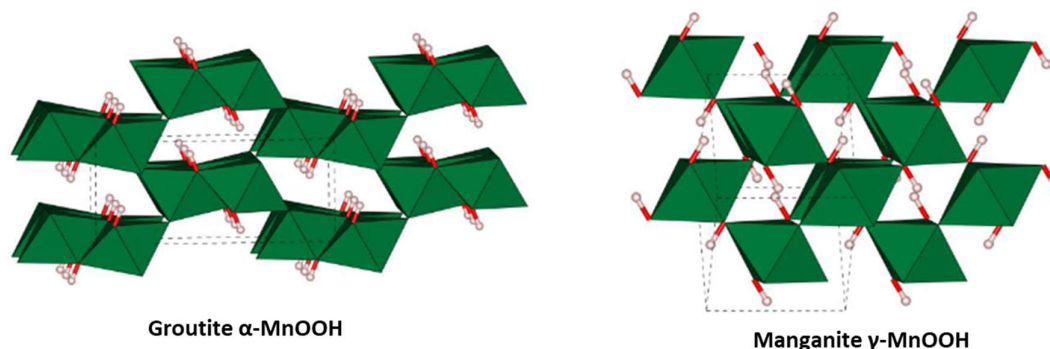


Figure 3: Structure of (left) Groutite and (right) Manganite [2].

Several authors tried to understand the mechanisms of H_2 trapping by γ - MnO_2 / Ag_2O getters [1], [2], [4], [5]. The one proposed by Galliez is the most recent and complete one [2], [14], [15]. First of all, he demonstrated that Ag_2O is transformed in Ag_2CO_3 by carbonation with ambient CO_2 during the getter preparation. However, Farcy [16] demonstrated that Ag_2CO_3 is transformed back to its original Ag_2O form in high pH conditions. In a first step (step 1 in figure 4), Galliez describes that there is a competition between the catalytic effect of Ag_2O on the dihydrogen dissociation and its reduction into metal silver by reacting with hydrogen ($Ag_2O + H_2 \rightarrow Ag + H_2O$). Due to this partial reduction of Ag_2O in metal Ag, it is more appropriate to call it a promoter rather than a catalyst. The formed hydrogen atoms can then be inserted in the tunnel structure of nsutite. Initially, they are preferentially inserted in 2x1 tunnels, which are more easily accessible (step 2 in figure 4). Progressively, this leads to Jahn-Teller deformations of adjacent 1x1 tunnels (step 3 in figure 4). Hydrogen atoms are then

Since that patent, two main studies have been conducted on the $\gamma\text{-MnO}_2/\text{Ag}_2\text{O}$ getter efficiency in cementitious materials without drying, for the purpose of gaseous tritium confinement [18].

On the one hand, Lanier [19] studied the getter efficiency in Portland cements (of CEMI and CEMV types) and designed low permeability mortars for tritiated waste confinement. On another hand, Farcy [16] studied the getter efficiency in magnesium potassium phosphate (MKP) and calcium sulfoaluminate (CSA) cements in order to limit the presence of water in the cement system. **These studies demonstrated an excellent hydrogen trapping efficiency of the getter in Portland, MKP and CSA cements, without the need of a preliminary thermal treatment step. However, interactions between the getter and the cementitious porewaters were brought to light and this might affect the getter efficiency.**

Several parameters might have an impact on the getter efficiency in cementitious environments:

- Despite its efficiency in wet conditions [1], [4], several authors agree that the getter efficiency is higher in dry conditions [1], [2], [16]. Figure 5 exemplifies the strong impact of humid conditions on the getter efficiency [16]. Hence, the amount of free water, present in the porous network of cementitious materials, might have an impact on the getter efficiency.

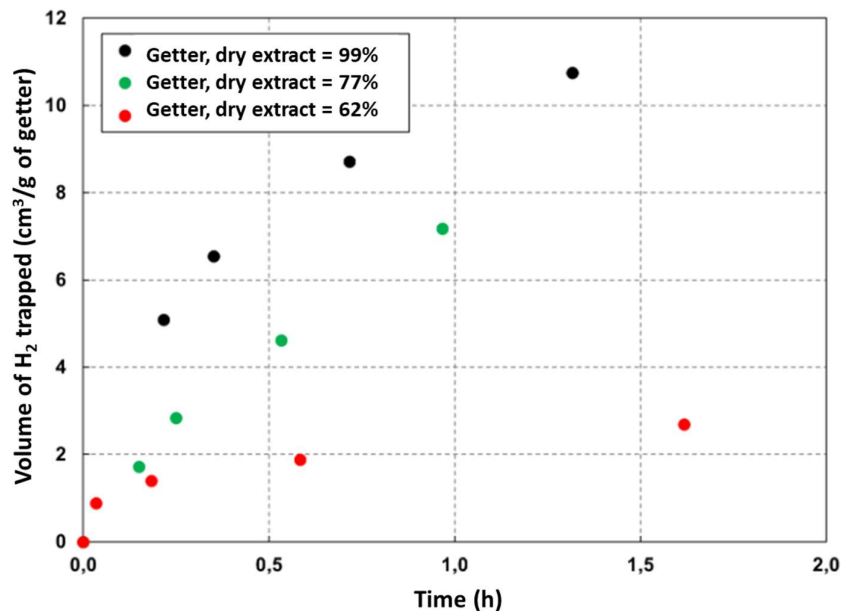


Figure 5: Trapping kinetic of $\gamma\text{-MnO}_2/\text{Ag}_2\text{O}$ at different rates of humidity [16].

- The packing of MnO_6 octahedrons creates a variety of voids that form sublattices of structurally equivalent interstitial sites, and allow the intercalation of cations and water into the MnO_2 frameworks. For instance, manganese dioxides are widely used to remove metal ions from wastewater by adsorption [20], [21] and Figure 6 illustrates the predicted sites for alkali intercalation [22]. Farcy [16] demonstrated that the nsutite structure has a strong tendency to adsorb various ions present in cementitious porewaters (Ca^{2+} , Mg^{2+} , Na^+ ...). This might have an impact on the accessibility of reactive sites for hydrogen.

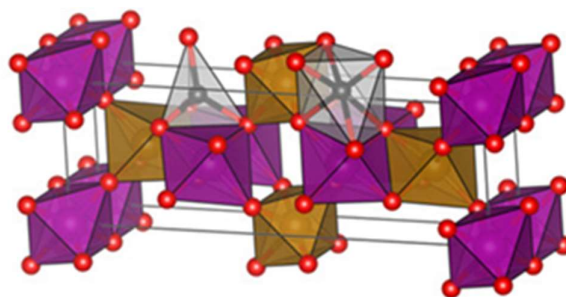
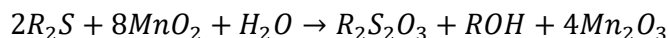


Figure 6: Nsutite polymorph of MnO_2 and predicted sites for alkali intercalation. The purple and yellow spheres and surrounding octahedrons denote spin-up and spin-down Mn atoms and MnO_6 octahedrons. The black spheres and surrounding gray polyhedrons denote potential intercalation sites for alkali and ions in the structure. Each presented site defines a distinct sublattice, while a single site of each type is shown [22].

- The literature reports that sulfide species reduce MnO_2 and $MnOOH$ via a two-electron inner-sphere transfer process, because these solids have an empty and partially filled conduction band of orbitals, respectively, that can accept two electrons. In the case of MnO_2 , this results in the reduction of Mn (+IV) to Mn (+III) [23]. In addition, a recent patent describes that manganese dioxide reacts with sulfide species present in BFS mortars through the following reaction [24]:



If happening, this reaction would reduce the trapping capacity of the getter.

In conclusion, AAM are considered in this work for their ability to efficiently immobilize industrial oils. In the case of tritiated oils, the functionalization with a γ - MnO_2/Ag_2O hydrogen/tritium getter is considered to limit HT/ T_2 outgassing. This chapter aims at studying the hydrogen trapping performance of the γ - MnO_2/Ag_2O getter in AAM. In particular, potential detrimental interactions between AAM porous environments and the getter will be examined. In addition, this chapter also aims at ascertaining that the presence of oil does not interfere with the trapping performances.

References

- [1] A. Kozawa and K. V. Kordesch, « Silver-catalysed MnO₂ as hydrogen absorber », *Electrochimica Acta*, 1981, doi: 10.1016/0013-4686(81)90020-7.
- [2] K. Galliez, « Study and understanding of the irreversible trapping of hydrogen using a mixture of MnO₂/Ag₂O », PhD, University of Nantes, France, 2012.
- [3] C. Maruejols et al., « Mitigation of the hydrogen risk in fusion facilities: The first experimental results », *Fusion Eng. Des.*, 2003, doi: 10.1016/S0920-3796(03)00150-9.
- [4] V. Chaudron, « Etude de la mitigation du risque hydrogène dans un réacteur de fusion thermonucléaire par réduction d'un oxyde métallique », PhD, University of Nancy, 1998.
- [5] Y. Chabre and J. Parnetier, « Structural and electrochemical properties of the proton / γ -MnO₂ system », *Prog. Solid State Chem.*, 1995.
- [6] K. Galliez, P. Deniard, D. Lambertin, S. Jobic, and F. Bart, « Influence of MnO₂ polymorphism form on MnO₂/Ag₂O hydrogen getter », *J. Nucl. Mater.*, 2013, doi: 10.1016/j.jnucmat.2013.03.053.
- [7] S. K. Ghosh, « Diversity in the Family of Manganese Oxides at the Nanoscale: From Fundamentals to Applications », *ACS Omega*, 2020, doi: 10.1021/acsomega.0c03455.
- [8] J. Shin, J. K. Seo, R. Yaylian, A. Huang, and Y. S. Meng, « A review on mechanistic understanding of MnO₂ in aqueous electrolyte for electrical energy storage systems », *Int. Mater. Rev.*, 2020, doi: 10.1080/09506608.2019.1653520.
- [9] N. L. P. Magnard, S. A. Anker, A. Kirsch, and K. M. Ø. Jensen, « Characterisation of intergrowth in metal oxide materials using structure mining: the case of γ -MnO₂ », *Dalton Transactions*, 2022, doi.org/10.1039/D2DT02153F.
- [10] P. M. De Wolff, « Interpretation of some γ -MnO₂ diffraction patterns », *Acta Crystallogr.*, 1959, doi: 10.1107/S0365110X59001001.
- [11] T. Kohler and T. Armbruster, « Hydrogen Bonding and Jahn–Teller Distortion in Groutite, -MnOOH, and Manganite, -MnOOH, and Their Relations to the Manganese Dioxides Ramsdellite and Pyrolusite », *J. Solid State Chem.*, 1997.
- [12] W. C. Maskell, J. E. A. Shaw, and F. L. Tye, « Manganese dioxide electrode - IV. Chemical and electrochemical reduction of an electrolytic γ -MnO₂ », *Electrochem. Acta*, 1981.
- [13] L. A. H. MacLean and F. L. Tye, « The Structure of Fully H-Inserted γ -Manganese Dioxide Compounds », *J. Solid State Chem.*, 1996.
- [14] K. Galliez et al., « Pair Distribution Function and Density Functional Theory Analyses of Hydrogen Trapping by γ -MnO₂ », *Inorg. Chem.*, 2015, doi: 10.1021/ic5026334.
- [15] K. Galliez, P. Deniard, P.-E. Petit, D. Lambertin, F. Bart, and S. Jobic, « Modelling and quantification of intergrowth in γ -MnO₂ by laboratory pair distribution function analysis », *J. Appl. Crystallogr.*, 2014, doi: 10.1107/S1600576714000375.
- [16] O. Farcy, « Formulation et caractérisation de mortiers fluides pour le conditionnement de déchets tritiés », PhD, University of Montpellier, 2020.
- [17] D. Lambertin and C. Cau Dit Coumes, « Hydrogen-trapping material, method of preparation and uses », WO 2010/066811, 2010
- [18] « Appel à projets ANDRA : MACH3 (Matrices Cimentaires pour le piégeage du tritium ³H) », 2018.
- [19] S. Lanier, « Mise au point d'un mortier de piégeage à réseau poreux contrôlé », PhD, Centrale Lille Institut, 2020.
- [20] N. C. Le and D. Van Phuc, « Sorption of lead (II), cobalt (II) and copper (II) ions from aqueous solutions by γ -MnO₂ nanostructure », *Adv. Nat. Sci. Nanosci. Nanotechnol.*, 2015, doi: 10.1088/2043-6262/6/2/025014.
- [21] R. Yang and al., « MnO₂-Based Materials for Environmental Applications », *Adv. Mater.*, 2021, doi: 10.1002/adma.202004862.

- [22] D. A. Kitchev, S. T. Dacek, W. Sun, and G. Ceder, « Thermodynamics of Phase Selection in MnO₂ Framework Structures through Alkali Intercalation and Hydration », *J. Am. Chem. Soc.*, 2017, doi: 10.1021/jacs.6b11301.
- [23] G. W. Luther, A. Thibault de Chanvalon, V. E. Oldham, E. R. Estes, B. M. Tebo, and A. S. Madison, « Reduction of Manganese Oxides: Thermodynamic, Kinetic and Mechanistic Considerations for One-Versus Two-Electron Transfer Steps », *Aquat. Geochem.*, 2018, doi: 10.1007/s10498-018-9342-1.
- [24] X. Gao, L. Frouin, M. Cyr, and C. Musikas, « Ground granulated blast furnace slag based binder, discolored mortar or concrete including said binder and their preparation methods », WO2017080577A1, 2017.

Chapter IV: Trapping performance of alkali-activated materials incorporating a hydrogen/tritium getter for the conditioning of tritiated organic liquids (Published in *Journal of Nuclear Materials*)

Charles Reeb^{1,2}, Catherine Davy^{1,3}, Christel Pierlot¹, David Lambertin²

¹Univ. Lille, CNRS, Centrale Lille, ENSCL, Univ, Artois, UMR 8181-UCCS-Unité de Catalyse et de Chimie du Solide – F-59000 Lille, France

²CEA, DES, ISEC, DE2D, SEAD, LCBC, Univ Montpellier, Marcoule, France

³Sorbonne Université, CNRS, EPHE, UMR 7619 METIS, 4 place Jussieu 75005 Paris, France

Abstract

In this research, novel alkali-activated materials (AAM) are developed for the conditioning of tritiated organic liquids OL. Their originality is to ensure both radioactive OL waste conditioning and hydrogen or tritium ($^1\text{H}_2$ or $^3\text{H}_2$) trapping. Two types of AAM are compared, either based on metakaolin MK (i.e., on geopolymer GEO solid structure) or on blast furnace slag BFS (i.e., Portland cement solid structure). For $^1\text{H}_2$ or $^3\text{H}_2$ trapping, both AAM incorporate a $\gamma\text{-MnO}_2/\text{Ag}_2\text{O}$ getter powder at 10 wt.%, as in former research.

The efficiency of $^1\text{H}_2$ trapping in the two AAM is assessed *via in situ* $^1\text{H}_2$ production, using two distinct methods: (1) gamma irradiation (short term $^1\text{H}_2$ production) and (2) magnesium metal Mg corrosion (longer term $^1\text{H}_2$ production). Complementarily, the $^1\text{H}_2$ trapping efficiency of the getter is analyzed in both AAM porewaters.

Gamma irradiation with a cumulative dose up to 500 kGy shows that GEO-based AAM added with getter have a H_2 trapping efficiency of almost 100% without OL, and 87-92% with OL, when compared to identical materials made with non-trapping $\gamma\text{-MnO}_2$. BFS-based AAM made with getter have a trapping efficiency of 52-65% without OL and 16-25% with OL.

After 443-464 days Mg corrosion, the cumulative amount of $^1\text{H}_2$ trapped in BFS AAM reaches an asymptote of 0.7 mmol/g of getter, while it keeps increasing in GEO AAM. This proves the excellent $^1\text{H}_2$ trapping efficiency of getter-functionalized GEO compared to BFS AAM.

The contact of the getter with the extracted porewaters of the two AAM shows a strong ion adsorption on its surface. This reduces the $^1\text{H}_2$ trapping capacity by 50% (in both cases). When the getter is placed in contact with sulfides, which are present in BFS AAM only, X-Ray Diffraction (XRD) and Scanning Electron Microscopy (SEM) evidence that the structure of the getter is modified. This explains the limited $^1\text{H}_2$ trapping efficiency of the getter in BFS AAM, whereas the getter-functionalized GEO AAM remains efficient.

Keywords: Alkali-activated materials, blast furnace slag, geopolymer, tritium, getter, radioactive waste, organic liquids, organics, tritium trapping

1. Introduction

1.1. Industrial context

Industrial countries are responsible for the management of their hazardous radioactive waste, generated mainly by the nuclear industry, but also from medical or military applications [1], [2]. The stabilization/solidification (S/S) of these waste is a safe conditioning method, e.g. by vitrification for long lived and high activity waste, or by immobilization into cement-based materials. Ordinary Portland cement (OPC) materials are widely used for radioactive waste immobilization because their long-term durability is well documented [3], and they are a robust and economically viable solution [4].

However, alternative materials are required for specific applications, where OPC are inadequate, e.g., for immobilizing aluminum [5], [6], or organic liquids (OL) [7], [8]. In the latter case, with OPC, the incorporation of OL may prove difficult, the setting and strength development are significantly hindered [9]-[12], and durability is uncertain [13]-[16]. Instead, alkali-activated materials (AAM) have proven their excellent behavior for OL conditioning [8], [16]-[23]. They are currently investigated in the framework of the European H2020 PREDIS project [24].

An alternative to OL treatment is to resort to incineration, but this method presents strong restrictions, with significant limitations on radiologic activity or prohibiting the presence of specific chemical compounds in the wastes. In particular, tritium gas, an isotope of hydrogen, is released by waste from current fission nuclear reactors, and significantly more will be produced in the near future by the nuclear fusion reactor ITER [1], [25]. Although tritium is a short-lived radionuclide, it is very difficult to confine and can easily migrate in the environment. Numerous tritiated waste exceed the allowed annual limits for tritium emission in gaseous and liquid effluents from incineration units [1], [26]. In practice, tritiated OL are currently not allowed in incineration units. Rather, immobilization into cement-based materials has been considered [27], [28], but until now this has been done without any means to limit tritium gas release and hence, to provide sufficient resistance against internal cracking (due to gas pressure build-up) and sufficient durability.

1.2. Scientific background

Although they are based on OPC, the developed matrices in [27], [28] also have a very limited compressive strength (below 100 kPa after 28 days curing, at an OL incorporation rate of 15-20%wt cement). This is too low for current international regulations, which impose a minimal compressive strength of 8 MPa. As developed above, to achieve such minimal strength for cement matrices encapsulating OL, alkali-activated materials (AAM) are more adequate than

OPC [8], [16]-[23]. In practice, two types of AAM exist depending on their Ca content [30]. Both are investigated here. Low Ca content AAM is based on alkali-activated metakaolin (MK); this provides a geopolymer matrix, made of an amorphous 3D aluminosilicate solid framework. High content Ca AAM is based on alkali-activated blast furnace slag (BFS); setting leads to amorphous calcium aluminate and silicate hydrates.

1.3. Aims and scopes

Complementarily to using an AAM matrix for the immobilization of radioactive OL wastes, *tritiated* OL also require the confinement of tritium gas.

An international patent [31] shows that significant trapping of H₂ is possible in different conditioning matrices, including AAM, provided that they include a dedicated hydrogen-tritium getter, and that a preliminary drying of the cement matrix is performed (at 32°C for 14 days followed by 2 days at 60°C). The getter is a mix of γ -MnO₂ and Ag₂O, aiming at irreversibly trapping gaseous hydrogen [32]-[34] and its isotopes (deuterium and tritium forms) [35]. It has been successfully used in the development of Portland cement-based mortars [36] or calcium sulfoaluminate cements [37] for the conditioning of tritiated waste, without requiring any heat treatment, although the latter was suggested in [31]. These cement matrices incorporate a fixed amount of 10% γ -MnO₂/Ag₂O getter in a powdered form (expressed in% of the total mortar mass) with a ¹H₂ trapping efficiency of over 90% after exposure to gamma irradiations.

However, the getter efficiency after incorporation in an AAM without heat treatment is not known. Potential detrimental interactions may occur between the γ -MnO₂/Ag₂O getter and the AAM pore-waters such as 1) significant cations and/or anions sorption on the γ -MnO₂ surface [37], 2) a high amount of free water present in the pore structure of MK-based AAM (i.e., geopolymers) and 3) the presence of reductive species in BFS-based AAM [38], which might react with the oxidative components of the γ -MnO₂/Ag₂O getter. The influence of the immobilized OL on the hydrogen trapping efficiency is also a question on hold.

The purpose of this research is precisely to determine the hydrogen/tritium trapping efficiency of AAM added with getter for OL immobilization. Hydrogen gas is used, and results are assumed extendable to tritium. Following the promising materials developed in [36], [37], [39], the AAM developed in this research contain 10 wt.% of γ -MnO₂/Ag₂O getter, or a non-trapping γ -MnO₂ powder used for comparison purposes. The AAM are either based on blast furnace slag (BFS) or on metakaolin (MK). They are neither dried nor heat treated. Following industrial requirements, a fixed OL incorporation rate of 20% by volume is used. The OL is a pure non-reactive mineral oil.

The efficiency of H₂ trapping in the two AAM is assessed via in situ hydrogen production, using

two distinct methods: (1) gamma irradiation (short term hydrogen production) on three-month old AAM, and (2) magnesium metal Mg corrosion (longer term hydrogen production). The first method generates *in situ* H₂ gas by water and OL radiolysis [40]-[42]. The second method produces H₂ gas *in-situ* through the corrosion of Mg powder added in the AAM [42]. Complementarily, the hydrogen trapping efficiency of the getter is analyzed in both AAM porewaters, by combining (1) X-Ray Diffraction (XRD) and Scanning Electron Microscopy (SEM) to observe any structural change, (2) ICP-AES to assess ion sorption and (3) trapping efficiency characterizations.

2. Materials and methods

2.1. Raw materials

All raw materials used in this study are listed in Table 1.

The γ -MnO₂/Ag₂O getter is produced by A3I (France) using manganese oxide (γ -MnO₂) and silver oxide (Ag₂O).

A pure mineral oil (Nevastane EP100) is chosen as the OL to incorporate into the AAM. The reasons are its purity (i.e., its absence of additives) and its easy incorporation in cementitious materials, related to its viscosity comparable to that of the fresh AAM [22], [44].

Table 1: Raw materials used in this study.

Category	Name	Supplier
Solid precursors	Metakaolin (M1000)	Imerys
	Blast Furnace Slag	Ecocem
Alkaline sources	Sodium hydroxide (purity > 99 %)	VWR Int.
	Sodium silicate solution (Betol 39T)	Woellner
Getter constituents	Manganese Oxide (ref n°8.05958.1000)	Sigma-Aldrich
	Silver Oxide (ref n°1.19208.0100)	Merck
Mineral oil	Nevastane EP100	Total
Other powders	Magnesium (-325 mesh, purity > 99 %)	Alfa Aesar
	Sodium sulfide	Sigma-Aldrich

2.2. Materials preparation

Two formulations of AAM cements are selected from the literature, one for MK-based AAM [7], [18], [19], [45], [46], the other for slag-based AAM [47]. An alkali-activation with sodium silicate is chosen for MK to obtain a stoichiometry providing good mechanical performance. Sodium hydroxide is preferred for BFS. Indeed, a preliminary study in our laboratory has

shown that the OL emulsification is better (with smaller and more homogeneously distributed droplets) in sodium hydroxide activated BFS than in sodium silicate activated BFS.

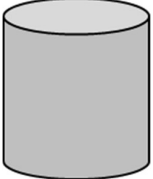
Figure 1 summarizes the different materials prepared with their processing steps and the associated experimental measurements.

The first step (Figure 1, Step 1) consists in preparing the fresh material grouts:

- For the MK-based geopolymer (GEO), the components are Betol 39T, sodium hydroxide, water and MK. They are weighed in order to obtain a molar composition of $3.5 \text{ SiO}_2 : 1.0 \text{ Al}_2\text{O}_3 : 1.0 \text{ Na}_2\text{O} : 13.0 \text{ H}_2\text{O}$, following (Cantarel 2015, Cantarel 2018).
- For the alkali-activated blast furnace slag (BFS), the components (sodium hydroxide, water and BFS) are weighed with a water/BFS mass ratio equal to 0.45 and a mass concentration of sodium hydroxide representing 10% by mass of the mass of BFS, following [47].

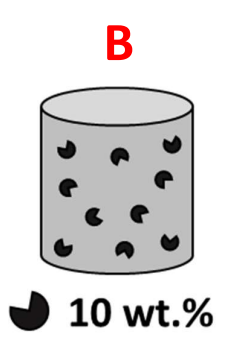
For both AAM, the alkali-activating solutions are prepared first. Sodium hydroxide pellets are dissolved in distilled water. In the GEO case, the sodium silicate solution (Betol 39T) is also added to the mix. The solutions are left to cool down to room temperature for several hours. At this stage, activating solutions are stirred mechanically at 2000 rpm with a helical blade and the solid precursor powders (MK or BFS) are quickly added. The mixing is carried out for 3 minutes until homogenization. Fresh grouts are either used in the second step (Figure 1, Step 2) or cured under endogenous conditions at 25°C for 28 days to provide **material A**. A detailed composition is given in Table 2.

Table 2: Formulation details of materials A presented for a total mass of 100 g.

	Material (g)	GEO	BFS
	H ₂ O	2.95	28.82
NaOH	6.87	7.12	
Betol 39T	47.85	-	
MK	42.33	-	
BFS	-		64.06

The second step (Figure 1, Step 2) consists in adding 10% mass $\gamma\text{-MnO}_2$ or the $\gamma\text{-MnO}_2/\text{Ag}_2\text{O}$ getter powders to the fresh grouts. These powders are quickly introduced in the fresh pastes and the mixing is carried out for 5 minutes at 2000 rpm until homogenization. At this stage, the fresh mixtures are either used in the third step (Figure 1, Step 3) or cured under endogenous conditions at 25°C for 90 days to provide **material B**. A detailed composition is given in Table 3.

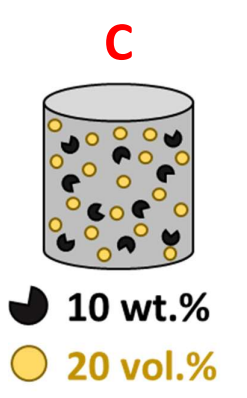
Table 3: Formulation details of materials B presented for a total mass of 100 g.

	Material (g)	GEO	BFS
	H ₂ O	4.95	25.94
	NaOH	6.02	6.40
	Betol 39T	41.94	-
	MK	37.10	-
	BFS	-	57.65
	γ -MnO ₂ or getter	10.00	10.00

The third step (Figure 1, Step 3) is divided into two distinct paths:

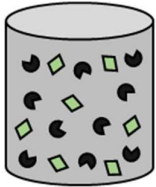


- Step 3a (Figure 1) consists in adding the OL in proportions representing 20% volume of the total volume of the material. The OL is quickly introduced in each fresh paste and the mixing is carried out for 5 minutes at 2000 rpm until homogenization. Fresh mixtures are then cured under endogenous conditions at 25°C for 90 days to provide material C. A detailed composition is given in Table 4. Due to the easy incorporation of the OL, no phase separation is observed until hardening of the AAM.

Table 4: Formulation details of materials C presented for a total mass of 100 g.

	Material (g)	GEO	BFS
	H ₂ O	4.40	23.42
	NaOH	5.34	5.78
	Betol 39T	37.23	-
	MK	32.93	-
	BFS	-	52.05
	γ -MnO ₂ or getter	10.00	10.00
Nevastane EP100	10.10	8.74	

- Step 3b (Figure 1) consists in adding Mg powder in proportions representing 2% by mass of the total mass of the material. It is quickly introduced in the fresh grout and the mixing is carried out for 3 min at 2000 rpm until homogenization. Each fresh mixture is then directly placed in a sealed stainless-steel container and cured under endogenous conditions at 25°C to provide material D. A detailed composition is given in Table 5.

Table 5: Formulation details of materials D presented for a total mass of 100 g.

 D  10 wt.%  2 wt.%	Material (g)	GEO	BFS
	H ₂ O	4.84	25.37
	NaOH	5.88	6.26
	Betol 39T	41.00	-
	MK	36.27	-
	BFS	-	56.37
	γ-MnO ₂ or getter	10.00	10.00
	Magnesium	2.00	2.00

With this strategy, the effect of the OL on the trapping performance of the AAM added with getter is characterized independently of the trapping performance of the AAM added with getter alone. Gamma irradiation tests are used for the former (Step 3a), and magnesium corrosion is used for the latter (Step 3b).

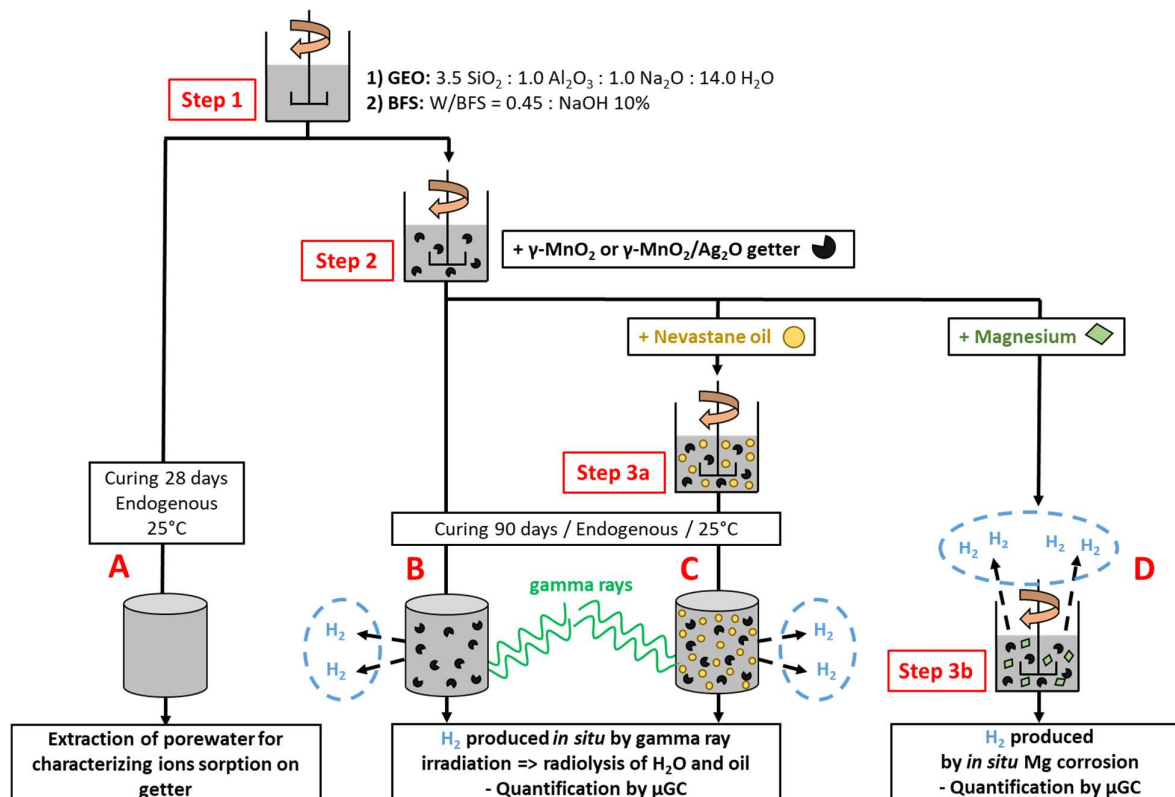


Figure 1: Graphical representation of the experimental strategy developed in this four-step research (1 to 3b), for four different material types (A to D).

2.3. Hydrogen trapping performance

Two complementary methods are used to produce dihydrogen *in-situ*:

- Gamma irradiation exposure allows producing H₂ *in-situ* by radiolysis of water and OL present in the materials. This method best represents real-life storage conditions. However, it is performed on cured materials (i.e., not from early age) and the amount of H₂ is measured at a specific cumulative dose (i.e., for a specific amount of H₂ produced).
- The presence of magnesium in alkaline conditions produces H₂ *in-situ* by magnesium corrosion. This is not representing real-life storage conditions, because in practice, no Mg powder will be dispersed into AAM for storage purposes. However, this method allows measuring the amount of H₂ produced over time directly from fresh materials (i.e. from an early age) and this can be continuously, over long periods of time. In this research, measurements are performed for 460 days (16 months).

Moreover, all AAM (materials B, C and D) are made either with the γ -MnO₂/Ag₂O getter, or with a γ -MnO₂ powder. The latter is used as a non-trapping reference powder, in order to quantify (by comparison) the H₂ trapping performance of the AAM incorporating the γ -MnO₂/Ag₂O getter, without changing the material microstructure.

2.3.1. Gamma irradiation experiments

After 90 days curing (3 months), materials B and C, with a cylindrical shaped volume of 10 mL are demolded, weighed and placed in glass vials of 105 mL. The glass vials are flame sealed under 900 mbar of pure argon (after 3 cycles of depressurization at 30 mbar and pressurization with argon to ensure air removal). The sealing ensures the confinement of any gas emitted during irradiation and radiolysis.

Each sample is subjected to external gamma irradiations (⁶⁰Co) in the experimental Gammatec irradiator in Marcoule (France). A dose rate of 1000 Gy.h⁻¹ is applied to achieve total doses of 250 kGy and 500 kGy respectively, on distinct samples (made at the same time). A Perspex dosimeter provided by Harwell [48] is used according to the ISO-ASTM 51261 procedure [49]. The temperature is regulated between 20 and 25 °C during irradiation.

After irradiation, the amount of H₂ present in the gas volume of each sealed glass vial is directly analyzed using a micro-gas chromatography (GC) analyzer Fusion from INFICON. The device is equipped with a capillary column (Restek Rt-Msieve 5A) and a thermal conductivity detector with a detection limit of 0.0001% H₂. In this experiment, pure argon is used as the carrier gas.

The H₂ molar amount $n(H_2)$ (in mol) is determined from the percentage of H₂ present in the vial gas volume (directly given by micro-GC), from the gas pressure P in the vial after irradiation (Pa) and from the free volume V in the glass vials (m³) as:

$$n(H_2) = \frac{P \cdot V \cdot \% (H_2)}{R \cdot T} \quad (1)$$

where R is the gas constant (8.314 J.mol⁻¹.K⁻¹) and T is temperature (298.15 K).

The amount of trapped H₂ per mass unit of getter (mmol/g of getter) is expressed as:

$$n(H_2)_{trapped} = \frac{n(H_2)_{MnO_2} - n(H_2)_{getter}}{m_{getter}} \quad (2)$$

where n(H₂)_{MnO₂} (in mol) is the amount of H₂ measured in the sample containing γ-MnO₂ and n(H₂)_{getter} (in mol) is the amount of H₂ measured in the sample of the same material type, but containing the γ-MnO₂/Ag₂O getter.

The trapped H₂ fraction, expressed in %, is calculated as follows:

$$Trapped\ H_2\ (\%) = \frac{n(H_2)_{MnO_2} - n(H_2)_{getter}}{n(H_2)_{MnO_2}} \times 100 \quad (3)$$

Radiolysis results are usually expressed by the radiolysis gas yield G (in mol.J⁻¹):

$$G(H_2)_{material} = \frac{n(H_2)}{m \cdot D} \quad (4)$$

where n(H₂) is the measured amount of H₂ gas (in mol), D the cumulative dose of gamma radiation (in Gray) and m the mass of the irradiated sample (in kg).

For comparison purposes with the experimental $G(H_2)_{material}$ given by Eq. (4), the theoretical hydrogen radiolytic yields are also calculated for materials B and C. The radiolytic yield of pure water $G(H_2)_{water}$ is taken from the literature (at a reference value of 4.46.10⁻⁸ mol/J) [50], whereas the radiolytic yield of the OL $G(H_2)_{OL}$ has been determined experimentally (1.65.10⁻⁷ mol/J).

In material B (Figure 1), because water radiolysis is the main significant source of H₂, the theoretical radiolytic yield G is expressed as:

$$G(H_2)_{material} = G(H_2)_{water} \times w_{water} \quad (5)$$

where w_{water} is the total mass water fraction present in the sample (i.e., both free and bound water) and G(H₂)_{water} is the radiolytic yield of pure water.

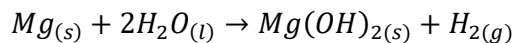
In material C (Figure 1), OL radiolysis is also a significant source of H₂ and the theoretical radiolytic yield G is then expressed as:

$$G(H_2)_{material} = G(H_2)_{water} \times w_{water} + G(H_2)_{OL} \times w_{OL} \quad (6)$$

where w_{OL} is the mass fraction of OL in the sample, and G(H₂)_{OL} the radiolytic yield of the OL.

2.3.2. Magnesium corrosion

The Pourbaix diagram of magnesium describes that in the presence of sufficiently alkaline solutions (i.e., pH > 11.5), metallic magnesium reacts with water, leading to the formation of a solid Mg(OH)₂ (brucite) layer and H₂ [43] as:



The Mg(OH)₂ layer protects the Mg metal and slows down corrosion reactions. Therefore, Mg is chosen in this study because it provides a controlled corrosion rate, and hence, a controlled H₂ production rate.

A volume of 100 mL of material D is prepared and placed in a plastic container following the procedure presented in (Figure 1), and it is directly introduced in a 1 L stainless steel reactors. The latter is tightly closed to avoid air pollution under 900 mbar of pure nitrogen (after 3 cycles of depressurization at 30 mbar and pressurization with nitrogen to ensure air removal). For each material D sample, the reactor is kept at 25°C and the evolution of the H₂ present in the vapor volume of the reactor is followed over time using micro-GC. The same device as in II.3.1 is used but with nitrogen as the carrier gas.

At given time t (expressed in days), the H₂ molar content is determined using Eq. (1) and normalized with respect to the Mg mass present in the material, as:

$$n(H_2, t) = \frac{P \cdot V \cdot \% (H_2, t)}{R \cdot T \cdot m_{Mg}} \quad (7)$$

At given time t also, the amount of trapped H₂ per unit mass of getter (mmol/g of getter) is calculated using Eq. (2). The cumulative fraction (CF) of trapped H₂ from time t=0 to time t is deduced as:

$$CF H_2 (\%) \text{ at time } t = \frac{\sum_{i=0}^t n(H_2, i)_{MnO_2} - \sum_{i=0}^t n(H_2, i)_{Getter}}{\sum_{i=0}^t n_i(H_2, i)_{MnO_2}} \times 100 \quad (8)$$

The instantaneous fraction of trapped H₂, expressed in %, is calculated from time t=1 day, as follows:

$$Trapped H_2 \text{ at time } t (\%) = \frac{[\Delta n(H_2)_{MnO_2}(t) - \Delta n(H_2)_{getter}(t)]}{\Delta n(H_2)_{MnO_2}(t)} \times 100 \quad (9)$$

where $\Delta n(H_2)_{MnO_2}(t) = n(H_2)_{MnO_2}(t) - n(H_2)_{MnO_2}(t - 1)$ is the change in the amount of H₂ measured in the sample containing γ -MnO₂ between time t and time t-1, and $\Delta n(H_2)_{getter}(t) = n(H_2)_{getter}(t) - n(H_2)_{getter}(t - 1)$ is the change in the amount of H₂ measured in the sample containing the γ -MnO₂/Ag₂O getter between time t and time t-1.

2.4. Interactions between the AAM porewaters and the getter

This part aims to determine the influence of the AAM porewater chemistry on the γ -MnO₂/Ag₂O getter, and, hence, to explain its relative efficiency in each AAM. The AAM porewater solutions are directly extracted from the solid AAM, to represent the composition of the actual porewater solutions as closely as possible.

Complementarily, the sulfides species present in the BFS-based AAM porewater are assumed to affect the getter efficiency. To prove this, a simplified interacting solution, containing sulfite species and mimicking reductive conditions present in BFS-based materials [51], is used.

The getter is put in contact with both solution types, and several analysis methods are used to characterize the changes in its structure.

Details of the solutions, experimental protocol and analysis methods are given in Appendix.

3. Results and analysis

3.1. H₂ trapping performance of hardened AAM in presence of getter and OL (materials B and C)

Figure 2 displays the experimental radiolytic yields $G(H_2)_{material}$ for all samples made with γ -MnO₂ or γ -MnO₂/Ag₂O getter, compared to the theoretical radiolytic yield of hydrogen.

With γ -MnO₂, materials B (i.e. without oil) have a significant H₂ production rate with $G(H_2)_{material}$ ranging from $9.3 \cdot 10^{-9}$ mol/J (BFS at 500 kGy) to $1.33 \cdot 10^{-8}$ mol/J (GEO at 250 kGy) depending on the material and on the cumulative dose considered. The experimental radiolytic yields are close to the theoretical values for the two AAM.

With the γ -MnO₂/Ag₂O getter, all materials B have a significantly lower hydrogen production, with values ranging from $0.07 \cdot 10^{-10}$ mol/J (GEO at 500 kGy) to $4.45 \cdot 10^{-9}$ mol/J (BFS at 500 kGy), again depending on the material and on the cumulative dose considered. This means that in presence of getter, for GEO, the H₂ production is lower by more than two orders of magnitude when compared with γ -MnO₂-based materials. For BFS-based AAM, however, the H₂ production only decreases by 52-65%, depending on the cumulative dose.

With γ -MnO₂, materials C (i.e. with oil) have a significant H₂ radiolytic yield ranging from $1.15 \cdot 10^{-8}$ mol/J (BFS at 250 kGy) to $3.41 \cdot 10^{-8}$ mol/J (GEO at 250 kGy) depending on the material and on the cumulative dose considered. GEO displays experimental radiolytic yields close to the theoretical value, meaning that the OL produces H₂ as expected. On the contrary, BFS displays a radiolytic yield significantly lower than (i.e., about half lower than) the theoretical one; in both cases, $G(H_2)_{material}$ is of the same order of magnitude. This could be attributed

to the fine pore structure of BFS-based AAM, which slows down the release of H₂ produced from the samples.

With the γ -MnO₂/Ag₂O getter, the radiolytic yield $G(H_2)_{material}$ of GEO materials with OL (materials C) is on average of $2.71 \cdot 10^{-9}$ mol/J (at 250 kGy) and $4.23 \cdot 10^{-9}$ mol/J (at 500 kGy). This is one order of magnitude lower than γ -MnO₂-based materials. In BFS, the H₂ production is slightly lower than that of the samples containing γ -MnO₂. For instance, at 250kGy cumulative dose, $G(H_2)_{material}$ is on average of $1.15 \cdot 10^{-8} \pm 0.22$ mol/J with γ -MnO₂ and $0.86 \cdot 10^{-8} \pm 0.12$ mol/J with the γ -MnO₂/Ag₂O getter. This means that the getter does not have an actual efficiency towards H₂ trapping.

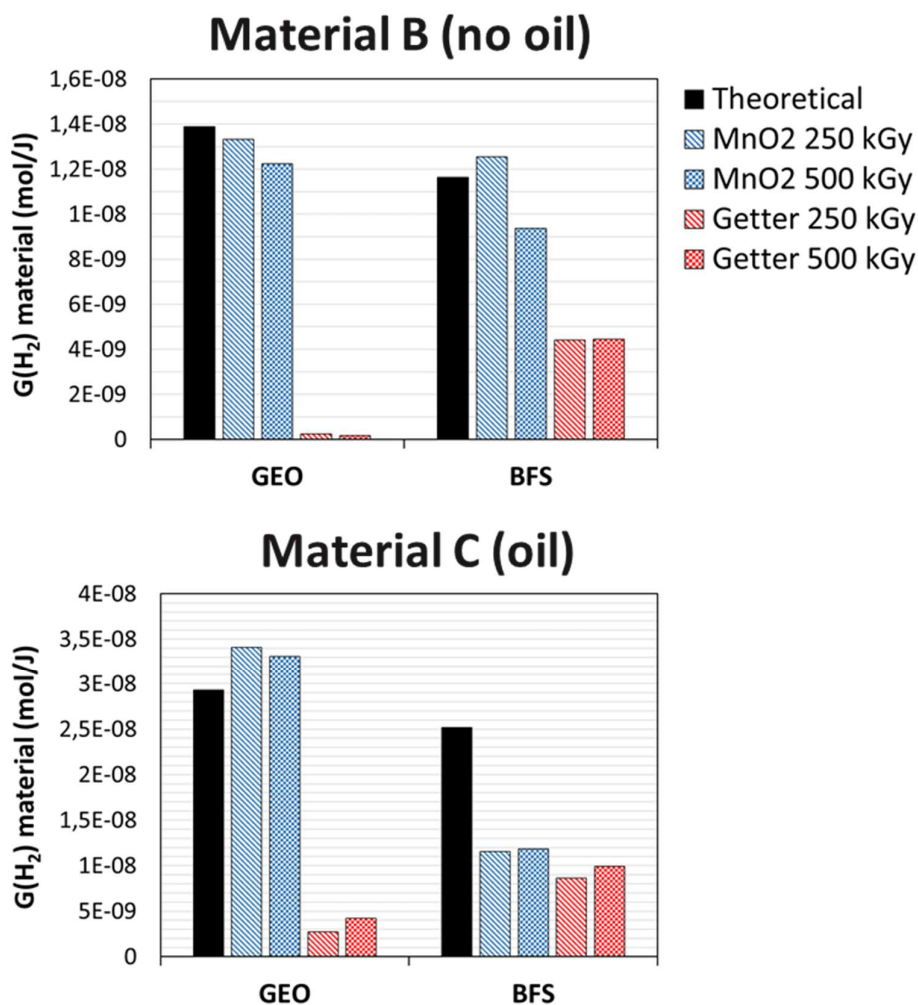


Figure 2: Experimental hydrogen radiolytic yields in (mol/J) for materials B and C made with γ -MnO₂ (blue columns) or γ -MnO₂/Ag₂O getter (red columns), depending on the cumulative dose (striped pattern at 250 kGy and checkered pattern at 500 kGy), compared to theoretical radiolytic yields (black columns on the left).

Figure 3 summarizes the H₂ trapping efficiency of both AAM after 250 or 500 kGy gamma irradiation. The trapping efficiency is either expressed in mmol/g of getter (left) or normalized relatively to the same material made with γ -MnO₂ in % (right).

In GEO, in the absence of OL (i.e. in materials B), the trapping efficiency reaches almost 100% (with average values of 98.1-98.7% depending on the cumulative dose), whereas in BFS, the trapping efficiency is between 52 and 65% (depending on the cumulative dose).

In presence of OL (i.e. in materials C), again in GEO, the trapping efficiency remains high, with a value of 87-92% (depending on the cumulative dose). In BFS+OL, the trapping efficiency is very low, with values between 16 and 25%.

It is concluded that the trapping efficiency of the γ -MnO₂/Ag₂O getter efficiency is poor in BFS-based AAM.

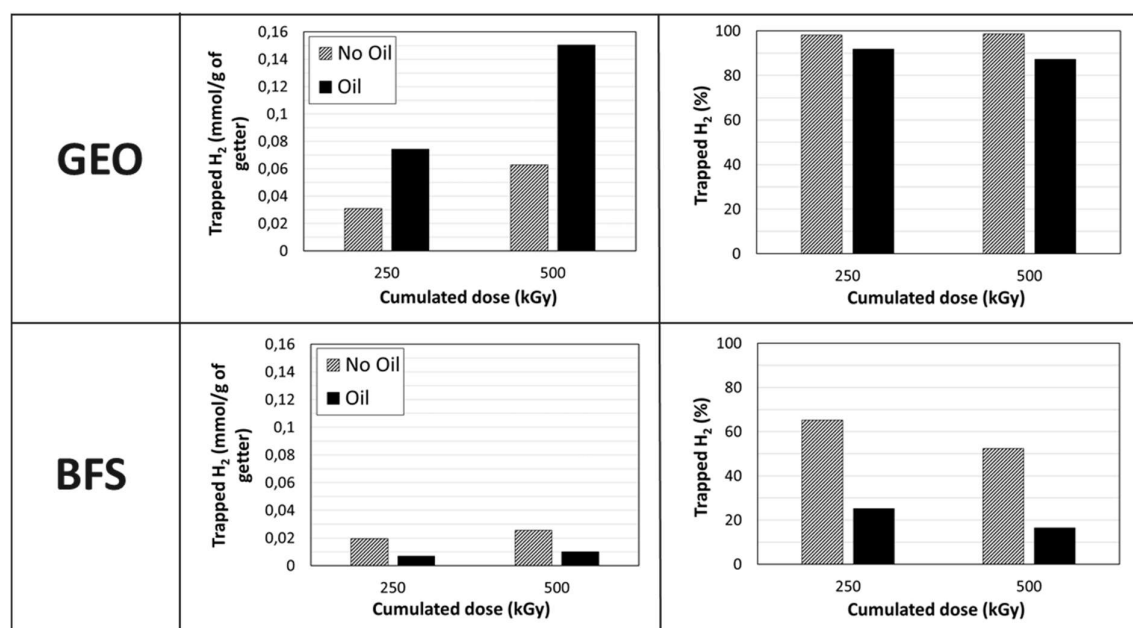


Figure 3: Trapped H₂ expressed in (mmol/g of getter) or relatively to the same material made with γ -MnO₂ in (%) for the three materials (GEO and BFS) after gamma irradiation (in kGy).

3.2. Continuous H₂ trapping performance of AAM in presence of getter (materials D)

The corrosion of Mg powder introduced in material D (Figure 1) provides continuous *in situ* H₂ release for long periods of time (for over a year, see [52]). These are recorded and analyzed in the following, in presence of non-trapping γ -MnO₂ or of getter inside the AAM (and no OL).

3.2.1. Trapping kinetics

Figure 4 displays the amount of hydrogen released by γ -MnO₂-based materials and γ -MnO₂/Ag₂O getter-based materials as a function of time. Each experiment is duplicated. The amount of Mg is slightly different in each material (from 3.085 to 3.55g Mg for samples of 154.25 to 177.5g). Therefore, results are normalized with respect to the mass of Mg initially introduced in each sample.

Given the amount of H₂ released from non-trapping γ -MnO₂-based materials, Mg corrosion is very fast at an early age in both AAM materials (for the first 28 days), and then it progressively decelerates, without reaching an asymptote after 443 to 464 days (depending on the sample considered). This deceleration is attributed to (1) the hardening of the AAM, which pore structure decreases the mobility of the reactive species and (2) mainly to the formation of a brucite (i.e. Mg(OH)₂) protective layer at high pH (i.e. for a pH > 11.5), as observed in [53]. Moreover, for all samples, Mg corrosion continues even after the end of the recordings because Mg corrosion continues [51].

In the absence of getter, the lowest cumulative amount of released H₂ is in GEO-based AAM. On average, the cumulative amount of released H₂ in GEO is of 4.84 mmol/g Mg +/-0.04 and it is of 5.69 mmol/g Mg +/- 0.3 in BFS-based AAM.

In contrast, in getter-based materials, the amount of released H₂ is significantly lower, with cumulative amounts of 0.19-0.44 mmol/g Mg for GEO and of 2.29-2.38 mmol/g Mg for BFS-based AAM. At an early age, and until 28-91 days for BFS and 190-308 days for GEO, the amount of released H₂ is below 0.1 mmol/g Mg.

3.2.2. Trapping efficiency

Figure 5 summarizes the cumulative trapped H₂ of both AAM materials. It is either expressed in mmol/g of getter (top graph) or in % (with respect to the same material made with γ -MnO₂, bottom graph).

As a matter of comparison, the cumulative amount of trapped H₂ is significantly greater with the corrosion method than after exposure to gamma radiations. For instance, for BFS, the cumulative amount of trapped H₂ is of 0.02 mmol/g of getter after gamma irradiation (Figure 3), whereas it is of 0.67 mmol/g of getter +/-0.07 after 443-464 days Mg corrosion (Figure 5).

For up to about 200 days, the amount of trapped H₂ is significant in both AAM. No statistically significant difference is observed between them. After that, the amount of trapped H₂ stabilizes in BFS materials, while it keeps increasing in GEO materials, without reaching an asymptote at the end of the tests (after 443 to 464 days).

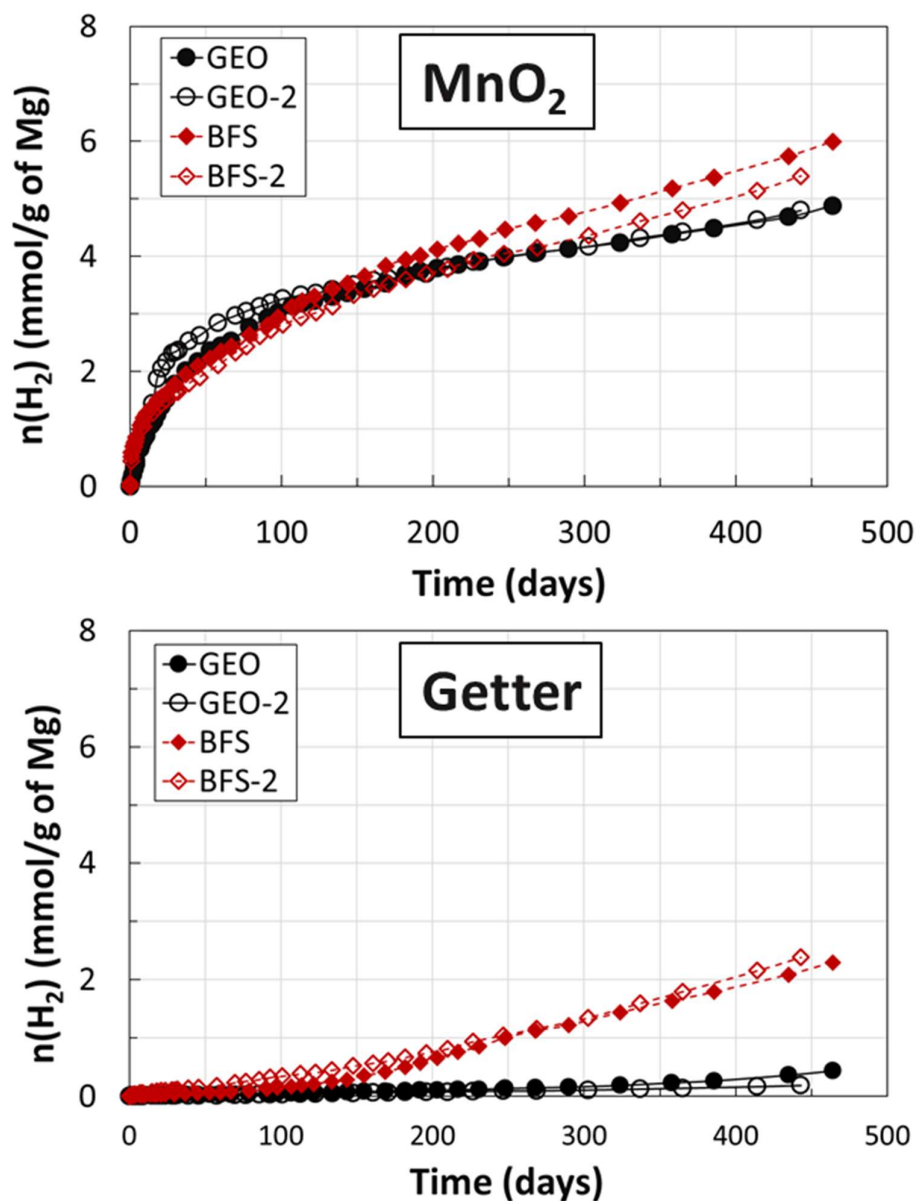


Figure 4: H₂ released over time in materials D made with γ -MnO₂ or γ -MnO₂/Ag₂O getter for the three materials (GEO and BFS) expressed in (mmol/g of Mg). Each experiment is duplicated (GEO or GEO-2 and BFS or BFS-2).

After 443-464 days, the cumulative amount of trapped H₂ in BFS materials is limited to 0.67 mmol/g of getter +/-0.07. During the continuous corrosion process, the cumulative trapped H₂ percentage (with respect to the same material made with γ -MnO₂) decreases in BFS materials, down to 59% +/-3 after 443-464 days.

Comparatively, in GEO materials, the cumulative amount of trapped H₂ is greater (0.91 mmol/g of getter +/- 0.01) after 443-464 days. Simultaneously, the cumulative trapped H₂ percentage remains stable, with an average value of 93.5% +/-2.5 after 443-464 days.

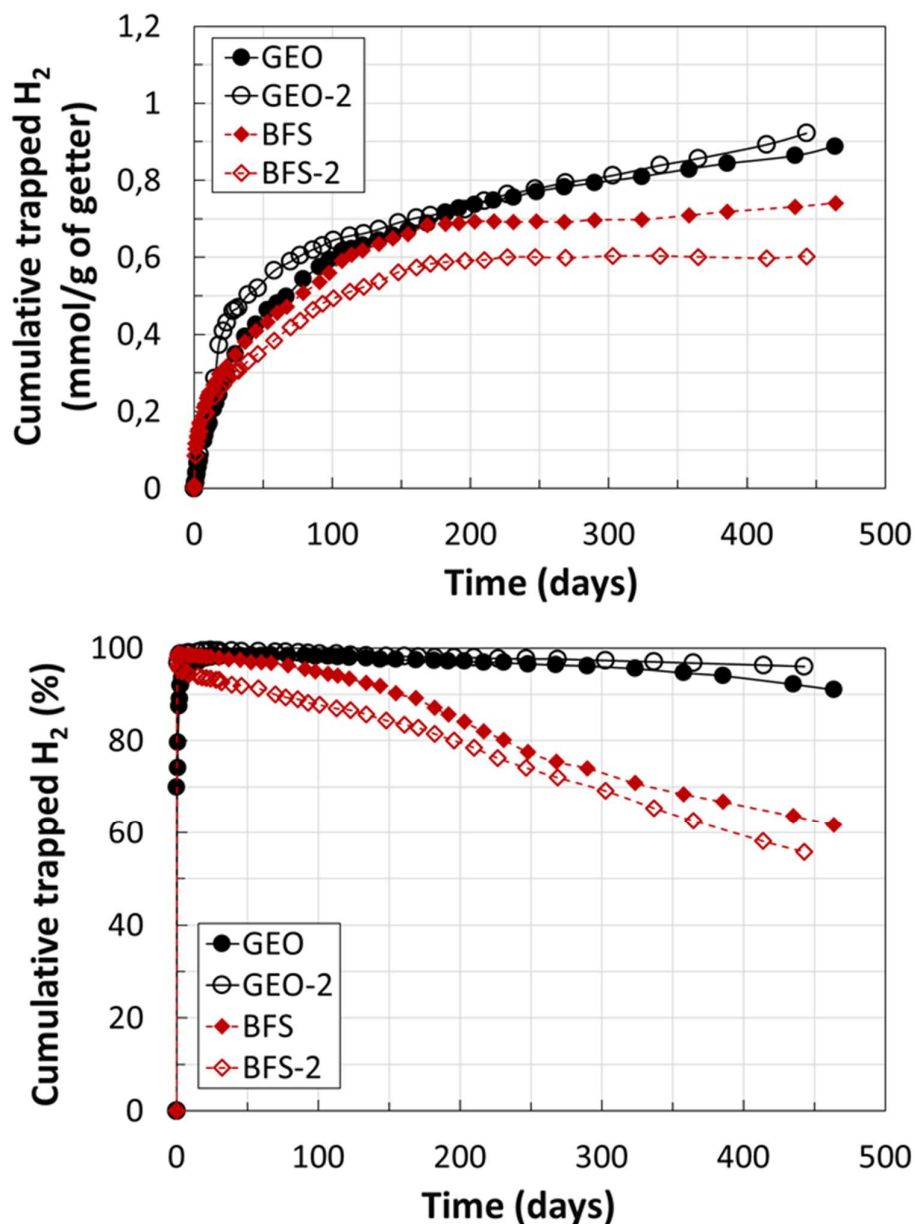


Figure 5: Evolution of trapped H₂ over time in materials D for both AAM (GEO and BFS) expressed (top) in (mmol/g of getter) or (bottom) in % (with respect to the same material made with γ -MnO₂). Each experiment is duplicated (GEO or GEO-2 and BFS or BFS-2).

Finally, the instantaneous trapped H₂ percentage is calculated for both AAM (Figure 6). In BFS materials, this parameter remains greater than 75% during the first 100 days. After that period of time, the instantaneous trapped H₂ percentage decreases significantly, down to 0% reached at about 215 days (7 months and a half). After that duration, the trapped H₂ percentage oscillates around zero, meaning that the getter-added BFS material no longer provides H₂ trapping. The instantaneous trapped H₂ percentage remains significant in GEO AAM, with values ranging between 63 and 88% after 443-464 days.

Comparatively, after the gamma irradiation test of BFS materials, the amount of trapped H₂ is very limited. In such instance, the production of H₂ starts only after 3 months curing. This means that the γ -MnO₂/Ag₂O getter has probably lost a significant part of its efficiency after such duration. In the Mg corrosion test, H₂ is produced at an early age, as it will be in the industrial case. In such instance, from an early age, H₂ can be trapped by the γ -MnO₂/Ag₂O getter before it loses efficiency.

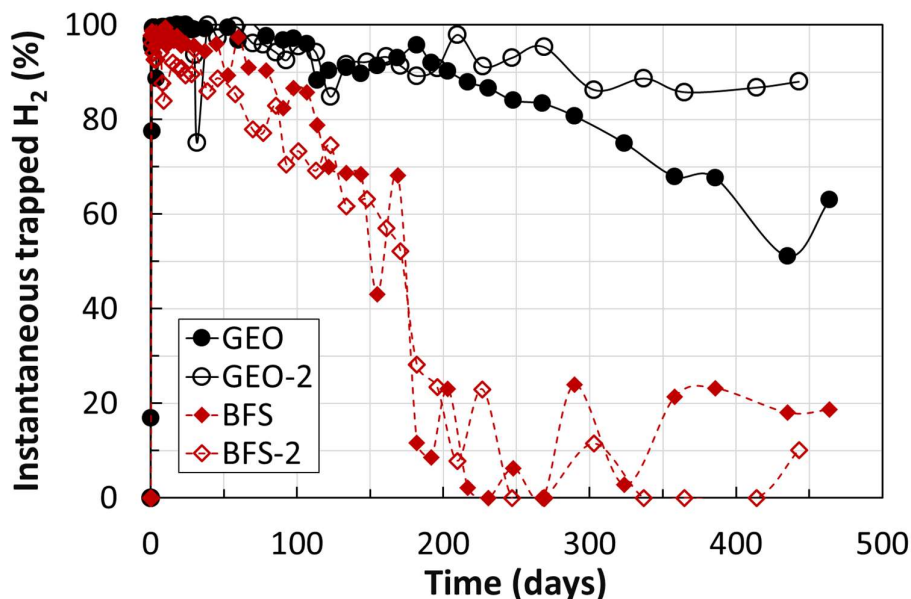


Figure 6: Trapping efficiency - evolution of instantaneous trapped H₂ fraction in materials D made with γ -MnO₂ or γ -MnO₂/Ag₂O getter for both materials (GEO and BFS), calculated at a given time and expressed relatively to the same material made with γ -MnO₂ in %.
Each experiment is duplicated (GEO or GEO-2 and BFS or BFS-2).

3.3. Influence of the porewater chemistry on the γ -MnO₂/Ag₂O getter

In this section, the γ -MnO₂/Ag₂O getter powder is placed in contact with two types of aqueous solutions. The first ones are directly extracted from materials A (Figure 1) to represent the actual AAM porewaters, and the second one is a sodium sulfide solution, used to mimic the reductive species present in the BFS-based material at an early age.

3.3.1. Interactions between porewaters and γ -MnO₂/Ag₂O getter

This experiment aims, in a qualitative way, to highlight the strong tendency of the γ -MnO₂/Ag₂O getter to adsorb ions present in the AAM porewaters on its surface.

The γ -MnO₂/Ag₂O getter is placed in contact with the AAM porewaters directly extracted from 28 days cured materials (see Appendix A.1 and A.2).

3.3.1.1 Ion sorption at the surface of the γ -MnO₂/Ag₂O getter

The composition of the extracted porewaters is analyzed by ICP-AES before and after contact with the γ -MnO₂/Ag₂O getter. Results are given in Figure 7 (black columns are before contact with getter and striped columns are after contact with getter).

In both AAM (i.e. GEO and BFS), the alkaline activating solutions contain high amounts of sodium ions, which significantly adsorb at the surface of the getter (Figure 7, bottom). In GEO material, small amounts of potassium and phosphorus-based ions (cations and anions) are released by the getter, whereas sulfur and silicon-based ions (mainly anions) are trapped. In BFS, aluminum-based ions are slightly adsorbed, whereas calcium cations, potassium cations and sulfur anions are all adsorbed on the getter surface; silicon and phosphorus-based ions are not present.

According to [37], the getter surface is negatively charged in alkaline conditions ($\equiv\text{Mn-O}^-$) and therefore has a strong tendency to adsorb cations by electrostatic interactions. For instance, a strong sorption of calcium cations is observed in Portland cements, as reported earlier [54]. According to these earlier researches, anions were not expected to adsorb on the getter surface. However, the sorption of anions observed in this research is attributed to the preliminary sorption of cations, which changes the surface charge of the getter from negative to positive, allowing the sorption of anions in a double layer.

Overall, this section shows that the γ -MnO₂/Ag₂O getter has a strong tendency to adsorb ions on its surface, both anions and cations, and this may have an impact on the getter H₂ trapping properties.

3.3.1.2 XRD results

Before and after contact with the different porewater solutions, the crystalline phase blend of the γ -MnO₂/Ag₂O getter is determined by qualitative XRD (Figure 8). According to the literature [36], the γ -MnO₂/Ag₂O getter is supposed to have a hardly crystalline structure, so that the phase identification is not straightforward. Some bumps on the XRD patterns actually indicate the presence of non-crystalline matter.

However, the presence of crystallized pyrolusite (PDF 01-071-0071) is observed on the XRD pattern of the getter powder used in this paper. According to [55], the presence of pyrolusite strongly decreases the H₂ trapping kinetics of the γ -MnO₂/Ag₂O getter. There is also a slight presence of metallic silver (PDF 03-065-2871), which has no catalytic effect on H₂ dissociation [56], [57]. However, the first part of this paper highlighted the significant efficiency of the γ -MnO₂/Ag₂O getter, indicating that these two unwanted species are present as impurities. Their presence may be due to the manufacturing process of the γ -MnO₂/Ag₂O getter.

The main observation is that porewater solutions extracted from the AAM do not impact the γ - $\text{MnO}_2/\text{Ag}_2\text{O}$ getter crystalline structure (Figure 8).

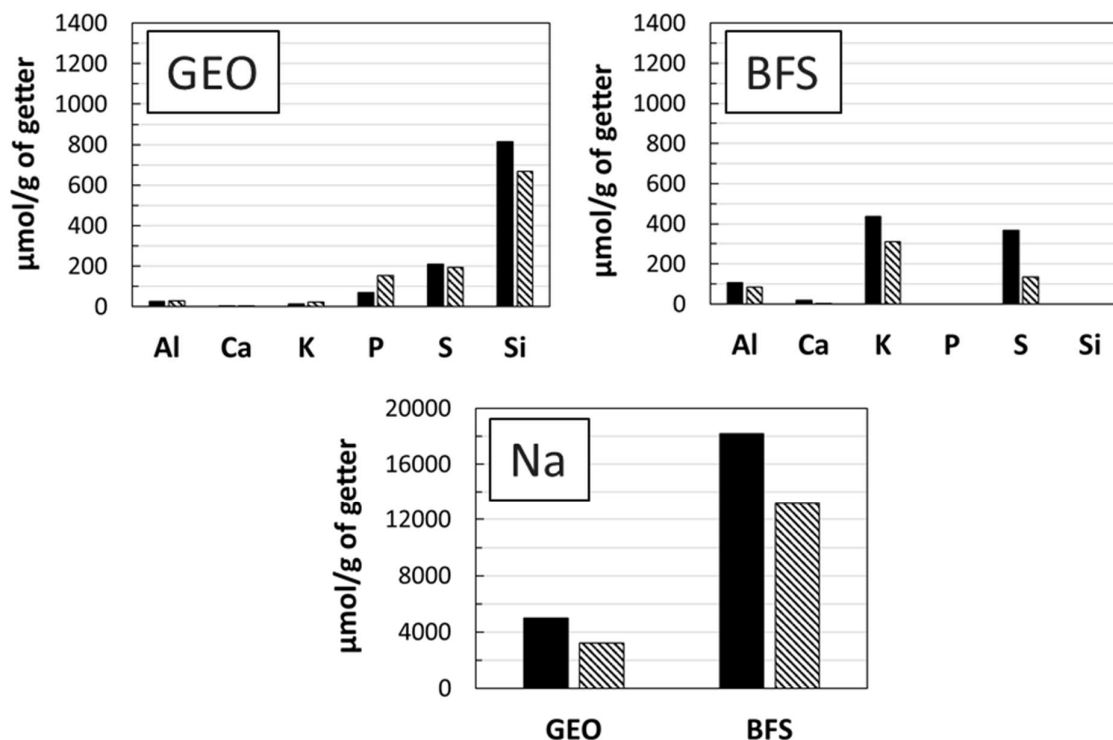


Figure 7: Sorption of Al, Ca, K, P, S, Si and Na elements present in pore-water. Solid columns represent the concentration of elements before contact with the getter and striped column represent the concentration after contact with the getter. The sorption of Na is on a separate graph due to an important concentration requiring a dedicated scale.

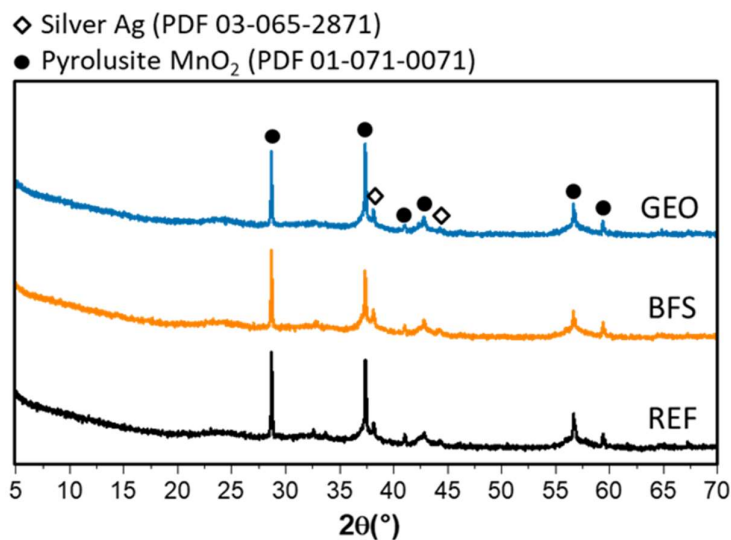


Figure 8: Comparison of XRD patterns for γ - $\text{MnO}_2/\text{Ag}_2\text{O}$ getter powder before contact with pore-water solutions (black) and after contact with pore-waters extracted from BFS (orange) and GEO (blue) materials.

3.3.1.3 Hydrogen trapping capacity of $\gamma\text{-MnO}_2/\text{Ag}_2\text{O}$ getter powder

The trapping capacity of the $\gamma\text{-MnO}_2/\text{Ag}_2\text{O}$ getter before and after contact with the alkaline pore-waters is given in Figure 9. First of all, the trapping efficiency of the unaltered getter powder is on the order of 4 mmol/g of getter, which is lower than the experimental trapping capacity of about 5.7 mmol/g of getter determined by Farcy [37]. This difference is attributed to the presence of crystallized pyrolusite and metallic silver observed on the XRD pattern in Figure 8.

After contact with the alkaline porewaters for 116-120 days, the H_2 trapping capacity of the getter powder is reduced by about 50%, with only a slight difference between the two distinct porewaters (slightly more H_2 is trapped in GEO than in BFS). This is attributed to the sorption of ions observed in Figure 7, which decreases the H_2 trapping kinetics and/or the trapping efficiency by making the reactive sites of the $\gamma\text{-MnO}_2$ less accessible and/or inaccessible. This is an important result as it highlights that the theoretical trapping efficiency of the $\gamma\text{-MnO}_2/\text{Ag}_2\text{O}$ getter powder is no to be considered when incorporated into cementitious materials. However, this test is not discriminatory and does not explain why the $\gamma\text{-MnO}_2/\text{Ag}_2\text{O}$ getter is less efficient in BFS-based AAM.

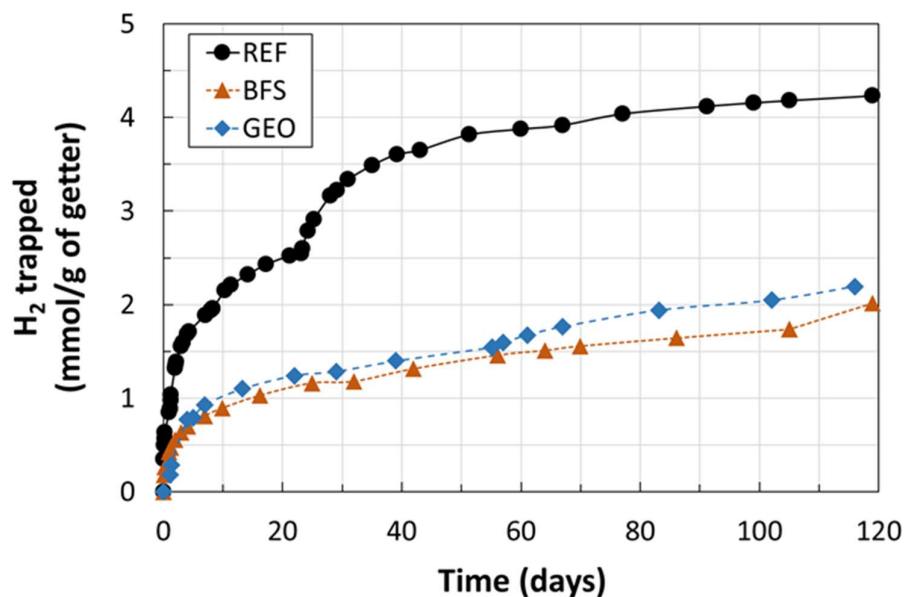


Figure 9: Comparison of the $\gamma\text{-MnO}_2/\text{Ag}_2\text{O}$ getter powder H_2 trapping capacity before contact with alkaline pore-waters (black) and after contact with pore-waters extracted from BFS (orange) and GEO (blue) materials.

3.3.2. Interaction between sulfides and γ -MnO₂/Ag₂O hydrogen getter

3.3.2.1 SEM observations of the γ -MnO₂/Ag₂O getter powder

Macro-photographs and SEM micrographs of the γ -MnO₂/Ag₂O getter are given before and after contact with the sodium sulfide solution (Figure 10).

First, after contact with sulfides, visual observations highlight that the getter powder has undergone a color change from black (Figure 10 top left) to brown (Figure 10 top right). As γ -MnO₂ is the major constituent of the getter, this color change is attributed to a possible change in the oxidation state of γ -MnO₂. A structural change of Ag₂O is also possible.

With SEM observations (Figure 10 second and third lines, left), the γ -MnO₂/Ag₂O getter powder, before contact with the sulfides solution, displays a typical ovoid form of γ -MnO₂ particles, with varied size ranging from a few microns to 40 μ m. The surface roughness is attributed to the presence of Ag₂O at the surface of γ -MnO₂ [39]. After contact with the sulfides solution (Figure 10 second and third lines, right), γ -MnO₂/Ag₂O getter particles have a different surface state, marked by the presence of small crystallites at the surface of γ -MnO₂ grains. Due to surface roughness and small crystal size, the EDX analysis is not conclusive to determine what crystals have formed. Let now use XRD to observe possible crystalline structure changes.

3.3.2.2 XRD results

The crystalline phase blend of the γ -MnO₂/Ag₂O getter powder after contact with the sodium sulfides solution is determined by qualitative XRD and compared to the XRD pattern of untreated getter powder (Figure 11). After contact with the sulfide species, many peaks appear on the getter XRD pattern. They are attributed to the presence of silver sulfide Ag₂S (PDF 01-080-5476). The emergence of low intensity peaks (32°, 37°) corresponding to the powder diffraction profile of Mn₃O₄ is also observed (PDF 01-075-1560). Finally, a strong peak at $2\theta = 20^\circ$ could not be attributed by the computing system to any powder diffraction profile corresponding to the elements in presence. According to [58], this peak could be attributed to MnSO₄ salt.

3.3.2.3 Hydrogen trapping capacity of γ -MnO₂/Ag₂O getter

The trapping capacity of the γ -MnO₂/Ag₂O getter before and after contact with the sodium sulfides solution is given in Figure 12. After contact with the sulfides solution, the trapping capacity of the getter is divided by a factor of 11; the trapping capacity is lower than 0.4 mmol/g of getter and remains stable. This is attributed both to the change of amorphous Ag₂O into crystalline Ag₂S and to the possible reduction of γ -MnO₂ in Mn₃O₄ or other species. Previous studies highlighted the reduction of MnO₂ into Mn₂O₃ by reacting with sulfides

present in BFS [59]. The γ - $\text{MnO}_2/\text{Ag}_2\text{O}$ trapping mechanism involves the reduction of MnO_2 in MnOOH supported by amorphous Ag_2O catalysis [55]. The crystalline Ag_2S that is formed might not be as efficient as Ag_2O to promote the dissociation of dihydrogen molecules. Additionally, if γ - MnO_2 is already in a reduced state (Mn_2O_3 , Mn_3O_4 , etc.), the trapping capacity will be consequently reduced. Further X-ray photoelectron spectroscopy (XPS) analysis could allow confirming the chemical changes occurring to the getter constituents when placed into contact with sulfide species.

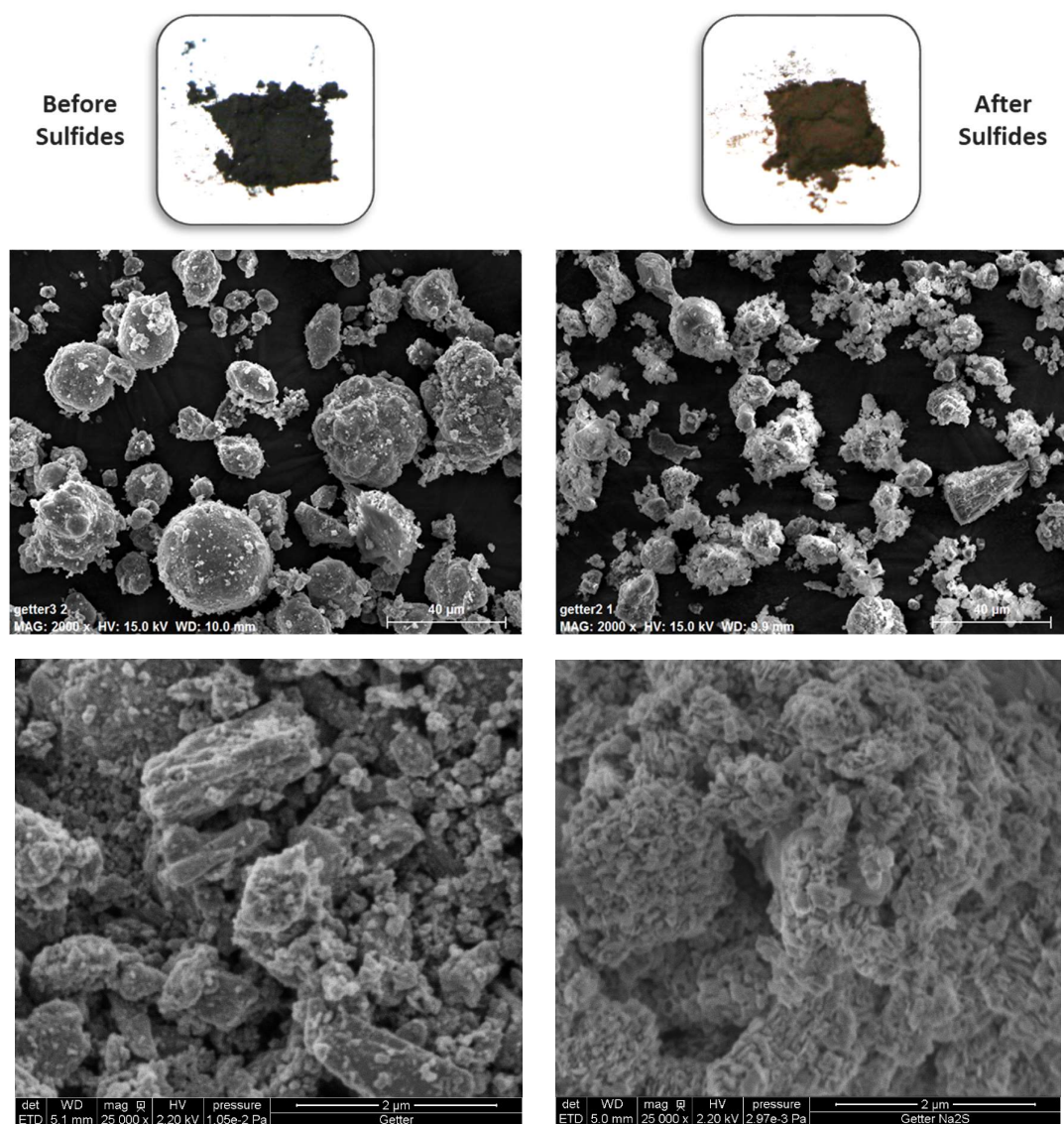


Figure 10: Photographs and SEM observations in backscattered electron mode of γ - $\text{MnO}_2/\text{Ag}_2\text{O}$ getter powder before contact with sulfides (left) and after contact with sulfides (right).

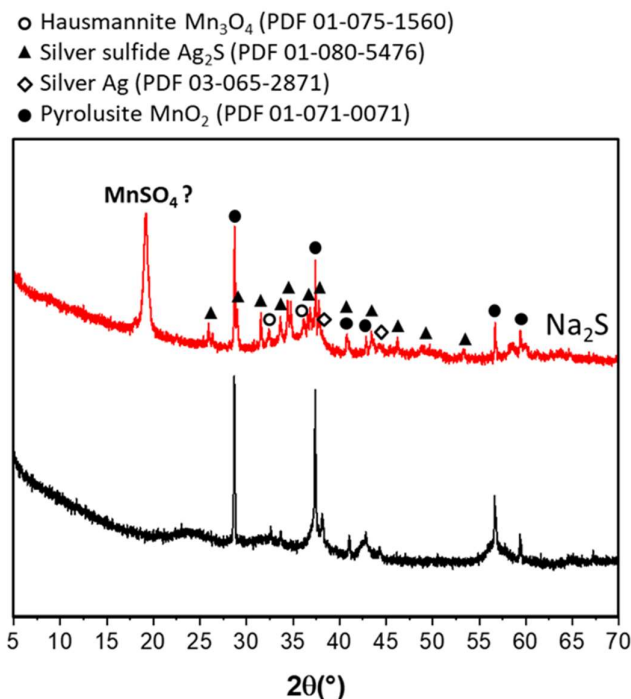


Figure 11: Comparison of XRD patterns for γ - MnO_2/Ag_2O getter powder before contact with sulfides (black) and after contact with sulfides (red).

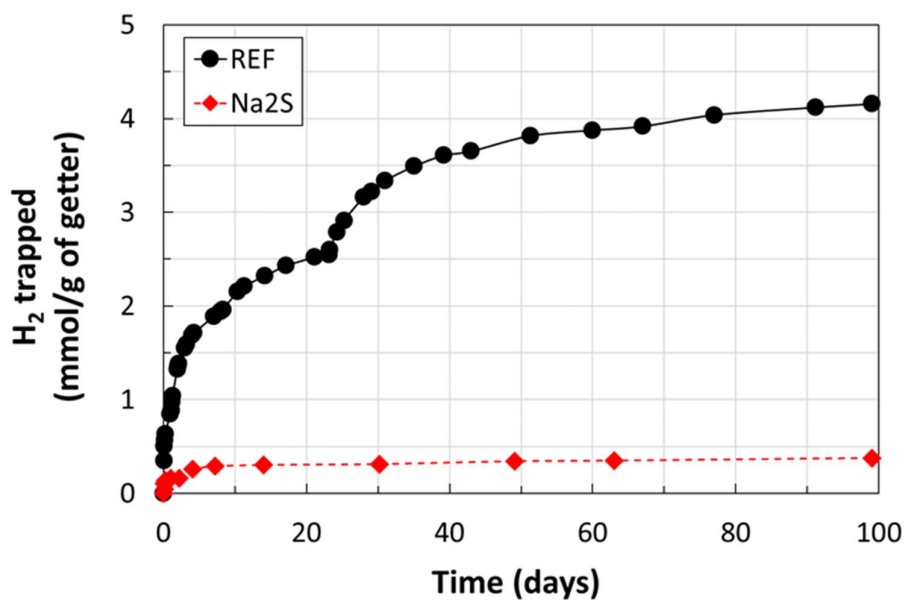


Figure 12: Comparison of the γ - MnO_2/Ag_2O getter powder H₂ trapping capacity before contact with the sodium sulfides solution (solid circle) and after contact with the sodium sulfides solution (empty circles).

4. Conclusion

This research has determined the hydrogen trapping efficiency of two novel AAM, either based on MK or on BFS, functionalized with 10 wt.% of a γ -MnO₂/Ag₂O getter. Results are summarized as follows:

- The efficiency of the γ -MnO₂/Ag₂O getter is assessed in AAM by in-situ hydrogen production. After gamma irradiation with cumulative doses of up to 500 kGy, GEO materials made with getter have a hydrogen trapping efficiency of almost 100% in the absence of OL and about 90% in the presence of OL, when compared to the irradiation of identical materials made with a non-trapping γ -MnO₂ powder. On the contrary, BFS-based materials with getter have a trapping efficiency of 50% in the absence of OL and about 20% in the presence of OL.
- The presence of OL does not reduce the trapping capacity, but it has an impact on the H₂ trapping kinetics.
- After 443-464 days Mg corrosion, without OL, the amount of trapped H₂ in BFS material is limited to 0.7 mmol/g of getter, while is it higher in GEO material. This means that GEO functionalized with γ -MnO₂/Ag₂O getter display excellent hydrogen trapping efficiency, but it is not the case of BFS-based materials.
- Complementarily, the contact of the γ -MnO₂/Ag₂O getter powder with the AAM porewaters highlights the strong tendency of the getter to adsorb ions on its surface, both cations and anions. With both types of alkaline porewaters, this reduces the H₂ trapping capacity of the getter by 50%.
- Finally, the γ -MnO₂/Ag₂O getter is placed into contact with sulfides, which are present in BFS-based materials. X-Ray Diffraction (XRD) and Scanning Electron Microscopy (SEM) evidence that the structure of the getter is modified after contact with sulfide species. The amorphous Ag₂O promoter reacts into crystalline Ag₂S and the γ -MnO₂ is most likely reduced, but the exact reaction product could not be determined. This leads to a surface-modified getter powder and explains its poor efficiency for H₂ trapping in alkali-activated BFS materials.

In further research, the efficiency of H₂ mitigation should be tested with greater gamma doses (> 1000 kGy), at varying dose rates, to assess the H₂ trapping capacity of the getter in GEO materials and also the trapping kinetics. More generally, the influence of the γ -MnO₂/Ag₂O getter on the reactivity and final properties of GEO materials should be assessed.

Considering the tritium issue, the proposed getter is able to reduce T₂ or HT releases but does not prevent tritiated water (HTO) to move out from waste packages. This will also require additional investigations (HTO diffusion experiments).

Appendix: Interactions between the AAM porewaters and the getter

A.1- Preparation of the different solutions

- Solutions 1 (S1): After 28 days curing, a sample of material A is broken into centimetric pieces. 30 g are mixed with 30 g distilled water and left under stirring for half an hour. The mixture is then filtered using a Buchner funnel over 0.20 μm filters. The clear solution obtained represents the composition of the porewater of material A. The pH is measured to ensure the quality of the extraction. For both BFS and GEO materials, the pH of the extracted solutions is greater than 12.
- Solution 2 (S2): 2 g of Na₂S salt are dissolved in 100 mL of distilled water. The mixture is left under stirring until complete dissolution.

A.2- Experimental approach

The $\gamma\text{-MnO}_2/\text{Ag}_2\text{O}$ getter powder is placed in contact with one of the two solutions S1 or S2, with the following protocol:

- Protocol for S1: 5 g of getter powder are suspended in 100 mL of S1 and left under stirring for a week. This period allows the getter to interact with the ionic species present in S1 and to reach equilibrium. The getter is then filtered using a Buchner funnel and 0.20 μm filters. The S1 solutions are kept, and the getter powder is dried at 80°C for 24 hours.
- Protocol for S2: 2 g of getter powder are suspended in 100 mL of S2 during 24h. The getter powder is then filtered using a Buchner funnel and 0.20 μm filters. The getter powder is dried at 80°C for 24 hours.

A.3- Analysis

The $\gamma\text{-MnO}_2/\text{Ag}_2\text{O}$ getter powder is characterized before and after contact with the two solution types.

SEM observations. Microscopic observations of $\gamma\text{-MnO}_2/\text{Ag}_2\text{O}$ getter powder are performed by Scanning Electron Microscopy (SEM) (FEI Inspect S50, high vacuum mode, acceleration voltage of 15 kV, current intensity of 50 nA, and working distance of 10 mm).

XRD analysis. X-ray diffraction (XRD) patterns of $\gamma\text{-MnO}_2/\text{Ag}_2\text{O}$ getter powder are identified with the Bragg Brentano geometry (PANalytical X'Pert PRO MPD - copper anode $\lambda\text{K}\alpha_1 = 1.54056 \text{ \AA}$ generated at 45 mA and 40 kV, X'celerator detector). The XRD patterns are collected in the 2θ range 5–70° with 0.017° steps, corresponding to 0.625 s measurement time per step.

ICP-AES analysis. The composition of S1 is evaluated before and after contact with the $\gamma\text{-MnO}_2/\text{Ag}_2\text{O}$ getter by inductively coupled plasma atomic emission spectroscopy (ICP-AES, using a Thermo Scientific iCAP 6000 Series device). According to the literature, the focus is

given on the main elements present in OPC and AAM pore-waters, i.e. Na, Al, Ca, K, P, S, Si [60].

Trapping efficiency. This test aims at assessing the trapping efficiency of the γ -MnO₂/Ag₂O getter powder. 1 g of getter powder is introduced in a 1L stainless steel reactor. This reactor is then tightly closed in order to avoid air pollution. As in [30], a gas mixture of H₂/N₂ in molar proportions 4/96 is introduced in the reactor at a pressure of 1.3 bar. The evolution of the H₂ present in the vapor phase of the reactor is then followed over time using GC (the same device as in 3.1 is used but with nitrogen as carrier gas). The H₂ molar quantification is made using Eq. (1).

The molar amount of H₂ trapped as a function of time, per unit of mass of getter, is determined as follows:

$$n(H_2)_{trapped} = \frac{[n(H_2)_0 - n(H_2)_t]}{m_{getter}}$$

where $n(H_2)_0$ is the amount of H₂ initially present in the reactor (in mol), $n(H_2)_t$ is the amount of H₂ present in the reactor at time t (in mol), and m_{getter} the mass of getter initially introduced inside the reactor (in g). If necessary, i.e. when the molar proportion of H₂ in the gas mixture of H₂/N₂ is lower than 1/99, the vapor phase in the reactor is renewed with the same H₂/N₂ (4/96) gas mixture until saturation of the getter powder is achieved.

References

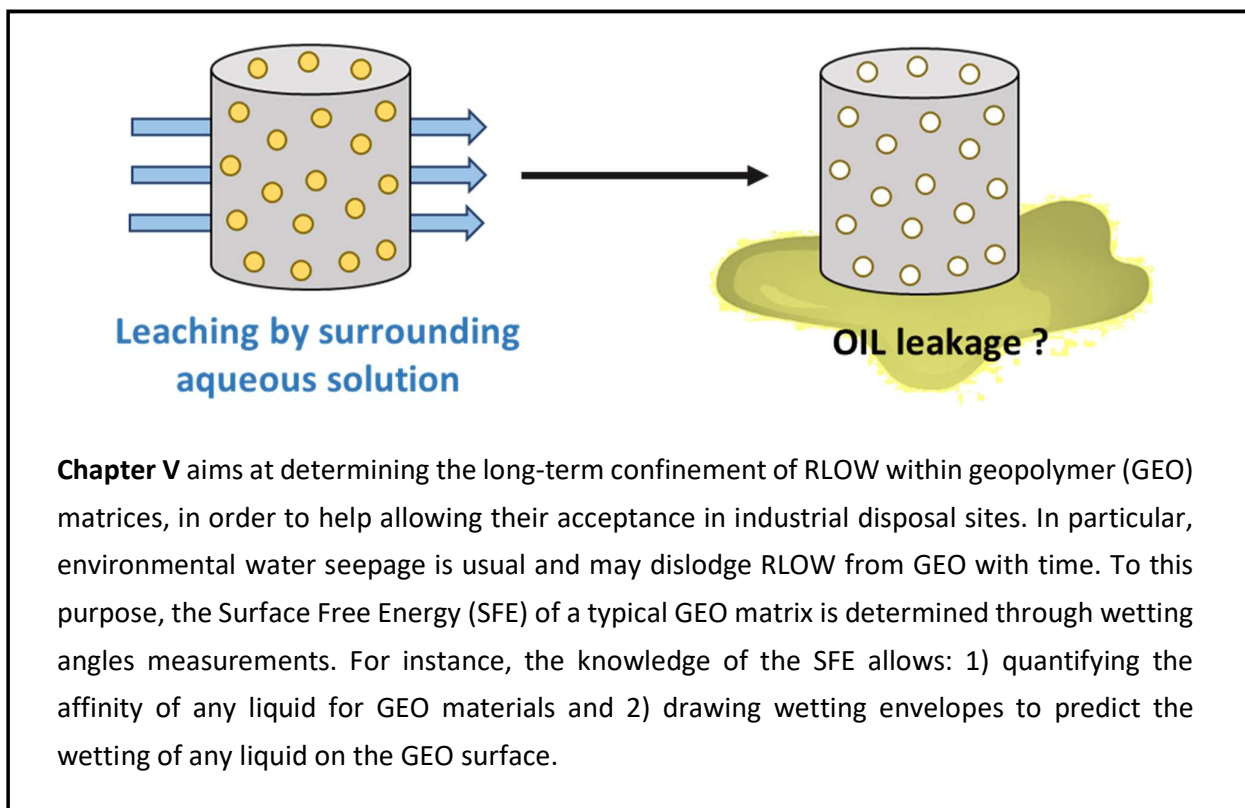
- [1] ANDRA (Agence Nationale de gestion des Déchets RADIOactifs), Synthesis report: National Inventory of Radioactive Materials and Waste, France, 2018, https://international.andra.fr/sites/international/files/2019-03/Andra-Synthese-2018_EN_relu_HD.pdf
- [2] Status and trends in Spent Fuel and Radioactive Waste Management', International Atomic Energy Agency (IAEA), 2022, https://www-pub.iaea.org/MTCD/Publications/PDF/PUB1963_web.pdf
- [3] IAEA (International Atomic Energy Agency), 'Retrieval and conditioning of solid radioactive waste from old facilities', Technical Reports series n. 456, 2007, https://www-pub.iaea.org/MTCD/Publications/PDF/TRS456_web.pdf.
- [4] M. I. Ojovan, W. E. Lee, and S. N. Kalmykov, An Introduction to nuclear waste immobilization, Third Edition. Elsevier, 2019
- [5] C. Cau Dit Coumes, D. Lambertin, H. Lahalle, P. Antonucci, C. Cannes, and S. Delpech, 'Selection of a mineral binder with potentialities for the stabilization/solidification of aluminum metal', J. Nucl. Mater., 2014, doi: 10.1016/j.jnucmat.2014.06.032.
- [6] H. Kinoshita, P. Swift, C. Utton, B. Carro-Mateo, G. Marchand, N. Collier and N. Milestone, 'Corrosion of aluminium metal in OPC- and CAC-based cement matrices', Cem. Concr. Res., 2013, doi: 10.1016/j.cemconres.2013.03.016.
- [7] V. Cantarel, F. Nouaille, A. Rooses, D. Lambertin, A. Poulesquen, and F. Frizon, 'Solidification/stabilisation of liquid oil waste in metakaolin-based geopolymer', J. Nucl. Mater., 2015, doi: 10.1016/j.jnucmat.2015.04.036.
- [8] C. Reeb, C. Pierlot, C. Davy, and D. Lambertin, 'Incorporation of organic liquids into geopolymer materials - A review of processing, properties and applications', Ceram. Int., 2020, doi: 10.1016/j.ceramint.2020.11.239.
- [9] S. J. T. Pollard, D. M. Montgomery, C. J. Sollars, and R. Perry, 'Organic compounds in the cement-based stabilisation/ solidification of hazardous mixed wastes—Mechanistic and process considerations', J. Hazard. Mater., 1991, doi: 10.1016/0304-3894(91)87082-D
- [10] D. M. Montgomery, C. J. Sollars, R. Perry, S. E. Tariingt, P. Barnes, and E. Henderson, 'Treatment of organic-contaminated industrial wastes using cement-based S/S - I. Microstructural analysis of cement-organic interactions', Waste Manag. Res., 1991.
- [11] S. Trussell and R. D. Spence, 'A review of solidification/stabilization interferences', Waste Manag., 1994.
- [12] N. Nestle, C. Zimmermann, M. Dakkouri, and R. Niessner, 'Action and Distribution of Organic Solvent Contaminations in Hydrating Cement: Time-Resolved Insights into Solidification of Organic Waste', Environ. Sci. Technol., 2001, doi: 10.1021/es015528y.
- [13] A. Eddhahak, S. Drissi, J. Colin, S. Caré, and J. Neji, 'Effect of phase change materials on the hydration reaction and kinetic of PCM-mortars', J. Therm. Anal. Calorim., 2014, doi: 10.1007/s10973-014-3844-x.
- [14] D. E. Clark, P. Colombo, and R. M. Jr. Neilson, 'Solidification of oils and organic liquids', Nuclear Waste Management, BNL-51612, 1982. doi: 10.2172/6462993.
- [15] M. Masrulita, P. Burhan, and Y. Trihadiningrum, 'Stabilization / Solidification of Waste Containing Heavy Metals and Hydrocarbons Using OPC and Land Tras Cement', J. Ecol. Eng., 2018, doi: 10.12911/22998993/92926.
- [16] M. H. Almabrok, R. McLaughlan, and K. Vessalas, 'Investigation of oil solidification using direct immobilization method', Sydney, Australia, 2011.
- [17] C. Shi and A. Fernández-Jiménez, 'Stabilization/solidification of hazardous and radioactive wastes with alkali-activated cements', J. Hazard. Mater., 2006, doi: 10.1016/j.jhazmat.2006.05.008.
- [18] V. Cantarel, D. Lambertin, A. Poulesquen, F. Leroux, G. Renaudin, and F. Frizon, 'Geopolymer assembly by emulsion templating: Emulsion stability and hardening mechanisms', Ceram. Int., 2018, doi: 10.1016/j.ceramint.2018.03.079.
- [19] C. A. Davy, G. Hauss, B. Planel, and D. Lambertin, '3D structure of oil droplets in hardened geopolymer emulsions', J. Am. Ceram. Soc., 2018, doi: 10.1111/jace.16142.

- [20] X. Liu, S. Nair, K. Aughenbaugh, and E. van Oort, 'Mud-to-cement conversion of non-aqueous drilling fluids using alkali-activated fly ash', *J. Pet. Sci. Eng.*, 2019, doi: 10.1016/j.petrol.2019.106242.
- [21] B. Planel, C. A. Davy, P. M. Adler, G. Hauss, M. Bertin, V. Cantarel, D. Lambertin, Water permeability of geopolymers emulsified with oil, *Cem. Concr. Res.*, 2020, doi: 10.1016/j.cemconres.2020.106108
- [22] C. Pierlot, H. Hu, C. Reeb, J. Bassetti, M. Bertin, D. Lambertin, C. Davy, V. Nardello-Rataj, 'Selection of suitable surfactants for the incorporation of organic liquids into fresh geopolymer pastes', *Chem. Eng. Sci.*, 2022, doi: 10.1016/j.ces.2022.117635x.
- [23] M. De Campos, Ch. Reeb, C. A. Davy, J. Hosdez, D. Lambertin, Solidification/stabilization (S/S) of high viscosity organics in geopolymers, *Journal of Nuclear Materials*, in press, 2022, doi: 10.1016/j.jnucmat.2022.153979.
- [24] 'EU-project PREDIS, WP5 - Innovations in liquid organic waste treatment and conditioning', <https://predis-h2020.eu/work-packages/>
- [25] ASN (Autorité de sûreté nucléaire), Livre Blanc du Tritium. 2019, <https://www.asn.fr/sites/tritium/>
- [26] CENTRACO, Rapport annuel d'information du public relatif aux installations nucléaires du site de Centraco, Cyclife France, Groupe EDF, 2020 version (in French), https://www.cyclife-edf.com/sites/cyclife/files/edf_rapport_centraco_2020_basse_def_2.pdf
- [27] M. Dianu and N. Deneanu, 'Conditioning Experiments of Organic Solvents Solutions Contaminated With Tritium', 2003, doi: 10.1115/ICEM2003-4740.
- [28] M. Dianu, 'Conditioning Matrices of Liquid Scintillation Cocktails Contaminated with Tritium', *Fusion Sci. Technol.*, 2005, doi: 10.13182/FST05-A918.
- [29] IAEA (International Atomic Energy Agency), 'Treatment and conditioning of radioactive organic liquids', 1992. https://www-pub.iaea.org/MTCD/publications/pdf/te_656_web.pdf
- [30] J. L. Provis and S. A. Bernal, 'Geopolymers and Related Alkali-Activated Materials', *Annu. Rev. Mater. Res.*, 2014, doi: 10.1146/annurev-matsci-070813-113515.
- [31] D. Lambertin and C. Cau Dit Coumes, 'Hydrogen-trapping material, method of preparation and uses', WO 2010/066811, 2010, <https://patentimages.storage.googleapis.com/9b/39/0d/a1739fc869efa7/EP2367627B1.pdf>
- [32] A. Kozawa and K. W. Kordesch, 'Silver Catalyzed Manganese Dioxide Hydrogen Gas Absorber', US4252666A, 1981
- [33] A. Kozawa and K. V. Kordesch, 'Silver-catalysed MnO₂ as hydrogen absorber', *Electrochimica Acta*, 1981, doi: 10.1016/0013-4686(81)90020-7.
- [34] K. Galliez, 'Study and understanding of the irreversible trapping of hydrogen using a mixture of MnO₂/Ag₂O', PhD, University of Nantes, France, 2012.
- [35] K. Liger, P. Trabuc, X. Lefebvre, M. Troulay, and C. Perrais, 'Limitation of Tritium Outgassing from Tritiated Solid Waste Drums', *Fusion Sci. Technol.*, 2015, doi: 10.13182/FST14-T53.
- [36] S. Lanier, C. A. Davy, C. Albert-Mercier, O. Farcy, C. Cau-Dit-Coumes, and D. Lambertin, 'Novel Portland cement matrices incorporating a γ -MnO₂/Ag₂O hydrogen/tritium getter -structure changes and trapping performance', *J. Nucl. Mater.*, 2022, doi: 10.1016/j.jnucmat.2022.153819.
- [37] O. Farcy, 'Formulation et caractérisation de mortiers fluides pour le conditionnement de déchets tritiés', PhD, 2020.
- [38] M. Chaouche, X. X. Gao, M. Cyr, M. Cotte, and L. Frouin, 'On the origin of the blue/green color of blast-furnace slag-based materials: Sulfur K-edge XANES investigation', *J. Am. Ceram. Soc.*, vol. 100, no. 4, pp. 1707–1716, Apr. 2017, doi: 10.1111/jace.14670.
- [39] S. Lanier, 'Mise au point d'un mortier de piégeage à réseau poreux contrôlé', PhD, Centrale Lille Institut, 2020.
- [40] L. Acher, 'Etude du comportement sous irradiation γ et électronique de matrices cimentaires et de leurs hydrates constitutifs', PhD, 2017.

- [41] F. Chupin, A. Dannoux-Papin, Y. Ngono Ravache, and J.-B. d'Espinose de Lacaillerie, 'Water content and porosity effect on hydrogen radiolytic yields of geopolymers', *J. Nucl. Mater.*, 2017, doi: 10.1016/j.jnucmat.2017.07.005.
- [42] A. Olejniczak, A. G. Shostenko, S. Truszkowski, and J. Fall, 'Radiolysis of synthetic oils based on polyalphaolefins', *High Energy Chem.*, 2008, doi: 10.1134/S0018143908020057
- [43] M. Pourbaix, 'Atlas of electrochemical equilibria in aqueous solutions', *J. Electroanal. Chem. Interfacial Electrochem.*, 1967, doi: 10.1016/0022-0728(67)80059-7
- [44] C. Reeb, C. A. Davy, C. Pierlot, M. Bertin, V. Cantarel, D. Lambertin, 'Emulsification of low viscosity oil in alkali-activated materials', *Cement and Concrete Research*, *under revision*, March 2022.
- [45] P. Duxson, A. Fernández-Jiménez, J. L. Provis, G. C. Lukey, A. Palomo, and J. S. J. van Deventer, 'Geopolymer technology: the current state of the art', *J. Mater. Sci.*, 2007, doi: 10.1007/s10853-006-0637-z.
- [46] D. Lambertin, A. Rooses, and F. Frizon, 'Process for preparing a composite material from an organic liquid and resulting material', WO2014/044776 A1, 2014.
- [47] A. Blyth, C. A. Eiben, G. W. Scherer, C. E. White, Impact of activator chemistry on permeability of alkali-activated slags, *J Am Ceram Soc.* 2017, doi: 10.1111/jace.14996.
- [48] '<http://www.harwell-dosimeters.co.uk/perspex/>'.
- [49] 'ISO-ASTM 51261 Guide for Selection and Calibration of Dosimetry Systems for Radiation Processing.'
- [50] J. A. LaVerne, M. R. Ryan, and T. Mu, 'Hydrogen production in the radiolysis of bromide solutions', *Radiat. Phys. Chem.*, 2009, doi: 10.1016/j.radphyschem.2009.07.001.
- [51] J. Couvidat, C. Diliberto, E. Meux, L. Izoret, and A. Lecomte, 'Greening effect of concrete containing granulated blast-furnace slag composite cement: Is there an environmental impact?', *Cem. Concr. Compos.*, 2020, doi: 10.1016/j.cemconcomp.2020.103711.
- [52] C. F. Barros, B. Muzeau, R. François, and V. L'Hostis, 'Corrosion behavior of Mg-Zr alloy in alkaline solutions and in Na- geopolymer', 2018.
- [53] A. Setiadi, N. B. Milestone, J. Hill, and M. Hayes, 'Corrosion of aluminium and magnesium in BFS composite cements', *Adv. Appl. Ceram.*, 2006, doi: 10.1179/174367606X120142.
- [54] P. J. Pretorius and P. W. Linder, 'The adsorption characteristics of d-manganese dioxide: a collection of diffuse double layer constants for the adsorption of H⁺, Cu²⁺, Ni²⁺, Zn²⁺, Cd²⁺ and Pb²⁺', *Appl. Geochem.*, 2001
- [55] K. Galliez, P. Deniard, D. Lambertin, S. Jobic, and F. Bart, 'Influence of MnO₂ polymorphism form on MnO₂/Ag₂O hydrogen getter', *J. Nucl. Mater.*, 2013, doi: 10.1016/j.jnucmat.2013.03.053.
- [56] A. B. Mohammad, K. Hwa Lim, I. V. Yudanov, K. M. Neyman, and N. Rösch, 'A computational study of H₂ dissociation on silver surfaces: The effect of oxygen in the added row structure of Ag (110)', *Phys Chem Chem Phys*, 2007, doi: 10.1039/B616675J.
- [57] A. B. Mohammad, I. V. Yudanov, K. H. Lim, K. M. Neyman, and N. Rösch, 'Hydrogen Activation on Silver: A Computational Study on Surface and Subsurface Oxygen Species', *J. Phys. Chem. C*, 2008, doi: 10.1021/jp0765190.
- [58] S. M. Reddy, S. S. Rao, N. Venkanna, and K. N. Reddy, 'Electrical and structural studies of pure and MnSO₄ doped Poly (Vinyl Alcohol) polymer electrolyte films', *International Journal of Chemical and Analytical Science*, 2011
- [59] X. Gao, L. Frouin, M. Cyr and C. Musikas, 'Ground granulated blast furnace slag based binder, discoloured mortar or concrete including said binder and their preparation methods', WO 2017/080577, 2017.
- [60] K. Andersson, B. Allard, M. Bengtsson, and B. Magnusson, 'Chemical composition of cement pore solutions', *Cem. Concr. Res.*, 1989, doi: 10.1016/0008-8846(89)90022-7.

Chapter V

A new approach for evaluating the long-term confinement of radioactive organic liquids



Summary Chapter V

CHAPTER V: A NEW APPROACH FOR EVALUATING THE LONG-TERM CONFINEMENT OF RADIOACTIVE ORGANIC LIQUIDS IN GEOPOLYMERS.....	205
ABSTRACT	205
1. INTRODUCTION.....	206
1.1. INDUSTRIAL AND SCIENTIFIC CONTEXT.....	206
1.2. AIMS AND SCOPE.....	206
2. THEORETICAL BACKGROUND	207
2.1. SURFACE WETTING PROPERTIES.....	207
2.2. EXPERIMENTAL STRATEGY	209
2.2.1. <i>Determination of the SFE of GP.....</i>	<i>209</i>
2.2.2. <i>Determination of wetting envelopes.....</i>	<i>210</i>
2.2.3. <i>Prediction of wetting on a GP surface and experimental validation of the Owens-Wendt approach</i>	<i>210</i>
3. MATERIALS AND METHODS	210
3.1. MATERIALS.....	210
3.1.1. <i>Preparation of the GP material</i>	<i>210</i>
3.1.2. <i>Organic liquids.....</i>	<i>211</i>
3.2. CONTACT ANGLE MEASUREMENTS	211
4. RESULTS AND DISCUSSION.....	211
4.1. CHARACTERIZATION OF Γ^S , Γ^{SP} AND Γ^S	211
4.2. DETERMINATION OF THE GP WETTING ENVELOPES.....	213
4.3. EXPERIMENTAL VALIDATION OF THE OWENS-WENDT APPROACH	214
4.4. DISCUSSION ON THE PREFERENTIAL WETTING OF OL OR WATER ON GP SURFACE	215
5. CONCLUSIONS.....	216
REFERENCES	217

Chapter V: A new approach for evaluating the long-term confinement of radioactive organic liquids in geopolymers **(Under review in the *Journal of Nuclear Materials*)**

Charles Reeb^{1,2}, Catherine A. Davy¹, Christel Pierlot¹, David Lambertin²

¹*Univ. Lille, CNRS, Centrale Lille, ENSCL, Univ, Artois, UMR 8181-UCCS-Unité de Catalyse et de Chimie du Solide – F-59000 Lille, France*

²*CEA, DES, ISEC, DE2D, SEAD, LCBC, Univ Montpellier, Marcoule, France*

Abstract

Geopolymers (GP) are efficient matrices for confining radioactive organic liquids (OL) prior to their final disposal. However, on the long term, the OL must remain inside the GP, even in case of water seepage coming from the environment.

This research quantifies the wettability of OL and water on GP. The GP Surface Free Energy (SFE) is determined using the Owens-Wendt approach, and wetting envelopes are deduced. The low contact angles (i.e. high affinity) of two OL, widely used in nuclear applications, are determined theoretically and confirmed experimentally. Accordingly, their spreading coefficient S on the GP surface is significantly greater than that of water, ensuring stronger bonding and promoting long term confinement.

Keywords: Geopolymer, radioactive waste, organic liquid, wetting, contact angle

1. Introduction

1.1. Industrial and scientific context

Currently, non-negligible amounts of radioactive organic liquids (OL) are stored temporarily in nuclear facilities, without an industrially validated treatment route. However, from a research and development viewpoint, their incorporation in a cement matrix is generally a favorite procedure, because it ensures an easy and direct chemical solidification/stabilization (S/S) of many compounds, and produces a mechanically stable waste form [1], [2]. Contrarily to most cements (including Portland-based ones), alkali-activated materials (AAM), and particularly geopolymers (GP), display better performances for OL immobilization [3], [4]. GP can incorporate up to 60 %vol. of OL [5], [6]. The final composite materials, referred to as GEOIL, display high mechanical performance (above 10 MPa in uniaxial compression) [7], [8].

For industrial-scale radioactive waste disposal, the GEOIL solution still needs to comply with usual acceptance criteria. One of the most challenging aspects is its long-term behavior, i.e. its long-term durability. Under typical radioactive waste disposal conditions, the durability of GEOIL has mainly been investigated on the short term [6]. Over a long period of time (several years and more), ensuring an adequate confinement of OL inside geopolymers still remains an unanswered question.

1.2. Aims and scopes

The confinement of an OL into a GP matrix is promoted by strong physico-chemical interactions (wetting and adhesion) between the OL and the GP surface. However, in a typical radioactive wastes disposal site, natural water seepage is usual. On the long term, any greater affinity of the water for the GP surface, compared to the OL, could lead to water replacing the OL, and OL migrating through to the environment.

In this context, for safety assessment, it is useful to determine and compare the wetting properties of OL and of water on a typical GP substrate. The aim here is to determine which liquid (OL or water) has the greatest spreading on the GP surface. To this purpose, the surface free energy (SFE) of a typical GP needs to be identified. SFE is a first order parameter, which allows determining the affinity of liquids (OL or water) for the GP surface.

The characterization of the SFE of a solid is not straightforward, even for an ideal surface. Several semi-empirical analytical models based on contact angle measurements have been developed [9]. The commonly used method developed by Owens-Wendt is adopted in this work [10], because it has already been used to determine the SFE of ordinary Portland cement and slag-based materials [11]-[13]. In this research, the SFE of GP is determined

experimentally by contact angle measurements and from the Owens-Wendt model, using four selected OL, including water.

Further, by using the identified SFE values and the Owens-Wendt model, the corresponding wetting envelopes are represented [14]. They are theoretical tools predicting the wetting (i.e. the contact angle) of any liquid on the GP surface. After plotting, they are validated experimentally, by measuring contact angles of liquids different from those used for model identification. In this work, these will be two OL typically used in the nuclear industry.

Finally, the spreading ability of these two OL and water is quantified using the SFE of the GP surface. The preferential wetting of OL or water on the GP surface is discussed.

2. Theoretical background

2.1. Surface wetting properties

The affinity of a liquid for a solid surface is characterized by wettability. At equilibrium, wettability is captured by the contact angle θ of a spherical cap-shaped droplet, where the liquid-vapor interface meets the solid-liquid interface (Figure 1). θ depends on the interfacial free energies of solid-vapor (γ_{SV}), solid-liquid (γ_{SL}) and liquid-vapor (γ_{LV}) interfaces, expressed in N.m^{-1} or J.m^{-2} . For small relative vapors, $\gamma_{SV} = \gamma_S$ and $\gamma_{LV} = \gamma_L$. By convention, γ_S refers to the surface free energy (SFE) of the solid and γ_L refers to the surface tension of the liquid. At equilibrium, they are all related in the thermodynamics approach of Young [15] by:

$$\gamma_S = \gamma_{SL} + \gamma_L \cos \theta \quad (1)$$

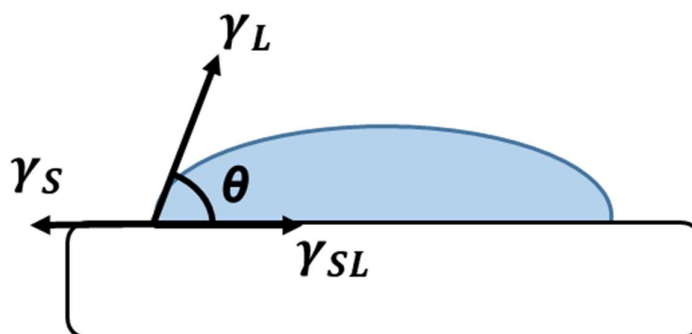


Figure 1: Schematic representation of the Young equation relating the contact angle θ to the interfacial free energies γ_S (i.e. the SFE) and γ_L (i.e. the surface tension).

The wettability of a liquid on a solid surface is determined by (1) the work of adhesion W_A between liquid and solid and (2) the work of cohesion W_C . W_A measures the strength of contact between two distinct phases and corresponds to the work required to disjoin a unit

area of the solid-liquid interface (γ_{SL}) by creating a unit area of liquid-vapor (γ_L) and of solid-vapor (γ_S). W_C is the work produced per unit area when dividing a homogeneous liquid. In other words, while W_A contributes to the spread of liquid over the solid surface, W_C offers resistance to liquid spreading, inducing a liquid contraction. They are related to the interfacial free energies in Eq. 2 and Eq. 3 as [16], [17]:

$$W_A = \gamma_S + \gamma_L - \gamma_{SL} \quad (2)$$

$$W_C = 2 \cdot \gamma_L \quad (3)$$

According to Eq. 2, a significant W_A does not only require significant free energies of both liquid (γ_L) and solid (γ_S), but also a low interfacial energy (γ_{SL}).

Complementarily, the spreading coefficient S measures the tendency of a liquid to spread on a solid surface. It is defined as the difference between the work of adhesion and the work of cohesion. For spontaneous spreading to occur, it is necessary that S is positive, according to Eq. 4 below [18]:

$$S = W_A - W_C = \gamma_S - \gamma_L - \gamma_{SL} \quad (4)$$

The Dupré equation (Eq. 2) combined with the Young equation (Eq. 1), results in Eq. 5 below:

$$W_A = \gamma_L(1 + \cos \theta) \quad (5)$$

Eq. 5 is often called the Young–Dupré equation and relates the work of adhesion to the equilibrium contact angle θ . It is inherently a mechanical expression which does not take into account chemical aspects of the liquid–solid interaction.

Fundamentally, wetting is also a chemical phenomenon, and models taking into account chemical interactions have greater explanatory power, i.e. they have the potential to be more predictive than purely mechanical theories. Accordingly, several models use Eq. 1 as a starting point, but they also capture the chemical aspects of solid–liquid and liquid–vapor interactions [9]. One of the most common chemical models is the Owens–Wendt approach [10]. This approach assumes that the interfacial free energy has two contributions, namely the polar (p) and the dispersive (d) ones, due to intermolecular interactions. Polar interactions (p) comprise Coulomb interactions between permanent dipoles and between permanent and induced dipoles, such as hydrogen bonds. Dispersive interactions (d) are caused by random fluctuations of the charge distribution in atoms and molecules; these are the Van der Waals London forces between induced dipoles. The polar and dispersive contributions to the interfacial free energy are expressed in Eqs. 6 and 7 for liquids and solids, respectively, as:

$$\gamma_L = \gamma_L^d + \gamma_L^p \quad (6)$$

$$\gamma_S = \gamma_S^d + \gamma_S^p \quad (7)$$

Owens and Wendt expressed the interfacial free energy of the liquid-solid interface as the geometric mean between these contributions, as [10]:

$$\gamma_{SL} = \gamma_S + \gamma_L - 2 \left(\sqrt{\gamma_S^d \gamma_L^d} + \sqrt{\gamma_S^p \gamma_L^p} \right) \quad (8)$$

From Eqs. 2 and 6, the work of adhesion is evaluated as follows:

$$W_A = W_A^d + W_A^p = 2 \left(\sqrt{\gamma_S^d \gamma_L^d} + \sqrt{\gamma_S^p \gamma_L^p} \right) \quad (9)$$

From Eqs. 1 and 8, the Owens-Wendt model is deduced as:

$$\boxed{\frac{\gamma_L(1 + \cos \theta)}{2\sqrt{\gamma_L^d}}} = \sqrt{\gamma_S^p} \boxed{\sqrt{\frac{\gamma_L^p}{\gamma_L^d}}} + \sqrt{\gamma_S^d} \quad (10)$$

2.2. Experimental strategy

2.2.1. Determination of the SFE of GP

The linear relationship in Eq. 10 provides the SFE of the GP solid (γ_S) by plotting $Y = (\gamma_L(1 + \cos \theta_{GP}))/2\sqrt{\gamma_L^d}$ as a function of $X = \sqrt{\gamma_L^p/\gamma_L^d}$. The square of the slope of the (X,Y) plot is γ_S^p ; the square of the intercept is γ_S^d . Parameters (X,Y) are plotted for at least two different liquids (four are used here), and γ_S^p and γ_S^d are derived from their linear interpolation in the least squares sense. The greater the number and the difference in the liquid chemistry, the more accurate γ_S^p , γ_S^d and the SFE $\gamma_S = \gamma_S^d + \gamma_S^p$. This process requires to identify preliminarily γ_L^d , γ_L^p and θ_{GP} (γ_L is the sum of γ_L^d and γ_L^p).

Firstly, the γ_L^d and γ_L^p values of four different liquids are determined by rearranging Eq. 10 and by considering polytetrafluoroethylene (PTFE) as a standard reference surface. Pure untreated PTFE has a surface energy of 20.0 mJ/m², and it is assumed devoid of polar interactions, i.e., for PTFE, $\gamma_S = \gamma_S^d = 20.0 \text{ mJ/m}^2$ and $\gamma_S^p = 0 \text{ mJ/m}^2$ [19], [20]. Substituting these values into Eq. 10 yields:

$$\gamma_L^d = \frac{\gamma_L^2(1 + \cos \theta_{PTFE})^2}{80} \quad (11)$$

Where θ_{PTFE} is the contact angle measured between PTFE and the probed liquid. Therefore, with Eq. 11, by simply measuring θ_{PTFE} , and by knowing γ_L , the dispersive component γ_L^d is determined for the selected liquid. The value of γ_L^p is deduced as $\gamma_L^p = \gamma_L - \gamma_L^d$ (Eq. 6).

Secondly, the contact angle θ_{GP} is measured for the liquids of known γ_L , γ_L^d and γ_L^p , but on the GP solid surface instead of PTFE.

2.2.2. Determination of wetting envelopes

When both (γ_S^d and γ_S^p) are known, the so-called “wetting envelopes” are determined. For a given set (γ_S^d , γ_S^p , θ_{GP}), each value of γ_L^d corresponds to a single value of γ_L^p , obtained by the numerical resolution of Eq. 10. Wetting envelopes are then deduced by plotting the dispersive component γ_L^d of a liquid against the polar component γ_L^p . For a given solid SFE, wetting envelopes are bow-shaped curves at constant equilibrium contact angles θ_{GP} .

2.2.3. Prediction of wetting on a GP surface and experimental validation of the Owens-Wendt approach

In practice, wetting envelopes are used to predict the wetting of the GP surface (i.e. the contact angle θ_{GP}) for any liquid, provided that the polar and dispersive components of its surface tension γ_L^p and γ_L^d are known [21]. In the following, they are used to predict the θ_{GP} of two OL widely used in the nuclear industry.

For these OL, using γ_S^p and γ_S^d identified for the GP, together with γ_L and θ_{PTFE} values from the literature (or from experimental measurements), γ_L^d and γ_L^p are derived and plotted in the wetting envelope diagram, and the corresponding contact angle θ_{GP} is deduced from Eq. 10.

Further, the predicted θ_{GP} values for the two OL are compared to experimental measurements of θ_{GP} for the same liquids. This aims to validate experimentally the Owens-Wendt approach for GP, and to enable a wide use of the wetting envelopes for any other liquid in contact with GP.

Finally, the work of adhesion W_A , the work of cohesion W_C and the spreading coefficient S are deduced and compared for the two OL and water.

3. Materials and methods

3.1. Materials

3.1.1. Preparation of the GP material

An aqueous sodium silicate solution (Betol 39T) is obtained from Woellner (Germany), sodium hydroxide (purity > 99%) is purchased from VWR International (USA) and metakaolin (MK) powder of M1000 grade is obtained from Imerys (France). The components (sodium silicate,

sodium hydroxide, water and MK) are weighed in order to have a reference molar composition of 3.5 SiO₂ : 1.0 Al₂O₃ : 1.0 Na₂O : 14.0 H₂O. The preparation of the GP is detailed elsewhere [6], [22]. Samples are cured in endogenous conditions at 20°C under atmospheric pressure for at least 14 days to ensure complete geopolymerization.

3.1.2. Organic liquids

Deionized water and ethylene glycol, dimethylformamide (DMF) and dodecane with analytical-reagent quality (purchased from Sigma-Aldrich, USA) are used for determining the SFE of GP.

In order to validate experimentally the wetting envelopes, analytical-reagent quality Tributylphosphate (TBP), from Sigma-Aldrich, USA, and an industrial mineral oil (labelled IO for industrial oil, reference Shell SPIRAX S2 A80W-90, Shell Company, France) are selected.

3.2. Contact angle measurements

θ_{PTFE} is measured with the sessile drop method using an optical tensiometer (Kruss K100). Liquid drops are stable over time on PTFE substrates (they are measured without any time constraint). For each sample, θ_{PTFE} is the average of three measurements.

The process for θ_{GP} is slightly different. After demolding, the GP monolithic sample is dried by air exposure for at least 24h. This decreases the liquid penetration rate into the porous solid material when measuring contact angles; in a first approach, it is assumed not to affect the contact angle value. θ_{GP} is measured with the same method as for θ_{PTFE} . After the liquid drop is deposited on the GP surface, it fully penetrates into the GP in less than 10 s, because GP are porous materials and liquids may easily penetrate by capillarity. This phenomenon may lead to underestimate contact angle values. Therefore, contact angles on the GP surface are measured 1 s only after the drop deposition. For each sample, θ_{GP} is the average of three measurements.

4. Results and discussion

4.1. Characterization of γ_S^d , γ_S^p and γ_S

Table 1 provides, first, θ_{GP} values as measured on the GP surface (Figure 2a), followed by θ_{PTFE} values, measured on PTFE. From experimental θ_{PTFE} values and reference values for γ_L , the components γ_L^d and γ_L^p are deduced using Eq. 11. The literature also provides reference values for γ_L^d and γ_L^p , used for comparison purposes. Good agreement is obtained for DMF [23], dodecane [24] and water [25], with less than 10% difference for all values except one at 20% (γ_L^d for water). For ethylene glycol, the polar contribution is strongly

underestimated in comparison with [26], possibly because the authors use a specific method, relying on water-ethylene glycol mixes.

Table 1: Measured contact angles θ_{GP} on GP surface, and θ_{PTFE} on PTFE followed by total surface tension γ_L taken from the literature, and corresponding dispersive and polar components (γ_L^d , γ_L^p), either deduced from experimental θ_{PTFE} or from the literature (same references as for γ_L)

Liquids	Experimental		Literature	Experimental		Literature (same ref. as for γ_L)	
	θ_{GP} (°)	θ_{PTFE} (°)	γ_L (with reference)	γ_L^d	γ_L^p	γ_L^d	γ_L^p
Water	38.82 (± 0.71)	111.80 (± 1.50)	72.80 (Janiszewska 2020)	26.18 (± 2.02)	46.62 (± 2.02)	21.80	51.00
DMF	21.34 (± 0.65)	65.34 (± 1.65)	37.30 (Tang 2018)	34.93 (± 1.29)	2.37 (± 1.29)	32.42	4.88
Dodecane	11.79 (± 0.91)	36.57 (± 0.98)	25.90 (Pan 2018)	25.90 (± 0.31)	0 (± 0.31)	25.90	0
Ethylene glycol	21.68 (± 1.54)	77.43 (± 1.00)	48.00 (Zhang 2019)	42.70 (± 1.19)	5.30 (± 1.19)	29.00	19.00

Eq. 10 is then applied to the measured values θ_{GP} in combination with experimental or literature γ_L^d and γ_L^p values (Table 1). This yields two distinct sets of four (X, Y) values for the GP surface (Fig. 2b).

With the experimental γ_L^d and γ_L^p values, the linear fitting parameters (slope a and intercept b) are a = 5.824 and b = 4.871. This provides $\gamma_S^d = 23.7 \text{ mN.m}^{-1}$, $\gamma_S^p = 33.9 \text{ mN.m}^{-1}$ and $\gamma_S = 57.6 \text{ mN.m}^{-1}$. With the γ_L^d and γ_L^p values from the literature, the linear fitting parameters are a = 5.908 and b = 4.417, yielding $\gamma_S^d = 19.5 \text{ mN.m}^{-1}$, $\gamma_S^p = 34.9 \text{ mN.m}^{-1}$ and $\gamma_S = 54.4 \text{ mN.m}^{-1}$. These two sets of results for the GP SFE are comparable, with less than 10% difference.

To our knowledge, the literature does not report any SFE for metakaolin-based GP, but the total SFE γ_S (54.4-57.6 mN.m^{-1}) is of the same order of magnitude as for ordinary Portland cement (47.9-54.4 mN.m^{-1}) or slag-based alkali-activated materials (66.3 mN.m^{-1}) [13].

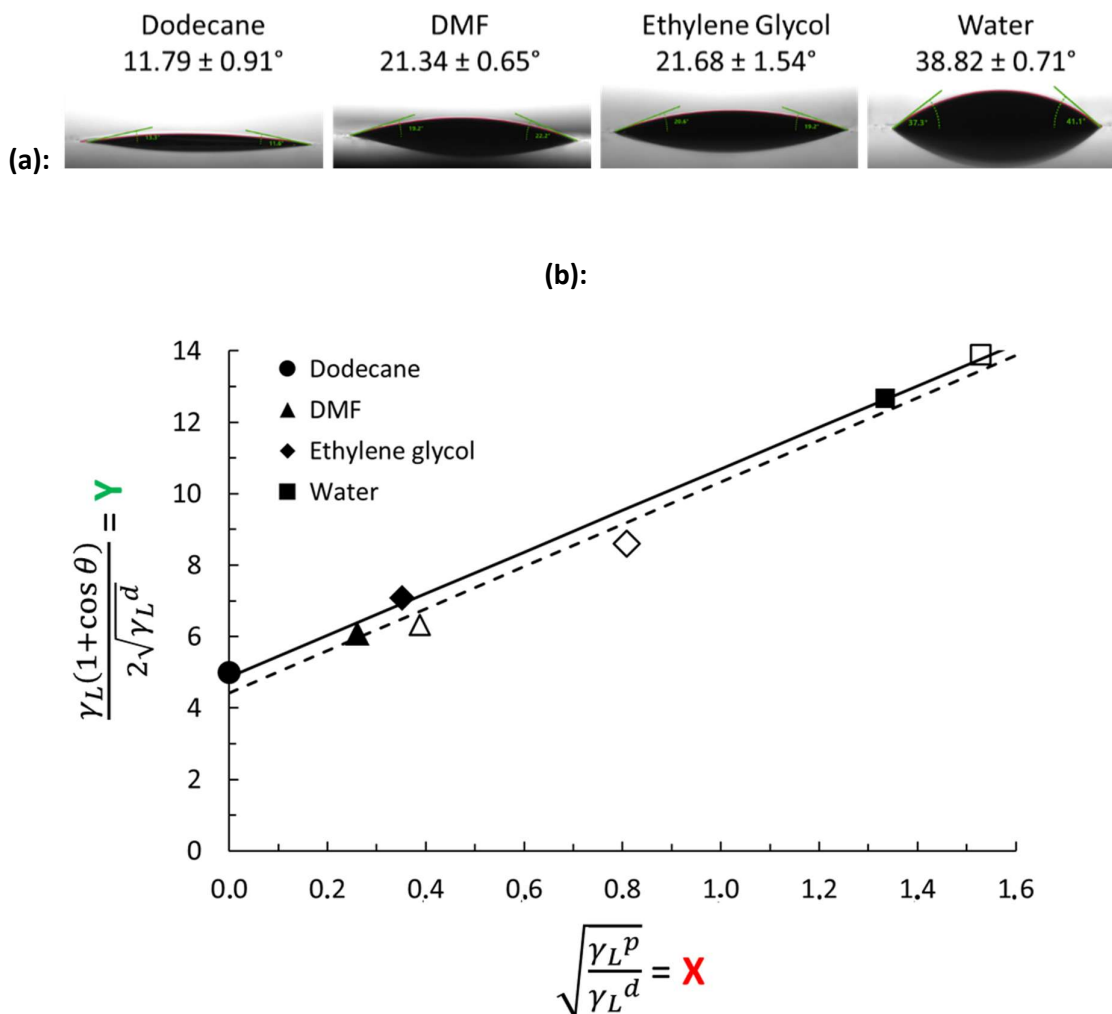


Figure 2: (a) Photographs of the drop of each liquid on the GP surface with the corresponding θ_{GP} value. (b): Variation of Y with X for the solid GP surface using experimental γ_L^d and γ_L^p values (continuous line and black marks), or using γ_L^d and γ_L^p from the literature (dashed lines and hollow marks). Each line represents the data best linear fit in the least squares sense (with a Pearson's coefficient $R^2 > 0.97$).

4.2. Determination of the GP wetting envelopes

Using (γ_s^d, γ_s^p) obtained either from contact angle experiments or from the literature, wetting envelopes for the GP surface are plotted in Figure 3, for fixed theoretical contact angles values θ_{GP} of 0° , 20° , 40° and 60° . For instance, the 20° wetting envelope corresponds to the set of liquids (with variable γ_L^d and γ_L^p) for which the theoretical contact angle on GP is 20° in Eq. 10. Accordingly, any liquid with γ_L^d and γ_L^p laying within this contour will theoretically wet the GP surface with a contact angle lower than 20° . On the contrary, any liquid with γ_L^d and γ_L^p laying outside this contour will theoretically wet the geopolymer surface with a contact angle greater than 20° . For instance, water is very close to the 40°

wetting envelope, in good agreement with its measured contact angle on GP of 38.82° (Table 1 and Figure 2a).

4.3. Experimental validation of the Owens-Wendt approach

For water, TBP and an industrial oil (IO), the predicted contact angles θ_{GP} are given in Table 2. They are based on (γ_S^d, γ_S^p) deduced from the experimental measurement of (γ_L^d, γ_L^p) or from their values from the literature (for water only). For TBP and the IO, their positioning on the wetting envelopes plot (Figure 3) predicts full wetting on the GP surface (i.e. a contact angle of 0°). This means that they have a very high affinity for the GP material.

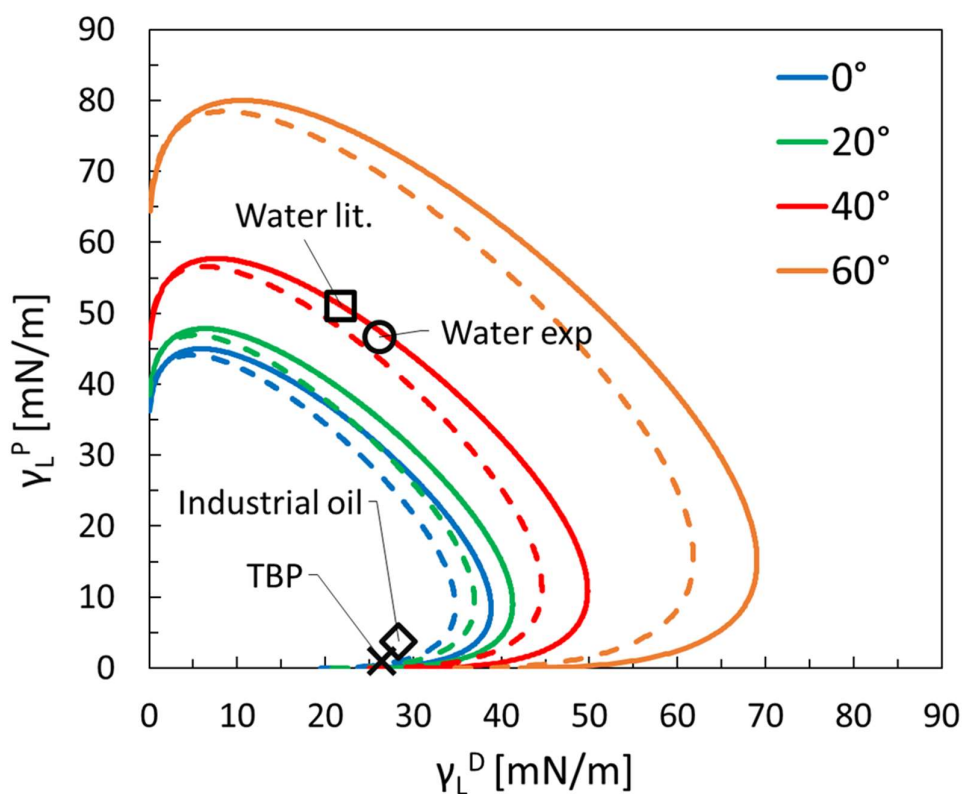


Figure 3: Geopolymer wetting envelopes for contact angles of 0° , 20° , 40° and 60° using the (γ_S^d, γ_S^p) values obtained either experimentally (solid lines) or from the literature (dashed lines). Water, tributylphosphate (TBP) and an industrial oil (IO) are plotted for validation purposes.

The contact angles of the two liquids are also measured experimentally on the GP surface (right column, Table 2). In the case of TBP, the prediction is perfectly in accordance with the experiment. On the contrary, the experimental contact angle obtained for the IO (24°) is higher than the prediction (0°). This difference is explained by the higher viscosity of the IO, which slows down the spreading on the GP surface. The measurement of the contact angle is taken only 1 s after drop deposition; very possibly, this does not allow enough time for the

viscous IO to spread. However, the contact angle measured is low, and significantly lower than that of water.

Table 2: Comparison of predicted contact angle values with experimental contact angle values: case of TBP and an IO. Surface tension is expressed in mN.m⁻¹.

Liquid	Measured θ_{PTFE} (°)	γ_L	γ_L^d	γ_L^p	θ_{GP} (°)		Measured
					Predicted using experimental (γ_S^d, γ_S^p) ²	Predicted using (γ_S^d, γ_S^p) from the literature ³	
Water	111.80 (± 1.50)	72.80	26.18	46.62	38.99	43.47	38.82
IO	61.09 (± 2.39)	32.09 ¹	28.33	3.76	0	N/A	24.2
TBP	47.44 (± 1.14)	27.42 ¹	26.41	1.01	0	N/A	0

¹: The total surface tension of the OL was measured using a Wilhelmy plate (not from the literature)

²: Experimental values are $\gamma_S^d = 23.7$ mN.m⁻¹, $\gamma_S^p = 33.9$ mN.m⁻¹ and $\gamma_S = 57.6$ mN.m⁻¹

³: Values deduced from the literature are $\gamma_S^d = 19.5$ mN.m⁻¹, $\gamma_S^p = 34.9$ mN.m⁻¹ and $\gamma_S = 54.4$ mN.m⁻¹

4.4. Discussion on the preferential wetting of OL or water on GP surface

The knowledge of the geopolymer SFE allows calculating the work of cohesion W_C , the work of adhesion W_A , the spreading coefficient S and the interfacial free energy γ_{SL} for any liquid of known surface tension. These are calculated for water, TBP and the IO, using Eq. 9, Eq. 3, Eq. 4 and Eq. 5 respectively (Table 3). The work of adhesion W_A for TBP and the IO is much lower than that of water, due to the low surface tension γ_L of these liquids (Table 2). However, due to a significant work of cohesion W_C water displays a negative spreading coefficient S and is unlikely to spread on the GP surface, whereas TBP and the IO spread on the geopolymer surface (positive S). In case of water seepage at disposal sites, water is therefore unlikely to migrate in GP materials and dislodge confined OL. Additionally, the GP formulation could be modified to change the SFE in order to optimize the OL affinity and reduce that of water.

Table 3: Work of cohesion W_C , work of adhesion W_A , spreading coefficient S and interfacial tension γ_{SL} between liquids and GP surface. All are expressed in $\text{mN}\cdot\text{m}^{-1}$.

Liquids	W_C	Calculated using experimental (γ_S^d, γ_S^p)			Calculated using (γ_S^d, γ_S^p) from literature data		
		W_A	S	γ_{SL}	W_A	S	γ_{SL}
IO	64.18	74.45	10.27	15.28	69.94	5.76	16.57
TBP	54.84	61.77	6.93	23.29	57.27	2.43	24.57
Water	145.60	129.38	-16.22	1.06	125.64	-19.96	1.58

5. Conclusions

This paper determines experimentally the surface free energy of a GP using the Owens Wendt approach. By solely measuring liquid/solid contact angles (on PTFE or on GP paste), four different liquids (water and 3 OL) are used for model identification. Further, the Owens-Wendt model is validated experimentally using two other OL. The corresponding wetting envelopes are used to predict the contact angle of any liquid on the GP surface.

The knowledge of the geopolymer SFE allows calculating several interesting parameters (W_A , W_C , S , etc.). For instance, the spreading coefficient S shows the preferential wetting of GP by typical OL used in nuclear application, rather than by water. This is positive for ensuring the long-term confinement of OL within GP materials: Because OL have an excellent affinity for GP, long-term water seepage is not likely to dislodge OL from GP. The SFE parameter can be further used to optimize the GP formulation in order to optimize the OL affinity. In the context of nuclear wastes management, this appears as a positive contribution for ensuring long-term confinement of OL within GP materials and could be extremely useful for the acceptance of GEOIL at industrial disposal sites.

References

- [1] S. Trussell and R. D. Spence, 'A review of solidification/stabilization interferences', *Waste Manag.*, 1994.
- [2] International Atomic Energy Agency (IAEA), 'Treatment and conditioning of radioactive organic liquids', 1992.
- [3] M. H. Almabrok, R. McLaughlan, and K. Vessalas, 'Investigation of oil solidification using direct immobilization method', presented at the Environmental Research Event, Sydney, Australia, 2011.
- [4] X. Liu, S. Nair, K. Aughenbaugh, and E. van Oort, 'Mud-to-cement conversion of non-aqueous drilling fluids using alkali-activated fly ash', *J. Pet. Sci. Eng.*, 2019, doi: 10.1016/j.petrol.2019.106242.
- [5] V. Cantarel, D. Lambertin, A. Poulesquen, F. Leroux, G. Renaudin, and F. Frizon, 'Geopolymer assembly by emulsion templating: Emulsion stability and hardening mechanisms', *Ceram. Int.*, 2018, doi: 10.1016/j.ceramint.2018.03.079.
- [6] B. Planel, C.A. Davy, P.M. Adler, G. Hauss, M. Bertin, V. Cantarel, D. Lambertin, 'Water permeability of geopolymers emulsified with oil', *Cem. Concr. Res.*, 2020, doi: 10.1016/j.cemconres.2020.106108.
- [7] V. Cantarel, F. Nouaille, A. Roosees, D. Lambertin, A. Poulesquen, and F. Frizon, 'Solidification/stabilisation of liquid oil waste in metakaolin-based geopolymer', *J. Nucl. Mater.*, 2015, doi: 10.1016/j.jnucmat.2015.04.036.
- [8] M. H. Almabrok, R. G. McLaughlan, K. Vessalas, and P. Thomas, 'Effect of oil contaminated aggregates on cement hydration', *Am. J. Eng. Res.*, 2019.
- [9] M. Żenkiewicz, 'Methods for the calculation of surface free energy of solids', *J. Achiev. Mater. Manuf. Eng.*, 2007.
- [10] D. K. Owens and R. C. Wendt, 'Estimation of the surface free energy of polymers', *J. Appl. Polym. Sci.*, vol., 1969, doi: 10.1002/app.1969.070130815.
- [11] H. R. Pakravan, M. Jamshidi, and M. Latifi, 'Relationship between the surface free energy of hardened cement paste and chemical phase composition', *J. Ind. Eng. Chem.*, 2014, doi: 10.1016/j.jiec.2013.08.025.
- [12] D. Barnat-Hunek and P. Smarzewski, 'Influence of hydrophobisation on surface free energy of hybrid fiber reinforced ultra-high performance concrete', *Constr. Build. Mater.*, 2016, doi: 10.1016/j.conbuildmat.2015.11.008.
- [13] C. Zhu, Y. Guo, Z. Wen, Y. Zhou, L. Zhang, Z. Wang, Y. Fang and W. Long, 'Hydrophobic Modification of a Slag-based Geopolymer Coating', *IOP Conf. Ser. Earth Environ. Sci.*, 2021, doi: 10.1088/1755-1315/783/1/012015.
- [14] Z. Żółek-Tryznowska and A. Kałuża, 'The Influence of Starch Origin on the Properties of Starch Films: Packaging Performance', *Materials*, 2021, doi: 10.3390/ma14051146.
- [15] T. Young, 'III. An essay on the cohesion of fluids', *Philos. Trans. R. Soc. Lond.*, 1805, doi: 10.1098/rstl.1805.0005.
- [16] Dupré, 'Théorie mécanique de la chaleur', *Gauthier-Villars*, 1869.
- [17] C.M.S Vicente, P.S André and R.A.S Ferreira, 'Simple Measurement of surface free energy using a web cam', *Revista Brasileira de Ensino de Física*, 2012.
- [18] M. Riazi and A. Golkari, 'The influence of spreading coefficient on carbonated water alternating gas injection in a heavy crude oil', *Fuel*, 2016, doi: 10.1016/j.fuel.2016.03.021
- [19] B. Jańczuk and T. Białłopiotrowicz, 'Surface free-energy components of liquids and low energy solids and contact angles', *J. Colloid Interface Sci.*, 1989, doi: 10.1016/0021-9797(89)90019-2.
- [20] C. Jie-Rong and T. Wakida, 'Studies on the surface free energy and surface structure of PTFE film treated with low temperature plasma', *J. Appl. Polym. Sci.*, 1997.
- [21] D. Janssen, R. De Palma, S. Verlaak, P. Heremans, and W. Dehaen, 'Static solvent contact angle measurements, surface free energy and wettability determination of various self-assembled monolayers on silicon dioxide', *Thin Solid Films*, 2006, doi: 10.1016/j.tsf.2006.04.006.

- [22] C. Pierlot, H. Hu, C. Reeb, J. Bassetti, M. Bertin, D. Lambertin, C. Davy and V. Nardello-Rataj, 'Selection of suitable surfactants for the incorporation of organic liquids into fresh geopolymer pastes', *Chem. Eng. Sci.*, 2022, doi: 10.1016/j.ces.2022.117635.
- [23] F. Tang, G. Xu, T. Ma, and L. Kong, 'Study on the Effect of Demulsification Speed of Emulsified Asphalt based on Surface Characteristics of Aggregates', *Materials*, 2018, doi:10.3390/ma11091488.
- [24] Y. Pan, S. Huang, F. Li, X. Zhao, and W. Wang, 'Coexistence of superhydrophilicity and superoleophobicity: theory, experiments and applications in oil/water separation', *J. Mater. Chem. A*, 2018, doi: 10.1039/C8TA04725A.
- [25] N. Janiszewska, J. Raczowska, A. Budkowski, K. Gajos, Y. Stetsyshyn, M. Michalik and K. Awiuk, 'Dewetting of Polymer Films Controlled by Protein Adsorption', *Langmuir*, 2020, doi: 10.1021/acs.langmuir.0c01718.
- [26] Z. Zhang, W. Wang, A. N. Korpacz, C. R. Dufour, Z. J. Weiland, C. R. Lambert and M. T. Timko 'Binary Liquid Mixture Contact-Angle Measurements for Precise Estimation of Surface Free Energy', *Langmuir*, 2019, doi: doi.org/10.1021/acs.langmuir.9b01252

Conclusions and **further research**

1. Main achievements

The objective of this work consisted in developing a novel solution for the management of tritiated oils based on the direct conditioning in alkali-activated materials (AAM), additionally functionalized with a $\gamma\text{-MnO}_2/\text{Ag}_2\text{O}$ hydrogen tritium getter (Figure 1). Two types of AAM, either based on metakaolin (geopolymer or GEO) or on blast furnace slag (AABFS) were considered. The scientific approach first consisted in understanding the emulsion of a model mineral oil in fresh AAM added with various surfactants. The properties of hardened AAM-OIL composites were then characterized. Secondly, the trapping efficiency of the $\gamma\text{-MnO}_2/\text{Ag}_2\text{O}$ getter was assessed in AAM. Finally, a new methodology was proposed to demonstrate the oil affinity for geopolymer materials in order to prove the long-term confinement capacity.

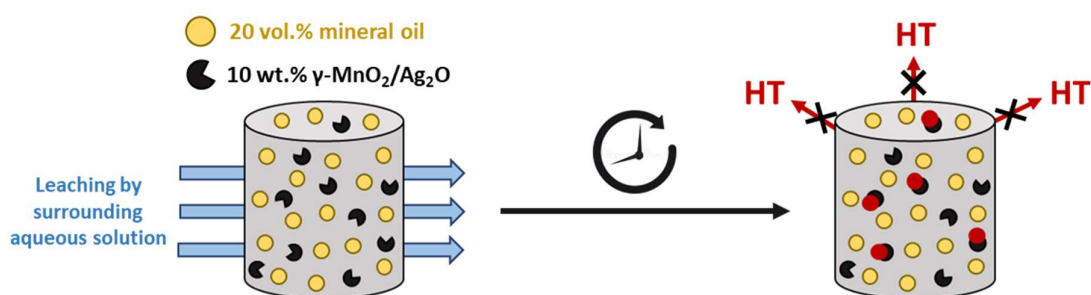
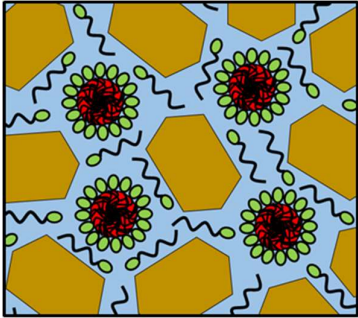
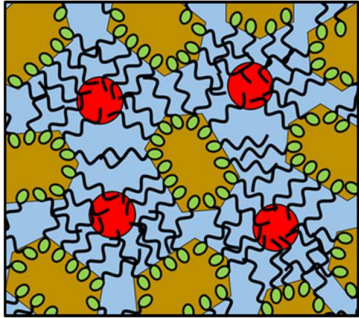


Figure 1: Graphical representation of this work objectives.

1.1. Fresh state oil emulsion

The emulsification of oil in a proportion of 20%vol. was successfully performed in both types of fresh AAM grouts. However, this requires the addition of surfactants as the oil incorporation would be insufficient due to the presence of heterogeneous and large visible droplets otherwise. Several surfactants (CTAB, SDS, Glucopon 225DK, Span 80, Tween 80, Brij O10) have successfully improved the oil emulsion (smaller and homogeneous oil droplets) but with varying efficiencies and more importantly, following two distinct mechanisms that are summarized in table 1.

Table 1: Schematic representation of the two action mechanisms of surfactants for the incorporation of oil in AAM. The light blue background represents the aqueous activating solution, the red circles represent the oil droplets and the brown hexagons correspond to the solid particles (BFS or MK). The green circles and the black lines correspond to the surfactant heads and tails respectively.

	Mechanism 1	Mechanism 2
Viscosity	Constant	Increases
Interfacial tension	Effective decrease	Poor decrease
Oil-solid particles interactions	Low	High
Graphical description		
GEO	Glucopon SDS	Span 80 CTAB Tween 80 Brij O10
AABFS	Glucopon SDS CTAB Tween 80 Brij O10	Span 80

Mechanism 1 proceeds simply by reducing the interfacial tension, while maintaining the workability of the fresh mixtures. Mechanism 2 acts by promoting interactions between solid precursor particles and oil droplets, leading to thick and non-flowing fresh mixtures. Surprisingly, even if fresh AAM can be conceptualized as similar (both are aqueous alkaline solutions containing high amounts of particles), the behavior of surfactants can be opposite in the two types of AAM and should be a focus of attention in the future development of AAM for oil immobilization.

1.2. Oil immobilization in the hardened state

The advantage of using surfactants for oil immobilization was also highlighted in hardened AAM-oil composites. It was first observed that when the composite materials fracture, the oil

remains confined in the presence of surfactants owing to smaller droplets, whereas oil leakage is clearly observed in the absence of surfactants due to larger droplets.

More importantly, we have shown that there is no influence of the oil on the setting time and strength development of AAM materials. At the low concentration of that study ($3 \cdot 10^{-3} \text{ mol} \cdot \text{L}^{-1}$), surfactants do not influence these parameters. In addition, the main AAM reaction products (C-A-S-H in AABFS and N-A-S-H in GEO) are not impacted by the addition of oil or surfactants. **The impact on mechanical properties is therefore only attributed to a physical reason, i.e. the increase in fluid volume (oil and/or entrained air bubbles).**

We have highlighted that the addition of surfactants, with the aim of improving the oil immobilization/emulsion, leads to the side effect of increasing the porosity of AAM by stabilizing air bubbles. In both types of AAM, GlucoPON is by far the surfactant stabilizing the highest amount of air bubbles, which is highly detrimental to the short-term mechanical properties and the long-term durability of solid composite materials. However, AAM-OIL composites immobilizing 20%vol. of oil all have significant compressive strengths, of 25 MPa on average for GEO-OIL composites and 20 MPa on average for AABFS-OIL composites. This is significantly higher than the 8 MPa required by ANDRA.

In conclusion, we have demonstrated that both GEO and AA-BFS materials are suitable for immobilizing 20%vol. of oil provided that a surfactant is added, most preferentially CTAB in AABFS or Brij O10 in GEO. According to both fresh and hardened states observations, GEO exhibits higher performances for the immobilization of oil than AA-BFS, mainly based on droplets size characterizations. The type and concentration of surfactant must be carefully chosen, not only for the purpose of stabilizing the oil emulsion but also to avoid side effects, such as an excessive porosity increase that will impact the final properties of composite materials.

1.3. Getter efficiency in AAM

The efficiency of the $\gamma\text{-MnO}_2/\text{Ag}_2\text{O}$ getter was assessed in AAM by using *in-situ* dihydrogen production in two distinct ways:

- **Gamma irradiations (up to 500 kGy):** GEO materials containing the getter demonstrated a H_2 trapping efficiency of almost 100% in the absence of oil and about 90% in the presence of oil. On the contrary, BFS-based materials containing the getter exhibited only a H_2 trapping efficiency of 50% in the absence of oil and about 20% in the presence of oil.
- **Magnesium corrosion:** The trapping of H_2 in AABFS material is limited to about 0.7 mmol/g of getter; it is greater in GEO and still carries on after 500 days.

Complementarily, the contact of the $\gamma\text{-MnO}_2/\text{Ag}_2\text{O}$ getter powder with AAM pore-waters, directly extracted from solid AAM, highlighted the strong tendency of the getter to sorb ions on its surface (Ca^{2+} , Mg^{2+} , Na^+ , but also silicates, aluminates, etc.). The sorption of these ions at the surface of the getter hinders the access of hydrogen atoms to their reactive sites, which reduces the H_2 trapping capacity by 50%.

Lastly, it was evidenced that the structure of the $\gamma\text{-MnO}_2/\text{Ag}_2\text{O}$ getter was modified after contact with sulfide species, which led to an ineffective getter powder. Most probably, sulfide species naturally present in raw BFS reduce the oxidant components of the getter powder.

In conclusion, it was demonstrated that the $\gamma\text{-MnO}_2/\text{Ag}_2\text{O}$ getter is significantly more effective in GEO than in AABFS due to its reactivity with reducing sulfur species present in the AABFS systems.

1.4. Oil confinement on the long-term

The surface free energy (SFE) of a GEO surface was determined experimentally by contact angle measurements and using the Owens-Wendt approach. The spreading coefficient S , which can be calculated from the SFE, shows the preferential wetting of GEO materials by typical organic liquids used in nuclear applications (such as industrial oils), rather than by water. **Because organic liquids have an excellent affinity for GEO materials, long term water seepage is not likely to dislodge them from GEO-OIL composites. In the context of nuclear waste management, this appears as a positive contribution to the long-term durability of geopolymer immobilizing oil (GEOIL) and it is extremely important for their acceptance in industrial disposal sites.**

2. Further research

2.1. Ensuring oil confinement over time

This work has provided adequate formulations of strong AAM-OIL composite materials. Thus far, the remaining questions from waste regulators concern the proof that the oil will remain confined in AAM over long periods of time and under specific conditions arising from the nature of the disposal sites. Hence, the topic initiated in chapter V should be further investigated to prove, in a thermodynamic approach, that the oil strongly interacts with GEO matrices and will remain confined on the long term, even in the case of surrounding water exposure. First, the method used for contact angle measurements may not be the most adapted as the liquid droplets quickly penetrate in AAM by capillarity. The Washburn method may be more adapted for measuring contact angles on cementitious-like materials. In addition, the impact of AAM formulation parameters or ageing (e.g. irradiation exposure) on

the surface free energy of AAM should be evaluated to assess if changes in the oil-GEO affinity could occur over time.

2.2. Ensuring tritium confinement

To ensure the confinement of gaseous tritium, the $\gamma\text{-MnO}_2/\text{Ag}_2\text{O}$ getter is added in significant proportions (10 wt%). It would be interesting to assess its influence on the reactivity and on the final properties of AAM. In particular, the sorption of ions at the surface of the getter could delay the setting time of AAM, while the getter might also act as a nucleation site accelerating the setting of AAM. This work demonstrated that the H_2 trapping efficiency is very effective in GEO materials. In further research, the efficiency of H_2 mitigation should be studied at higher gamma doses (> 1000 kGy) and at varying dose rates, in order to assess the maximum trapping capacity and kinetics of the $\gamma\text{-MnO}_2/\text{Ag}_2\text{O}$ getter in GEO materials.

Although this work focused on gaseous tritium (HT), it is not to be forgotten that tritiated oils also release tritium in the form of tritiated water (HTO). The proposed $\gamma\text{-MnO}_2/\text{Ag}_2\text{O}$ getter aims at ensuring gaseous tritium (HT) confinement but does not prevent tritiated water (HTO) to be released from AAM. Hence, this will require additional investigations, in particular the development of AAM with water transport properties as low as possible. First trials have been initiated to determine the HTO diffusion coefficient of the composite materials studied in this work. Four formulations (GEO and AABFS samples, with or without oil immobilization), with optimized water contents, are currently under investigation at CEA Cadarache. All samples contain 10 wt% of MnO_2 , in order to be representative of the $\gamma\text{-MnO}_2/\text{Ag}_2\text{O}$ getter. The test consists in subjecting fully saturated slices of composite materials to a continuous HTO flow in order to determine their HTO diffusion coefficient. More information about the experimental design and subsequent data exploitation can be found in [1]. **Final results are not yet available but the current trend is that the HTO diffusion is much lower in AABFS than in GEO, which confirms the relevance of studying AABFS materials for the immobilization of tritiated oils. In particular, it could be interesting to improve the $\gamma\text{-MnO}_2/\text{Ag}_2\text{O}$ getter efficiency in AABFS, by preventing its reactivity with sulfur species.** This could be achieved by adding a strong oxidant (e.g. KMnO_4), which will preferentially react with the sulfur-reducing species present in AABFS materials, hence protecting the oxidative constituents of the $\gamma\text{-MnO}_2/\text{Ag}_2\text{O}$ getter.

References

- [1] T. Wattez, A. Duhart-Barone, and S. Lorente, 'Tritium through-diffusion test in non steady state: Can the effective diffusion coefficient be determined?', *Constr. Build. Mater.*, 2015, doi: 10.1016/j.conbuildmat.2015.05.111.

Appendix 1

Selection of suitable surfactants for the incorporation of organic liquids into fresh geopolymer pastes



Selection of suitable surfactants for the incorporation of organic liquids into fresh geopolymer pastes



Christel Pierlot^{a,*}, Hanyu Hu^a, Charles Reeb^{a,b}, Jordan Bassetti^a, Matthieu Bertin^b, David Lambertin^b, Catherine Davy^a, Véronique Nardello-Rataj^a

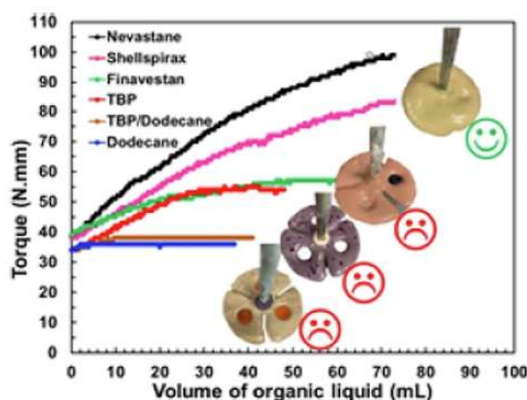
^a Centrale Lille, Université de Lille, CNRS, Université Artois, UMR 8181-UCCS-Unité de Catalyse et Chimie du Solide, Lille, France

^b CEA, DES, ISEC, DE2D, SEAD, LCBC, Univ Montpellier, Marcoule, France

HIGHLIGHTS

- Torque monitoring during emulsification of OL into fresh GP allows to have one-line viscosity.
- Torque evolution allows to predict if OL will be successfully incorporated in GP or not.
- Quaternary ammonium salts such as CTAB are well adapted to adjust the viscosity of fresh GEOIL.
- Capillary forces between OL and MK were shown using Zêta potential measurements and Washburn tests.

GRAPHICAL ABSTRACT



ARTICLE INFO

Article history:
Received 27 September 2021
Received in revised form 9 March 2022
Accepted 21 March 2022
Available online 25 March 2022

Keywords:
Geopolymers
Metakaolin
Torque
Quaternary ammonium salts
Zeta potential

ABSTRACT

Geopolymers (GP) have recently emerged as suitable binders for the conditioning of radioactive organic liquids (OL). The condition for suitably incorporating high amounts of OL into GP is assessed in this research. A series of OL has been selected, comprising alkanes (dodecane and 2 paraffinic mineral oils), an industrial gear oil and tributylphosphate (TBP), in order to cover a wide range of viscosities (0.001–2.33 Pa.s). The incorporation of viscous OL (>0.2 Pa.s) into fresh GP results in a regular torque increase, indicating a suitable process with the dispersion of the OL in the form of fine micrometric droplets. When the torque remains stable, for OL of low viscosity (<0.2 Pa.s) like TBP/Dodecane mixtures, the incorporation is not possible, or only partial in the form of large droplets quickly coalescing and leading to an organic supernatant above the hardened GP.

For low viscosity OL, surfactants are required. The use of quaternary ammoniums (QAs) like cetyltrimethylammonium bromide (CTAB) has been studied. Torque monitoring shows that the OL is incorporated similarly in the GP slurry, whether the surfactant is introduced at the beginning, through the course or at the end of the mixing process. The torque evolution also provides the optimum surfactant concentration, by evidencing that beyond a certain concentration, the medium hardens too quickly, preventing the incorporation of OL. Finally, torque monitoring highlights that QAs with shorter alkyl chains,

* Corresponding author.

such as hexamethyltrimethylammonium, are able to replace CTAB with the same efficiency. Therefore, the powerful action of CTAB on the incorporation of alkanes into GP is attributed to its positive charge rather than to its surfactant effect.

© 2022 Elsevier Ltd. All rights reserved.

1. Introduction

1.1. Oil incorporation into geopolymer suspensions

Geopolymers (GP) are inorganic aluminosilicate materials synthesized at room temperature by the activation of a solid aluminosilicate precursor (e.g. metakaolin, fly ash F) in alkaline conditions (fresh GP) (Davidovits, 1991; Provis et al., 2009). The resulting mixture hardens to form a solid material (hardened GP). Mixing organic liquids (OL) with such aqueous suspensions (Bai and Colombo, 2018; Davidovits, 1991; Duxson et al., 2007; Provis et al., 2009) has been recently described for the synthesis of porosity-controlled media, thermal insulating foams or filtration supports (Bai et al., 2016; Barbosa et al., 2018; Cilla et al., 2017; Glad and Kriven, 2015; Medpelli et al., 2014) and for the treatment of radioactive wastes (Cantarel et al., 2018, 2015). Vegetable oils (Bai et al., 2016; Cilla et al., 2017) were also used as the organic phase. Because of the strong alkaline medium, the triglycerides contained in the vegetable oils are converted into glycerol and sodium salt of carboxylic acids, which act as surfactants during GP stirring. Therefore, unlike OL containing alkanes, incorporation of vegetable oils into aqueous geopolymer suspensions does not cause any process issue.

1.2. Two-steps oil incorporation process

With the aim of immobilizing radioactive organic wastes, alkanes (Cantarel et al., 2018; Lambertin et al., 2018) and paraffin oil (Liu et al., 2018) have been used as model oils. In (Cantarel et al., 2018; Lambertin et al., 2018), the two-steps incorporation process first requires the formulation of an oil in alkaline water emulsion at high shear rate in a first reactor, followed by its incorporation into an aqueous and viscous metakaolin suspension in a second reactor. Even if this process allows an efficient incorporation up to 20 %v of OL in GP, by providing oil droplets of about 10–100 μm , this two-steps protocol is hardly applicable at the industrial scale.

Moreover, the surfactant choice to form the initial emulsion is critical, since this conditions not only the stability of the emulsion, but also the easiness of incorporating the emulsion in the GP suspension. Among the different surfactants that have been tested, alkyl quaternary ammoniums, and in particular cetyl trimethyl ammonium bromide (CTAB), appears as a promising emulsifier. When using CTAB, the viscosity of the fresh hexadecane/geopolymer composite pastes at 20% by volume of hexadecane is between 100 and 1000 times greater than the viscosity of the fresh geopolymer free from alkane (Cantarel, 2016).

1.3. One-step oil incorporation process

Former studies highlight that when paraffin oil is dispersed into a GP slurry, the suspension is not stable with time (Thakur et al., 2019). However, it is worth noting that it is possible to incorporate motor oils (Cantarel et al., 2015; Davy et al., 2019) in a GP cement directly, in a one step process, without using any surfactant. Even if no details are given concerning the composition of these industrial oils, which probably contain additives like surfactants with some emulsifying and/or stabilizing properties, it was the first time that a one-step process had been successfully used. Cantarel et al.

(Cantarel et al., 2015) noted an increase in viscosity during the incorporation of the oil.

1.4. Offline rheological measurements

Most of the time, rheological measurements are performed offline, which requires to transfer the fresh GP from the reactor to the measurement cell of the rheometer. The rheological properties of these fresh pastes are generally determined using rotational rheometers with a parallel plate (Sun et al., 2020), a cone plate (Dusserre et al., 2020) or a bowl with an helical steel ribbon impeller (Steins et al., 2012) type geometry. Offline rheological measurements can be carried out using several sample solicitations. As an example, by simply measuring the evolution of viscosity versus time on a scale of several hours, the setting time of geopolymers can be estimated (Autef et al., 2013).

Moreover, typical rheological shear stress/shear rate curves also provide apparent viscosity, yield stress and plastic viscosity. In Sun et al. (Sun et al., 2020), these last two basic parameters have been characterized to determine to what extent geopolymers meet the requirements for extruding and molding processes.

In Dusserre et al. (Dusserre et al., 2020), thixotropic curves of fresh geopolymers have been studied using a cone plate geometry. From the interpretations of the rheological changes with time, a model for the dissolution mechanism of metakaolin followed by polycondensation is proposed.

Oscillatory rheological experiments allow the determination of viscoelastic parameters (G' , G'' , and $\tan \delta$). With these information, Steins et al. (Steins et al., 2012) have shown that a rigid percolating network in fresh GP occurs more quickly with alkali activator. Hussain et al. (2005, 2004) have shown that the relaxation strength ($\tan \delta$) is correlated to the glass transition temperature (T_g) of geopolymer-modified composites. In Rouyer et al. (2015), the elastic and viscous moduli are also measured to investigate the percolation and aggregation mechanisms during geopolymer paste hardening.

1.5. Online rheological measurement

To our knowledge, there are not many articles dealing with online rheological measurement, and even less when it is related to oil incorporation in fresh geopolymer.

In some cases (Autef et al., 2013), rheological measurements are performed using an unconventional geometry to facilitate mixing, using a bowl and a helical steel ribbon impeller. In that case, the torque measured during stirring can be converted to a viscosity thanks to a preliminary calibration, performed with standard oils (Autef et al., 2013). However, geopolymer pastes may exhibit high stiffness and cohesion, which makes common shear-driven rheometers inappropriate. In that case, a homemade small-scale ramp-type rheometer has been used to simulate an extrusion process and to convert the applied pressure (i.e. the resulting torque) to the rheological behavior of the pastes (Yunsheng et al., 2008).

Online torque measurements have already been used to follow emulsification processes of viscous organic polymers such as epoxy resin (Akay, 1997), polyethylene (Akay and Tong, 2001), polyester (Catte et al., 2018; Pierlot et al., 2018), polyurethane (Saw et al., 2004), rosin resins (Song et al., 2011), silicon resin (Galindo-

Alvarez et al., 2011), bisphenol A-polyester (Goger et al., 2015) or bitumen (Edward et al., 2014). The torque may be converted to viscosity by calibration curves or by mathematical models (Allouche et al., 2004; Edward et al., 2014; Song et al., 2011).

In this article, the aim is to take advantage of the high viscosity of fresh geopolymers to perform online torque tracking into the reactor before and during organic liquid incorporation. The objective is to determine to what extent torque tracking provides relevant information on both the process of oil incorporation and its repartition into the GP. A series of organic liquids (OL) have been selected for this study, comprising alkanes (dodecane, 2 paraffinic mineral oils (Finavestan and Nevastane)) as well as an industrial motor oil (Shellspirax) and tributylphosphate (TBP), in a view of covering a wide range of viscosity (0.0018 to 2.33 Pa.s).

The effects of different quaternary ammoniums on the oil incorporation have been studied, including the well-known cetyltrimethylammonium bromide (CTAB), with the aim of confirming the positive effect of CTAB on the organic liquid incorporation.

2. Materials and methods

2.1. Chemicals

Geopolymers with the following molar composition $3.8 \text{ SiO}_2 : 1 \text{ Al}_2\text{O}_3 : 1 \text{ Na}_2\text{O} : 13 \text{ H}_2\text{O}$ were synthesized using a sodium silicate solution (Woellner, Betol® 39 T: 27.8 wt% SiO_2 , 8.3 wt% Na_2O and 63.9 wt% H_2O), sodium hydroxide (Sigma Aldrich, 99%) and an aluminosilicate source (metakaolin, ARGICAL-M 1000, Imerys). Metakaolin was chosen in this study for its stable chemical composition and easy supply, which is not the case of other raw materials used for geopolymer formulation (e.g. fly ash F, red mud).

Hexa, tetra, dode, de, octa, hexa-decyltrimethylammonium bromide and Sudan IV were purchased from Sigma-Aldrich. Mineral oils Nevastane EP100 and Finavestan A360B were obtained from Total, Shellspirax S2 A 80 W-90 is a commercially available oil, Dodecane, and Tributyl phosphate were purchased from VWR with an announced purity of 99%. Chemicals were used as received without any further purification. Water was deionized using a Milli-QR® Water Purification System and was collected with a resistivity $\geq 18.2 \text{ M}\Omega\text{-cm}$.

2.2. Propeller and reactor

The stirring system is a propeller (Table 1) with three contiguous blades (6.0 cm diameter) fixed on a stainless steel rod (0.6 cm diameter). The reactor is a cm beaker with an internal diameter of

Table 1

Viscosity at 25 °C measured at 100 s^{-1} for different organic liquids, fresh geopolymer pastes with and without incorporated Shellspirax oil (20 %v) and p ratio (viscosity of OL/ viscosity of fresh GP).

Organic liquids	Viscosity at 100 s^{-1} at 25 °C (Pa.s)	p ratio (viscosity of OL/ viscosity of GP)
<i>Suspension of fresh geopolymer with 20 %v Shellspirax alone</i>		
	5.59	
	1.92	
<i>Organic liquid</i>		
Nevastane oil	2.33	1.214
Shellspirax oil	0.32	0.167
Finavestan	0.13	0.068
Tributyl phosphate (TBP)	0.0036	0.002
Dodecane	0.0018	0.001

8.0 cm. During the mixing step, the propeller is placed at 1 cm from the bottom of the beaker.

2.3. Geopolymer/oil preparation

First, 12.92 g of sodium hydroxide, 82.16 g of Betol® 39 T silicate solution and 11.04 g of deionized water are introduced into a 500 mL reactor to form the activating solution: The mixture was first stirred at 400 rpm with the Heidolph RZR 2051 control to ensure the complete dissolution of sodium hydroxide, and then allowed to cool down to room temperature during 1 h. Afterwards, 72.12 g of ARGICAL-M 1000 are added during 2 min and the mixture is stirred at 800 rpm during 15 min until both visual homogeneity of the dispersion and torque stability. At this stage, the fresh geopolymer paste is obtained. The last step consists of introducing the organic liquid colored with Sudan IV into the reactor at a flow rate of $4.0 \text{ mL}\cdot\text{min}^{-1}$ with a Syringe pump Legato (kdScientific). The organic liquid is introduced into the geopolymer paste so that the point of impact is located at equal distance from the center and the periphery of the beaker. The fresh mixture (called fresh "geoil") is poured into graduated test tubes for liquid state characterization (discussed below) or directly transferred into open cylindrical polystyrene containers and aged at room temperature for 2 days before solid-state characterization.

2.4. Rheological experiments

3 mL of the liquid geopolymer suspension is placed in the gap of a cone-plate (6 cm, 4°) Kinexus rheometer (Malvern). A shear stress gradient from zero to the maximum value (Pa), chosen in accordance to the consistency of the sample, is applied in 1 min followed by the return in the same conditions, in order to reach at least a shear rate of 100 s^{-1} . Experiments were carried out at a constant temperature of 25.0 °C. The linear profiles obtained allow the determination of the viscosity (shear stress divided by shear rate) in the studied scale.

2.5. Torque measurements

The torque is measured in function of time using a Heidolph RZR 2051 control at a selected stirring rate (100 to 800 rpm) and recorded via a specific software (Watch/Control 200) provided by Heidolph.

2.6. Optical microscopic analysis

Optical microscopic observations are carried out using an Axios-tar microscope Zeiss in transmission-mode for fresh geopolymers. Due to their important opacity, geopolymer suspensions are directly diluted with water (1/10) on the small glass plate before observation. A Keyence VHX-5000 microscope is also used in reflection-mode for hardened geopolymer observations.

2.7. Zeta potential

10 mg of metakaolin and an appropriate amount of alkyl trimethyl ammonium bromide are dispersed in 10 mL of aqueous solutions for 5 min using ultrasonic waves and left for 12 h at rest. The pH of the aqueous solutions is adjusted by the addition of sodium hydroxide or hydrochloric acid and controlled before the Zeta Potential analysis, which is performed using a Nanosizer Malvern instrument.

2.8. Washburn tests

Washburn tests are carried out using a Krüss Force Tensiometer - K100 in combination with Krüss Windows based Laboratory Desktop software in the sorption mode. 1.0 g of (natural or hydrophobically modified) metakaolin is placed in an appropriate sample holder, packed for 30 s using 2 kg weight and finally suspended from the balance in the tensiometer. The liquid is raised until it just touches the bottom of the porous sample and mass² (w^2) versus time (t) data are then collected as liquid penetrates into the solid.

Hydrophobically metakaolin powders were obtained as follow: 5.0 g of natural metakaolin were introduced in 50 mL of 10^{-2} M CTAB aqueous solution of and let for stirring during 2 h. The powders were then filtered on paper and dried in an oven at 60 °C overnight.

3. Results and discussion

3.1. Torque/Viscosity correspondence

The selected organic liquids (OL) of interest comprising alkanes (dodecane, 2 paraffinic mineral oils (Finavestan and Nevastane) as well as an industrial motor oil (Shellspirax) and tributylphosphate (TBP) have been first analyzed by shear stress/shear rate rheological curves. Viscosity profiles are presented in Fig. 1. A. The maxi-

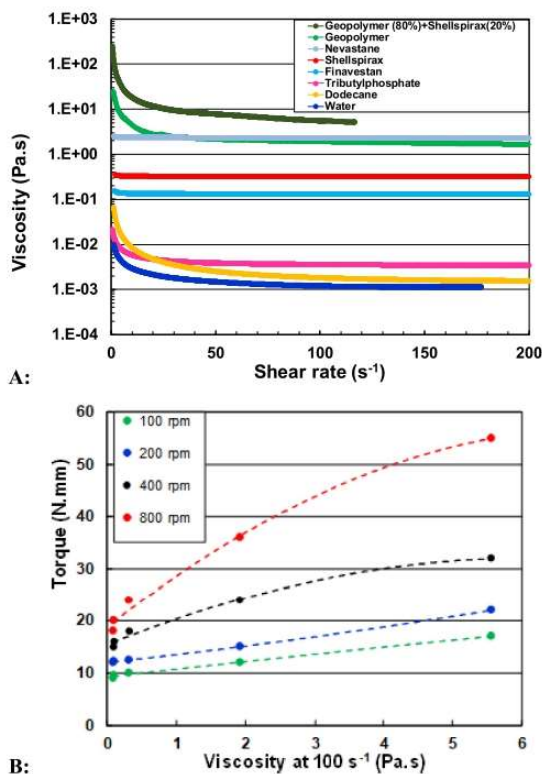


Fig. 1. A: Viscosity (Pa.s) versus shear rate (s^{-1}) measured at 25.0 °C for water, different organic liquids, fresh geopolymers (with 0 %v and 20 %v of incorporated Shellspirax oil). Viscosity curve have been obtained during increase in shear stress from 0 to σ_{max} during 1 min. σ_{max} is fixed in order to obtain a maximum shear rate around $100 s^{-1}$. B: Correspondence between viscosity at $100 s^{-1}$ and torque (N.mm) at different stirring speeds (100, 200, 400 and 800 rpm).

imum shear stress applied is selected in order to reach $100 s^{-1}$ that could be representative of a mean shear rate generated in the reactor during fresh geopolymer mixing.

The tested OLs are almost Newtonian since their viscosity is relatively constant with the shear rate. The small variations in viscosity for extremely flowing OLs (water, dodecane, TBP) at low speed gradients ($<10 s^{-1}$) are due to experimental conditions. The viscosity at $100 s^{-1}$ (Table 1) versus the torque obtained in the reactor at different speed rates have been plotted (Fig. 1B).

In order to extend the viscosity/torque correlation curve with more consistent fluids, data obtained with fresh geopolymers (1.92 Pa.s) and with 20 %v of Shellspirax oil incorporated (5.59 Pa.s) have been added in Fig. 1B. For very fluid media (<0.2 Pa.s), the torque only slightly varies whatever the stirring speed (from 100 to 800 rpm). Thus, the correlation between viscosity and torque is not relevant for OL of viscosity lower than 0.2 Pa.s. For low speeds of rotation (100 or 200 rpm), the torque only increases by 10 N.mm when the viscosity rises from 0.1 to 5.0 Pa.s. On the other hand, at 800 rpm, a large torque amplitude of more than 50 N.mm is observed. Fig. 1B. shows that a mixing speed of 800 rpm is well adapted to both ensure a good mixing of the geopolymer and to follow the torque evolution during OL incorporation.

3.2. Choice of geometry / transferability to other mixing geometries

Different stirring propeller (vortex, anchor, dispersing homogenising blades) have been tested without success. Only the propeller with three contiguous blades made it possible to incorporate organic liquids with a minimum speed of 800 rpm. Estimation of Reynold number ($Re = 23$) has been done using $Re = N \cdot d^2 \cdot \rho / \mu$ with $N = 13.33$ rounds/s (800 rpm), $d = 6.10^{-2}$ m, $\rho = 1672$ kg.m⁻³, $\mu = 3.5$ Pa.s. Estimation of the maximum shear rate at the extremity of the blade is $151 s^{-1}$.

Given the high viscosity of the reaction medium, it is important to note that the mixture can be stirred homogeneously as long as the quantity of geopolymer is at a distance from the helix of the order of a few cm. Beyond this distance, the geopolymer at the surface of the reactor is no longer agitated. In the case of an industrial dimensioning, it would probably be necessary to choose more suitable systems with multi-blade systems for example.

3.3. Organic liquids incorporation into fresh geopolymer

The incorporation of OL (Fig. 2) was carried out by always following the same protocol. First, the geopolymer suspension is prepared by adding metakaolin to the activating solution. Once the torque value is stable, the OL is added at a constant flow rate of 4.0 mL per minute. The addition is stopped at 100 mL if the geopolymer is able to accept this volume (Fig. 1, Nevastane, Shellspirax). If not the addition is stopped when the organic liquid can no longer penetrate inside the geopolymer (Fig. 1, Finavestan, ..., Dodecane). At this stage, the mixture is removed from the reactor and a picture of the fresh GEOIL, fixed on the 6 cm diameter propeller is presented in Table 2. At this step an observation of the GEOIL can be obtained by optical microscopy (Fig. 3).

All the points in Fig. 2 for which there is no OL added ($v = 0.0$ mL) correspond to the same fresh geopolymer composition, thus the small torque variations (35–40 N.mm) can be attributed to slight position change of the propeller in the reactor. In any case, this difference of 5.0 N.mm is negligible in comparison with the torque variation obtained during OL incorporation (see Fig. 3).

Three torque evolution profiles can be distinguished in Fig. 2 depending of the type of OL that is incorporated, whose corresponding GEOIL aspect (Type I, II or III) are presented in Table 2 before and after hardening. In the case of dodecane or TBP/dode-

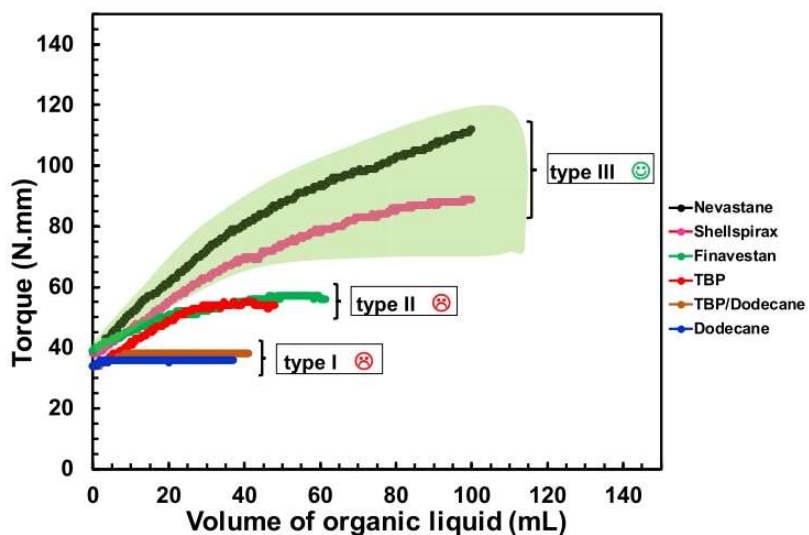
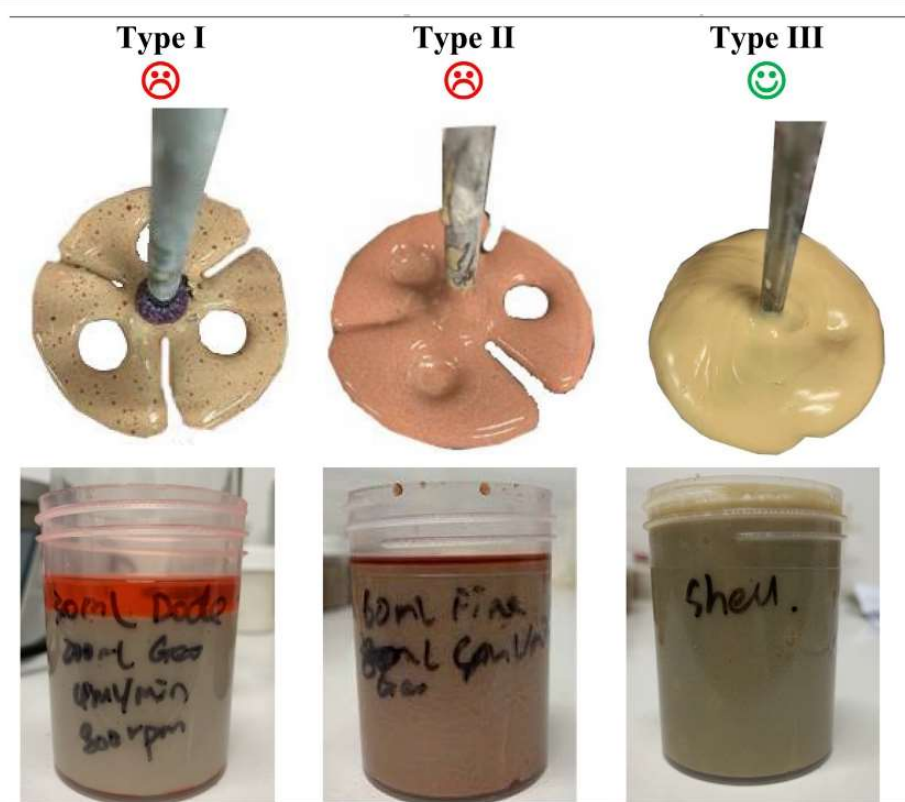


Fig. 2. Torque (N.mm) variation versus volume (mL) of different organic liquids incorporated (flow rate = 4.0 mL.min⁻¹ and stirring speed = 800 rpm) into 80.0 mL of fresh geopolymer. Type I, II and III physical aspects of geopolymers are represented in Table 2.

Table 2

Type I, II, III GEOIL before (top) and after (bottom) hardening.



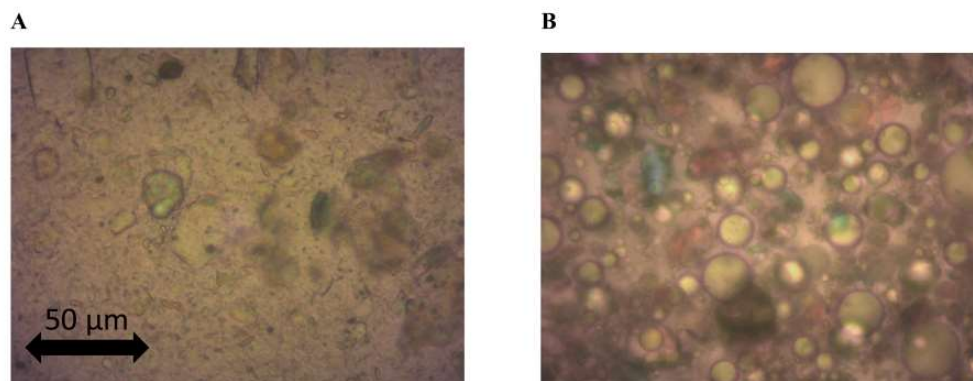


Fig. 3. Optical microscopy in transmission mode of fresh geopolymer (A) and with incorporation of 56% of Shellspirax organic liquid (B). Observations have been carried out with preliminary dilution in water (1/10). Small colored (blue, green, red) parts correspond to solid particles that appear under polarized light. Circular oil droplets with sizes ranging from 1.0 to 50 μm are also visible (B). (For interpretation of the references to colour in this figure legend, the reader is referred to the web version of this article.)

cane, the torque remains constant. The torque recording was proceeded until introduction of 40 mL of OL, but in fact, the oil incorporation into the GP was not taking place. After stopping the agitation, the organic liquid directly coalesced at the surface of the GP. The small amount of OL that is being incorporated is in the form of big droplets of a few millimeters diameter, as can be seen on the picture of the paste (Table 2, first column). In the end, the paste corresponds practically to the fresh geopolymer in terms of viscosity and is defined as **type I GEOIL**.

In case of TBP and Finavestan, the torque increases regularly up to 54 N.mm and then stabilizes after 22 mL of TBP or 42 mL of Finavestan have been incorporated. This late stabilization results from the limit of incorporation and the appearance of big droplets of oil in the GEOIL that can be seen on the propeller (Table 2, second column). The fresh paste is still a bit too fluid to avoid coalescence of OL droplets on the surface of the geopolymer until the hardening phase. GEOIL **type II** will characterize such systems for which the incorporation of oil is possible in a limited proportion and for which an oil resurgence appears before hardening.

In case of Nevastane and Shellspirax mineral oils, the torque increases constantly even after adding 100 mL of oil (55% oil incorporation) and the dispersion seems macroscopically very homogeneous as shown by the appearance of the GEOIL on the propeller (Table 2, third column). The microscopic state (picture not presented) shows the dispersion of numerous oil droplets ranging from 1.0 to 50 μm . GEOIL **type III** will characterize these fresh geoil with an adapted viscosity after oil incorporation that allows the organic liquid to remain trapped in the solid matrix until the hardening is completed. The green area in Fig. 2 is a schematic representation of torque variation versus volume of organic liquid that leads to GEOIL **type III**.

Finally, with regards to the OL tested, it seems that if its viscosity is greater than 0.13 Pa.s (at 100 s^{-1}) like Nevastane or Shellspirax oils, the incorporation into geopolymer is properly done. If the viscosity is about 0.13 Pa.s, such as the Finavestan oil, incorporation is possible but only at a limited extent of about 43% and the droplets are relatively big (100 μm). For OL with very low viscosities (lower than 0.004 Pa.) such as TBP, dodecane and their mixtures, incorporation is not possible.

3.4. Effect of the viscosity difference on the incorporation

The effect of the viscosity ratio ($p = \eta_D / \eta_C$) between the dispersed and the continuous phases on the ability of a dispersed liquid to be burst has been studied by Grace (Grace, 1982). This study concluded that there is a range of most favorable ratios ($10^{-2} < p <$

3) to produce a high quality dispersion. It appears that these conclusions are also valid in the present study if the fresh geopolymer is considered as the continuous phase ($\eta^c = 1.92 \text{ Pa.s}$) and the organic liquid as the dispersed phase. In fact, for Nevastane ($p = 1.2$) and Shellspirax ($p = 0.17$), the oil incorporation is successful (Table 1). For OL with lower p ratio such as Finavestan ($p = 0.13$) and TBP ($p = 0.004$), the incorporation of oil is still possible but at a limited amount, especially in the case of TBP for which the p ratio is outside the good interval conditions ($10^{-2} < p < 3$). As expected, dodecane, which does not incorporate into the geopolymer has indeed the lowest p ratio ($p = 0.002$). Organic liquids with a viscosity high enough to reach a p ratio higher than 3.0 have not been tested in this study. However, Grace's observations might be applicable to geopolymer suspensions with organic liquids having superior viscosities, as observed during the bad dispersion of excessively viscous epoxy liquids into fresh geopolymer resin (Wang et al., 2019).

3.5. Effect of CTAB added at different steps of the process

To see whether the addition of CTAB in geopolymer paste facilitates OL incorporation, Finavestan oil was selected for its moderate incorporation (Type II) without any additives.

In the protocol of the present study, the components are added in the following order: activating solution, metakaolin and oil. The CTAB is introduced at three different steps of the process: directly in the activation solution, just after the addition of metakaolin, or at the end, just after the oil incorporation. The concentration of CTAB (10^{-2} M) was calculated with respect to the volume of the fresh geopolymer. Without CTAB (black and green curves in Fig. 4), the torque typically increases from 35–40 to 55 N.mm during the addition of Finavestan, as already observed in Fig. 2. The optical microscopy visualization of the hardened GEOIL without oil are presented in Fig. 5A. Angular micron particles can be observed that probably corresponds to metakaolin (noted MK in the photo) trapped in the polymerized aluminosilicate matrix. (Fig. 5B) confirms the presence of large Finavestan oil droplets of more than 50 μm , the reflection of which is materialized by a small white disc in the center of the drop.

The addition of CTAB in the activating solution containing metakaolin already induces an increase in torque (50–55 N.mm) compared to the sample free of CTAB (25–40 N.mm). Oil addition then leads to a strong increase of the torque profile, up to 160 N.mm. After hardening, the microscopic analysis shows a homogeneous size distribution with droplets smaller than 10 μm that can be detected by the numerous small white points (Fig. 5C). An

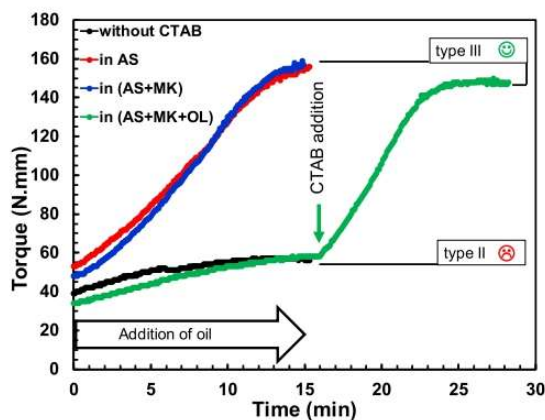


Fig. 4. Torque (N.mm) variation versus time (min) at stirring speed = 800 rpm. The addition of Finavestan (60 mL/23%) happens during the first 15 min (flow rate = 4.0 mL.min⁻¹) into 200 mL of geopolymer without CTAB (black), with introduction of 10⁻² M CTAB in the activating solution (AS, red), after the addition of metakaolin (AS + MK, blue) and after the oil incorporation (AS + MK + oil, green). In case of AS + MK + oil, the torque is monitored during 15 additional min. (For interpretation of the references to colour in this figure legend, the reader is referred to the web version of this article.)

enlargement of a central portion of the photo in Fig. 5C (see insert) allows the small drops to be seen better.

Even more surprising, when CTAB is added after the incorporation of Finavestan, the torque progressively increases during 10 min, leading to a similar torque value (150 N.mm) as when the CTAB is directly introduced in the activating solution. Again, the droplet size is about a few microns (Fig. 5D).

The huge increase of torque experienced when adding CTAB could be due to the adsorption of CTAB on the surface of MK particles. The polar head of CTAB is positively charged and is therefore likely to adsorb on the surface of MK particles, which are negatively charged in alkaline conditions (Zhang et al., 2008). The hydrophobic forces arising from the interaction between hydrophobic tails of CTAB molecules cause the formation of agglomerates of MK particles (Suzzoni et al., 2018). These agglomerates are responsible for the viscosity increase due to higher effective volume. This phenomenon is even much more significant in the presence of oil, probably due to the fact that the mixture is getting close to the maximum packing fraction (Guazzelli and Pouliquen, 2018).

3.6. Effect of CTAB concentration

Since the positive effect of CTAB has been shown on the incorporation of a moderately viscous oil (Fig. 4), the incorporation of a

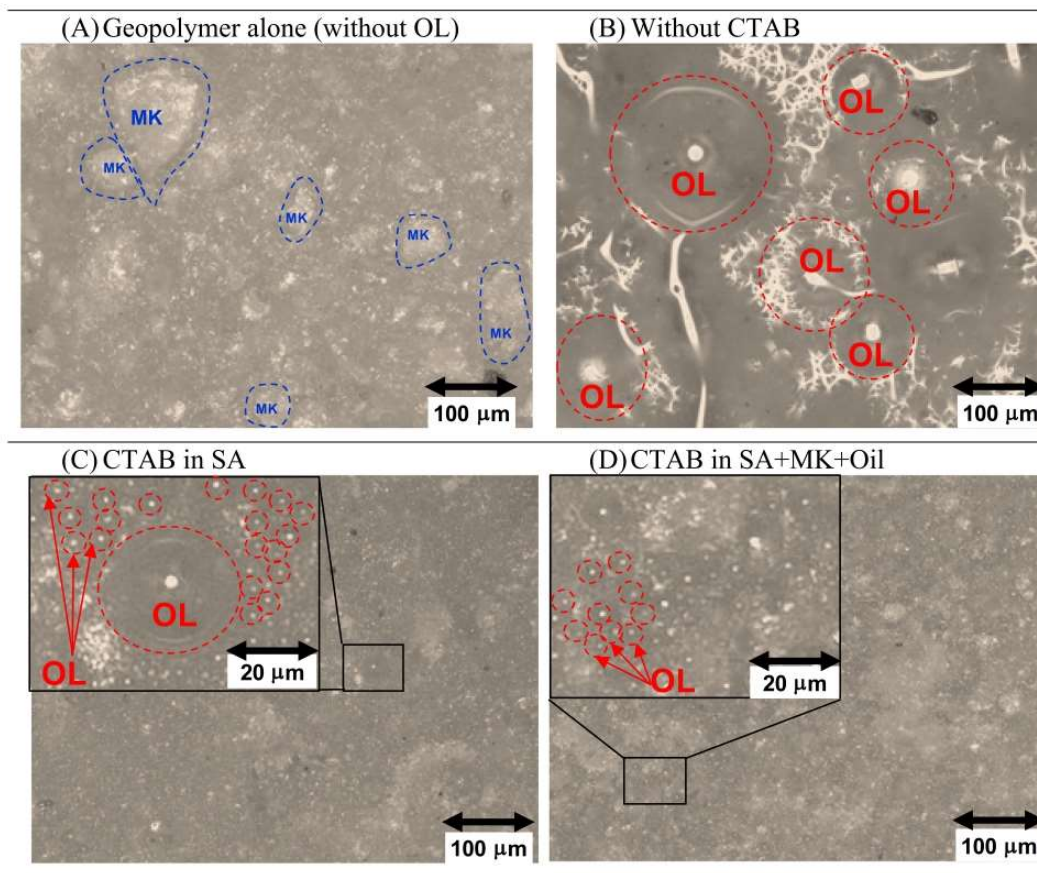


Fig. 5. Optical microscopy in reflexion mode of cured geopolymers: (A) without Organic Liquid (OL) and with of 23% of incorporated of Finavestan OL as described in Fig. 4; (B) without CTAB, (C) with addition of CTAB in the activating solution and (D) with addition of CTAB after Finavestan incorporation.

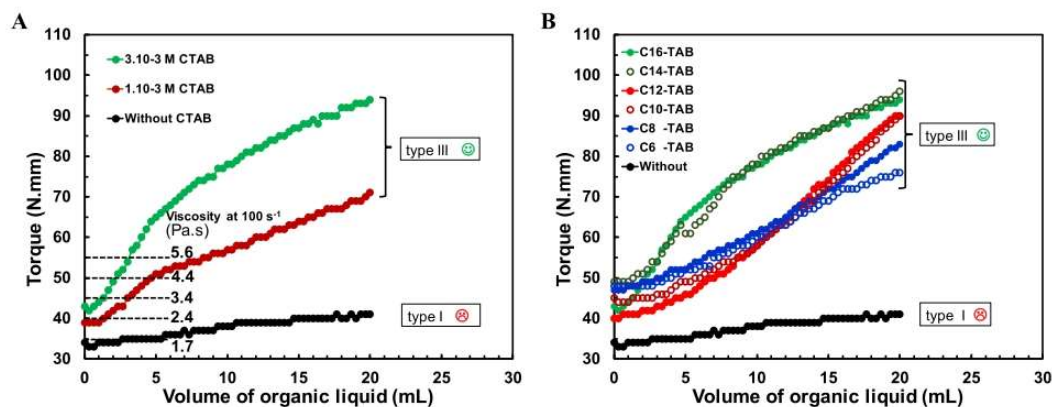


Fig. 6. Torque (N.mm) variation versus TBP/Dodecane volume (mL) added at a flow rate of $4.0 \text{ mL}\cdot\text{min}^{-1}$ at a stirring speed of 800 rpm in 80 mL of geopolymer. (A): Different concentrations of CTAB ($0, 1, 3, 5$ and $10 \cdot 10^{-3} \text{ M}$) and (B): Different quaternary ammonium ($\text{C}_6, \text{C}_8, \text{C}_{10}, \text{C}_{12}, \text{C}_{14}, \text{C}_{16}\text{-TAB}$) at $3 \cdot 10^{-3} \text{ M}$ are introduced in the activating solution.

very fluid oil mixture TBP/dodecane (7/3) will be tried using CTAB. The CTAB is introduced in the activation solution at different concentrations ($0, 1, 3, 5$ and $10 \cdot 10^{-3} \text{ M}$).

The black curve (Fig. 6) corresponds to the experience without CTAB. The correspondence between the torque and the viscosity was reported using the calibration curve (Fig. 1). Before oil addition, the viscosity of the GP increases with the amount of CTAB, from $1.7 \text{ Pa}\cdot\text{s}$ without CTAB to $3 \text{ Pa}\cdot\text{s}$ for $3 \cdot 10^{-3} \text{ M}$ of CTAB and to $4.5 \text{ Pa}\cdot\text{s}$ if $10 \cdot 10^{-3} \text{ M}$ of CTAB was used. For less important CTAB concentrations of $1 \cdot 10^{-3} \text{ M}$ and $3 \cdot 10^{-3}$, the torque strongly increases up to 5 mL of organic liquid added, then further increases but less quickly up to 20 mL . In the end, the quality of the dispersion is high and corresponds to a geoil type III. As previously observed, when the addition of 20 mL of oil is completed, the torque reaches a certain value ($60\text{--}90 \text{ N}\cdot\text{mm}$, $\approx 10 \text{ Pa}\cdot\text{s}$) and further increases, leading to a successful incorporation. On the other hand, for the highest CTAB concentrations ($5 \cdot 10^{-3} \text{ M}$ and $10 \cdot 10^{-3} \text{ M}$), the torque increases too quickly up to $85 \text{ N}\cdot\text{mm}$ at just 5 mL of LO incorporated. At this stage, the viscosity is so high (around $20 \text{ Pa}\cdot\text{s}$) that the rotation of the propeller can no longer drive the geopolymer from the outside towards the center of the reactor. Thus, the organic liquid can no longer penetrate inside the GP and accumulates at the surface of the slurry. In such a case, the torque signal is very noisy and the mixture heterogeneous. The torque tracking was therefore not reported on Fig. 6A, for such high concentrations of CTAB ($5 \cdot 10^{-3} \text{ M}$ and $10 \cdot 10^{-3} \text{ M}$).

3.7. Effect of the alkyl chain length of trimethyl ammonium bromide surfactants

Several quaternary ammoniums (QA) with different chain lengths ($\text{C}_6, \text{C}_8, \text{C}_{10}, \text{C}_{12}, \text{C}_{14}, \text{C}_{16}$) were tested in this study. Using the results of Fig. 6A, a QA concentration of $3 \cdot 10^{-3} \text{ M}$ was chosen for the incorporation of a TBP/dodecane mixture. Fig. 6B shows that whatever the quaternary ammonium that is used, the oil incorporation is successful, providing with a final geoil type III, similar to the one previously obtained with CTAB (C_{16}). The torque profiles are identical for each pairs of compounds $\text{C}_6\text{--}\text{C}_8, \text{C}_{10}\text{--}\text{C}_{12}$ and $\text{C}_{14}\text{--}\text{C}_{16}\text{-TAB}$. The profiles are convex for $\text{C}_6\text{--}\text{C}_{12}\text{-TAB}$ and concave for $\text{C}_{14}\text{--}\text{C}_{16}\text{-TAB}$. Torque monitoring shows that quaternary ammonium with short alkyl chains such as hexamethyltrimethylammonium are able to replace CTAB for the incorporation of oil with the same efficiency. The positive action of CTAB on the incor-

poration of alkane type fluids is therefore due to its positive charge rather than its surfactant activity.

It can be observed that the magnitude of the torque increase tends to be smaller with decreasing alkyl chain length. This is in accordance with the presence of hydrophobic forces between MK particles. Shorter alkyl chains decrease the range of attraction between MK particles, which decreases the size of particles agglomerates, the effective volume and ultimately the impact on the viscosity.

3.8. Zeta potential of metakaolin particles in the presence of QA

Quaternary ammonium salts (QAs) have been used to obtain high surface area nanoporous geopolymers (Kang et al., 2005; Pei et al., 2020; Singhal et al., 2017; Yu et al., 2020) improve the compressive strength of geopolymers (Petlitckaia and Poulesquen, 2019) or to increase the hydrophobicity of mineral particles to improve the adsorption capacity of organic compounds (Chen et al., 2019; Falah et al., 2016; Montgomery et al., 1991; Siyal et al., 2018). The interaction between metakaolin and QAs, responsible for an increase in viscosity of fresh geopolymers has already been observed when using CTAB (Cantarel, 2016; Revathi et al., 2017).

To demonstrate the interaction between metakaolin and QAs, suspensions of metakaolin in the presence of QAs with different chain lengths have been formulated and left at rest for 12 h . This period of rest allows the QAs species to fully adsorb on the surface of the particles. Despite the fact that geopolymer formation requires very basic conditions, the range of pH was extended from 2 to 12 in this study. In the absence of QAs, the Zeta potential of metakaolin (Fig. 7) decreases from -10 mV to -60 mV with increasing pH value. In the presence of QAs, the Zeta potential/pH curves are strongly translated to higher values and the greater the length of the alkyl chain, the higher the value of the Zeta potential. When using CTAB, the Zeta potential is high and almost constant ($60/50 \text{ mV}$) along de pH, even in highly alkaline conditions. These experiments demonstrate the affinity of QAs for metakaolin, and the interactions appear to be stronger with a longer alkyl chain like CTAB.

The concentration of hydroxide ions in a geopolymer activation solution is about $6.75 \text{ mol}\cdot\text{L}^{-1}$. This high concentration of NaOH is intended to accelerate the dissolution of the Metakaolin and thus the polymerization of the geopolymer. Since the most basic conditions used in zetametry never exceeded $10^{-2} \text{ mol}\cdot\text{L}^{-1}$, we consid-

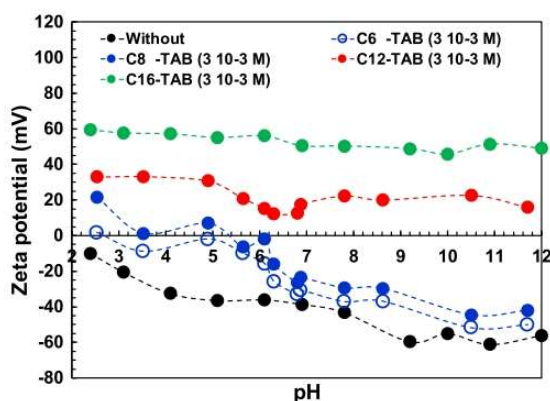


Fig. 7. Zeta potential (mV) versus pH of metakaolin suspensions without and with C_8 , C_{12} and C_{16} -TAB species at 3.10^{-3} M.

ered that our basic conditions used did not influence the zeta potential measurement. Despite the fact that geopolymer formation requires very basic conditions, the range of pH was extended from 2 to 12 in this study.

3.9. Influence of the H_2O/Na_2O molar ratio (MR) without QAs

Surprisingly, it was observed that an increase in viscosity of the starting geopolymer slurry facilitates the incorporation of very fluid organic liquids such as TBP/dodecane mixtures, even in the absence of QAs. To increase the viscosity of a geopolymer slurry, the amount of water can be reduced while keeping other formulation parameters constant. The GP that serves as a reference in this study has a molar ratio (MR) H_2O/Na_2O of 13. Two others GPs with less water have been prepared (MR = 12 and MR = 11). The viscosities of the fresh geopolymers and the p ratio reported in Table 3 show that the viscosity of fresh GPs is increasing with decreasing amount of water. This is particularly observed for the formulation with the lowest amount of water (MR = 11, torque = 65 N.mm) which corresponds to a viscosity of about 10 Pa.s in comparison with 2.4 and 2.0 Pa.s for MR = 12 and 13 respectively.

During the addition of the organic liquid in the MR = 12 formulation, the torque remains slightly higher than the reference formulation MR = 13 (type I). The incorporation is therefore being slightly improved (type II) but the geoil that is obtained is still too fluid (3.5 Pa.s) to end with a high quality incorporation. In the case of the MR = 11 formulation, the torque measurement is linearly increasing with the amount of OL added and displaying a significant slope ($1.7 \text{ N.mm. min}^{-1}$) up to 100 N.mm. In the end, the incorporation is of quality and behave as a geoil type III.

3.10. Capillary forces

The interfacial tension between TBP/Dodecane and the activating solution is the same for the three experiments presented in

Table 3
Viscosity of geopolymer (Pa.s) at 25°C at 100 s^{-1} for different H_2O/Na_2O molar ratio (MR) and corresponding p ratio (viscosity of TBP/Dodecane/viscosity of geopolymer).

	Geopolymer		
	MR = 13	MR = 12	MR = 11
Viscosity of geopolymer (Pa.s) at 25°C at 100 s^{-1}	2.0	2.4	10
p ratio	$1.8 \cdot 10^{-3}$	$1.5 \cdot 10^{-3}$	$0.36 \cdot 10^{-3}$

Fig. 8, but there is a change in the viscosity of the aqueous metakaolin suspension. The p ratio $\eta_{oil}/\eta_{Geopolymer}$ is always lower than 2.10^{-3} . According to Grace's observations (Grace, 1982), it is logic to consider that TBP/Dodecane cannot be incorporated as droplets into geopolymer slurries, and it is indeed the case with geopolymers (MR = 12 and 13). Such observations have also been confirmed in other studies⁴⁷ in which the incorporation of dodecane in geopolymers was only possible if p is higher than 10^{-2} . Moreover, this rule seems to be verified as well for organic liquid polymers, for which the viscosity adjustment of the geopolymer slurries represents the key parameter in the process of incorporating the resins into geopolymers (Colangelo et al., 2013). However, in the present study, the incorporation of TPB/dodecane in the MR = 11 geopolymer, for which the p ratio is the lowest (lower than 3.10^{-3}), the oil can be dispersed in a better way than for MR = 12 or 13 formulations.

To find an explanation, one has to consider that the system of interest is not just a liquid/liquid system, which would be governed by surface tension and viscosity forces only but also includes metakaolin particles. Ternary particle-liquid-liquid systems, composed of particles dispersed in two immiscible liquids can form a variety of structures depending on the ratio of the three components and their chemical affinity. Even when a tiny amount of the second immiscible liquid is added into the first liquid containing the particles (i.e. particles suspension), the rheological properties of the initial suspension can be dramatically altered from a fluid-like to a gel-like state or from a weak to a strong gel. In that case, the viscosity further increases as the volume fraction of the second fluid increases and is attributed to capillary forces between the two fluids and the solid particles. The so-called "capillary suspensions" are a typical phenomenon for these ternary systems, in which capillary or pendular states are building up depending on the wetting properties of each liquid towards the solid particles.

These capillary forces also depend on the interfacial tension between the two liquids and can be observed when the proportion of solid particles is important. This phenomenon could explain why the incorporation of TBP/dodecane is possible in a highly concentrated aqueous suspension (MR = 11) and not in a more diluted medium (MR = 12 or 13).

An experiment carried out with hydrophilic glass beads (SiO_2) in water with small amount of diisononyl phthalate (DINP) as second immiscible fluid shows that the water preferentially wets the glass beads. However, oil droplets are also wetting the glass beads to a lesser extent, but high enough to create bridges joining beads with each other, thus forming the pendular state. The same experiment with hydrophobic glass beads instead of hydrophilic ones changes the system from pendular to capillary state in which water, being the continuous phase, does not preferentially wet the treated beads (Koos, 2014; Koos and Willenbacher, 2011). Such capillary associations can be observed by microscopy using fluorescent dyes.

Unfortunately, through the course of this study, it was not possible to show such water/oil/metakaolin associations by microscopy. However, to demonstrate these capillary forces, Washburn tests were performed. Water, dodecane and Finavestan were allowed to rise along conventional and hydrophobically modified (using CTAB) metakaolin.

Fig. 9 presents the results of the Washburn methods that can be described as follow. After the contact of a glass tube filled with metakaolin powder has been made, the liquid is rising along the powder as a result of capillarity, inducing an increase in mass, whose square can be plotted in function of time. If considering the metakaolin powder as a bundle of capillaries, the liquid migration into the solid can be described thanks to the Washburn equation (Eq. (1)) below:

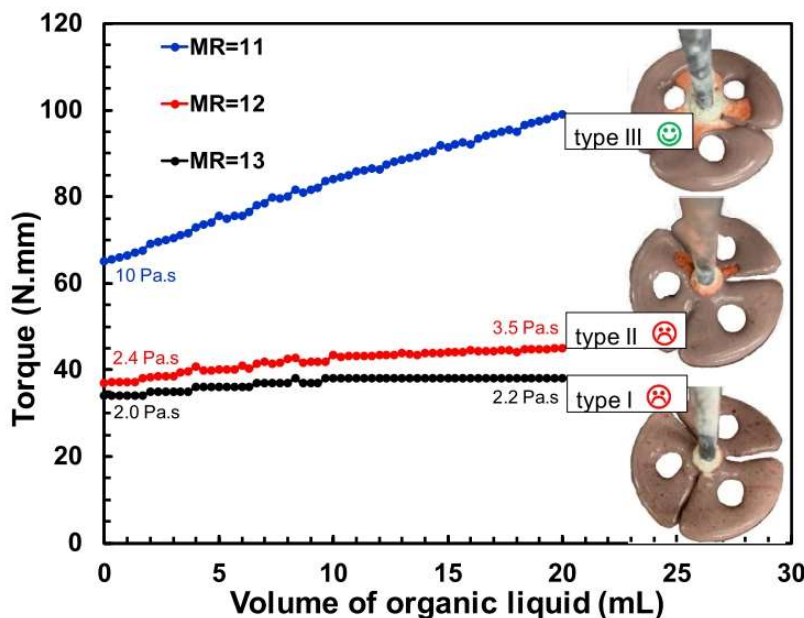


Fig. 8. Torque (N.mm) variation versus TBP/Dodecane volume (mL) added at a flow rate of 4.0 mL.min⁻¹ at stirring speed = 800 rpm in 80 mL of geopolymer. Formulated with water molar ratio of 11, 12 and 13.

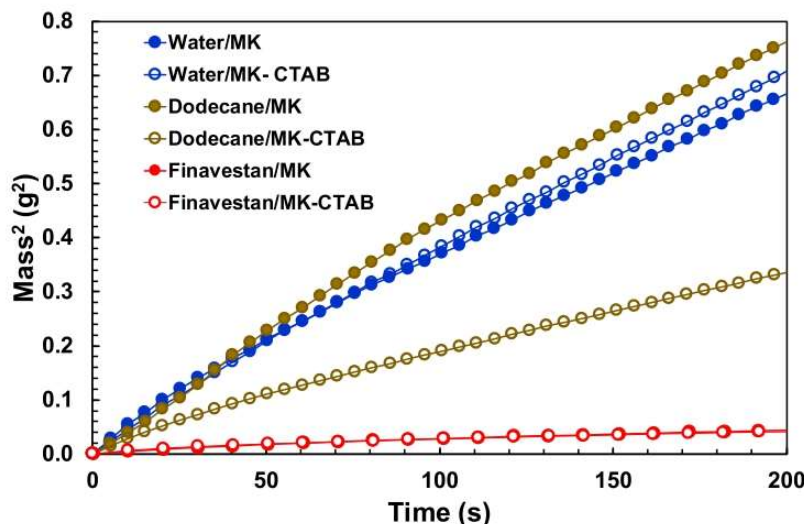


Fig. 9. Washburn tests representing the square of liquid mass (g²) on metakaolin powders (MK) allowed to rise via capillarity in function of time. Liquids are water (blue circles), dodecane (brown circles) and Finavestan (red circles). Full circles corresponds to non-modified metakaolin and open circles to metakaolin impregnated with 10⁻² M of CTAB. (For interpretation of the references to colour in this figure legend, the reader is referred to the web version of this article.)

$$\frac{m^2}{t} = \frac{C \times \gamma \times \cos \theta \times \rho^2}{\eta} \quad (1)$$

where m , C , ρ , γ , η , θ , t are respectively the mass of liquid adsorbed, the capillary constant of the powder, the density, the superficial tension and the viscosity of the liquid, the contact angle between the liquid and the solid and the time.

Dodecane and water show the same migration rate in untreated metakaolin. Concerning water, the speed of migration is almost

identical on the two kinds of metakaolin particles, which is not the case for dodecane, which seems to be more retained by the hydrophobic powder. About Finavestan, there is no difference in behavior depending on the nature of the metakaolin, the migration speed being rather governed by the high viscosity of the oil (Eq. (1)), as can be confirmed by the low value of $\rho^2 \cdot \gamma / \eta$ (Table 4). From the slopes measurements ($\Delta m^2 / \Delta t$) and the calculated $\rho^2 \cdot \gamma / \eta$, $C \cdot \cos(\theta)$ values can be determined (Table 4). The value of $C \cdot \cos(\theta)$ is the highest for water, followed by dodecane and finally

Table 4

 Density ($\text{kg}\cdot\text{m}^{-3}$), Viscosity (Pa.s), Superficial tension ($\text{N}\cdot\text{m}^{-1}$) and $\rho^2\cdot\gamma/\eta$ ($\text{kg}^2\cdot\text{m}^{-3}\cdot\text{s}^{-1}$) at 25 °C for water, dodecane and Finavestan oil. Slope ($\Delta\text{m}^2/\Delta\text{t}$ in $\text{kg}^2\cdot\text{s}^{-1}$) and $C\cdot\cos(\theta)$ are extracted from the Washburn equation.

Liquid	Density at 25 °C (ρ) ($\text{kg}\cdot\text{m}^{-3}$)	Viscosity at 25 °C (η) (Pa.s = $\text{N}\cdot\text{s}\cdot\text{m}^{-2}$)	Superficial Tension at 25 °C (γ) ($\text{N}\cdot\text{m}^{-1}$)	$\rho^2\cdot\gamma/\eta$ ($\text{kg}^2\cdot\text{m}^{-3}\cdot\text{s}^{-1}$)	Slope ($\Delta\text{m}^2/\Delta\text{t}$) ($\text{kg}^2\cdot\text{s}^{-1}$)	$C\cdot\cos(\theta)$ (m^{-3})
Dodecane	749	0.0013	0.0254	$3.7 \cdot 10^2$	$3.8 \cdot 10^{-9\text{a}}$ $1.6 \cdot 10^{-9\text{b}}$	$1.0 \cdot 10^{-7\text{a}}$ $4.3 \cdot 10^{-8\text{b}}$
Finavestan	900	0.143	0.0314	$6.2 \cdot 10^0$	$1.9 \cdot 10^{-10\text{a}}$ $1.9 \cdot 10^{-10\text{b}}$	$3.1 \cdot 10^{-11\text{a}}$ $3.1 \cdot 10^{-11\text{b}}$
Water	1000	0.001	0.0725	$5.3 \cdot 10^3$	$3.2 \cdot 10^{-9\text{a}}$ $3.5 \cdot 10^{-9\text{b}}$	$6.0 \cdot 10^{-7\text{a}}$ $6.0 \cdot 10^{-7\text{b}}$

^aSlope ($\Delta\text{m}^2/\Delta\text{t}$) with metakaolin (MK), ^b with hydrophobic metakaolin (MK-CTAB).

Finavestan, which indicates that water is better wetting natural or hydrophobically treated metakaolin than dodecane or Finavestan. However, the most important observation to keep in mind for this study is that these three different liquids are capable of wetting metakaolin particles, since capillary rises are observed.

The capillary interactions seen in the Washburn experiments presented in Fig. 9 bring to light the importance of the interactions between metakaolin and the two immiscible liquids. When metakaolin is impregnated with CTAB, the behavior of dodecane towards the powder changes, whereas the behavior of water remains unchanged. Thus, by concentrating an aqueous suspension of metakaolin even more, the solid-liquid interactions with the introduced oil will increase, and the strength of capillary forces will be enhanced. This could explain why the incorporation of organic liquid is made possible in very high viscosity geopolymers, even if the p ratio is lower than 10^{-3} (Fig. 8).

4. Conclusion

Torque monitoring, which is very convenient in the case of industrial applications, was used to follow the incorporation of OL in geopolymer. First, in-line torque monitoring during OL incorporation into geopolymer (GP) slurries provides information on the viscosity of the mixtures using a prior calibration. This avoids off-line rheological measurements and allows observing the impact of each component on the rheology of the mixtures. In addition, in-line torque monitoring allows having relevant information about the OL incorporation process. In particular, three types of torque evolution were identified upon OL addition, corresponding to three types of fresh GEOIL textures (Type I, II and III). When the OL is not incorporated and remains at the surface of the geopolymer slurry, the torque remains constant, which corresponds to Type I GEOIL. On the contrary, effective OL incorporation processes are those displaying an increase in torque. If the torque increases at the start of OL incorporation, but remains constant from a specific amount of OL incorporated, Type II GEOIL is obtained, with an excess of OL at the surface of the mixture. In order to obtain a continuous increase in torque, corresponding to a full incorporation of the OL, the addition of quaternary ammonium (QAs) has proven to be very efficient (Type III). It was demonstrated that the effectiveness of QAs is due to the positive charge of the quaternary ammonium part rather than to the length of the alkyl chain. More specifically, QAs species increase the viscosity of fresh GP and act on the viscosity ratio (p) between the OL and the GP. This ratio is an important parameter to obtain a suitable OL incorporation (Type III). In accordance with Grace's observations, a ratio greater than 10^{-2} constitutes favorable conditions. However, even at very low p ratio ($<10^{-3}$), when highly viscous geopolymers are used ($\text{MR} = 11$), the incorporation of OL is possible. In that case, metakaolin particles (MK) are concentrated enough to consider the presence of strong particle/liquid interactions. These capillary forces were demonstrated using the Washburn method, showing

different behavior between OL, water and MK particles, depending on whether the latter has been hydrophobically treated with QAs or not.

The alkali-activation of metakaolin, poor in Ca, leads to the formation of a 3D reticulated alumino-silicate gel (N-A-S-H), the so-called geopolymer structure. Other raw materials used for alkali-activation, rich in Ca (e.g. fly ash C or slag) lead to the formation of 2D calcium alumino-silicate hydrates (C-A-S-H) as in Portland cements. This type of material is less suitable for OL immobilization. On the contrary, the literature reports the very good compatibility of various organic liquids with geopolymer materials (Reeb et al., 2021). It would indeed be interesting to investigate other Ca-poor raw materials with the purpose of recycling industrial wastes (e.g. fly ash F, red mud). However, metakaolin (MK) was chosen in this study for its stable composition and easy supply.

In conclusion, the in-line torque monitoring is useful to ensure OL incorporation (i.e. when the torque increases) but also to maintain sufficient workability of the final GEOIL mixture. The addition of QAs surfactants is required for the incorporation of some OL in fresh GP. It can be noticed that QAs can be added directly in the activation solution or after the OL incorporation step with no significant differences. However, the addition of QAs leads to a strong viscosity increase of fresh GEOIL, which can be an issue at an industrial scale. In this work, only QAs surfactants were tested and other types should be considered to better control the rheology of GEOIL mixtures. Finally, in the case of successful OL incorporation (Type III), droplets are efficiently dispersed and smaller than 10 μm in the GEOIL composite.

CRediT authorship contribution statement

Christel Pierlot: Writing – original draft. **Hanyu Hu:** Investigation. **Charles Reeb:** Investigation. **Jordan Bassetti:** Investigation. **Mathieu Bertin:** Investigation. **David Lambertin:** Funding acquisition, Supervision. **Catherine Davy:** Resources, Writing – review & editing. **Véronique Nardello-Rataj:** Resources, Funding acquisition.

Declaration of Competing Interest

The authors declare that they have no known competing financial interests or personal relationships that could have appeared to influence the work reported in this paper.

Acknowledgments

Chevreur Institute (FR 2638), Ministère de l'Enseignement Supérieur et de la Recherche, Région Hauts de France, and FEDER are acknowledged for supporting and funding part of this work.

References

- Akay, G., 1997. Flow-induced phase inversion in the intensive processing of concentrated emulsions. *Chem. Eng. Sci.* 53 (2), 203–223. [https://doi.org/10.1016/S0009-2509\(97\)00199-1](https://doi.org/10.1016/S0009-2509(97)00199-1).
- Akay, G., Tong, L., 2001. Preparation of colloidal low-density polyethylene latexes by flow-induced phase inversion emulsification of polymer melt in water. *J. Colloid Interface Sci.* 239 (2), 342–357. <https://doi.org/10.1006/jcis.2001.7615>.
- Allouche, J., Tyrode, E., Sadtler, V., Choplin, L., Salager, J.-L., 2004. Simultaneous conductivity and viscosity measurements as a technique to track emulsion inversion by the phase-inversion-temperature method. *Langmuir* 20 (6), 2134–2140. <https://doi.org/10.1021/la035334r>.
- Autef, A., Joussein, E., Poulesquen, A., Gagnier, G., Pronier, S., Sobrados, I., Sanz, J., Rossignol, S., 2013. Influence of metakaolin purities on potassium geopolymer formulation: The existence of several networks. *J. Colloid Interface Sci.* 408, 43–53. <https://doi.org/10.1016/j.jcis.2013.07.024>.
- Bai, C., Colombo, P., 2018. Processing, properties and applications of highly porous geopolymers: A review. *Ceram. Int.* 44 (14), 16103–16118. <https://doi.org/10.1016/j.ceramint.2018.05.219>.
- Bai, C., Franchin, G., Elsayed, H., Conte, A., Colombo, P., 2016. High strength metakaolin-based geopolymer foams with variable macroporous structure. *J. Eur. Ceram. Soc.* 36 (16), 4243–4249. <https://doi.org/10.1016/j.jeurceramsoc.2016.06.045>.
- Barbosa, T.R., Foletto, E.L., Dotto, G.L., Jahn, S.L., 2018. Preparation of mesoporous geopolymer using metakaolin and rice husk ash as synthesis precursors and its use as potential adsorbent to remove organic dye from aqueous solutions. *Ceram. Int.* 44 (1), 416–423. <https://doi.org/10.1016/j.ceramint.2017.09.193>.
- Cantarel, V., 2016. Etude de la synthèse de composites liquides organiques/géopolymère en vue du conditionnement de déchets nucléaires. Université Blaise Pascal-Clermont-Ferrand II.
- Cantarel, V., Lambertin, D., Poulesquen, A., Leroux, F., Renaudin, G., Frizon, F., 2018. Geopolymer assembly by emulsion templating: Emulsion stability and hardening mechanisms. *Ceram. Int.* 44 (9), 10558–10568. <https://doi.org/10.1016/j.ceramint.2018.03.079>.
- Cantarel, V., Nouaille, F., Rooses, A., Lambertin, D., Poulesquen, A., Frizon, F., 2015. Solidification/stabilisation of liquid oil waste in metakaolin-based geopolymer. *J. Nucl. Mater.* 464, 16–19. <https://doi.org/10.1016/j.jnucmat.2015.04.036>.
- Catte, M., Ontiveros, J.F., Aramaki, K., Pierlot, C., 2018. Catastrophic emulsion inversion process of highly viscous isosorbide biobased polyester monitored in situ by torque and light backscattering. *J. Oleo Sci.* 67, 925–931. <https://doi.org/10.5650/jos.ess18057>.
- Chen, S., Qi, Y., Cossa, J.J., Deocleciano Salomao Dos, S.J., 2019. Efficient removal of radioactive iodide anions from simulated wastewater by HDTMA-geopolymer. *Prog. Nucl. Energy* 117, 103112. <https://doi.org/10.1016/j.pnucene.2019.103112>.
- Cilla, M.S., de Mello Innocentini, M.D., Morelli, M.R., Colombo, P., 2017. Geopolymer foams obtained by the saponification/peroxide/gelcasting combined route using different soap foam precursors. *J. Am. Ceram. Soc.* 100 (8), 3440–3450.
- Colangelo, F., Roviello, G., Ricciotti, L., Ferone, C., Cioffi, R., 2013. Preparation and characterization of new geopolymer-epoxy resin hybrid mortars. *Materials* 6 (7), 2989–3006.
- Davidovits, J., 1991. Geopolymers: inorganic polymeric new materials. *J. Therm. Anal.* 37 (8), 1633–1656.
- Davy, C.A., Hauss, G., Planel, B., Lambertin, D., 2019. 3D structure of oil droplets in hardened geopolymer emulsions. *J. Am. Ceram. Soc.* 102, 949–954. <https://doi.org/10.1111/jace.16142>.
- Dusserre, G., Farrugia, A., Cutard, T., 2020. Rheology evolution of a geopolymer precursor aqueous suspension during aging. *Int. J. Appl. Ceram. Technol.* Ahead of Print 17 (4), 1802–1810. <https://doi.org/10.1111/ijac.13508>.
- Duxson, P., Fernández-Jiménez, A., Provis, J.L., Lukey, G.C., Palomo, A., van Deventer, J.S.J., 2007. Geopolymer technology: The current state of the art. *J. Mater. Sci.* 42 (9), 2917–2933. <https://doi.org/10.1007/s10853-006-0637-z>.
- Edward, A.C., Veronique, S., Philippe, M., Lionel, C., Frederic, D., Michel, M., 2014. Preparation of highly concentrated bitumen emulsions by catastrophic phase inversion: Follow-up of the emulsification process. *Colloids Surf. A* 458, 25–31. <https://doi.org/10.1016/j.colsurfa.2014.02.030>.
- Falah, M., MacKenzie, K.J.D., Knibbe, R., Page, S.J., Hanna, J.V., 2016. New composites of nanoparticle Cu (I) oxide and titania in a novel inorganic polymer (geopolymer) matrix for destruction of dyes and hazardous organic pollutants. *J. Hazard. Mater.* 318, 772–782.
- Galindo-Alvarez, J., Sadtler, V., Choplin, L., Salager, J.-L., 2011. Viscous oil emulsification by catastrophic phase inversion: influence of oil viscosity and process conditions. *Ind. Eng. Chem. Res.* 50 (9), 5575–5583. <https://doi.org/10.1021/ie102224k>.
- Glad, B.E., Kriven, W.M., Colombo, P., 2015. Highly porous geopolymers through templating and surface interactions. *J. Am. Ceram. Soc.* 98 (7), 2052–2059.
- Goger, A., Thompson, M.R., Pawlak, J.L., Lawton, D.J.W., 2015. In situ rheological measurement of an aqueous polyester dispersion during emulsification. *Ind. Eng. Chem. Res.* 54 (21), 5820–5829. <https://doi.org/10.1021/acs.iecr.5b00765>.
- Grace, H.P., 1982. Dispersion phenomena in high viscosity immiscible fluid systems and application of static mixers as dispersion devices in such systems. *Chem. Eng. Commun.* 14 (3–6), 225–277.
- Guazzelli, E., Pouliquen, O., 2018. Rheology of dense granular suspensions. *J. fluid mech.* 852, P1/P1/73. <https://doi.org/10.1017/jfm.2018.548>.
- Hussain, M., Varely, R., Cheng, Y.B., Mathys, Z., Simon, G.P., 2005. Synthesis and thermal behavior of inorganic-organic hybrid geopolymer composites. *J. Appl. Polym. Sci.* 96 (1), 112–121. <https://doi.org/10.1002/app.21413>.
- Hussain, M., Varley, R.J., Cheng, Y.B., Simon, G.P., 2004. Investigation of thermal and fire performance of novel hybrid geopolymer composites. *J. Mater. Sci.* 39 (14), 4721–4726. <https://doi.org/10.1023/B:JMSE.0000034180.35216.ba>.
- Kang, F., Wang, Q., Xiang, S., 2005. Synthesis of mesoporous Al-MCM-41 materials using metakaolin as aluminum source. *Mater. Lett.* 59 (11), 1426–1429.
- Koos, E., 2014. Capillary suspensions: Particle networks formed through the capillary force. *Curr. Opin. Colloid Interface Sci.* 19 (6), 575–584.
- Koos, E., Willenbacher, N., 2011. Capillary forces in suspension rheology. *Science* 331 (6019), 897–900.
- Lambertin, D., Cantarel, V., Poulesquen, A., Frizon, F., 2018. Production of geopolymer composites comprising organic phase change materials.
- Liu, J., Li, F., Zhang, R., Dong, E., Gong, X., Lun, Y., Zhang, T., Zhu, J., 2018. Foam geopolymer for tunnel composite lining and preparation method thereof.
- Medpelli, D., Seo, J.-M., Seo, D.-K., Glasser, F., 2014. Geopolymer with hierarchically meso-/macroporous structures from reactive emulsion templating. *J. Am. Ceram. Soc.* 97 (1), 70–73.
- Montgomery, D., Sollars, C., Perry, R., 1991. Optimization of cement-based stabilization/solidification of organic-containing industrial wastes using organophilic clays. *Waste Manage. Res.* 9 (1), 21–34.
- Pei, Y.-R., Yang, J.-H., Choi, G., Choy, J.-H., 2020. A geopolymer route to micro- and meso-porous carbon. *RSC Adv.* 10 (12), 6814–6821. <https://doi.org/10.1039/C9RA06988A>.
- Petlitskaia, S., Poulesquen, A., 2019. Design of lightweight metakaolin based geopolymer foamed with hydrogen peroxide. *Ceram. Int.* 45 (1), 1322–1330.
- Pierlot, C., Ontiveros, J.F., Royer, M., Catte, M., Salager, J.-L., 2018. Emulsification of viscous alkyl resin by catastrophic phase inversion with nonionic surfactant. *Colloids Surf. A* 536, 113–124. <https://doi.org/10.1016/j.colsurfa.2017.07.030>.
- Provis, J.L., van Deventer, J.S.J., Editors., 2009. Geopolymers: Structure, Processing, Properties and Industrial Applications. Woodhead Publishing Ltd.
- Reeb, C., Pierlot, C., Davy, C., Lambertin, D., 2021. Incorporation of organic liquids into geopolymer materials-A review of processing, properties and application. *Ceram. Int.* 47, 7369–7385. <https://doi.org/10.1016/j.ceramint.2020.11.239>.
- Revathi, T., Jeyalakshmi, R., P. Rajamane, N., Sivasakthi, M., 2017. Evaluation of the role of Cetyltrimethylammoniumbromide (CTAB) and Acetylenicglycol (AG) admixture on fly ash based geopolymer. *Orient J. Chem.* 33 (2), 783–792.
- Rouyer, J., Poulesquen, A., Struble, L., 2015. Evidence of a fractal percolating network during geopolymerization. *J. Am. Ceram. Soc.* 98 (5), 1580–1587.
- Saw, L.K., Brooks, B.W., Carpenter, K.J., Keight, D.V., 2004. Catastrophic phase inversion in region II of an ionomeric polymer-water system. *J. Colloid Interface Sci.* 279 (1), 235–243. <https://doi.org/10.1016/j.jcis.2004.06.056>.
- Singhal, A., Gangwar, B.P., Gayathry, J.M., 2017. CTAB modified large surface area nanoporous geopolymer with high adsorption capacity for copper ion removal. *Appl. Clay Sci.* 150, 106–114.
- Siyal, A.A., Shamsuddin, M.R., Khan, M.I., Rabat, N.E., Zulfiqar, M., Man, Z., Siame, J., Azizi, K.A., 2018. A review on geopolymers as emerging materials for the adsorption of heavy metals and dyes. *J. Environ. Manage.* 224, 327–339.
- Song, D., Zhang, W., Gupta, R.K., Melby, E.G., 2011. Role of operating conditions in determining droplet size and viscosity of tackifier emulsions formed via phase inversion. *AIChE J.* 57 (1), 96–106. <https://doi.org/10.1002/aic.12238>.
- Steins, P., Poulesquen, A., Diat, O., Frizon, F., 2012. Structural Evolution during geopolymerization from an Early Age to Consolidated Material. *Langmuir* 28 (22), 8502–8510. <https://doi.org/10.1021/la300868v>.
- Sun, C., Xiang, J., Xu, M., He, Y., Tong, Z., Cui, X., 2020. 3D extrusion free forming of geopolymer composites: Materials modification and processing optimization. *J. Cleaner Prod.* 258, 120986. <https://doi.org/10.1016/j.jclepro.2020.120986>.
- Suzzoni, A., Barre, L., Kohler, E., Levitz, P., Michot, J.J., MHamdi, J., 2018. Interactions between kaolinite clay and AOT. *Coll. Surf. A* 556, 309–315. <https://doi.org/10.1016/j.colsurfa.2018.07.049>.
- Thakur, N., Weatherly, C.A., Wimalasinghe, R.M., Armstrong, D.W., 2019. Fabrication of interconnected macroporosity in geopolymers via inverse suspension polymerization. *J. Am. Ceram. Soc.* 102 (8), 4405–4409.
- Wang, S., Ma, X., He, L., Zhang, Z., Li, L., Li, Y., 2019. High strength inorganic-organic polymer composites (IOPC) manufactured by mold pressing of geopolymers. *Constr. Build. Mater.* 198, 501–511.
- Yu, Z., Song, W., Li, J., Li, Q., 2020. Improved simultaneous adsorption of Cu (II) and Cr (VI) of organic modified metakaolin-based geopolymer. *Arabian J. Chem.* 13 (3), 4811–4823.
- Yunsheng, Z., Wei, S., Zongjin, L., Xiangming, Z., Eddie, C., 2008. Impact properties of geopolymer based extrudates incorporated with fly ash and PVA short fiber. *Constr. Build. Mater.* 22, 370–383. <https://doi.org/10.1016/j.jconbuildmat.2006.08.006>.
- Zhang, X.-P., Hu, Y.-H., Liu, R.-Q., 2008. Hydrophobic aggregation of ultrafine kaolinite. *J. Cent. South Univ. Tech. ing Hydrophobic aggregation of ultrafine kaolinite* 15 (3), 368–372. <https://doi.org/10.1007/s11771-008-0069-9>.

Appendix 2

**Solidification/Stabilization (S/S) of high viscosity
organics in geopolymers**



Contents lists available at ScienceDirect

Journal of Nuclear Materials

journal homepage: www.elsevier.com/locate/jnucmat

Solidification/stabilization (S/S) of high viscosity organics in geopolymers

M. De Campos^a, C. Reeb^{a,b}, C.A. Davy^{b,*}, J. Hosdez^c, D. Lambertin^a^a CEA, DES, ISEC, DE2D, SEAD, LCBC, Marcoule, Univ. Montpellier, France^b UMR 8181 - UCCS - Unité de Catalyse et de Chimie du Solide, Univ. Lille, CNRS, Centrale Lille, ENSCL, Univ. Artois, Lille F-59000, France^c Laboratoire de Mécanique, Univ. Lille, CNRS, Centrale Lille, Multiphysique et Multiéchelle (LaMcube) UMR CNRS 9013, Lille F-59000, France

ARTICLE INFO

Article history:

Received 24 May 2022

Revised 15 July 2022

Accepted 11 August 2022

Available online 13 August 2022

Keywords:

Solidification/stabilization
Alkali-activated materials (AAM)
Geopolymers
Tributylphosphate
Dodecane
Organics
Grease
Oils
Viscosity

ABSTRACT

This research contributes to nuclear waste management by proposing a simple treatment route for high viscosity (HV) organics (oils and greases). These are currently without an industrial solution, because they are not directly pourable into a cementation matrix. Their solidification/stabilization (S/S) into geopolymers (GP) is investigated. Incorporation is achieved by assembling the HV organics (a model oil MO, an industrial oil IO or a grease G) with a low viscosity (LV) solvent, either dodecane (C12) or a mix of tributylphosphate (TBP)/C12, prior to mixing with the fresh GP.

First, the minimal solvent amount is determined to achieve sufficient fluidity of the HV oil or grease mix. Two different criteria are used, one for the Newtonian oils and the other for the non-Newtonian grease. Secondly, the immobilization of 20%vol of assembled mix is performed into a GP paste or mortar. The organics bleeding, the GP setting, the rheological properties of the mix, and the mechanical performance at 28 days endogenous curing are assessed. The morphology of the oil or grease emulsion inside the hardened GP mortar is determined by 2D SEM observations and 3D quantitative X Ray micro-computed tomography. The efficiency of the immobilization is proven by cross analyzing these properties. In particular, a minimal compressive strength of 25.4 MPa \pm 4.6 is achieved for a GP mortar immobilizing 20%vol HVG assembled with TBP/C12; it corresponds to an emulsion made of 12.9%vol droplets in the 10–480 μ m size range, and 7.1%vol smaller than 10 μ m, without organics bleeding.

© 2022 Elsevier B.V. All rights reserved.

1. Introduction

1.1. Industrial and scientific context

The Stabilization/Solidification (S/S) of organic liquids (OL) in geopolymers is a well-known process [3,8,9,11,15,27,28,31,40,48,56]. It is useful for varied applications, e.g. after oil removal, where mechanically stable highly porous ceramics are an asset (as membrane supports for photocatalytic degradation applications, as catalyst supports, or heavy metals adsorbents, etc.) [3–5,15,27,31,48], or for the manufacturing of phase change materials [28,48]. One particularly useful application is the direct immobilization of nuclear OL waste [8,9,11,27,40].

Indeed, more traditional Portland cement-based matrices, or alkali-activated materials with high Ca content (e.g. based on blast furnace slag or Class C fly ash), are less adapted to incorporating significant amounts of OL [19,25,32,34,40,42,52]. For instance, after

incorporating 40% by weight of oily waste into Portland cement matrices [19], a very low compressive strength of 0.5 MPa is obtained; this does not comply with current Waste Acceptance Criteria [54]. In [40], formulations incorporating alkali-activated Class C fly ash and 20%vol pump oil demonstrate a weak resistance to water flow.

On the opposite, geopolymers have proven effective to incorporate up to 60%vol low viscosity oils [8,11,40]. Geopolymers (GP) are aluminosilicate amorphous cements, generally obtained by the activation of powdered solid precursors (metakaolin, Class F fly ash, silica fume, etc.) with a highly alkaline silicate liquid [10]. Several routes exist to incorporate the OL into the GP [56]. The direct route is the simplest option; provided that the OL is sufficiently fluid, it consists in simply pouring the OL into the fresh GP paste while stirring the mix, which results in emulsifying the OL, and creating a 3D droplet distribution throughout the GP matrix.

For instance, the compressive strength of GP mortars added with 20%vol OL are high, with values of 33.6 MPa \pm 3 at 30 days [40], and durability is significant; water permeability is on the order of 4×10^{-19} m² for at least 40 days experiments, and this value is on the order of High Performance Portland-cement based

* Corresponding author at: Sorbonne Université, CNRS, EPHE, UMR 7619 METIS, 4 place Jussieu 75005 Paris, France.

E-mail address: catherine.davy@enscm.fr (C.A. Davy).

Glossary

C12	dodecane
TBP	tributylphosphate
GP	geopolymer
MK-GP	metakaolin-based geopolymer
OL	organic liquid
LV	low Viscosity
HV	high Viscosity
LVOL	low viscosity organic liquid
HVOL	high viscosity organic liquid
MO	model oil
IO	industrial oil
SEM	Scanning Electron Microscope
X Ray micro-CT	X ray micro-computed tomography

Concretes (HPC) [6,46,53]. The connectivity between the spherical OL droplets, leading to a percolating oil system, is shown to be obtained from 27%vol OL and more [11,13]; nevertheless, depending on the actual 3D morphology of the waste inside the GP (e.g. as elongated droplets), this proportion may be significantly lower [13,21,35].

Despite all this, for high viscosity OL (i.e. organics with a viscosity > 1 Pa.s), the direct S/S process is not possible, because these OL cannot be simply poured into the fresh GP paste.

1.2. Aims and scopes

Currently, in Europe and in a number of industrialized countries, some amounts of radioactive high viscosity (HV) oils and greases are awaiting a long-term treatment route, because they cannot be directly conditioned in a cement-based matrix, due to their poor flowability and fluidity. Due to the presence of radionuclides, they cannot be heated or calcined easily (due to WAC regulations [54]); it would be preferable to make them more fluid, so that they can be further incorporated into a S/S cementing process. According to the literature dedicated to the fluidization of petroleum compounds for their transport by pipelines, HV oils and greases can be fluidized in different ways, particularly by assembly with low viscosity (LV) solvents [12,36].

For an assembly with nuclear OL waste, the adequate choice of the solvent is important, because it must not react with the OL, and not evaporate at room temperature. Usual solvents in the nuclear industry are alkanes, such as dodecane (C12) with a low viscosity of 1.32 mPa.s, or mixtures of such solvents. The mixture of TriButylPhosphate (TBP) and dodecane (TBP/C12, at 30 and 70%vol respectively) is currently used as an extraction solvent in the PUREX (Plutonium Uranium Reduction Extraction) process, for fuel recycling [14]; TBP/C12 has a low viscosity of about 1.90 mPa.s [26]. Its use for the assembly of oils and viscous grease would allow a double conditioning in a single process, with a circular economy perspective.

This research aims to determine in what practical conditions the assembly of C12 or TBP/C12 with HVOL (oils and grease) is feasible, and what are its main performances. It is divided into two parts.

The first part determines the conditions for an assembly (dilution) of HVOL with LV solvents prior to their incorporation into GP paste. To this purpose, the cases of HV oils and greases are distinguished, due to their different rheological behavior (Newtonian or non-Newtonian, respectively). Two main LV solvents for HVOL are tested, either C12 alone or TBP/C12 (mix of 30%vol TBP+70%vol C12); the solvent amount is varied in order to determine a threshold below which the HVOL+LV solvent mix is considered pourable.

The second part investigates the immobilization of 20%vol of the assembled OL mixtures into GP materials. A minimum OL amount of 20%vol is necessary to justify industrial scaling of the immobilization process. This involves (1) the incorporation quality: what is the GP+OL rheological behavior? does the OL remain immobilized inside the GP after hardening? (2) how is the GP paste setting impacted by OL presence? (3) is the mechanical performance of hardened GP+OL mortars sufficient and compliant with industrial practice? and (4) how is the OL microstructure inside the hardened GP: is the emulsion made of 3D small, dispersed, spherical and disconnected droplets, corresponding to non-percolating OL?

2. Materials and methods

2.1. Raw materials

2.1.1. Geopolymer matrices

Metakaolin (MK, of M1000 grade) is supplied by Imerys (France). A sodium silicate solution, Betol 52T is supplied by Woellner (Germany). Sodium hydroxide is purchased from VWR (France). Silica Sand (0–5 mm grain size distribution) from Le Beausset is supplied by Lafarge.

2.1.2. Organics - oils and greases

The OL used in this study are summarized in Table 1. They are divided in two categories: high viscosity organic liquids (HVOL) or low viscosity organic liquids (LVOL). HVOL are the compounds to be stabilized into the GP matrix (a model oil, an industrial oil and a grease), and the LVOL (solvents) aim to lower their viscosity, and hence, ease the stabilization, by an assembly method.

The selected LVOL are Tributylphosphate (TBP) (CAS Number 126-73-8) and Dodecane (C12), both supplied by VWR (France). A mixture of TBP/C12 (30/70 v/v) is also studied because it is the most common extraction solvent used in the nuclear fuel cycle.

A HV pure mineral oil (Nevastane EP1000) is obtained from Total (France). This oil is chosen for its purity (i.e. its absence of additives) and for its absence of reactivity in alkaline media.

A HV industrial oil (Mobil 600XP680) is obtained from Lubexcel (France). The additives present in Mobil 600XP680 are various amines, such as C12-14-tert-alkyl (CAS Number 68955-53-3) and tris(methylphenyl) phosphate (CAS Number 1330-78-5) [20].

A HV grease of grade NLGI 3 is chosen (Gadus S2 V100 3, supplied by Lubexcel, France). The grade corresponds to the consistency of the grease and can vary between 0 (fluid) and 6 (hard). Greases differ from oils by the presence of a thickener in their composition, which operates as a sponge retaining the oil in its structure [44,45]. Lithium stearate is the main thickener present in NLGI 3 grease (CAS Number 4485-12-5). Lithium stearate molecules arrange as arrays or networks of twisted and entangled fibers (or filaments) of several tens of nm diameter [18]. Oil in the grease is assumed to flow into the structure of the solid thickener. Forming a porous matrix, the thickener is viewed as a "sponge" that holds and releases the oil contained in the grease, due to van der Waals and capillary forces, dipole-dipole and ionic interactions, or hydrogen bonds [30]. The grease of that study also contains additives such as zinc naphthenate (CAS Number 12001-85-3), N,N-Bis(2-ethylhexyl)-1,2,4-triazol-1-ylmethanamine (CAS Number 91273-04-0) and alkyl thiaziazole (EC Number 948-020-7).

Fourier transform infrared (FT-IR) spectra of oils and greases are recorded on a ThermoScientific iS50 Nicolet FT-IR spectrometer in attenuated total reflection (ATR) mode, using a thin film of the analyzed solution, for wave numbers ranging from 400 to 4000 cm⁻¹ at a resolution of 1 cm⁻¹. The resulting FTIR spectra are presented

Table 1
Classification and properties of the studied OL.

Name	Description	Density (g.cm ⁻³)	Viscosity at 25 °C (Pa.s) ²	Category
Dodecane (C12)	Solvent	0.750	0.0013	LVOL
Tributylphosphate (TBP)	Solvent	0.973	0.0034	LVOL
Mix of TBP/C12 (30/70)	Solvent	0.823	0.0019	LVOL
Nevastane EP1000	Mineral oil (MO)	0.886	3.67	HVOL
Mobil 600XP680	Industrial oil (IO) ¹	0.914	2.95	HVOL
Gadus S2 V100 3	Grease (NLGI 3, also G)	0.900	– ³	HVOL

¹ Industrial oil = Mineral oil + various additives.

² All organic liquids (except the grease) have a Newtonian behavior.

³ The grease displays a non-Newtonian behavior and is characterized by its yield stress (102.7 Pa).

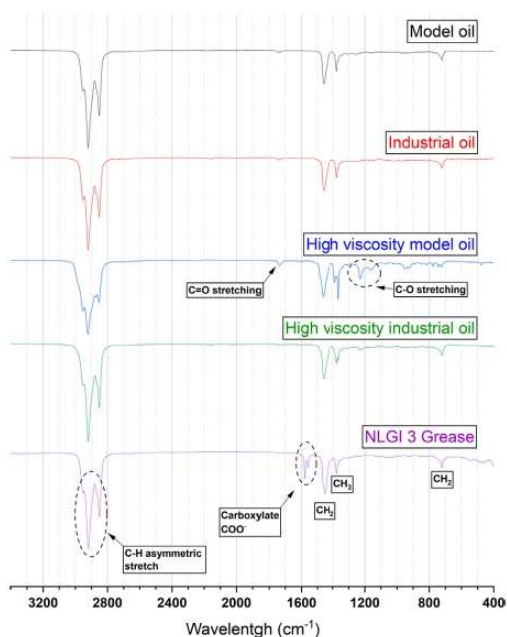


Fig. 1. FTIR analysis of the organic liquids used in this study.

in Fig. 1. The oil additives are not concentrated enough to be visible on FTIR spectra.

2.2. Preparation of composite materials

2.2.1. Preparation of GP paste

The GP is manufactured with a stoichiometry of 3.8 SiO₂: 1.0 Al₂O₃: 1.0 Na₂O: 11.0 H₂O, which is the reference selected in [8,9,40].

The first step consists in preparing the alkali-activating solution. Sodium hydroxide pellets are dissolved in water mixed with Betol 52T. The alkali-activating solution is left to cool down for several hours before use. The aqueous solution is then mechanically stirred at 2000 rpm and the solid precursor powder (MK) is quickly added. The blend is mixed for 2 min until homogenization. The water-to-MK ratio (W/MK) is 0.40. The fresh paste is used immediately for OL incorporation (see below).

For mortar formulations, intended for compressive strength measurements, sand is quickly introduced, and the mixing is carried out for 1 additional min. In such case, only a small quantity of sand is used. It represents a sand-to-metakaolin mass ratio S/MK of 0.5. Because the OL cannot penetrate inside the sand grains, the choice of a small amount of sand allows the presence of a greater

GP paste proportion, favorable for 20%vol OL incorporation into the mortar.

2.2.2. Incorporation of the OL

HVOL and the solvents used for their assembly (dilution) are introduced sequentially in the same container. Mixtures are then subjected to magnetic stirring for an hour at 200 rpm (for oil) and 1000 rpm (for grease) respectively. This method is identical whatever the solvent used, i.e. C12 or TBP/C12 mixture.

The homogenized and assembled OL mixtures are then incorporated into the fresh GP paste (or mortar) under strong agitation (2000 rpm) and the mixing is carried out for 2 min, in order to obtain composite materials with an OL volume concentration of 20%vol (% of the total GP matrix + OL volume).

2.3. Characterization methods

2.3.1. Rheology measurements

All rheology measurements are carried out on a rheometer AR-G2 (TA instruments, USA) at 25 °C. The rheology of the oils corresponds to Newtonian fluids, whereas grease, GP pastes and GP+OL pastes are non-Newtonian. This induces different experimental protocols, as follows.

• Rheology of OL

The viscosity of oils and solvents (pure or as mixtures) is characterized by applying a gradually increasing shear rate from 1 to 10³ s⁻¹ followed by a gradually decreasing shear rate from 10³ to 0.1 s⁻¹ using a plane geometry with a diameter of 40 mm. All these samples display a Newtonian behavior and the viscosity is calculated by averaging 10 values obtained for different shear rates.

The viscosity of grease (pure or after assembly) is characterized by applying a gradually increasing shear rate from 10⁻³ to 10² s⁻¹ followed by a gradually decreasing shear rate from 10² to 10⁻⁴ s⁻¹ using a vane geometry. The grease of that study has a shear-thinning behavior and the apparent yield stress is considered at 10⁻⁴ s⁻¹.

• Rheology of GP pastes + OL

The viscosity of GP pastes alone or incorporating assembled HVOL is characterized by applying a gradually increasing shear rate $\dot{\gamma}$ from 1.0 to 10² s⁻¹ followed by a gradually decreasing shear rate from 10² to 0.1 s⁻¹ using a vane geometry. Flow curves are modeled using the Herschel-Bulkley relationship, which is usually a suitable candidate to describe the geopolymer rheological behavior [41,43]. This relationship involves three parameters. It is applicable to fluids with non-linear evolution, as follows [38]:

$$\sigma = \sigma_0 + K\dot{\gamma}^n \quad (1)$$

where σ is the shear stress at given shear rate (in Pa), σ_0 is the yield stress (in Pa), K is the consistency index (in Pa.s), $\dot{\gamma}$ is the shear strain (in s⁻¹) and n is the flow index (no unit). Comparing K values is possible for fluids with similar n values. Shear thinning is observed when $n < 1$, and shear thickening for $n > 1$.

Table 2
Main characteristics of the samples investigated by 3D X Ray micro-CT (voxel size = 5 μm).

GP + assembled HVOL	Industrial oil + C12	Industrial oil + TBP/C12	Grease + C12	Grease + TBP/C12
Size of the raw image stack (pixels ³)	868 × 947 × 1250	833 × 756 × 1251	1070 × 1140 × 1260	689 × 836 × 1260
Size of the cropped image stack (pixels ³)	582 × 420 × 500	487 × 264 × 840	506 × 646 × 400	290 × 504 × 822
Size of the cropped image stack (mm ³)	15.3	13.5	16.3	15.0
Manual threshold (grey level)	60	37	61	72
Observed relative volume of the OL emulsion (%)	3.7	2.0	9.3	12.9
in a given object size range (microns)	(10–700 μm)	(10–440 μm)	(10–670 μm)	(10–480 μm)

2.3.2. Isothermal micro-calorimetry

The reactivity of GP pastes with or without OL is characterized in the fresh state by isothermal micro-calorimetry. The measurements are carried out on a TAM-air micro-calorimeter (from TA instruments, USA). The preparation of the slurry is performed outside the calorimeter. Right after mixing (see procedure in Section 2.2.2), about 2 g of GP paste are introduced into dedicated glass containers, which are sealed to avoid possible evaporation of water from the samples. The sealed containers are then introduced into the calorimeter. The heat flow and the cumulative heat are recorded over time at a stable temperature of 25 °C. The first 30 min are omitted in the calculation of cumulative heat due to the perturbation induced by introducing the sample into the calorimeter.

2.3.3. Mechanical characterization

The compressive strength of reference mortars (without OL) and of composite mortars incorporating OL is measured on a hydraulic press (3R RP 40/400 N), following the European standard EN 196-1. For this purpose, cubic specimens of 40 × 40 × 40 mm are prepared by pouring the fresh mortar pastes into PTFE molds; they are then cured in a climatic chamber for 2 days at 20 °C and 95% RH.¹ After demolding, the specimens undergo endogenous curing in a sealed bag. Their compressive strength is evaluated at 28 days. Complementary samples are made specifically for 3D X Ray micro-computed tomography (see below); they are cured in endogenous conditions for 28 days, as for mechanical tests.

2.3.4. Microstructure analysis

• Scanning Electron Microscopy (SEM)

Microscopic observations of hardened samples are performed on a Scanning Electron Microscope (SEM), (FEI Inspect S50, high vacuum mode, acceleration voltage of 15 kV, current intensity of 50 nA, and working distance of 10 mm). The samples are sliced using a diamond saw blade and placed in an oven at 350 °C for 3 h. This thermal treatment aims at removing the OL (by calcination) before introduction in the SEM chamber.

• 3D X-ray micro-CT

With this observation method, the samples do not require drying or polishing, or even resin impregnation. They are simply cut to a 1 cm³ size using a diamond saw. Four image series are acquired in less than 30 min each, and processed by X ray micro-CT at the ISIS4D platform (Lille, France) [29,37,50]. Each image series corresponds to one different sample of GP mortar (S/MK = 0.5) incorporating 20%vol assembled HVOL, one stabilizing HV oil with C12, one of HV oil with TBP/C12, one of HV grease with C12 and one of HV with TBP/C12 (Table 2). For all of them, an identical voxel size of 5 μm is used.

The X Ray micro-CT apparatus is equipped with a nano focus tube operated at a 60 kV tension and 35 μA current, with a flat

detector panel of 1874 × 1496 pixels². At each given angular position of the sample, the projection image is the average of four images in order to limit noise. After the reconstruction procedure (along the Z axis, with a filtered retro-projection algorithm [22–24]) and acquisition artifacts removal, an output volume is computed, composed of 1250–1260 images in a (X, Y) plane (at 0.57–1.22 × 10⁶ pixels² each) regularly spaced from one another by one voxel size (5 μm). Each sample corresponds to huge datasets of 0.72–1.53 × 10⁹ voxels³, linearly scaled into a 16-bit format.

Before quantitative analysis, all images are cropped in a (X, Y) plane so that sample boundaries and exterior are removed. The remaining image volumes, ranging between 13.5 and 16.3 mm³, are given in Table 2. For each given formulation, similar volumes are selected, in order to provide comparable droplet structures; the volumes are considered representative of the emulsion morphology, with a number of segmented droplets of several thousands and more.

The images are filtered and segmented with the ImageJ software [47], in a minimal manner to avoid information loss. The grey level histogram of the whole image stack is spread over the whole 0–255 available range. Contrast is enhanced and a limited Gaussian Blur filter (0.8 pixel radius) is applied. Thresholding is then performed using the image stack histogram, by selecting the local minimum grey level value between darker pores and lighter solids. This provides realistic binary images (with pores in black and the rest in white).

Further, the pore size distribution is quantified as in [11], with the Beat plugin [33] for 3D Continuous Pore Size Distributions (3D CPSD). By assuming that in each 2D image, every individual pore object is modeled by an ellipse, the ImageJ tool “analyze Particles > Ellipses” provides a so-called shape factor, defined as the ratio between the minor and the major axis [49,55]; the shape factor thus defined is comprised between 0 and 1, and the closest the pore is to a sphere, the greater the shape factor value; a perfect sphere has a shape factor of 1. Conversely, the more elongated the droplet is, the smaller the shape factor.

3. Results and discussion

3.1. Assembly of HVOL with LV solvents

In the following, the amount of solvent is expressed in%vol of the assembly. For example, a dilution with 20%vol solvent corresponds to a mixture of HVOL/solvent in the proportions of 80/20 v/v.

3.1.1. Assembly of high viscosity oils (HVO)

HV oils have a Newtonian rheological behavior, identical to that of LV oils. Therefore, based on former research on the stabilization of OL into GP pastes [11,39,40], the criterion proposed here for an adequate incorporation of the assembled HV oil is to impose that it corresponds to that of a LV model oil (Finavestan A360B, pure linear alkane oil provided by Total, France), which is at a value of

¹ RH = Relative Humidity.

Table 3
Summary of HV oil (HVO) assemblies selected for immobilization in geopolymer pastes.

Nomenclature (HVO-solvent-%vol.)	HVO	Solvent	Quantity of solvent (%vol.)	Viscosity (Pa.s) before assembly	Viscosity (Pa.s) after assembly
HVMO-C12-25	HVMO	C12	25	3.70	0.16
HVMO-TBP/C12-27	HVMO	TBP/C12	27	3.70	0.18
HVIO-C12-20	HVIO	C12	20	2.95	0.10
HVIO-TBP/C12-25	HVIO	TBP/C12	25	2.95	0.19

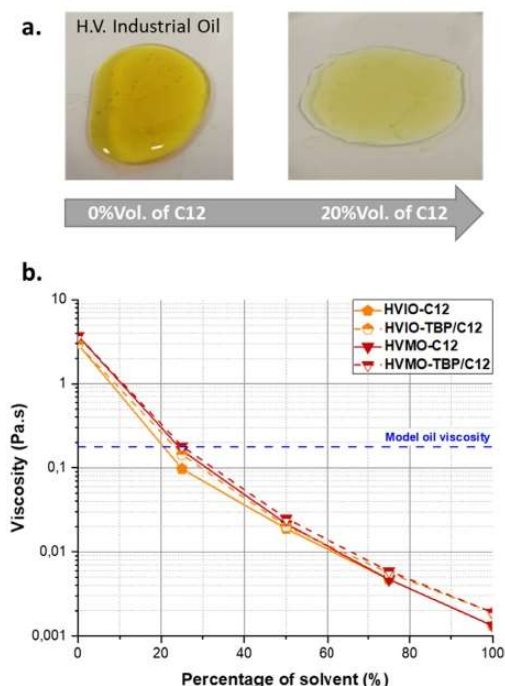


Fig. 2. (a): macrophotographs of the progressive assembly of HV oil with an increasing amount of C12; (b): Viscosity evolution of HV oils after assembly with LV solvents, as a function of solvent%vol. IO stands for Industrial Oil; MO stands for Model Oil.

0.2 Pa.s \pm 0.05. Any oil with an equivalent viscosity is considered adequately stabilized; any oil with a greater viscosity is assumed not adequately stabilized (it is considered not sufficiently pourable); any oil with a smaller viscosity is neither considered adequately stabilized (phase separation may occur before full GP hardening). This criterion ensures that the oil will be easily and efficiently poured into the GP paste.

The fluidization of the HV industrial oil (HVIO) is illustrated in Fig. 2(a). When 20%vol C12 is added to the HVIO, the mix becomes very fluid, and it is homogeneous and stable. Accordingly, viscosity decreases exponentially with the solvent content (Fig. 2(b)), so that it reaches the 0.2 Pa.s threshold at slightly different solvent content, depending on the solvent (C12 or TBP/C12) and on the HV oil considered (MO or IO). For HVMO, the addition of (at least) 25%vol of C12 or 27%vol of TBP/C12 is required. For HVIO, which is less viscous than HVMO, a minimum amount of 20%vol is required with C12 and a slightly greater amount of 25%vol with TBP/C12. This is attributed to the greater viscosity of TBP/C12 compared to C12 (see Table 1). In both cases however, the solvents are very efficient to reduce the initial viscosity of the HV oil down to a pourable oil.

Table 3 summarizes the selected mixes for further incorporation in GP pastes.

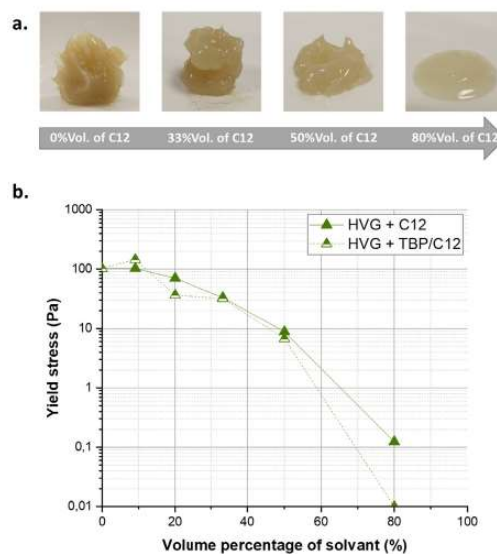


Fig. 3. (a): macrophotographs of the progressive assembly of HV grease with increasing amounts of C12; (b): Yield stress evolution of HV grease through assembling with LV solvents C12 or TBP/C12.

3.1.2. Assembly of highly viscous grease (HVG)

The grease has a typical shear-thinning behavior, with a non-zero shear stress at very low shear rate (i.e. a yield stress). Since its viscosity varies with shear rate, the selection of the adequate solvent proportion to obtain a pourable assembled mix cannot be identical to that for the HV oils. It is determined as follows.

The solvent/grease mix is studied visually for C12 (Fig. 3(a)) and TBP/C12 (with a behavior similar to C12), and by recording the change in yield stress with increasing solvent amount (Fig. 3(b)). It is observed that the assemblies are stable and homogeneous, even at high solvent concentration. However, the evolution of the grease texture is slow with solvent addition; insufficient spread (i.e. an insufficient ability to be poured) remains up to 50%vol solvent; a sufficient spread of the mix is obtained at 80% solvent addition.

Results in Fig. 3(b) show that the initial yield stress of the grease is decreased by one order of magnitude (i.e. one decade) when adding 50%vol solvent, by two decades at 60%vol, and by three to four decades at 80%vol solvent; compared to an initial value of 100 Pa (without solvent), the yield stress at 80%vol is of 0.12 Pa with C12 and 0.01 Pa with TBP/C12. Owing to this evolution, and to visual inspection, a decrease by a factor of 500 is retained for further addition to a GP paste, i.e. a yield stress lower than 0.2 Pa. This corresponds to a solvent content of 79%vol of C12 or 66%vol of TBP/C12. The corresponding mixes have a similar spread to that at 80%vol (Fig. 3(a)).

Table 4 summarizes the selected mixes for further incorporation into GP pastes.

Table 4
Summary of grease assemblies selected for immobilization in geopolymer pastes.

Nomenclature (HVG-solvent-%vol.)	HVG	Solvent	Quantity of solvent (%vol.)	Yield stress (Pa) before assembly	Yield stress (Pa) after assembly
HVG-C12-79	HVG	C12	79	102.7	0.12
HVG-TBP/C12-66	HVG	TBP/C12	66	102.7	0.21

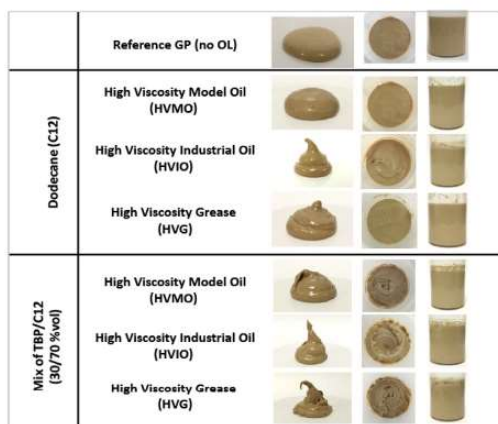


Fig. 4. Macrophotographs of the fresh GP pastes, either the reference without OL (1st line), or added with 20%vol of assembled HVMO (2nd and 5th lines), HVIO (3rd and 6th lines) or HVG (4th and 7th lines). The assembly is done either with C12 (2nd to 4th lines) or with TBP/C12 (5th to 7th lines). In each column, the GP-HVOL is represented in the fresh state (left), or in the hardened state (middle and right photographs, corresponding to top and side views respectively). No HVOL is observed on the hardened paste surface.

3.2. Incorporation of assembled HVOL into GP pastes

The visual observation of the GP+OL composite pastes is provided in Fig. 4, in the fresh state (left image for each mix) and in the hardened state (middle and right image for each mix). Comparison is done with the reference GP paste (without any OL), see the top line in Fig. 4. In both fresh and hardened states, whatever the OL and the solvent considered, the OL does not bleed out of the GP paste, neither in the fresh state nor in the hardened state. The general aspect of the pastes has a similar homogeneity to that of the reference GP paste. It is considered that the HVOL immobilization is effective from a macroscopic viewpoint. However, strong variations in rheology may be observed. This will be the focus of the following section.

3.3. Rheological properties of geopolymer pastes incorporating assembled HVOL

Flow curves of GP pastes immobilizing 20%vol HVOL are presented in Fig. 5. They are compared to the reference GP paste (i.e. without HVOL). All rheological curves display the general shape of the reference GP paste, described by the Herschel-Bulkley model, see Table 5 for the calculated values of the model parameters. Despite the OL addition, the rheological behavior is that typical of a GP paste.

For shear rates below 100 s^{-1} , the OL incorporation increases the paste viscosity; this increase is more pronounced with TBP/C12 compared to C12 alone, except for HVIO. This result means that for two HVOL out of three, the use of TBP/C12 tends to make the paste more viscous than the C12 solvent, i.e. TBP/C12 has a greater structuring effect on the GP+HVOL mix, possibly due to interactions of the GP paste with the phosphate functions present in TBP. Such

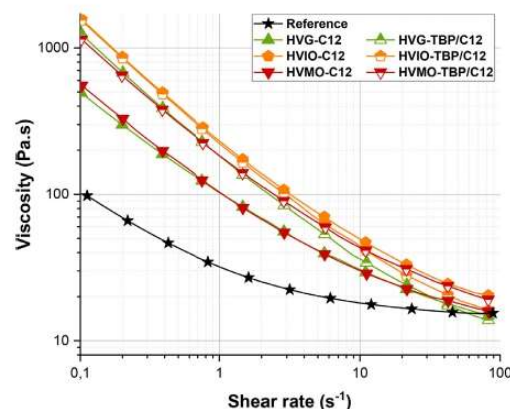


Fig. 5. Flow curves of GP pastes incorporating 20%vol. of HVOL assembled with a given proportion of LV solvent. Reference GP paste (without OL) is provided for comparison.

interactions have been reported in the literature, but only in the case of Portland cement [7]. For HVIO, the presence of additives is possibly predominant over that of GP/TBP interactions (see also below).

For HVMO and HVG, when considering each solvent individually, the rheological behavior of the GP+assembled HVMO is close to that of GP+assembled HVG, with almost superposed curves. In more quantitative terms, with the C12 solvent, the yield stress for GP+ assembled HVMO is of 60.4 Pa, and 51.0 Pa for GP + assembled HVG; with the TBP/C12 solvent, the yield stress for GP+ assembled HVMO is of 118.4 Pa, and 128.3 Pa for GP + assembled HVG.

For HVIO, either with C12 or TBP/C12, the same viscosity increase is noted, with flow curves almost superposed, and a yield stress value of 167.2 and 161.0 Pa respectively (Table 5). It is the greatest increase in paste viscosity (i.e. the greatest structuring effect) of all the mixes. In that case, the main structuration is attributed to the additives present in the HVIO, interacting with the MK particles of the fresh GP. Although the exact nature of these additives is not provided by the industrial supplier, they are very possibly surfactants, owing to their typical structuring effect.

Finally, since no significant difference is observed for the two assemblies of HVG (with or without TBP), the effect of the IO additives is considered predominant compared to possible interactions between TBP phosphate functions and GP paste.

3.4. Influence of assembled HVOL on the reactivity of GP pastes

Micro-calorimetry results for GP pastes immobilizing assembled HVOL are given in Fig. 6. Whether for reference GP, GP+assembled MO, GP+assembled IO or GP+assembled HVG, the heat flow curves are almost superposed. There is only a slight shift of the heat flow curves for GP+assembled HVG in the first 10–100 h, with a maximum delayed by about 10 h; all curves are superposed at 100 h and later. Because it is similar whether HVG is assembled with C12 or TBP/C12, and it is not observed for HV oils, this effect can-

Table 5

Identified values of the Herschel-Buckley model parameters for the geopolymer pastes incorporating 20% vol. of assembled HVOL

Incorporated HVOL	Herschel-Buckley parameter		
	σ_0 (Pa)	K (Pa.s)	n
Reference GP (without oil)	13.7	17.8	0.96
GP + HVMO-C12-25	60.4	39.5	0.78
GP + HVIO-C12-20	167.2	58.9	0.73
GP + HVG-C12-79	51.0	47.5	0.72
GP + HVMO-TBP/C12-27	118.4	60.2	0.72
GP + HVIO-TBP/C12-25	161.0	56.5	0.68
GP + HVG-TBP/C12-66	128.3	49.4	0.68

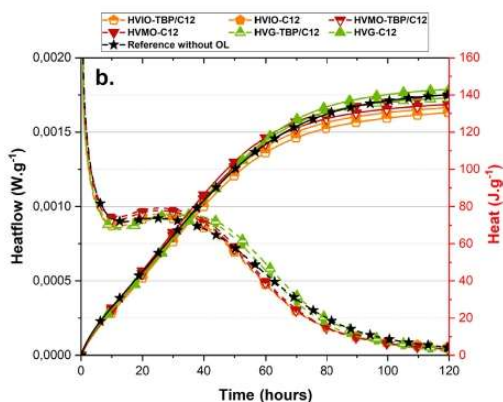


Fig. 6. Micro-calorimetry results (heat flow as dashed curves, cumulative heat as solid lines) for reference GP paste and 20%vol assembled HVOL stabilized into GP paste.

not be attributed to the solvent used for the assembly. It is attributed to possible interactions between components of the grease (e.g. its additives) and the GP paste. However, the value of the heat flow maximum is of the same order of magnitude in all samples. Interestingly, the results highlight that the assembled HVOL have no impact on the cumulative heat curves, i.e. on the extent of geopolymerization. On the whole, the assembled HVOL have a very limited effect on the geopolymerization process.

3.5. Mechanical properties of geopolymer materials incorporating assembled HVOL

The 28-days compressive strength of the hardened GP+assembled HVOL composites is given in Fig. 7. The reference geopolymer (i.e. without OL incorporation) has a high compressive strength of 65.1 MPa \pm 10.3. For GP mortars incorporating assembled HVMO or HVIO, the compressive strength f_c is identical whatever the LV solvent. For HVMO mortars, $f_c = 31.1$ MPa \pm 1.1 with C12 solvent, and $f_c = 33.8$ MPa \pm 1.2 with TBP/C12 solvent. For HVIO mortars, $f_c = 33.6$ MPa \pm 1.5 with C12 solvent, and $f_c = 33.6$ MPa \pm 1.5 with TBP/C12 solvent. This is consistent with micro-calorimetry observations, showing that assembled HV oils have no impact on the cumulative heat. Moreover, these values, on the order of 30 MPa, are in good agreement with compressive strengths provided in the literature for GP mortars containing 20%vol OL [8,9].

For GP incorporating HVG, the choice of the solvent impacts compressive strength. For HVG mortars, $f_c = 32.0$ MPa \pm 3.0 with C12 solvent, and $f_c = 25.4$ MPa \pm 4.6 with TBP/C12 solvent. This difference in compressive strength may be explained by either an incorporation of air in the composite material, or a difference in the morphology of the HVG droplets. This hypothesis is verified by using 2D SEM and 3D X-ray micro-CT.

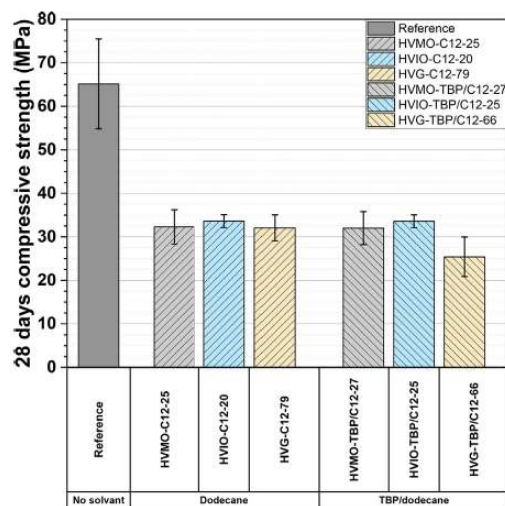


Fig. 7. Compressive strength of geopolymer mortars incorporation 20%vol. of assembled HVOL after 28 days of curing in endogenous conditions.

3.6. Microstructural analysis of GP mortars containing assembled HVOL

3.6.1. 2D SEM observations

The SEM observations focus on the GP paste present in GP mortars incorporating assembled HVOL, see Fig. 8 (magnification $\times 1000$ on the left and $\times 2000$ on the right). The homogeneously distributed holes at the sample surface correspond to the location of the OL, removed by calcination during sample preparation. HVMO mortar images are not presented, because they are analogous to HVIO mortar images. For HVIO (1st and 2nd lines), whatever the solvent, the GP paste is interspersed with homogeneously distributed OL droplets, most of which are smaller than 10 μm (i.e. smaller than the 1/4th of the scale on the right side images); no significant difference is observed between the two pastes. For HVG (3rd and 4th lines), bigger OL droplets than with HVIO are observed whatever the solvent; droplets of spherical shape are observed for the HVG assembled with C12 (3rd line), whereas a more elongated shape is observed for the assembly with TBP/C12; with both solvents, the OL is homogeneously distributed inside the GP paste. Let analyze and quantify the HVOL droplet emulsions in 3D, with X Ray micro-CT observations (Fig. 9).

3.6.2. 3D X ray micro-CT observations

Because the samples require no preliminary preparation (e.g. no calcination), X Ray micro-CT provides unaltered observation of the GP + assembled HVOL mortar composites (Fig. 9 left). A single dark grey range is observed for the droplets, meaning

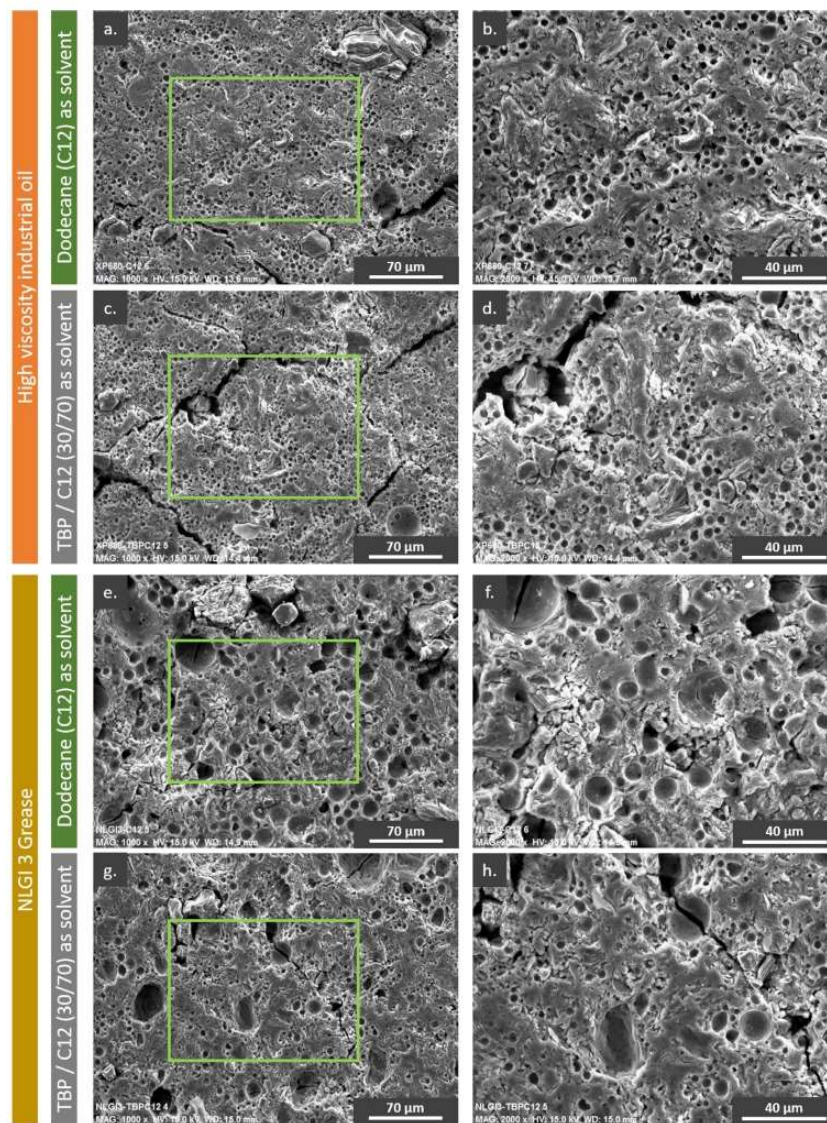


Fig. 8. SEM observations of the GP-HVOL composites in the hardened state, after 350 °C calcination (i.e. the OL is removed): (1st line) HVIO assembled with C12; (2nd line): HVIO assembled with TBP/C12; (3rd line): HV grease assembled with C12; (d): HV grease assembled with TBP/ C12. The left column is a general view of the material, and the right column is a close-up, as indicated by a green rectangle on the left image.

that all of them correspond to HVOL, and not to entrained air bubbles (these would appear in a darker grey range than the OL).

After thresholding to retain only the OL (in black, see Fig. 9 right), a quantification of the 3D HVOL emulsion is also performed in the image observation range (Table 2 and Fig. 10). With 3D X Ray micro-CT, the image observation range is bounded; for the smallest observable object, it corresponds to two voxel sizes (here, 10 μm for all image stacks), and for the biggest object, to 1/3rd of the smallest image size (between 440 and 840 μm depending on the sample considered, see Table 2). Owing to macroscopic observations (no bleeding is observed in Fig. 4) and SEM imaging (droplets of 10 μm and smaller values are present in Fig. 8), it is assumed in the following that the HVOL not visible

by 3D X Ray micro-CT is very probably located in objects smaller than 10 μm.

For HVIO, Fig. 9(a) and (b) show that the retained OL (measured after thresholding) is of limited proportions, with amounts of 3.7%vol for HVIO assembled with C12 and 2.0%vol for HVIO assembled with TBP/C12 (Table 2). The assembled HVIO droplets, which are not visible with X Ray micro-CT (i.e. smaller than 10 μm), are therefore of significant proportions. When calculated as the difference between the added amount of 20%vol and the observed HVIO amount, this proportion is of 16.4 or 18%vol, depending on the solvent. Because the smaller the OL droplets, the more stable the emulsion is, having a majority of the OL in the form of droplets smaller than 10 μm means that the incorporation of assembled HVIO is very efficient in GP paste.

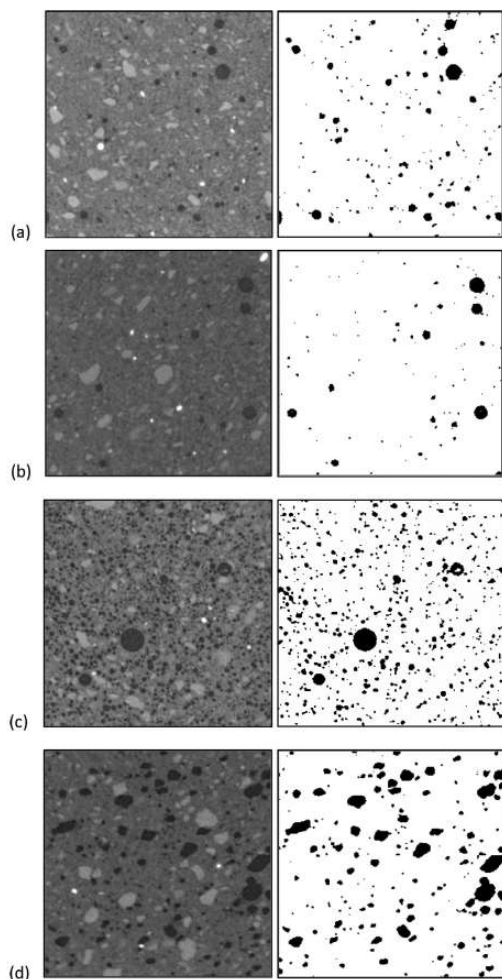


Fig. 9. Example of a raw X-ray micro-tomography image (limited to an identical 260×260 pixels2 i.e. 1.3×1.3 mm² for each) – left and same image after filtering and thresholding for hardened GP composite mortars ($S/MK = 0.5$) incorporating assembled (a): HVIO with C12; (b): HVIO with TBP/C12; (c): HV grease with C12; (d): HV grease with TBP/C12.

For assembled HVG immobilized into GP mortar paste, the visible amount of HVG is of 9.3% with C12 solvent, and 12.9% with TBP/C12 (Table 5); this is greater than for HVIO, see Fig. 9(c) and (d). With the same analysis as with HVIO, it means that 10.7 or 7.1% are in droplets smaller than 10 μ m, depending on the solvent considered. In other words, for HVG, despite an efficient process, the emulsion has bigger droplets than for HVIO.

Fig. 10(a) presents the droplet size distributions for the four GP+assembled HVOL composites, obtained from the 3D X Ray micro-CT image stacks. Compared to the qualitative SEM images (Fig. 8), these measurements encompass both droplets observed with the SEM (below 40–70 μ m diameter) on the left side of the distributions, and bigger droplets (up to 440–700 μ m depending on the sample, see Table 2).

For both HVIO and HVG, the use of C12 (as a solvent) provides generally bigger OL droplets, with a wider distribution, of up to 0.32 mm diameter (for HVG) and 0.65 mm (for HVIO).

Compared to C12, TBP/C12 provides narrower droplet size distributions, with maxima of 0.22 mm diameter (HVG) and 0.12 mm

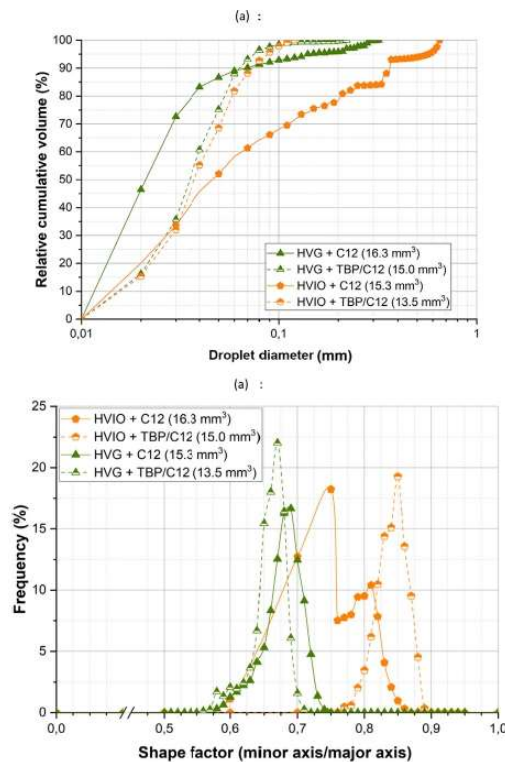


Fig. 10. 3D X-ray micro-CT results of hardened GP mortars immobilizing 20%vol HVOL (i.e. HVIO and HVG): (a): droplet size distributions of the assembled HVOL; (b): Shape factor of the assembled HVOL (by assuming an ellipsoidal shape for the HVOL droplets).

(HVIO). This is explained by the amphiphilic (i.e. surfactant) nature of TBP, promoting lower interfacial tension between the OL droplets and the fresh GP paste. Indeed, when considering an organic molecule as a surfactant, the notion of Hydrophilic-Lipophilic Balance (HLB) in the Griffin's sense [16,17] refers to the proportion of hydrophilic and hydrophobic (i.e. lipophilic) functions present in the molecule. An HLB value between 1 and 8 corresponds to a lipophilic molecule, leading to emulsions of water into an oil continuous phase, and to surfactant molecules adsorbed at the oil/water interface (with lipophilic portions of the surfactant oriented towards the oil); this adsorption decreases the oil/water interfacial tension [51]. On the opposite, an HLB value greater than 8 promotes the formation of oil emulsions into an aqueous continuous phase. When considered as a surfactant, TBP has been attributed a HLB value of 5.46 [1,2], meaning that it is significantly lipophilic. Therefore, when considering the assembled organics as the oil phase and the GP paste as a highly concentrated aqueous solution i.e. as the water phase, TBP tends to adsorb at the oil/water interface, which reduces the oil/water interfacial tension, leading to smaller OL droplets inside the GP paste.

Moreover, when analyzing the droplet shape (Fig. 10(b)), assembled HVG has generally more elongated droplets than assembled HVIO. The smaller the shape factor, the greater the elongation (i.e. the less spherical the droplet). In particular, the smallest peak of the shape factor is obtained at a value of 0.67 for HVG assembled with TBP/C12, and 0.69 for HVG assembled with C12. Comparatively, the shape factor for assembled HVIO is closer to 1, with two peak values of 0.75 and 0.81 with C12 and a single peak at

0.86 with TBP/C12. For HVIO assembled with C12, the major peak of the shape factor at 0.75 is attributed to partial droplet coalescence, whereas the secondary peak at 0.81 corresponds to more spherical individual droplets.

3.7. Discussion

For GP mortars immobilizing HVG + TBP/C12, the smaller compressive strength, when compared to the other 20%vol OL incorporations (Fig. 7), is attributed to two main factors. First, a greater OL proportion is present in the 10–480 μm range (of 12.9%) and, hence, a smaller OL proportion (of 7.1%) is present below 10 μm size, meaning that the OL emulsion is less refined than for the other assemblies. Secondly, a smaller shape factor i.e. significantly more elongated droplets are present in the GP mortar. This induces smaller droplet curvatures, and hence, greater stress concentrations at the tips of elongated droplets.

In terms of OL immobilization, using TBP/C12 for the assembly of HVOL allows to stabilize and solidify two distinct nuclear waste types, namely the TBP/C12 PUREX solvent, and HVIO or HVG. In order to comply with current regulations for nuclear waste storage (at least in France), the developed process allows to pour the OL into the fresh GP mortar, whether it is a HV oil or a grease; this provides hardened materials with sufficient compressive strength ($f_c = 25.4 \text{ MPa} \pm 4.6$, where a minimum of 8 MPa is required by the French national nuclear waste management agency ANDRA), and no bleeding is observed. The major part of the OL is made of droplets smaller than 0.12–0.65 mm diameter, depending on the assembly considered.

4. Conclusion

The present work has shown that it is possible to incorporate HV oils and greases directly into a GP matrix. This only requires an assembly step with low viscosity solvents (C12 or TBP/C12). With the OL studied in this research, a minimum amount of 20–25%vol C12, or 25–27%vol TBP/C12, is required to fluidify HV oils (either model or industrial ones), and 79%vol C12 for HV grease or 66%vol TBP/C12.

Although the assembly rate is higher for the TBP/C12 mixture than for C12 alone, its incorporation into the conditioning process for HV oil and grease wastes would allow for a double disposal in a single process. The process simply consists in assembling the HVOL with one of the two solvents (preferably TBP/C12 for double conditioning) and pouring it into a GP paste (or alternately pouring a GP paste over the assembled HVOL). However, it should be noted that assembling HV oils or grease with TBP/C12 induces a significant viscosity increase of the GP paste; the greatest viscosity increase is observed for a HV industrial oil, whatever the solvent. It is interpreted that the additives present in the HVIO, and the TBP phosphate functions, both act as structuring agents in the GP paste. However, the viscosity increase is compatible with a lost drum process, where the GP+HVOL composite remains into the drum until hardening and storage.

In the hardened state, the composite mortars synthesized with the HVOL have sufficient mechanical strength, no bleeding, and they form fine emulsions with droplet sizes smaller than 0.12–0.65 mm in the hardened state. With TBP/C12, the HV grease has bigger and more elongated droplets; both effects are responsible for a smaller compressive strength of GP mortar made with HVG+TBP/C12 than with assembled HV oils or with HVG+C12.

Further, in order to ensure long term immobilization of HV oils and greases, it will be useful to study their durability in the usual storage environmental conditions, and particularly their leaching durability (e.g. due to underground water seepage). In the context of radioactive waste immobilization, ensuring that no leakage of

the organics is achieved in leaching environmental conditions is of paramount importance.

Declaration of Competing Interest

The authors declare that they have no known competing financial interests or personal relationships that could have appeared to influence the work reported in this paper.

CRediT authorship contribution statement

M. De Campos: Conceptualization, Methodology, Investigation, Data curation, Writing – original draft, Writing – review & editing, Visualization. **C. Reeb:** Methodology, Investigation, Writing – review & editing, Visualization. **C.A. Davy:** Conceptualization, Methodology, Investigation, Data curation, Writing – review & editing, Supervision. **J. Hosdez:** Investigation, Resources, Data curation, Writing – review & editing. **D. Lambertin:** Conceptualization, Methodology, Resources, Writing – review & editing, Supervision.

Data Availability

Data will be made available on request.

References

- [1] W. Apostoluk, W. Robak, Analysis of the aqueous solubility of trialkyl phosphates, dialkyl alkylphosphonates, dialkylphosphites and alkyl dialkylphosphinates, *SN Appl. Sci.* 1 (2019) 801, doi:10.1007/s42452-019-0763-2.
- [2] K.J. Babu, Analysis on crystal formation and physio-tribological properties of lithium based grease developed from coconut oil (*Cocos Nucifera*), *IOP Conf. Ser. Mater. Sci. Eng.* 1132 (2021) 012003, doi:10.1088/1757-899X/1132/1/012003.
- [3] C. Bai, G. Franchin, G. Elsayed, A. Conte, P. Colombo, High strength metakaolin-based geopolymer foams with variable macroporous structure, *J. Eur. Ceram. Soc.* 33 (16) (2016) 4243–4249, doi:10.1016/j.jeurceramsoc.2016.06.045.
- [4] C. Bai, P. Colombo, Processing, properties and applications of highly porous geopolymers: a review, *Ceram. Int.* 44 (14) (2018) 16103–16118, doi:10.1016/j.ceramint.2018.05.219.
- [5] C. Bai, T. Ni, Q. Wang, H. Li, P. Colombo, Porosity, mechanical and insulating properties of geopolymer foams using vegetable oil as the stabilizing agent, *J. Eur. Ceram. Soc.* 38 (2018) 799–805, doi:10.1016/j.jeurceramsoc.2017.09.021.
- [6] V. Baroghel-Bouny, Conception des bétons pour une durée de vie donnée des ouvrages—Maîtrise de la durabilité vis-à-vis de la corrosion des armatures et de l'alcali-réaction, in: *Etat de l'art et Guide Pour la Mise en Oeuvre D'une Approche Performantielle et Prédictive sur la base D'indicateurs de Durabilité*, AFGC, Bagneux, 2004, p. 252. Scientific and Technical Report of the French Civil Engineering Association In press.
- [7] P. Bernard, S. Garraut, A. Nonat, C. Cau-Dit-Coumes, Hydration process and rheological properties of cement pastes modified by orthophosphate addition, *J. Eur. Ceram. Soc.* 25 (2005) 1877–1883, doi:10.1016/j.jeurceramsoc.2004.06.017.
- [8] V. Cantarel, F. Nouaille, A. Rooses, D. Lambertin, A. Poulesquen, F. Frizon, Solidification/stabilisation of liquid oil waste in metakaolin-based geopolymer, *J. Nucl. Mater.* 464 (2015) 16–19, doi:10.1016/j.jnucmat.2015.04.036.
- [9] V. Cantarel, D. Lambertin, A. Poulesquen, F. Leroux, G. Renaudin, F. Frizon, Geopolymer assembly by emulsion templating: emulsion stability and hardening mechanisms, *Ceram. Int.* 44 (9) (2018) 10558–10568, doi:10.1016/j.ceramint.2018.03.079.
- [10] J. Davidovits, Geopolymers: inorganic polymeric new materials, *J. Therm. Anal.* (1991), doi:10.1007/bf01912193.
- [11] C.A. Davy, G. Hauss, B. Paniel, D. Lambertin, 3D structure of oil droplets in hardened geopolymer emulsions, *J. Am. Ceram. Soc.* (2018) 1–6, doi:10.1111/jace.16142.
- [12] A.H.S. Dehaghani, M.H. Badizad, Experimental study of Iranian heavy crude oil viscosity reduction by diluting with heptane, methanol, toluene, gas condensate and naphtha, *Petroleum 2* (4) (2016) 415–424, doi:10.1016/j.petlm.2016.08.012.
- [13] E.J. Garboczi, K.A. Snyder, J.F. Douglas, M.F. Thorpe, Geometrical percolation threshold of overlapping ellipsoids, *Phys. Rev. E* 52 (1) (1995) 819–828, doi:10.1103/PhysRevE.52.819.
- [14] A. Geist, J.M. Adnet, S. Bourg, C. Ekberg, H. Galan, P. Guilbaud, M. Miguiditchian, G. Modolo, C. Rhodes, R. Taylor, An overview of solvent extraction processes developed in Europe for advanced nuclear fuel recycling, part 1—heterogeneous recycling, *Sep. Sci. Technol.* 56 (11) (2021) 1866–1881, doi:10.1080/01496395.2020.1795680.
- [15] B. Glad, W.M. Kriven, Highly porous geopolymers through templating and surface interactions, *J. Am. Ceram. Soc.* 98 (7) (2015) 2052–2059, doi:10.1111/jace.13584.

- [16] W.C. Griffin, Calculation of HLB values of non-ionic surfactants, *J. Soc. Cosmet. Chem.* 5 (4) (1954) 249–256.
- [17] L. Grunberg, A.H. Nissan, Mixture law for viscosity, *Nature* 164 (4175) (1949) 799–800 nov, doi:10.1038/164799b0.
- [18] A. Hodapp, A. Conrad, B. Hochstein, K.H. Jacob, N. Willenbacher, Effect of base oil and thickener on texture and flow of lubricating greases: insights from bulk rheometry, optical micro rheology and electron microscopy, *Lubricants* 10 (2022) 55, doi:10.3390/lubricants10040055.
- [19] IAEA, Treatment and Conditioning of Radioactive Organic Liquids, 656, IAEA, 1992 TECDOC.
- [20] D.W. Johnson, J.E. Hils, Phosphate esters, thiophosphate esters and metal thiophosphates as lubricant additives, *Lubricants* 1 (4) (2013) 132–148, doi:10.3390/lubricants1040132.
- [21] J.M. Juoi, M.I. Ojovan, W.E. Lee, Microstructure and leaching durability of glass composite wasteforms for spent clinoptilolite immobilisation, *J. Nucl. Mater.* 372 (2008) 358–366, doi:10.1016/j.jnucmat.2007.04.047.
- [22] A.C. Kak, M. Slaney, Principles of Computerized Tomographic Imaging, IEEE Press, Piscataway, NJ, 1988.
- [23] A.C. Kak, M. Slaney, Principles of Computerized Tomographic Imaging, Society of Industrial and Applied Mathematics, Philadelphia, 2001, doi:10.1137/1.9780898719277.
- [24] J.A. Kent, J.A. Kent, Soap, fatty acids, and synthetic detergents, Riegel's Handbook of Industrial Chemistry, Springer, Boston, MA, 2003, doi:10.1007/0-387-23816-6_27.
- [25] R.B. Kogbara, A review of the mechanical and leaching performance of stabilized/solidified contaminated soils, *Environ. Rev.* 22 (1) (2014), doi:10.1139/er-2013-0004.
- [26] S. Kumar, S.B. Koganti, Prediction of liquid mixture viscosity for dry and water-saturated TBP/n-dodecane solutions, *Nucl. Technol.* 123 (3) (1998) 335–340, doi:10.13182/NT98-A2903.
- [27] D. Lambertin, A. Rooses, F. Frizon, "Process for preparing a composite material from an organic liquid and resulting material", 2014, Patent no. WO 2014044776, available at <https://patents.google.com/patent/WO2014044776A1/en>
- [28] D. Lambertin, V. Cantarel, A. Poulesquen, F. Frizon, "Geopolymer comprising organic phase change material, production methods thereof and use of same", 2018, Patent no. WO 2018083411, available at <https://patents.google.com/patent/WO2018083411A1/en>
- [29] N. Limodin, T. Rougelot, J. Hosdez, 2013, access to the platform website for full publication list at <http://isis4d.univ-lille.fr/>
- [30] P.M. Lugt, A review on grease lubrication in rolling bearings, *Tribol. Trans.* 52 (2009) 470–480, doi:10.1080/10402000802687940.
- [31] D. Medpelli, R. Sandoval, L. Sherrill, K. Hristovski, D.K. Seo, Iron oxide-modified nanoporous geopolymers for arsenic removal from ground water, *Resour. Effic. Technol.* (1) (2015) 19–27, doi:10.1016/j.refit.2015.06.007.
- [32] D.M. Montgomery, C.J. Sollars, R. Perry, Optimization of cement-based stabilization/solidification of organic-containing industrial wastes using organophilic clays, *Waste Manag. Res.* 9 (1) (1991) 21–34, doi:10.1177/0734242X9100900103.
- [33] B. Münch, L. Holzer, Contradicting geometrical concepts in pore size analysis attained with electron microscopy and mercury intrusion, *J. Am. Ceram. Soc.* 91 (12) (2008) 4059–4067, doi:10.1111/j.1551-2916.2008.02736.x.
- [34] I. Natali Sora, R. Pelosato, D. Botta, G. Dotelli, Chemistry and microstructure of cement pastes admixed with organic liquids, *J. Eur. Ceram. Soc.* 22 (9–10) (2002) 1463–1473, doi:10.1016/S0955-2219(01)00473-3.
- [35] M.I. Ojovan, W.E. Lee, in: *An Introduction to Nuclear Waste Immobilisation*, Elsevier, 2005, pp. 179–200.
- [36] M. Orea, Y. Mujica, A. Diaz, T. Árraga, E. Pacific, Dilution of heavy crude oils for pipeline transportation purposes : the asphaltene instability issue, in: *Proceedings of the Conference: Heavy Oil Latin American Conference (HOLA 2015)*, 2015 Sept.
- [37] G. Peix, P. Duvauchelle, N. Freud, in *X-ray tomography in material science*, Edited by Hermes science (London), 2000, Chap. 1:15–27
- [38] A. Peverè, G. Guibaud, E. van Hullebusch, P. Lens, M. Baudu, Viscosity evolution of anaerobic granular sludge, *Biochem. Eng. J.* 27 (3) (2006) 315–322 janv, doi:10.1016/j.bej.2005.08.008.
- [39] C. Pierlot, H. Hu, C. Reeb, J. Bassetti, M. Bertin, D. Lambertin, C.A. Davy, V. Nardello-Rataj, Selection of suitable surfactants for the incorporation of organic liquids into fresh geopolymer pastes, *Chem. Eng. Sci.* (2022), doi:10.1016/j.ces.2022.117635.
- [40] B. Planel, C.A. Davy, P.M. Adler, G. Hauss, M. Bertin, V. Cantarel, D. Lambertin, Water permeability of geopolymers emulsified with oil, *Cem. Concr. Res.* 135 (2020) 106108 February, doi:10.1016/j.cemconres.2020.106108.
- [41] F. Puertas, B. Gonzalez-Fonteboa, I. Gonzalez-Fonteboa, M.M. Alonso, M. Torres-Carrasco, G. Rojo, F. Martinez-Abella, Alkali-activated slag concrete: fresh and hardened behaviour, *Cem. Concr. Compos.* 85 (2018) 22–31, doi:10.1016/j.cemconcomp.2017.10.003.
- [42] M. Riaz, E. Zamorani, A study of the effects of 1,3,5-trichlorobenzene solidified in cement, *Cem. Concr. Res.* 19 (1) (1989) 124–130 janv, doi:10.1016/0008-8846(89)90072-0.
- [43] M. Romagnoli, C. Leonelli, E. Kamse, M. Lassinantti Gualtieri, Rheology of geopolymer by DOE approach, *Constr. Build. Mater.* 36 (2012) 251–258 nov, doi:10.1016/j.conbuildmat.2012.04.122.
- [44] A. Saatchi, P.J. Shiller, S.A. Eghtesadi, T. Liu, G.L. Doll, A fundamental study of oil release mechanism in soap and non-soap thickened greases, *Tribol. Int.* 110 (2017) 333–340, doi:10.1016/j.triboint.2017.02.004.
- [45] L. Salomonsson, G. Stang, B. Zhmud, Oil/thickener interactions and rheology of lubricating greases, *Tribol. Trans.* 50 (3) (2007) 302–309, doi:10.1080/10402000701413471.
- [46] R. San Nicolas, M. Cyr, G. Escadeillas, Performance-based approach to durability of concrete containing flash-calcined metakaolin as cement replacement, *Constr. Build. Mater.* 55 (2014) 313–322, doi:10.1016/j.conbuildmat.2014.01.063.
- [47] J. Schindelin, I. Arganda-Carreeras, E. Frise, V. Kaynig, M. Longair, T. Pietzsch, Fiji: an open-source platform for biological-image analysis, *Nat. Methods* 9 (7) (2012) 676.
- [48] D.K. Seo, D. Medpelli, J.M. Seo, "Porous geopolymer materials", 2013, US Patent Application Publication no.: US 20130055924A1 ; Mar. 7, 2013, available at <https://patents.google.com/patent/US20130055924A1/en>
- [49] Y. Song, C.A. Davy, D. Troadec, A.M. Blanchet, F. Skoczylas, J. Talandier, J.C. Robinet, Multi-scale pore structure of COx claystone: towards the prediction of fluid transport, *Mar. Pet. Geol.* 65 (2015) 63–82, doi:10.1016/j.marpetgeo.2015.04.004.
- [50] Y. Song, C.A. Davy, T.N. Kim, D. Troadec, G. Hauss, L. Jeannin, Two-scale analysis of a tight gas sandstone, *Phys. Rev. E* 94 (2016) 043316, doi:10.1103/PhysRevE.94.043316.
- [51] T.F. Tadros, T.F. Tadros, Emulsion formation, stability, and rheology, in: *Emulsion Formation and Stability*, Wiley-VCH Verlag GmbH & Co. KGaA, Weinheim, Germany, 2013, pp. 1–75, doi:10.1002/9783527647941.ch1.
- [52] S. Trussell, R.D. Spence, A review of solidification/stabilization interferences, vol. 14, no 6, p. 507–519, 2008, doi:10.1016/0956-053X(94)90134-1.
- [53] W. Wang, J. Liu, F. Agostini, C.A. Davy, F. Skoczylas, J. Talandier, Durability of an ultra high performance fiber reinforced concrete (UHPC) under progressive aging, *Cem. Concr. Res.* 55 (2014) 1–13, doi:10.1016/j.cemconres.2013.09.008.
- [54] Western European Nuclear Regulators Association (WENRA), 2018, 54p, report available at: https://wenra.eu/sites/default/files/publications/report_radioactive_waste_treatment_and_conditioning_safety_reference_levels.pdf
- [55] A. Yamaji, F. Masuda, Improvements in graphical representation of fabric data, showing the influence of aspect ratios of grains on their orientations, *J. Sediment. Res.* 75 (3) (2005) 514–519, doi:10.2110/jsr.2005.040.
- [56] C. Reeb, C. Pierlot, C. Davy, D. Lambertin, Incorporation of organic liquids into geopolymer materials – A review of processing, properties and applications, *Ceram. Int.* (2020), doi:10.1016/j.ceramint.2020.11.239.

Résumé détaillé

1. Contexte de l'étude

L'utilisation des propriétés radiologiques depuis le début du XIX^{ème} siècle a conduit à la formation d'une importante quantité de déchets radioactifs. Ces déchets sont de nature très différentes, aussi bien en terme de composition, d'état physique ou d'activité radiologique. De nos jours, la plupart de ces déchets possèdent une voie de traitement spécifique pour leur stockage garantissant la protection de l'environnement. Cependant, certains déchets ne possèdent toujours pas d'exutoire et sont temporairement entreposés sur leurs sites de production. C'est par exemple le cas de certains déchets liquides organiques radioactifs (DLOR) qui sont strictement interdits dans les sites de stockages, et ce peu importe leur activité radiologique. A l'échelle mondiale, le procédé de référence pour le traitement des DLOR est la minéralisation par incinération. En France, à l'unité d'incinération de CENTRACO gérée par Cyclife, les cendres issues de l'incinération sont par la suite immobilisées dans des matrices cimentaires à destination des centres de stockage de l'ANDRA. Néanmoins, certains DLOR ne respectent pas les spécifications de l'incinérateur en termes de composition chimique ou d'activité radiologique et ne peuvent donc pas être incinérés. **Plus particulièrement, les huiles industrielles tritiées ne peuvent pas être incinérées.** En l'absence d'une voie de traitement, un volume significatif d'huiles tritiées s'est accumulé au cours du temps et une quantité importante sera produite à l'avenir avec la mise en fonctionnement et le démantèlement du réacteur ITER. Cette thèse s'inscrit donc dans le contexte de la recherche d'un procédé de traitement pour ces huiles tritiées qui soit à la fois robuste, fiable et économiquement réalisable. Une alternative prometteuse concerne le conditionnement direct en matrice cimentaire. Les ciments sont en effet très utilisés pour le conditionnement des déchets radioactifs de par leurs nombreux avantages comme leur flexibilité vis-à-vis de la variabilité des déchets, leur faible cout, leur résistance à l'irradiation et la possibilité de traiter de grandes quantités de déchets.

2. Objectifs de la thèse

Bien que leur composition soit très variable, les huiles industrielles (lubrifiant, huile de pompe, huile de coupe, ...) sont majoritairement composées d'huiles minérales. **Dans un souci de compréhension, ce travail s'articule donc autour de l'immobilisation d'huiles minérales.**

Le premier objectif consiste à assurer que l'immobilisation d'huiles minérales en matrices cimentaires soit bien maîtrisée, sans ressuage d'huile, tout en maintenant de bonnes propriétés mécaniques des composites obtenus. Comme dans le secteur du génie civil, le ciment de référence pour le conditionnement des déchets nucléaires est le ciment Portland.

Néanmoins, des études ont montré que la présence d'espèces organiques pouvait interférer avec la réactivité des ciments Portland, impactant fortement leurs propriétés mécaniques. De plus, l'émulsion (l'incorporation) des DLOR est généralement difficile dans les coulis de ciment Portland. **Pour pallier ces problèmes, l'utilisation des matériaux alcali-activés (MAA) s'est avérée efficace, particulièrement les géopolymères.**

Le second objectif concerne la limitation du rejet en tritium des colis finaux. Des essais réalisés en interne au CEA Marcoule ont montré que les rejets en tritium des huiles tritiées sont principalement sous la forme d'eau tritiée (HTO), mais une quantité significative de tritium gazeux (HT) a également été mesurée. **La forme HT est particulièrement difficile à confiner et sera l'objet de ce travail.** La stratégie envisagée consiste à fonctionnaliser les matériaux cimentaires avec un piègeur à hydrogène/tritium. A cet effet, les oxydes minéraux sont de bons candidats, de par leur stabilité à l'irradiation, à la température et leur capacité de piégeage à température ambiante. Plus particulièrement, de nombreuses études ont mis en évidence l'efficacité des mélanges à base de MnO_2/Ag_2O pour le piégeage d'hydrogène. L' Ag_2O agit comme catalyseur permettant la dissociation des molécules de dihydrogène en atomes d'hydrogènes qui peuvent ensuite s'insérer dans la structure du MnO_2 . La réaction est irréversible et conduit à la formation de $MnOOH$.

Afin de satisfaire ces objectifs, deux MAA sont considérés dans cette étude :

- **Les géopolymères**, pour leur très bonne efficacité concernant l'immobilisation des DLOR. Néanmoins, l'importante quantité d'eau libre présente dans les pores des géopolymères pourrait altérer l'efficacité du piègeur à hydrogène et ainsi limiter ses performances vis-à-vis du confinement du tritium.
- **Les laitiers activés**, dans lesquels l'immobilisation des DLOR est plus difficile que dans les géopolymères. Néanmoins, la quantité d'eau libre y est moins importante, ce qui pourrait être un atout pour l'efficacité du piègeur à hydrogène et ainsi assurer le confinement du tritium.

3. Stratégie expérimentale

Ce manuscrit de thèse est divisé en cinq chapitres indépendants :

- **Le chapitre I** est une revue de la littérature concernant l'incorporation de liquides organiques (LO) dans des MAA, plus particulièrement dans des géopolymères. La première partie présente de façon générale les différentes voies d'incorporation des LO dans des matériaux cimentaires à l'état frais. La deuxième partie présente les avantages des géopolymères par rapport aux ciments Portland pour l'incorporation de LO. En particulier, les trois principales applications découlant de la bonne compatibilité entre géopolymères et LO sont discutées.

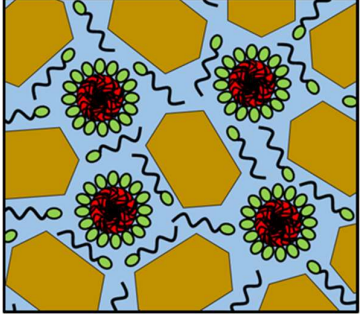
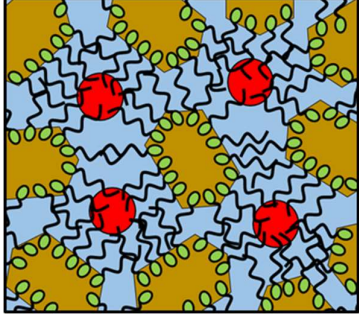
- **Le chapitre II** se concentre sur l'émulsification d'une huile minérale dans des MAA à l'état frais. A cet effet, six tensioactifs de nature chimiques différentes (cationique, anionique, non-ionique) sont évalués. Toutes les caractérisations sont réalisées à l'état frais, c'est-à-dire avant la prise des matériaux avec pour but de formuler l'émulsion la plus stable (gouttelettes de tailles fines et homogènes).
- **Le chapitre III** a pour but de déterminer la matrice la plus adéquate pour l'immobilisation d'huile minérale : géopolymère ou laitier activé. L'originalité de ce chapitre réside dans la comparaison de ces deux types de MAA pour l'immobilisation d'une huile minérale, dans les mêmes conditions, ce qui n'a pas été réalisé précédemment. De plus, ce chapitre vise à comprendre comment les MAA sont impactés par la présence d'huile minérale, à savoir si l'impact est uniquement physique et dû à une augmentation de la porosité (présence d'huile) ou bien également chimique (impact sur la réactivité des MAA).
- **Le chapitre IV** détermine l'efficacité du piègeur à hydrogène/tritium choisi à base de MnO_2/Ag_2O dans les deux types de MAA. Cela est nécessaire puisque l'efficacité du piègeur peut être affectée par l'environnement porale des matériaux cimentaires (quantité d'eau libre, sorption d'ions, réaction redox, ...).
- **Le chapitre V** propose une méthode visant à assurer le confinement à long-terme des LO dans des matrices géopolymères, de manière à consolider leur acceptation au stockage. Cette méthode est basée sur la détermination de l'énergie de surface des géopolymères par mesures d'angles de contact et en utilisant le modèle d'Owens-Wendt. La connaissance de cette énergie de surface permet ensuite de théoriquement quantifier l'affinité des LO pour la matrice géopolymère.

4. Principaux résultats expérimentaux

4.1. Etude de l'émulsion de l'huile minérale à l'état frais

Une huile minérale a été incorporée avec succès à raison de 20%vol. dans des MAA à l'état frais à base de métakaolin (MK) ou de laitier de hauts fourneaux (LHF), formant ainsi des matériaux composites (immobilisation de l'huile). Dans les deux types de MAA, de grosses gouttelettes d'huile sont observables sans ajout de tensioactif et l'incorporation d'huile est considérée insuffisante. Plusieurs tensioactifs (CTAB, SDS, GlucoPON 225DK, Span 80, Tween 80, Brij O10) ont permis d'améliorer l'émulsion d'huile (gouttelettes d'huile plus petites et homogènes) mais avec des efficacités variables. En particulier, des études rhéologiques, des mesures de tensions interfaciales et l'analyse de suspensions ternaires diluées montrent que les tensioactifs agissent selon deux mécanismes distincts pour émulsifier l'huile dans les MAA (Tableau 1).

Tableau 1: Représentation schématique des deux mécanismes d'actions des tensioactifs proposés. Le fond bleu clair représente la solution d'activation alcaline, les cercles rouges représentent les gouttelettes d'huiles et les hexagones bruns représentent les particules solides (MK ou laitier). Les cercles verts et les lignes noires correspondent respectivement aux « têtes » hydrophiles et aux « queues » lipophiles des tensioactifs.

	Mécanisme 1	Mécanisme 2
Viscosité	Constante	Augmente
Tension interfaciale	Décroit significativement	Décroit peu
Interactions huile-particules	Faible	Forte
Représentation schématique		
Géopolymère	Glucopon SDS	Span 80 CTAB Tween 80 Brij O10
Laitier activé	Glucopon SDS CTAB Tween 80 Brij O10	Span 80

Le mécanisme classique (Mécanisme 1 ou M1) réduit la tension interfaciale pour stabiliser l'émulsion d'huile ; c'est le principal mécanisme observé dans la matrice laitier activé. Le mécanisme singulier (Mécanisme 2 ou M2) favorise l'interaction des particules solides avec l'huile pour stabiliser l'émulsion d'huile ; c'est le principal mécanisme observé dans la matrice géopolymère. Il semblerait que le mécanisme dépende de la solubilité des tensioactifs dans les solutions d'activations. Étonnamment, même si les MAA à l'état frais peuvent être conceptualisés comme étant similaires (suspensions alcalines concentrées de particules solides), le comportement des tensioactifs peut être opposé dans les deux types de MAA et devra être au centre de l'attention lors du développement futur de MAA immobilisant des huiles. D'un point de vue applicatif, M1 est à privilégier si l'ouvrabilité des MAA frais est recherchée, tandis que M2 est à viser afin d'avoir une meilleure stabilisation de l'huile dans

les composites durcis. Enfin, en accord avec les mesures de tailles de gouttelettes, l'incorporation d'huile minérale présente des performances plus élevées dans la matrice géopolymère que dans la matrice laitier activé.

4.2. Etude des matériaux composites

Une huile minérale pure (ci-après huile) a été immobilisée avec succès dans des matrices géopolymère (GEO) et laitier activé (LA) jusqu'à un taux d'incorporation de 40%vol. Les principales conclusions et orientations de l'étude sont les suivantes :

- En plus d'être observé à l'état frais avec l'amélioration de l'émulsion d'huile, l'avantage d'utiliser des tensioactifs pour l'immobilisation d'huile dans des MAA peut également être observé dans les composites durcis. Dans le cas de la fracturation des matériaux composites, l'huile reste confinée en présence de tensioactifs du fait de la petite taille des gouttelettes, alors qu'un écoulement important d'huile est observé en l'absence de tensioactifs du fait de la présence de grosses gouttelettes.
- L'ajout de tensioactifs, dans le but d'améliorer l'incorporation de l'huile, a pour effet secondaire d'augmenter la porosité des MAA. Dans les deux types de MAA, le Glucopon 225DK est le tensioactif incorporant et stabilisant la plus grande quantité de bulles d'air, ce qui est préjudiciable aux propriétés mécaniques à court-terme et à la durabilité à long-terme des matériaux obtenus.
- Les composites « MAA-Huile » immobilisant 20%vol. d'huile possèdent tous une résistance à la compression importante, de 25 MPa en moyenne pour les composites à base de GEO et de 20 MPa en moyenne pour les composites à base de laitier, soit bien plus que les 8 MPa exigés par l'ANDRA. Les composites GEO-huile incorporant 40%vol. d'huile ont une résistance à la compression moyenne de 15 MPa, tandis que les composites LA-Huile incorporant 40%vol. d'huile n'ont pas de résistances à la compression mesurables, même ceux contenant des tensioactifs.
- Cette étude montre qu'il n'y a pas d'influence de l'huile minérale ou des tensioactifs sur le temps de prise et le développement des propriétés mécaniques des MAA. Les principaux produits réactionnels des MAA (C-A-S-H dans les laitiers et N-A-S-H dans les géopolymères) ne sont pas non plus impactés par l'ajout d'huile minérale ou de tensioactifs. L'impact sur les propriétés mécaniques peut donc être essentiellement attribué à des raisons physiques, à savoir l'augmentation de la porosité (incorporation d'huile et/ou d'air).

Ce chapitre a permis de démontrer que les matrices géopolymère et laitier activé conviennent à l'immobilisation de 20%vol. d'huile minérale à condition d'ajouter un tensioactif, préférentiellement le CTAB dans le laitier activé ou le BrijO10 dans le géopolymère. Le choix et la concentration des tensioactifs doivent être déterminés avec soin, non seulement dans le

but de stabiliser l'émulsion d'huile mais aussi d'éviter les effets secondaires, comme une augmentation excessive de la porosité. Enfin, comme ce fut le cas à l'état frais, les observations à l'état durci confirment que le géopolymère présente des performances plus élevées pour l'immobilisation d'huile minérale que le laitier activé.

4.3. Efficacité du piègeur « γ -MnO₂/Ag₂O » dans les MAA

Le piègeur à hydrogène/tritium choisi dans cette étude est un mélange à base de γ -MnO₂ et d'Ag₂O. L'efficacité de ce piègeur a été évaluée dans les MAA par production d'hydrogène *in-situ*, de deux manières distinctes:

- Irradiations gamma (500 kGy): Les matrices géopolymères contenant le piègeur ont démontré une efficacité de piégeage d'H₂ de presque 100% en l'absence d'huile et d'environ 90% en présence d'huile. Au contraire, les matériaux à base de laitier activé contenant le piègeur ne présentent qu'une efficacité de piégeage d'H₂ de 50% en l'absence d'huile et d'environ 20% en présence d'huile.
- Corrosion du magnésium: Le piégeage d'H₂ dans la matrice laitier activé est limité à 0,7 mmol.g⁻¹ de piègeur, alors qu'il est d'ores et déjà plus élevé dans la matrice GEO et persiste après 500 jours d'analyse.

Les deux types d'expériences ci-dessus s'accordent donc sur les meilleures performances du piègeur γ -MnO₂/Ag₂O dans une matrice type géopolymère que dans une matrice type laitier activé.

Pour comprendre ce dernier résultat, des expériences ont mis en évidence que la structure du piègeur γ -MnO₂/Ag₂O est modifiée au contact d'espèces réductrices à base de soufre, conduisant à la formation d'une poudre de piègeur inefficace. Cela explique pourquoi le piègeur est moins efficace dans les laitiers activés car ces derniers contiennent naturellement des espèces soufrées.

En complément, la mise en contact du piègeur γ -MnO₂/Ag₂O avec des solutions interstitielles directement extraites de MAA durcis, a mis en évidence la forte tendance du piègeur à adsorber des ions à sa surface (Ca²⁺, Mg²⁺, Na⁺, silicates, aluminates ...). La sorption de ces ions semble gêner l'accès des atomes d'hydrogène aux sites réactifs du piègeur, réduisant d'environ 50% la capacité de piégeage d'H₂ dans les deux types de MAA. La capacité de piégeage théorique n'est donc plus valable en environnement cimentaire.

4.4. Confinement de l'huile à long terme

Ce dernier chapitre a permis de déterminer expérimentalement l'énergie libre de surface d'un géopolymère en utilisant le modèle d'Owens-Wendt basé sur la mesure d'angles de contact. Les enveloppes de mouillage correspondantes permettent de prédire théoriquement l'angle de contact de tout liquide à la surface du GEO. La connaissance de l'énergie de surface du GEO permet également de quantifier des paramètres d'interactions solide/liquide. Par exemple, le coefficient d'étalement « S » démontre le mouillage préférentiel du GEO par des LOs

typiquement utilisés dans l'industrie du nucléaire, plutôt que par l'eau. Cela est un résultat positif pour assurer le confinement à long-terme des LOs dans des matrices GEO. Puisque les LOs ont une excellente affinité pour le GEO, une infiltration d'eau à long-terme n'est pas susceptible de les déloger des GEO. Dans le cadre de la gestion des déchets nucléaires, ces premiers résultats apparaissent comme une contribution positive à l'acceptation des GEO immobilisant des huiles dans les sites de stockages industriels.

5. Conclusions et perspectives

Que ce soit concernant l'incorporation de l'huile minérale, ou bien l'efficacité du piègeur à hydrogène, ce travail de thèse a mis en évidence que la matrice géopolymère est plus adaptée que la matrice laitier activé vis-à-vis de l'immobilisation d'huile tritiées. Les principales questions restantes concernent le comportement à long terme de ces matériaux composites, avec notamment la question du relargage d'huile. A cet effet, la thématique initiée dans le dernier chapitre devra être approfondie.

Synthesis and characterization of composites based on alkali-activated materials incorporating mineral oils for the management of tritiated oils

This work deals with the conditioning of tritiated industrial oils in the context of nuclear wastes that are still deprived of an appropriate treatment solution. The strategy consists in directly conditioning model mineral oils in alkali-activated materials (AAM), additionally functionalized with a $\gamma\text{-MnO}_2/\text{Ag}_2\text{O}$ hydrogen/tritium getter. Geopolymer (GEO) and alkali-activated blast furnace slag (AABFS) are considered as AAM. In the presence of surfactants, the oil was successfully emulsified (small and homogeneous droplets) in both types of AAM. Two surfactant mechanisms are distinguished acting by: 1) decreasing the interfacial tension or 2) promoting oil-particles interactions. Mechanism 1 should be favored if workability of fresh mixtures is required, while mechanism 2 should be targeted to provide a better confinement of oil owing to strong oil-particles interactions. After curing, AAM-OIL composites are obtained. There is no influence of the oil and surfactants on the setting time and strength development of AAM. The main reaction products (C-A-S-H in AABFS and N-A-S-H in GEO) are not impacted. However, the addition of surfactants leads to increased porosity of AAM due to air bubbles stabilization. AAM-OIL composites immobilizing 20%vol. of oil all have compressive strengths higher than 20 MPa, which is a more than the 8 MPa required from ANDRA. Overall, according to both fresh and hardened states observations, GEO exhibit higher performances for the immobilization of oil than AABFS. The efficiency of the $\gamma\text{-MnO}_2/\text{Ag}_2\text{O}$ getter was assessed in AAM via *in-situ* hydrogen production by gamma irradiations or magnesium corrosion. Both types of experiments agree to the higher performances of the getter in GEO than in AABFS. This is explained by reducing sulfur species present in AABFS, which react with the oxidizing getter components. Finally, wetting measurements demonstrated that industrial oils have an excellent affinity for GEO, testifying that long-term water seepage is not likely to dislodge them from GEO-OIL composites. In the context of nuclear waste management, GEO functionalized with $\gamma\text{-MnO}_2/\text{Ag}_2\text{O}$ getter appears as a promising option for disposal of tritiated oils. However, additional investigations of HTO confinement need to be performed that could renew the interest of using AABFS.

Keywords: Alkali-activated materials (AAM), blast furnace slag (BFS), geopolymer (GEO), nuclear waste, oil, emulsion, surfactant, composite, tritium/hydrogen, $\gamma\text{-MnO}_2/\text{Ag}_2\text{O}$ getter.

Synthèse et caractérisation de composites à base de matériaux alcali-activés incorporant des huiles minérales pour la gestion des huiles tritiées

Ce travail a pour but le conditionnement des huiles tritiées et s'inscrit dans la problématique des déchets nucléaires sans filière de gestion. La stratégie consiste à directement conditionner des huiles minérales modèles dans des matrices alcali-activés (MAA), également fonctionnalisées avec un piègeur à hydrogène/tritium $\gamma\text{-MnO}_2/\text{Ag}_2\text{O}$. Géopolymères (GEO) et laitiers de hauts fourneaux (LHF) sont considérés comme MAA. En présence de tensioactifs, l'huile est émulsionnée avec succès (gouttelettes fines et homogènes) dans les deux types de MAA. Deux modes d'actions des tensioactifs sont observés agissant par: 1) réduction de la tension interfaciale ou 2) promotion d'interactions huile-particules. Le mécanisme 1 doit être favorisé si l'ouvrabilité des coulis est requise alors que le mécanisme 2 doit être ciblé afin de permettre un meilleur confinement de l'huile grâce aux interactions huile-particules. Après durcissement, des composites MAA-Huile sont obtenus. Il n'y a pas d'influence de l'huile et des tensioactifs sur la prise et le développement des propriétés mécaniques des MAA. Les principaux produits de réaction (C-A-S-H pour LHF et N-A-S-H pour GEO) ne sont pas impactés. Néanmoins, l'addition de tensioactifs entraîne une porosité plus importante à cause de la stabilisation de bulles d'air. Les composites MAA-Huile contenant 20%vol. d'huile ont tous des résistances en compression supérieures à 20 MPa, ce qui est plus que les 8 MPa requis par l'ANDRA. Globalement, en accord avec les observations aux états frais et durci, les GEO possèdent de meilleures performances pour l'immobilisation d'huile que les LHF. L'efficacité du piègeur $\gamma\text{-MnO}_2/\text{Ag}_2\text{O}$ a été caractérisée dans les MAA par production d'hydrogène *in-situ* par irradiations gamma et corrosion du magnésium. Les deux types d'expérience s'accordent sur la meilleure performance de piégeage dans le GEO que dans le LHF. Cela s'explique par la présence d'espèces soufrés réductrices dans le LHF qui réagissent avec les oxydants constituant le piègeur. Finalement, des mesures de mouillabilité ont démontré que les huiles industrielles ont une excellente affinité pour le GEO, démontrant qu'une exposition longue durée à de l'infiltration d'eau ne délogera pas l'huile des composites MAA-Huile. Dans le contexte du traitement des déchets nucléaires, les GEO fonctionnalisés avec un piègeur $\gamma\text{-MnO}_2/\text{Ag}_2\text{O}$ semblent être une option intéressante pour le stockage des huiles tritiées. Néanmoins, des études complémentaires doivent être menées au sujet du confinement de l'HTO, ce qui pourrait faire renaitre l'intérêt d'utiliser le LHF.

Mots-clés: Matériaux alcali-activés (MAA), laitier de hauts fourneaux (LHF), géopolymère (GEO), déchet nucléaire, émulsion, tensioactif, composite, piègeur à hydrogène/tritium $\gamma\text{-MnO}_2/\text{Ag}_2\text{O}$.